Determining Pavement Design Criteria for Recycled Aggregate Base and Large Stone Subbase

NRRA GEOTECHNICAL TEAM

Authors: Bora Cetin (Michigan State University), Haluk Sinan Coban (Michigan State University), Tuncer B. Edil (University of Wisconsin-Madison), Halil Ceylan (Iowa State University), William Likos (University of Wisconsin-Madison), Junxing Zheng (Iowa State University), Ashley Buss (Iowa State University)

A pooled fund project administered by the Minnesota Department of Transportation

Report No. NRRA202103

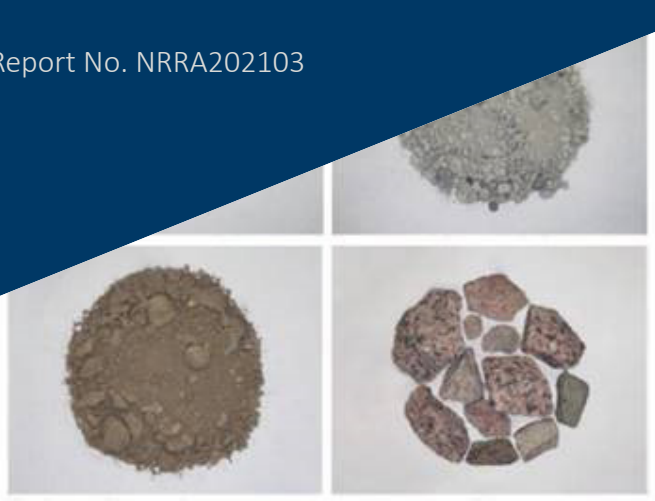

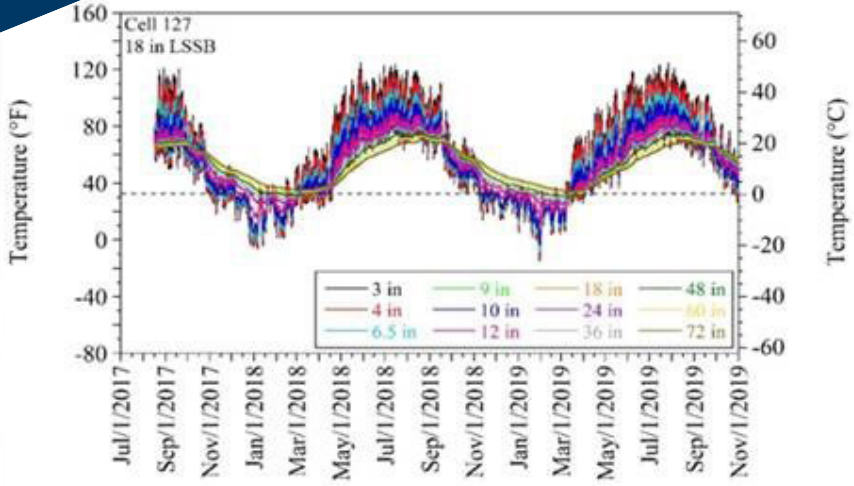

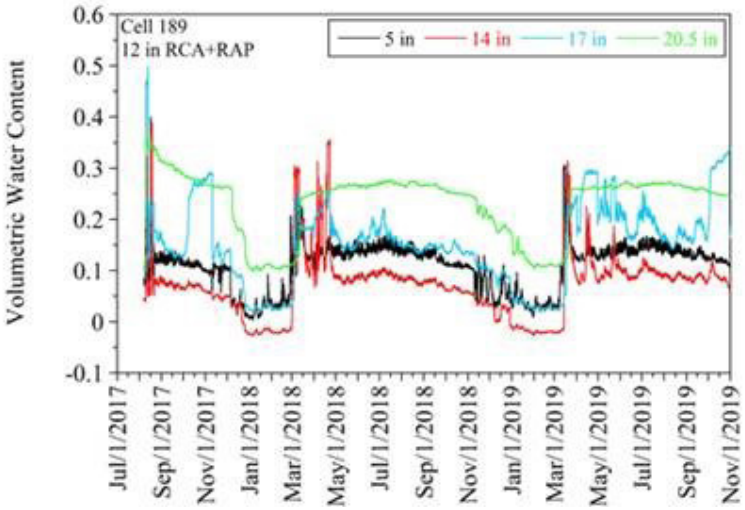

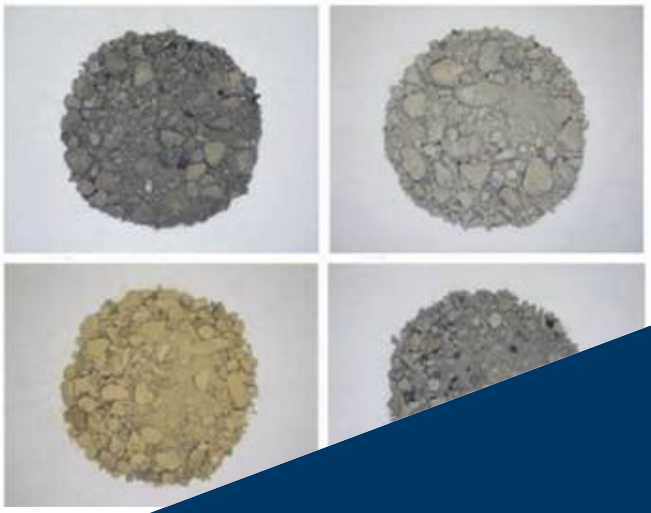

To request this document in an alternative format, such as braille or large print, call 651-366-4718 or 1-800-657-3774 (Greater Minnesota) or email your request to ADArequest.dot@state.mn.us. Please request at least one week in advance.

Technical Report Documentation Page

1. Report No.	2.	3. Recipients Accession No.	
NRRA202103			
4. Title and Subtitle Determining Pavement Design Criteria for Recycled Aggregate Base and Large Stone Subbase		5. Report Date June 2021 6.	
7. Author(s) Bora Cetin, Haluk Sinan Coban, Tuncer B. Edil, Halil Ceylan, William Likos, Junxing Zheng, Ashley Buss		8. Performing Organization Report No.	
9. Performing Organization Name and Address Civil, Construction and Environmental Engineering Iowa State University 813 Bissell Road Ames, IA 50011		10. Project/Task/Work Unit No. 11. Contract (C) or Grant (G) No. (c) 1003320 (wo) 2	
12. Sponsoring Organization Name and Address National Road Research Alliance Minnesota Department of Transportation Office of Research & Innovation 395 John Ireland Boulevard, MS 330 St. Paul, Minnesota 55155-1899		13. Type of Report and Period Covered Final Report 14. Sponsoring Agency Code	
15. Supplementary Notes https://www.mndot.gov/research/reports/2021/NRRA202103.pdf https://www.mndot.gov/research/reports/2021/NRRA202103A.pdf			
16. Abstract (Limit: 250 words) This project was performed to evaluate the performance of recycled aggregates and large stones used in the aggregate base/subbase layers of pavement systems and provide recommendations regarding pavement design and material selection. As part of this project, eleven test cells were built at MnROAD to evaluate the impact of recycled aggregates and large stones on the long-term pavement performance via a series of laboratory [permeability, soil-water characteristic curve (SWCC), stereophotography (image analysis), gyratory compaction, and resilient modulus (M_R) tests] and field tests [intelligent compaction (IC), falling weight deflectometer tests (FWD), rutting measurements, international roughness index (IRI) measurements, light weight deflectometer (LWD) tests, and dynamic cone penetrometer (DCP) tests]. In addition, a pavement mechanistic-empirical (ME) design approach was used to provide recommendations for designs of pavement systems containing recycled aggregate base (RAB) and large stone subbase (LSSB) layers. Overall, this project found that finer recycled concrete aggregate (RCA) material would be preferable to coarser RCA material and a blend of RCA and recycled asphalt pavement (RAP) materials would be preferable to natural aggregate for aggregate base layers. RCA materials provided better performance than the blend of RCA and RAP materials, indicating that RCA materials would be preferable to the blend. For LSSB layers, this project found that geosynthetics would be required to successfully construct thinner LSSB layers. Overall, thicker LSSB layers provided better structural support than thinner LSSB layers both in the short term and the long term.			
17. Document Analysis/Descriptors Recycled materials, Subbase materials, Subbase (Pavements), geosynthetics, pavement performance, modulus, image analysis, permeability, mechanistic-empirical pavement design, Falling weight deflectometers, Compaction		18. Availability Statement No restrictions. Document available from: National Technical Information Services, Alexandria, Virginia 22312	
19. Security Class (this report) Unclassified	20. Security Class (this page) Unclassified	21. No. of Pages 377	22. Price

DETERMINING PAVEMENT DESIGN CRITERIA FOR RECYCLED AGGREGATE BASE AND LARGE STONE SUBBASE

FINAL REPORT

Prepared by:

Bora Cetin, *Department of Civil and Environmental Engineering, Michigan State University*
Haluk Sinan Coban, *Department of Civil and Environmental Engineering, Michigan State University*
Tuncer B. Edil, *Department of Civil and Environmental Engineering, University of Wisconsin-Madison*
Halil Ceylan, *Department of Civil, Construction and Environmental Engineering, Iowa State University*
William Likos, *Department of Civil and Environmental Engineering, University of Wisconsin-Madison*
Junxing Zheng, *Department of Civil, Construction and Environmental Engineering, Iowa State University*
Ashley Buss, *Department of Civil, Construction and Environmental Engineering, Iowa State University*

Published by:

Minnesota Department of Transportation
Office of Research & Innovation
395 John Ireland Boulevard, MS 330
St. Paul, Minnesota 55155-1899

June 2021

ACKNOWLEDGMENTS

The authors would like to thank the National Road Research Alliance (NRRA) for sponsoring this project. They also would like to thank Raul Velasquez, Terry Beaudry, Tim Andersen, John Siekmeier, and Dave Van Deusen, at the Minnesota Department of Transportation (MnDOT), for providing the field data collected from MnROAD and for their help throughout this project. The authors would also like to thank MnROAD operations staff, including Benjamin Worel, Michael Vrtis, Len Palek, and Steven Henrichs, for providing field data and access and assistance to the database. The authors would also like to acknowledge the members of the project's technical advisory panel (TAP) for their invaluable feedback during the research project: James Bittmann, MnDOT; Richard Endres, Michigan DOT; Thomas Fennessey, Missouri DOT; Ed Johnson, MnDOT; Jeff Horsfall, Wisconsin DOT; Deepak Maskey, Caltrans; and Heather Shoup, Illinois DOT. Thanks also to Dr. Askin Ozocak and the University of Wisconsin-Madison for performing permeability and soil-water characteristics curve (SWCC) tests. The authors would also like to thank Dr. Soheil Nazarian and the Center for Transportation Infrastructure Systems at the University of Texas at El Paso (UTEP) for performing the laboratory resilient modulus (M_R) tests. Finally, thanks to Dr. David White and Ingios Geotechnics for performing intelligent compaction (IC).

TABLE OF CONTENTS

LIST OF FIGURES

LIST OF TABLES

EXECUTIVE SUMMARY

The majority of virgin aggregates (VAs) produced in the U.S. has been used for roadway constructions and maintenance. The price of VA has increased significantly due to huge demand, the loss of natural sources, and federal/local restrictions regarding aggregate production over the last two decades. Changes in availability and a reduction in the cost-effectiveness of VA have directed the attention of researchers and contractors to using alternative aggregates, which result in similar or better performance than VA. The alternative materials studied in this project include recycled aggregates and unconventionally large aggregates (i.e., large stones). Using these alternative aggregates can also aid the environment by reducing the consumption of natural resources, improving waste utilization and decreasing greenhouse gas emissions and energy consumption. While recycled materials have been used in roadway base layers for many years, specific field performance comparisons and prediction of the characteristics of these materials from simple index properties has not existed. There is also a lack of information about the use of large stone subbase (LSSB) materials as subbase layers in pavement systems.

This project evaluates the performance of these alternative materials, including recycled aggregates and unconventionally large aggregates (i.e., large stones), that can be used in the aggregate base/subbase layers of pavement systems and provides practical recommendations with respect to material selection and pavement layer design. This final report presents the findings and details the pavement design criteria for recycled aggregate base (RAB) and LSSB.

Several different types of recycled aggregates, a VA, and a large stone were used during the course of this project. The recycled aggregates included three different recycled concrete aggregate (RCA) materials (i.e., Coarse RCA, Fine RCA, and Class 5Q Aggregate) and two blends of RCA and recycled asphalt pavement (RAP) materials (i.e., RCA+RAP and Class 6 Aggregate). A crushed limestone aggregate (i.e., Limestone) was used as a VA. A crushed granite stone (i.e., LSSB Material) was used as a large stone. Around 0.4 miles (0.64 km) of the Minnesota Road Research Project (MnROAD) low-volume road (LVR) was dedicated to eleven test cells constructed with RAB and LSSB layers. Four of the cells were constructed with 12-in thick RAB layers, two were constructed with 18-in LSSB layers, and five with 9-in LSSB layers (with or without geosynthetics). All of the cells except for two (Cells 185 and 186) were constructed on clay subgrade soils, and the same paving material was applied after the completion of the aggregate base layers. For the cells containing 18-in and 9-in LSSB layers, a very non-traditional subgrade preparation procedure was followed to create weak clay subgrade layers with a dynamic cone penetration (DCP) index (DCPI) value between 2.5 and 3.5 in/blow (65 and 90 mm/blow) (ASTM D6951) for the upper 1 ft (0.3 m) of the subgrade soil. The reason behind weakening the clay subgrade layers before the placement of LSSB layers was to simulate undesired very weak subgrade conditions to effectively observe the performance of LSSB layers used as working platforms and structural elements in pavement systems.

This report consists of six main chapters: (1) literature review, (2) construction monitoring and preliminary performance evaluation of the test cells, (3) laboratory testing, (4) long-term performance evaluation of the test cells, (5) estimation of laboratory and field characteristics, and (6) pavement performance predictions.

The literature review chapter is an in-depth review of the use of recycled aggregates and large stones in pavement systems. Detailed information about the overall findings regarding the index, engineering, and environmental properties of such alternative materials is provided. In the previous studies, using these alternative materials to replace conventional VA was determined to be effective to obtain well-performing and long-lasting pavement systems. Information with respect to various geosynthetics applications, functions of geosynthetics, and the effects of using geosynthetics in pavements is also presented. AASHTO 1993 and mechanistic-empirical (ME) pavement design methods are provided along with the techniques that can be used to implement alternative materials in pavement design. Lastly, selected practices of state departments of transportation (DOTs) with respect to using alternative materials in pavement systems are summarized.

In the construction monitoring and preliminary performance evaluation chapter, detailed information regarding the cross-sections and the construction of the test cells was provided. It was observed during construction monitoring that the construction of the LSSB layers was problematic in general. However, solutions were found in a short span of time and required modifications (use of geosynthetics between the LSSB and subgrade layers) were made to the design of the cells containing LSSB layers. Using geosynthetics between LSSB and subgrade layers mitigated rutting and subgrade soil pumping issues during construction of the test cells. An evaluation of the data collected from nuclear density, DCP, light weight deflectometer (LWD), gas permeameter tests, intelligent compaction (IC), and falling weight deflectometer (FWD) tests was presented. Field test results observed during and shortly after construction showed that the cells constructed with Coarse RCA and Fine RCA base layers performed better than the other cells. The cells constructed with thicker LSSB layers showed relatively higher modulus values and lower deflections than the cells constructed with thinner LSSB layers. In fact, the worst field performance was observed with the cells constructed with thinner LSSB layers. It was concluded that the tests performed on the test cells (LWD, FWD, and IC) were not suitable to evaluate the structural benefits of the geosynthetics placed between thinner LSSB and subgrade layers. It is thought that the loads applied by LWD, FWD, or IC testing were not sufficient to cause adequate stress on LSSB and subgrade layers to observe the structural benefits of the geosynthetics.

In the laboratory testing chapter, the index and engineering properties of the materials, used in the cells, were presented. Laboratory tests included fundamental geotechnical engineering laboratory tests [i.e., sieve analyses, hydrometer tests, specific gravity (G_s) and absorption tests, and Proctor compaction tests] as well as other laboratory tests. These tests were asphalt binder and residual mortar content determination, water repellency/contact angle, permeability, soil-water characteristic curve (SWCC), stereophotography (i.e., image analysis), and gyratory compaction tests. Permeability and SWCC tests were performed to determine the saturated and unsaturated properties of the materials. Stereophotography and gyratory compaction tests were used to evaluate the abrasion characteristics of the materials. Laboratory test results showed that specifications and guidelines with respect to material

selection and pavement design should be updated based on gradation, absorption, residual mortar content, and abrasion. For example, while the recycled aggregates used in this study were found to be preferable to the VA to construct stiff aggregate base layers, laboratory test results showed that the recycled aggregates showed considerably higher degradation than the VA. Therefore, not only the stiffness but also the degradation characteristics of recycled aggregates should be considered to obtain well-performing and long-lasting pavement systems.

In the long-term performance evaluation of test cells chapter, detailed information with respect to data, collected by environmental monitoring systems (e.g., weather information, soil temperature and moisture monitoring), FWD tests, frost heave and thaw settlement measurements, rutting measurements, international roughness index (IRI) measurements, and pavement distress evaluations, was provided. Annual frost penetration depths and the freezing and thawing periods were determined using the environmental monitoring data to support the seasonal FWD test results. Overall, the RAB layers constructed with Coarse RCA, Fine RCA, and RCA+RAP performed superior to those built with Limestone [Coarse RCA contained 61.7% gravel, 34.9% sand, and 3.4% fines (silt and clay). Fine RCA contained 38.3% gravel, 54.6% sand, and 7.1% fines]. Results also showed that Fine RCA performed the best, followed by Coarse RCA and RCA+RAP, while Limestone performed the lowest within the test cells that were not built with LSSB. Per these results, it was concluded that Fine RCA would be preferable to Coarse RCA and RCA+RAP to achieve well-performing and long-lasting aggregate base layers. In addition, it could be said that Coarse RCA would be more preferable to RCA+RAP for the same purpose. The thickness of the LSSB layers should be sufficient enough to provide good drainage and structural support, and the results of this study showed that thicker LSSB layers performed better than thinner LSSB layers.

In the next chapter, an effort was made to develop simple and easily interpretable models to estimate laboratory and field characteristics of the materials. A forward stepwise regression method was used for the development of these models. With respect to the estimation of laboratory test results, regression models were developed to estimate the Proctor compaction, saturated hydraulic conductivity (K_{sat}), SWCC, resilient modulus (M_R), and degradation characteristics of the materials. With respect to the estimation of field test results, regression models were developed to estimate DCPI, California bearing ratio (CBR), LWD elastic modulus (E_{LWD}), FWD elastic modulus (E_{FWD}), and IC M_R properties of the base layers constructed using recycled aggregates and Limestone.

In the pavement performance predictions chapter, the AASHTOWare Pavement ME Design program was used to evaluate the long-term performance prediction models of different pavement systems containing different RAB and LSSB layers with respect to IRI, rutting, alligator cracking, and longitudinal cracking. Various aggregate base/subbase layer thicknesses and traffic levels were used in the analyses. The effects of the layer thickness, base layer aggregate type, and traffic level on the performance prediction models were evaluated. The optimal thicknesses of the Coarse RCA, Fine RCA, and RCA+RAP base layers that had an equivalent (or similar) structural capacity as the 12-in Limestone base layer were determined for different subgrade conditions. It was concluded that thinner RAB layers (4, 6, 8, or 10 in) could be constructed with Coarse RCA, Fine RCA, or RCA+RAP materials rather than constructing a 12-in Limestone base layer depending on the pavement distress of interest to an agency.

CHAPTER 1: GENERAL INTRODUCTION

1.1 PAVEMENT SYSTEMS AND AGGREGATE BASE/SUBBASE LAYER APPLICATIONS

1.1.1 Pavement Systems

The total public road length in the US is approximately 6.6 million km (4.1 million miles), and the total lane length is reported as 14 million km (8.7 million miles) (FHWA 2016). Roads are classified into two main categories: paved and unpaved. In 6.6 million km (4.1 million miles) total public road length, the total length of the paved roads is around 4.3 million km (2.7 million miles) (about 66% of all roads), whereas the total length of the unpaved roads is around 2.3 million km (1.4 million miles) (about 34% of all roads) (BTS 2017). Unpaved roads do not have any asphalt or concrete top layers. Paved roads are also classified into two sub-categories: flexible and rigid pavements. More than 90% of the paved roads are flexible pavements with an asphalt surface (Copeland 2011). While most of the loads from vehicles are carried by a concrete layer in rigid pavements, they are mostly distributed to sublayers in flexible pavements (Figure 1.1).

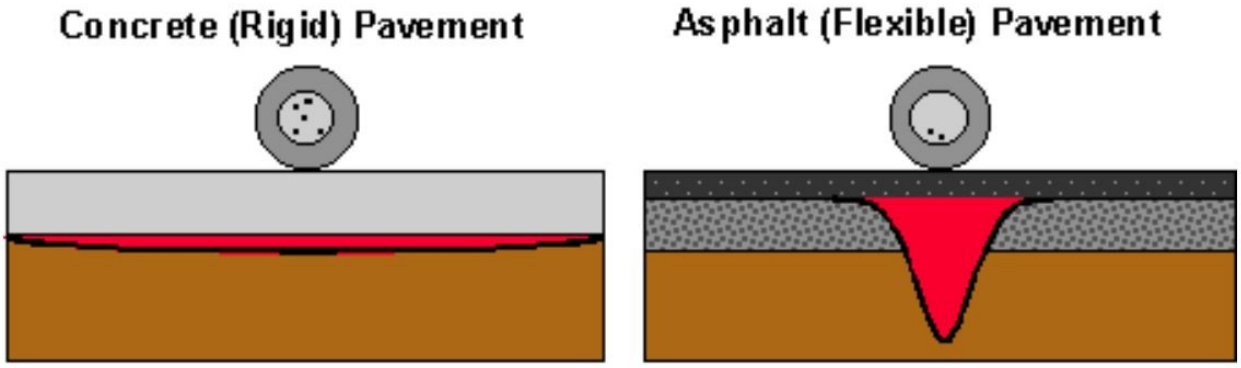

Figure 1.1. Load distribution mechanisms of rigid and flexible pavements [http://overlays.acpa.org/Concrete_Pavement/Technical/Fundamentals/Differences_Between_Concrete_and_Asphalt.asp (date accessed: January 23, 2021)].

Since the main working principle of flexible pavements is to distribute traffic loads from asphalt layers to pavement sublayers (aggregate base, subbase, and subgrade layers) (Mohod and Kadam 2016), the performance of such sublayers is very important for long-term pavement performance (Little and Nair 2009). Several cracking types (fatigue, block, transverse, and longitudinal), potholes, and permanent deformation are the main failure mechanisms commonly seen in flexible pavements (Figure 1.2). They are mainly caused by the horizontal tensile strain beneath the asphalt surface and vertical compressive strain on the subgrade layer (Selvi 2015).

Figure 1.2. (a) Fatigue cracking [https://texasmaterialsgroup.com/alligator-cracking-asphalt-repair/ (date accessed: January 23, 2021)], (b) pothole [https://theconversation.com/potholes-how-engineers-are-working-to-fill-in-the-gaps-102055 (date accessed: January 23, 2021)], and (c) permanent deformation [http://www.pavementinteractive.org/wp-content/uploads/2008/05/Mvc-037s.jpg (date accessed: January 23, 2021]

Aggregate base layer (Figure 1.3) is the primary load-carrying sublayer in flexible pavements (Cosentino and Kalajian 2001; Yohannes et al. 2009). Fatigue cracking and rutting, which are the main failure mechanisms of flexible pavements (Saeed et al. 2001), are primarily caused by quality or performance issues related to the aggregate base layer (improper compaction, poor aggregate quality, high fines content, etc.) (Saeed et al. 2001; Tamrakar and Nazarian 2016). Therefore, an aggregate base layer must exhibit adequate stiffness to resist cyclic stresses and to reduce vertical compressive strain (Schuettpelz et al. 2010; Bozyurt et al. 2012; Cooley and Hornsby 2012; Haider et al. 2014; Cetin et al. 2014; Edil and Cetin 2015; Zornberg 2017; Esfahani and Goli 2018). The high stiffness of an aggregate base layer improves the stability of the sublayers by improving the vertical load distribution (Zornberg 2017). Good-quality (i.e., stiff and durable) VAs are generally preferred to construct stiff aggregate base layers. An adequately stiff aggregate base layer reduces pavement deformations and increases the lifespan of the pavement (Edil et al. 2012).

Subbase layer (Figure 1.3) is the secondary load-carrying sublayer in flexible pavements (Schuettpelz et al. 2010) and is usually constructed with granular materials (Perkins et al. 2005). In fact, it is an optional layer and can be used to minimize potential instability of fine-grained subgrade soils due to frost-heave and thaw-weakening, minimize capillary water retention, and provide adequate filtering and drainage (Uhlmeyer et al. 2003; Zornberg 2012). The subbase layer can also provide a working platform over a weak or soft subgrade layer (Tanyu et al. 2004; Kazmee et al. 2016).

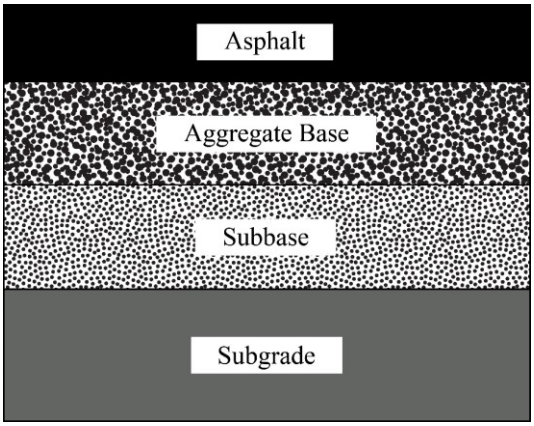

Figure 1.3. General structure of flexible pavements

1.1.2 Recycled Aggregates in Aggregate Base Layer Applications

About 1.33 billion tons of VAs were produced in the US in 2017, and about 76% of the aggregates were used for pavement construction and maintenance (USGS 2018). However, in the last decades, the increased demand for good-quality VAs has caused a depletion of their sources (ACPA 2009). The price of good-quality VAs has increased due to increasing demand, loss of natural resources, and federal/local restrictions regarding their production (ACPA 2009; Cooley and Hornsby 2012). The reduced availability and cost-effectiveness of VAs has directed the attention of researchers and contractors to alternative materials (Gonzalez and Moo-Young 2004; Westover et al. 2007; Edil et al. 2012). Use of recycled aggregates to construct recycled aggregate base (RAB) layers is a promising approach since such layers can perform similarly to VA base layers or even better than them (Bennert et al. 2000; Westover et al. 2007). Several positive environmental consequences, such as reduced consumption of natural sources, improved waste utilization, reduced need for landfills, and decreased greenhouse gas emissions and energy consumption, can be achieved by using recycled aggregates (Cetin et al. 2010; Lee et al. 2010; Cooley and Hornsby 2012). Use of recycled aggregates can also provide overall project savings by minimizing transportation costs for VAs (Gonzalez and Moo-Young 2004; Edil 2011).

Recycled concrete aggregate (RCA) and recycled asphalt pavement (RAP) materials [Figure 1.4(a) and Figure 1.4(b), respectively] are the two most commonly used alternative materials for pavement construction. Such materials have been used in hot-mix asphalt (HMA) and aggregate base layers by several state departments of transportation (DOTs) such as Minnesota DOT (MnDOT) and Wisconsin DOT. RCA materials are produced by crushing and processing hardened concrete recovered from rigid pavements or other structures (e.g., buildings and bridges) and removing the construction debris and steel reinforcement (Edil et al. 2012; LRRB 2016). RAP materials are produced by milling old or failed asphalt pavement surfaces and processing the milled material (Edil 2011). Because of the presence of unhydrated cement in concrete mortar residue, RCA materials are hydrophilic (Edil 2011; Edil et al. 2012; Rahardjo et al. 2010). RAP materials exhibit hydrophobic properties due to the presence of remnant asphalt coating (Rahardjo et al. 2010; Edil et al. 2012) and tend to exhibit a higher saturated hydraulic conductivity than RCA materials and VAs (Rahardjo et al. 2010; Nokkaew et al. 2012). In general, RCA and RAP materials exhibit greater stiffness than VAs (MacGregor et al. 1999; Bennert et al.

2000; Kuo et al. 2002; Cosentino et al. 2003; Abdelrahman et al. 2010; Edil et al. 2012; Stolle et al. 2014; Rosa et al. 2017). RAP materials are less susceptible to water than RCA materials and VAs due to their hydrophobic properties; hence, moisture-induced changes are relatively less important for RAP materials (Cosentino et al. 2003). Due to hydration of their cement content, RCA materials can exhibit an increase in California Bearing Ratio (CBR) values in the soaked condition (Jayakody et al. 2012; Garach et al. 2015; Bestgen et al. 2016a).

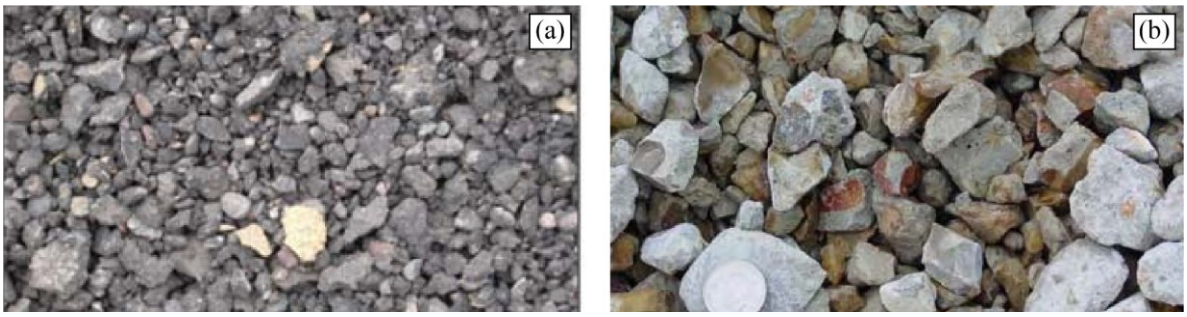

Figure 1.4. (a) Recycled asphalt pavement (RAP) (Copeland 2011) and (b) recycled concrete aggregate (RCA) (Gonzalez and Moo-Young 2004)

1.1.3 Large-Size Aggregates in Subbase Layer Applications

Pavement subgrade layers should be stiff and stable enough to withstand the loads and to increase the service life of pavements (Kazmee et al. 2016). Coarse-grained aggregate layers are constructed to minimize the instability caused by subgrade and protect the upper layers. The coarse-grained structure of aggregates minimizes the capillary action and helps to evacuate the water coming from the surface or groundwater (Uhlmeyer et al. 2003).

Although conventional size aggregates have been used for subbase layer construction, use of unconventionally large aggregates (generally top size $\geq$ 76 mm or 3 in) (such materials are called large stones in this study) for subbase layer construction [such subbase layers are called large stone subbase (LSSB) layers in this study] has become popular in recent years. Large stones can perform equally as or even better than conventional size aggregates; therefore, they are promising alternatives to conventional size aggregates (Kazmee et al. 2016). The amount of energy, which is used to break up rocks or stones to obtain conventional size aggregates, can be significantly reduced with the direct use of large stones for subbase layer construction (Kazmee et al. 2015). Use of large stones for LSSB layer construction has been investigated by several DOTs such as Idaho DOT, Illinois DOT, and Wisconsin DOT (Uhlmeyer et al. 2003; Tanyu et al. 2004; Kazmee et al. 2015; Kazmee et al. 2016). Crushed rock, breaker run, pit run, and rock cap materials were used as large stones for LSSB layer construction (Tanyu et al. 2004; Schuettpelz et al. 2010; Kazmee et al. 2015, 2016). The Illinois DOT Bureau of Design and Environment defined three new gradation specifications named CS01 (203 mm or 8 in top size), CS02 (150 mm or 6 in top size), and RR01 (76 mm or 3 in top size) to classify large-size aggregates (Kazmee et al. 2016).

1.1.4 Motivation and Purpose of This Research

Engineering properties of aggregates are affected by gradation (Saeed 2008), angularity, and texture (Tutumluer 2013; Tan et al. 2014; Haider et al. 2014; Cetin et al. 2014; Hatipoglu et al. 2020). Gradation, in particular, has a significant influence on the engineering properties of RCA materials. For instance, finer RCA materials tend to contain more unhydrated cement than coarser RCA materials (ACPA 2009). The literature contains a large amount of information about the effects of gradation on laboratory performance of RCA materials. However, interpretations of these effects on the performance of the sublayers built with RCA materials are lacking. In addition, while there is much information in the literature about using blends of RCA and VA or RAP and VA in pavement construction, there is a lack of information about using RCA and RAP materials blended together.

A survey regarding the use of recycled aggregates in aggregate base applications was conducted by MnDOT in 2016, and the target participants were local transportation agencies (66 respondents) (LRRB 2016). Initially, it was concluded that about 11% of the respondents indicated that they had not used recycled aggregates due to lack of specification and guidance, lack of experience, and low amount of available recycled aggregates. The rest of the respondents (about 89%) stated that they hesitated to use recycled aggregates for the first time due to some uncertainties related to gradation, durability, performance, and quality control. It was concluded from the survey that there was no agreement between the agencies regarding the use of a specific design method for determining RAB layer thickness during pavement design analyses (Figure 1.5). Another question in the survey was about selecting the correct proportions of recycled aggregates in their mixture with VA. While MnDOT specifications were preferred by 69% of the respondents, the rest indicated that they used their experiences. Although recycled aggregates have been used in roadway base layers for many years, a specific design method did not exist that described how to build roadways with these aggregates.

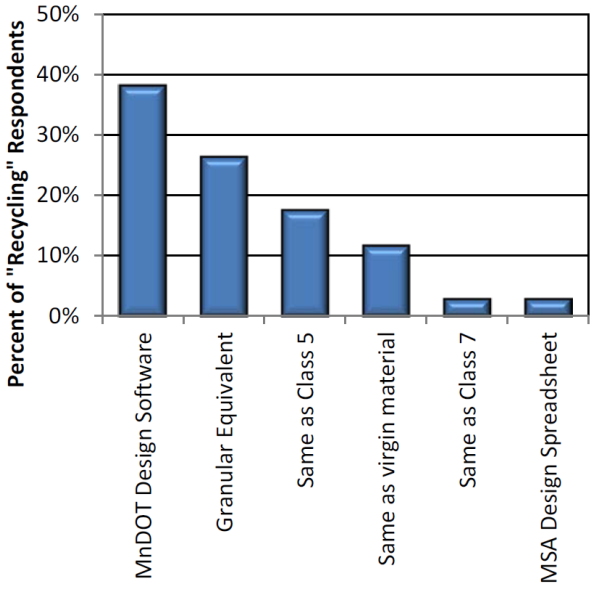

Figure 1.5. Methods for determining recycled aggregate base (RAB) layer thickness (LRRB 2016)

Limited information was available regarding the engineering properties of large stones and LSSB layers, primarily due to limitations of laboratory facilities and in-place testing techniques to be able to test these materials (Schuettpelz et al. 2010; Kazmee and Tutumluer 2015; Kazmee et al. 2016). Therefore, the suitability of large stones for pavement construction must be evaluated by constructing full-scale pavement test sections with such materials and then performing field tests to determine the performance-based engineering properties of these materials. Rock cap, pit run, and breaker run aggregates were used as large-size aggregates for aggregate base/subbase applications (Kazmee et al. 2016; Schuettpelz et al. 2010). However, there was a similar lack of an existing design methodology for pavement systems built with a LSSB as unconventional large-size aggregates.

As mentioned above, there were issues regarding the use/implementation of RAB and LSSB in pavement foundation systems that needed to be addressed adequately, so use of these materials could be increased in such applications. Therefore, this study was conducted to undertake and solve these concerns about RAB and LSSB materials.

This project had three main goals. The first goal was to determine the field and laboratory performances of the recycled aggregates, including two RCA materials with different gradations and a mixture of RCA and RAP, and test cells built with RAB layers. The first goal also included the evaluation of the field performance of LSSB layers. The second goal was to develop a method to estimate the stiffness (i.e., performance-based parameters) of RAB and LSSB layers. This goal was achieved by establishing correlations between common laboratory test data and both laboratory and field modulus values. The third goal was to prepare a pavement design and construction specification for pavements built with RAB and LSSB layers. This goal was accomplished by analyzing field and laboratory, and pavement performance prediction modelling. The results of this research could help agencies optimize the use of recycled aggregates and large stones in pavement systems and enable them to make proper pavement design analyses with RAB and LSSB materials.

CHAPTER 2: LITERATURE REVIEW

2.1 INDEX PROPERTIES OF RECYCLED ASPHALT PAVEMENT (RAP), RECYCLED CONCRETE AGGREGATE (RCA), AND LARGE STONE SUBBASE (LSSB) MATERIALS

Material characteristics such as mineralogy, gradation, angularity, texture, and durability are different for each aggregate, and these differences affect the engineering properties of aggregates (Tutumluer 2013; Tan et al. 2014). The index properties of RAP and RCA are highly affected by several factors, such as the aggregate source, the aggregate type, and the crushing operations. Unlike LSSB, RAP and RCA can contain various impurities such as steel, metal, and tire residual. The amount of the impurities is not constant and is affected by the original aggregate source and the crushing methods (Jayakody et al. 2012).

2.1.1 Grain and Gradation Characteristics

RCA particles tend to be relatively more angular than RAP particles. In addition, they tend to have rougher surface texture than RAP particles. Asphalt content (about 4.5 - 6%) and trapped air between asphalt and aggregate particles cause lower specific gravity values of RAP (Cosentino et al. 2003). On the other hand, RCA also has a relatively lower specific gravity than VA due to the presence of mortar bounds in the RCA matrix (Snyder et al. 1994).

Engineering properties of granular materials such as hydraulic conductivity, shear strength, and frost-susceptibility are highly affected by the gradation of the aggregates (Saeed 2008). Original aggregate type, milling operations, and the crushing methods affect the gradation of RAP and RCA (Cosentino and Kalajian 2001). Aggregate particles retaining on No. 4 sieve are classified as coarse aggregates, whereas those passing No. 4 sieve are classified as fine aggregates (Gonzalez and Moo-Young 2004; Van Dam et al. 2011). While coarse aggregates are suitable for pavement aggregate base applications, fine aggregates have limited use (Van Dam et al. 2011).

The gradation of RAP is generally similar to VA; however, it may contain higher fines content depending on the RAP production method (Chesner et al. 1998). A summary of the gradations of RAP and RCA used in similar types of studies are provided in Table 2.1 for RAP and Table 2.2 for RCA (Edil et al. 2012). The gradation of RCA affects its engineering properties considerably because finer particles may contain higher unhydrated cement compared to coarser particles mainly due to a higher surface area associated with finer particles (ACPA 2009).

Since it is not practicable to sieve large-size aggregates due to the limitations of the standard sieve sizes, image analysis techniques can be performed (Kazmee et al. 2016). As stated before, CS01 (203 mm or 8 in top size), CS02 (150 mm or 6 in top size), and RR01 (76 mm or 3 in top size) aggregates were defined by the Illinois DOT Bureau of Design and Environment. The angularity of aggregates increases as the crushing operation goes from the primary stage to further stages. However, large-size aggregates may have less angularity since they generally go through a single crushing operation (Kazmee et al. 2016).

Table 2.1. Different recycled asphalt pavement (RAP) gradations from similar studies (Edil et al. 2012)

Material	% Passing											
	#200	#100	#50	#30	#16	#8	#4	3/8"	1/2"	3/4"	1	1.5
Bejarano et al. (2003) Pulverized	2	3	7	12	20	31	46	68	---	100	---	---
Guthrie et al. (2007) R1	8	11	15	23	35	45	58	82	---	99	---	---
Guthrie et al. (2007) R2	1	3	8	12	21	39	59	82	---	97	---	---
Bennert et al. (2000) RAP	1	2	3	5	10	20	39	68	---	90	---	---
Saeed et al. (2008) RAP-LS-MS	3	5	9	12	19	27	38	62	75	95	95	100
Saeed et al. (2008) RAP-GR-CO	1	2	5	12	18	25	39	63	75	92	97	100
Saeed et al. (2008) RAP-GV-LA	0	2	6	11	17	23	33	61	76	92	98	100
Average Value	2.3	4.0	7.6	12.4	20.0	30.0	44.6	69.4	75.3	95.0	96.7	100
Standard Deviation	2.7	3.3	3.8	5.3	7.5	9.0	10.2	9.0	0.6	3.8	1.5	0.0
Coefficient of Variance	1.2	0.8	0.5	0.4	0.4	0.3	0.2	0.1	0.0	0.0	0.0	0.0

Table 2.2. Different recycled concrete aggregate (RCA) gradations from similar studies (Edil et al. 2012)

Material	% Passing												
	#200	#100	#50	#30	#16	#10	#8	#4	3/8"	1/2"	3/4"	1	2"
Bennert et al. (2000) RCA	7	10	15	24	28	---	32	42	56	---	76	---	---
Blankenagel et al. (2006) Demolition	3	6	9	12	15	---	20	31	60	---	---	---	---
Blankenagel et al. (2006) Haul-Back	8	10	13	23	37	---	46	60	72	---	---	---	---
Saeed (2008) RCP-LS-IL	4	8	15	26	36	---	48	60	89	---	99	100	---
Saeed (2008) RCP-GV-LA	8	11	16	26	32	---	48	64	74	---	89	96	---
Saeed (2008) RCP-GR-SC	3	5	9	13	19	---	27	38	62	76	95	98	---
Kuo et al. (2002) District 1	4	---	12	---	---	30	---	45	52	---	76	99	100
Kuo et al. (2002) District 2	5	---	17	---	---	30	---	40	53	---	76	99	100
Kuo et al. (2002) District 4	5	---	11	---	---	28	---	40	56	---	81	99	100
Kuo et al. (2002) District 5	4	---	18	---	---	45	---	56	80	---	100	100	100
Kuo et al. (2002) District 6	5	---	20	---	---	30	---	33	37	---	50	86	99
Kuo et al. (2002) District 7	5	---	20	---	---	40	---	50	63	---	82	99	100
Average Value	5.1	8.3	14.6	20.7	27.8	33.8	36.8	46.6	62.8	76.0	82.4	97.3	99.8
Standard Deviation	1.7	2.4	3.8	6.4	9.1	6.9	12.1	11.2	14.1	---	14.8	4.4	0.4
Coefficient of Variance	0.3	0.3	0.3	0.3	0.3	0.2	0.3	0.2	0.2	---	0.2	0.0	0.0

2.1.2 Compaction Characteristics

The relationship between dry unit weight and water content of aggregates greatly affects their engineering properties such as hydraulic conductivity, stiffness, and strength. RAP and RCA have different compaction characteristics than VA because of their different morphology, such as water absorption capacity and angularity. The general trend (of Proctor compaction tests) for the dry unit weight is that RAP and RCA have lower maximum dry unit weight compared to VA when compacted. On the other hand, while RAP has lower optimum water content than VA, RCA shows a higher optimum moisture content (Figure 2.1) (Edil et al. 2012; Nokkaew et al. 2012; Sayed et al. 1993). In addition, LSSB tends to be insensitive to compaction water content because of the high water flow (Kim et al. 2005).

While RAP shows hydrophobic properties because of the asphalt coating around particles, RCA shows hydrophilic properties due to concrete mortar residues (Rahardjo et al. 2010). Thus, a relatively higher optimum moisture content is observed with RCA because of higher water absorption capacity. Gradation affects the compaction characteristics of aggregates. The compaction effort is more efficient for well-graded aggregates rather than open-graded aggregates. In addition, fines content greatly affects the compaction curves of recycled aggregates, e.g., higher fines content in RCA may cause a higher maximum dry unit weight and higher optimum water content because of an increase in the surface area and absorption capacity (Jayakody et al. 2012). For all aggregate types, the voids cannot be filled effectively due to the lack of fines contents, and this can cause a reduction in maximum dry unit weight (Locander 2009; Blankenagel and Guthrie 2006). Since RAP has lower specific gravity than VA because of asphalt content and low fines content, lower maximum dry unit weights are observed. (Guthrie et al. 2007; Locander 2009). The hydration and cementation of unhydrated cement particles in RCA may reduce the dry unit weight of RCA (Chen and Brown 2012). An increase in the linking between particles increases the resistance of particles against the compaction effort and may yield a lower maximum dry unit weight values (Hussain and Dash 2010).

A similar trend is also observed in the RAP-VA and RCA-VA mixtures. The reduction in the maximum dry unit weight is directly proportional to the content of RAP and RCA in the RAP-VA and RCA-VA mixtures, respectively (Taha et al. 1999). Greater reductions in the maximum dry unit weight are seen with the use of more recycled aggregates in the mixtures (Bennert et al. 2000). While using higher RAP content in the RAP-VA mixtures causes a further reduction in the optimum water content (Locander 2009), the use of a higher amount of RCA in the RCA-VA mixtures leads to an increase in the optimum water content (Bennert et al. 2000).

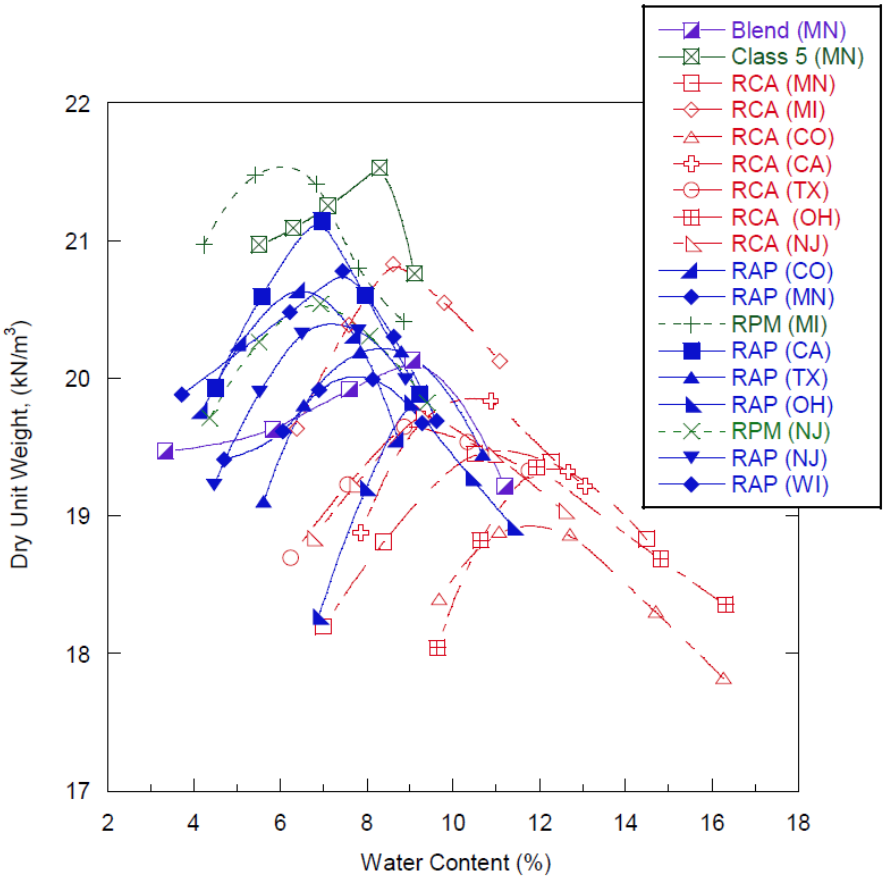

Figure 2.1. Compaction characteristics of recycled asphalt pavement (RAP), recycled concrete aggregate (RCA), and virgin aggregate (VA) (Abbreviations in parentheses represent locations of aggregate sources) (Edil et al. 2012)

It is stated by Kim et al. (2007) that gyratory compactor provided better results to simulate the in-situ conditions. Gyratory compaction results were closer to the densities obtained from the field by 4-in (102 mm) and 6-in (150 mm) sand cone tests (Figure 2.2).

The compaction characteristics of RAP changes with temperature (Soleimanbeigi and Edil 2015). Due to the softening of asphalt binder at higher temperatures, the binding quality between aggregate particles improves and dry unit weight increases, e.g., about 3.5% increase in the dry unit weight was observed in the specimens compacted at 49°C (120°F) rather than 21°C (70°F) (Montemayor 1998, as cited in Cosentino and Kalajian 2001).

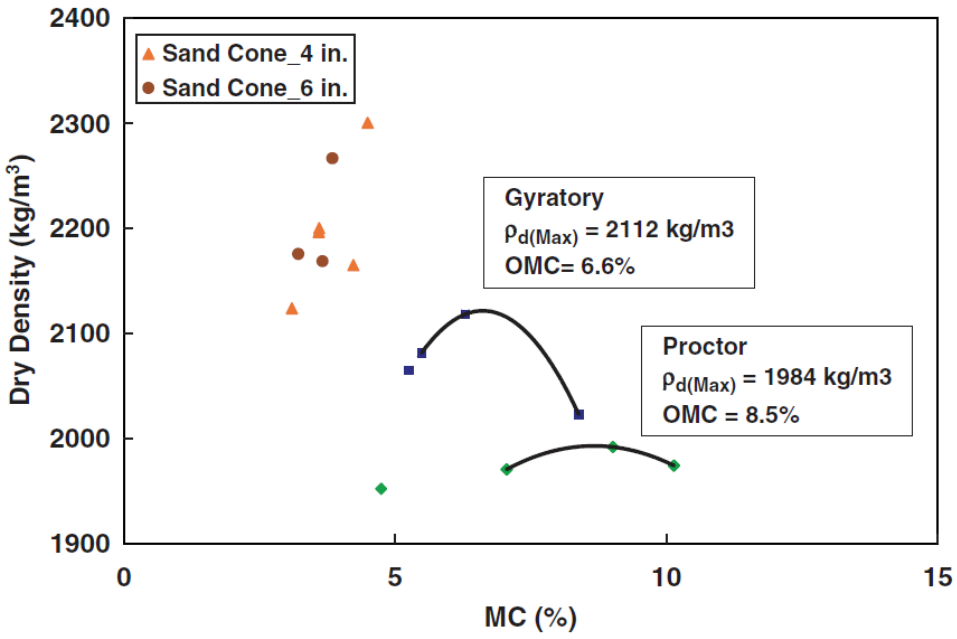

Figure 2.2. Difference between Proctor and gyratory compaction methods ($\rho_{d(Max)}$ = maximum dry density; OMC = optimum moisture content) (4 in and 6 in represent the diameters of sand cones) (Kim et al. 2007)

2.2 ENGINEERING PROPERTIES OF RECYCLED ASPHALT PAVEMENT (RAP), RECYCLED CONCRETE AGGREGATE (RCA), AND LARGE STONE SUBBASE (LSSB) MATERIALS

The previously stated index properties of RAP and RCA affect their engineering properties significantly. As a specific example, the stiffness of an aggregate base layer constructed with RAP is affected by the original aggregate type, asphalt content, and gradation of RAP (Thakur and Han 2015). The original structure from which RCA is produced may affect the unhydrated cement content of RCA. The amount of unhydrated cement affects the engineering behavior and the long-term performance of aggregate base layers constructed with RCA (Hiller et al. 2011).

Metallic objects, crushed clay bricks, pavement markings, which may be present in RAP or RCA matrix, may affect the engineering properties of the aggregates. Some specifications (AASHTO 2002; Greenbook 2009; ASTM 2016) regarding the content of an impurity, e.g., crushed clay brick, should be less than 5% for the aggregate base layer applications of RCA unless it is proven that its presence improves the engineering properties of aggregate base layer (Edil et al. 2012). Some agencies generate RAP and RCA only from their sources to minimize the presence of impurities (West 2010, as cited in Hoppe et al. 2015). For others who obtain recycled aggregates from various sources, it is important to understand the components and the engineering properties of the aggregates for constructing high-quality pavements (Gonzalez and Moo-Young 2004).

2.2.1 Hydraulic Properties

One of the main functions of aggregate base layers is to provide adequate drainage and prevent capillary action to increase the service life of pavements (Cedergren 1988). An increase in the pore water pressure in the aggregate base layers causes a reduction in the stiffness of aggregate base layers (Edil et al. 2012). Hydraulic properties of aggregates are affected by gradation. Fine particles fill the voids up and reduce drainage properties of aggregates (Cosentino et al. 2003). Saturated hydraulic conductivity (K_{sat}) and soil-water characteristics curve (SWCC) are the two parameters that should be evaluated for pavement designs (Nokkaew et al. 2012). K_{sat} is the ability of soil to let water flow in the presence of a hydraulic gradient. SWCC is used to describe the hydraulic properties of unsaturated soils. K_{sat} is used as a parameter for drainage design, and SWCC is used to determine the modulus of aggregate base layers (Gupta et al. 2004; NCHRP 2004a).

RAP shows hydrophobic properties, while RCA shows hydrophilic properties (Edil et al. 2012; Rahardjo et al. 2010). The liquid contact angle is one of the methods used to evaluate the water repellency of aggregates. The higher the contact angle, the greater the water repellency (Letey et al. 2000). While the apparent contact angle of RAP tends to be greater than 90°, it is about 0° for RCA (Figure 2.3) (Edil et al. 2012). Due to the hydrophobicity of RAP, it tends to have higher K_{sat} ($3.8x10^{-5}$ to $3.7x10^{-4}$ m/s) than RCA (about $1.8x10^{-5}$ m/s) (Figure 2.4) (Nokkaew et al. 2012).

Figure 2.3. Water repellency of (a) recycled asphalt pavement (RAP) and (b) recycled concrete aggregate (RCA) (Edil et al. 2012)

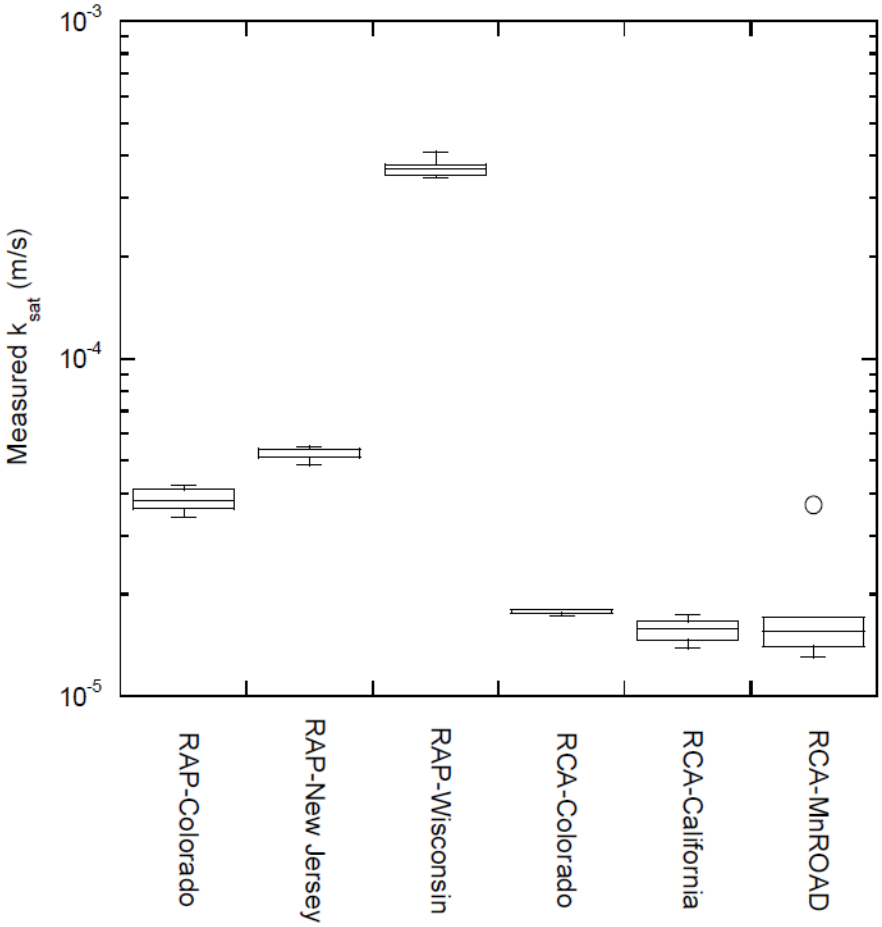

Figure 2.4. Saturated hydraulic conductivity (K_{sat}) of recycled asphalt pavement (RAP) and recycled concrete aggregate (RCA) (Nokkaew et al. 2012)

Hysteresis is a phenomenon that affects the unsaturated hydraulic properties of soils. It is basically a difference between the suctions on the wetting (absorption) and drying (desorption) mechanisms (Ebrahimi-Birang et al. 2007). Hysteresis can be described on SWCCs, which show the relationship between the suction and the volumetric water content (VWC) (Figure 2.5). For the same suction, it is seen that the drying curve shows higher water content than the wetting curve due to hysteresis (Likos et al. 2013). Air-entry pressure (Ψ_a) is the pressure required to start desaturation of the largest pores in the soil (Figure 2.5) (Fredlund and Rahardjo 1993).

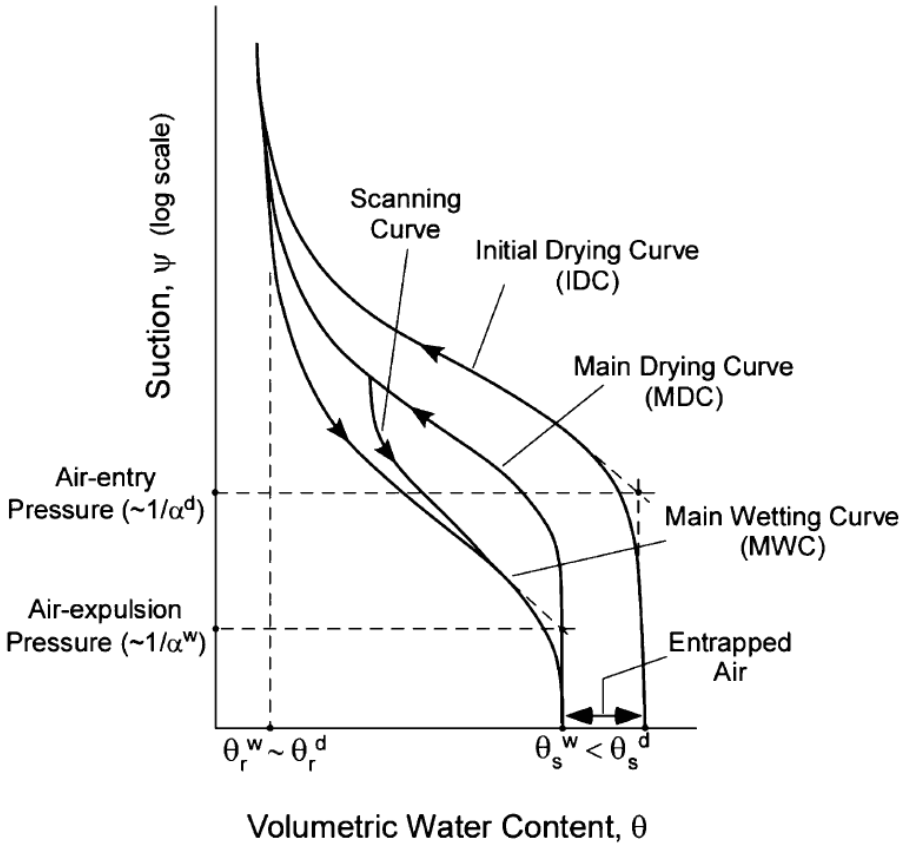

Figure 2.5. Soil-water characteristic curve (SWCC) and hysteresis (Likos et al. 2013)

In general, only the drying curve is measured for coarse-grained soils due to the difficulty of obtaining the wetting curve (Hillel 1980, as cited in Nokkaew et al. 2012). There is a relationship between the contact angles and the matric suction properties of soils. For RAP, positive matric suction is observed due to the high contact angle (> 90°). It means that water can move freely between the RAP particles. On the other hand, RCA has a contact angle of about 0°, which causes negative matric suction. As a result, water will not move through RCA as freely as in RAP (if RAP and RCA have similar gradations) (Edil et al. 2012). Thus, if the gradations are similar, RAP tends to provide a better drainage layer than RCA (Edil et al. 2012; Hoppe et al. 2015).

RAP and RCA have different Ψ_a values (Figure 2.6) (Nokkaew et al. 2012). There is a relationship between the contact angles and the air entry pressures of aggregates. A decrease in the contact angle yields an increase in the air entry pressure values. Thus, RAP tends to have lower air entry pressures (0.03 kPa or 0.004 psi to 2 kPa or 0.29 psi) than RCA due to its relatively higher contact angle (> 90°). While large pores drain first in RAP, small pores will drain first in RCA (Edil et al. 2012).

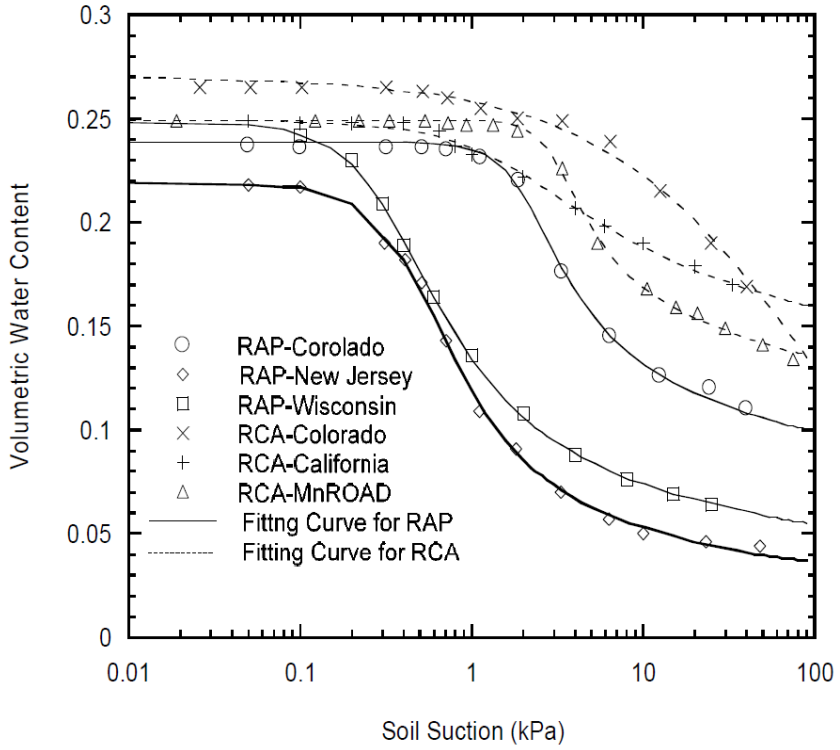

Figure 2.6. Drying curves of recycled asphalt pavement (RAP) and recycled concrete aggregate (RCA) (Nokkaew et al. 2012)

2.2.2 California Bearing Ratio (CBR) Properties

The California Bearing Ratio (CBR) test is a commonly used test in which the strength characteristics of materials are observed. Although it is a commonly used test method, it should only be used to select the most suitable material for the aggregate base layer application (Bennert and Maher 2005). The minimum CBR values of the aggregate base and subbase layers should be 80 and 60, respectively (Jayakody et al. 2012; Ooi et al. 2010). In Florida, Limerock Bearing Ratio (LBR), a modified version of the conventional CBR test, is commonly used (Cosentino et al. 2003). In addition to the specified minimum CBR values, LBR should be at least 100 (LBR = 1.25 x CBR) for aggregate base layers (FDOT 2018).

The general trend is that RAP has lower CBR than VA. In addition, an increase in the RAP content of the RAP-VA mixtures reduces the CBR (Bennert and Maher 2005; Guthrie et al. 2007) (Figure 2.7). Due to the asphalt coating around the particles, the presence of RAP reduces the CBR. Asphalt coating reduces the particle bonding quality and interlocking mechanism of particles (Ooi et al. 2010; Taha et al. 1999). In addition, a lower fines content of RAP may leave unfilled voids (open-graded structure), which may be the reason for a reduction in the CBR (Sayed et al. 1993). Relatively higher strength values are observed in effectively compacted materials than the ones compacted loosely because of their open-graded structure (Cosentino et al. 2003). However, depending on the physical, chemical, and morphological characteristics of RAP, different trends could be observed (Thakur and Han 2015). There might be an optimum RAP content (about 80%), which indicates a higher CBR than VA (Cosentino et al. 2003).

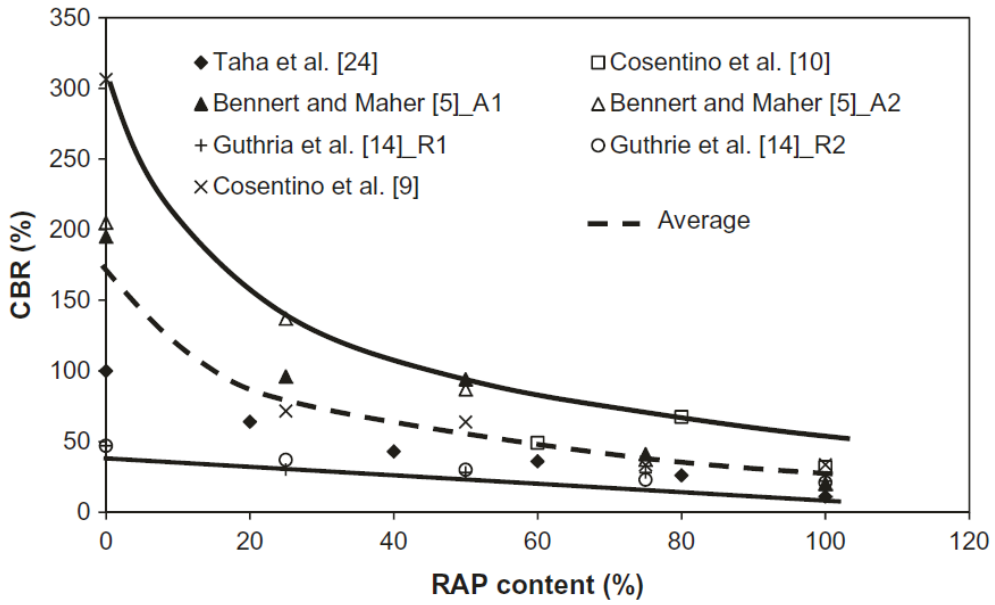

Figure 2.7. California bearing ratio (CBR) values of mixtures of recycled asphalt pavement (RAP) and virgin aggregate (VA) with different RAP contents (Thakur and Han 2015)

As stated before, compacting RAP at a relatively higher temperature increases its dry unit weight by improving the binding between particles. An increase in the dry unit weight leads to an increase in the LBR values, e.g., when compacted at 49°C (120°F), the observed LBR range of RAP was increased from 25-50 to 42-125 (Montemayor 1998, as cited in Cosentino and Kalajian 2001). Regardless of the compaction temperature, the ambient temperature when the LBR tests are performed affects the LBR of RAP considerably (Figure 2.8). While an increase in temperature causes a decrease in the LBR of RAP, a decrease in temperature leads to an increase in the LBR due to the hardening of asphalt material (Cosentino and Kalajian 2001).

A fully-saturated condition is more critical than a partially-saturated or a dry condition in terms of the CBR; thus, observing the behavior of materials after soaking is more important (Jayakody et al. 2012). Different behaviors are observed in RCA for soaked and unsoaked conditions. While lower CBR values are seen in RCA for unsoaked conditions, an increase in the CBR is observed for soaked conditions (Jayakody et al. 2012). The difference in the behavior of RCA is attributed to the presence of unhydrated cement content. With an increase in the soaking period, relatively higher CBR values can be obtained (Figure 2.9) (Garach et al. 2015; Bestgen et al. 2016a). Cementitious reactions are time-dependent, and more reactions could occur with an increase in the curing period (Poon et al. 2006; Garach et al. 2015; Bestgen et al. 2016a).

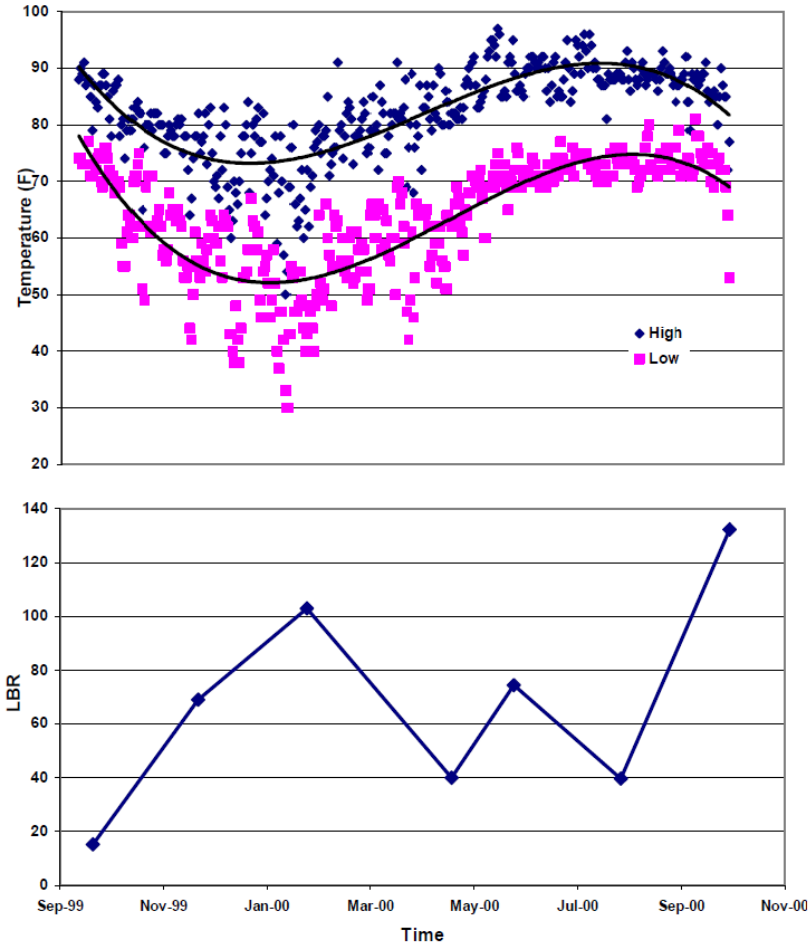

Figure 2.8. Changes in limerock bearing ratio (LBR) of recycled asphalt pavement (RAP) with temperature (Cosentino and Kalajian 2001)

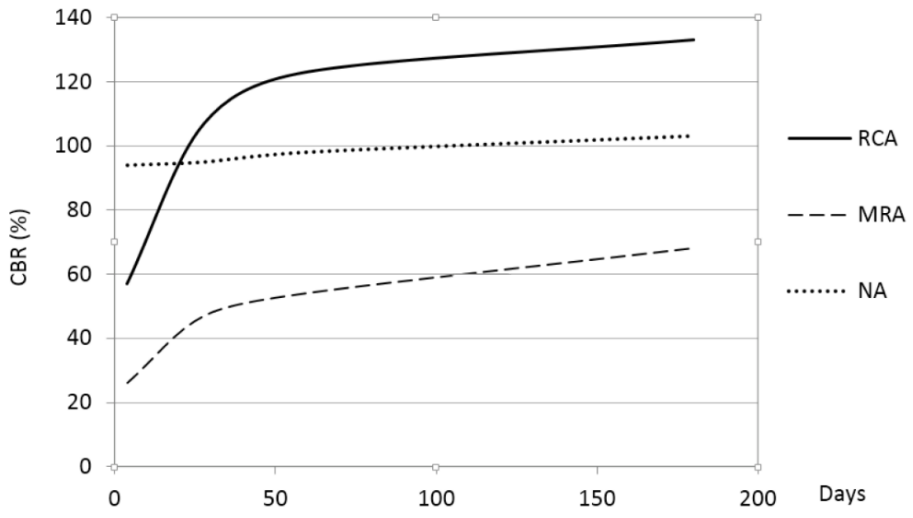

Figure 2.9. Effect of soaking period on California bearing ratio (CBR) of recycled concrete aggregate (RCA), mixed recycled aggregate (MRA), and natural aggregate (NA) (Garach et al. 2015)

2.2.3 Shear Strength Properties

Shear strength is defined as the maximum shear stress that soil can resist. Shear strength of an unbound base layer is a significant parameter that needs to be considered for designing successful and durable pavement structures (Attia 2010, as cited in Thakur and Han 2015). Normal and confining stresses, cohesion, and internal friction angle are the main parameters that affect the shear strength properties of soils (Thakur and Han 2015).

Under the same confining pressure (e.g., 103.4 kPa or 15 psi), RAP, RCA, and VA tend to behave differently during static triaxial loading (Figure 2.10). In addition, depending on the gradation and morphology, e.g., fines content and angularity, VA tends to have higher friction angle and cohesion values than RAP and RCA. For instance, according to the static triaxial tests performed by Bennert et al. (2000), while a natural aggregate had 53° friction angle and 103.4 kPa (15 psi) cohesion, RCA had 47° friction angle and 48.3 kPa (7 psi) cohesion. In addition, RAP had 44° friction angle and 15.9 kPa (2.3 psi) cohesion. RAP and RCA have comparable or generally lower shear strength than VA (Thakur and Han 2015).

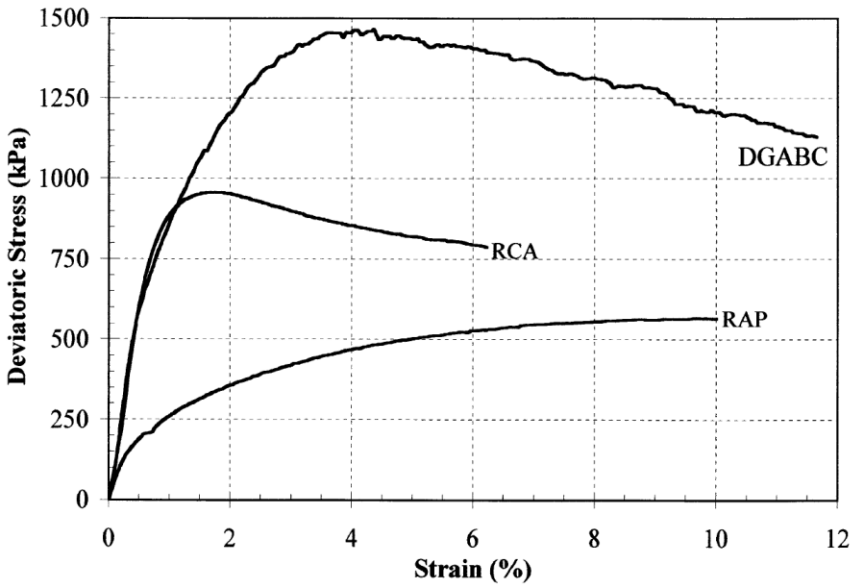

Figure 2.10. Stress-strain relationship for dense-graded aggregate base coarse (DGABC), recycled concrete aggregate (RCA), and recycled asphalt pavement (RAP) (Bennert et al. 2000)

The RAP content of the RAP-VA mixtures affects the friction angle and cohesion values of the mixtures. While an increase in the RAP content causes an increase in the friction angle, it leads to a decrease in the cohesion values in static (or rapid) triaxial tests (Figure 2.11) (Thakur and Han 2015).

RAP tends to show different shear strength characteristics at different temperatures due to the temperature-sensitive asphalt content. There is an optimum temperature that increases the shear strength of RAP. In addition, RAP tends to give lower shear strength values at lower and higher temperatures than the optimum temperature (Figure 2.12). In the static triaxial tests performed at

various temperatures by Cosentino and Kalajian (2001), the highest principal stress at failure was observed at 37.8°C (100°F). While performing tests at various temperatures did not affect the internal friction of RAP considerably, increasing the temperature caused an increase in its cohesion (Cosentino and Kalajian 2001). The increase in the cohesion was attributed to an improvement in the linking between particles.

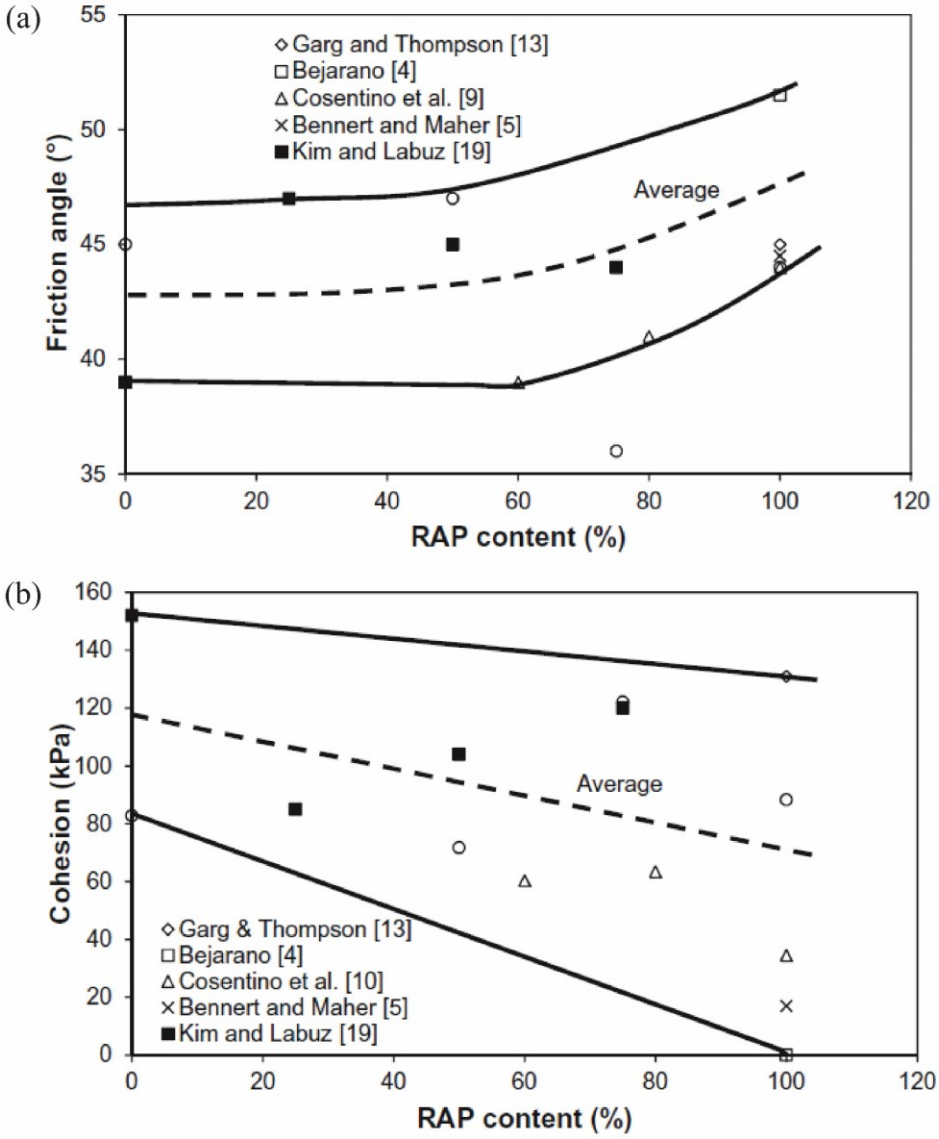

Figure 2.11. Effect of recycled asphalt pavement (RAP) content of mixtures of RAP and virgin aggregates (VAs) on (a) friction angle and (b) cohesion (Thakur and Han 2015)

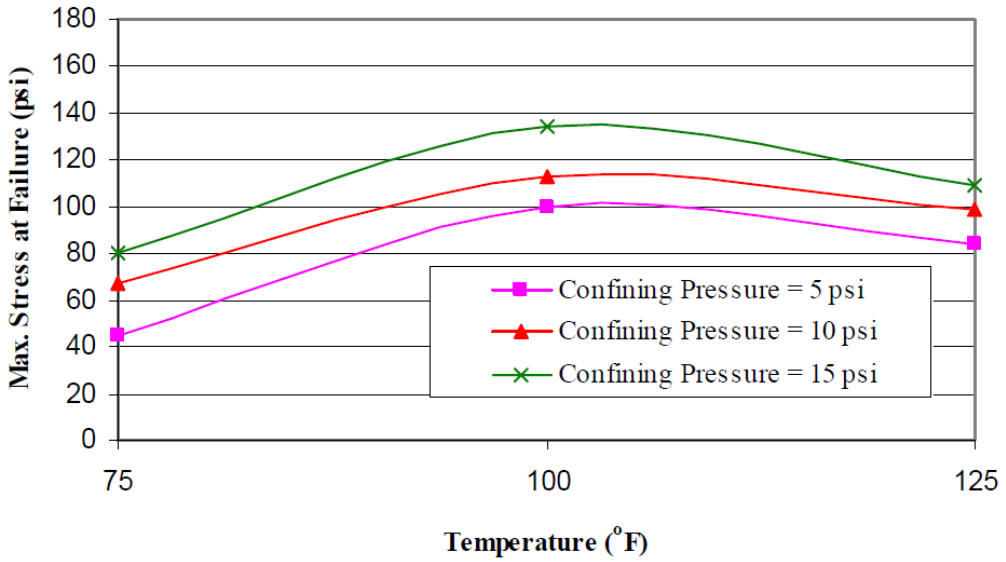

Figure 2.12. Effect of temperature on maximum stress of recycled asphalt pavement (RAP) at failure (Cosentino and Kalajian 2001)

2.2.4 Stiffness Properties

Pavement systems are subjected to repeated loadings due to the traffic flow. As a result of the repeated loading, deformations may be observed in the surface (asphalt layer) and aggregate base layers. Since the main load-carrying and load-distribution mechanisms are related to aggregate base layers, it is very important to understand the responses of these sublayers to the repeated loadings (Lekarp et al. 2000). Elastic modulus (E) is a parameter used for measuring the soil stiffness against slowly applied loads. It is the ratio between stress and elastic strain. However, to better simulate the traffic flow, which creates rapidly applied cyclic loading, the resilient modulus (M_R) is used to determine the elastic deformation of soil under cyclic loading (Edil et al. 2012). M_R is one of the main parameters used in the two most commonly used pavement design methods called AASHTO 1993 and Mechanistic-Empirical (ME) pavement design (Thakur and Han 2015; NCHRP 2017a). In the field, light weight deflectometer (LWD), falling weight deflectometer (FWD), Clegg impact test (CIT), and soil stiffness gauge (SSG) can be used to determine the soil stiffness. In addition, intelligent compaction (IC) (Mooney et al. 2010; White and Vennapusa 2017) and automated plate load testing (APLT) (White and Vennapusa 2017) can be performed for the determination of the in-situ M_R values (White and Vennapusa 2017).

The general trend is that, unlike the trend observed in the shear strength, higher M_R values are observed for RAP and RCA compared to VA (MacGregor et al. 1999; Bennert et al. 2000; Cosentino et al. 2003; Abdelrahman et al. 2010; Rosa et al. 2017). In addition, higher M_R values are observed with an increase in bulk stress as observed for typical aggregates (Figure 2.13) (Bestgen et al. 2016a; Cosentino et al. 2003). Higher M_R values are seen with an increase in the RAP and RCA contents of the RAP-VA and RCA-VA mixtures, respectively (Figure 2.14 for RAP and Figure 2.15 for RCA) (Thakur and Han 2015; Bennert et al. 2000; Edil et al. 2012). However, some exceptions could exist, e.g., RCA may not improve the stiffness of VA when they are mixed due to an increase in the fines content (Bestgen et al. 2016a).

Moisture content, absorption capacity, stress history, the degree of compaction (DOC), aggregate origin and type, gradation, and temperature could affect the behavior of recycled aggregates significantly (Thakur and Han 2015).

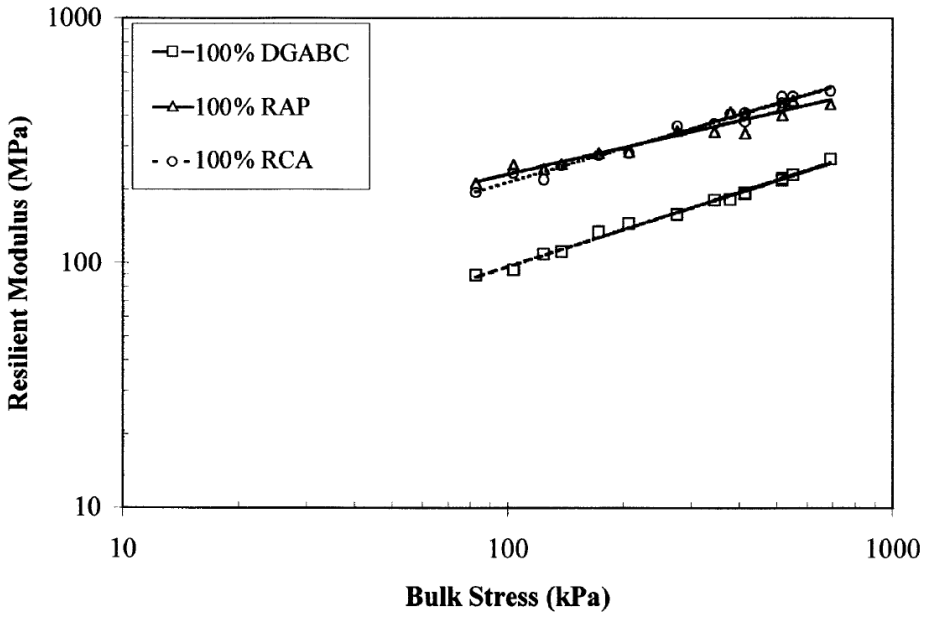

Figure 2.13. Resilient modulus of dense-graded aggregate base coarse (DGABC), recycled concrete aggregate (RCA), and recycled asphalt pavement (RAP) (at ambient temperature) (Bennert et al. 2000)

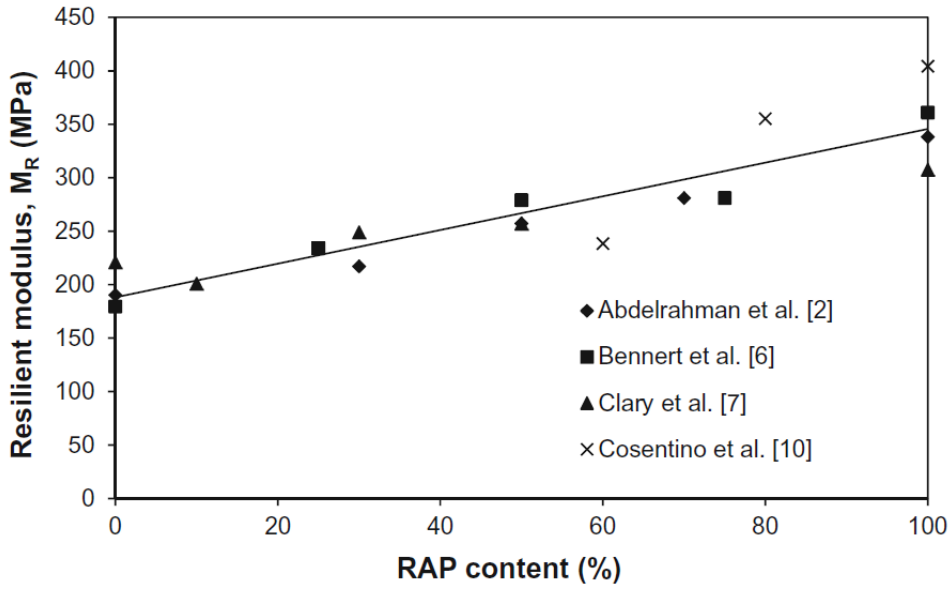

Figure 2.14. Effect of recycled asphalt pavement (RAP) content on resilient modulus (MR) (Thakur and Han 2015) [M_R values shown in the figure are for the bulk stress (θ) model ($M_R=K_1\theta^{K_2}$) where θ = 345 kPa]

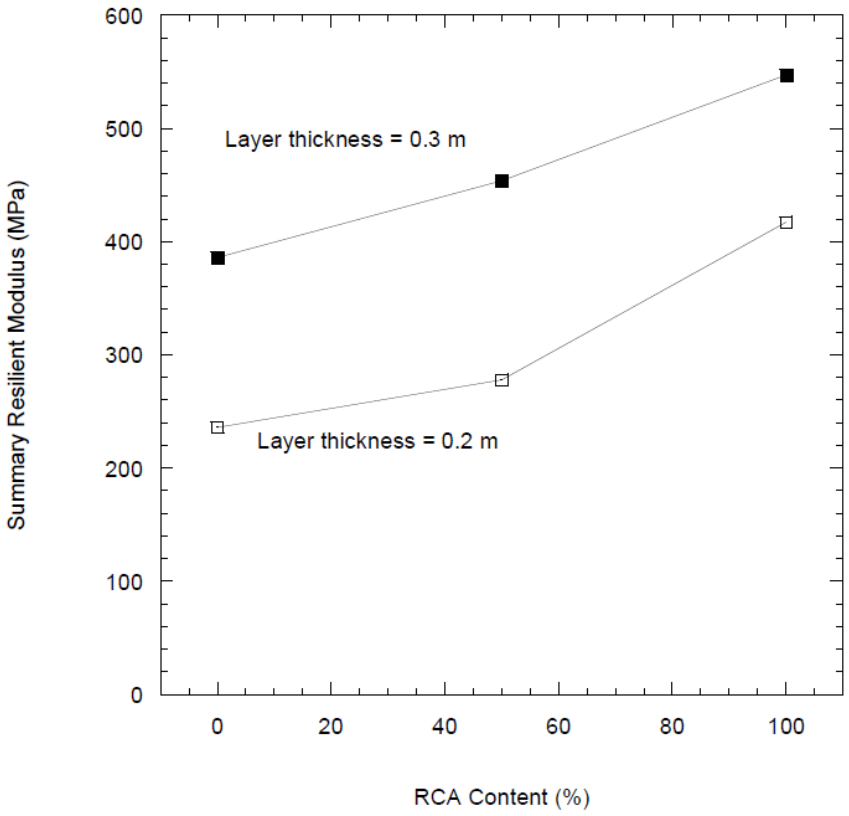

Figure 2.15. Effect of recycled concrete aggregate (RCA) content on summary resilient modulus [modulus at bulk stress of 208 kPa (NCHRP 1-28A)] (Edil et al. 2012)

Angularity and surface texture affect the stiffness characteristics of aggregates by improving the interlocking between particles. Since RCA has angular particles and a rough surface due to the crushing operations and the cement content, it shows a relatively higher M_R than VA (Edil et al. 2012; Stolle et al. 2009; Kuo et al. 2002). In addition, secondary cementation of unhydrated cement content in the presence of water is another reason for higher observed M_R values (Bestgen et al. 2016a). On the other hand, elongated particles in RCA may reduce the M_R since elongated particles are prone to degradation. A relatively lower M_R sometimes may be observed due to the elongated particles in RCA (Nataatmadja and Tan 2001, as cited in Edil et al. 2012).

Falling weight deflectometer (FWD) is one of the non-destructive in-situ test methods that is used to measure the stiffness of pavement layers. Data obtained from FWD can be converted into impulse stiffness modulus (ISM) and elastic modulus (Abdelrahman et al. 2010; Cosentino et al. 2003). The ISM is the ratio of the load (kips) divided by the center plate deflection (mils) (Bush and Thompson 1990, as cited in Cosentino et al. 2003). RAP is less susceptible to water than VA; hence, water-related changes are relatively less important for RAP than VA. A high variance in stiffness is observed in water-sensitive aggregates (Figure 2.16). The same trends can be observed by performing the Clegg impact test (CIT) and soil stiffness gauge (SSG) test (Cosentino et al. 2003).

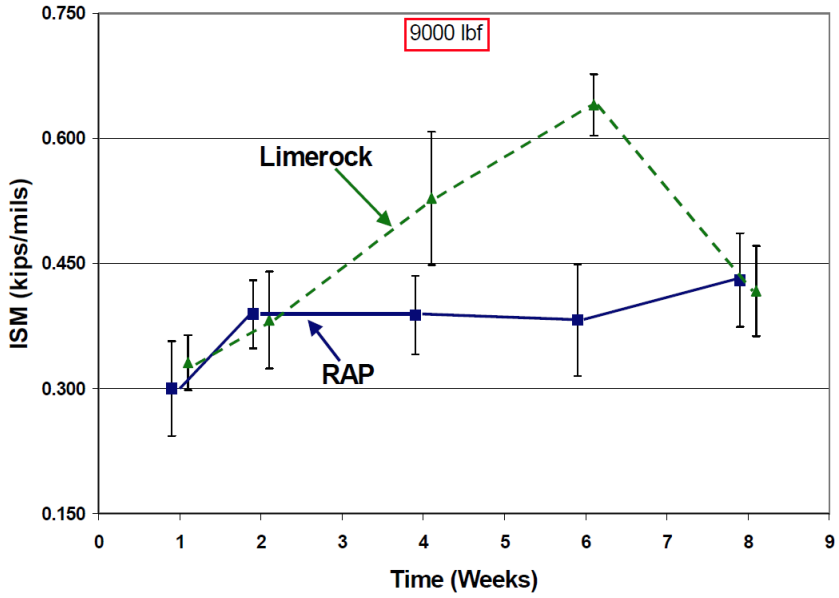

Figure 2.16. Change in impulse stiffness modulus (ISM) of recycled asphalt pavement (RAP) and limerock with time (Cosentino et al. 2003)

The large-scale modeling experiment (LSME) is an alternative laboratory test method used to simulate the in-situ conditions better. In the LSME, a test pit is built to model the pavement system and the desired cycling loading is applied (Tanyu et al. 2003; Edil et al. 2012). In general, while the LSME and FWD give comparable summary M_R (SM_R) values, the conventional M_R test gives relatively lower SM_R values than those observed in the LSME and FWD tests. However, there is no direct correlation observed between the data obtained from the LSME and conventional M_R tests. Although the LSME simulates the in-situ conditions more accurately than the conventional M_R test, it is sensitive to layer thicknesses. A higher M_R is expected for thicker layers due to an improvement in the load distribution with an increase in the layer thickness due to the strain effect (Tanyu et al. 2003).

Relatively higher stiffness values can be observed in LSSB with the light weight deflectometer (LWD) test depending on the size of the LWD equipment. In addition to the higher stiffness values, the fluctuation of the stiffness data can be observed with the LWD test due to the large voids present in LSSB (Kazmee et al. 2016).

RCA and VA are not as sensitive to temperature changes as RAP. RAP is sensitive to temperature due to its asphalt content, a temperature-sensitive material (Figure 2.17) (Wen et al. 2011; Soleimanbeigi et al. 2015). RAP and the RAP-VA mixtures show a decreasing stiffness trend as temperature increases (Soleimanbeigi et al. 2015). After reaching a softening point of an asphalt material, which is in the range of 45°C (113 °F) and 80°C (176 °F) in general, the viscosity of asphalt starts reducing, and the reduction in stiffness is observed (Read and Whiteoak 2003, as cited in Edil et al. 2012; Wen et al. 2011).

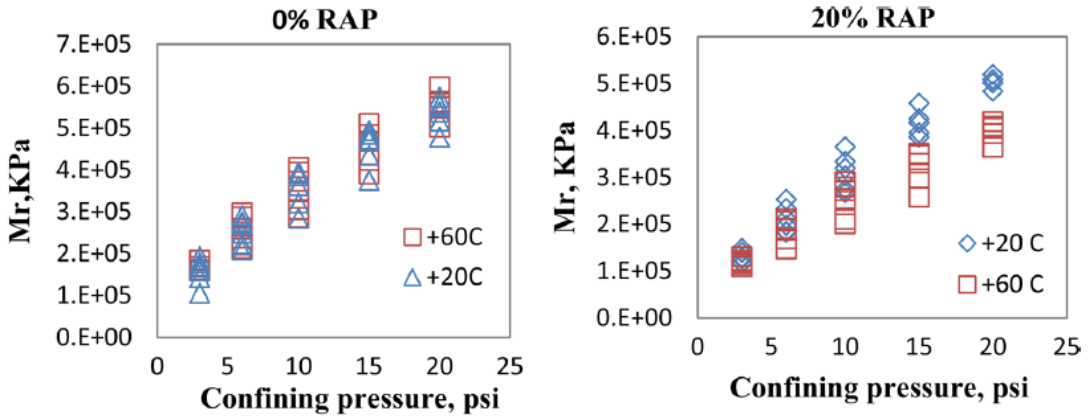

Figure 2.17. Effect of temperature on resilient modulus (M_r) of virgin aggregate (VA) [0% recycled asphalt pavement (RAP)] and its blend with 20% RAP (Wen et al. 2011)

2.2.5 Permanent Deformation Properties

Permanent deformation (or rutting) of pavements due to the repeated loading conditions is one of the most significant parameters that affect the performance of flexible pavement systems and failure mechanisms (Thompson and Smith 1990). Vertical compressive strains that occur in the pavement layers are the reasons for the permanent deformation failure (Bennert et al. 2000). The permanent deformation occurring in the aggregate base layers contributes to the total permanent deformation of flexible pavements (Wen and Wu 2011).

Permanent deformation is determined by performing a cyclic triaxial test in which the confining pressure, deviatoric stress, and the number of cycles are predetermined, e.g., permanent deformation tests were performed by Bennert et al. (2000) under the confining pressure and cyclic deviatoric stress of 103.42 kPa (15 psi) and 310.26 kPa (45 psi), respectively. In addition, 100,000 load repetitions were applied (AASHTO TP46-94). A permanent deformation test can also be conducted during the conditioning phase of the M_R test in which 1,000 load repetitions are applied with the set confining pressure and cyclic deviatoric stress (Garg and Thompson 1996). Different deviator stresses can also be used for the tests (e.g., 207 kPa or 30 psi) (Kim and Labuz 2007).

In general, RCA shows the lowest permanent deformation, while RAP shows the highest permanent deformation (Figure 2.18) (Bennert et al. 2000; Edil et al. 2012; LRRB 2016). In addition, increasing the loading cycle leads to an increase in the permanent deformation regardless of the aggregate type. A relatively higher permanent deformation occurs with an increase in the RAP content of the RAP-VA mixture (Kim and Labuz 2007; Thakur and Han 2015). On the other hand, an increase in the RCA content of the RCA-VA mixture leads to a relatively lower permanent deformation (Bennert et al. 2000). The reason why RAP shows the highest permanent deformation while it shows better stiffness properties than VA is the progressive breakdown of its asphalt binder (Bennert et al. 2000). In addition, the viscous creep behavior of asphalt material is attributed as one of the reasons for observed high plastic deformation of RAP (Edil et al. 2012). In addition, plastic deformation is not accounted for in the estimation of M_R.

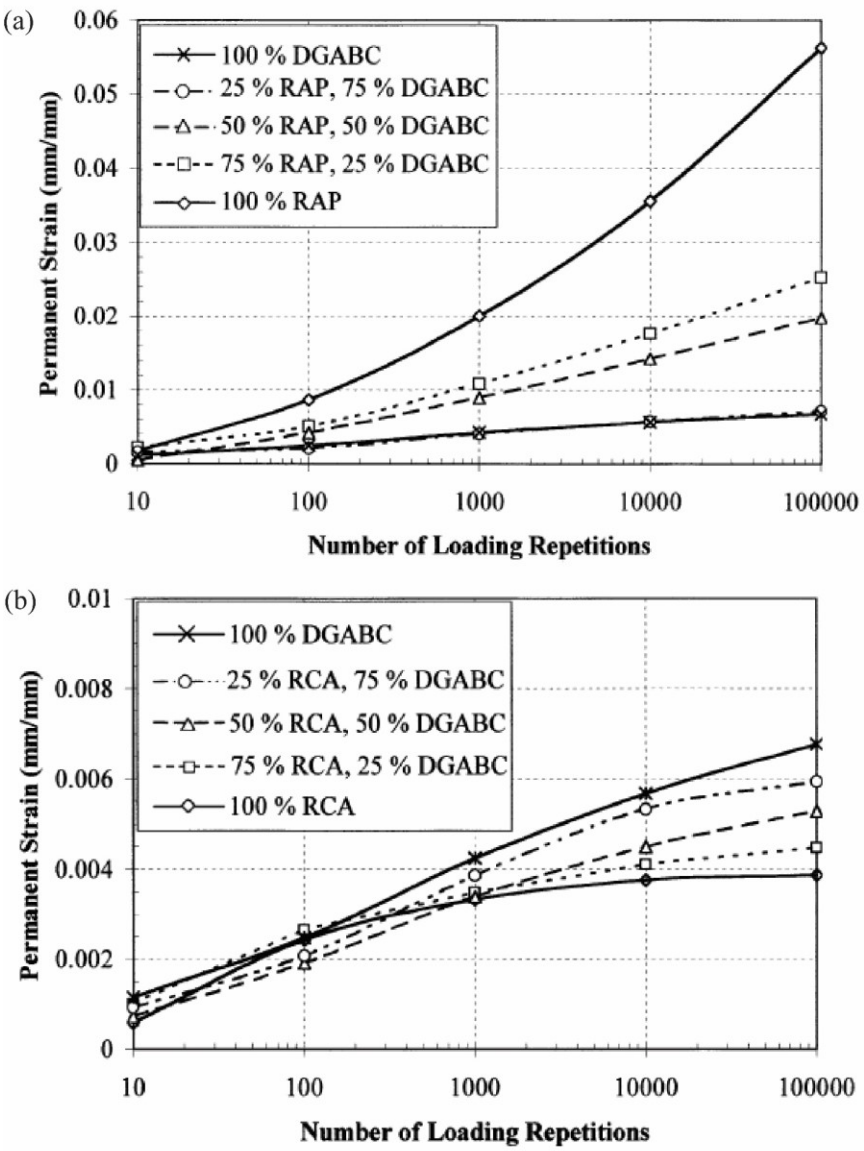

Figure 2.18. Permanent deformations of (a) mixtures of recycled asphalt pavement (RAP) and dense-graded aggregate base coarse (DGABC) and (b) mixtures of recycled concrete aggregate (RCA) and DGABC (Bennert et al. 2000)

Different trends between RAP, RCA, and VA can be observed due to their different fines contents. VA may show lower permanent deformation than RCA due to its lower fines contents (Bestgen et al. 2016a). While fines content has no significant effect on the M_R values of aggregates, it affects the permanent deformation mechanisms considerably. A relatively higher fines content leads to a higher permanent deformation of aggregates (Figure 2.19) (Mishra and Tutumluer 2012). Another reason for different trends between RCA and VA in terms of permanent deformation may be the angularity of RCA. Highly-angular RCA particles (especially hydrated cement particles) may tend to deform easier than relatively more rounded particles, and relatively higher permanent deformation may be observed in RCA (Bestgen et al. 2016a).

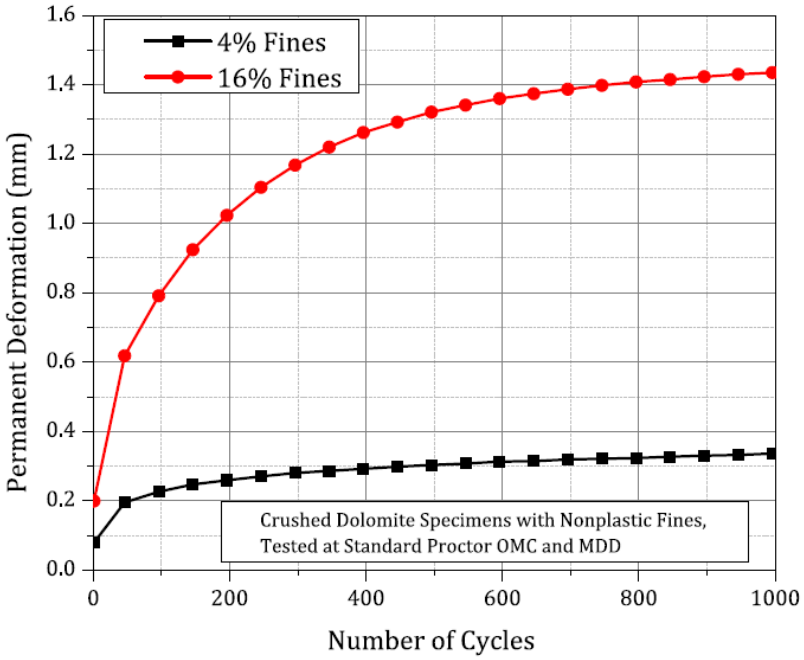

Figure 2.19. Effect of fines content on permanent deformation of aggregates (OMC = optimum moisture content; MDD = maximum dry density) (Mishra and Tutumluer 2012)

An increase in the layer thickness provides lower permanent deformation values because of the improved stress distribution. Stress is distributed more effectively throughout a thicker layer (Cetin et al. 2010, Schaertl 2010, as cited in Edil et al. 2012), and this mechanism is significant for the determination of the aggregate base layer performance. In addition, the presence of larger aggregates in the material matrix contributes to the strength and the resistance against deformation (Gray 1962; Kazmee et al. 2016).

Different modes of permanent deformation failures can be observed, and three main modes are classified: mode 0, mode 1, and mode 2 (Figure 2.20). Initial improper compaction of aggregates may leave large voids, and mode 0 failure may be seen under the loading. Shear failure of an aggregate layer may cause a horizontal movement of particles beneath the wheel path, and mode 1 failure may be seen. Failure of a weak subgrade layer leads to mode 2 type failure (Dawson and Kolisoja 2006). Less permanent deformation is observed in well-graded aggregates compared to uniformly-graded aggregates because of a denser structure and less porous structure (Kazmee et al. 2016).

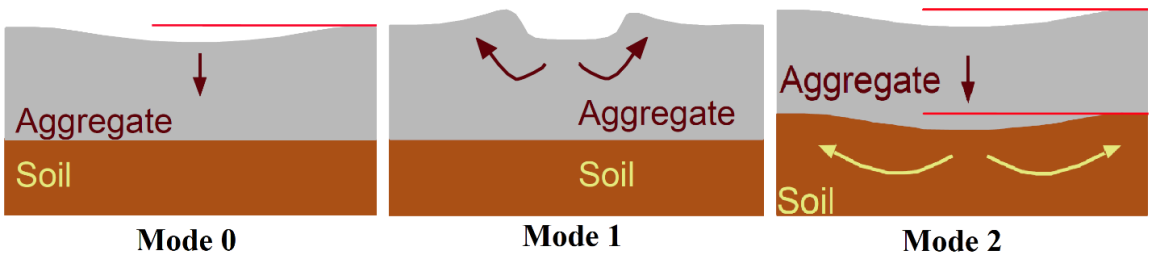

Figure 2.20. Permanent deformation failure modes of aggregate layers (Dawson and Kolisoja 2006)

An increase in temperature causes similar trends observed in strength and stiffness properties of RAP regarding the permanent deformation. Asphalt loses its viscosity under higher temperatures (Edil et al. 2012; Soleimanbeigi et al. 2015). Thus, the increase in temperature leads to an increase in permanent deformation because of the temperature-sensitivity of RAP. On the other hand, the temperature has little to no effect on RCA and VA (Figure 2.21).

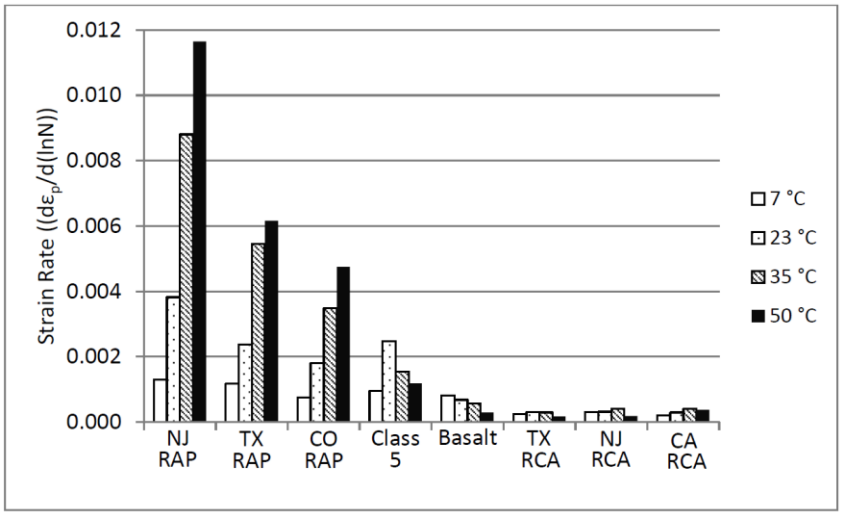

Figure 2.21. Effect of temperature on strain rate of recycled asphalt pavement (RAP), recycled concrete aggregate (RCA), and virgin aggregate (VA) (Edil et al. 2012)

2.2.6 Creep Properties

Creep is defined as a long-term (time-dependent) deformation of a material subjected to a constant static loading which is lower than its maximum loading capacity (Thakur and Han 2015). In general, creep is expected to occur in cohesive soils showing high plastic properties (Cosentino et al. 2012). In other words, granular materials are expected to show little to zero creep potential (Thakur and Han 2015). While RAP is a granular material, it tends to show creep potential due to its asphalt content. Asphalt material has viscoelastic properties, and the presence of asphalt in the RAP matrix leads to a reorientation of particles under static loading in the long-term (Cosentino et al. 2012; Yin et al. 2016). Repositioning of particles in the long-term due to the asphalt content causes the creep of RAP.

Under the constant static loading, the creep potential of RAP increases at elevated temperatures, e.g., Yin et al. (2016) observed that the RAP specimens prepared and tested at 22°C (72°F) showed lower axial strain compared to the triaxial tests performed at elevated temperatures (test specimens were prepared at 35°C (95°F) or 50°C (122°F) (Figure 2.22). As stated before, the compaction of RAP at high temperatures improves its engineering properties because it improves the binding between aggregates (Montemayor 1998, as cited in Cosentino and Kalajian 2001). Yin et al. (2016) also demonstrated that lower axial strain (triaxial tests were run at 22□ or 72□) was observed in the RAP specimens compacted and consolidated at 35°C (95°F) or 50°C (122°F) compared to the specimens prepared at 22°C (72°F) (Figure 2.23). Lower void ratio values were observed in the RAP specimens compacted at elevated temperatures.

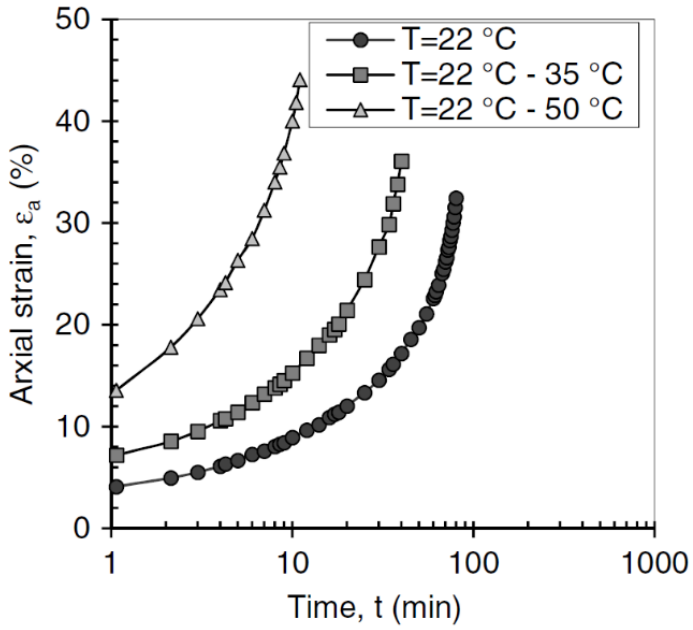

Figure 2.22. Creep properties of recycled asphalt pavement (RAP) under different temperatures (Yin et al. 2016)

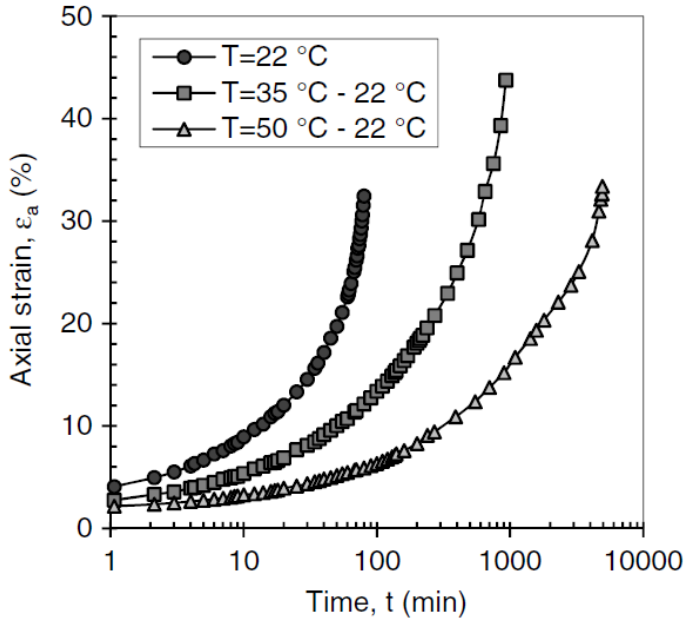

Figure 2.23. Creep properties of recycled asphalt pavement (RAP) compacted at different temperatures (Yin et al. 2016)

An increase in the RAP content in the RAP-VA mixtures leads to an increase in the creep potential (Figure 2.24) (Dikova 2006; Bleakley et al. 2014). In addition, the rate of creep deformation reduces as time progresses (Thakur and Han 2015). RAP should be mixed with a minimum of 75% of VA to obtain the best improvement in creep potential (Cosentino et al. 2012; Bleakley et al. 2014). In addition, applying higher vertical stress increases the creep deformations (Cosentino et al. 2003).

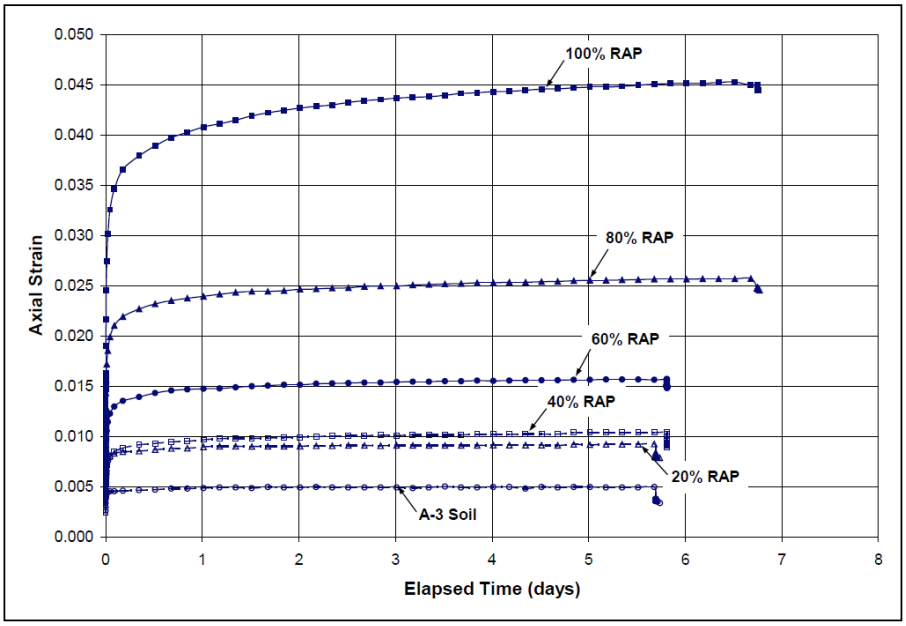

Figure 2.24. Creep behavior of mixtures of recycled asphalt pavement (RAP) and virgin aggregate (VA) prepared with different RAP contents (at ambient temperature) (Dikova 2006)

2.2.7 Freeze-Thaw (F-T) and Wet-Dry (W-D) Durability

In cold regions, pavement structures may be subjected to severe freezing and thawing cycles in the long-term. Long-term pavement performance is highly affected by climatic changes. The engineering properties of pavement systems change seasonally due to the seasonal variations (Rosa et al. 2016). The stiffness of the pavement layers increases during the freezing phase, whereas a reduction in stiffness is observed during the thawing phase (Kootstra et al. 2010). As a result of the seasonal freeze-thaw cycles, various failure mechanisms such as potholes, permanent deformation, frost heave, and thaw weakening can be observed in pavement systems.

During the freezing phase, water freezes and turns into ice with an increase in its volume (around 10%). Expansion of water molecules when they turn into ice produces internal pressures and may deteriorate aggregates. During the thawing phase, ice turns into water with a reduction in its volume and leaves a relatively more porous structure because of the formation of larger voids during freezing. In addition, fines content may increase due to aggregate deterioration. While increased porous medium can worsen the engineering properties of pavements, an increase in the fines content may fill the voids up more effectively, which may cause an improvement in the engineering properties (Edil et al. 2012; Mishra et al. 2010). However, after a certain fines content (e.g., 12%), the generation of more fines decreases the stiffness as excessive fines content reduces the bonding between particles (Mishra et al. 2010). In addition, an increase in the fines content yields an increase in the water absorption capacity of the aggregates due to an increase in the specific surface area in the aggregate matrix (Edil et al. 2012; Rosa et al. 2017). Coarse-grained aggregates are less susceptible to the freeze-thaw action than fine-grained aggregates due to their more porous structure. However, containing fine-grained particles more than 5-10% may cause the coarse-grained aggregates to be more frost susceptible (Konrad and Lemieux 2005).

The stiffness of RAP consistently decreases as freeze-thaw cycles continue. The first couple of freeze-thaw cycles are the most deteriorative ones (Edil et al. 2012; Soleimanbeigi et al. 2015; Rosa et al. 2017). As time progresses, RAP becomes more stable against freeze-thaw cycles, and a reduction in the stiffness decrease rate of RAP is observed (Figure 2.25). Although the stiffness of RAP reduces with freeze-thaw cycles, it still has a higher M_R than VA (Edil et al. 2012). The weakening of asphalt with the freeze-thaw effect may be another reason for the stiffness reduction of RAP (Bozyurt et al. 2013). Hydrophobicity of RAP may cause a reduction in its water content during the M_R test, and this reduction may cause an increasing trend of stiffness as freeze-thaw cycles progress (Attia and Abdelrahman 2010).

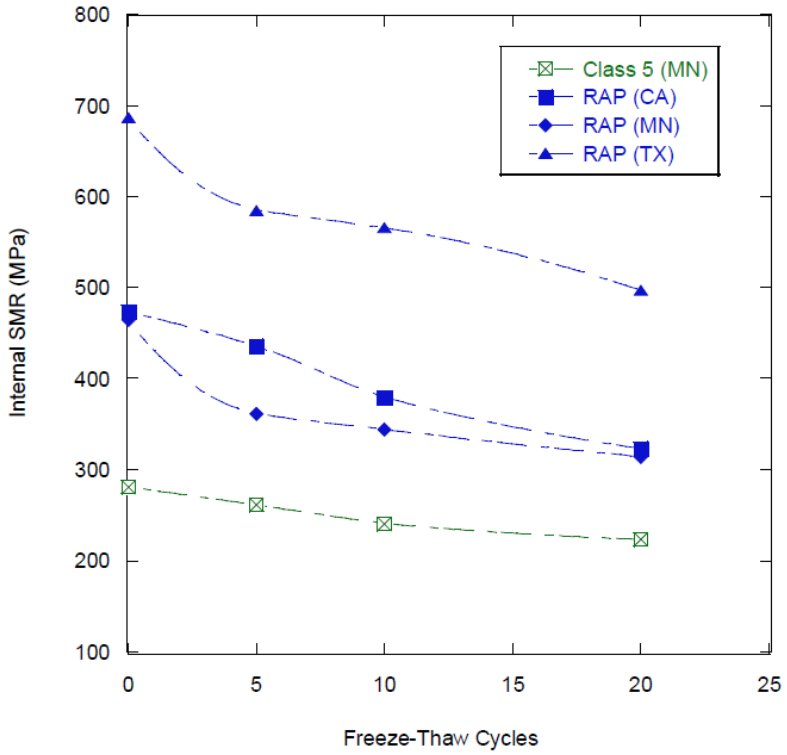

Figure 2.25. Effect of freeze-thaw cycles on stiffness of recycled asphalt pavement (RAP) (internal SMR means the summary resilient modulus measured by using internal LVDTs) (Edil et al. 2012)

Although RAP and RCA show similar stiffness properties at room temperature, they perform differently under the freeze-thaw cycles. While the decrease in the stiffness of RCA is similar to that observed in RAP for the first couple of freeze-thaw cycles, an increasing trend in the stiffness of RCA in the laboratory tests is observed as the freeze-thaw cycles continue due to the self-cementing properties of RCA (Figure 2.26) (Poon et al. 2006; Edil et al. 2012; Soleimanbeigi et al. 2015; Bestgen et al. 2016a, Rosa et al. 2017). In addition, an increase in the fines content of RCA may have a contribution to the increasing trend of stiffness (Edil et al. 2012). However, compared to the effect of the self-cementing of RCA, the gradation of RCA does not seem to affect the stiffness properties of RCA as much (Molenaar and van Niekerk 2002).

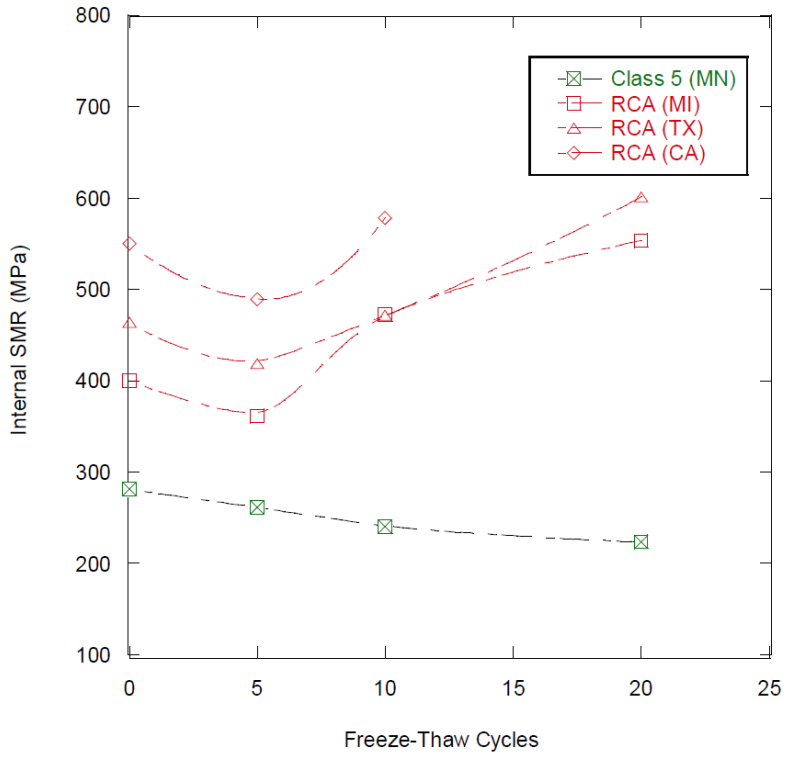

Figure 2.26. Effect of freeze-thaw cycles on stiffness of recycled concrete aggregate (RCA) (internal SMR means the summary resilient modulus measured by using internal LVDTs) (Edil et al. 2012)

Wetting and drying is the other important climate-related event that can affect the long-term performance of pavements (Edil et al. 2012). Materials used in pavements must be durable enough to resist the negative impact caused by the wet-dry cycles (Wu et al. 1998, as cited in Edil et al. 2012). Although the fines in the RCA matrix may be washed away during wetting, there is an increasing trend for the fines content of RCA due to the exposure to the wet-dry cycles (Figure 2.27).

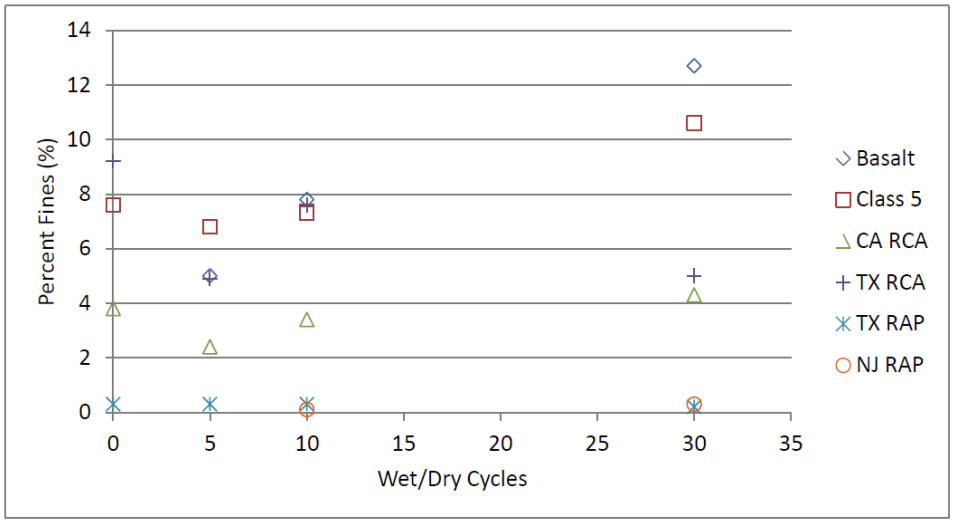

Figure 2.27. Effect of wet-dry cycles on fines content of aggregates (Edil et al. 2012)

2.3 ENVIRONMENTAL PROPERTIES OF RECYCLED ASPHALT PAVEMENT (RAP) AND RECYCLED CONCRETE AGGREGATE (RCA) MATERIALS

2.3.1 Properties of Recycled Asphalt Pavement (RAP) Materials

RAP is mainly composed of natural aggregates and asphalt binder. Asphalt is a material which oxides as time progresses. The oxidation of asphalt causes age hardening, which affects the engineering properties of RAP (Roberts et al. 1996, as cited in Hoppe et al. 2015). Thus, the chemical properties of RAP should be well investigated for constructing high-quality and long-lasting pavement systems.

2.3.1.1 pH Characteristics

Various pH values have been determined for RAP in the literature. In one of the studies performed by Shedivy et al. (2012), it was observed from the batch leaching tests that the pH of RAP varied in the range of 8.59 to 9.58. In another study, it was found that the pH of RAP was around 9.67 from the same test (Kang et al. 2011, as cited in Hoppe et al. 2015). Edil et al. (2012) observed from batch leaching (per ASTM D3987) and field leaching tests that the pH values of RAP were between 8-10.5 in the laboratory batch leaching tests and around 8 in the field leaching tests (Figure 2.28).

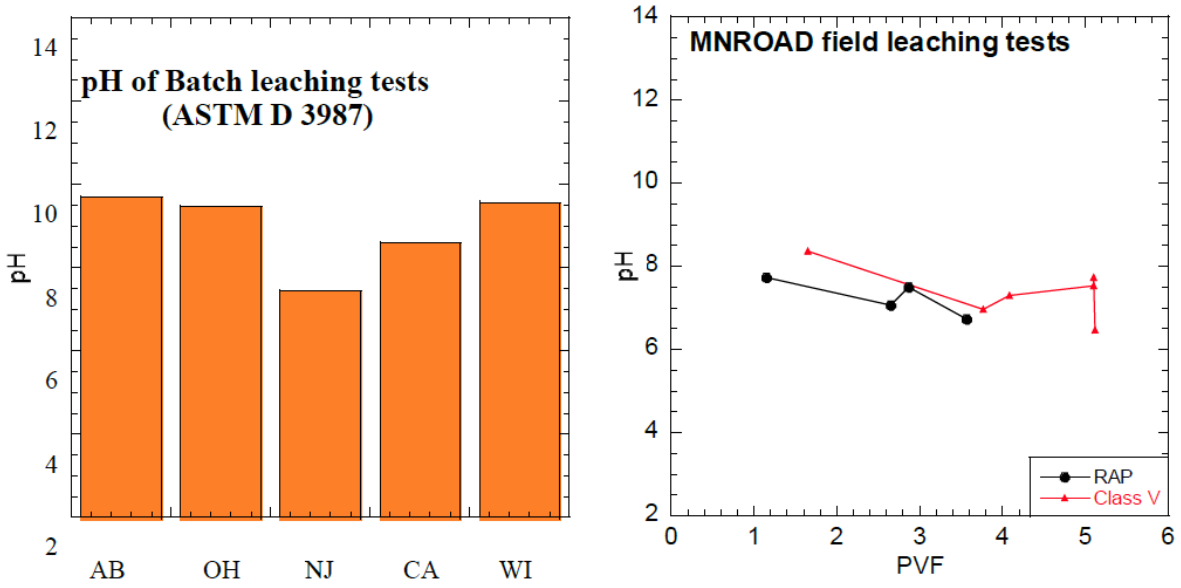

Figure 2.28. pH of recycled asphalt pavement (RAP) materials from batch leaching and field leaching tests (Edil et al. 2012)

Bituminous asphalt material consists of heavy metals and poly-aromatic hydrocarbons (PAHs), which are hazardous to the environment and human health (Shedivy et al. 2012). In a rainfall event, leaching of heavy metals and PAHs may be an issue and may affect groundwater quality and damage nature (Gupta et al. 2009).

2.3.1.2 Heavy Metal Leaching Characteristics

Asphalt surface, which will be crushed for RAP production, is directly subjected to traffic flow. Tire residuals, corrosion of steel crash barriers, or brake pad/disc residuals of vehicles may introduce several heavy metals to the asphalt surface (Muschack 1990; Hewitt and Rashed 1990, as cited in Shedivy et al. 2012). The main heavy metals that may create environmental issues are arsenic (As), aluminum (Al), cadmium (Cd), chromium (Cr), lead (Pb), silver (Ag), antimony (Sb), and selenium (Se) (Hoppe et al. 2015; Edil et al. 2012).

In general, heavy metal leaching from RAP is not a hazardous environmental issue, and almost all heavy metals found in leachates are equal to or lower than the EPA drinking water standards (Edil et al. 2012; Cosentino et al. 2003; Shedivy et al. 2012). A higher concentration of heavy metal may not indicate that RAP itself has the potential for hazardous metal leaching. For instance, a study conducted by Townsend and Brantley (1998) showed that the column leaching test concentrations of lead (Pb) was higher than the standard (15 ppb) in a RAP generated from a relatively aged asphalt surface. It was concluded that traffic flow or other environmental structures cause a lead (Pb) pollution in the asphalt surface (Townsend and Brantley 1998, as cited in Cosentino et al. 2003).

The liquid used in the batch or column leaching tests may affect the leaching characteristics of heavy metals, e.g., Cosentino et al. (2003) observed that while the concentration of cadmium (Cd) was below the detection limit when distilled-deionized water (DDW) was used, the concentration of Cd was higher than the detectable limit with the use of synthetic acid rain (SAR) as a liquid (Figure 2.29). In addition, an observed heavy metal concentration, which is initially higher, may reduce as time progresses because the leaching characteristics of RAP become more stable over time (Figure 2.29) (Cosentino et al. 2003).

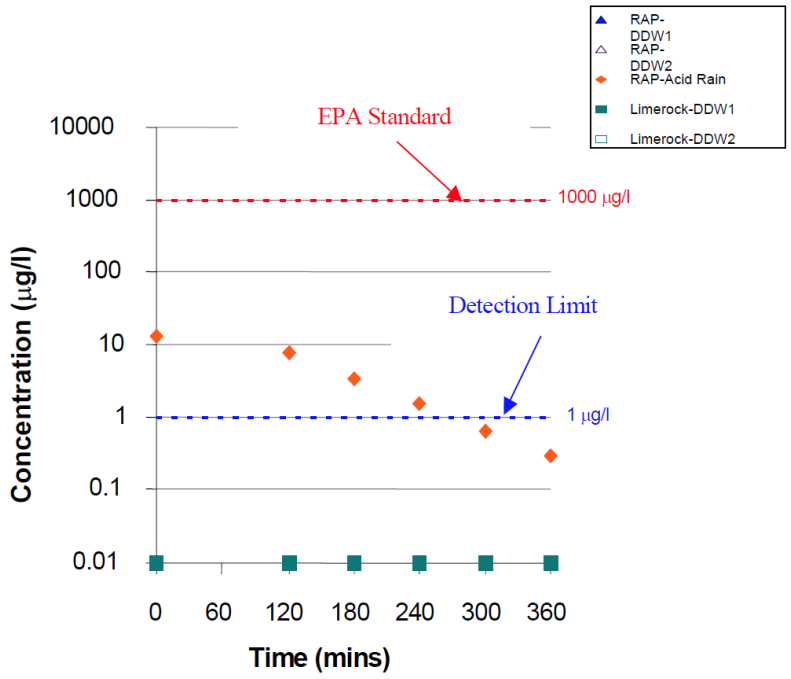

Figure 2.29. Column leaching test results of cadmium (Cd) with different test fluids (Cosentino et al. 2003)

2.3.1.3 Poly-Aromatic Hydrocarbons (PAHs) Leaching Characteristics

Incomplete burning of organic compounds is the main source of PAHs. It is speculated that tire residuals, exhaust gases, gasoline or diesel fuels are the sources of PAHs present in asphalt surface (Takada et al. 1990; Baek et al. 1991; Sadler et al. 1999; Brandt and De Groot 2001; Kriech et al. 2002, as cited in Shedivy et al. 2012). Some of the important PAHs that needed to be tested for better understanding the environmental properties of RAP are acenaphthylene, benzo(a)anthracene, and benzo(ghi)perylene (Grosenheider et al. 2006). In general, leaching of PAHs does not cause an environmental issue since their concentrations tend to be lower than the EPA drinking water standards according to laboratory leaching tests (Hoppe et al. 2015; Shedivy et al. 2012). The rate of dilution of RAP affects PAH concentrations. The general trend is that an increase in the liquid-solid ratio causes an increase in the amount of PAHs leached out (Shedivy et al. 2012).

2.3.2 Properties of Recycled Concrete Aggregate (RCA) Materials

Chemical and environmental properties of RCA have been investigated by several researchers (Bestgen et al. 2016a-b; Abbaspour et al. 2016; Engelsen et al. 2017). Leaching characteristics of RCA have been one of the major focus areas in terms of environmental properties because of the presence of the cement paste (Engelsen et al. 2010; Van Dam et al. 2011). In addition, other cement additives such as fly ash may be present in RCA, and they may intensify the leaching concern (Cetin et al. 2012). The other concern has been the alkalinity of the aqueous solutions of RCA (Van Dam et al. 2011).

Deicing applications to pavements during winter seasons may increase the chloride content of concrete pavement surfaces, which is one of the RCA sources. Chloride may cause corrosion of steel pipes or may affect the durability of RCA. Crushing of concrete surface into fine-grained RCA may contain a risk for potential failures due to the high chloride content; however, using coarse-grained RCA reduces the risk (ACPA 2009). In addition, since the aggregate base layer constructed with RCA has a porous structure, there is no serious concern about the volume change of the RCA base layer due to alkali-silica reactions (Van Dam et al. 2011). The cement paste contents of RCA should be well investigated because the cement content is the main parameter that affects the environmental properties of RCA (Bestgen et al. 2016b). Environmental properties of RCA are highly influenced by the source of the aggregate, the source of the contaminants, and the climate (Engelsen et al. 2017). As a result, the environmental properties of RCA should be investigated and should not be generalized because of the high variance of the parameters that affect the environmental properties.

2.3.2.1 pH Characteristics

The alkalinity of RCA is caused by the CaO and total Ca^{2+} compounds present in the cement paste (Cetin et al. 2013). As a result of the cement content of RCA, it is expected to demonstrate high pH values (Engelsen et al. 2009). Understanding the pH characteristics of RCA is important not only to assess the environmental effects of alkalinity but also to understand its leaching characteristics better since the pH has a great influence on the leaching of heavy metals (Engelsen et al. 2012; Bestgen et al. 2016a). The pH of RCA may be in a range of 10.5 to 13 (Steffes 1999; Chen et al. 2013; Abbaspour et al. 2016).

When RCA is exposed to the atmosphere, dissolved CO_2 from the atmosphere reacts with calcium hydroxide (or portlandite - $Ca(OH)_2$) and calcium-silicate-hydrate (C-S-H) gel present in the hardened concrete. The reaction forms calcium carbonate (calcite - $CaCO_3$), which reduces the pH and the leaching potential (Garrabrants et al. 2004; Gervais et al. 2004, as cited in Bestgen et al. 2016b). The carbonation content increases over time (Figure 2.30) (Abbaspour et al. 2016), and the pH of RCA decreases over time (Figure 2.31). pH values lower than 10 can be observed in fully carbonated concrete (Engelsen et al. 2017).

The stockpiled RCA tends to experience higher carbonation rates than the freshly crushed ones because the stockpiled RCA is exposed to weather events such as rain, which initiates more carbonation (Abbaspour et al. 2016). The initially-recorded pH values are the indication of whether a high degree of carbonation has occurred. For instance, the initial pH values of less than 12 show that RCA has undergone some previous carbonation (Abbaspour et al. 2016; Edil et al. 2012). Previously carbonated RCA could minimize further carbonation when used in the field which could be advantageous in terms of providing adequate drainage during its service life. However, it needs to be further studied to be determined. After the first contact with water, carbonation film around the particles, which is the reason for low pH values, dissolves, and the pH of RCA starts increasing due to the hydration of cement (Chen and Brown 2012).

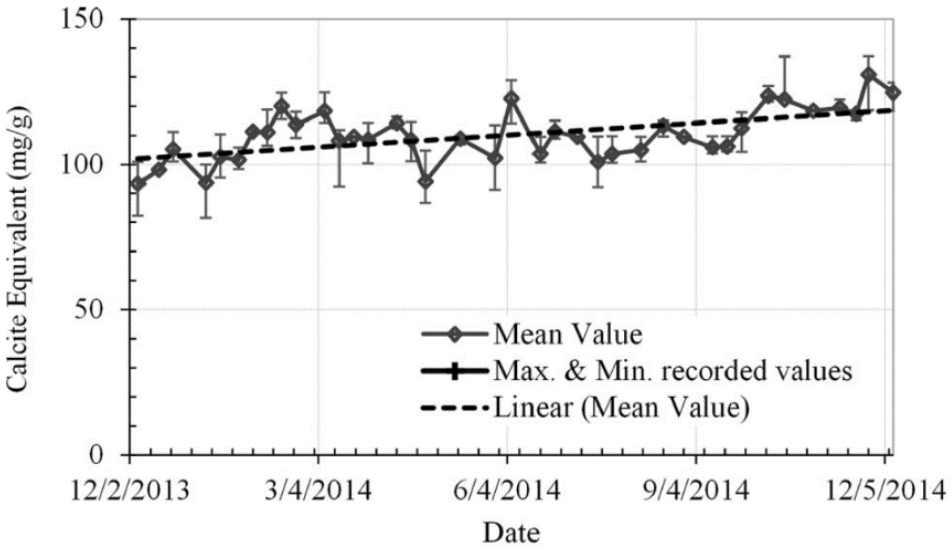

Figure 2.30. Change in carbonation over time (Abbaspour et al. 2016)

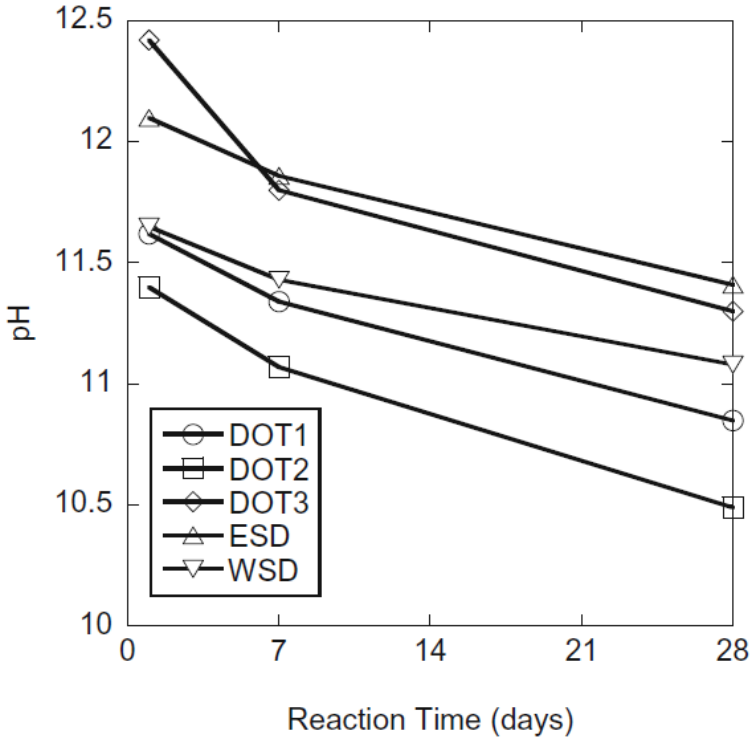

Figure 2.31. Change in pH of different recycled concrete aggregate (RCA) materials over time (Bestgen et al. 2016b)

2.3.2.2 Heavy Metal Leaching Characteristics

Unlike RAP, RCA is suspected of having a high leaching potential for several metals such as aluminum (Al), silicon (Si), calcium (Ca), magnesium (Mg), chromium (Cr), copper (Cu), iron (Fe), and zinc (Zn) at a high pH environment (Engelsen et al. 2009; Engelsen et al. 2010; Edil et al. 2012; Bestgen et al. 2016b; Abbaspour et al. 2016). Different leaching characteristics can be observed in the field and the laboratory since the laboratory conditions are more controlled (Figure 2.32). Each RCA shows different behaviors because of their different cement properties and different source materials. Some metals may exceed the EPA drinking water standards in some RCA; however, some of them may not show any hazardous leaching characteristics (Figure 2.33) (Edil et al. 2012; Gupta et al. 2018). However, it should be known that RCA has a higher potential for hazardous metal leaching than RAP due to its cement content.

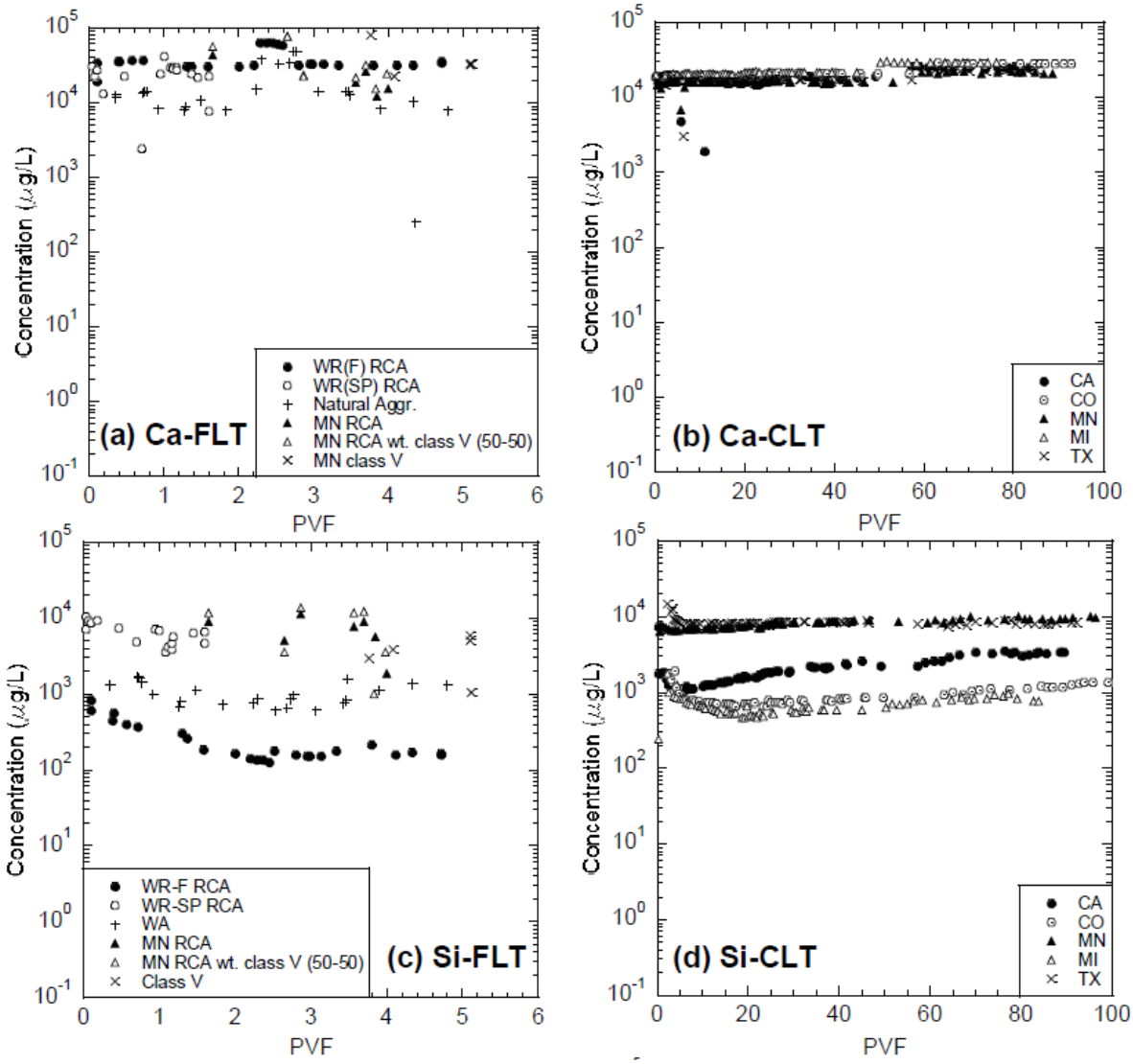

Figure 2.32. Difference between field leaching test (FLT) and column leaching test (CLT) as a function of pore volumes of flow (PVF) (Edil et al. 2012)

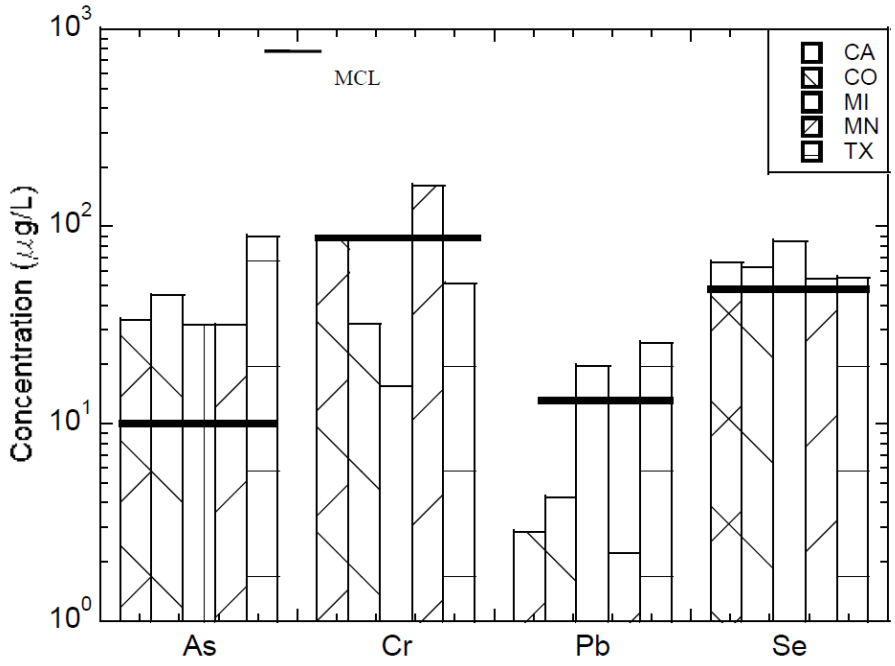

Figure 2.33. Concentrations of different metals and maximum contaminant levels (MCLs) for Environmental Protection Agency (EPA) drinking water standards (Edil et al. 2012)

Along with the pH, several other factors can affect the leaching characteristics of RCA, such as aging, the liquid-to-solid ratio (L/S ratio), and gradation (Bestgen et al. 2016a-b; Abbaspour et al. 2016). The total metal content of RCA does not significantly affect its leaching characteristics compared to the aforesaid parameters (Bestgen et al. 2016b).

The general trend for the effect of aging is that metal concentrations decrease with an increase in aging (Figure 2.34) (Bestgen et al. 2016a). The reason is that carbonation occurs as time progresses. Initially, carbonation occurs on the surface of the aggregate, and moves toward the center of the particle with time, and decrease the pH of the pore matrix (Roy 1986 and Taylor 1997, as cited in Abbaspour et al. 2016). Different leaching behaviors may be observed between the freshly crushed RCA and the stockpiled RCA, e.g., silicon (Si) concentration is lower in the freshly-crushed RCA compared to the stockpiled one (Edil et al. 2012).

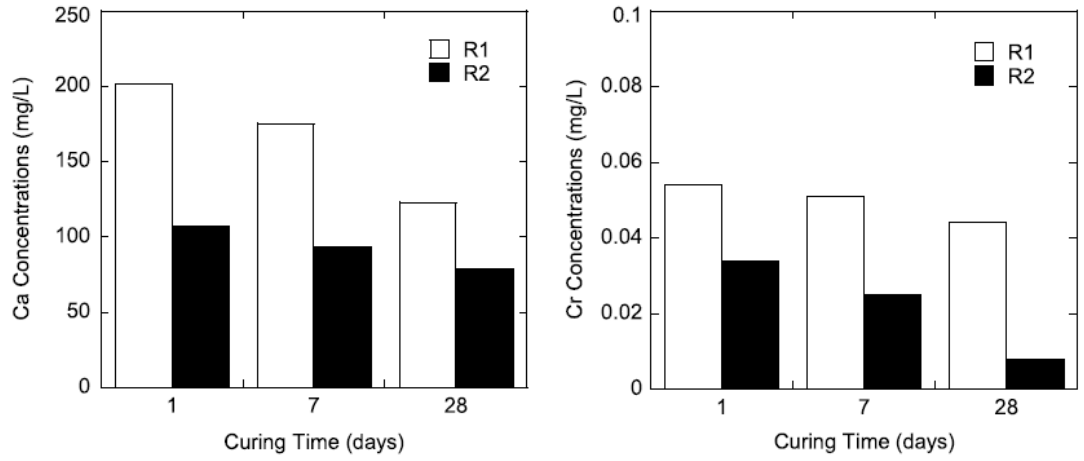

Figure 2.34. Concentrations of calcium (Ca) and chromium (Cr) with curing time (R1 and R2 represent RCA materials) (Bestgen et al. 2016a)

Increasing the liquid-to-solid ratio lowers the dissolved metal concentrations due to a higher dilution (Figure 2.35) (Bestgen et al. 2016a). The higher dilution causes a decrease in the pH of the aqueous solution, and a reduction of the pH may reduce the leaching activity of heavy metals from RCA (Gupta et al. 2018).

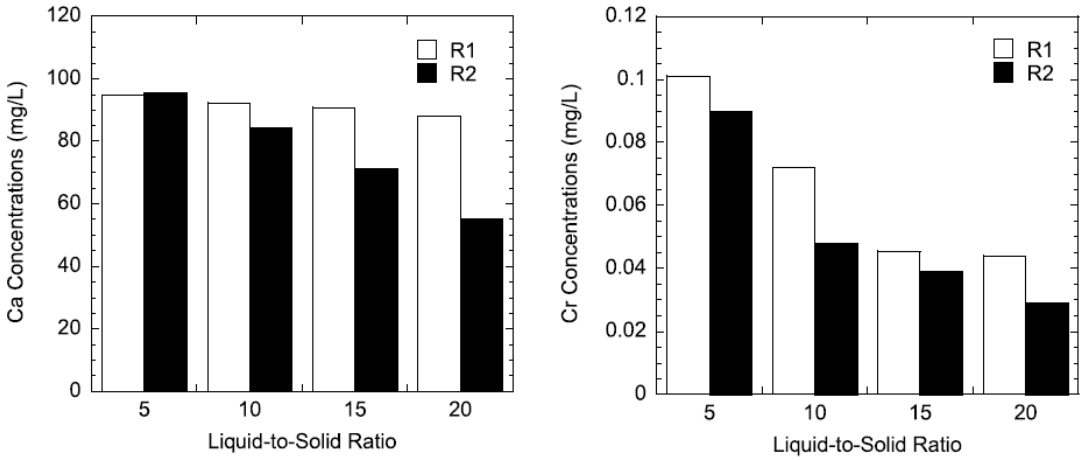

Figure 2.35. Effects of liquid-to-solid ratio on concentrations of calcium (Ca) and chromium (Cr) in leachates of different recycled concrete aggregate (RCA) (Bestgen et al. 2016a)

The specific surface area of the fine-grained aggregates is higher than that of the coarse-grained aggregates. Leaching is enhanced with a higher specific surface area because of increased interaction between the cement and the aqueous solution. In other words, the finer the aggregate, the higher the leaching concentrations (Figure 2.36) (Edil et al. 2012; Bestgen et al. 2016a). On the other hand, leaching of metals may decrease in the presence of fine-grained aggregates because more carbonation may occur on more particle surfaces with a high specific surface area (Chen et al. 2013). Lastly, more cement content may present in the fine-grained particles, which may be the reason for higher metal concentrations (Bestgen et al. 2016a).

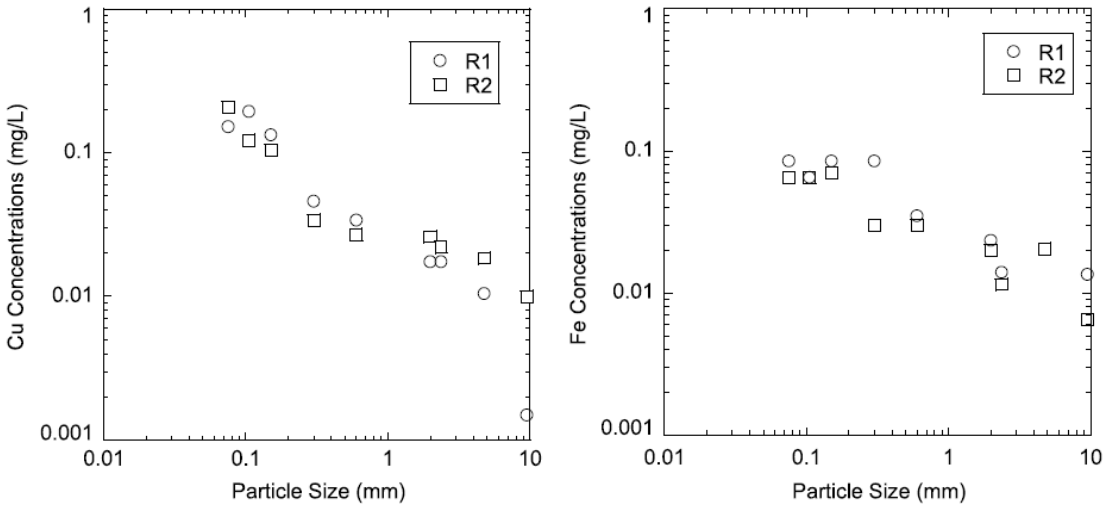

Figure 2.36. Effect of gradation of recycled concrete aggregate (RCA) on heavy metal concentrations in leachates (Bestgen et al. 2016a)

Another concern may arise with the use of RCA in aggregate base applications due to the tufaceous formation by leaching and precipitation of heavy metals (Ceylan et al. 2013; Abbaspour et al. 2016). First, CO_2 from the atmosphere and H_2O present in the aqueous solution of RCA react to form carbonic acid (H_2CO_3). Then, H^+ and CO_3 form after the two-step ionization of H_2CO_3. In the final step, Ca^{2+} released from the cement at the high pH environment reacts with CO_3 coming from the ionization of H_2CO_3, and the reaction forms calcite ($CaCO_3$) (Feldmann et al. 1982).

Drainage properties of aggregate base layers constructed with RCA and granular subbase layers can be reduced due to tufa formation. In addition, the pipes located beneath a pavement system for drainage purposes can be clogged by the tufa formation (Figure 2.37) (Ceylan et al. 2013). An effective drainage system is very critical in the long-term pavement performance, and a reduction in the drainage performance may cause severe pavement failures such as transverse cracking (Ceylan et al. 2015a). To minimize the problems related to the tufa formation, coarse-sized (bigger than No. 4 sieve) RCA can be used (Gupta and Dollimore 2002). Another method would be washing RCA before the aggregate base construction to fasten the carbonation process and move the cementitious materials away from the RCA matrix (Snyder and Bruinsma 1996).

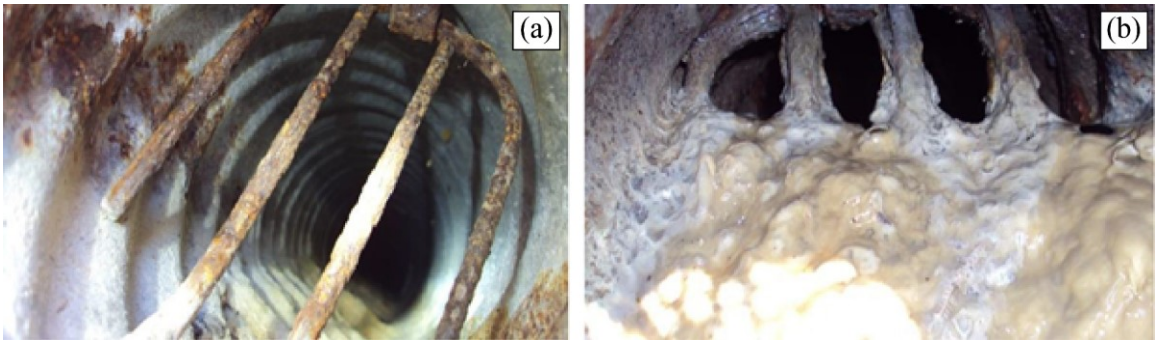

Figure 2.37. (a) Clean pipe and (b) partially-clogged pipe (Ceylan et al. 2013)

2.4 GEOSYNTHETIC APPLICATIONS

2.4.1 Functions of Geosynthetics

Weak subgrade soils reduce the general performance and service life of pavements. To improve the performance of pavements, geosynthetics, which are environmentally friendly, can be used (Abu-Farsakh et al. 2016). There are various types of geosynthetics (geotextiles, geogrids, geonets, geocomposites) used in different engineering applications (Skok et al. 2003a). In pavements, geotextiles and geogrids (Figure 2.38) are the two main geosynthetic types that are commonly used (Clyne 2011; Siekmeier and Casanova 2016; Zornberg 2017). Geotextiles can be woven or nonwoven. Along with that, geogrids can be uniaxial, biaxial, or multiaxial (Erickson and Drescher 2001; Zornberg 2017).

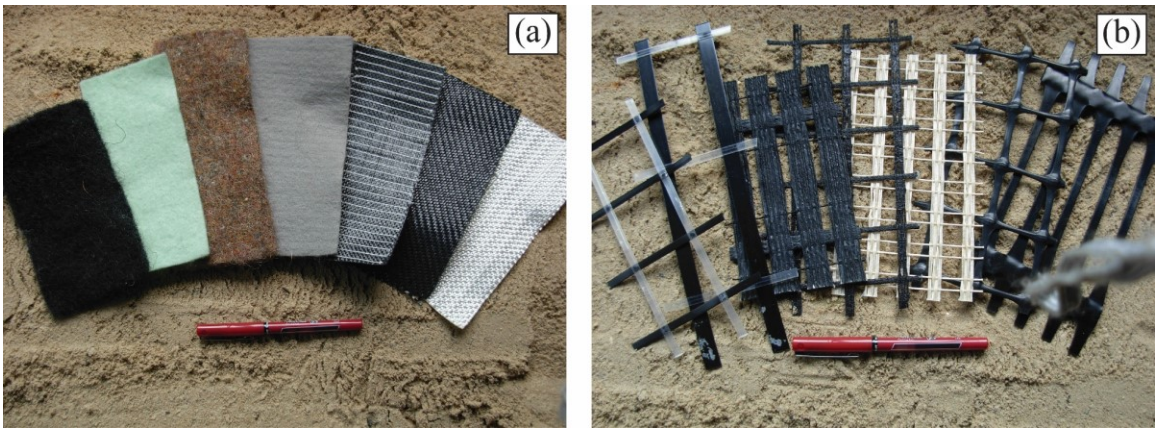

Figure 2.38. (a) Geotextiles [https://commons.wikimedia.org/wiki/File:Geotextile-GSI.JPG (date accessed: January 23, 2021)] and (b) geogrids [https://commons.wikimedia.org/wiki/File:Geogrids.JPG (date accessed: January 23, 2021)]

The main functions of geosynthetics in pavement systems are providing separation, filtration, and reinforcement (Zornberg 2012). To improve the performance of the layers beneath the surface, they can be used between the aggregate base and subbase or between subbase and subgrade (Clyne 2011; Zornberg 2017). Aggregate base layers tend to move into the soft subgrade layer because of the traffic loads and the compaction efforts during construction. The contamination of subgrade may cause serious problems as a result of a reduction in structural support. The presence of fine-grained aggregate particles in aggregate base layers may reduce the shear strength and permeability of the layers. It may also cause an increase in the frost-susceptibility of aggregate base layers, which may cause detrimental problems in the long term (Zornberg 2017). To prevent the dangerous interaction between aggregate base and subgrade layers, geosynthetics (mostly geotextiles) are used as a separation layer (Figure 2.39) (Erickson and Drescher 2001).

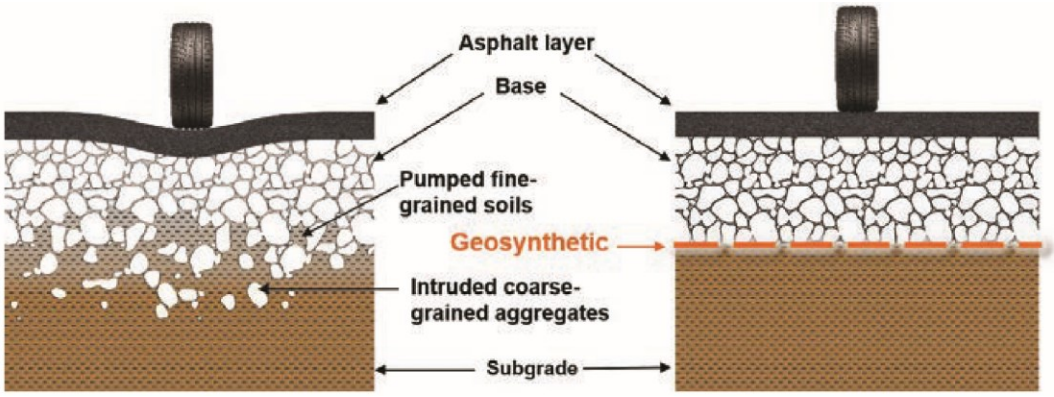

Figure 2.39. Separation function of geosynthetics (Zornberg 2017)

Fine-grained subgrade soils tend to move towards the aggregate base layers due to the upward movements of water. Geosynthetics can be used as a filtration layer between the aggregate base layers and subgrade to prevent the movement of fine-grained soils while allowing the free movements of the water molecules (Figure 2.40) (Zornberg 2012; Erickson and Drescher 2001). Due to the large opening sizes of geogrids, geotextiles are more suitable for filtration applications.

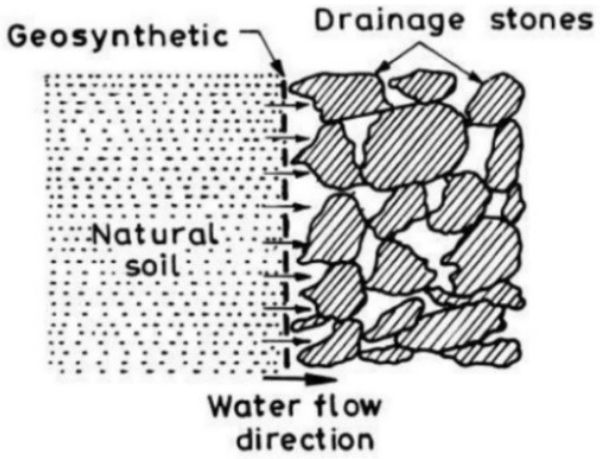

Figure 2.40. Filtration function of geosynthetics [https://www.slideshare.net/samirsinhparmar/lec-2-functions-and-selection-of-geosynthetics (date accessed: January 23, 2021)]

Using suitable geosynthetics can improve the bearing capacity of subgrade layers and minimize the permanent deformation (Perkins et al. 2005). A better load distribution mechanism can be obtained, and the stresses acting on subgrade soils can be reduced (Figure 2.41) (Zornberg 2012). Providing a lateral resistance, increasing the bearing capacity, and acting as a tensioned membrane are the three main mechanisms of the geosynthetic reinforcement (Holtz et al. 1998). The aggregate base layer thicknesses of pavements can be reduced by using geosynthetics. The use of these materials to reduce the aggregate base layer thickness usually does not affect the expenses for maintenance purposes in the long term. On the other hand, if geosynthetics are used without any change in the aggregate base layer thickness, the maintenance costs can be reduced (Perkins et al. 2005).

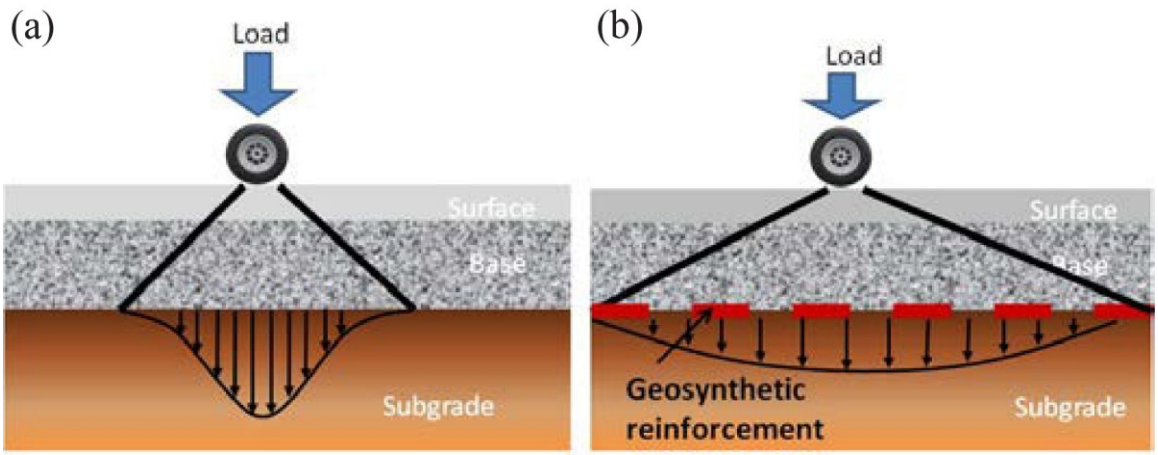

Figure 2.41. Load distribution mechanisms of (a) unreinforced pavement and (b) reinforced pavement (Zornberg 2012)

2.4.2 Effects of Using Geosynthetics

The most important benefit of using geosynthetics is a reduction in the overall pavement aggregate base layer deflection. Lower vertical stresses are observed in the pavement layers as a result of an enhanced load distribution mechanism. The layer thickness overlying the geosynthetic affects the performance and efficiency of geosynthetics. Kim et al. (2005) observed that the type of the geosynthetic used had no significant effect on the deflections in the presence of a thin pavement layer overlying the geosynthetic while a geogrid and a woven geotextile reduced the deflections more than a nonwoven geotextile under a thicker pavement layer. On the other hand, the effect of geosynthetics reduced with the increase in the layer thickness because more effective load distribution occurred throughout the thicker layer. The better load distribution caused lower strains in the region where geosynthetic was located (Kim et al. 2005). The geosynthetic used in pavement systems should have a higher stiffness than the layers that are intended to be improved. Otherwise, no improvement would be observed. The deflection of reinforced pavement layers is also dependent on Young's modulus of the used geosynthetic material (Figure 2.42) (Erickson and Drescher 2001).

The presence of a frictional interface and an interlocking mechanism are the other parameters that affect the performance of geosynthetics. If the loading is high, different behaviors would be seen between geogrids and geotextiles because of their different surface textures. For instance, coarse-grained aggregates can interlock between grid openings of geogrids, and the interlocking mechanism increases the integrity and stiffness of pavement layers (Tutumluer et al. 2012). On the other hand, if the loading is low, not much difference can be observed between geogrids and geotextiles (Erickson and Drescher 2001).

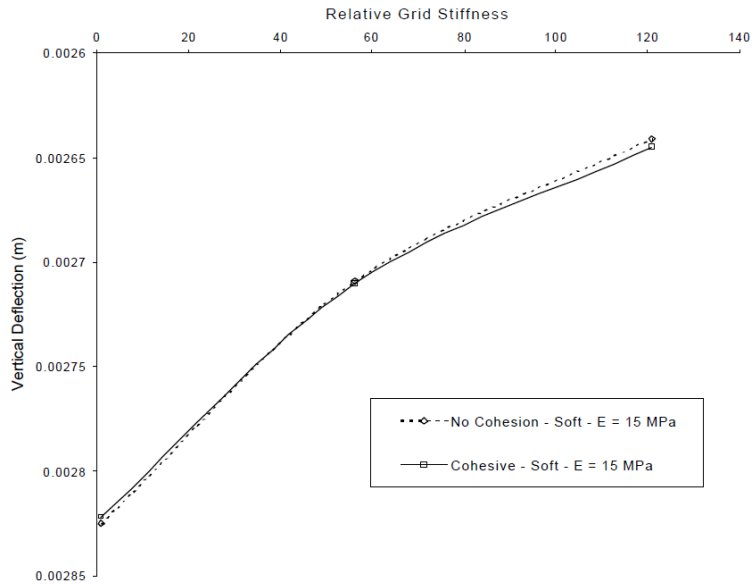

Figure 2.42. Effect of geosynthetics on deflections (Erickson and Drescher 2001)

Depending on the type, geosynthetics can be used as a tension member to avoid the failures caused by horizontal loading (Kim et al. 2005). Horizontal loads are transferred to geosynthetics (Figure 2.43), and if the geosynthetic used is stiff enough, it creates resistance against the loading thanks to its tensile strength. Thus, the shear strength of pavement layers increases. In addition to the improvements observed in the deflections and shear strength, the designed service life of pavements can be increased using geosynthetics (Erickson and Drescher 2001).

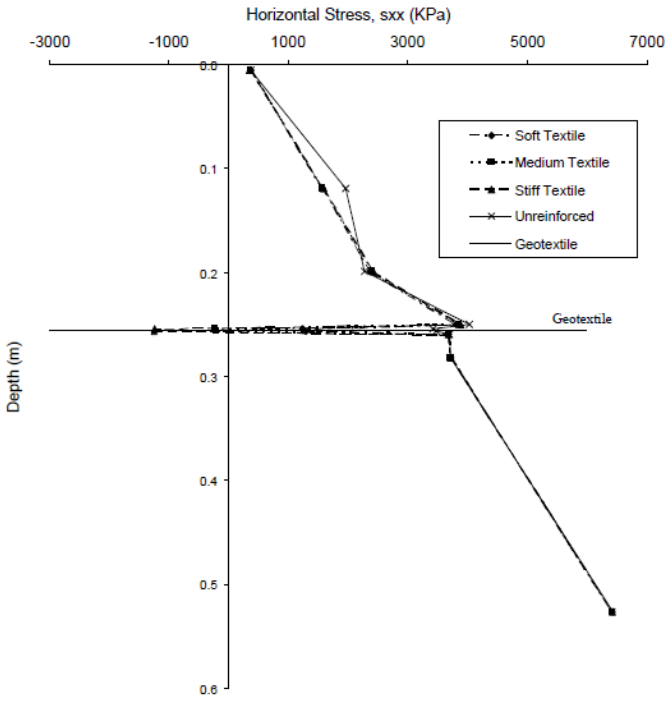

Figure 2.43. Horizontal load transfer through geosynthetic (Erickson and Drescher 2001)

2.5 DESIGN METHODS

The determination of surface, aggregate base, and subbase layers thicknesses is a very important step for constructing high-quality and long-lasting pavement systems. There have been methods and assumptions for using VA as an aggregate base or subbase layers; however, designing pavement systems with recycled (RAP and RCA) or unconventional aggregates (LSSB) may be challenging (Edil 2011; LRRB 2016). The engineering properties of aggregates are considered for design purposes; thus, the properties of RAP, RCA, and LSSB should be well understood. AASHTO 1993 and mechanistic-empirical (ME) pavement design methods are the most commonly used design methods for flexible and rigid pavements (Edil 2011; LRRB 2016). In addition, several local design methods are followed by some DOTs, such as the MnDOT Granular Equivalent Method or MnPAVE (Skok et al. 2003b; LRRB 2016).

2.5.1 AASHTO 1993 Pavement Design Method

2.5.1.1 General Design Method for Conventional and Recycled Aggregates

AASHTO 1993 pavement design method is an empirical method based on structural numbers (SN), indicating the structural capacity and role of each pavement layer. The thickness and stiffness of each layer are the main parameters that are needed to be determined to calculate the SN of each layer (Edil 2011). The overall SN of the entire flexible pavement system is calculated using Equation (2.1) (MacGregor et al. 1999; Zornberg 2012).

$$\log W_{18} = Z_R \times S_o + 9.36 \times \log(SN + 1) - 0.20 + \frac{\log\left(\frac{\Delta PSI}{2.7}\right)}{0.40 + \frac{1094}{(SN + 1)^{5.19}}} + 2.32 \times \log M_{R,SG} - 8.07 \qquad (2.1)$$

where W_{18} is the predicted number of 18-kip equivalent single-axle load (ESAL) over the design life of pavement, Z_R is the standard normal deviate for the reliability level, S_o is the combined standard error of traffic prediction and performance prediction, ΔPSI is the difference between the initial design serviceability index (p_o) and the design terminal serviceability index (p_t), and $M_{R,SG}$ is the resilient modulus of subgrade (psi).

From Equation (2.1), the total SN is calculated. Equation (2.2) is then used to determine the layer thicknesses (Locander 2009; Zornberg 2012; MacGregor et al. 1999). To determine the thicknesses, iterations are made (Zornberg 2012). The layer thicknesses are determined by considering not only the performance but also the minimum design requirements and economic aspects (MacGregor et al. 1999).

$$SN = (a_1 \times D_1) + (a_2 \times D_2 \times m_2) + (a_3 \times D_3 \times m_3) \qquad (2.2)$$

where a_1, a_2, and a_3 are the structural layer coefficients of surface, aggregate base, and subbase layers, respectively, D_1, D_2, and D_3 are the thicknesses of surface, aggregate base, and subbase layers (in), respectively, m_2 and m_3 are the drainage coefficients of aggregate base and subbase layers, respectively.

The structural layer coefficients of a_2 (for aggregate base) and a_3 (for subbase) are determined based on the stiffness of layers (Kim et al. 2005; Cetin et al. 2010). Equations (2.3) and (2.4) can be used to calculate the structural layer coefficients of aggregate base (a_2) and subbase (a_3) layers, respectively (AASHTO 1993; Edil 2011).

$$a_2 = 0.249 \times \log SRM - 0.44 \quad (2.3)$$

where a_2 is the structural layer coefficient of aggregate base layer, and SRM is the summary resilient modulus of aggregate (MPa).

$$a_3 = 0.227 \times \log M_{R3} - 0.839 \quad (2.4)$$

where a_3 is the structural layer coefficient of subbase layer, and M_{R3} is the resilient modulus of granular material (psi).

The general trend is that the layer coefficients increase with an increase in the M_R values of aggregate base and subbase layers (Figure 2.44) (Rada and Witczak 1982).

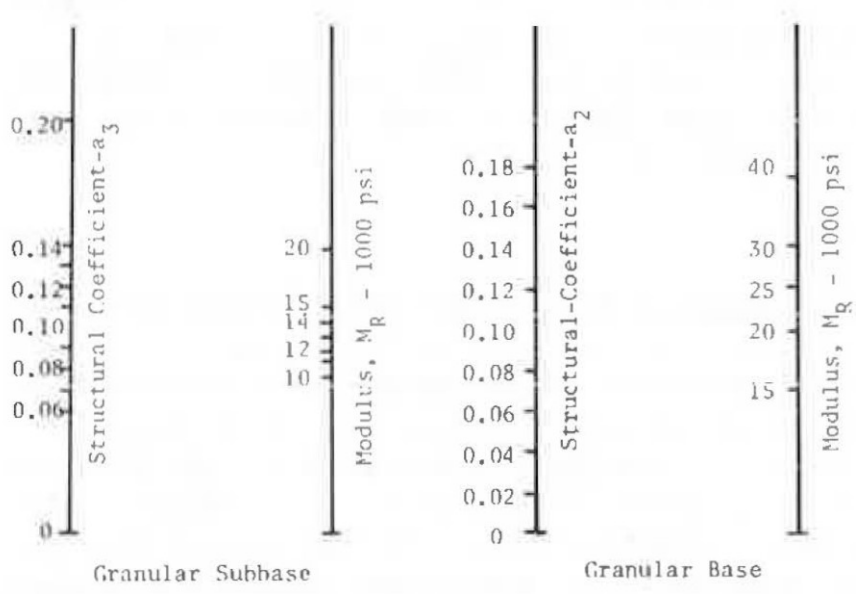

Figure 2.44. Structural layer coefficients of aggregate base and subbase layers (Rada and Witczak 1982)

In general, higher M_R values are observed for RAP and RCA compared to VA (MacGregor et al. 1999; Bennert et al. 2000; Cosentino et al. 2003; Abdelrahman et al. 2010). Thus, higher structural layer coefficients (a_2 and a_3) are expected for the layers constructed with RAP or RCA (MacGregor et al. 1999). A thinner aggregate base layer may be preferred if RCA having a relatively higher structural layer coefficient (a_2) than VA is used (Bestgen et al. 2016a). In addition to Equation (2.3), some values are recommended by Locander (2009) for a_2 (Table 2.3).

Table 2.3. Some recommended structural layer coefficients (Locander 2009)

Component	Coefficient
Aggregate Base with R-Value ≥ 83	0.14
Aggregate Base with 77 ≤ R-Value <83	0.12
Aggregate Base with 69 ≤ R-Value < 77	0.11
Aggregate Base with R-Value < 69	0.10
RAP Base, with RAP portion of material ≤ 30% of mixture	0.10 - 0.14
RAP Base, with RAP portion of material > 30% of mixture	0.15 - 0.25

R-value - response of aggregate to a vertically applied pressure

Effective drainage systems are critical in pavement designs because the long-term pavement performance is highly affected by water-related pavement performances and failures. Layer thickness, drainage path, the slope of the drainage layers, and hydraulic conductivity are the parameters that affect the drainage coefficients (MacGregor et al. 1999). Firstly, the time required to drain aggregate base layer to 50% saturation should be determined (Table 2.4). Secondly, the quality of drainage should be determined according to the time required obtained from Table 2.4 before determining drainage coefficients, m_2 and m_3 (Table 2.5). Lastly, the drainage coefficients are selected according to the quality of drainage, and the percent of the time pavement structure is exposed to moisture levels close to saturation (Table 2.6) (Locander 2009).

As mentioned before, RAP shows hydrophobic properties, while RCA shows hydrophilic properties (Edil et al. 2012; Rahardjo et al. 2010). Due to the hydrophobicity of RAP, it tends to have higher K_{sat} ($3.8x10^{-5}$ to $3.7x10^{-4}$ m/s) than RCA (about $1.8x10^{-5}$ m/s) (Nokkaew et al. 2012). If other parameters are constant, there is a direct relationship between the hydraulic conductivity and the drainage coefficients, e.g., the higher the hydraulic conductivity, the higher the drainage coefficient (MacGregor et al. 1999). Thus, it is expected that higher drainage coefficients should be used for RAP than those used for RCA.

Table 2.4. Determination of time to drain aggregate base layer to 50% saturation (Locander 2009)

Permeability, k (ft/day)	Porosity, n	Slope, S	Base Thickness			
			1 Foot		2 Feet	
			Drainage Path		Drainage Path	
			12 feet	24 feet	12 feet	24 feet
0.1	0.015	0.01	10	36	6	20
		0.02	9	29	5	18
1.0	0.027	0.01	2	6	5	18
		0.02	2	5	1	3
10.0	0.048	0.01	0.3	1	0.2	0.6
		0.02	0.3	1	0.2	0.6
100	0.08	0.01	0.05	0.2	0.03	0.1
		0.02	0.05	0.2	0.03	0.1

Note: the time required to drain the unbound layers presented in days.

Table 2.5. Determination of quality of drainage (AASHTO 1993; Locander 2009)

Water Removed Within	Quality of Drainage
2 Hours	Excellent
1 Day	Good
1 Week	Fair
1 Month	Poor
Water Will Not Drain	Very Poor

Table 2.6. Determination of drainage coefficients of aggregate base & subbase layers (AASHTO 1993; Locander 2009)

Quality of Drainage	Percent of Time Pavement Structure Is Exposed to Moisture Levels Approaching Saturation			
	Less Than 1%	1 - 5%	5 - 25%	Greater Than 25%
Excellent	1.40 - 1.35	1.35 - 1.30	1.30 - 1.20	1.20
Good	1.35 - 1.25	1.25 - 1.15	1.15 - 1.00	1.00
Fair	1.25 - 1.15	1.15 - 1.05	1.05 - 0.80	0.80
Poor	1.15 - 1.05	1.05 - 0.80	0.80 - 0.60	0.60
Very Poor	1.05 - 0.95	0.95 - 0.75	0.75 - 0.40	0.40

m_i can be used as 1 unless specific drainage information indicates otherwise.

2.5.1.2 Equivalency-Based Design Method

A pavement structure consisting of an aggregate base layer constructed with recycled aggregate is designed to obtain a structural capacity similar to a pavement structure consisting of an aggregate base layer constructed with conventional aggregates (Edil 2011). Designers and DOTs are familiar with designing pavement structures when conventional and well-known aggregates are used. In the Equivalency-Based Design Method, the overall structural numbers of pavements with or without recycled aggregates in the aggregate base layer are equalized.

In Equivalency-Based Design Method, the MnDOT Class 5 Aggregate is used as a standard aggregate for equating the structural numbers with the pavements built with recycled aggregates (MnDOT 2005, as cited in Edil 2011). Equations (2.5) and (2.6) are used for conventional (c) and recycled (r) aggregate base layer materials for the profiles provided in Figure 2.45 (Edil 2011).

$$SN_c = (a_1 \times D_1) + (a_c \times D_c) \quad (2.5)$$

$$SN_r = (a_1 \times D_1) + (a_r \times D_r) \quad (2.6)$$

where SN_c and SN_r are the structural numbers of the pavement structures containing conventional and recycled aggregate base layers, respectively, a_1, a_c and a_r are the structural layer coefficients of surface, conventional aggregate base, and recycled aggregate base layers, respectively, and D_1, D_c, and D_r are the thicknesses of surface, conventional aggregate base, and recycled aggregate base layers, respectively.

It is assumed that $SN_c = SN_r$. If the same HMA layers are used, Equation (2.7) is established (Edil 2011).

$$\frac{a_c}{a_r} = \frac{D_r}{D_c} \rightarrow \frac{D_r}{D_c} = \frac{0.249 \times \log SRM_c - 0.44}{0.249 \times \log SRM_r - 0.44} \quad (2.7)$$

where a_c and a_r are the structural layer coefficients of conventional and recycled aggregate base layers, respectively, D_c and D_r are the thicknesses of conventional and recycled aggregate base layers, respectively, and SRM_c and SRM_r are the summary resilient modulus of conventional and recycled aggregates (MPa), respectively.

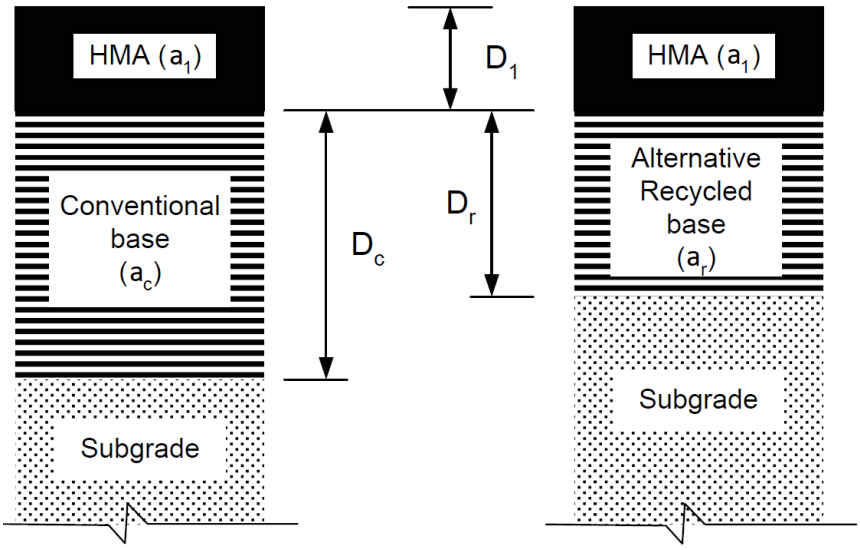

Figure 2.45. Pavement structures with conventional and recycled aggregate base layers (Edil 2011)

2.5.2 Mechanistic-Empirical (ME) Pavement Design Method

Unlike the AASHTO 1993 pavement design method, which is an empirical approach, plastic deformation is considered in the ME design, which is a mechanistic-empirical approach. Several parameters, such as the modulus values of layers, climate zone, traffic conditions, the designed service life of the pavement, and failure criteria, are used to predict the most suitable design conditions (Table 2.7). Design

thicknesses can be determined by making iterations for specific materials and other related conditions (Edil 2011). The required parameters for the analysis can be obtained for RAP, RCA, and VA, and the RAP-VA and RCA-VA mixtures for performance estimates of pavement systems.

Table 2.7. Some input parameters for mechanistic-empirical (ME) design (Edil 2011)

Traffic	Initial Two-Way	4000 AADTT		
	Number of Lanes	2		
	Operation Speed	110 km/h		
	Dual Tire Spacing	0.3 m		
	Tire Pressure	800 kPa		
Environment	I-94 Minnesota - USA			
Asphalt Binder Superpave Binder Grading	Thickness	0.1 m		
	A	10.98		
	VTS	-3.60		
Base Course A-1-a	Thickness	0.3 m		
	Modulus	RSG = 246 MPa RPM = 492 MPa Class 5 = 405 MPa SRPM = 845 MPa SRSG = 918 MPa		
Subgrade	Thickness	0.5 m		
	Modulus	70 MPa		
Rutting for Granular Materials				
Rutting Calibration Factor	RSG	RPM	Class 5	SRPM/ SRSG
B_{s1}	1.70	1.40	1.00	0.10

AADTT = annual average daily truck traffic; A = regression intercept; VTS = regression slope of viscosity temperature susceptibility; RSG = road surface gravel; RPM = recycled pavement material; SRPM = RPM with 10% fly ash (by weight); SRSG = RSG with 10% fly ash (by weight).

For conventional and recycled aggregates, M_R values should be obtained from laboratory or field tests. To determine the service life of pavements, rut depth or IRI values can be kept constant (Edil 2011). In addition, the modulus of a reinforced pavement layer can be entered directly (Kim et al. 2005).

2.5.3 Design Method for Large Stone Subbase (LSSB) Layers

Figure 2.46 provided by the Illinois Department of Transportation (IDOT) Subgrade Stability Manual (2005) shows remedial thickness (above subgrade) recommendations depending on the strength/stiffness of subgrades. As shown in Figure 2.46, the thickness of subbase layers can be determined considering several subgrade layer properties, such as cone index (CI), shear strength, and unconfined compressive strength (Q_u), etc.

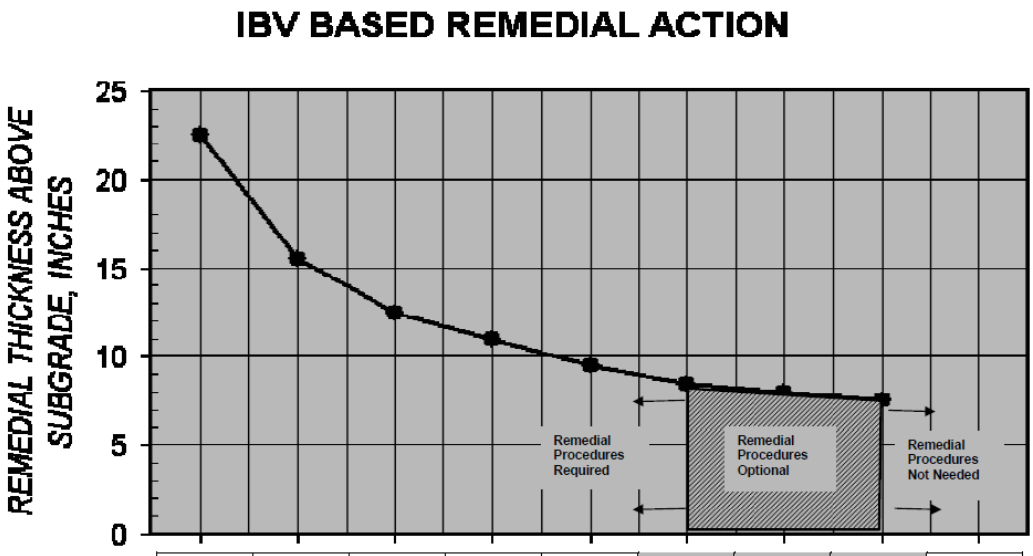

IBV	1	2	3	4	5	6	7	8	9
Cone Index(CI)	40	80	120	160	200	240	280	320	360
Shear Strength (psi)	2.25	4.50	6.75	9.00	11.25	13.50	15.75	18.00	20.25
Qu (tsf)	0.32	0.64	1.00	1.28	1.60	1.94	2.24	2.56	2.88
Rate (in./Blow)	4.6	2.6	2.0	1.5	1.3	1.1	1.0	0.9	0.8
Rate (Blows/6")	1.3	2.3	3.0	4.0	4.6	5.5	6.0	6.7	7.5
Treatment Thickness	22.5	15.5	12.5	11	9.5	8.5	8	7.5	0

Figure 2.46. Remedial thickness (above subgrade) recommendations depending on the subgrade conditions (IDOT 2005)

From the same manual (IDOT 2005), Table 2.8 also provides aggregate cover thickness reduction guidance when using geosynthetics [the table was developed by Kwon and Tutumluer (2003)]. Overall, the manual shows that aggregate cover thickness can be reduced using geosynthetics (geotextile or geogrid).

Table 2.8. Aggregate cover thickness reduction guidance when using geosynthetics (Kwon and Tutumluer 2003; IDOT 2005)

IBV/CI	Aggregate Cover without Geosynthetics in. (mm)	Aggregate Cover with Geotextile in. (mm)	Aggregate Cover with Geogrid in. (mm)
1/40	22 (560)	16 (405)	15 (375)
1.5/60	18 (450)	12 (300)	12 (300)
2/80	16 (400)	12 (300)	10 (250)
3/120	12 (300)	12 (300)	9 (230)

Wisconsin DOT's Facilities Development Manual (FDM) (2019) also provides thickness recommendations for several materials, including breaker run (100% passing through a 6-inch sieve) and select crushed material (90-100% passing through a 5-in sieve, 20-50% passing through a 1½-in sieve, and 0-10% passing through a No. 10 sieve). Figure 2.47 shows recommended thicknesses for breaker run stone and select crushed material with or without geogrids as an example. As can be seen from Figure 2.47, instead of constructing a 16-in large stone layer without any geogrid, a 12-in large stone layer with a geogrid could be constructed.

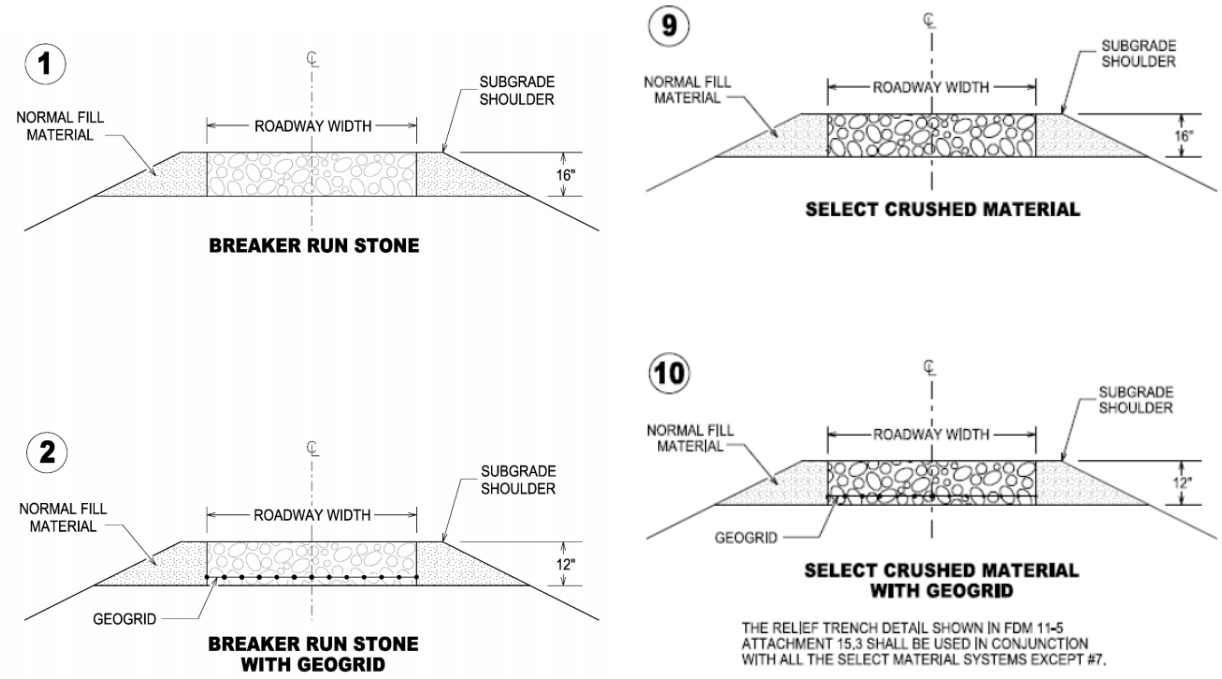

Figure 2.47. Thickness recommendations for breaker run and select crushed material (WisDOT 2019)

2.6 SELECTED PRACTICES OF DEPARTMENTS OF TRANSPORTATION (DOTS)

The state DOTs have established material specifications for pavement constructions for providing Quality Assurance (QA) practices. The materials that do not satisfy the specifications should be avoided because there is a higher risk of failure with the use of the off-specification materials (NCHRP 2017b).

2.6.1 California Department of Transportation (Caltrans)

In California, recycled aggregates generated from crushed existing asphalt concrete (AC) and Portland cement concrete (PCC) are commonly used in paved roads as aggregate base and subbase layers. Recycled aggregates must meet the grading and quality specifications stated for VA in the Caltrans Standard Specifications (CalRecycle 2014). While RAP and RCA were allowed up to 50% in their blends with VA before 2006, their uses have been allowed up to 100% since 2006 for aggregate base applications (CalRecycle 2014).

Sections 25 and 26 of the Caltrans Standard Specifications published in 2015 cover aggregate base and subbase applications of the recycled aggregates, respectively (Caltrans 2015). According to the stated sections, clean broken stone, crushed gravel, natural rough-surfaced gravel, sand, and reclaimed processed PCC and AC can be used as subbase and aggregate base layers. Per section 25, the aggregates used as subbase aggregate must meet the gradation ranges of Class 1, Class 2, or Class 3 Aggregate provided in Table 2.9. The aggregates should also show good quality characteristics provided in Table 2.10, depending on its class. Per section 26, the aggregates used as base aggregate must meet the gradations and show good quality characteristics of Class 2 or Class 3 Aggregate provided in Table 2.11 (Class 2 gradation), Table 2.12 (Class 2 quality specs), Table 2.13 (Class 3 gradation), Table 2.14 (Class 3 quality specs).

Table 2.9. Aggregate gradation for subbase applications (Caltrans 2015)

Sieve size	Percentage passing					
	Class 1		Class 2		Class 3	
	Operating range	Contract compliance	Operating range	Contract compliance	Operating range	Contract compliance
3"	100	100	100	100	100	100
2 1/2"	90–100	87–100	90–100	87–100	90–100	87–100
No. 4	35–70	30–75	40–90	35–95	50–100	45–100
No. 200	0–20	0–23	0–25	0–29	0–30	0–34

Table 2.10. Aggregate quality characteristics for subbase applications (Caltrans 2015)

Quality characteristic	Requirement					
	Class 1		Class 2		Class 3	
	Operating range	Contract compliance	Operating range	Contract compliance	Operating range	Contract compliance
Sand equivalent, (min)	21	18	21	18	21	18
Resistance, (R-value, min)	--	60	--	50	--	40

Table 2.11. Class 2 Aggregate gradation for aggregate base applications (Caltrans 2015)

Sieve size	Percentage passing			
	1-1/2 inch maximum		3/4 inch maximum	
	Operating range	Contract compliance	Operating range	Contract compliance
2"	100	100	--	--
1-1/2"	90–100	87–100	--	--
1"	--	--	100	100
3/4"	50–85	45–90	90–100	87–100
No. 4	25–45	20–50	35–60	30–65
No. 30	10–25	6–29	10–30	5–35
No. 200	2–9	0–12	2–9	0–12

Table 2.12. Class 2 Aggregate quality characteristics for aggregate base applications (Caltrans 2015)

Quality characteristic	Requirement	
	Operating range	Contract compliance
Resistance (R-value, min)	--	78
Sand equivalent (min)	25	22
Durability index (min)	--	35

Table 2.13. Class 3 Aggregate gradation for aggregate base applications (Caltrans 2015)

Sieve size	Percentage passing			
	1-1/2 inch maximum		3/4 inch maximum	
	Operating range	Contract compliance	Operating range	Contract compliance
2"	100	100	--	--
1-1/2"	90–100	87–100	--	--
1"	--	--	100	100
3/4"	50–90	45–95	90–100	87–100
No. 4	25–60	20–65	40–70	35–75
No. 30	10–35	6–39	12–40	7–45
No. 200	3–15	0–19	3–15	0–19

Table 2.14. Class 3 Aggregate quality characteristics for aggregate base applications (Caltrans 2015)

Quality characteristic	Requirement	
	Operating range	Contract compliance
Resistance (R-value) (min)	--	50
Sand equivalent (min)	21	18

2.6.2 Illinois Department of Transportation (IDOT)

While RAP is sometimes used as a subbase aggregate underlying VA, there is no application and specification related to the use of RAP as an aggregate base layer in Illinois (McGarrah 2007). Sections 311 and 351 of the IDOT Standard Specifications for Road and Bridge Construction published in 2016 allow crushed concrete produced from Portland cement concrete to be used along with crushed gravel and crushed stone for the aggregate base/subbase layers (IDOT 2016). Per section 1004, 20 different coarse aggregate types are defined for various applications (Table 2.15). Along with other suitable aggregates, crushed concrete should meet the requirements of CA6 or CA10 aggregates for aggregate base applications (Table 2.16) (IDOT 2016).

Per section 1004, different requirements are defined by Illinois DOT for quality control of aggregates (Table 2.17). Crushed concrete should be evaluated as a Class D Aggregate to check its quality in terms of Illinois Test Procedure (ITP) 96 (LA abrasion test). According to the LA Abrasion limit defined for Class D Aggregate, % abrasion loss should be less than 45%. In addition, crushed concrete should be evaluated as a Class C Aggregate for Illinois Test Procedure (ITP) 203, which is used to determine deleterious particles in coarse aggregate. However, instead of the given limit for deleterious materials (2%), the content of other deleterious materials should be limited to 7% with no more than 5% RAP (IDOT - Bureau of Materials and Physical Research). While the bearing ratio should be 80 for the aggregate base applications of typical materials, there is no requirement when crushed concrete is used (IDOT 2016).

Table 2.15. Gradation ranges of different aggregates (IDOT 2016)

Grad No.	COARSE AGGREGATE GRADATIONS												
	Sieve Size and Percent Passing												
	3 in.	2 1/2 in.	2 in.	1 1/2 in.	1 in.	3/4 in.	1/2 in.	3/8 in.	No. 4	No. 8	No. 16	No. 50	No. 200 [1/]
	75 mm	63 mm	50 mm	37.5 mm	25 mm	19 mm	12.5 mm	9.5 mm	4.75 mm	2.36 mm	1.18 mm	300 µm	75 µm [1/]
CA 1	100	95±5	60±15	15±15	3±3								
CA 2		100	95±5		75±15		50±15		30±10		20±15		8±4
CA 3		100	93±7	55±20	8±8		3±3						
CA 4			100	95±5	85±10		60±15		40±10		20±15		8±4
CA 5				97±3 [2/]	40±25		5±5		3±3				
CA 6				100	95±5		75±15		43±13		25±15		8±4
CA 7				100	95±5		45±15 [7/]		5±5				
CA 8				100	97±3	85±10	55±10		10±5		3±3 [3/]		
CA 9				100	97±3		60±15		30±15		10±10		6±6
CA 10					100	95±5	80±15		50±10		30±15		9±4
CA 11					100	92±8	45±15 [4/7/]		6±6		3±3 [3/ 5/]		
CA 12						100	95±5	85±10	60±10		35±10		9±4
CA 13						100	97±3	80±10	30±15		3±3 [3/]		
CA 14							90±10 [6/]	45±20	3±3				
CA 15							100	75±15	7±7		2±2		
CA 16							100	97±3	30±15		2±2 [3/]		
CA 17	100								65±20		45±20	20±10	10±5
CA 18	100				95±5				75±25		55±25	10±10	2±2
CA 19	100				95±5				60±15		40±15	20±10	10±5
CA 20							100	92±8	20±10	5±5	3±3		

Table 2.16. Typical aggregates for various applications (IDOT 2016)

Use	Gradation
Granular Embankment, Special	CA 6 or CA 10 [1/]
Granular Subbase:	
Subbase Granular Material, Ty. A	CA 6 or CA 10 [2/]
Subbase Granular Material, Ty. B	CA 6, CA 10, CA 12, or CA 19 [2/]
Subbase Granular Material, Ty. C	CA 7, CA 11, or CA 5 & CA 7 [3/]
Stabilized Subbase	CA 6 or CA 10 [4/]
Aggregate Base Course	CA 6 or CA 10 [2/]
Aggregate Surface Course:	
Type A	CA 6 or CA 10 [1/]
Type B	CA 6, CA 9, or CA 10 [5/]
Aggregate Shoulders	CA 6 or CA 10 [2/]

Table 2.17. Coarse aggregate quality control specifications (IDOT 2016)

COARSE AGGREGATE QUALITY				
QUALITY TEST	CLASS			
	A	B	C	D
Na_2SO_4 Soundness 5 Cycle, ITP 104 [1/], % Loss max.	15	15	20	25 [2/]
Los Angeles Abrasion, ITP 96, % Loss max.	40 [3/]	40 [4/]	40 [5/]	45
Minus No. 200 (75 µm) Sieve Material, ITP 11	1.0 [6/]	---	2.5 [7/]	---
Deleterious Materials [10/]				
Shale, % max.	1.0	2.0	4.0 [8/]	---
Clay Lumps, % max.	0.25	0.5	0.5 [8/]	---
Coal & Lignite, % max.	0.25	---	---	---
Soft & Unsound Fragments, % max.	4.0	6.0	8.0 [8/]	---
Other Deleterious, % max.	4.0 [9/]	2.0	2.0 [8/]	---
Total Deleterious, % max.	5.0	6.0	10.0 [8/]	---

Per section 303, crushed aggregate (crushed gravel, crushed stone, or crushed concrete) or RAP can be used for aggregate subgrade improvement (IDOT 2016). IDOT - Bureau of Design and Environment defines three new aggregates with gradation specifications named CS01 (8 in top size), CS02 (6 in top size), and RR01 (3 in top size) (Table 2.18) in addition to conventional CA2 and CA6 aggregates (Table 2.15) to widen the range of aggregates that can be used (Kazmee et al. 2016). RAP should be selected according to "Reclaimed Asphalt Pavement (RAP) for Aggregate Applications" provided by IDOT - Bureau of Materials and Physical Research. Up to 40% of well-graded RAP with a maximum of 100 mm (4 in) aggregate size can be mixed with CS01, CS02, and RR01 aggregates.

Table 2.18. CS01, CS02, and RR01 gradations (Kazmee and Tutumluer 2015)

Gradation Band	Coarse Aggregate Subgrade Gradations							
	Sieve Size and Percent Passing							
	203 mm	152 mm	102 mm	76 mm	51 mm	38 mm	4.76 mm	0.074 mm
	8"	6"	4"	3"	2"	1 ½"	#4	#200
CS 01	100	97 ± 3	90 ± 10		45 ± 25		20 ± 20	
CS 02		100	80 ± 10		25 ± 15			
RR 01				100		53 ± 23		

2.6.3 Minnesota Department of Transportation (MnDOT)

Section 2211 of the MnDOT Standard Specifications for construction published in 2018 allows both RAP and RCA to be used as aggregate base layer materials (MnDOT 2018). Per section 3138, aggregates are classified according to their quality characteristics, and they should meet the quality requirements of one of the classes described (Table 2.19). In addition, RAP and RCA should meet the quality requirements, which are the same for all aggregate classes (Table 2.20) (MnDOT 2018). Unless RAP content is less than 25% (by volume), the blend of RAP and aggregate is named recycled blend. A small percentage of aggregate (< 25%) can be mixed with aggregate with no change in the class of aggregate and no change in the quality control measurements specified for aggregate (McGarrah 2007). However,

when the RAP content exceeds 10% of the blend by volume, the gradation of RAP and aggregate blend must meet the specified gradation for the aggregate class (McGarrah 2007). RAP and VA must be blended at the crushing site, not at the job site with stockpiles aggregates (McGarrah 2007).

Almost all concrete pavements in Minnesota are recycled as dense-graded base aggregate material (Gonzalez and Moo-Young 2004). To avoid the drainage problems related to RCA (e.g., tufa formation), fine-grained (< No. 4 sieve) RCA particles must be eliminated. In addition, open-graded RCA can be mixed with natural aggregates to reduce the heavy metal leaching while improving the gradation of the blend (Snyder 1995, as cited in Gonzalez and Moo-Young 2004).

Per section 3138, the blends of VA and recycled aggregates containing less than 25% recycled aggregates used as a pavement aggregate base material should meet the gradations specified for different aggregate classes depending on the project (Table 2.21) (MnDOT 2018). If 25% or more recycled aggregates are used in the blends and if 75% or less recycled concrete is used, the mixture should meet the gradation criteria provided in Table 2.22. Lastly, if 75% or more recycled concrete is used, the mixture should meet the gradation criteria shown in Table 2.23 (MnDOT 2018).

Table 2.19. Quality requirements for virgin aggregates (VAs) (MnDOT 2018)

Requirement	Class			
	1 and 2	3 and 4	5 and 5Q	6
Max Shale, if No. 200 ≤ 7% by mass	NA	10.0%	10.0%	7.0%
Max Shale, if No. 200 > 7% by mass	NA	7.0%	7.0%	7.0%
Minimum Crushing Requirements *	NA	NA	10%	15%
Maximum Los Angeles Rattler (LAR) loss from carbonate quarry rock	40%	40%	40%	35%
Maximum Insoluble residue for the portion of quarried carbonate aggregates passing the No. 200 sieve	10%	10%	10%	10%
* Material crushed from quarries is considered crushed material.				

Table 2.20. Quality requirements for recycled aggregates (MnDOT 2018)

Requirement	Classes 1, 3, 4, 5, 5Q, and 6
Maximum Bitumen Content of Composite	3.5%
Maximum Masonry block %	10%
Maximum percentage of glass *	10%
Maximum size of glass *	¾ in
Crushing (Class 1, 5, 5Q, and 6) ‖	10% for Class 1 & 5 †, 60% for Class 5Q †, and 15% for Class 6 †
Maximum amount of Brick	1.0% #
Maximum amount of other objectionable materials including but not limited to: wood, plant matter, plastic, plaster, and fabric	0.3% #
* Glass must meet certification requirements on the Grading and Base website. Combine glass with other aggregates during the crushing operation. † If material ≥ 20% RAP and/or Concrete, Class 5 crushing requirement is met. † If material ≥ 60% RAP and/or Concrete, Class 5Q crushing requirement is met. † If material ≥ 30% RAP and/or Concrete, Class 6 crushing requirement is met. ‖ Material crushed from quarries is considered crushed material. # The Contractor/Supplier may not knowingly allow brick and other objectionable material and must employ a QC process to screen it out, before it becomes incorporated into the final product.	

Table 2.21. Gradation of base aggregate containing less than 25% recycled aggregates (MnDOT 2018)

Sieve Size	Class 1 (Surfacing £)	Class 2 (Surfacing β)	Class 3 (Subbase)	Class 4 (Subbase)	Class 5 (Base)	Class 5Q (Base)	Class 6 (Base)
2 in	—	—	100	100	—	100	—
1½ in	—	—	—	—	100	—	100
1 in	—	—	—	—	—	65 - 95	—
¾ in	100	100	—	—	70 - 100	45 - 85	70 - 100
⅜ in	65 - 95	65 - 90	—	—	45 - 90	35 - 70	45 - 85
No. 4	40 - 85	35 - 70	35 - 100	35 - 100	35 - 80	15 - 45	35 - 70
No. 10	25 - 70	25 - 45	20 - 100	20 - 100	20 - 65	10 - 30	20 - 55
No. 40	10 - 45	12 - 35	5 - 50	5 - 35	10 - 35	5 - 25	10 - 30
No. 200	8.0 - 15.0	5.0 - 16.0	5.0 - 10.0	4.0 - 10.0	3.0 - 10.0	0.0 - 10.0	3.0 - 7.0

* If product contains recycled aggregate, add letters in parentheses for each aggregate blend designating the type of recycled products included in the mixture.
(B) = Bituminous, (C) = Concrete, (G) = Glass
(BC) = Bituminous and Concrete, (BG) = Bituminous and Glass
(CG) = Concrete and Glass, (BCG) = Bituminous, Concrete, and Glass
£ Recycled concrete when used for surfacing is only allowed for shoulders
β Class 2 must be composed of 100% crushed quarry rock per 3138.2.B.2.

Table 2.22. Gradation of base aggregate containing 25% or more recycled aggregates & 75% or less recycled concrete (MnDOT 2018)

Sieve Size	Class 1 (Surfacing £)	Class 3 (Subbase)	Class 4 (Subbase)	Class 5 (Base)	Class 5Q (Base)	Class 6 (Base)
2 in	—	100	100	—	100	—
1½ in	—	—	—	100	—	100
1 in	—	—	—		65 - 95	
¾ in	100	—	—	70 - 100	45 - 85	70 - 100
⅜ in	65 - 95	—	—	45 - 90	35 - 70	45 - 85
No. 4	40 - 85	35 - 100	35 - 100	35 - 80	15 - 45	35 - 70
No. 10	25 - 70	20 - 100	20 - 100	20 - 65	10 - 30	20 - 55
No. 40	10 - 45 † 5 - 45	5 - 50	5 - 35	10 - 35	5 - 25	10 - 30
No. 200	5.0 - 15.0 † 0 - 15.0	0 - 10.0	0 - 10.0	0 - 10.0	0 - 10.0	0 - 7.0

* Add letters in parentheses for each aggregate blend designating the type of recycled products included in the mixture.
(B) = Bituminous, (C) = Concrete, (G) = Glass
(BC) = Bituminous and Concrete, (BG) = Bituminous and Glass
(CG) = Concrete and Glass, (BCG) = Bituminous, Concrete, and Glass
† Note: For Class 1, if the bitumen content is ≥ 1.5%, the gradation requirement is modified to 5 – 45% for the #40 sieve and 0 – 15.0% for the #200 sieve.
£ Recycled concrete is only allowed for shoulders

Table 2.23. Gradation of base aggregate containing more than 75% recycled concrete (MnDOT 2018)

Sieve Size	Class 1 (Surfacing £)	Class 3 (Subbase)	Class 4 (Subbase)	Class 5 (Base)	Class 5Q (Base)	Class 6 (Base)
2 in	—	100	100	100	100	100
1½ in	—	—	—	—		—
1 in	—	—	—	—	65 - 95	—
¾ in	100	—	—	45 - 100	45 - 85	45 - 100
⅜ in	65 - 95	—	—	25 - 90	35 - 70	25 - 85
No. 4	40 - 85	35 - 100	35 - 100	15 - 65	15 - 45	15 - 65
No. 10	25 - 70	20 - 100	20 - 100	10 - 45	10 - 30	10 - 45
No. 40	10 - 45	0 - 20	0 - 20	0 - 20	0 - 20	0 - 20
No. 200	5.0 - 15.0	0 - 6.0	0 - 6.0	0 - 6.0	0 - 6.0	0 - 6.0

* Add letters in parentheses for each aggregate blend designating the type of recycled products included in the mixture.
(B) = Bituminous, (C) = Concrete, (G) = Glass, (BC) = Bituminous and Concrete,
(BG) = Bituminous and Glass, (CG) = Concrete and Glass, (BCG) = Bituminous, Concrete, and Glass
£ Recycled concrete is only allowed for shoulders

As stated before, the price of VA has increased due to the huge demand in aggregate, the loss of natural resources, and federal/local restrictions regarding the aggregate production (ACPA 2009). Recycled aggregates are allowed to be used as base aggregates as alternatives to VA by MnDOT. However, investigations have been made by the Aggregate Resources Task Force (ARTF 2018) for increasing the efficiency of selecting and using VA sources. The investigation was about encouraging the use of the Aggregate Mapping Program developed by the Minnesota Department of Natural Resources (DNR) to widen the aggregate mapping across the State of Minnesota. The stated mapping tool is practical to locate the high-quality aggregate sources and ease accessing the aggregate deposits. In addition, the size of the aggregate resources can be identified. While some counties have mapping information available, 61 counties in Minnesota do not have any information regarding the aggregate qualities and their resources.

2.6.4 Missouri Department of Transportation (MoDOT)

Sections 304 and 1007 of the MoDOT Standard Specifications for Highway Construction published in 2018 allow the use of reclaimed asphalt and concrete aggregates as base aggregates as long as they meet the gradation specifications of Type 1 (Table 2.24), Type 5 (Table 2.25), and Type 7 (Table 2.26) Aggregates (MoDOT 2018). Type 1, Type 5, and Type 7 aggregates are defined as the aggregates that can be used for aggregate base applications (MoDOT 2018). Per section 1007, Type 1, Type 5, and Type 7 Aggregates should contain deleterious materials no more than 15%. Deleterious materials should be distributed uniformly along with sand, silt, and clay contents. The plasticity index (PI) of particles passing No. 40 sieve should not be more than 6 (MoDOT 2018).

Table 2.24. Gradation criteria of Type 1 Aggregate (MoDOT 2018)

Sieve	Percent by Weight
Passing 1-inch	100
Passing 1/2-inch	60-90
Passing No. 4	35-60
Passing No. 30	10-35

Table 2.25. Gradation criteria of Type 5 Aggregate (MoDOT 2018)

Sieve	Percent by Weight
Passing 1-inch	100
Passing 1/2-inch	60-90
Passing No. 4	35-60
Passing No. 30	10-35
Passing No. 200	0-15

Table 2.26. Gradation criteria of Type 7 Aggregate (MoDOT 2018)

Sieve	Percent by Weight
Passing 1 1/2-inch	100
Passing 1-inch	70-100
Passing No. 8	15-50
Passing No. 200	0-12

Per Section 303, durable stones containing no more than 10% (by weight) of earth, sand, shale, and non-durable rock are allowed for aggregate base applications in addition to Type 1, 5, and 7 Aggregates. The maximum particle size depends on the layer thickness. The maximum size should be about 12 in for an 18-in rock base. In addition, the maximum size should be about 9 in for a 12-in rock base. The size and quality of material are visually inspected for acceptance at the job site (MoDOT 2018).

2.6.5 Wisconsin Department of Transportation (WisDOT)

Section 301 of the WisDOT Standard Specifications published in 2018 allows various types of materials such as aggregates, breaker run, crushed gravel, crushed stone, pit run, reclaimed asphalt, and crushed concrete for different aggregate base applications (Table 2.27). Reclaimed asphalt is only suitable for dense 1 ¼-in aggregate base type, whereas crushed concrete is suitable for dense ¾-in, dense 1 1/4-in, and dense 3-in aggregate base types (WisDOT 2018). Materials should be free of deleterious materials such as shale, soft or porous rock fragments, coal, and organic particles.

Per section 301, reclaimed asphalt aggregates should contain at least 75% of reclaimed asphaltic pavement or surfacing. Crushed concrete aggregate should contain at least 90% crushed concrete, which is free of steel reinforcement or any other impurity. In addition, asphaltic pavement and surfacing material content should be lower than 10% in crushed concrete aggregate.

Crushed natural aggregates and recycled aggregates can be mixed at various percentages to create reprocessed materials or blended materials. Every single aggregate of blended materials must meet the specified aggregate base physical properties requirements (Table 2.28), and the final blend must meet the specified gradation (WisDOT 2018). Per section 305, dense-graded aggregates such as crushed stone, crushed gravel, and crushed concrete (except reclaimed asphalt) should meet the gradations provided in Table 2.29. For reclaimed asphalt, a material with 100% passing a 1 ¼-in sieve may be used for aggregate base layer application (WisDOT 2018).

Per section 301, crushed concrete can be mixed with up to 12% of glass, 7% of foundry slag, 75% of steel mill slag, 8% of bottom ash, and 7% of pottery cull (contents are by weight). Also, the listed by-products should be free of deleterious materials. Physical tests are conducted for the predominant material (WisDOT 2018).

Table 2.27. Suitability of various aggregate base materials (WisDOT 2018)

BASE TYPE	CRUSHED STONE	CRUSHED GRAVEL	CRUSHED CONCRETE	RECLAIMED ASPHALT	REPROCESSED MATERIAL	BLENDED MATERIAL
Dense 3/4-inch	Yes	Yes	Yes	No	Yes[1]	Yes[1]
Dense 1 1/4-inch	Yes	Yes	Yes	Yes	Yes	Yes
Dense 3-inch	Yes	Yes	Yes	No	Yes[2]	Yes[2]
Open-graded	Yes	Yes	No	No	No	No

[1] The contractor may provide reprocessed material or blended material as 3/4-inch base only if the material contains 50 percent or less reclaimed asphalt, by weight.

[2] Ensure that material is substantially free of reclaimed asphalt.

Table 2.28. Aggregate base physical properties (WisDOT 2018)

PROPERTY	CRUSHED STONE	CRUSHED GRAVEL	CRUSHED CONCRETE	RECLAIMED ASPHALT	REPROCESSED MATERIAL	BLENDED MATERIAL
Gradation AASHTO T27						
dense	305.2.2.1	305.2.2.1	305.2.2.1	305.2.2.2	305.2.2.1	305.2.2.1[1]
open-graded	310.2	310.2	not allowed	not allowed	not allowed	not allowed
Wear AASHTO T96 loss by weight	≤50%	≤50%	note[2]	___	note[2]	note[3]
Sodium sulfate soundness AASHTO T104 loss by weight						
dense	≤18%	≤18%	___	___	___	note[3]
open-graded	≤12%	≤12%	not allowed	not allowed	not allowed	not allowed
Freeze/thaw soundness AASHTO T103 loss by weight						
dense	≤18%	≤18%	___	___	___	note[3]
open-graded	≤18%	≤18%	not allowed	not allowed	not allowed	not allowed
Liquid limit AASHTO T89	≤25	≤25	≤25	___	___	note[3]
Plasticity AASHTO T90	≤6[4]	≤6[4]	≤6[4]	___	___	note[3]
Fracture ASTM D5821[6] min one face by count						
dense	58%	58%	58%	___	note[5]	note[3]
open-graded	90%	90%	not allowed	not allowed	not allowed	not allowed

[1] The final aggregate blend must conform to the specified gradation.

[2] No requirement for material taken from within the project limits. Maximum of 50 percent loss, by weight, for material supplied from a source outside the project limits.

[3] Required as specified for the individual component materials defined in columns 2 - 6 of the table before blending.

[4] For base placed between old and new pavements, use crushed stone, crushed gravel, or crushed concrete with a plasticity index of 3 or less.

[5] ≥75 percent by count of non-asphalt coated particles.

[6] as modified in CMM 8-60.

Table 2.29. Gradation requirements of dense-graded aggregate base materials except for reclaimed asphalt (WisDOT 2018)

	PERCENT PASSING BY WEIGHT		
SIEVE	3-INCH	1 1/4-INCH	3/4-INCH
3-inch	90 - 100	___	___
1 1/2-inch	60 - 85	___	___
1 1/4-inch	___	95 - 100	___
1-inch	___	___	100
3/4-inch	40 - 65	70 - 93	95 - 100
3/8-inch	___	42 - 80	50 - 90
No. 4	15 - 40	25 - 63	35 - 70
No. 10	10 - 30	16 - 48	15 - 55
No. 40	5 - 20	8 - 28	10 - 35
No. 200	2.0 - 12.0	2.0 - 12.0[1][3]	5.0 - 15.0[2]

Per section 312, crushed stone or crushed concrete are allowed for subgrade correction and improvement. Materials should be free of topsoil, organic materials, steel, or overburden materials. Crushed materials from deteriorated concrete or non-durable rock may be rejected. Materials should meet the specified gradation shown in Table 2.30 (WisDOT 2018).

Table 2.30. Gradation of large crushed materials (WisDOT 2018)

SIEVE	PERCENT PASSING (by weight)
5-inch	90 - 100
1 1/2-inch	20 - 50
No. 10	0 - 10

2.6.6 Michigan Department of Transportation (MDOT)

Sections 302 and 902 of the MDOT Standard Specifications for Construction published in 2012 allows the use of crushed concrete along with natural aggregate and iron blast furnace slag as long as they meet the gradation (Table 2.31) and quality (Table 2.32) specifications for Class 21AA, 21A, 22A, and 23A Dense-Graded Aggregates. Dense-graded aggregates can be mixed with fine-grained aggregates to satisfy the specifications. While crushed concrete should not contain more than 5% of brick, wood, plaster or asphalt by particle count, steel reinforcement pieces are allowed as long as they meet the specified gradation of stated dense-graded aggregate classes.

For environmental concerns such as heavy metal leaching, crushed concrete should not be used if there is no additional granular layer of at least 12 in (with Class I, II, IIA, or IIAA Aggregate - Table 2.33) between the dense-graded aggregate base and an underdrain which the dense-graded aggregate base drains into. In addition, a geotextile liner or geomembrane can be used as an alternative to a granular layer between the dense-graded aggregate base and the underdrain (MDOT 2012).

Table 2.31. Grading requirements for dense-graded aggregates (MDOT 2012)

Series/Class	Sieve Analysis (MTM 109) Total Percent Passing								Loss by Washing (MTM 108) % Passing
	1½ in	1 in	¾ in	½ in	⅜ in	No. 4	No. 8	No. 30	No. 200
21 AA	100	85-100	-	50-75	-	-	20-45	-	4-8
21 AA	100	85-100	-	50-75	-	-	20-45	-	4-8
22 A	-	100	90-100	-	65-85	-	30-50	-	4-8
23 A	-	100	-	-	60-85	-	25-60	-	9-16

Table 2.32. Physical requirements for dense-graded aggregates (MDOT 2012)

Series/Class	Crushed Material, % min (MTM 117)	Loss, % max, Los Angeles Abrasion (MTM 102)
21 AA	95	50
21 AA	25	50
22 A	25	50
23 A	25	50

Table 2.33. Grading requirements for granular materials (MDOT 2012)

Material	Sieve Analysis (MTM 109), Total % Passing (a)									Loss by Washing % Passing No. 200 (a), (b)
	6 in	3 in	2 in	1 in	½ in	⅜ in	No. 4	No. 30	No. 100	
Class I	—	—	100	—	45–85	—	20–85	5–30		0–5
Class II (c)	—	100	—	60–100	—	—	50–100	—	0–30	0–7
Class IIA (c)	—	100	—	60–100	—	—	50–100	—	0–35	0–10
Class IIAA	—	100	—	60–100	—	—	50–100	—	0–20	0–5
Class III	100	95–100	—	—	—	—	50–100	—	—	0–15
Class IIIA	—	—	—	—	—	100	50–100	—	0–30	0–15

a. Test results based on dry weights.
b. Use test method MTM 108 for Loss by Washing.
c. Except for use in granular blankets, Class IIA granular material may be substituted for Class II granular material for projects located in the following counties: Arenac, Bay, Genesee, Gladwin, Huron, Lapeer, Macomb, Midland, Monroe, Oakland, Saginaw, Sanilac, Shiawassee, St. Clair, Tuscola, and Wayne counties.

2.7 CHAPTER CONCLUSIONS AND RECOMMENDATIONS

In this chapter, a literature review was performed to provide detailed information about the index and engineering properties of recycled aggregates and LSSB materials used in pavement systems. General information about geosynthetics was provided. Methods to consider alternative materials and geosynthetics during pavement design were provided. Selected practices of departments of transportation (DOTs) were discussed. Based on the findings of this chapter, the following conclusions and recommendations were drawn.

- Changes in angularity and surface textures of recycled concrete and recycled asphalt aggregate particles should be investigated after compaction and under continuous traffic loads.
- Water retention curve characteristics of aggregates should be determined, and the effects of some material properties such as gradation, angularity, elongation, and water absorption capacity on this characteristic should be investigated.
- A methodology needs to be developed to determine the gradation of large stone-subbase (LSSB) materials.
- The impact of geosynthetics use with LSSB should be evaluated. This includes an evaluation of the impacts of geosynthetic types.

To address these issues, a test matrix including field and laboratory tests was developed in this project. Detailed information about these tests will be provided in the following chapters.

CHAPTER 3: CONSTRUCTION MONITORING AND PRELIMINARY PERFORMANCE EVALUATION OF TEST CELLS

3.1 TEST CELLS AND CONSTRUCTION

3.1.1 General Overview

The field study was conducted on eleven test cells constructed at the Minnesota Road Research Project (MnROAD) Low Volume Road (LVR), which is a pavement test facility owned by the Minnesota Department of Transportation (MnDOT) (MnDOT 2017). The MnROAD LVR, is a two-lane closed loop located near westbound I-94, northwest of Twin Cities, MN [Figure 3.1(a)]. Traffic on the MnROAD LVR is simulated by the MnROAD truck, which is a 5-axle tractor/trailer combination weighing 80 kip (36.3 Mg) (MnDOT 2013a). The MnROAD truck makes approximately 70 laps per day and it is operated in the inside lane (main traffic) only [Figure 3.1(b)]. The outside lane (occasional traffic) is dedicated to installing temperature and moisture sensors for environmental monitoring. Appendix A shows all the cells constructed at the MnROAD LVR and provides more information about the road lanes.

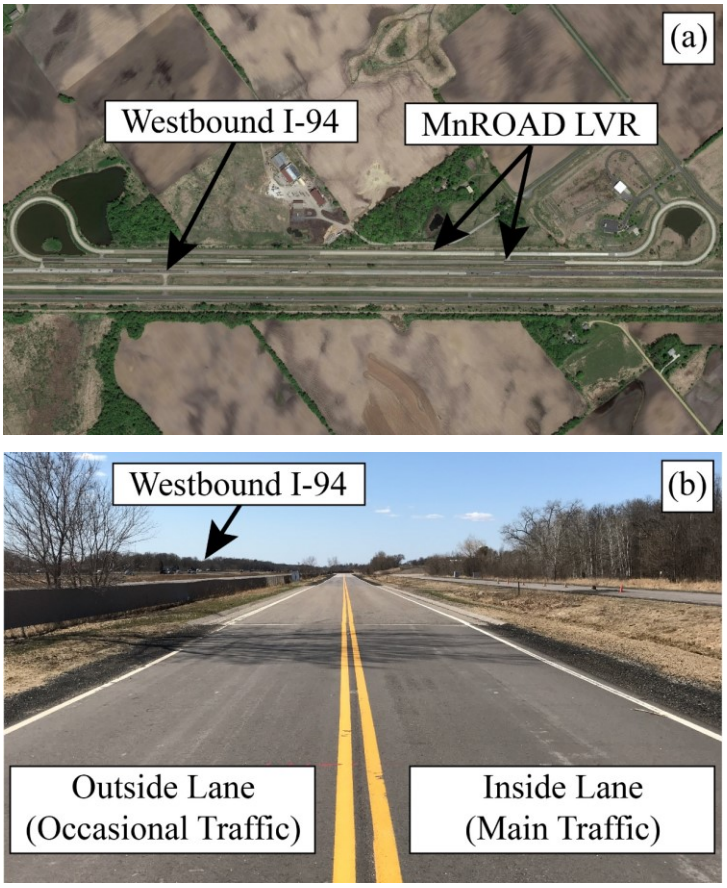

Figure 3.1. (a) Location and (b) traffic lanes of MnROAD LVR

The cells, located on the MnROAD LVR, contained three groups: (1) recycled aggregate base (RAB) group, (2) large stone subbase (LSSB) group, and (3) LSSB with geosynthetics group. A layout of the cells and their cross-sections are provided in Figure 3.2(a) and Figure 3.2(b), respectively. Cross-sectional elements and start and end stations of the cells are provided in Appendix B and Appendix C, respectively. More detailed information regarding the materials used to construct the cells is provided in Chapter 4.

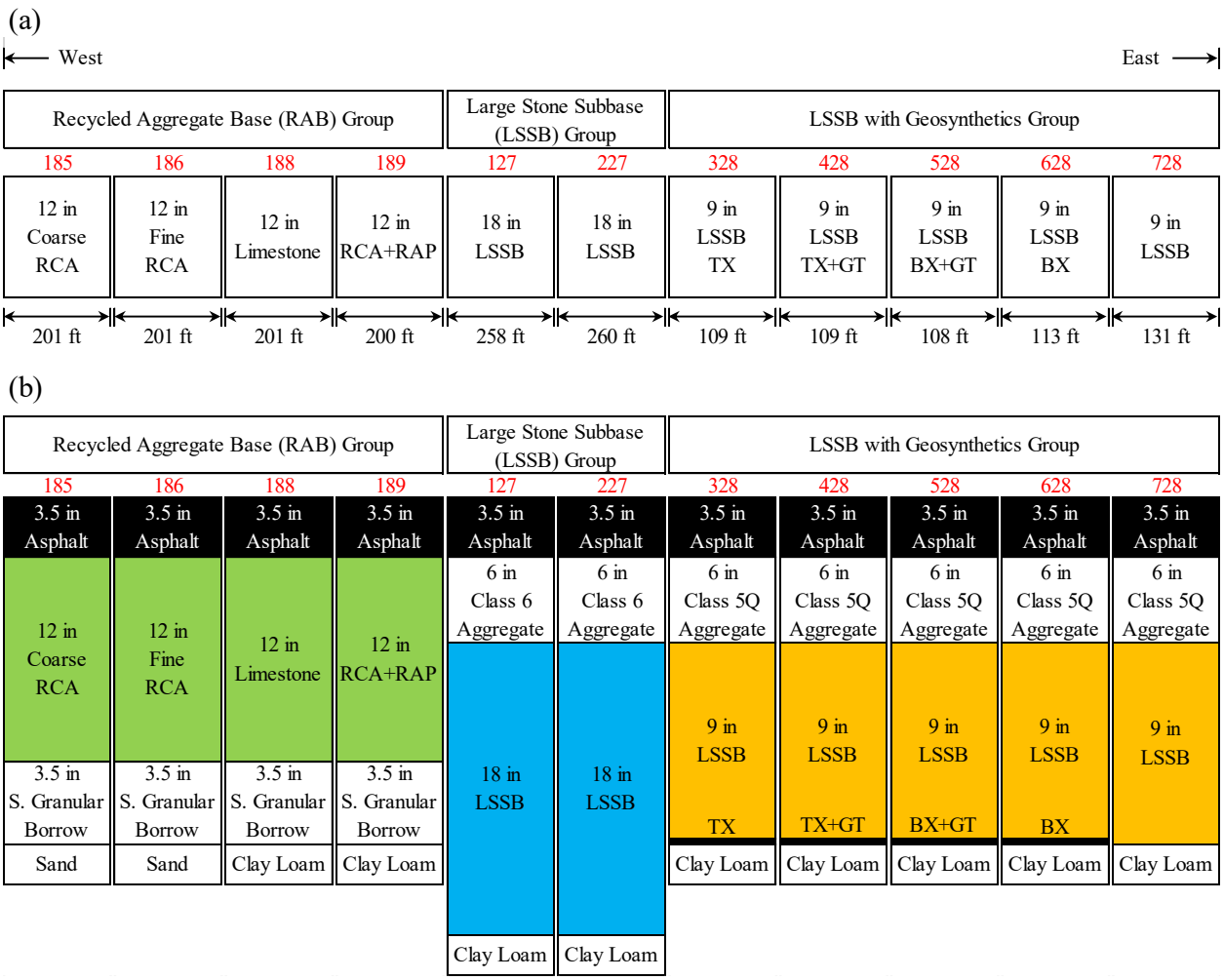

Figure 3.2. (a) Layout and (b) cross-sections of test cells (not to scale) (s. granular borrow = Select Granular Borrow, TX = triaxial geogrid, GT = needle-punched nonwoven geotextile, BX = biaxial geogrid)

3.1.2 Recycled Aggregate Base (RAB) Group

Cells 185, 186, 188, and 189 were designed to be approximately 200-ft (61 m) long [width of each lane is about 12 ft (3.7 m)]. Cells 185 and 186 were constructed over a sandy soil (named Sand Subgrade), and Cells 188 and 189 were constructed on a clayey soil (named Clay Loam). Each cell in this group contained identical 3.5-in (90-mm) subbase layers constructed using another sandy soil (named Select Granular Borrow (MnDOT 2018). Each cell contained 12-in (300-mm) aggregate base layers. Cells 185 and 186 were constructed with RAB layers using two RCA materials with different gradations. Coarser RCA

(named Coarse RCA) was used in the RAB layer of Cell 185, and finer RCA (named Fine RCA) was used in the RAB layer of Cell 186. A blend of RCA and RAP (named RCA+RAP) was used to construct the RAB layer in Cell 188. A crushed limestone aggregate (named Limestone) was used to construct the aggregate base layer in Cell 188. Each cell was covered with an identical 3.5-in (90-mm) asphalt layer. 0.5 in (12.5 mm) nominal maximum aggregate size (NMAS) Superpave was placed in two lifts [first and second lifts were 2.0-in (50-mm) and 1.5-in (40-mm) thick, respectively] for each asphalt layer (Van Deusen et al. 2018).

3.1.3 Large Stone Subbase (LSSB) Group

Cells 127 and 227 were designed to be approximately 260 ft (79.2 m) long [width of each lane is about 12 ft (3.7 m)]. Both cells were constructed on Clay Loam (AASHTO M 145). A very non-traditional subgrade preparation procedure was followed to create a weak subgrade with a dynamic cone penetration (DCP) index (DCPI) value between 2.5 and 3.5 in/blow (65 and 90 mm/blow) (ASTM D6951) for the upper 1 ft (0.3 m) of the subgrade soil. After constructing the subgrade to the desired elevation, the upper subgrade soil was loosened using shanks mounted to the back of a tracked dozer. Samples from the subgrade soil were taken to check moisture content. It was observed that the moisture content values were far below the optimum moisture content. A water truck was used to supply water to reach the target moisture content [Figure 3.3(a)]. The watered subgrade soil was mixed with dozer/ripper to obtain a somewhat uniform layer for the upper subgrade layer [Figure 3.3(b)]. Repetitive DCP tests (ASTM D6951) were performed to check whether the intended DCPI value was achieved. Minimum and maximum numbers of blows were determined as 3 and 5, respectively, to obtain 12 in (300 mm) of penetration in order to be within the target DCPI values. However, the higher end was relaxed as the construction schedule did not permit a waiting period for drying the soil (David Van Deusen, personal communication). The loosened subgrade soil at the optimum moisture content was mellowed overnight and checked to ensure that the subgrade soil satisfied the strength requirements. Then, LSSB layers were constructed over the prepared subgrade layers using a crushed granite stone (named LSSB Material) (Figure 3.4) (Van Deusen et al. 2018).

The original design was to construct 18-in (460-mm) LSSB layers with 1 lift and 2 lifts for Cells 127 and 227, respectively. However, Cell 227 was also constructed with 1 lift similar to Cell 127 because it was observed that dividing LSSB layer construction into 2 lifts was not practical. After the completion of 18-in (460-mm) LSSB layers, 6-in (150-mm) aggregate base layers were constructed with a recycled aggregate showing Class 6 material's gradation properties (MnDOT 2018) (named Class 6 Aggregate). Lastly, each cell was covered with similar asphalt layers used in the RAB group (Van Deusen et al. 2018).

Figure 3.3. (a) Moisture content adjustment for subgrade soil and (b) prepared subgrade (White and Vennapusa 2017)

Figure 3.4. Placement of LSSB Material (White and Vennapusa 2017)

3.1.4 Large Stone Subbase (LSSB) with Geosynthetics Group

Cells 328, 428, 528, and 628 were designed to be approximately 110 ft (33.5 m) long and Cell 728 was designed to be around 130 ft (39.6 m) long [width of each lane is about 12 ft (3.7 m)]. In fact, the original design was to build only two cells (Cells 128 and 228) with 9-in (230-mm) LSSB layers placed over specially prepared Clay Loam subgrade soil (AASHTO M 145) (similar preparation procedure described for Cells 127 and 227) with no geosynthetics [each cell was around 250 ft (76.2 m) long]. However, after the placement of LSSB layers, pumping of subgrade soil into LSSB layers (Figure 3.5) and aggregate base layer rutting were observed in those cells under construction traffic (Appendix E). A comparison between successfully constructed 18-in (460-mm) LSSB layer in Cell 227 and failed 9-in (230-mm) LSSB layer in Cell 128 is provided in Figure 3.6. Surface rutting was also observed shortly after paving the aggregate base layers (White and Vennapusa 2017); thus, Cells 128 and 228 were excavated to subgrade layers for reconstruction [Figure 3.7(a) and Figure 3.7(b)]. Cell 228 could not be fully removed because of the presence of near-surface utilities in an area to the east; thus, around 130 ft (39.6 m) of that cell was kept in place and numbered as Cell 728 (Van Deusen et al. 2018).

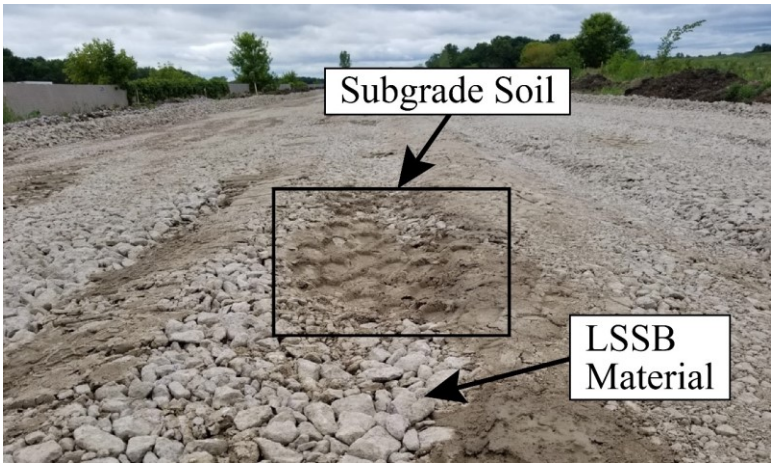

Figure 3.5. Pumped subgrade soil in Cells 128 and 228 (White and Vennapusa 2017)

Figure 3.6. Subbase layers of Cells 128 and 227 (Van Deusen et al. 2018)

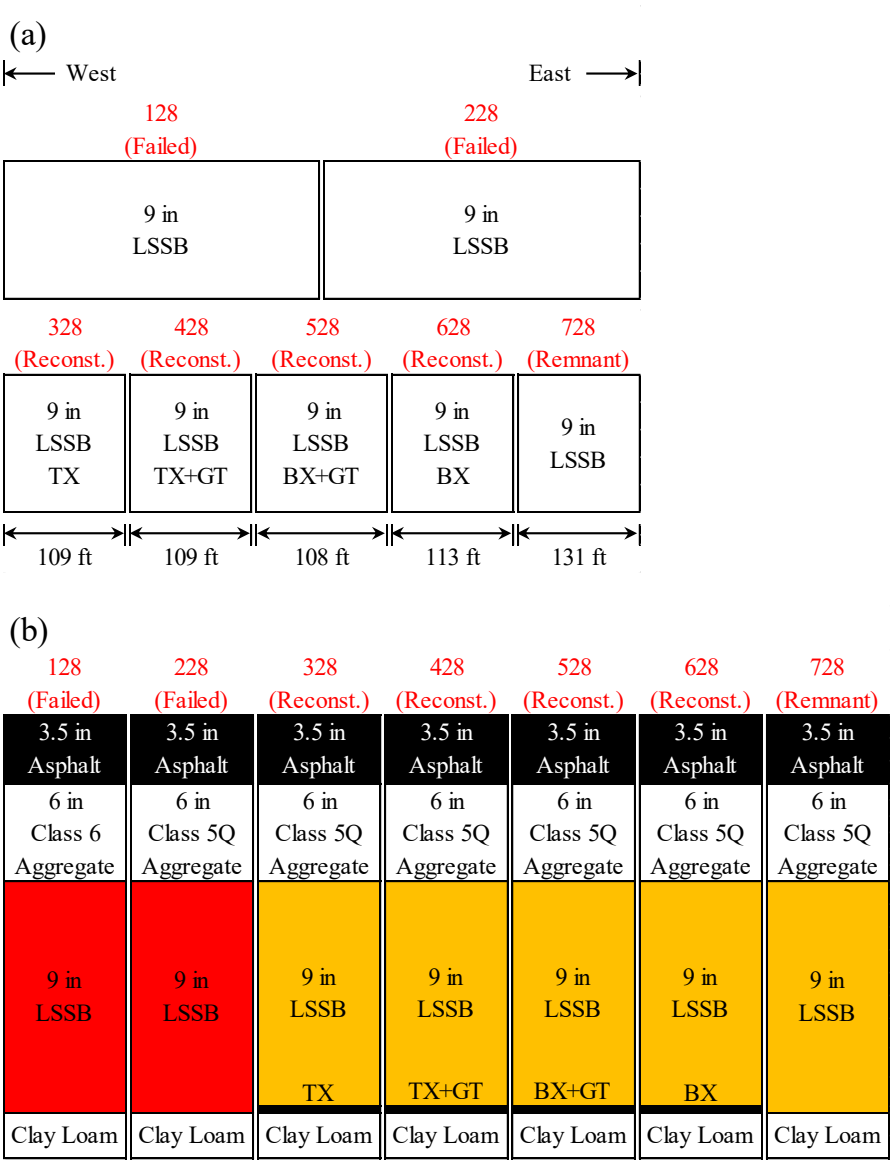

Figure 3.7. (a) Layout and (b) cross-sections of failed, reconstructed, and remnant cells (not to scale) (TX = triaxial geogrid, GT = needle-punched nonwoven geotextile, BX = biaxial geogrid)

Procedures similar to those followed for Cells 127 and 227 were used to prepare the subgrade soil for Cells 328, 428, 528, and 628. Geosynthetics were placed on top of the subgrade soil to prevent subgrade soil pumping into LSSB layers [Figure 3.8(a)]. More detailed information about geosynthetics used is provided in Appendix F. Tensar TriAx TX190L (triaxial geogrid - named TX) was used alone in Cell 328 and used with SKAPS GT-116 (needle-punched nonwoven geotextile - named GT) in Cell 428. In addition, Tensar BX1300 (biaxial geogrid - named BX) was used with the same geotextile in Cell 528 and used alone in Cell 628. Both geogrids were placed over geotextile to obtain the mechanical benefits from interlocking between geogrids and LSSB Material [Figure 3.8(b)]. Coarse-grained aggregates can interlock between grid openings of geogrids and the interlocking mechanism increases the integrity and stiffness of pavement layers (Tutumluer et al. 2012). No geosynthetic was placed in Cell 728 since it was

not reconstructed. After placing the geosynthetics, 9-in (230-mm) LSSB layers were constructed (Figure 3.9). A recycled aggregate showing Class 5Q material's gradation properties (named Class 5Q Aggregate) was used to construct 6-in (150-mm) aggregate base layers overlying LSSB layers. After completing the construction of LSSB layers and aggregate base layers successfully, all the cells except Cell 728 were paved with similar asphalt material (Cell 728 was already paved with similar asphalt material) (Van Deusen et al. 2018).

Figure 3.8. Placement of (a) geotextile and (b) triaxial geogrid over geotextile (White and Vennapusa 2017)

Figure 3.9. Placement of LSSB Material over geosynthetics (White and Vennapusa 2017)

3.2 DATA COLLECTED DURING AND SHORTLY AFTER CONSTRUCTION

3.2.1 Meteorological Data

Meteorological data including air temperature, relative humidity, wind speed, and precipitation were collected by external weather stations located at the MnROAD LVR before, during, and after construction. The variation of air temperature between 7/1/2017 and 12/1/2017 is provided in Figure 3.10. Data regarding relative humidity, average wind speed, and precipitation between the mentioned dates are provided in Appendix G. The minimum and maximum air temperatures were observed to be 40°F (4.4°C) and 91°F (32.8°C) during construction [average temperature was 67°F (19.4°C)]. In addition, relative humidity values ranging between 15 and 102% were observed during construction (Appendix G). Relative humidity values higher than 100% were observed only on 8/10/2017. Except for that day, the maximum relative humidity was 99.7% during construction.

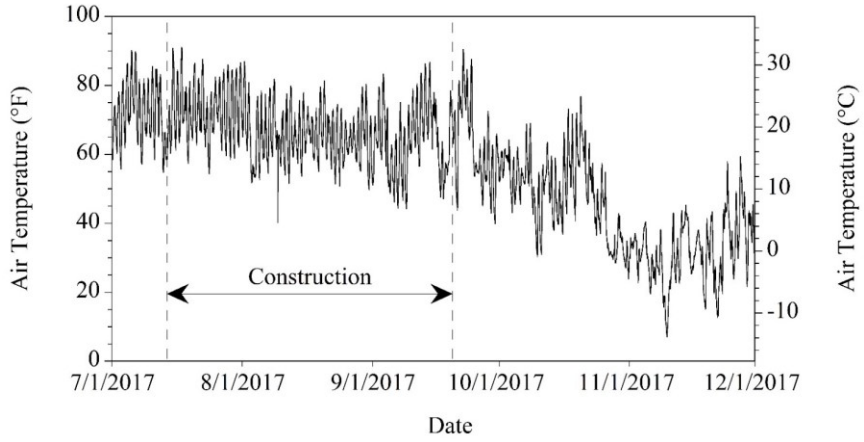

Figure 3.10. Air temperature data collected from weather stations

3.2.2 Nuclear Density Test

Seaman C-200 nuclear density gauge (NDG) was used to measure in-situ density and moisture content data from each cell (MnDOT 2009a). Data was collected from subgrade (for Cells 185 to 189), aggregate base (for each cell), and asphalt (for Cells 185, 127, 227) layers. For aggregate base and subgrade layers, direct transmission test method was performed at 4, 6, or 8 in depths (depending on the layer thickness) in cases where the test hole stayed open. Backscatter test method was performed when the test hole collapsed due to lack of moisture in the tested layer. For asphalt layers, backscatter test method was used.

Figure 3.11(a) and Figure 3.11(b) summarize the in-situ dry unit weight and moisture content data, respectively. Among aggregate base layers, Limestone base layer in Cell 188 provided the highest dry densities and the lowest moisture contents. RCA base layers (in Cells 185, 186, and 189) showed lower dry densities and higher moisture contents than Limestone base layer in Cell 188. In fact, the highest moisture contents were observed with RCA base layers. Class 6 Aggregate base layers in Cells 127 and 227 provided similar dry densities as RCA base layers; however, they showed lower moisture contents.

Class 5Q Aggregate base layers in Cells 328 to 728 showed the lowest dry unit weight values. The aggregate base layer in Cell 528 showed the lowest unit weight and moisture content values among these cells. Sand Subgrade layers in Cells 185 and 186 showed similar dry unit weight and moisture content values. Clay Loam subgrade layers in Cells 188 and 189 yielded higher moisture content values than Sand Subgrade layers. Subgrade soil in Cell 189 showed the lowest dry unit weight values. Comparisons of dry unit weight and moisture content values obtained from standard Proctor tests and in-situ unit weight and moisture content tests are provided in Figure 3.12(a) and Figure 3.12 (b), respectively. While in-situ dry unit weight values were higher than the values obtained from standard Proctor testing, in-situ moisture content values were lower than the values obtained from standard Proctor testing.

Figure 3.13 provides in-situ unit weight values of asphalt layers in Cells 185, 127, and 227. While the asphalt layer in Cell 185 showed a wider unit weight range, similar asphalt in-situ densities [around 141.6 pcf (22.24 kN/m^3)] were observed in all the cells.

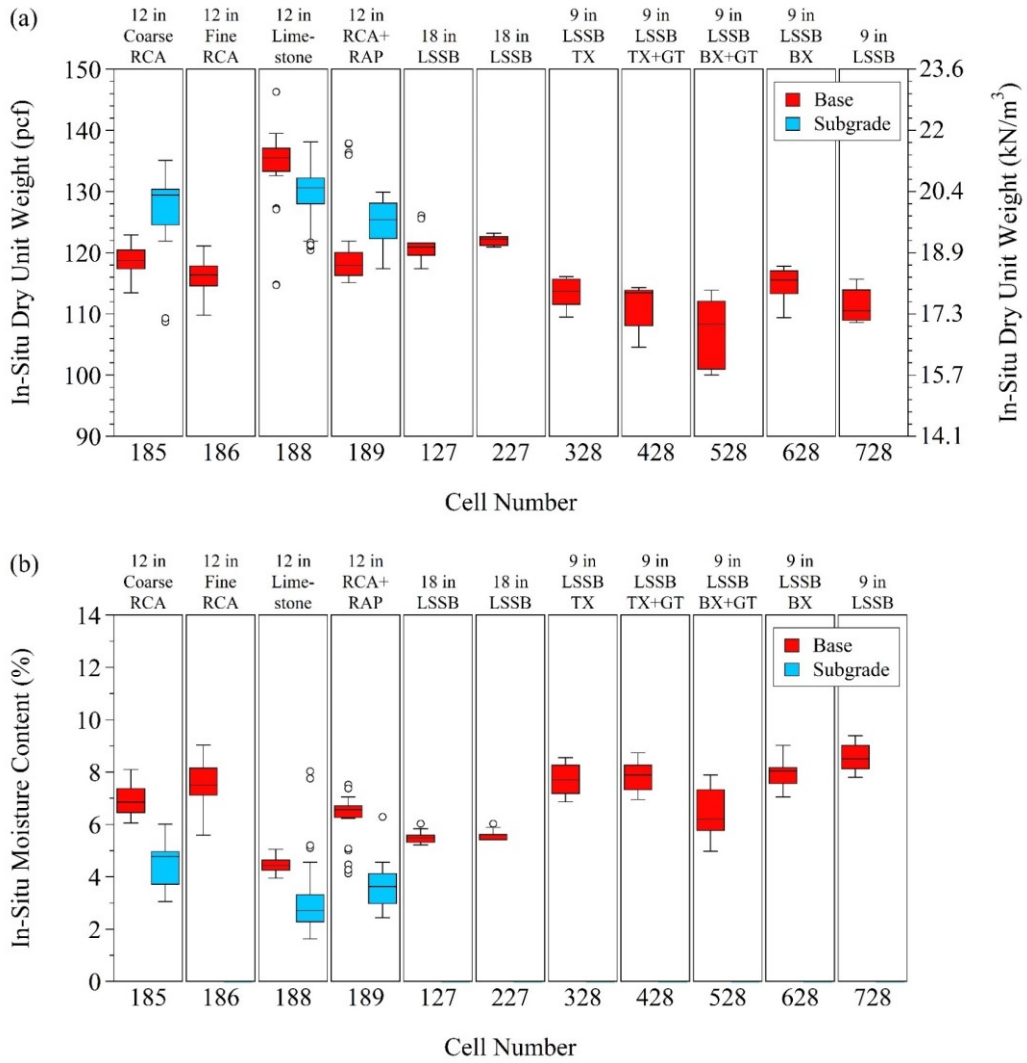

Figure 3.11. (a) In-situ dry unit weight and (b) moisture content measurements of Cells 185 to 728

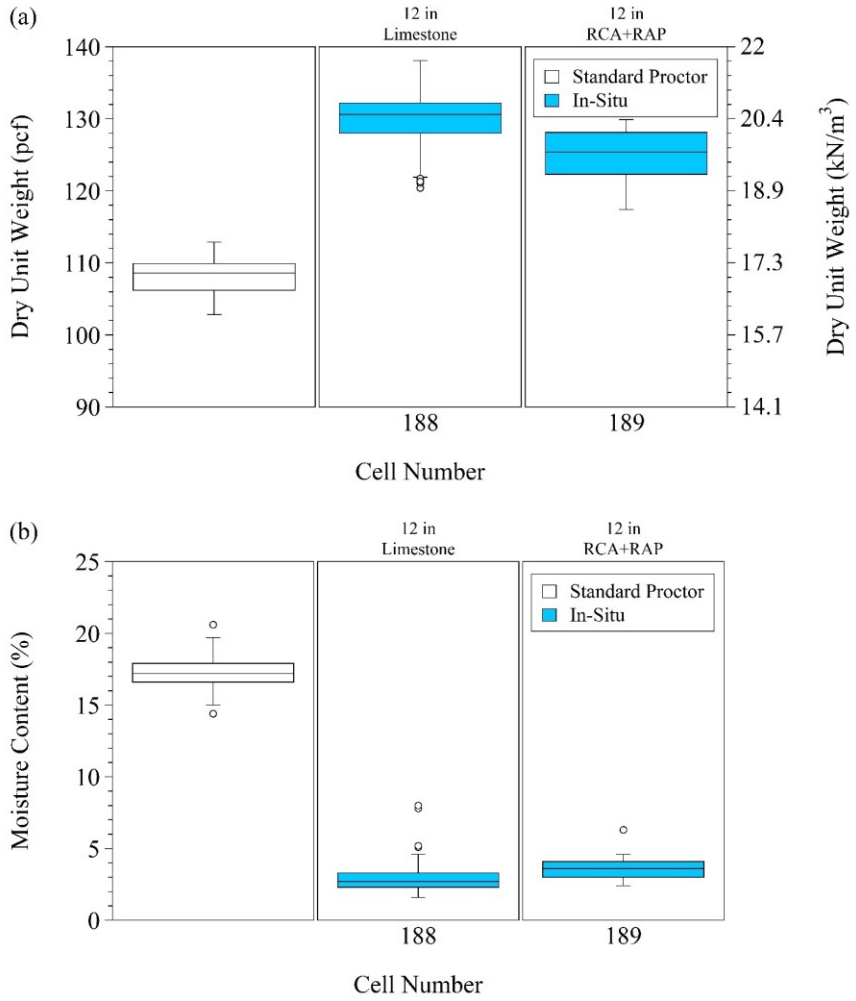

Figure 3.12. Standard Proctor and in-situ dry unit weight and moisture content values

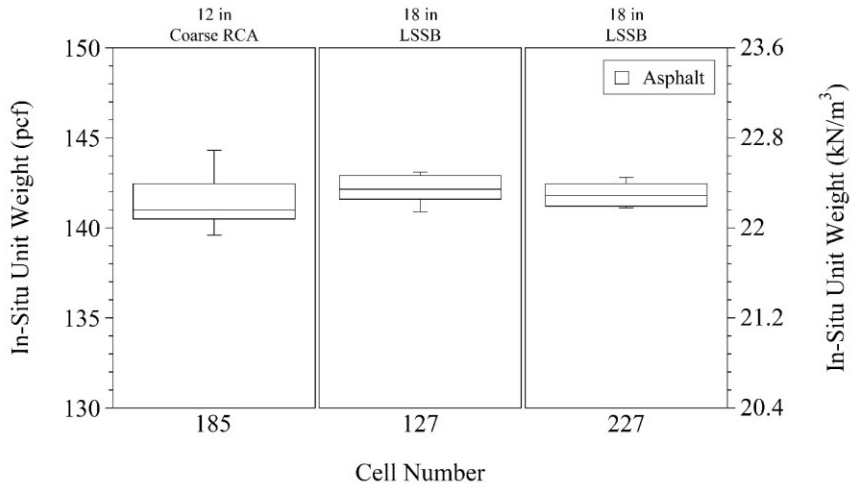

Figure 3.13. In-situ unit weight measurements of asphalt layers in Cells 185, 127, and 227

Figure 3.14(a) and Figure 3.14(b) show comparisons between the failed (Cells 128 and 228), reconstructed (Cells 328 to 628), and remnant (Cell 728) cells in terms of in-situ dry densities and moisture contents, respectively. Class 6 Aggregate base layer of Cell 128 showed relatively higher dry densities with no considerable difference in terms of moisture content compared to Class 5Q Aggregate base layers of Cells 228 to 728. Again, the aggregate base layer of Cell 528 showed the lowest dry unit weight and moisture content values.

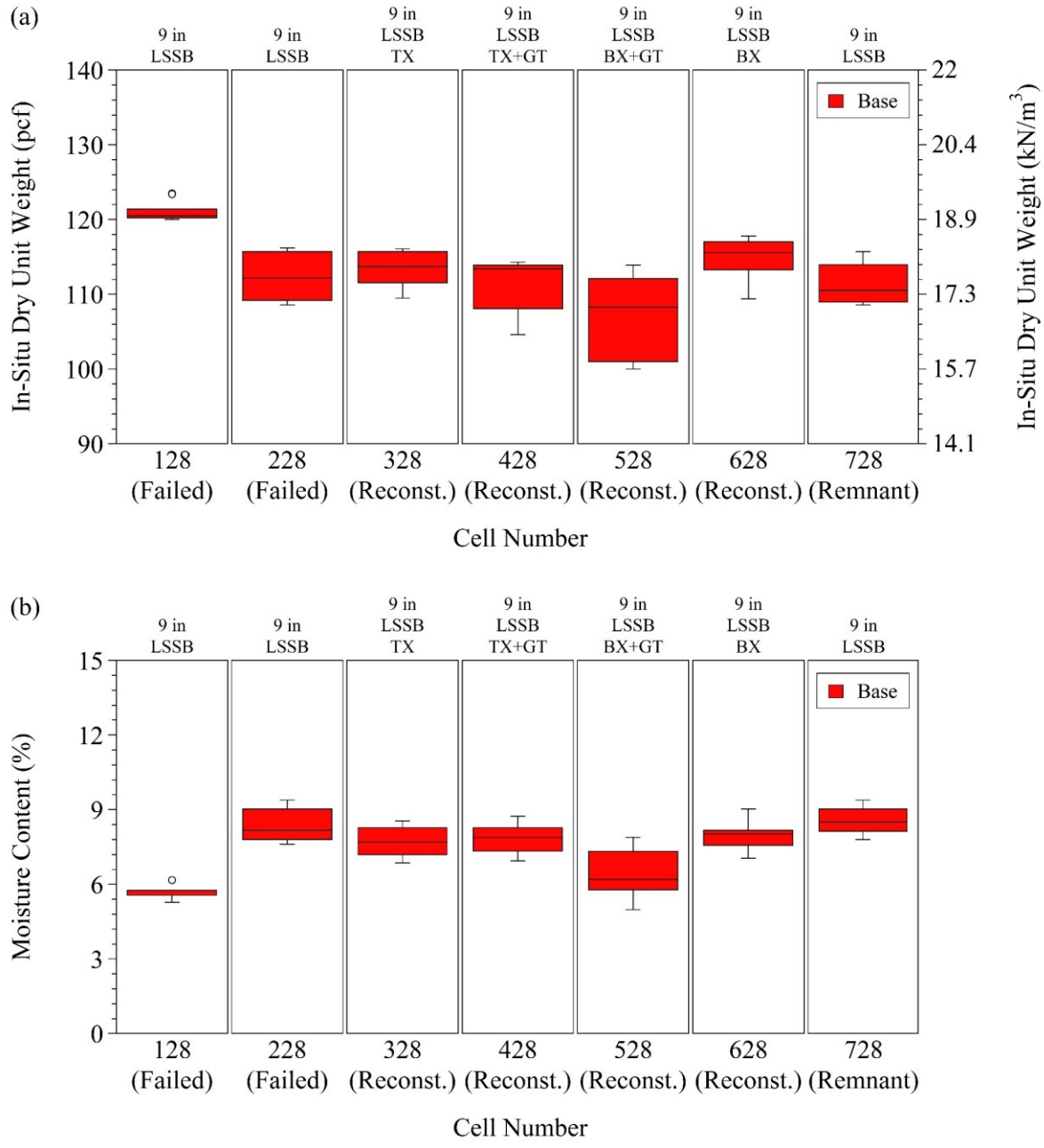

Figure 3.14. (a) In-situ dry unit weight and (b) moisture content values of failed, reconstructed, and remnant cells

3.2.3 Dynamic Cone Penetration (DCP) Test

DCP tests (ASTM D6951) were conducted on subgrade and aggregate base layers of the cells during construction. DCP equipment consisted of a 17.6-lb (8-kg) hammer dropped from a height of 22.6 in (575 mm). For the aggregate base layers of Cells 185 to 189, only the penetration depths after 12 drops at each location were recorded. For the aggregate base layers of the other cells, the target penetration depth was around 6 in (150 mm). Tests could not be performed on subgrade layers of Cells 185 and 186 due to rain which resulted in undesired testing condition. For subgrade layers of Cells 188 and 189, the drive rod was driven into subgrade layers to a depth of 18 in (460 mm). As stated previously, very soft subgrade conditions were created per project objectives in the cells constructed with LSSB layers (Cells 127 to 728); thus, traditional DCP testing was not conducted on weak subgrade layers. DCP testing was only used to estimate the target DCP index (DCPI) values [2.5 to 3.5 in/blow (65 to 90 mm/blow)] for subgrade layers in these cells. In addition, as stated previously, the higher end was actually kept flexible due to tight construction schedule (David Van Deusen, personal communication).

DCPI values calculated for several points in each cell are summarized in Figure 3.15 and estimated CBR values are shown in Appendix H. Coarse RCA and Fine RCA base layers in Cells 185 and 186, respectively, provided the lowest DCPI values (Figure 3.15). Limestone base (in Cell 188) and RCA+RAP base (in Cell 189) layers also provided relatively lower DCPI values (with no outliers) compared to the aggregate base layers placed over LSSB layers (in Cells 127 to 728). Wider DCPI ranges (mostly with outliers) were observed in the aggregate base layers constructed over LSSB layers (Figure 3.15).

A comparison between the failed (Cells 128 and 228), reconstructed (Cells 328 to 628), and remnant (Cell 728) cells is provided in Figure 3.16. While relatively narrower DCPI range was observed in the aggregate base layer of Cell 328, in general, no significant difference was observed between the failed (Cells 128 and 228), reconstructed (Cells 328 to 628), and remnant (Cell 728) cells (Figure 3.16).

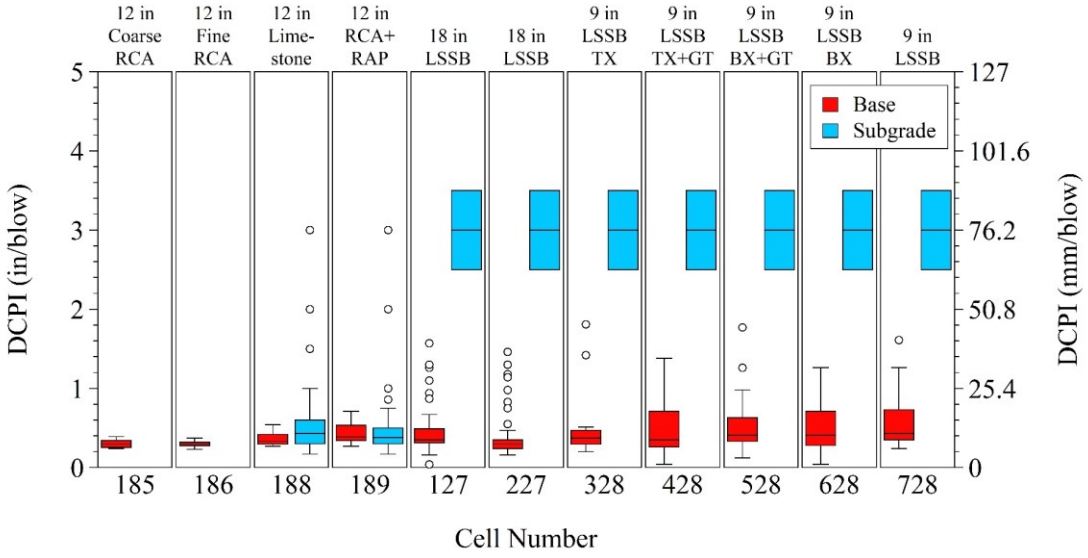

Figure 3.15. Summary of dynamic cone penetrometer (DCP) index (DCPI) values of Cells 185 to 728

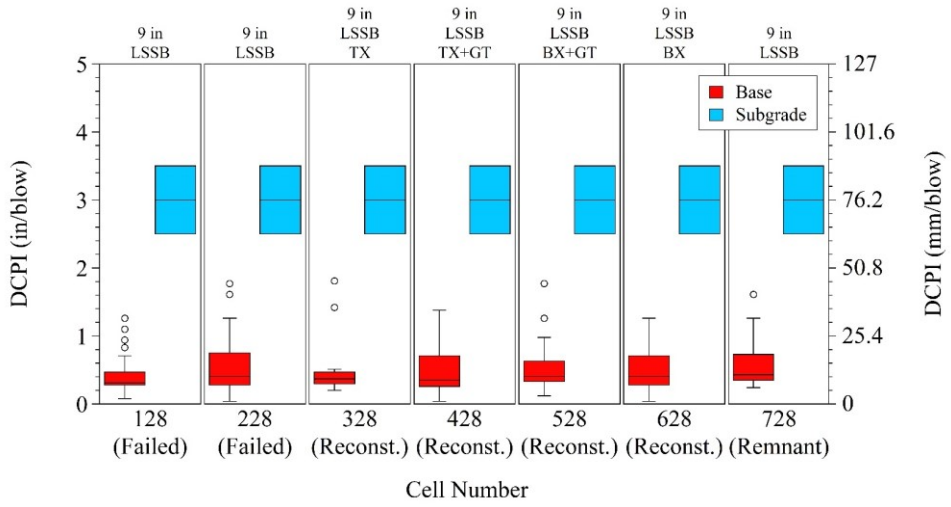

Figure 3.16. Dynamic cone penetrometer (DCP) index (DCPI) values of failed, reconstructed and remnant cells

3.2.4 Light Weight Deflectometer (LWD) Test

LWD tests (ASTM E2835) were performed on both subgrade (only for Cells 185 to 189) and aggregate base (for each cell) layers. LWD testing could not be operated on very weak subgrade layers, which were loosened intendedly to construct LSSB layers (for Cells 127 to 728). A Zorn ZFG 2000 LWD equipment having a plate diameter of 7.9 in (200 mm), drop mass of 22 lb (10 kg), and drop height of 19.7 in (500 mm) was used for testing [applied load was 1,340 lb (5.96 kN)]. Deflection from the last three drops (out of six drops) were recorded. Deflection values were compared systematically during the last three drops because a difference in deflections of more than 10% would be a sign of an insufficient compaction of the test zone (Siekmeier et al. 2009).

Boussinesq elastic solution was used to derive the LWD elastic modulus (E_{LWD}) of each test point (Vennapusa and White 2009). Parabolic stress distribution was assumed for tests performed on Sand Subgrade and aggregate base layers and a shape factor of 8/3 (rigid plate on granular material) was selected to determine the E_{LWD} values. On the other hand, inverse parabolic stress distribution was assumed for tests performed on Clay Loam subgrade layers and the shape factor was selected as $\pi/2$ (rigid plate on clay) (Vennapusa and White 2009). In addition, Poisson's ratios of 0.35 and 0.40 were used for tests performed on aggregate base and subgrade layers, respectively (Edil et al. 2012).

Figure 3.17 shows the E_{LWD} values calculated from tests performed on aggregate base and subgrade layers. Higher E_{LWD} values were observed from the tests conducted on the aggregate base layers of Cells 185 to 189 than the tests conducted on the subgrade layers of the same cells. Tests performed on Coarse RCA and Fine RCA base layers (in Cells 185 and 186, respectively) showed the highest E_{LWD} values. Similar median E_{LWD} values (from tests performed on aggregate base layers) were observed in Cells 188 to 227 while Cells 188 and 189 yielded a relatively wider E_{LWD} range. Tests performed on the aggregate base layers constructed over 9-in (230-mm) LSSB layers (Cells 328 to 728) showed the lowest E_{LWD} values in general. Particularly, Cell 528 showed considerably low E_{LWD} values which were as low as 3.43 ksi (23.64 MPa).

A comparison of the E_{LWD} values (from tests performed on the aggregate base layers) of the failed (Cells 128 and 228), reconstructed (Cells 328 to 628), and remnant (Cell 728) cells is provided in Figure 3.18. While Cells 328, 428, 628, and 728 provided E_{LWD} values equal to or greater than the values obtained from Cells 128 and 228 which were failed, reconstructed Cell 528 had lower E_{LWD} values than those of the failed cells. No significant effect of using geosynthetics during reconstruction was observed from LWD data, which is expected since the geosynthetics were placed below LSSB layers.

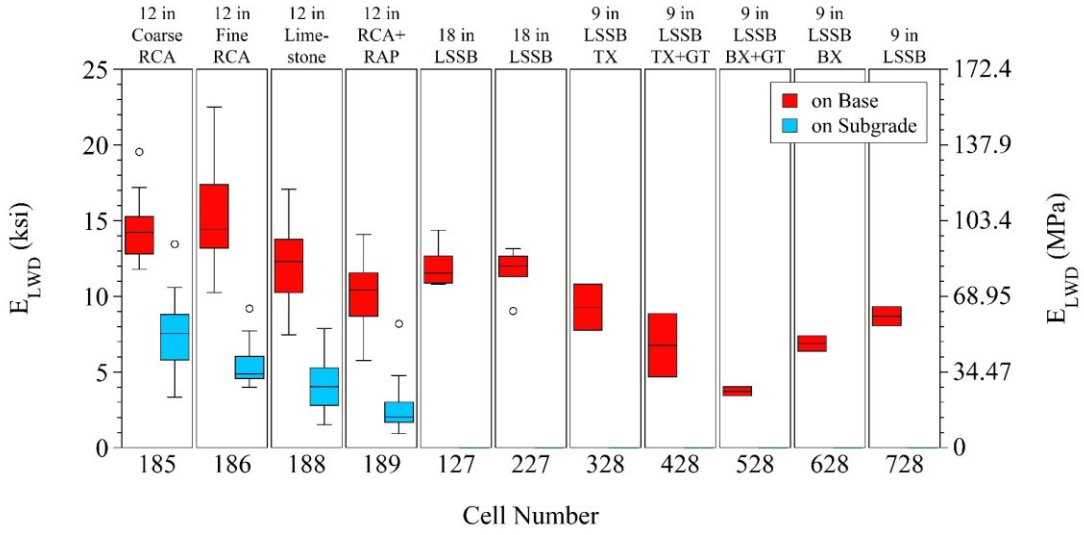

Figure 3.17. Light weight deflectometer (LWD) elastic modulus (E_{LWD}) values of Cells 185 to 728

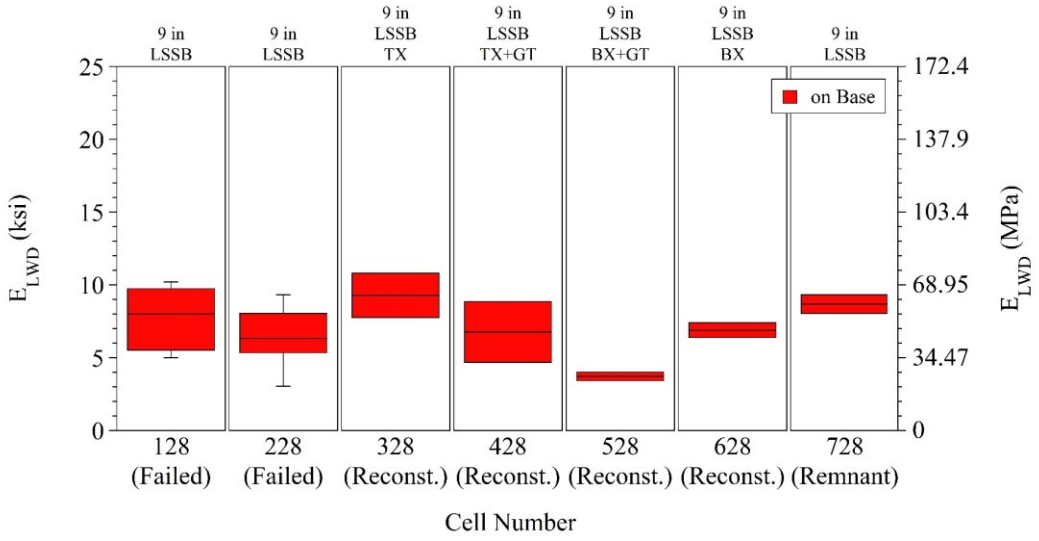

Figure 3.18. Light weight deflectometer (LWD) elastic modulus (E_{LWD}) values of failed, reconstructed, and remnant cells

3.2.5 Gas Permeameter Test (GPT)

A GPT device containing a self-contained pressurized gas system with a self-sealing base plate was used to estimate the saturated hydraulic conductivity (K_{sat}) of aggregate base layers of select cells (Appendix I) (White et al. 2010). TesCom Model 44-2213-242 regulator and precision orifice were used to control gas flow. Gas flow rate was calculated by digital pressure transducers which were used to monitor the gauge pressure at the inlet and outlet of the orifice. To prevent gas leakage, a polyurethane base seal was attached to the base plate. Saturated hydraulic conductivity (K_{sat}) values were derived from gas flow and pressure measurements by using Darcy's Law and considering viscosity and compressibility of gas, and gas flow under partially saturated conditions (White et al. 2007). More details are provided in White et al. (2010).

GPT tests were performed only on Cells 185, 186, 188, 189, and 728 by following the procedure outlined in White et al. (2010). Two different orifice types were used: (1) GPT(B) with a diameter of 34.29 mils (870.95 mm), and (2) GPT(C) with a diameter of 11.56 mils (293.66 mm) (White et al. 2010). Tests were performed on three different surface textures: (1) fine, (2) medium, and (3) coarse surface textures (Appendix I). Figure 3.19 shows ranges of saturated hydraulic conductivity (K_{sat}) values based on measurements and in-situ saturation levels. The aggregate base layers in Cells 186 (Fine RCA) and 728 (Class 5Q Aggregate) provided relatively lower K_{sat} values. Coarse RCA base layer in Cell 185 provided the highest K_{sat} values.

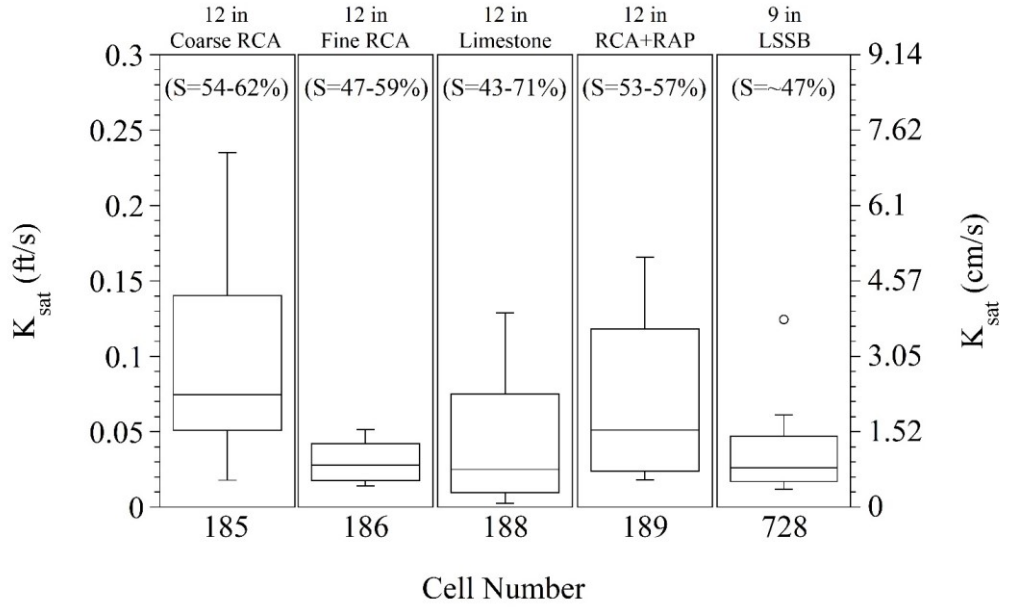

Figure 3.19. Gas permeameter test (GPT) measurements for Cells 185, 186, 188, 189, and 728 (in-situ saturation levels are shown in parenthesis)

As stated, in Figure 3.19, in-situ unit weight and moisture content values were used to calculate K_{sat} values. To observe the effect of saturation level (S), three different saturation levels (20, 40, and 60%) were selected and analyses were repeated (Zhao 2011). Figure 3.20 shows the variation of K_{sat} values

with different saturation levels. Lower saturation levels yielded relatively lower K_{sat} values. In addition, change of K_{sat} values between S=40% and S=60% were relatively higher than changes observed between S=20% and S=40%.

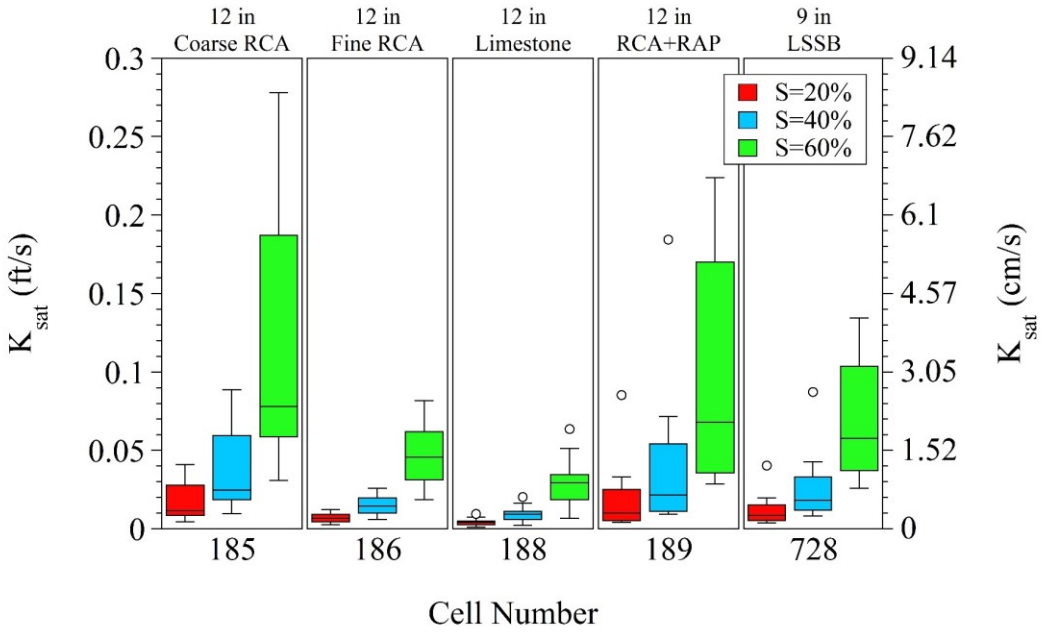

Figure 3.20. Effect of saturation levels on the saturated hydraulic conductivity (K_{sat}) values

3.2.6 Intelligent Compaction (IC)

The IC field testing, calibrated with automated plate load testing (APLT) to obtain cyclic stress-dependent composite and layered resilient modulus (M_R) values, was performed on the subbase (only for Cells 127 and 227) and aggregate base layers (for each cell) of the cells by Ingios Geotechnics. First, preliminary IC mapping results were obtained. Then, several test locations were selected for APLT testing based on the initial IC mapping results. APLT equipment (Appendix J) was used to measure in-situ M_R values directly (White and Vennapusa 2017). For IC testing and mapping, a Caterpillar CS56 vibratory smooth drum roller which weighs about 27,450 lb (122.1 kN) was outfitted with Ingios validated IC retrofit system (Appendix J). Stress-dependent M_R values at 10 psi (69 kPa) and 30 psi (207 kPa) plate contact stresses were calculated (White and Vennapusa 2017). More information about IC calibration and data analysis is provided by White and Vennapusa (2017).

For the evaluation of subbase layers, IC testing was only performed on 18-in LSSB layers in Cells 127 and 227 and their results are shown in Figure 3.21(a) and Figure 3.21(b) for both plate contact stresses. While Cell 127 showed relatively higher composite and subbase M_R values at both stress levels, both cells showed similar subgrade M_R values.

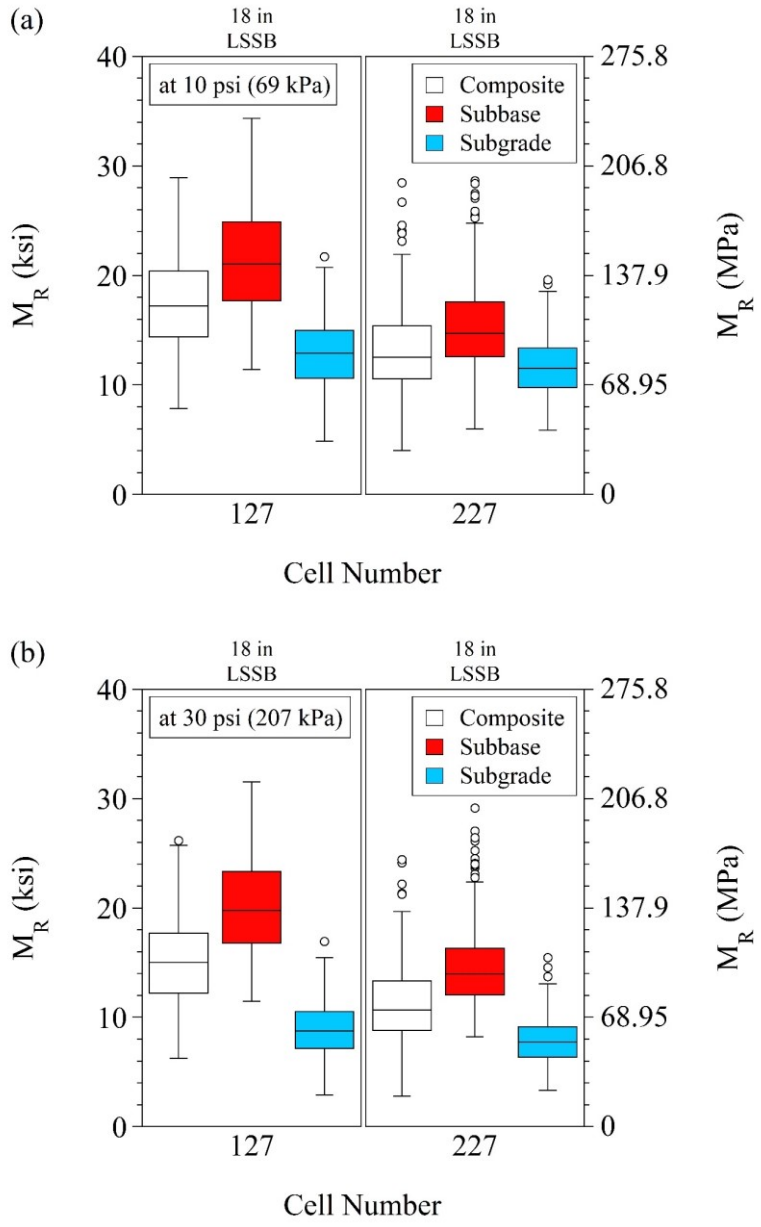

Figure 3.21. Resilient modulus (M_R) values of Cells 127 and 227 at (a) 10 psi (69 kPa) and (b) 30 psi (207 kPa)

As stated previously, rutting of subbase and aggregate base layers in Cells 128 and 228 was observed during construction and in-situ testing. After reconstruction, seven passes were made during mapping of Cells 328 to 628. An increase in the number of passes yielded an increase in M_R values in these cells and the M_R values obtained during the seventh pass (last pass) were used for overall comparison analyses. As an example, composite M_R values of Cell 328 during each roller pass is provided in Figure 3.22. Composite, base+subbase (they were combined and assumed as one layer), and subgrade M_R values of Cells 328 to 628 at each roller pass are provided in Appendix K.

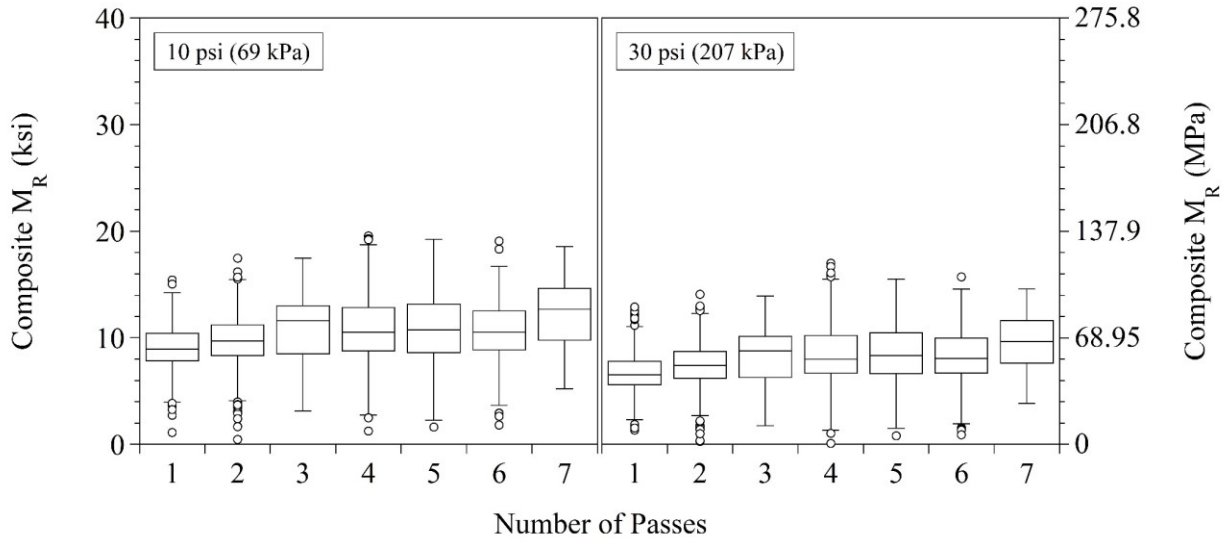

Figure 3.22. Composite resilient modulus (M_R) values of Cell 328 at each roller pass

For Cells 185 to 728, estimated composite, base+subbase (they were combined and assumed as one layer), and subgrade M_R values at 10 psi (69 kPa) and 30 psi (207 kPa) plate contact stress levels are summarized in Figure 3.23(a) and Figure 3.23(b), respectively. The highest M_R values at both stress levels were observed in Cells 185 (Coarse RCA base) and 186 (Fine RCA base). While Cell 127 with 18-in (460-mm) LSSB layer provided higher M_R values than Cells 188 (Limestone base) and 189 (RCA+RAP base), Cell 227 in which the same subbase layer was constructed provided comparable M_R values. At both stress levels, the cells constructed with 9-in (230-mm) LSSB layers (Cells 328 to 728) showed the lowest M_R values.

Figure 3.24(a) and Figure 3.24(b) provide a comparison of M_R values between the failed (Cells 128 and 228), reconstructed (Cells 328 to 628), and remnant (Cell 728) cells at 10 psi (69 kPa) and 30 psi (207 kPa) plate contact stress levels, respectively. It was observed that reconstructed Cell 528 provided the lowest M_R values at both stress levels. In addition, it was concluded that Cell 728, the remnant of Cell 228, had higher M_R values than the overall (removed part + remnant part) M_R values of Cell 228.

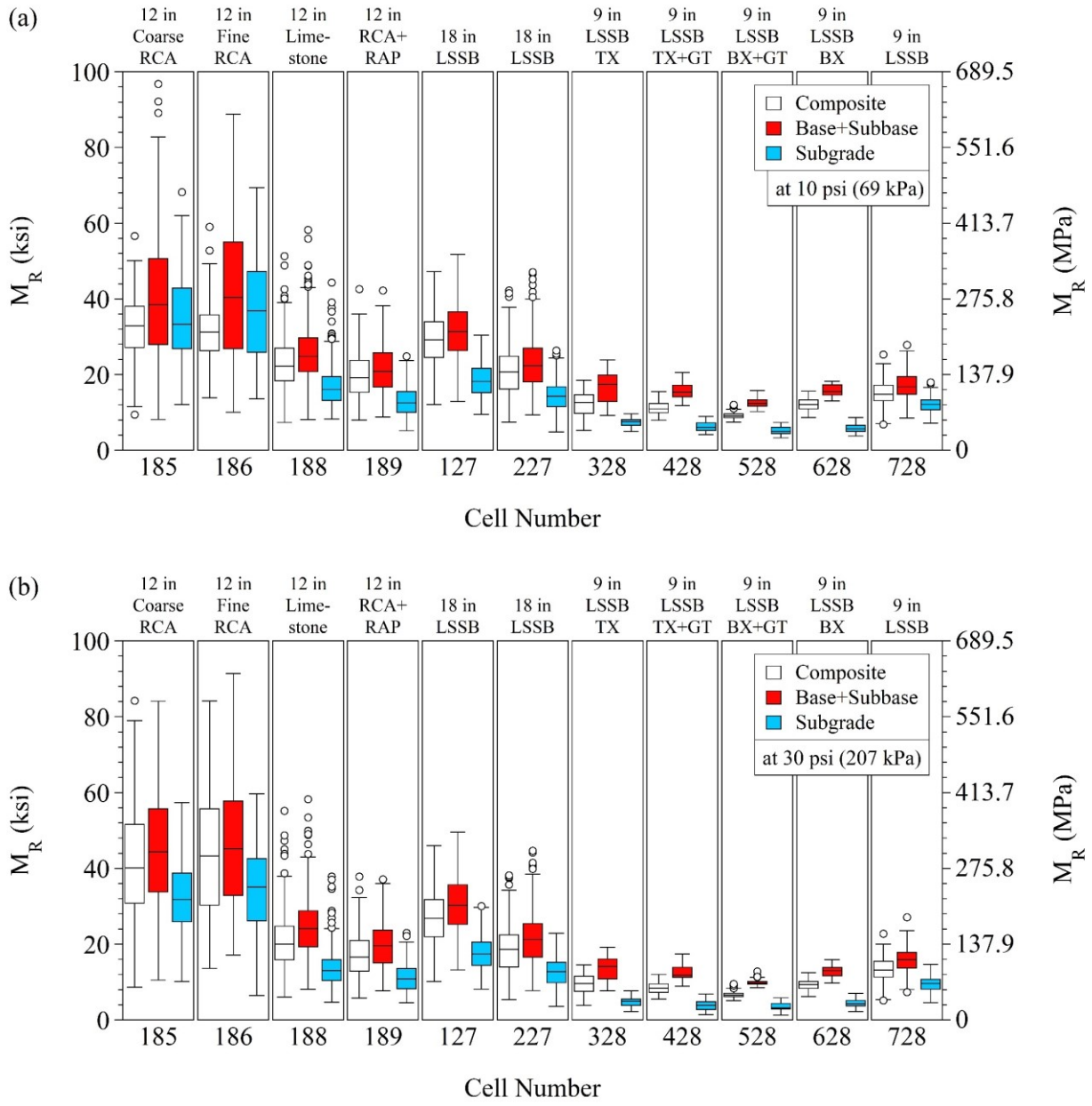

Figure 3.23. Resilient modulus (M_R) values of Cells 185 to 728 at (a) 10 psi (69 kPa) and (b) 30 psi (207 kPa)

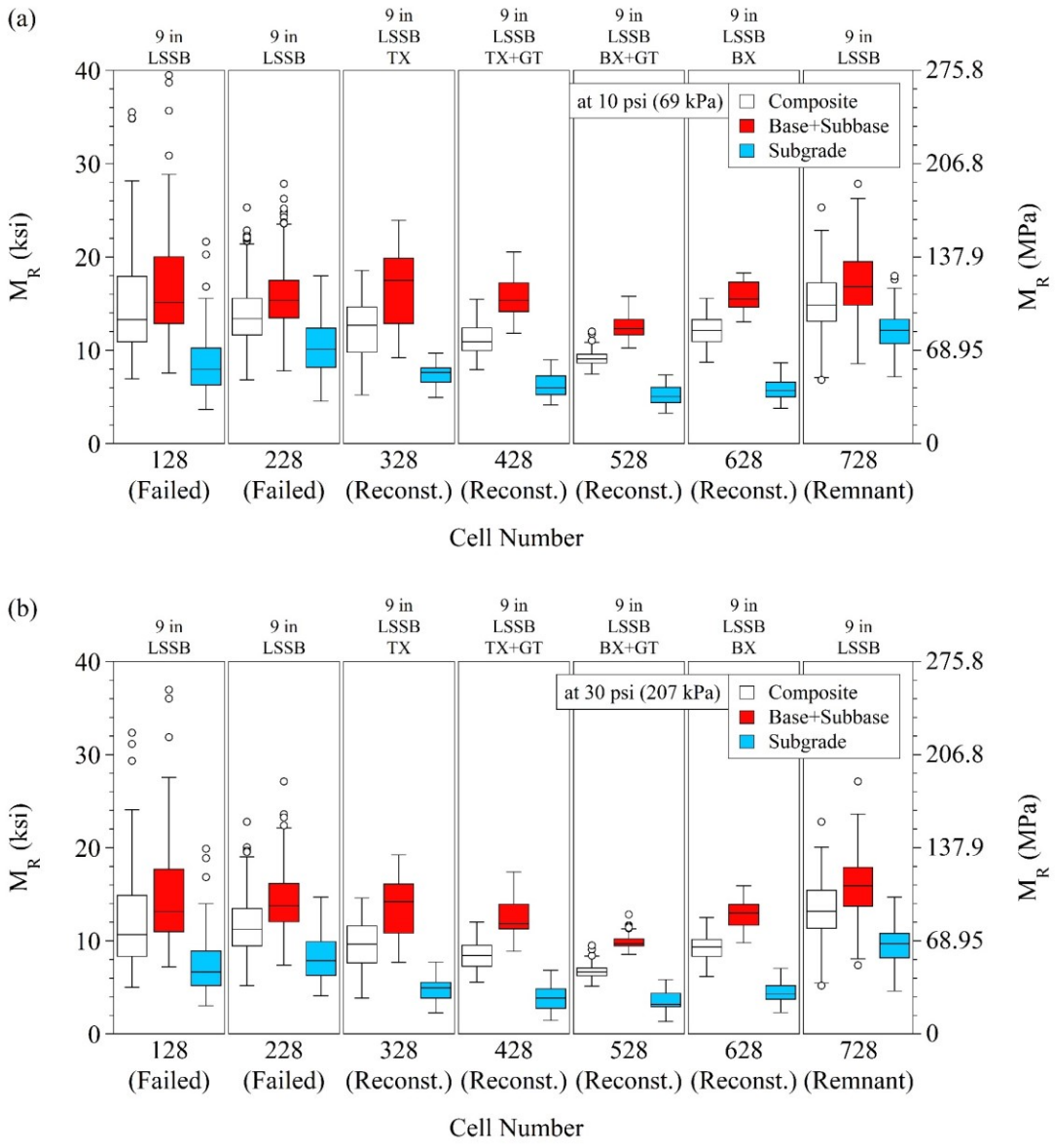

Figure 3.24. Resilient modulus (M_R) values of failed, reconstructed, and remnant cells at (a) 10 psi (69 kPa) and (b) 30 psi (207 kPa)

3.2.7 Falling Weight Deflectometer (FWD) Test

FWD testing, a non-destructive in-situ testing, was performed during construction and around two months after the final placement of asphalt surfacing to evaluate the deflection and FWD elastic modulus (E_{FWD}) of the cells. A trailer-mounted Dynatest Model 8002 FWD device (Appendix L) with two plate (rigid) diameters [17.7 in (450 mm) for subgrade and aggregate base layers, and 11.8 in (300 mm) for asphalt layers] were used. For deflection basin evaluation, eight geophones were located 8 in (203 mm), 12 in (300 mm), 18 in (460 mm), 24 in (610 mm), 36 in (914 mm), 48 in (1219 mm), 60 in (1524 mm), and 72 in (1829 mm) away from the center plate where the loading was applied. Three loading drops with increasing load levels were applied. Composite E_{FWD} values were calculated by Boussinesq

elastic solution (Vennapusa and White 2009) for the maximum deflections measured at the center of the loading plate. The shape factor was selected as 8/3 (rigid plate on granular material with parabolic stress distribution) for analyses of tests performed on Sand Subgrade, aggregate base, and asphalt layers. For tests performed on Clay Loam subgrade layers, the shape factor of $\pi/2$ (rigid plate on clay with inverse parabolic stress distribution) was used. Poisson's ratios of 0.30, 0.35 and 0.40 were used for asphalt, base+subbase (they were combined and assumed as one layer) and subgrade layers, respectively (Edil et al. 2012).

Layered E_{FWD} analyses were performed by MODULUS 7.0 program which was developed at Texas Transportation Institute (TTI) mainly for flexible pavements. MODULUS 7.0 uses database method for back-calculation and assumes linear-elastic theory to back-calculate E_{FWD} from recorded deflection basins during testing (Edil et al. 2012). It uses WESLEA program to create a deflection basin database which is then used to determine the layered modulus values that give deflection basins similar to the actually measured ones (William 1999; Baladi et al. 2011). The program only allows for seven sensors. Thicknesses of asphalt, aggregate base, and subbase layers are entered manually, and the program has three options for the subgrade thickness: (1) semi-infinite thickness, (2) depth-to-bedrock analysis, and (3) manual entry (William 1999). In this project, depth-to-bedrock analysis (Rohde et al. 1992; Newcomb et al. 1995) was selected as a result of potential relatively shallow water table. By using the depth-to-bedrock analysis, not only the presence of bedrock but also elevations of stiff clay layer and water table can be estimated (Liu and Scullion 2001; Chatti et al. 2017). Incorrect back-calculation for the upper layers can be made by selecting a semi-infinite subgrade layer when there is a relatively stiff layer (Newcomb et al. 1995). In general, if the stiff layer is deeper than around 450 in (11.43 m), it does not cause a significant effect (Chatti et al. 2017). In MODULUS 7.0, maximum 300 in (7.62 m) can be entered as the subgrade thickness (Liu and Scullion 2001). Figure 3.25 shows water table levels determined for the cells by the depth-to-bedrock analysis. Median values were used for back-calculation. The water table levels in Cells 185 and 186 were relatively deeper than the water tables in the other cells. In addition, subgrade/bedrock modular ratio of 100 is recommended for depth-to-bedrock model. However, a ratio of 5 was used for back-calculation because it was assumed that the stiffening was due to stiff clay soil (saturated soil where water table is high) (Liu and Scullion 2001).

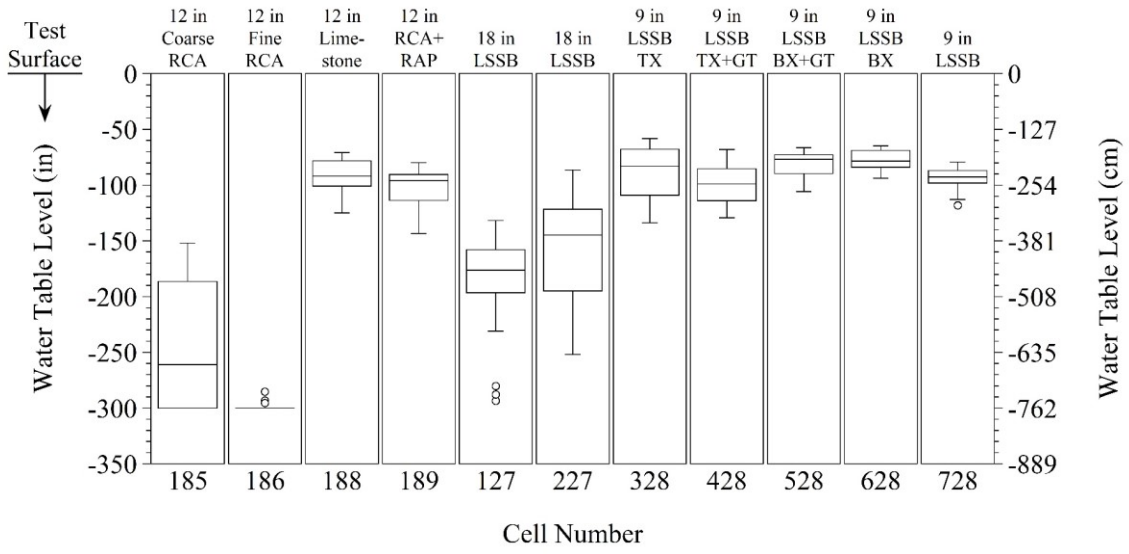

Figure 3.25. Water table levels determined by depth-to-bedrock analysis

During construction, tests were performed on the subgrade (only for Cells 185 to 189) and aggregate base (for each cell) layers. For subgrade layers of Cells 185 to 189, at each testing location, three loading drops that ranged between 3,700 lb (16.46 kN) and 7,700 lb (34.25 kN) were applied with increasing load levels and maximum deflections were recorded at the center of the loading plate (Figure 3.26). To calculate E_{FWD} values corresponding to deflections, the measured maximum deflections were normalized to 5,000 lb (22.2 kN) and 7,000 lb (31.1 kN) loads, respectively, because seating was observed after the first drop (Figure 3.26). Boussinesq elastic solution (Vennapusa and White 2009) was used to calculate composite E_{FWD} of subgrade layers (Figure 3.27). Sand Subgrade layers of Cells 185 and 186 provided lower maximum deflections and higher E_{FWD} values compared to Clay Loam subgrade layers of Cells 188 and 189.

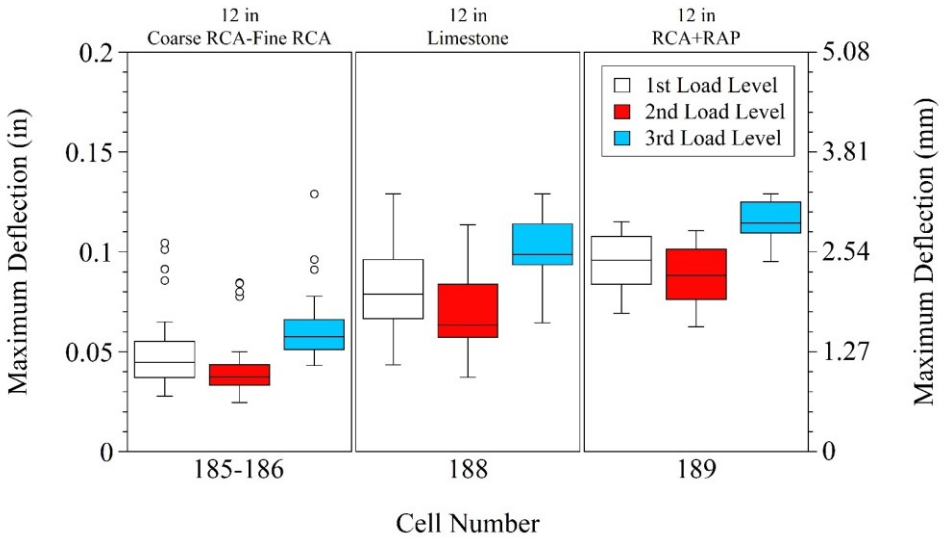

Figure 3.26. Maximum deflections of subgrade layers of Cells 185 to 189

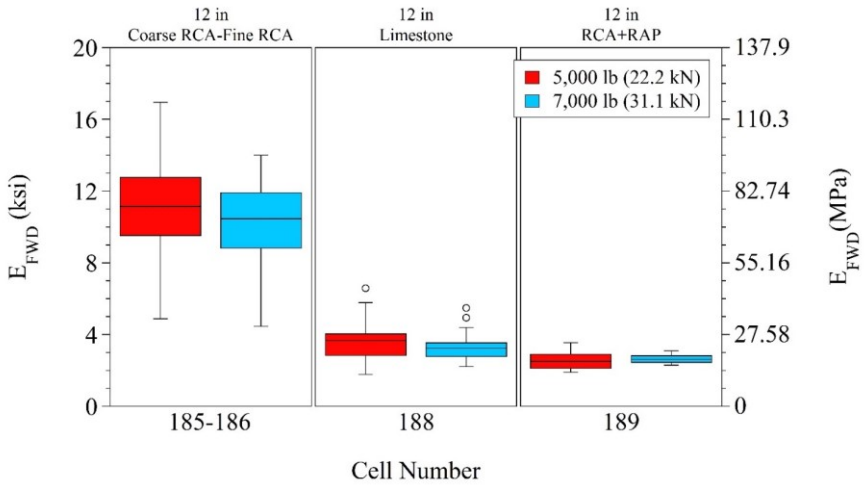

Figure 3.27. Falling weight deflectometer (FWD) composite elastic modulus (E_{FWD}) values of subgrade layers of Cells 185 to 189

For the aggregate base layers of the cells before paving, three loading drops ranged between 1,660 lb (7.38 kN) and 6,080 lb (27.04 kN) were applied with increasing load levels. Maximum deflections measured at the center of the loading plate for Cells 185 to 728 are summarized in Figure 3.28. While the first loading drop had the lowest load level, relatively higher maximum deflections were observed compared to the deflections caused by the second loading drop. Therefore, the first loading drop was assumed as a seating drop. As seen in Figure 3.28, the lowest maximum deflections were observed in Cells 185 and 186 constructed with Coarse RCA and Fine RCA base layers, respectively. Cells 188 (Limestone base), and 127 and 227 were also provided relatively lower maximum deflections. Cells 328 to 628 yielded relatively higher maximum deflections than the other cells (specifically, Cell 528 showed the highest maximum deflections). Compared to them, Cell 728 provided relatively lower maximum deflections.

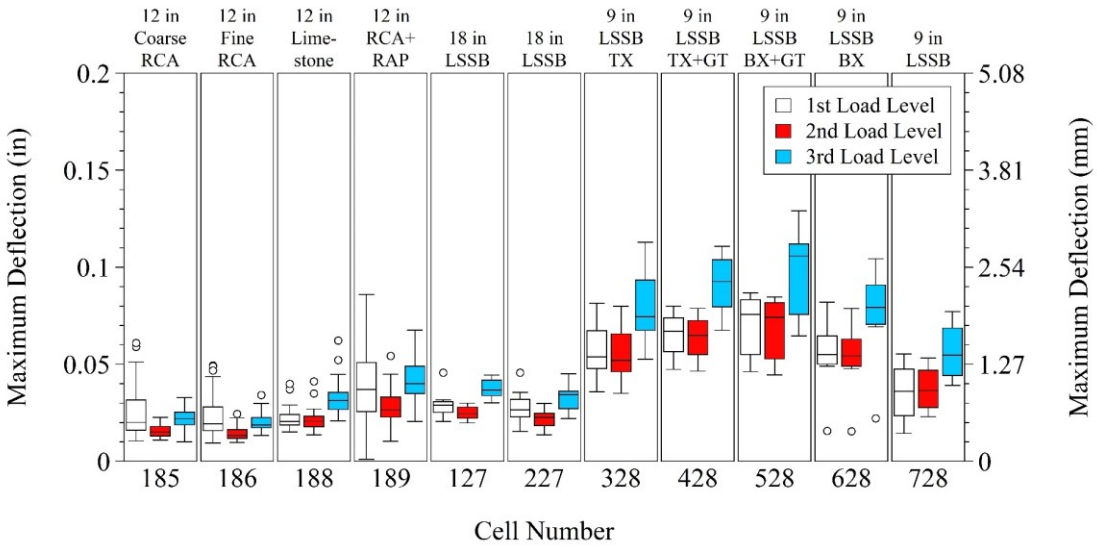

Figure 3.28. Maximum deflections of Cells 185 to 728 before paving

Actually, in addition to the first loading drop, the second loading drop was also assumed as the seating drop and composite analysis and back-calculation were performed only for the third loading drop in which the deflections were normalized to a 5,000-lb (22.2-kN) load (Figure 3.29). Since Cells 185 and 186 provided the lowest maximum deflections in Figure 3.28, they also provided the highest E_{FWD} values (Figure 3.29). In addition, the lowest E_{FWD} values were obtained for Cells 328 to 628, and Cell 728 yielded higher E_{FWD} values than them.

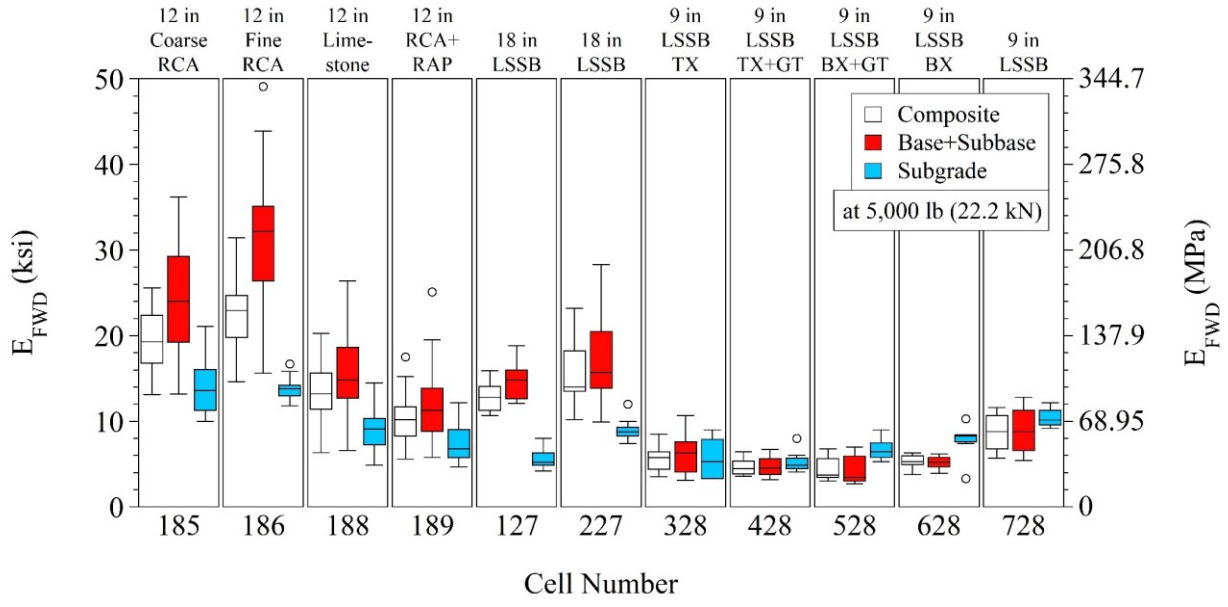

Figure 3.29. Falling weight deflectometer (FWD) elastic modulus (E_{FWD}) values of Cells 185 to 728 before paving

Comparisons of maximum deflections and E_{FWD} values of the failed (Cells 128 and 228), reconstructed (Cells 328 to 628), and remnant (Cell 728) cells are provided in Figure 3.30 and Figure 3.31, respectively. Overall, the failed cells (Cells 128 and 228) provided relatively lower maximum deflections and higher E_{FWD} values than the reconstructed cells (Cells 328 to 628). Since relatively lower maximum deflections and higher E_{FWD} values were observed in Cell 728 (remnant from Cell 228) compared to Cell 228, it was concluded that Cell 728 was the stiffer part of Cell 228.

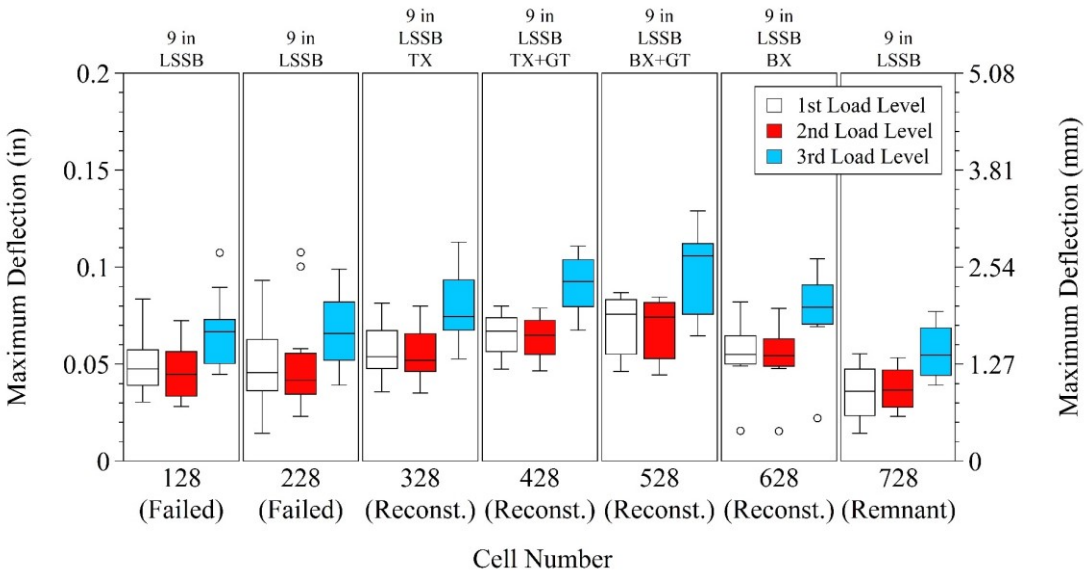

Figure 3.30. Maximum deflections of failed, reconstructed, and remnant cells

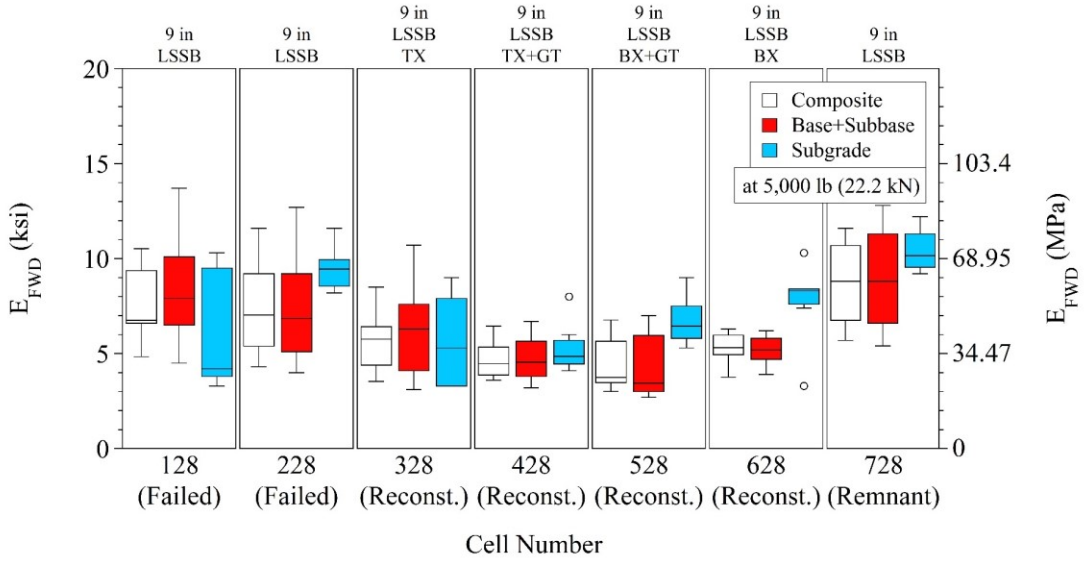

Figure 3.31. Falling weight deflectometer (FWD) elastic modulus (E_{FWD}) values of failed, reconstructed, and remnant cells at 5,000 lb (22.2 kN)

2 months after paving, three loading drops ranged between 5,700 lb (25.35 kN) and 12,900 lb (57.38 kN) were applied with increasing load levels. Initially, maximum deflections at three load levels (actual load levels) were compared and no apparent seating effect was observed. Thus, measured deflections were normalized to 6,000 lb (26.7 kN), 9,000 lb (40 kN), and 12,000 lb (53.4 kN) loads and chart showing maximum deflections were plotted based on normalization (Figure 3.32). As seen in Figure 3.32, Cells 185, 186, 127, and 227 yielded similar maximum deflections at each load level. Cells 188 and 189 showed intermediate maximum deflection values. Cells constructed with 9-in (230-mm) LSSB layers (Cells 328 to 728) showed the highest maximum deflections compared to the other cells.

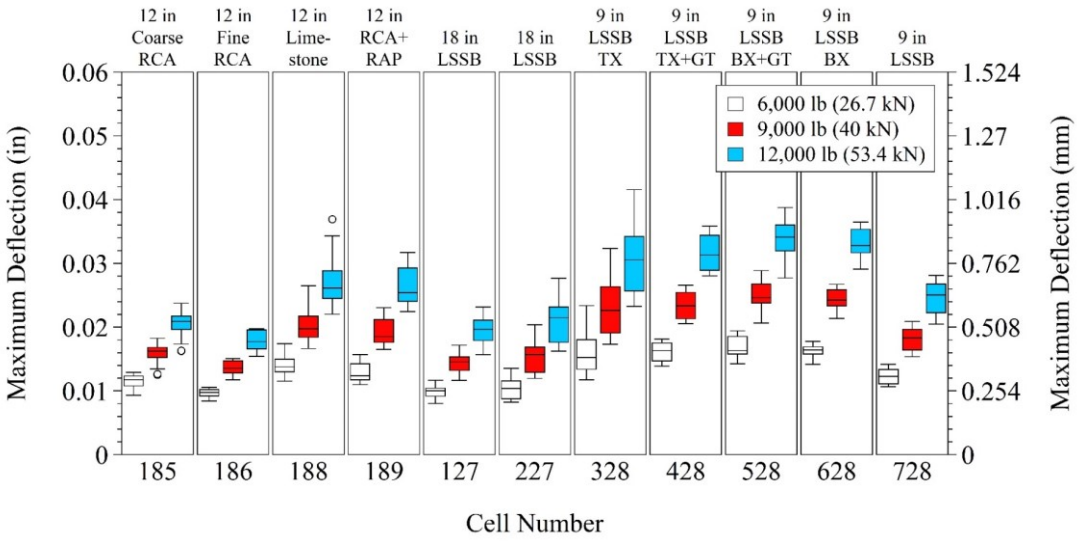

Figure 3.32. Maximum deflections of Cells 185 to 728 after paving

Very similar relationships were observed between the E_{FWD} values of the cells after paving at 6,000 lb (26.7 kN), 9,000 lb (40 kN), and 12,000 lb (53.4 kN); therefore, only the E_{FWD} values of the cells at 9,000-lb (40-kN) is shown in Figure 3.33. The E_{FWD} values at 6,000 lb (26.7 kN) and 12,000 lb (53.4 kN) are shown in Appendix M (separate charts for subgrade, base+subbase, asphalt, and composite E_{FWD} values are also provided in Appendix M). While similar maximum deflections (Figure 3.32) and composite E_{FWD} values (Figure 3.33) were observed in Cells 185, 186, 127 and 227. Cells 185 and 186 provided relatively higher base+subbase E_{FWD} values (Figure 3.33). Figure 3.34 provides the asphalt E_{FWD} values of the cells at 9,000 lb (40 kN). Although Cells 127 and 227 have lower base+subbase E_{FWD} values than Cells 185 and 186 (Figure 3.33), relatively higher asphalt E_{FWD} values of Cells 127 and 227 (Figure 3.34) improved their overall (composite) stiffness values.

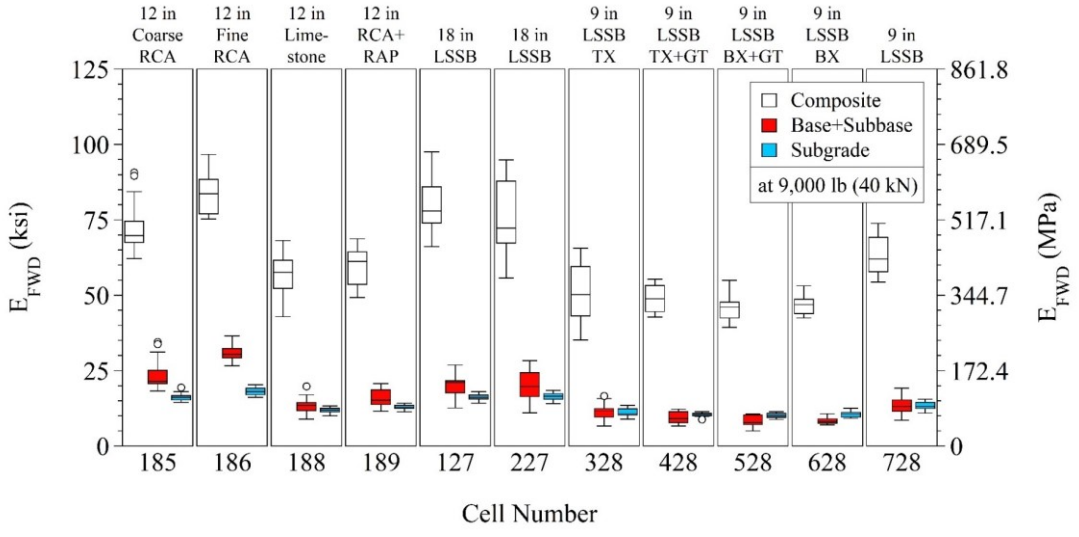

Figure 3.33. Falling weight deflectometer (FWD) elastic modulus (E_{FWD}) values of Cells 185 to 728 at 9,000 lb (40 kN) after paving

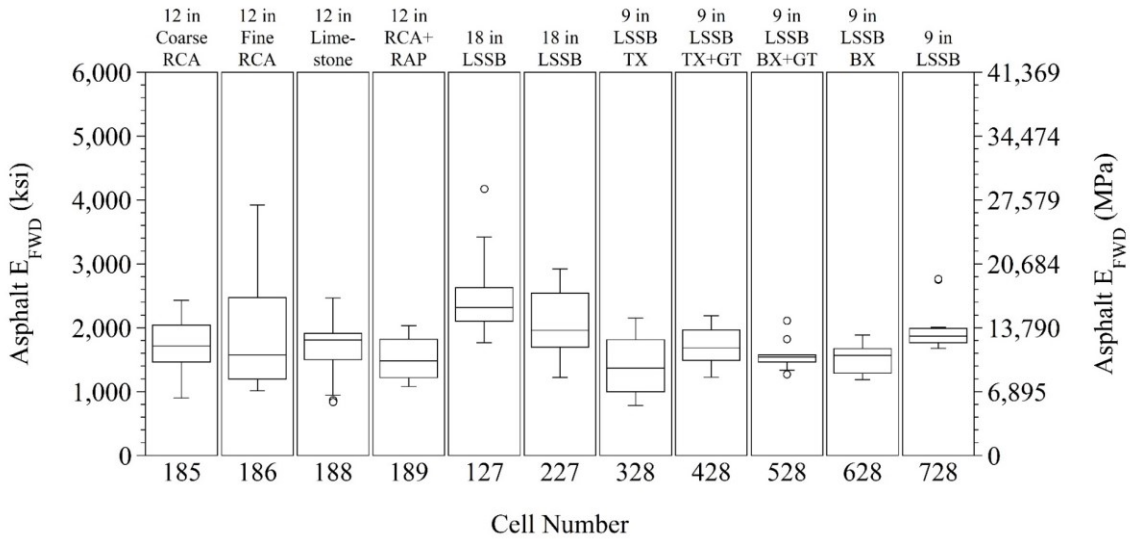

Figure 3.34. Falling weight deflectometer (FWD) elastic modulus (E_{FWD}) values of asphalt layers of Cells 185 to 728 at 9,000 lb (40 kN)

3.3 CHAPTER CONCLUSIONS

In this chapter, detailed information about the construction and preliminary performance of the built test cells was provided. Data collected during and shortly after construction was presented. Based on the findings of this chapter, the following conclusions were drawn:

- The observations made during construction show that there were some challenges with constructing 9-in (230-mm) LSSB layers placed directly over the subgrade layers. During compaction of these LSSB layers, subgrade soil pumping and rutting were observed. To solve these issues, the cells were reconstructed and geosynthetics were placed between thinner LSSB and subgrade layers. After the placement of geosynthetics, no significant problem was observed and construction could be completed successfully.

- As described by IDOT Subgrade Stability Manual (2005), the thickness of layers above subgrade depends on the strength/stiffness of subgrade layers (Figure 2.46). In this study, a very non-traditional subgrade preparation procedure was followed during construction to create a weak subgrade with a dynamic cone penetration index (DCPI) value between 2.5 and 3.5 in/blow (63.5 and 89 mm/blow) (ASTM D6951) for the upper 1 ft (0.3 m) of the clay loam subgrade soil. According to IDOT, the sufficient LSSB layer thickness would be between 15 and 20 in for the subgrade DCPI range of 2.5-3.5 in/blow (63.5 and 89 mm/blow). In addition, an 18-in LSSB layer is more sufficient than a 9-in LSSB layer. From the same manual, a 12-in LSSB with geotextile or geogrid could be constructed instead of constructing an 18-in LSSB without geosynthetics. In addition, instead of constructing a 9-in LSSB with geogrid, a 12-in LSSB could be constructed with geotextile or without any geosynthetics. As described by Wisconsin DOT's Facilities Development Manual (FDM) (2019), instead of constructing a 16-in large stone layer without any geogrid, a 12-in large stone layer with a geogrid could be constructed."

- The original plan was to construct 18-in (460-mm) LSSB layers with one lift and two lifts for Cells 127 and 227, respectively. However, Cell 227 was also constructed with one lift similar to Cell 127 because the subgrade soil pumping and rutting problems encountered during the construction of the 9-in (230-mm) LSSB layers without geosynthetics showed that dividing LSSB layer construction into two lifts would not be practical.

- DCP, LWD, IC, and FWD data collected during construction showed that the two cells constructed with Coarse RCA and Fine RCA base layers (Cells 185 and 186, respectively) (it should be noted that these two cells contained Sand Subgrade layers) performed better (lower DCPI, higher elastic and resilient moduli, and lower deflections) than the other cells that contained Clay Loam subgrade layers.

- Cells constructed with 18-in (460-mm) LSSB layers (Cells 127 and 227) showed relatively higher moduli and lower deflections than the cells constructed with 9-in (230-mm) LSSB layers (Cells 328 to 728) which indicated that thicker LSSB layers provided better structural support than thinner LSSB layers. In fact, among all the cells, the lowest performances (higher DCPI, lower moduli, and higher deflections) were observed in the cells constructed with 9-in (230-mm) LSSB layers (Cells 328 to 728).

- Although it was clearly observed during construction that using geosynthetics between 9-in (230-mm) LSSB and Clay Loam subgrade layers mitigated rutting and subgrade soil pumping under construction traffic, no superior performance was observed in the reconstructed cells compared to the failed cells.

CHAPTER 4: LABORATORY TESTING

4.1 MATERIALS

Ten different materials (Figure 4.1) were used to construct the cells (Figure 3.2). Two different subgrade soils were Sand Subgrade and Clay Loam [Figure 4.1(a) and Figure 4.1(b), respectively]. Two different subbase materials were Select Granular Borrow (MnDOT 2018) and LSSB Material [Figure 4.1(c) and Figure 4.1(d), respectively]. Base layer aggregates were Coarse RCA, Fine RCA, Limestone, RCA+RAP, Class 6 Aggregate, and Class 5Q Aggregate (MnDOT 2018) [Figure 4.1(e), 4.1(f), 4.1(g), 4.1(h), 4.1(i), and 4.1(j), respectively].

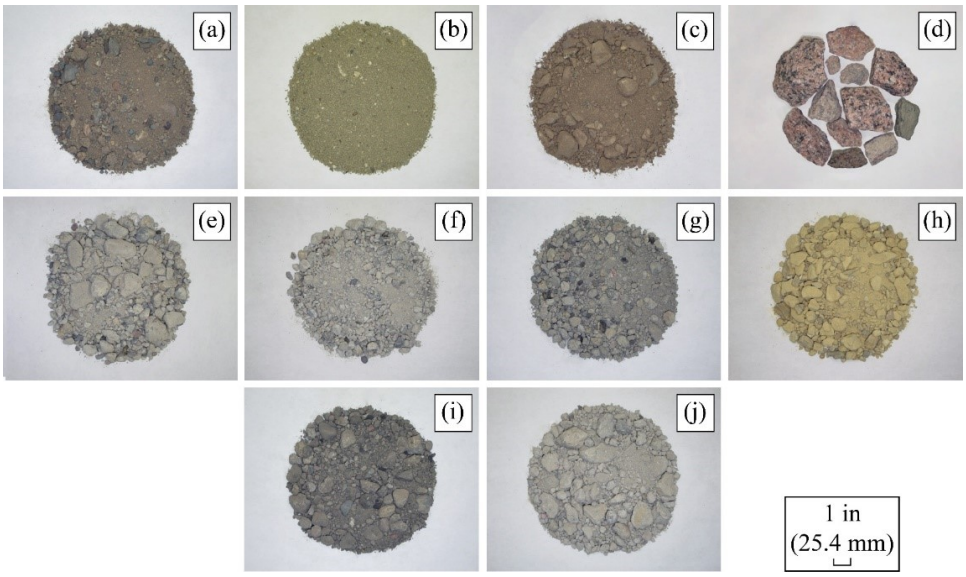

Figure 4.1. Materials used to construct test cells: (a) Sand Subgrade, (b) Clay Loam, (c) Select Granular Borrow, (d) LSSB Material, (e) Coarse RCA, (f) Fine RCA, (g) RCA+RAP, (h) Limestone, (i) Class 6 Aggregate, and (j) Class 5Q Aggregate

4.2 INDEX PROPERTIES

4.2.1 Deleterious Material Content

Each material was spread on a large pan and deleterious materials were identified visually. The deleterious materials that could be identified were plant roots, leaves, wood chips, plastic, and fabric. A magnet was used to remove metal, such as reinforcing steel, from the RCA materials' matrix. However, no steel pieces were observed. The collected deleterious materials were weighed. For each material, the weight of the deleterious materials was less than %0.1 of the dry weight of the material. Therefore, it was concluded that the materials satisfied the quality requirements determined by the MnDOT specification (MnDOT 2018). In addition, it was observed that the materials, other than RCA+RAP, also contained low amounts of RAP particles. However, those RAP particles were considered to be a part of those materials; therefore, they were not removed.

4.2.2 Classification of Materials

Particle size distributions of the materials were determined in accordance with ASTM C136, D6913, and D7928 (Figure 4.2). Atterberg limits were determined per BS 1377-2 (fall cone penetrometer) and ASTM D4318 (plastic limit rolling device) (Table 4.1). Classifications were determined according to the Unified Soil Classification System (USCS) (ASTM D2487) and the American Association of State Highway and Transportation Officials (AASHTO) soil classification system (AASHTO M 145) (Table 4.1).

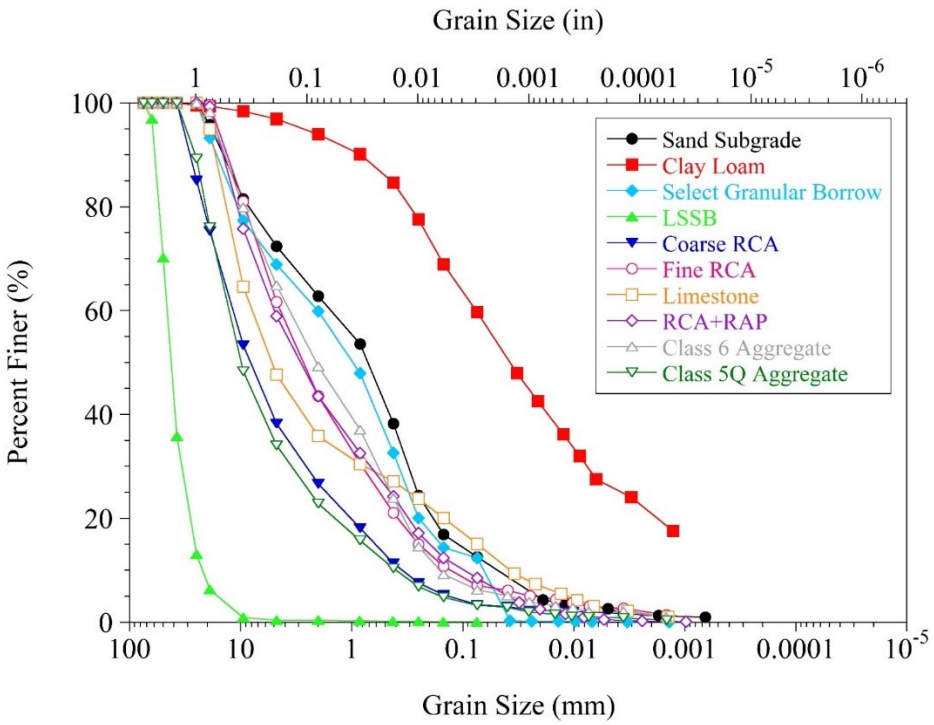

Figure 4.2. Particle size distributions of materials

Sand Subgrade and Clay Loam were classified as SM (silty sand with gravel) and CL (sandy lean clay) according to the USCS, respectively. The AASHTO soil classifications were determined to be A-1-b and A-6 for Sand Subgrade and Clay Loam, respectively. Select Granular Borrow and LSSB Material were classified as SM (silty sand with gravel) and GP (poorly graded gravel) according to the USCS, respectively. The AASHTO soil classifications were determined to be A-1-b and A-1-a for Select Granular Borrow and LSSB Material, respectively.

Coarse RCA, Fine RCA, Limestone, RCA+RAP, Class 6 Aggregate, and Class 5Q Aggregate were classified as GW (well-graded gravel with sand), SW-SM (well-graded sand with silt and gravel), GM (silty gravel with sand), SP-SM (poorly graded sand with silt and gravel), SP-SM (poorly-graded sand with silt and gravel), and GW (well-graded gravel with sand) according to the USCS, respectively. All base layer aggregates except Limestone were classified as A-1-a according to the AASHTO soil classification system. The AASHTO soil classification of Limestone was determined to be A-1-b.

Table 4.1. Index properties of materials

Material	Gravel (%)	Sand (%)	Fines (%)	C_u	C_c	LL	PI	USCS	AASHTO
Sand Subgrade	27.6	59.8	12.6	33.12	1.24	19.9	NP	SM	A-1-b
Clay Loam	3.1	37.2	59.7	NA	NA	36.3	12.4	CL	A-6
Select Granular Borrow	31.1	56.5	12.4	30.30	1.10	18.9	NP	SM	A-1-b
LSSB	99.6	0.3	0.1	1.84	1.08	NA	NP	GP	A-1-a
Coarse RCA	61.7	34.9	3.4	34.49	1.75	NA	NP	GW	A-1-a
Fine RCA	38.3	54.6	7.1	33.93	1.12	32.7	NP	SW-SM	A-1-a
Limestone	52.3	32.6	15.1	211.3	1.91	17.9	NP	GM	A-1-b
RCA+RAP	41	50.4	8.6	49.41	0.98	27.4	NP	SP-SM	A-1-a
Class 6 Aggregate	35.1	58.6	6.3	23.82	0.60	27.4	NP	SP-SM	A-1-a
Class 5Q Aggregate	65.9	30.9	3.2	33.69	2.60	NA	NP	GW	A-1-a

Fines = silt and clay; C_u = uniformity coefficient; C_c = coefficient of curvature; LL = liquid limit; PI = plasticity index; USCS = Unified Soil Classification System; AASHTO = American Association of State Highway and Transportation Officials; NP = non-plastic; NA = not available.

4.2.3 Specific Gravity (G_s) and Absorption

Specific gravity (G_s) and absorption of all the materials except Clay Loam were determined based on ASTM C127 and C128. For Clay Loam, ASTM D854 was followed. G_s and absorption of each material (except Clay Loam) were determined by taking the weighted average of the coarse [> No. 4 sieve (4.75 mm)] and fine (< No. 4) fractions of the material (Table 4.2). Three different specific gravity terms are provided in Table 4.2: (1) oven-dry (OD), (2) saturated-surface-dry (SSD), and (3) apparent G_s. However, only OD G_s, which is the most commonly used in Geotechnical Engineering, is discussed hereinafter.

Sand Subgrade and Clay Loam exhibited G_s values of 2.60 and 2.68, respectively. Sand Subgrade exhibited an absorption of 1.84%. Absorption could not be determined for Clay Loam because ASTM D854 does not include any testing procedure to determine absorption for Clay Loam. G_s and absorption of Select Granular Borrow were determined to be 2.62 and 1.53%, respectively. LSSB Material exhibited a G_s value of 2.60 and an absorption value of 0.36%.

Coarse RCA, Fine RCA, and RCA+RAP exhibited lower G_s (2.25, 2.17, and 2.28, respectively) and higher absorption (6.97, 8.65, and 4.34%, respectively) than Limestone (G_s and absorption were 2.66 and 1.72%, respectively). RCA materials tend to show lower G_s and higher absorption than VAs because of their residual mortar content and porous structure (Snyder et al. 1994; Abbas et al. 2007; Bhasya and Bharatkumar 2018; Titi et al. 2019). Low-density asphalt binder and trapped air between the asphalt and

aggregate particles cause lower G_s for RAP (Cosentino et al. 2003; Okafor 2010). Fine RCA exhibited lower G_s (2.17) and higher absorption (8.65%) than Coarse RCA (G_s and absorption were 2.25 and 6.97%, respectively). RCA+RAP exhibited lower absorption (4.34%) than Coarse RCA (6.97%) and Fine RCA (8.65%) and this was attributed to RAP material's hydrophobicity (Rahardjo et al. 2010; Nokkaew et al. 2012).

Class 6 Aggregate and Class 5Q Aggregate also exhibited lower G_s (2.35 and 2.28, respectively) and higher absorption (3.86% and 6.32%, respectively) than Limestone (G_s and absorption were 2.66 and 1.72%, respectively). Based on these results and the visual-manual soil identification procedure (ASTM D2488), it was determined that Class 6 Aggregate and Class 5Q Aggregate contained considerable amounts of RCA. In addition, Class 6 Aggregate also contained RAP (Class 5Q Aggregate also contained RAP but in a much smaller quantity compared to Class 6 Aggregate).

Table 4.2. Specific gravity (G_s) and absorption of materials

Material	Oven-Dry (OD) G_s	Saturated-Surface-Dry (SSD) G_s	Apparent G_s	Absorption (%)
Sand Subgrade	2.60	2.64	2.72	1.84
Clay Loam	NA	NA	2.68	NA
Select Granular Borrow	2.62	2.66	2.72	1.53
LSSB	2.60	2.61	2.63	0.36
Coarse RCA	2.25	2.40	2.64	6.97
Fine RCA	2.17	2.35	2.64	8.65
Limestone	2.66	2.71	2.79	1.72
RCA+RAP	2.28	2.38	2.52	4.34
Class 6 Aggregate	2.35	2.44	2.58	3.86
Class 5Q Aggregate	2.28	2.42	2.65	6.32

G_s = specific gravity; NA = not available.

4.2.4 Proctor Compaction

Maximum dry unit weight (MDU) and optimum moisture content (OMC) values of the materials were determined per ASTM D1557. Method C was used for all the materials except Clay Loam and LSSB Material. Method A was used for Clay Loam. Proctor compaction test could not be performed on LSSB Material due to the size limitations of the compaction testing equipment.

Corrections for the materials containing oversize particles were applied per ASTM D4718. Figure 4.3 shows the compaction curves determined by the Proctor compaction test. Both Proctor compaction test results (ASTM D1557) and corrected unit weight and moisture content values (ASTM D4718) are summarized in Table 4.3. Only the corrected unit weight and moisture content values will be discussed hereinafter.

Sand Subgrade exhibited relatively higher MDU (137.7 pcf) and lower OMC (5.6%) compared to Clay Loam (MDU and OMC were 124.9 pcf and 10%, respectively) (Table 4.3). MDU and OMC of Select Granular Borrow were determined to be 140.3 pcf and 5.3%, respectively.

Coarse RCA, Fine RCA, and RCA+RAP exhibited lower MDU (128.6, 121.7, and 125.8 pcf, respectively) and higher OMC (9.5, 11.1, and 10%, respectively) than Limestone (MDU and OMC were 143.2 pcf and 6.3%, respectively). RCA materials are prone to exhibit higher OMC compared to VAs because of their higher absorption and hydrophilicity (Rahardjo et al. 2010). RCA materials also tend to exhibit lower MDU than VAs because of the presence of residual mortar, which lowers G_s. Cementation of unhydrated cement particles in the RCA matrix increases the resistance of particles against compaction efforts, and this can also reduce MDU (Hussain and Dash 2010; Chen and Brown 2012). Fine RCA exhibited lower MDU (121.7 pcf) and higher OMC (11.1%) than Coarse RCA (MDU and OMC were 128.6 pcf and 9.5%, respectively) and RCA+RAP (MDU and OMC were 125.8 pcf and 10%, respectively).

Class 6 Aggregate and Class 5Q Aggregate exhibited lower MDU (128.5 and 128 pcf, respectively) and higher OMC (8.3 and 9.6%, respectively) than Limestone (MDU and OMC were 143.2 pcf and 6.3%).

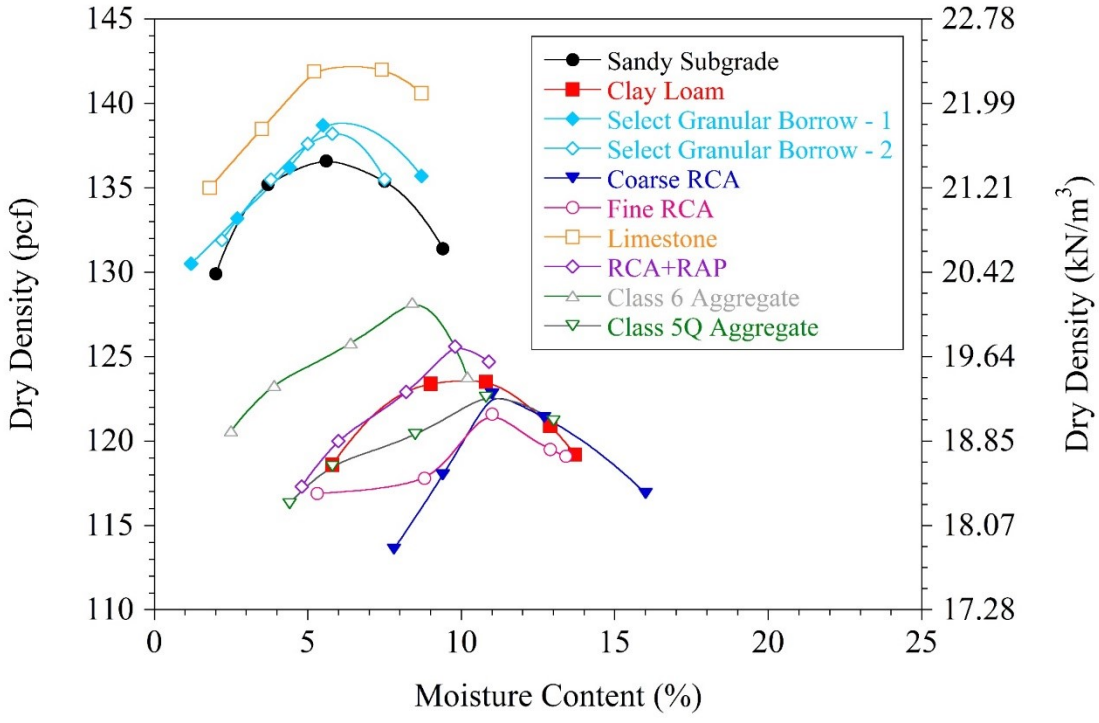

Figure 4.3. Proctor compaction curves of materials

Table 4.3. Uncorrected (actual) and corrected Proctor compaction test results

Material	Proctor Compaction Test Results			Corrected for Oversize Particles		
	MDU		OMC (%)	Corrected MDU		Corrected OMC (%)
	(pcf)	(kN/m^3)		(pcf)	(kN/m^3)	
Sand Subgrade	136.6	21.46	5.7	137.7	21.63	5.6
Clay Loam	123.9	19.46	10	124.9	19.62	10.0
Select Granular Borrow	138.6	21.77	5.4	140.3	22.03	5.3
LSSB	NA	NA	NA	NA	NA	NA
Coarse RCA	122.9	19.31	11.3	128.6	20.19	9.5
Fine RCA	121.6	19.10	11.1	121.7	19.12	11.1
Limestone	142.2	22.34	6.2	143.2	22.49	6.3
RCA+RAP	125.6	19.73	10	125.8	19.76	10.0
Class 6 Aggregate	128.2	20.14	8.3	128.5	20.19	8.3
Class 5Q Aggregate	122.6	19.26	11	128.0	20.11	9.6

MDU = maximum dry unit weight; OMC = optimum moisture content; NA = not available.

4.2.5 Asphalt Binder Content

In order to find the asphalt binder contents of the materials used, the ignition method (AASHTO T 308 and ASTM D6307) and the quantitative extraction method (AASHTO T 164 and ASTM D2172) were performed [Figure 4.4(a) and Figure 4.4 (b), respectively].

Figure 4.4. (a) Ignition furnace used in ignition method and (b) asphalt extraction bowl used in quantitative extraction

Overall, asphalt binder contents, determined by the ignition method, were relatively higher than the binder contents, determined by the quantitative extraction method (Table 4.4). Mineral fines and other organic materials may be burned away from the test material during ignition and cause higher asphalt

binder contents. In addition, loss of fines, which are lighter than the granular particles, by the ventilation system during ignition may be another reason for observed higher asphalt binder contents by the ignition method.

For both methods, RCA+RAP and Class 6 Aggregate exhibited the highest asphalt binder contents. Asphalt binder content of RCA+RAP was determined to be 3.18 and 1.58% by the ignition method and the quantitative extraction method, respectively. Asphalt binder content of Class 6 Aggregate was determined to be 3.17 and 1.77% by the ignition method and the quantitative extraction method, respectively. Asphalt binder contents of Coarse RCA, Fine RCA, Limestone, and Class 5Q Aggregate were not zero because they contained RAP in small quantities (Figure 4.5). According to the ignition method, asphalt binder content of Fine RCA (2.98%) was close to those of RCA+RAP (3.18%) and Class 6 Aggregate (3.17%). However, according to the quantitative extraction method, Fine RCA contained considerably lower asphalt binder (0.35%) compared to RCA+RAP (1.58%) and Class 6 Aggregate (1.77%). As stated previously, Fine RCA exhibited the lowest G_s (2.17) indicating that it consisted of lighter particles compared to other materials (Table 4.2). It was speculated that the presence of lighter fine particles in Fine RCA caused higher loss of fines by the ventilation system (lighter particles can be sucked by the ventilation system easier than heavier particles) for Fine RCA and this caused asphalt binder content (2.98%) for Fine RCA to be as high as asphalt binder content of RCA+RAP (3.18%) and Class 6 Aggregate (3.17%). According to the ignition method, Coarse RCA and Class 5Q Aggregate had relatively higher asphalt binder contents (2.02 and 2.15%, respectively) compared to Limestone (1.61%). However, according to the quantitative extraction, Coarse RCA and Class 5Q Aggregates had the lowest asphalt binder contents (0.10 and 0.28%, respectively). This result can also be attributed to lower G_s of Coarse RCA (2.25) and Class 5Q Aggregate (2.28) compared to Limestone (2.66).

Table 4.4. Asphalt binder content–s of materials

Material	Asphalt Binder Content (%)	
	Ignition Method	Quantitative Extraction Method
Coarse RCA	2.02	0.10
Fine RCA	2.98	0.38
Limestone	1.61	0.35
RCA+RAP	3.18	1.58
Class 6 Aggregate	3.17	1.77
Class 5Q Aggregate	2.15	0.28

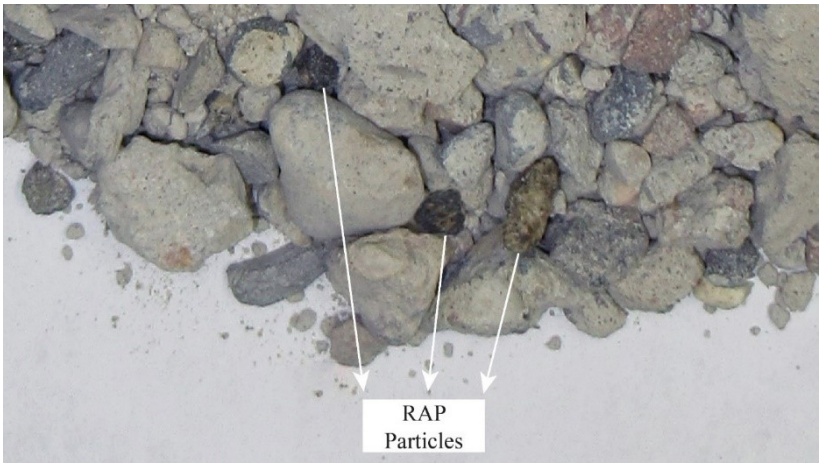

Figure 4.5. Recycled asphalt pavement (RAP) particles in Coarse RCA

4.2.6 Residual Mortar Content

Residual mortar contents of the materials used were determined based on a method developed by Abbas et al. (2007). A saturated sodium sulfate solution (26% by weight) was prepared as described in ASTM C88 (soundness test) (Figure 4.6). In fact, only a sodium sulfate concentration of 17% (by weight) would be enough for the saturated solution. However, according to ASTM C88, it is desirable that an excess of sodium sulfate crystals is to be present in the solution. Therefore, a more-than-needed amount of sodium sulfate (26% by weight) was used. Due to the high sodium sulfate concentration, salt cake formed in the solution (Figure 4.7). For each material, 2000 g of the particles retained on a 1-in sieve (if any), 2000 g of the particles retained on a 3/4-in sieve (if any), 1000 g of the particles retained on a 3/8-in sieve, and 1000 g of the particles retained on a No. 4 sieve were collected (Figure 4.8). The prepared samples were then dried for 24 h at 105°C. After drying, the oven-dried samples were immersed in the sodium sulfate solution for 24 h. While the samples were in the solution, they were subjected to five daily freeze-thaw cycles. Each freeze-thaw cycle included 16 h of freezing at -17°C (1.4°F) [Figure 4.9(a)] and 8 h of thawing at 80°C (176°F) [Figure 4.9(b)]. After the completion of the last cycle, the mixtures of the disintegrated mortar and natural aggregates (Figure 4.10) were washed over No. 4 (4.75 mm) sieve to get rid of the disintegrated mortar. As recommended by Butler et al. (2011), a rubber mallet was used to crush the remaining mortar and the samples were washed again over No. 4 sieve and dried at 105°C (221°F) for 24 h. Then, the final oven-dry mass of each sample was recorded, and the residual mortar content of each material was calculated. Upon visual inspection, 100% removal of the residual mortar could not be achieved as some aggregate particles still contained a thin mortar film on their surfaces (Figure 4.11). However, it was concluded that almost all the residual mortar was removed (Figure 4.12).

Class 5Q Aggregate and Coarse RCA contained the highest (37.1%) and the second highest (33.4%) residual mortar, respectively, compared to other base layer aggregates (Table 4.5). Fine RCA contained the third highest residual mortar (29.6%) (Table 4.5). Class 6 Aggregate exhibited relatively higher residual mortar content (25.6%) than RCA+RAP (20.1%) (Table 4.5). Limestone did not exhibit any considerable residual mortar content (1.3%), as expected (Table 4.5).

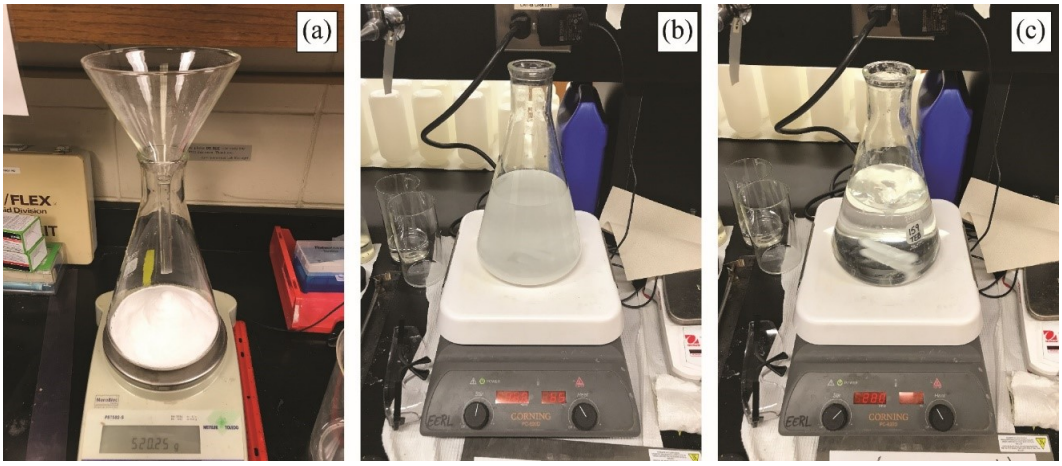

Figure 4.6. (a) Preparation of sodium sulfate solution, (b) early stage of mixing, and (c) end of mixing

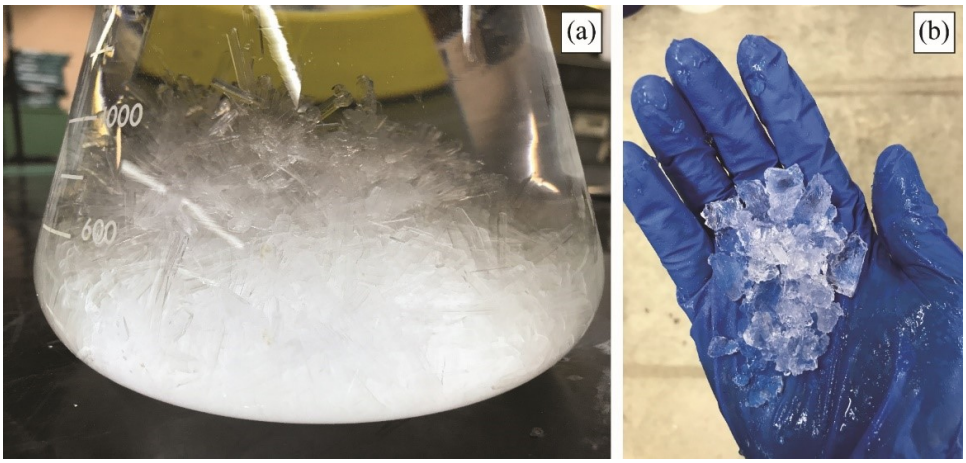

Figure 4.7. (a) Crystallization of sodium sulfate and (b) broken salt crystals

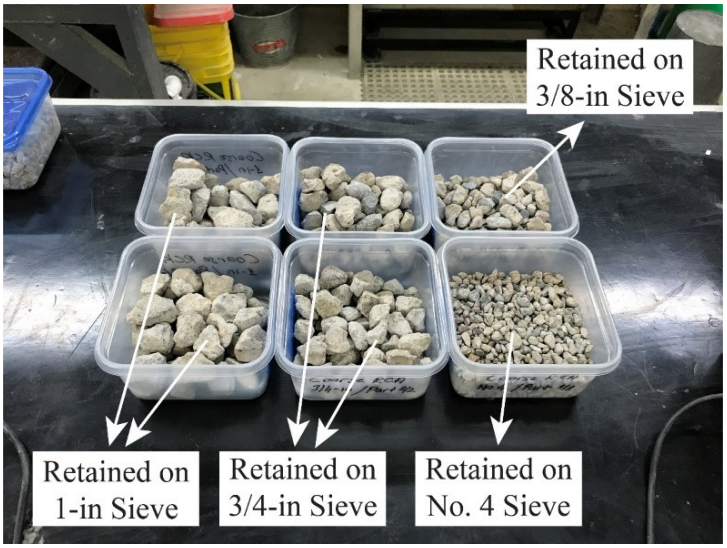

Figure 4.8. Samples prepared for Coarse RCA

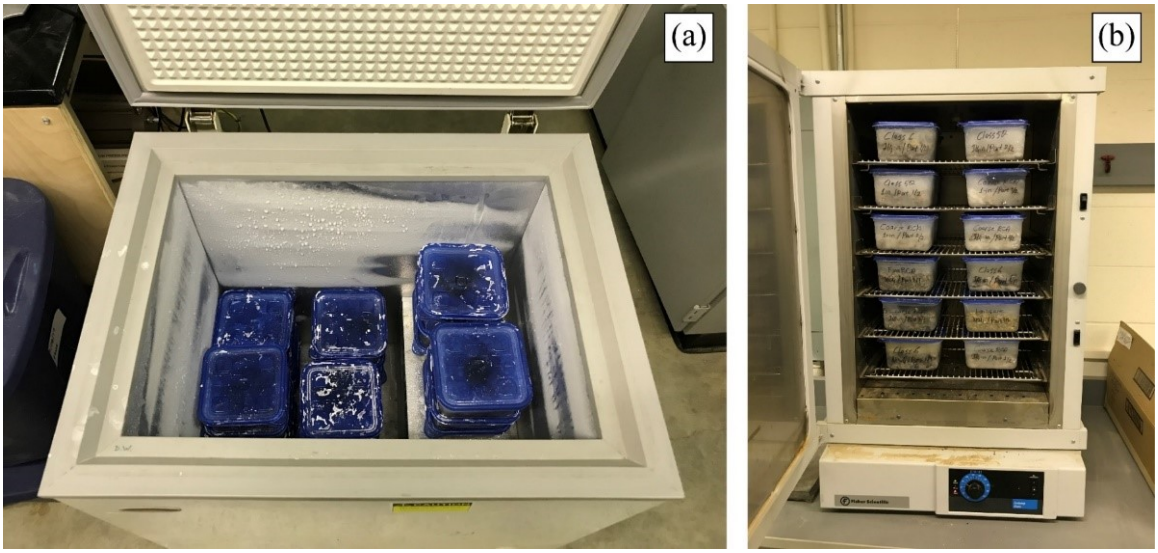

Figure 4.9. (a) Freezing phase and (b) thawing phase

Figure 4.10. Mixture of disintegrated mortar and aggregates

Figure 4.11. Remaining mortar film on particle surfaces

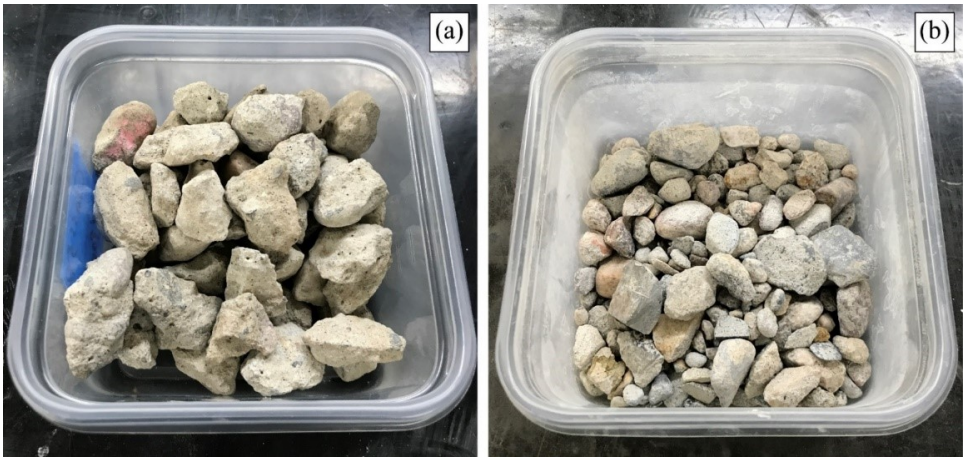

Figure 4.12. (a) Before (b) after residual mortar content determination test

Table 4.5. Residual mortar contents of materials

Material	Residual Mortar Content (%)
Coarse RCA	33.4
Fine RCA	29.6
Limestone	1.3
RCA+RAP	20.1
Class 6 Aggregate	25.6
Class 5Q Aggregate	37.1

4.2.7 Water Repellency

Water repellency of base layer aggregates was evaluated by the apparent contact angle and the water drop penetration time (WDPT) measurements. The apparent contact angle (the angle at zero energy state of water) is the angle between the tangent to the solid surface and the tangent to the liquid-fluid interface (Figure 4.13) (Wolansky and Marmus 1999). The WDPT is defined as the time required for a water drop to completely infiltrates through the materials after its placement at the surface of the aggregate particle (Edil et al. 2012). Mandal and Jayaprakash (2009) classify materials in terms of their water repellency based on their apparent contact angle and WDPT (Table 4.6).

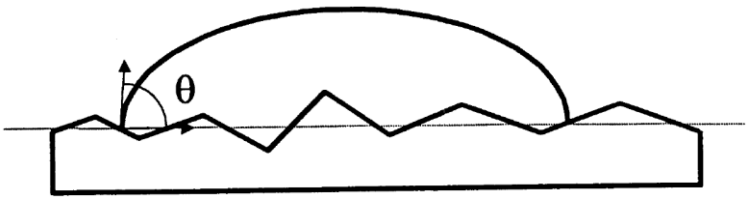

Figure 4.13. Apparent contact angle

Table 4.6. Water repellency classifications provided by Mandal and Jayaprakash (2009)

Water repellency	WDPT (s)	Apparent contact angle (°)
Wettable	<5	0
Slightly to moderately repellent	5–60	67
Strongly water-repellent	60–600	90
Severely water-repellent	600–3600	98
Extremely water-repellent	>3600	122

For Coarse RCA, Fine RCA, and Class 5Q Aggregate, 25 RCA particles were tested for each material. For RCA+RAP and Class 6 Aggregate, 25 RAP and 25 RCA particles were tested for each material. For Limestone, 25 particles were tested. Three examples for Coarse RCA, Fine RCA, Limestone, RCA+RAP, Class 6 Aggregate, and Class 5Q Aggregate are provided in Figure 4.14, Figure 4.15, Figure 4.16, Figure 4.17, Figure 4.18, and Figure 4.19, respectively. The average apparent contact angle and WDPT for each material are summarized in Table 4.7. Coarse RCA, Fine RCA, Limestone, and Class 5Q Aggregate exhibited 0° apparent contact angle and WDPT less than 5 seconds. Therefore, these materials were classified as wettable or hydrophilic. Apparent contact angles of RCA+RAP and Class 6 Aggregate were 83° and 86°, respectively. In addition, the water drops did not infiltrate through RCA+RAP and Class 6 Aggregate even after 3600 seconds from the placement of the water drops. As a result, these materials were classified as water repellent or hydrophobic.

Figure 4.14. Apparent water contact angle for Coarse RCA

Figure 4.15. Apparent water contact angle for Fine RCA

Figure 4.16. Apparent water contact angle for Limestone

Figure 4.17. Apparent water contact angle for RCA+RAP

Figure 4.18. Apparent water contact angle for Class 6 Aggregate

Figure 4.19. Apparent water contact angle for Class 5Q Aggregate

Table 4.7. Water repellency of materials

Material	Apparent Contact Angle (°)	Water Drop Penetration Time (WDPT) (s)	Water Repellency
Coarse RCA	~ 0	< 5	Wettable (Hydrophilic)
Fine RCA	~ 0	< 5	Wettable (Hydrophilic)
Limestone	~ 0	< 5	Wettable (Hydrophilic)
RCA+RAP	~ 83	> 3600	Water Repellent (Hydrophobic)
Class 6 Aggregate	~ 86	> 3600	Water Repellent (Hydrophobic)
Class 5Q Aggregate	~ 0	< 5	Wettable (Hydrophilic)

4.3 SATURATED AND UNSATURATED PROPERTIES

One of the main functions of aggregate base layers is to provide adequate drainage and prevent capillary action to increase the service life of pavements (Cedergren 1988). An increase in the pore water pressure in aggregate base layers causes a reduction in the stiffness of aggregate base layers (Edil et al. 2012).

K_{sat} is the ability of soil to let water flow in the presence of a hydraulic gradient. SWCC is used to describe the relationship between the volumetric water content (VWC) and the matric suction of unsaturated soils. K_{sat} is used as a parameter for drainage design, and SWCC is used to determine and evaluate the modulus of aggregate base layers (Gupta et al. 2004; NCHRP 2004a).

Saturated and unsaturated properties of aggregate base layers could be affected by the type of the recycled aggregate used (RCA or RAP). RCA materials are hydrophilic due to residual mortar content and unhydrated cement content emerging after the demolition of existing concrete (Rahardjo et al. 2010; Edil et al. 2012). The use of RCA materials could reduce the permeability of aggregate base layers due to further cementation of unhydrated cement particles. Another concern may arise with the use of RCA in aggregate base layers due to the tufa formation by leaching and precipitation of heavy metals (Ceylan et al. 2013; Abbaspour et al. 2016). First, CO_2 in the atmosphere and H_2O in the aqueous solution of RCA react to form carbonic acid (H_2CO_3). Then, H^+ and CO_3 form after the two-step ionization of H_2CO_3. In the final step, Ca2+ released from the cement at the high pH environment reacts with CO_3 coming from the ionization of H_2CO_3 and the reaction forms calcite ($CaCO_3$) (Feldmann et al. 1982). Drainage properties of aggregate base layers constructed with RCA can be reduced as a result of the tufa formation (Ceylan et al. 2013). In addition, the pipes located beneath a pavement system for drainage purposes can be clogged by the tufa formation (Figure 2.37) (Ceylan et al. 2013).

The use of RAP materials could improve the drainage characteristics of aggregate base layers since RAP materials exhibit hydrophobic properties due to the asphalt coating around particles (Rahardjo et al. 2010; Edil et al. 2012).

4.3.1 Permeability (K_{sat}) Test

K_{sat} tests were carried out on saturated specimens in accordance with ASTM D5084. For the tests, a permeability instrument with constant head principle (ASTM D5084 method A), which was suitable for coarser materials, was used. A sketch and a picture of the constant head permeability test equipment are provided in Figure 4.20 and Figure 4.21, respectively. For the tests, 6-in diameter and 4-in height specimens were prepared inside of the membrane by light hammering method (Figure 4.22). For Coarse RCA, Fine RCA, Limestone, and RCA+RAP, three specimens were prepared per material. For Sand Subgrade, Class 6 Aggregate, and Class 5Q Aggregate, four specimens were prepared per material. After the completion of the specimen preparation, each specimen was saturated per ASTM D5084. Saturation was controlled by two methods. The first method was observing the color change throughout the membrane. Homogeneous color distribution within the membrane during the saturation process was the first indication of the saturation (this indication may not be 100% accurate since the inside of the specimen may not be saturated even if the homogeneous color distribution was achieved). The second method was observing the K_{sat} measurements over time. During the test, the volume of water passing through the test specimen under the constant hydraulic load was measured with time and K_{sat} values were calculated by Darcy's law, as described in ASTM D5084. In the early stages of the tests, K_{sat} values were not stable. However, after a certain time, K_{sat} values became stable and this was believed to be the actual indication of saturation (Figure 4.23). The K_{sat} value which reached the stability was recorded to be the K_{sat} of the specimen.

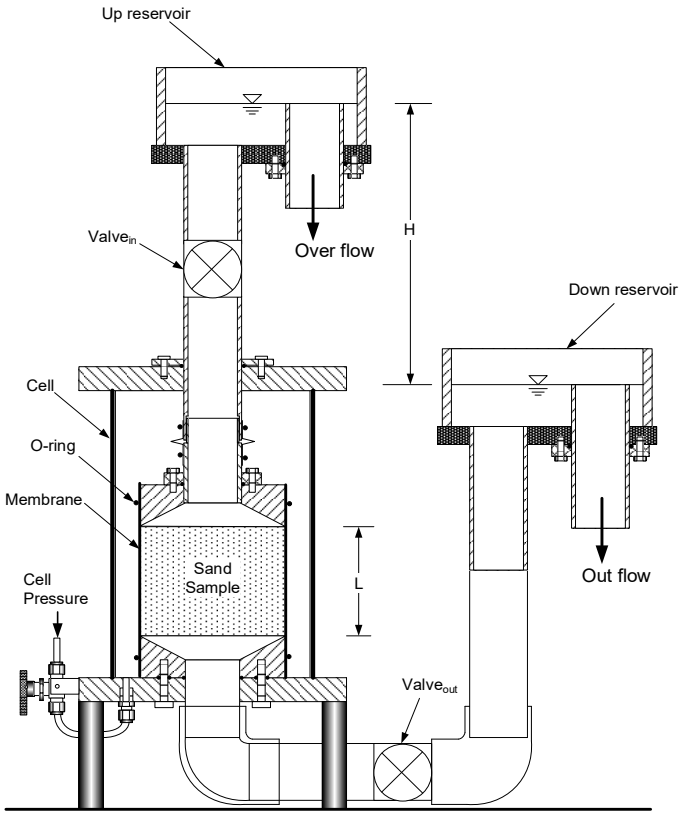

Figure 4.20. Sketch of constant head permeability test equipment

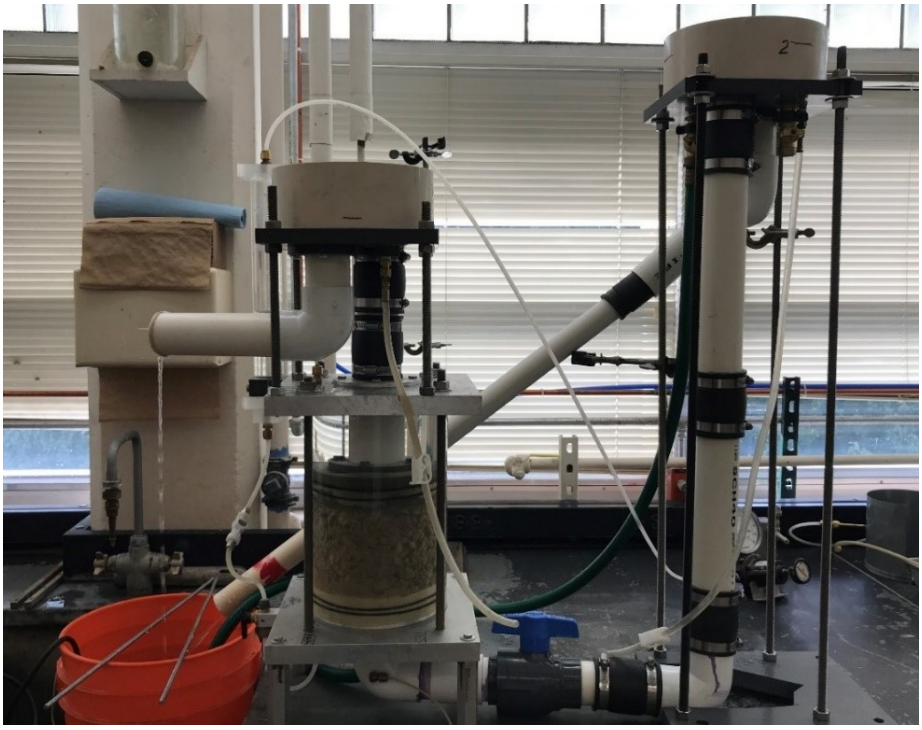

Figure 4.21. Picture of constant head permeability test equipment

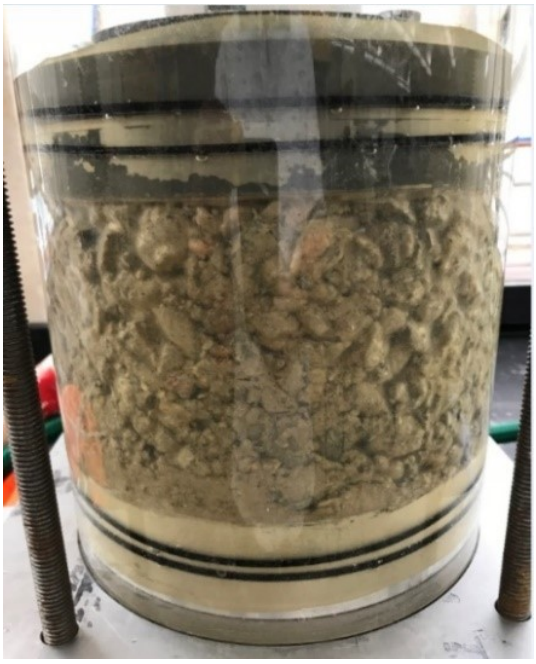

Figure 4.22. Specimen prepared for constant head permeability test

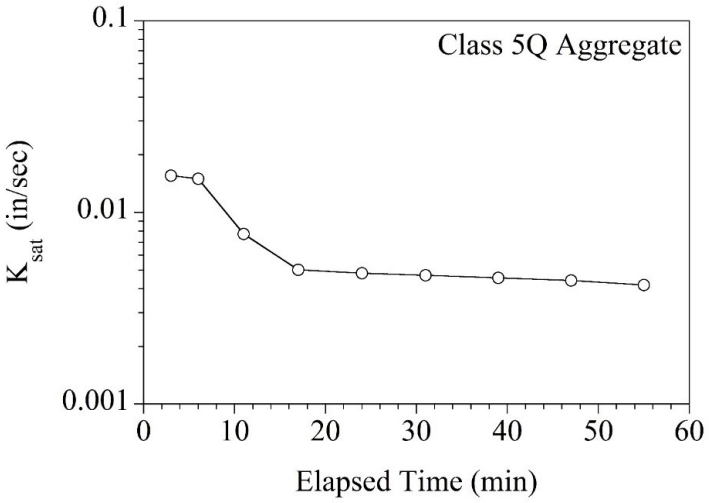

Figure 4.23. Saturated hydraulic conductivity (K_{sat}) versus elapsed time during constant head permeability test

K_{sat} and the degree of compaction (DOC) values of the materials, determined by the constant head permeability tests, are provided in Figure 4.24. Overall, it was concluded that the specimens could not be compacted sufficiently by the light hammering in the membrane because the DOC values were lower than 100% (as low as 84.6%). Fine RCA yielded the highest K_{sat} values with a narrower range (ranging from $1.41x10^{-2}$ to $3.26x10^{-2}$ in/sec). Sand Subgrade, Coarse RCA, and RCA+RAP exhibited relatively lower K_{sat} values with wider ranges (ranging from $3.35x10^{-5}$ to $6.57x10^{-3}$ in/sec). Class 6 Aggregate and Class 5Q Aggregate also exhibited similar K_{sat} values (Class 6 Aggregate exhibited a narrower range) (ranging from $2.07x10^{-3}$ to $9.41x10^{-3}$ in/sec). Limestone exhibited similar K_{sat} values compared to Class 6 Aggregate and Class 5Q Aggregate; however, the minimum K_{sat} value of Limestone ($1.70x10^{-4}$ in/sec) was much lower than those of Class 6 Aggregate ($2.78x10^{-3}$ in/sec) and Class 5Q Aggregate ($2.07x10^{-3}$ in/sec).

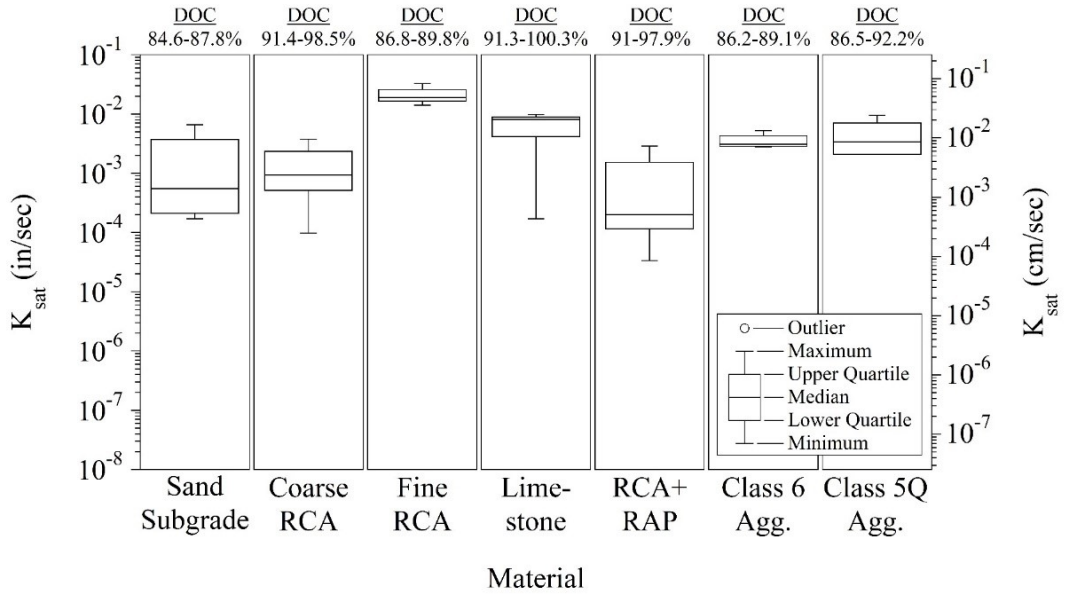

Figure 4.24. Constant head permeability test results (DOC = degree of compaction)

After evaluating the DOC values obtained by the light hammering in the membrane, a new specimen preparation method, in which the specimens were compacted in a 6-in compaction mold in five layers, was followed. First, all materials were sieved through a 3/4-in sieve and then the specimens were compacted to their MDU and OMC (Figure 4.3 and Table 4.3). After the compaction, the specimens were extruded from the compaction mold by a hydraulic jack (Figure 4.25) and placed into a membrane to be put into a triaxial cell. Clay Loam, Coarse RCA, Fine RCA, Limestone, and RCA+RAP specimens were prepared by this method for further testing. For Clay Loam, six specimens were prepared. For Coarse RCA, Fine RCA, Limestone, and RCA+RAP, three specimens were prepared per material.

The permeability test method was also switched to the standard falling head permeability tests (ASTM D5084 method C). The cell and the burette system of the falling head permeability test are provided in Figure 4.26.

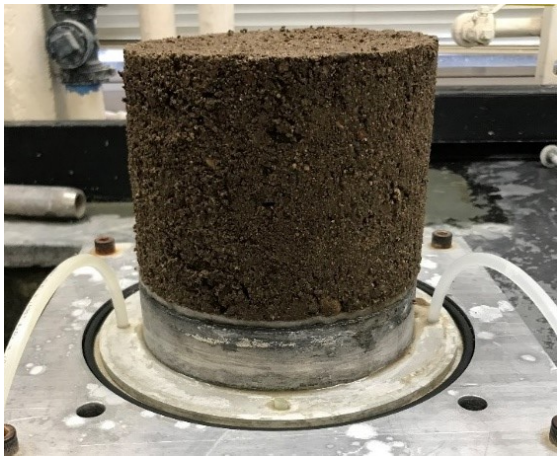

Figure 4.25. Specimen prepared in compaction mold for falling head permeability test

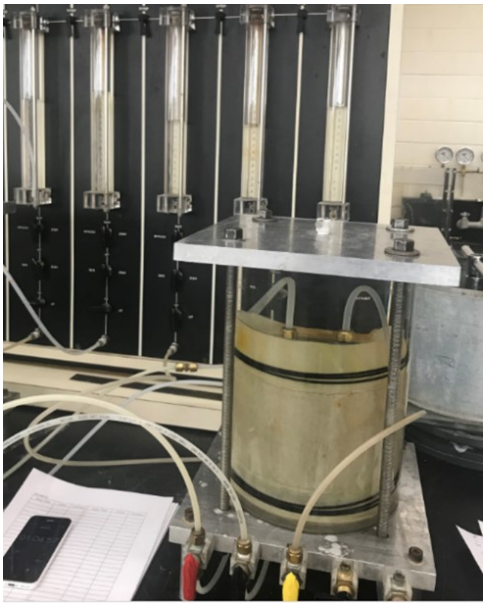

Figure 4.26. Picture of falling head permeability test system

K_{sat} and the DOC values of the specimens, which were prepared in the compaction mold and tested by the falling head permeability test, are provided in Figure 4.27. Relatively higher DOC values were observed with this method (the lowest DOC was 96.8%) compared to the light hammering in the membrane [the DOC values were as low as 84.6% (Figure 4.24)] due to the change in the compaction effort. Overall, the K_{sat} values obtained by the falling head permeability (Figure 4.27) were in narrower ranges compared to those obtained by the constant head permeability (Figure 4.24). Clay Loam exhibited the lowest K_{sat} values as expected (ranging from $3.75x10^{-8}$ to $2.59x10^{-7}$ in/sec). Coarse RCA, Fine RCA, and RCA+RAP exhibited similar K_{sat} values (K_{sat} values of Fine RCA were in a narrower range) (ranging from $3.93x10^{-5}$ to $3.28x10^{-4}$ in/sec). Limestone yielded lower K_{sat} values (ranging from $1.34x10^{-5}$ to $1.93x10^{-5}$ in/sec) than Coarse RCA, Fine RCA, and RCA+RAP.

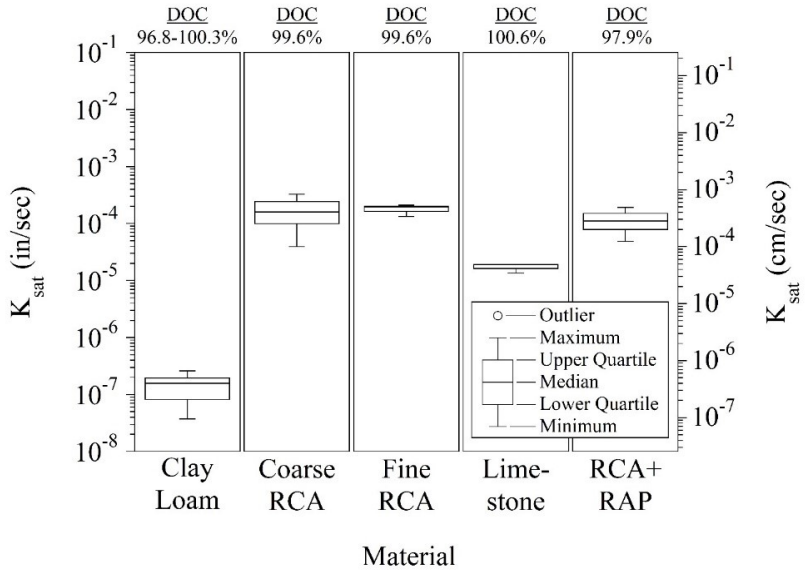

Figure 4.27. Falling head permeability test results (DOC = degree of compaction)

To observe the effects of the DOC on K_{sat} values of each material, more tests were prepared for all materials except Select Granular Borrow and LSSB Material. All specimens were compacted in the compaction mold at three different compaction energies to obtain 100, 95, and 90% DOC (Table 4.3). Specimens were compacted at their corresponding OMCs (Table 4.3) and OMCs were kept constant. Then, falling head permeability tests were performed on each material and results were evaluated (Figure 4.28). Particle size distributions of the materials used in the tests are summarized in Figure 4.29 and Table 4.8.

Overall, lowering the DOC yielded higher K_{sat} values for all materials. Less compaction, yielding lower DOC values, was obtained by applying lower compaction energies and these materials exhibited a more porous structure which allowed water to pass through faster. For all three cases, Clay Loam yielded the lowest K_{sat} values ($5.39x10^{-8}$, $5.94x10^{-7}$, and $2.70x10^{-6}$ in/sec for 100, 95, and 90% DOC, respectively). Then, Limestone exhibited the second lowest K_{sat} values for all three cases ($3.17x10^{-5}$, $7.52x10^{-5}$, and $1.29x10^{-4}$ in/sec for 100, 95, and 90%, respectively). Coarse RCA exhibited the third lowest K_{sat} values for 100 and 90% DOC ($5x10^{-5}$ and $2.63x10^{-4}$ in/sec). For 95% DOC, Coarse RCA exhibited the fourth lowest

K_{sat} value ($1.92x10^{-4}$ in/sec); however, it was very close to the K_{sat} value of RCA+RAP ($1.89x10^{-4}$ in/sec), which was the third lowest one. Fine RCA exhibited the highest K_{sat} values for 100 and 95% DOC ($1.88x10^{-4}$ and $3.90x10^{-4}$ in/sec, respectively). However, for 90% DOC, Fine RCA exhibited lower K_{sat} value ($3.98x10^{-4}$ in/sec) than Class 6 Aggregate ($6.18x10^{-4}$ in/sec), Class 5Q Aggregate ($6.14x10^{-4}$ in/sec), and RCA+RAP ($5.79x10^{-4}$ in/sec). Class 5Q Aggregate, Sand Subgrade, and Class 6 Aggregate exhibited the second, third, and fourth highest K_{sat} values for 100 and 95% DOC. Overall, it was concluded that the trends between the K_{sat} values of all materials were similar between 100 and 95% DOC. However, for 90% DOC, the trends changed for all materials except Clay Loam and Limestone.

Coarse RCA yielded lower K_{sat} values than Fine RCA at each DOC (Figure 4.28). This result could be attributed to the higher fines content of the representative sample taken from Coarse RCA. In fact, Coarse RCA contained fewer fines content (3.4%) than Fine RCA (7.1%). However, prior to tests, each material was sieved through the 3/4-in sieve for the preparation of the specimens and this caused a difference in the particle size distributions of the materials and test specimens. Since the amount of particles larger than the 3/4-in sieve in Coarse RCA (24.6%) was higher than that of Fine RCA (0.3%), removal of such particles during the specimen preparation caused a higher increase in Coarse RCA's fines content (from 3.4% to 12.4%) than Fine RCA's fines content (from 7.1% to 9.6%). Therefore, Coarse RCA had lower permeability than that of Fine RCA and other base layer aggregates.

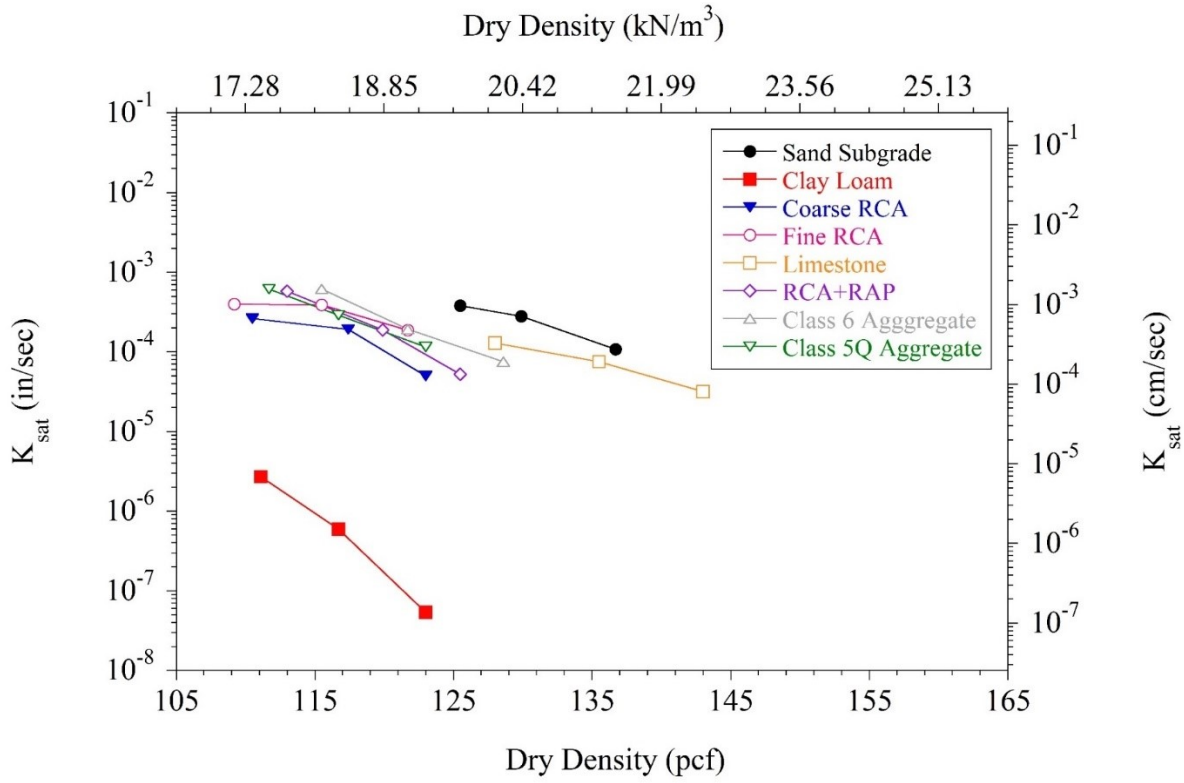

Figure 4.28. Effect of degree of compaction (DOC) on saturated hydraulic conductivity (K_{sat}) values of materials

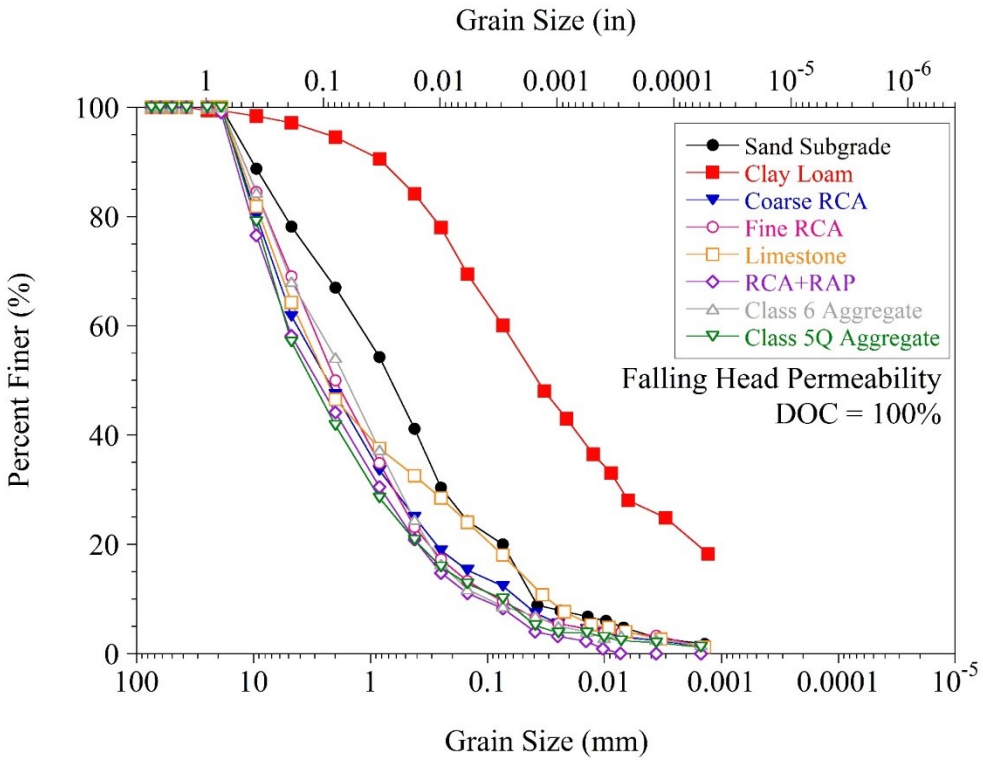

Figure 4.29. Particle size distributions of falling head permeability test specimens

Table 4.8. Compositions of falling head permeability test specimens

Material	Gravel (%)	Sand (%)	Fines (%)
Coarse RCA	38.2	49.4	12.4
Fine RCA	30.9	59.5	9.6
Limestone	35.7	46.2	18.1
RCA+RAP	41.8	49.9	8.3
Class 6 Aggregate	31.9	59.4	8.7
Class 5Q Aggregate	42.9	47	10.1
Sand Subgrade	21.8	58.2	20
Clay Loam	2.8	37.1	60.1

Fines = silt and clay

4.3.2 Soil-Water Characteristic Curve (SWCC)

SWCC describes the relationship between the VWC of the soil and the soil matric suction (i.e., negative matric potential). SWCC is used to describe the hydraulic, stiffness, and strength properties of unsaturated soils. The relationship between SWCC, permeability, stiffness, and shear resistance can be established. Gradation, morphology, mineralogy, stress history, and weathering of the soil affect the shape of the SWCC. Natural, compacted, and remolded soils also show different SWCC characteristics.

SWCC consists of two curves: wetting (absorption) and drying (desorption) curves (Likos et al. 2013) (Figure 4.30). Hysteresis is a phenomenon that affects the unsaturated hydraulic properties of soils. It is the difference between the matric suctions on the wetting and drying curves (Figure 4.30) (Ebrahimi-Birang et al. 2007). For the same matric suction, the drying curve shows relatively higher VWC than the wetting curve due to hysteresis (Likos et al. 2013). The difference between the two curves is influenced by several factors including the pore water composition and the pore structure. In general, only the drying curve is measured for soils due to the difficulty of obtaining the wetting curve (Hillel 1980, as cited in Nokkaew et al. 2012).

The VWC and matric suction relationship consist of three stages during drying (Figure 4.30). In the first stage, the saturation level of the soil does not decrease considerably in response to the increase in the matric suction. In this stage, the void ratio decreases due to shrinkage.

In the second stage, the so-called desaturation stage, the air starts to enter into the soil voids at the air-entry pressure (or bubbling pressure), which is the pressure required to start desaturation of the largest pores in the soil (Fredlund and Rahardjo 1993). When the matric suction keeps increasing after reaching the air-entry pressure, significant volumes of water begins to flow out of the soil as air enters the soil cavities. For well graded soils, the reduction in the water content is gentler. On the other hand, for uniformly graded soils, this reduction is steeper.

In the third stage, the so-called residual stage, some amount of water remains in the smallest voids. At this stage, a large increase in the matric suction is required for the discharge of water from the smallest voids. Many clayey soils can hold a significant amount of water and require very high matric suction to release the residual water content while still exhibiting a volume reduction and a high degree of saturation of up to 80%. In accordance with the laws of thermodynamics, the total suction value for soil at zero water content is around 145 ksi (1000 MPa).

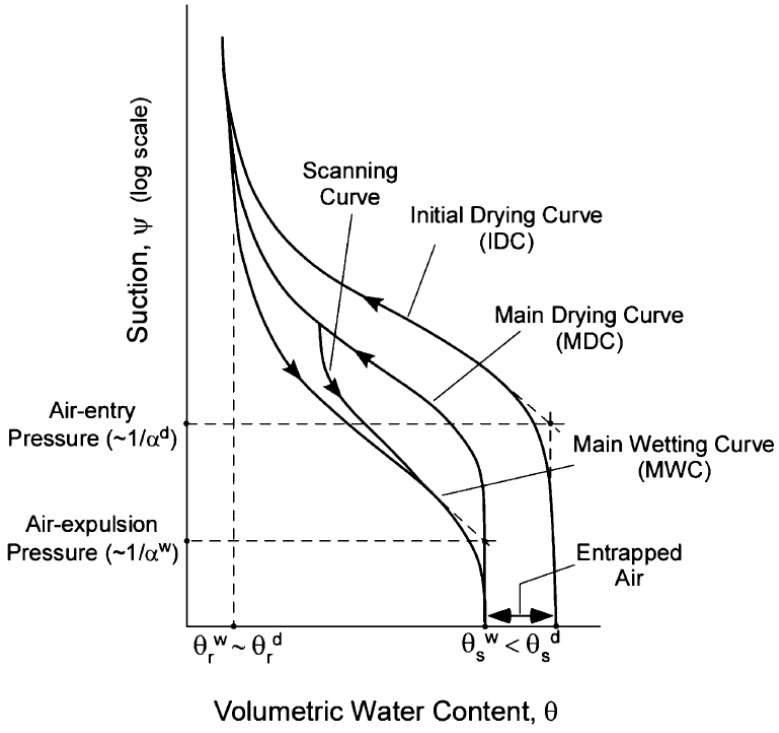

Figure 4.30. Drying curve, wetting curve, and typical hysteretic behavior of soil (Likos et al. 2013)

Three different tests were performed to determine the SWCCs of all the materials excluding Select Granular Borrow and LSSB Material. These tests included the hanging column test, the pressure plate test, and the activity meter test (ASTM D6836).

Hanging column tests were carried out on Sand Subgrade, Class 6 Aggregate, and Class 5Q Aggregate with matric suction values up to around 6 psi (40 kPa). A diagram of the hanging column test setup is provided in Figure 4.31. The pictures of the test setup are provided in Figure 4.32. The specimen, which was placed in a retaining ring, was placed on a ceramic disc into a glass funnel. Suction was created by the upper and lower reservoirs and applied to the specimen. The volume of the water, which was entering and leaving the specimen was observed in the horizontal tube. In this testing, the water content balance throughout the specimen was achieved within a period of not more than 1-2 days. To plot the SWCC curves, the test data was used to fit the van Genuchten model (van Genuchten 1980) described in Equation (4.1).

$$\Theta = \frac{\theta - \theta_r}{\theta_s - \theta_r} = \left[\frac{1}{1 + (\alpha\psi)^n}\right]^m \quad (4.1)$$

where Θ is the normalized volumetric water content (VWC), θ is the soil VWC, θ_r is the residual VWC, θ_s is the saturated VWC, Ψ is the matric suction (kPa), and α, n, and m are the van Genuchten fitting parameters (van Genuchten 1980).

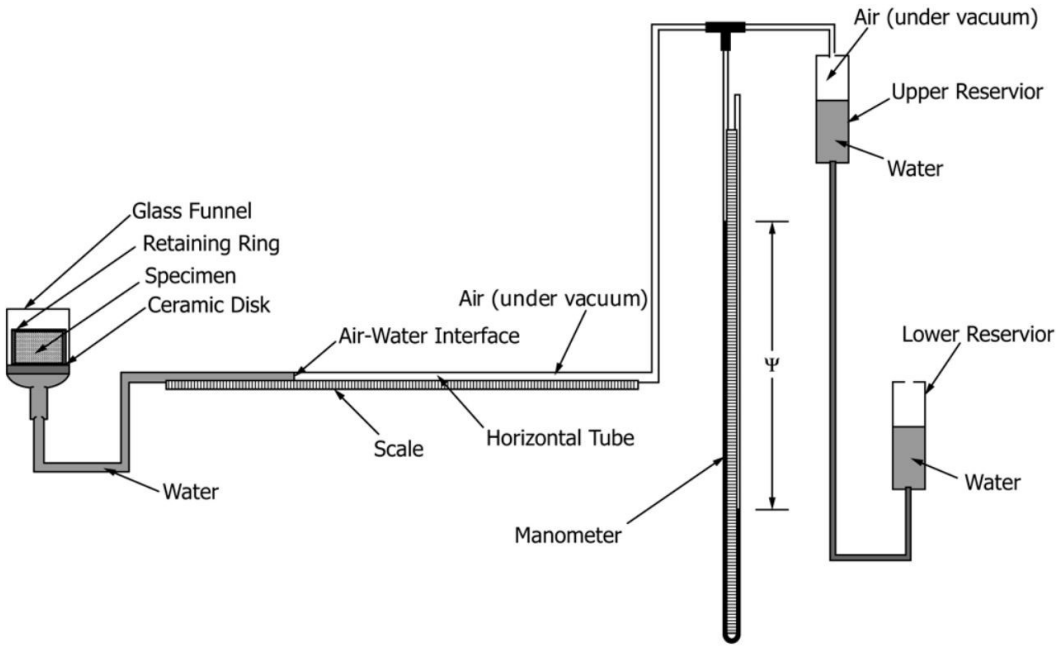

Figure 4.31. Schematic diagram of hanging column test setup (ASTM D6836)

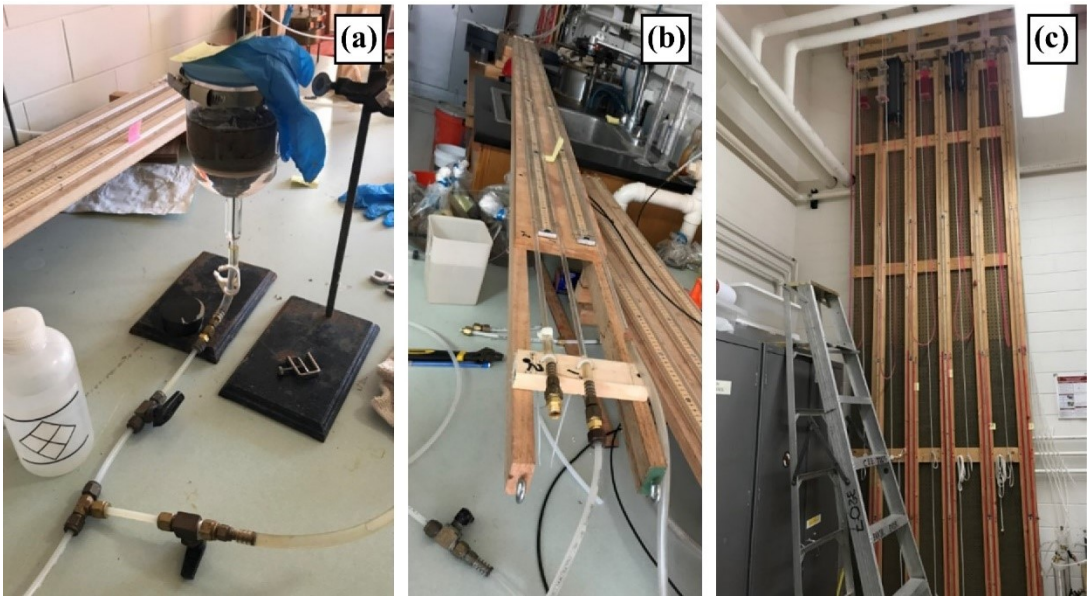

Figure 4.32. Pictures of hanging column test setup (a) glass funnel, (b) horizontal tube, and (c) manometer

The hanging column test results are provided in Figure 4.33, Figure 4.34, and Figure 4.35, for Sand Subgrade, Class 6 Aggregate, and Class 5Q Aggregate, respectively. The test methodology was successful for Sand Subgrade and Class 6 Aggregate overall. However, some of the tests on Class 5Q Aggregate had to be redone because no satisfactory model fitting could be obtained between the test data and the van Genuchten model (Figure 4.36). In addition, in the next step, another hanging column test was performed on Fine RCA and the test result did not exhibit a good fit with the van Genuchten model (Figure 4.37). Since both Fine RCA and Class 5Q Aggregate contained RCA particles, this result was

attributed to the cementation of the unhydrated cement in the RCA matrix (Figure 4.38). Cementation occurred during the long testing period and it caused difficulty for the water to flow out and created a risk regarding ceramic pore-clogging. In addition, the hanging column test is more suitable for coarse materials. Fines contents of the Class 5Q Aggregate and Fine RCA specimens could be higher than the hanging column test limitations. Therefore, instead of hanging column test, pressure plate and activity meter tests were performed on the rest of the materials.

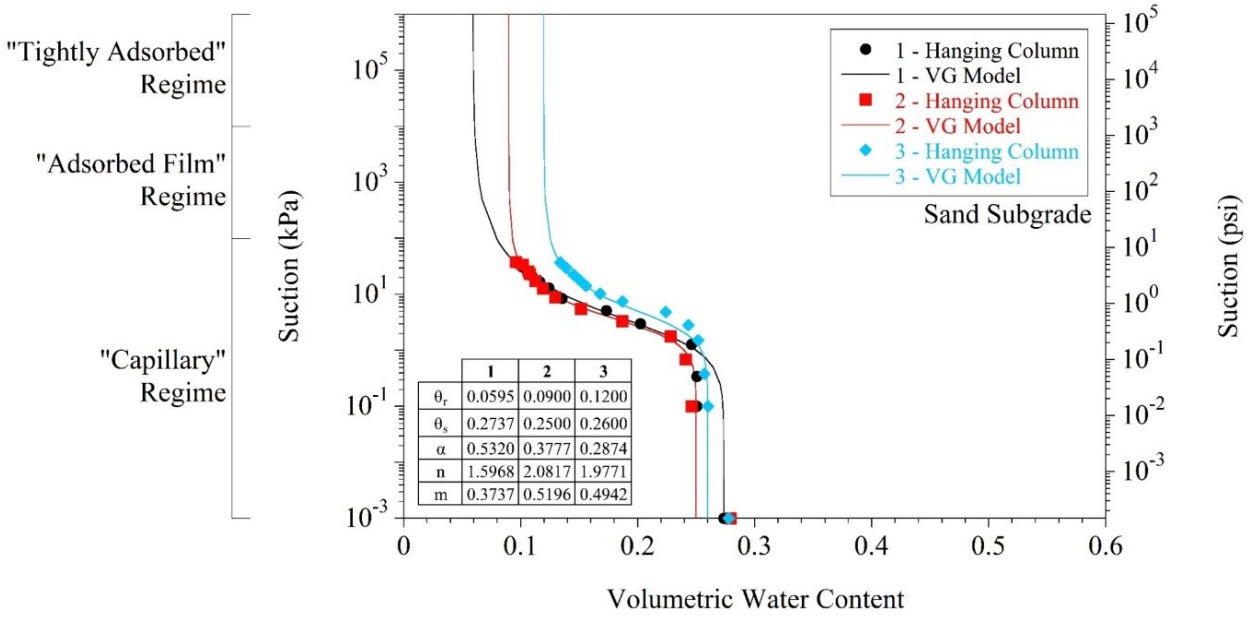

Figure 4.33. Soil-water characteristic curve (SWCC) of Sand Subgrade by hanging column test

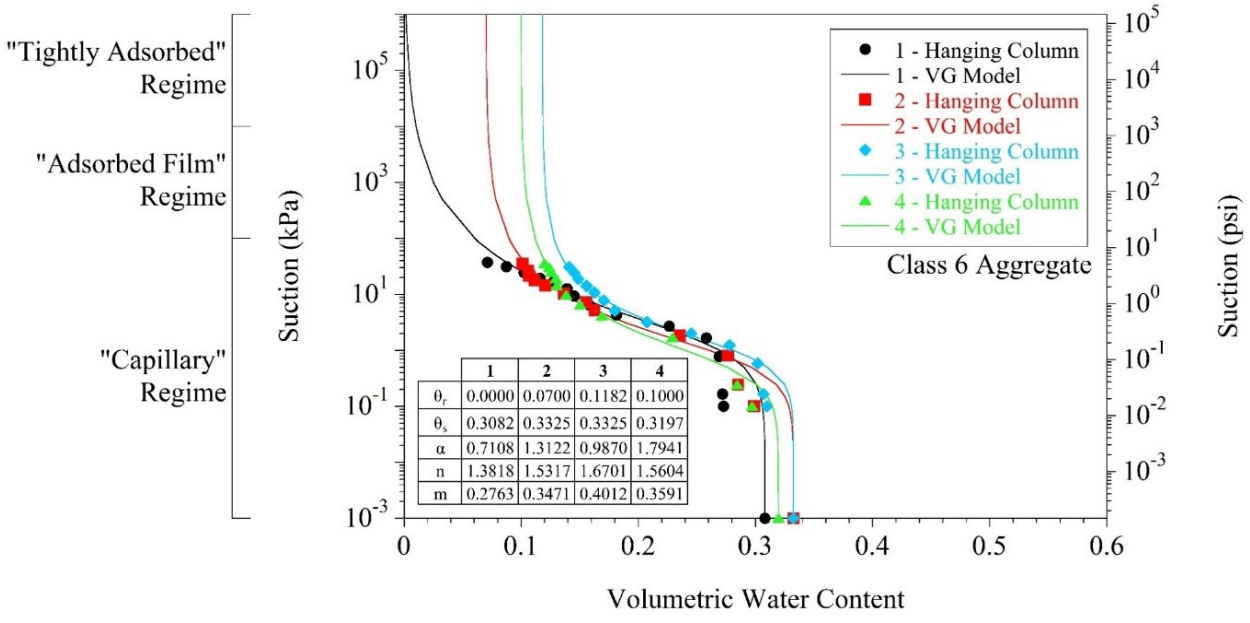

Figure 4.34. Soil-water characteristic curve (SWCC) of Class 6 Aggregate by hanging column test

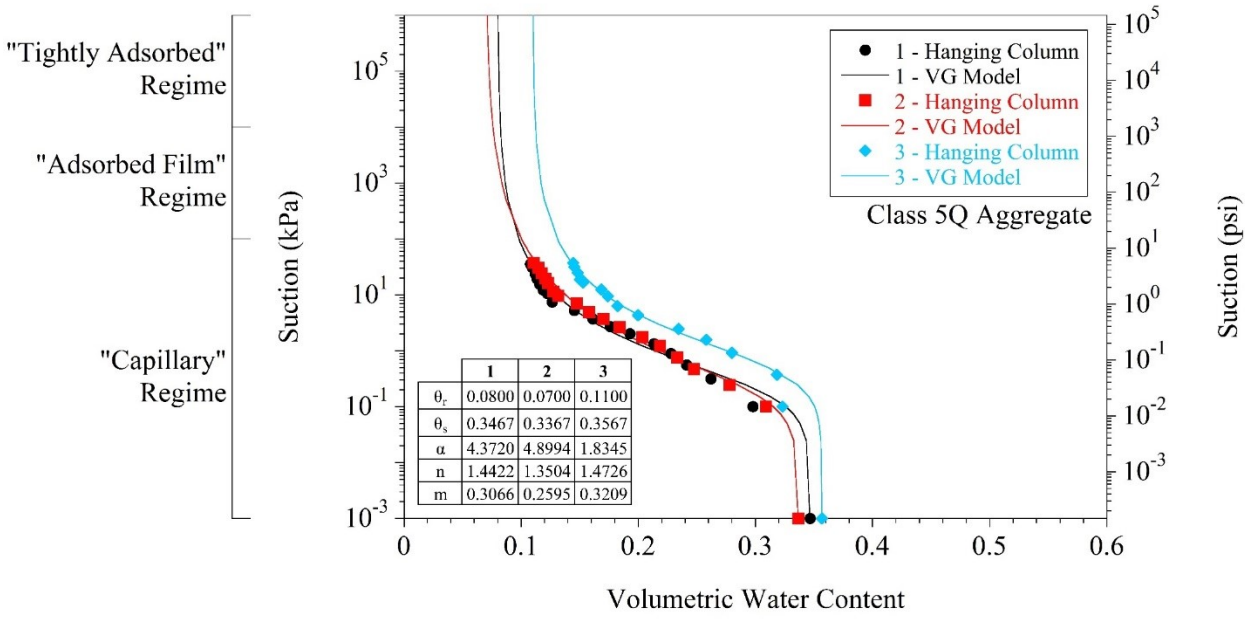

Figure 4.35. Soil-water characteristic curve (SWCC) of Class 5Q Aggregate by hanging column test

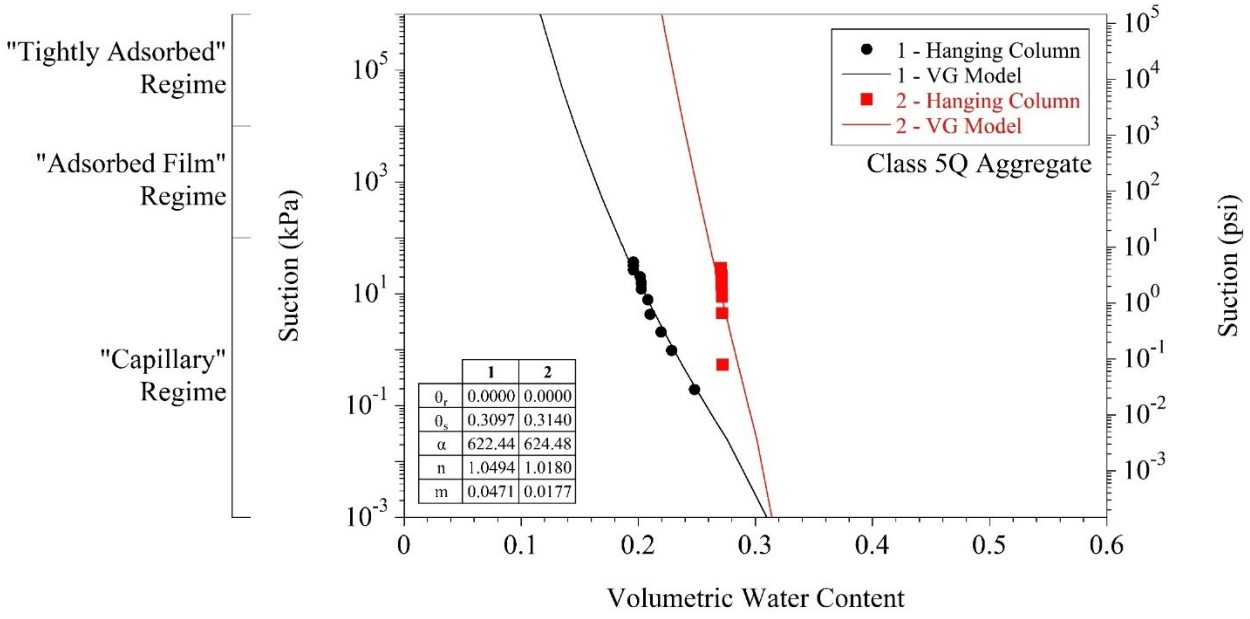

Figure 4.36. Hanging column test data and van Genuchten model for Class 5Q Aggregate

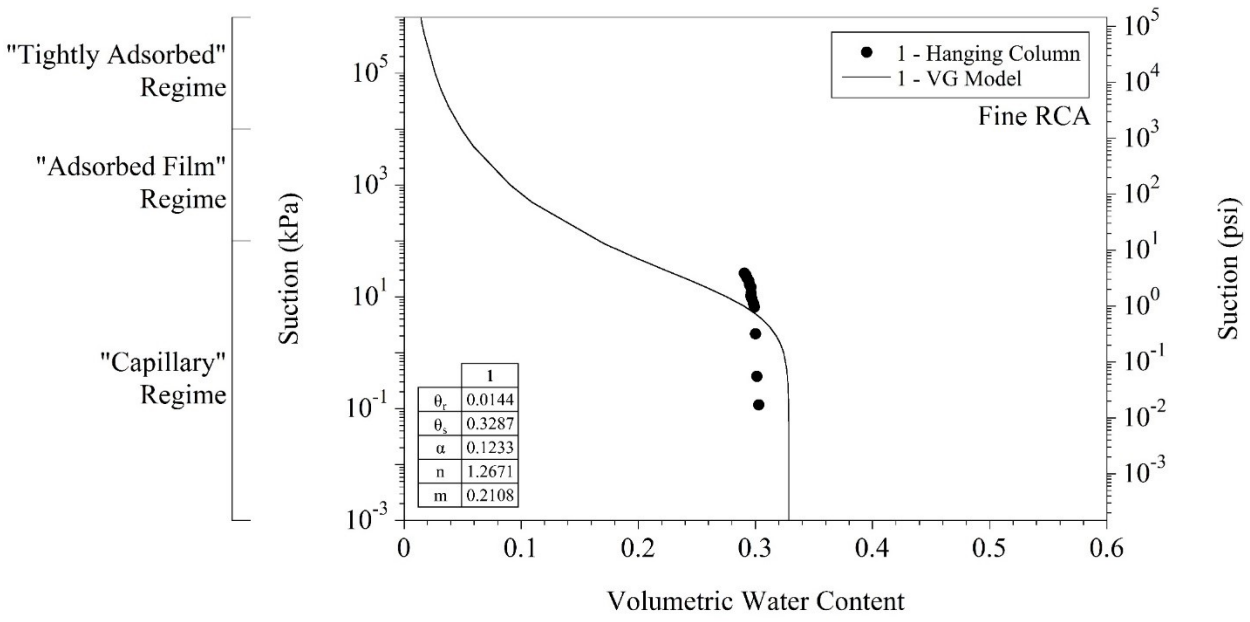

Figure 4.37. Hanging column test data and van Genuchten model for Fine RCA

Figure 4.38. Cementation of Fine RCA after hanging column test

The pressure plate and activity meter tests were carried out on Clay Loam, Coarse RCA, Fine RCA, Limestone, and RCA+RAP. Pressure plate tests were performed on the materials passing 3/8-in sieve at matric suction values up to around 220 psi (1500 kPa). Figure 4.39 shows the pressure chambers, which were used for the pressure plate tests. 3-in diameter and 1-in height specimens were compacted in three layers in a ring in the pressure chamber (Figure 4.40). The specimens were then saturated by applying a vacuum in the desiccator and placed in the pressure plate cell. The volume of the water entering and leaving the specimen was measured by means of the horizontal tube as in the hanging column method [Figure 4.31 and Figure 4.32(b)]. By checking the water level in the horizontal tube, it was observed whether the water content of the specimen was constant. This period took around 3 to 10 days for each suction stage.

Even higher suction values had to be applied to the specimens for being able to reach to the residual water contents. Depending on the fines content of the specimen, it was not always possible to reach the residual water content [the water content at which the slope of the SWCC becomes zero in the third stage, the so-called residual stage (van Genuchten 1980)] in the SWCC by the pressure plate test because of the maximum matric suction that could be created by that method [220 psi (1500 kPa)]. An activity meter device (Figure 4.41) was operated to obtain data at much higher suction values. In fact, the activity meter does not apply suction to the specimens directly. Instead, it measures the relative humidity and then converts the readings to matric suction values by Kelvin's Law, which indicates that the relative humidity and suction are directly related parameters (Sposito 1981; Likos and Lu 2003). The activity meter tests were performed on the finer fractions of the materials [passing No. 10 sieve (2 mm)] because the larger particles are not suitable for this method. 1.6-in (40-mm) diameter specimens were used for the activity meter tests. Since the specimen size that can be used in this testing was relatively smaller, it was actually not possible to provide a representative specimen in terms of the actual gradation of the corresponding material (Figure 4.2 and Table 4.1). It should be noted that the compaction status of the specimen was not important at a high level of suction. In other words, the pore structure of the specimen plays a negligible role at very high suction values. In the high suction rates, it is the properties of the mineral surfaces that dominate the SWCC behavior of the materials.

Figure 4.39. Single-specimen pressure chambers

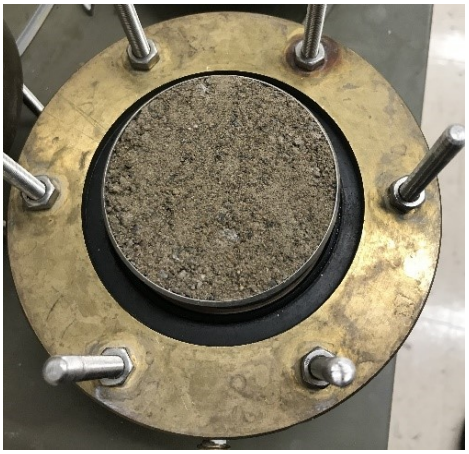

Figure 4.40. Compacted specimen prepared in a ring in pressure chamber

Figure 4.41. Activity meter device

The data collected by the pressure plate and the activity meter tests were combined and used to develop the van Genuchten model (van Genuchten 1980), as described previously in Equation (4.1). The data obtained from the activity meter was at very high suction [> 220 psi (1500 kPa)] and the data obtained from the pressure plate was at relatively lower suctions [< 220 psi (1500 kPa)]. Combining the data obtained from the two different methods caused discontinuities to some extent.

Pressure plate and activity meter test results are provided in Figure 4.42, Figure 4.43, Figure 4.44, Figure 4.45, and Figure 4.46 for Clay Loam, Coarse RCA, Fine RCA, Limestone, and RCA+RAP, respectively.

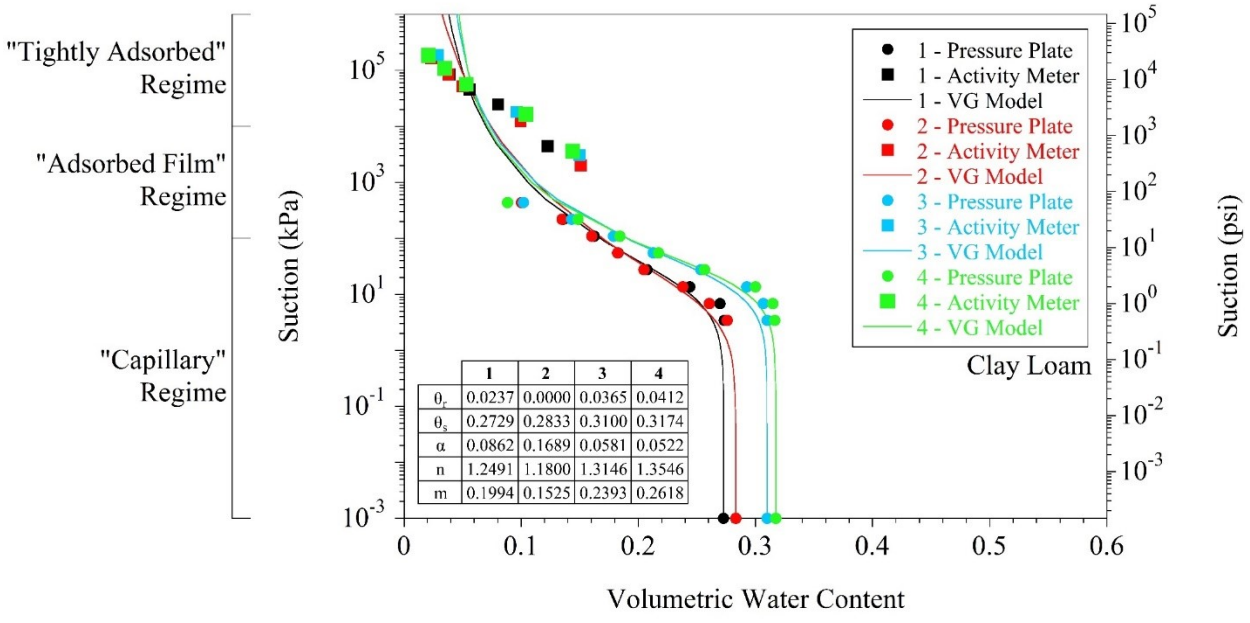

Figure 4.42. Soil-water characteristic curve (SWCC) of Clay Loam by pressure plate and activity meter tests

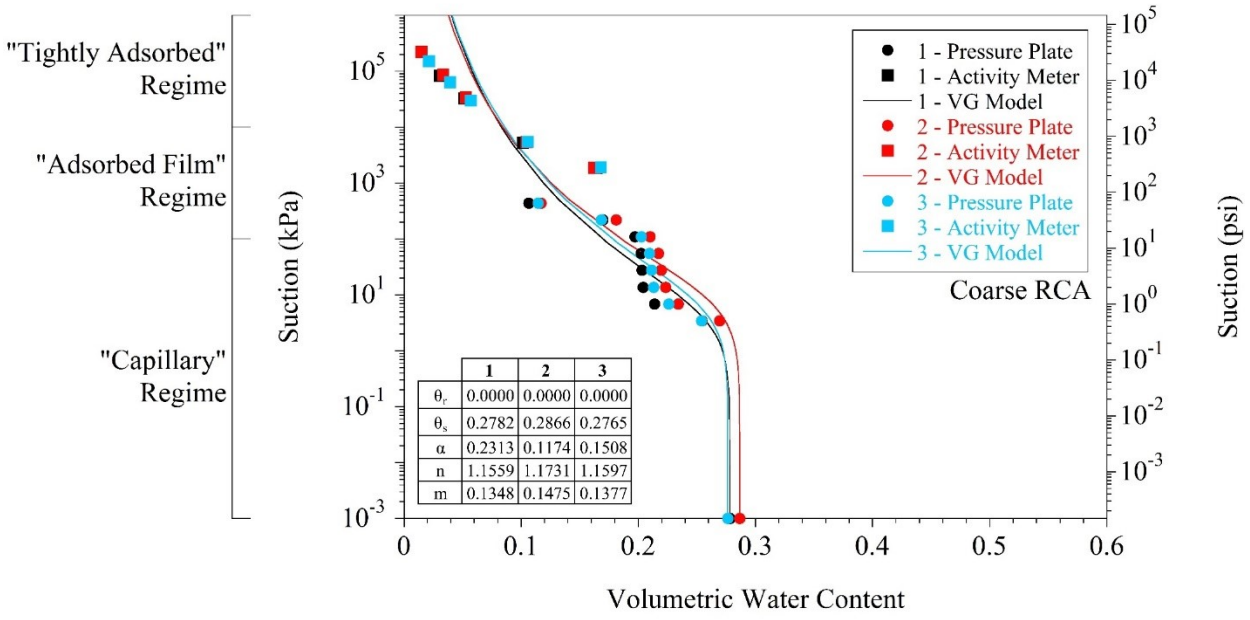

Figure 4.43. Soil-water characteristic curve (SWCC) of Coarse RCA by pressure plate and activity meter tests

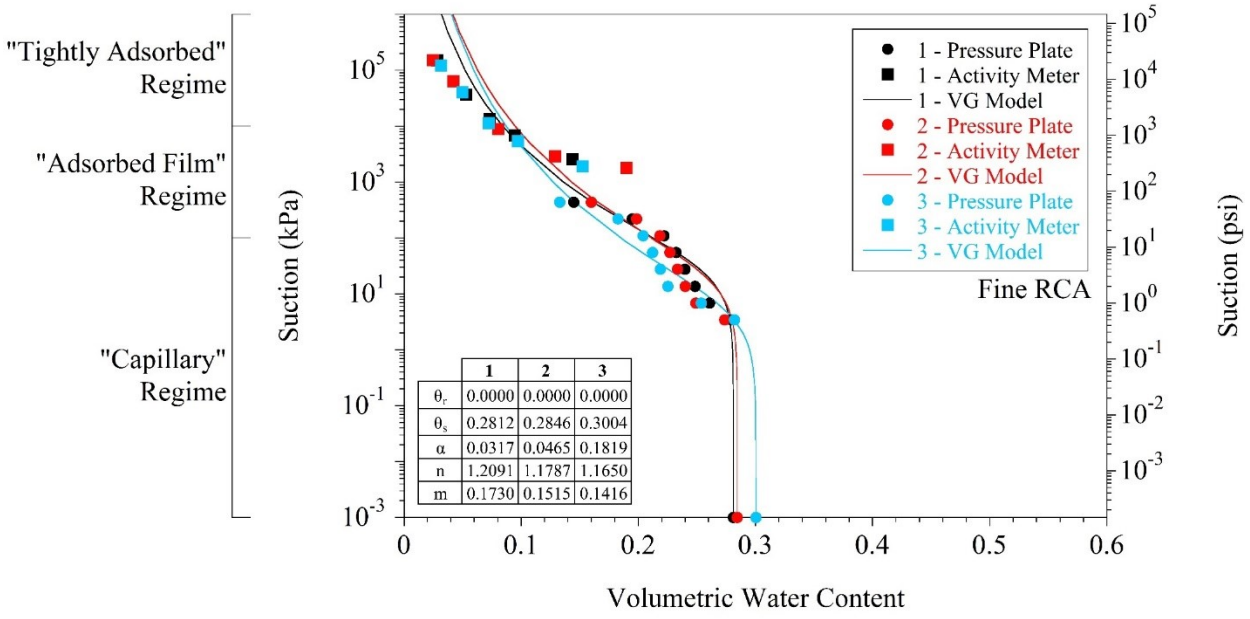

Figure 4.44. Soil-water characteristic curve (SWCC) of Fine RCA by pressure plate and activity meter tests

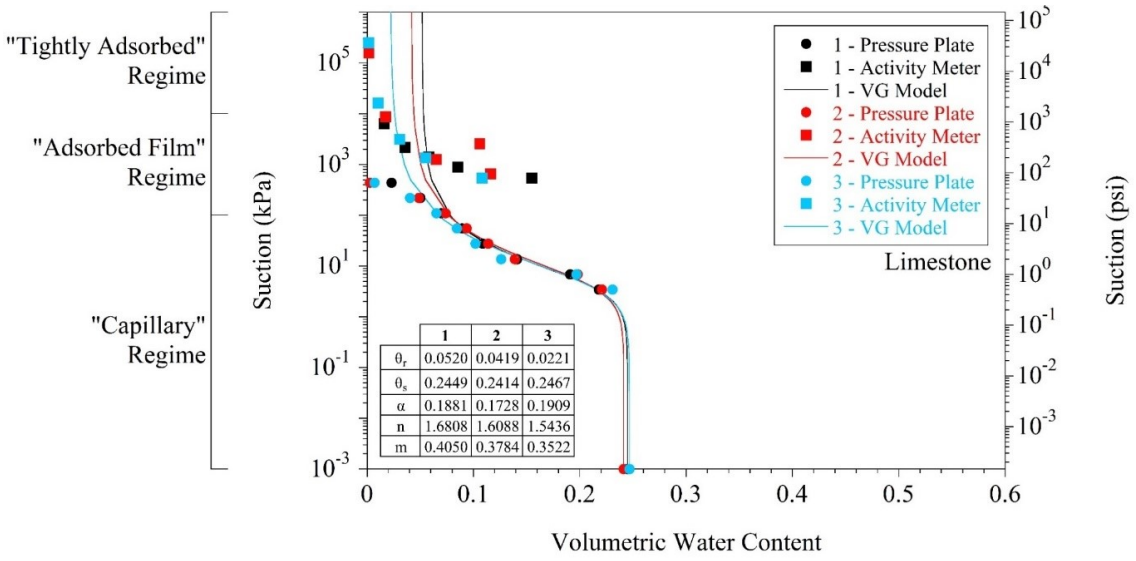

Figure 4.45. Soil-water characteristic curve (SWCC) of Limestone by pressure plate and activity meter tests

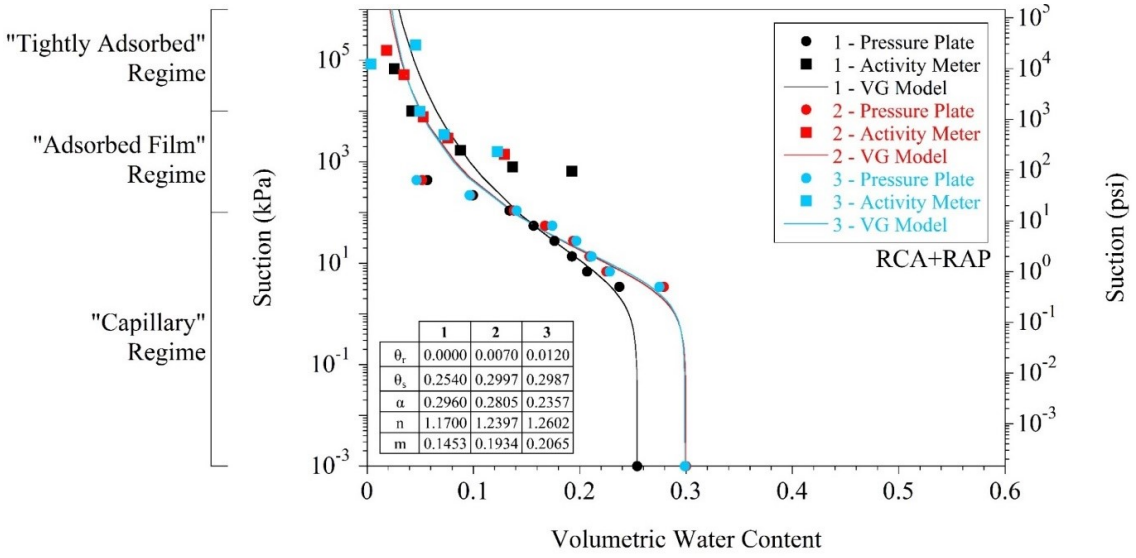

Figure 4.46. Soil-water characteristic curve (SWCC) of RCA+RAP by pressure plate and activity meter tests

The van Genuchten models of different specimens from the same material were averaged and one summary model for each material is shown in Figure 4.47. VWC at fully saturated condition and air-entry pressure of each material are summarized in Table 4.9. Class 5Q Aggregate and Class 6 Aggregate exhibited the highest and the second highest VWC at fully saturated conditions (0.347 and 0.323, respectively). In descending order, VWC values of 0.296, 0.289, 0.284, 0.280, 0.261, and 0.244 were observed for Clay Loam, Fine RCA, RCA+RAP, Coarse RCA, Sand Subgrade, and Limestone, respectively, at fully saturated conditions. Fine RCA and Clay Loam exhibited the highest air-entry pressures (4 and 3.5, respectively). Then, in descending order, air-entry pressure values of 2.5, 1.75, 1.40, 0.85, 0.30, and 0.10 kPa were observed for Coarse RCA, Limestone, RCA+RAP, Sand Subgrade, Class 6 Aggregate, and Class 5Q Aggregate, respectively.

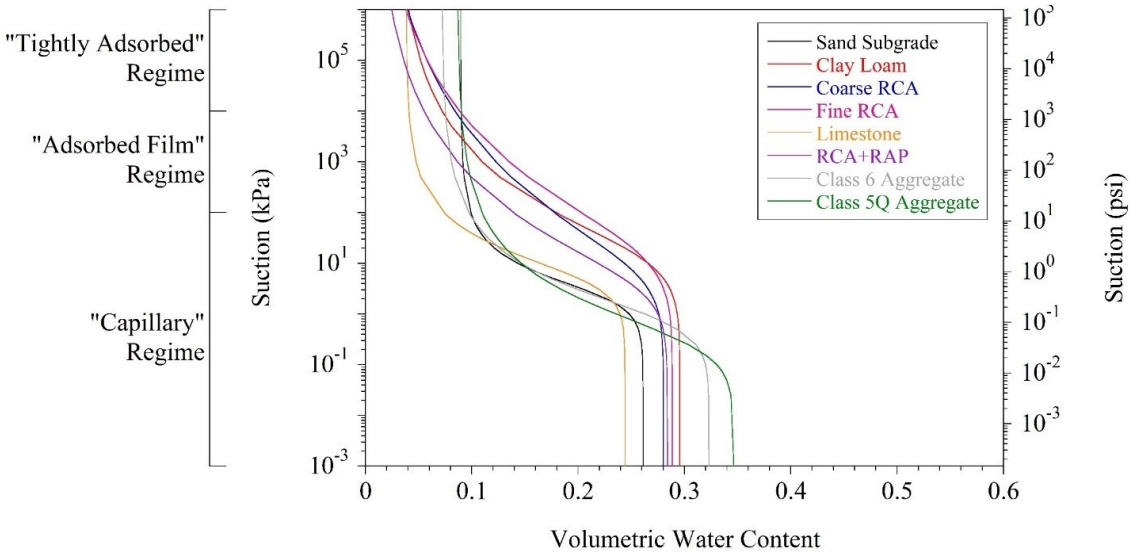

Figure 4.47. van Genuchten models of all materials

Table 4.9. Volumetric water content (VWC) at fully saturated condition and air-entry pressure of each material

Material	Initial VWC	Air-Entry Pressure	
		(kPa)	(psi)
Sand Subgrade	0.261	0.85	0.12
Clay Loam	0.296	3.50	0.51
Coarse RCA	0.280	2.50	0.36
Fine RCA	0.289	4.00	0.58
Limestone	0.244	1.75	0.25
RCA+RAP	0.284	1.40	0.20
Class 6 Aggregate	0.323	0.30	0.04
Class 5Q Aggregate	0.347	0.10	0.01

To observe the effects of the DOC on the SWCC characteristics of each material, the 3-in diameter and 1-in height specimens were prepared from all the materials except Select Granular Borrow and LSSB Material. All specimens except the Fine RCA specimens were compacted in three layers in the ring by three different compaction energies to obtain 100, 95, and 90% DOC [based on the uncorrected MDU of the materials (Figure 4.3 and Table 4.3)]. The Fine RCA specimens were compacted in the ring at 100, 90, and 80% DOC (Figure 4.3 and Table 4.3). In the beginning, the target DOC values were determined to be 100, 90, and 80%. All materials except Fine RCA could not be removed from the mold without significant disturbance when they were compacted at 80% DOC. Therefore, all materials except Fine RCA were compacted at 100, 95, and 90% DOC.

All specimens were compacted at their corresponding OMCs (Figure 4.3 and Table 4.3). The pressure plate and the activity meter tests were performed, and their result were evaluated. Test results for Sand Subgrade, Clay Loam, Coarse RCA, Fine RCA, Limestone, RCA+RAP, Class 6 Aggregate, and Class 5Q

Aggregate are provided in Figure 4.48, Figure 4.49, Figure 4.50, Figure 4.51, Figure 4.52, Figure 4.53, Figure 4.54, and Figure 4.55, respectively. VWC at the fully saturated condition and air-entry pressure of each material are summarized in Table 4.10. It was observed that the higher the DOC of the specimens, the lower the initial VWC of the specimens at fully saturated conditions. This was due to the denser structure of the specimens. The denser structure of the specimens yielded lower void ratio values, which in turn lowered the initial VWC at fully saturated conditions. Particle size distributions of the materials used in the tests are summarized in Figure 4.56 and Table 4.11 (gradation tests were performed after SWCC testing).

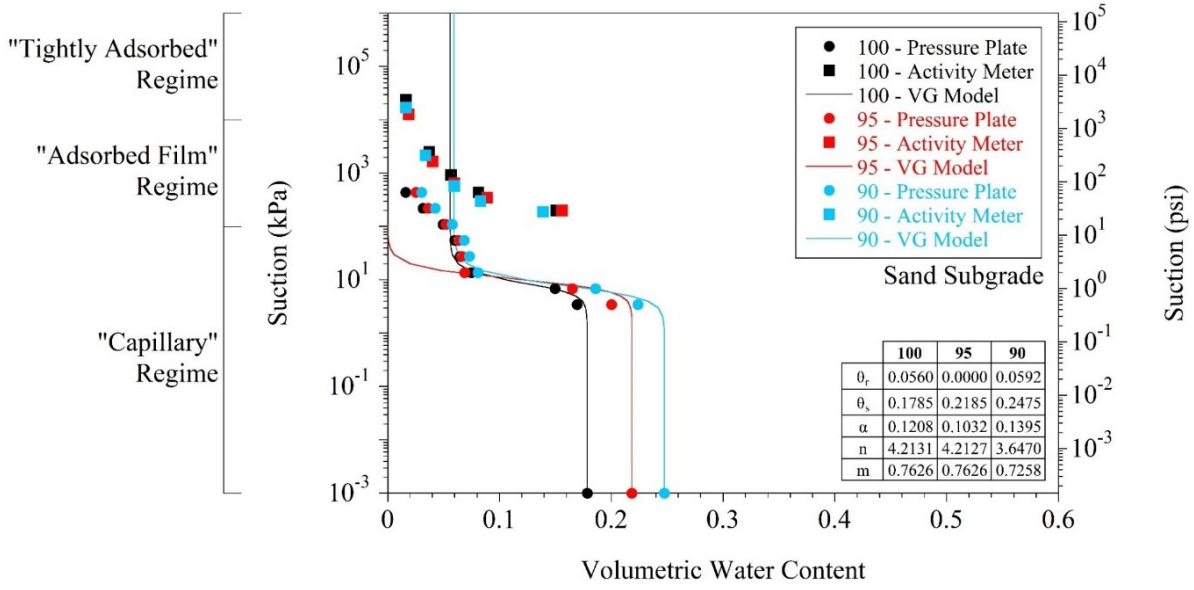

Figure 4.48. Effect of degree of compaction (DOC) on soil-water characteristic curve (SWCC) of Sand Subgrade

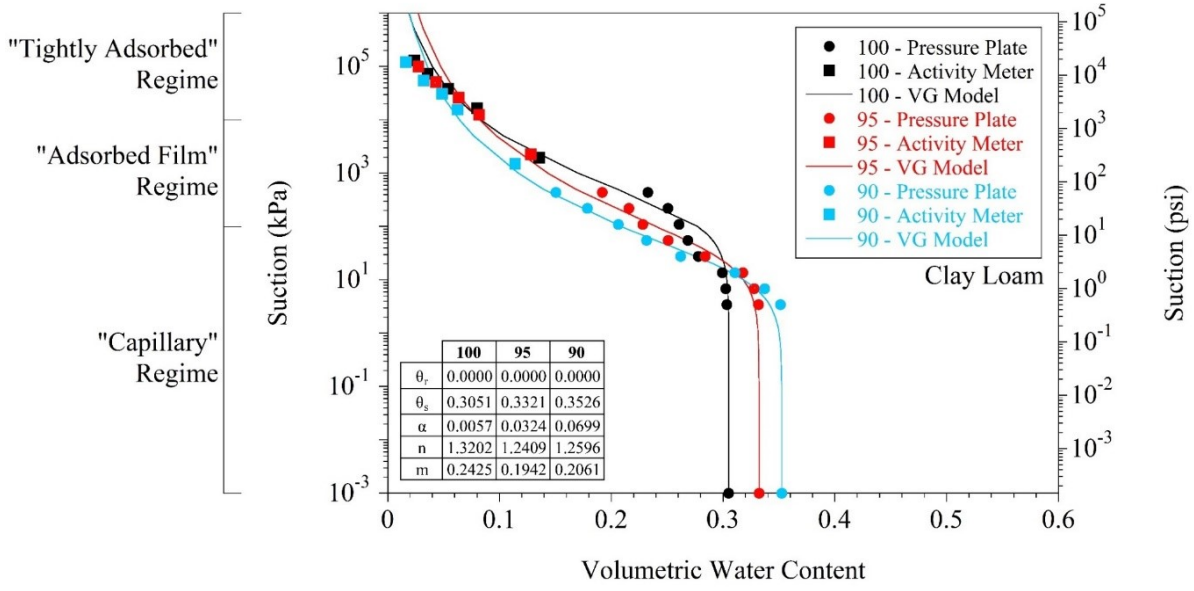

Figure 4.49. Effect of degree of compaction (DOC) on soil-water characteristic curve (SWCC) of Clay Loam

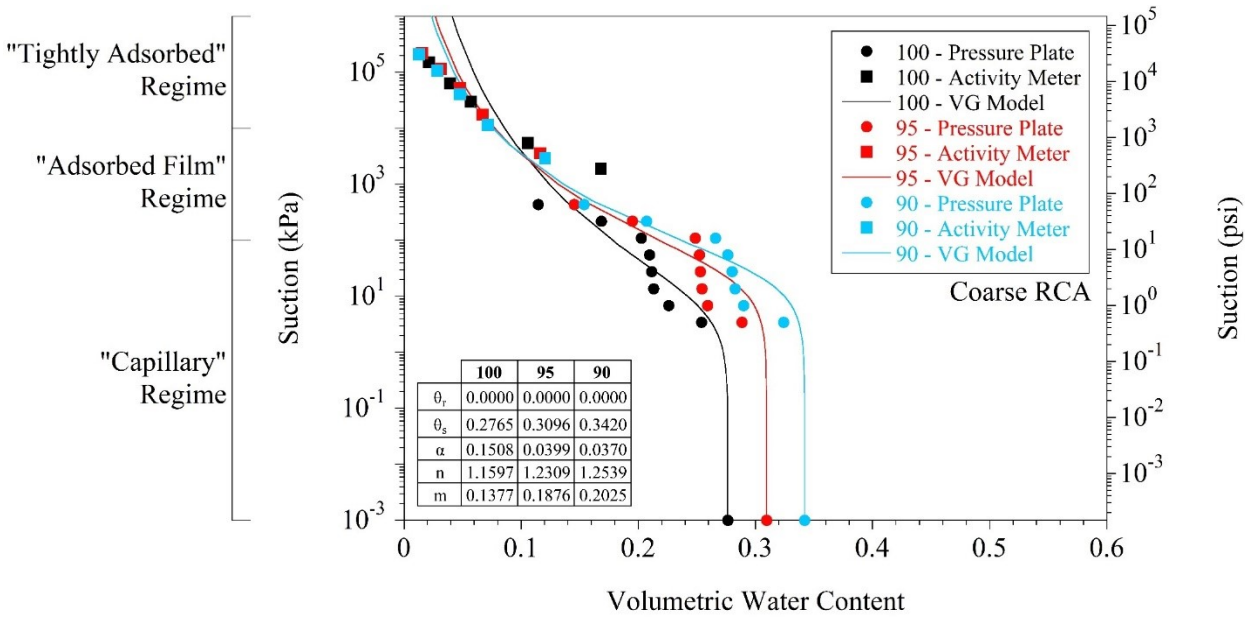

Figure 4.50. Effect of degree of compaction (DOC) on soil-water characteristic curve (SWCC) of Coarse RCA

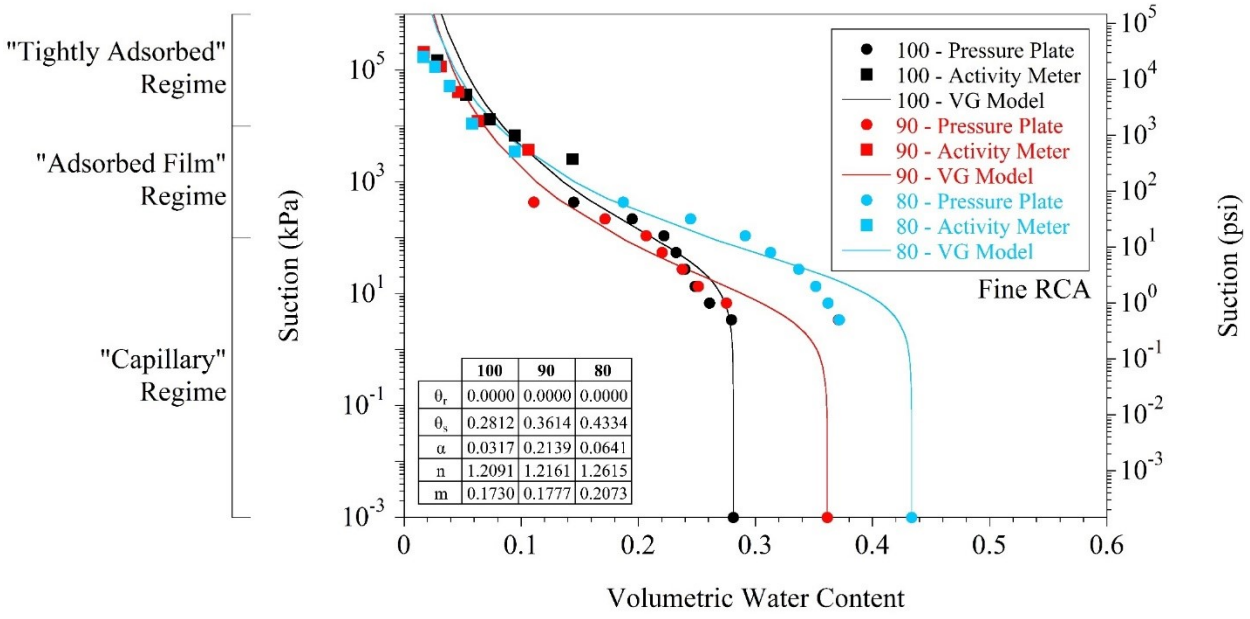

Figure 4.51. Effect of degree of compaction (DOC) on soil-water characteristic curve (SWCC) of Fine RCA

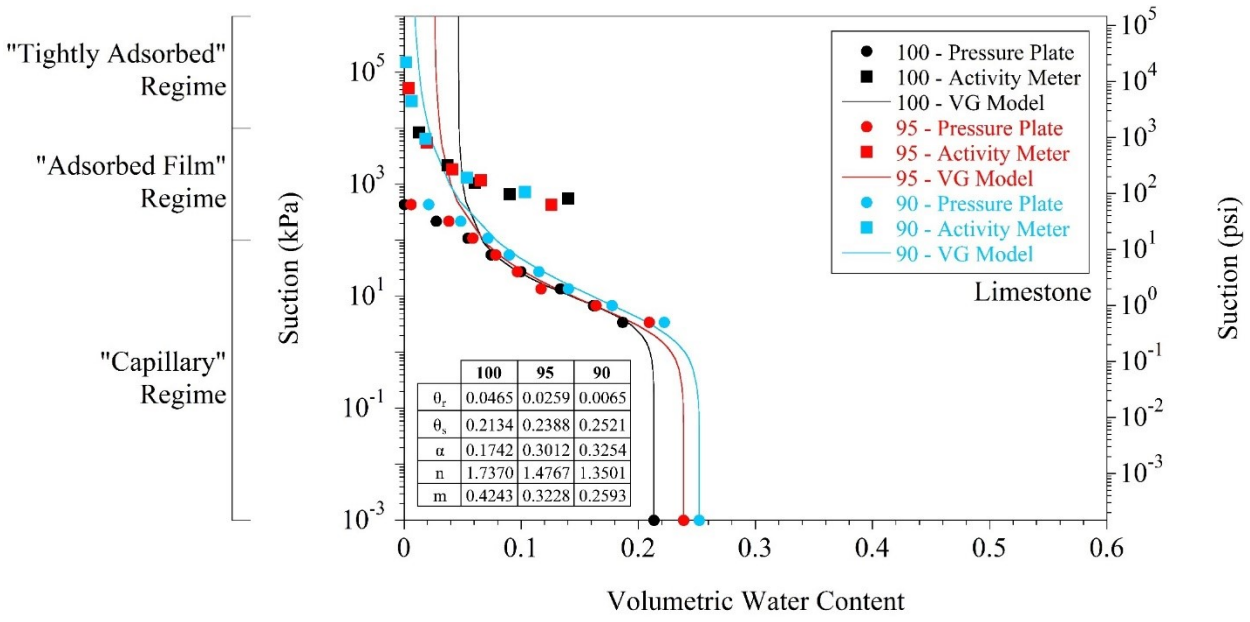

Figure 4.52. Effect of degree of compaction (DOC) on soil-water characteristic curve (SWCC) of Limestone

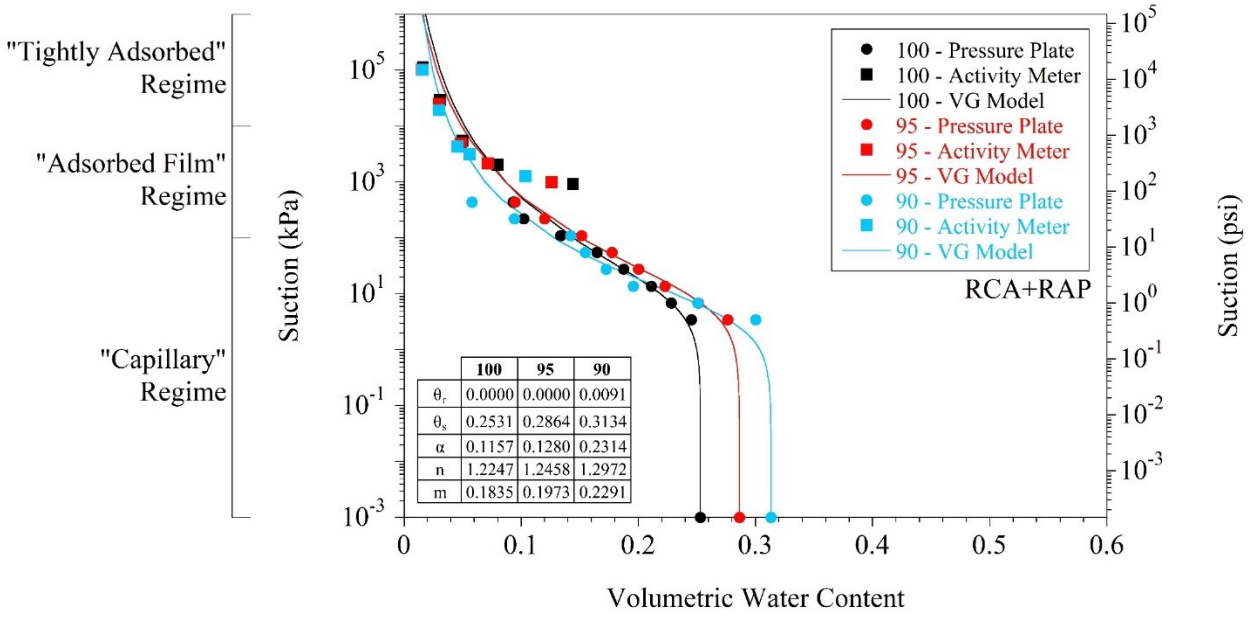

Figure 4.53. Effect of degree of compaction (DOC) on soil-water characteristic curve (SWCC) of RCA+RAP

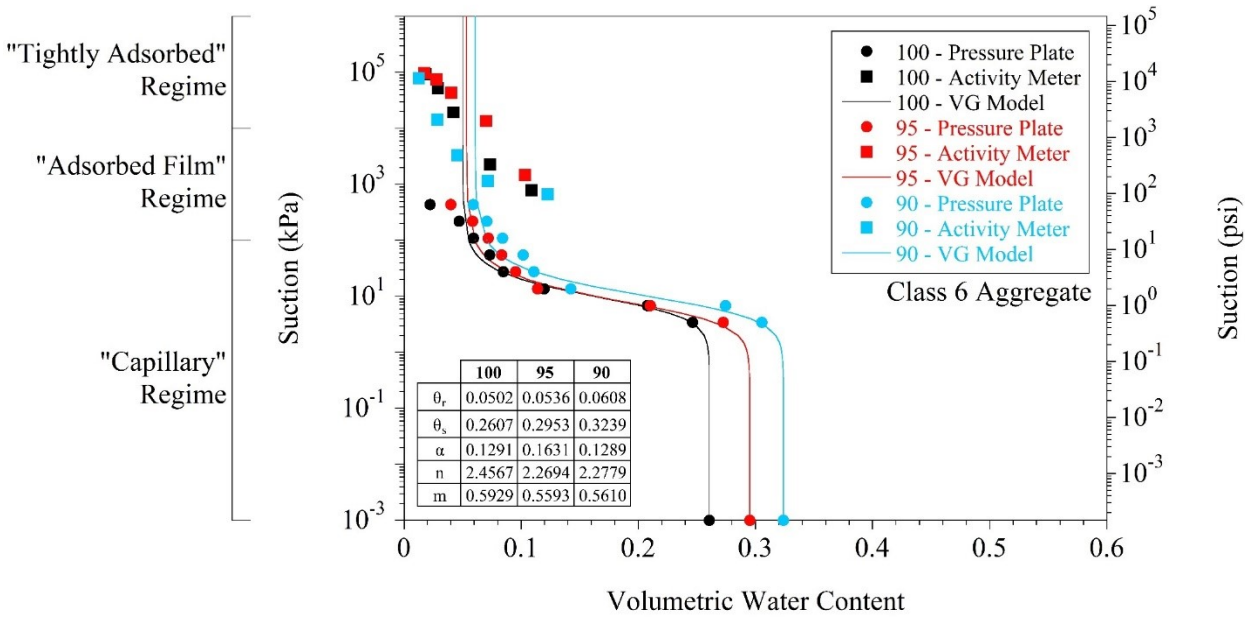

Figure 4.54. Effect of degree of compaction (DOC) on soil-water characteristic curve (SWCC) of Class 6 Aggregate

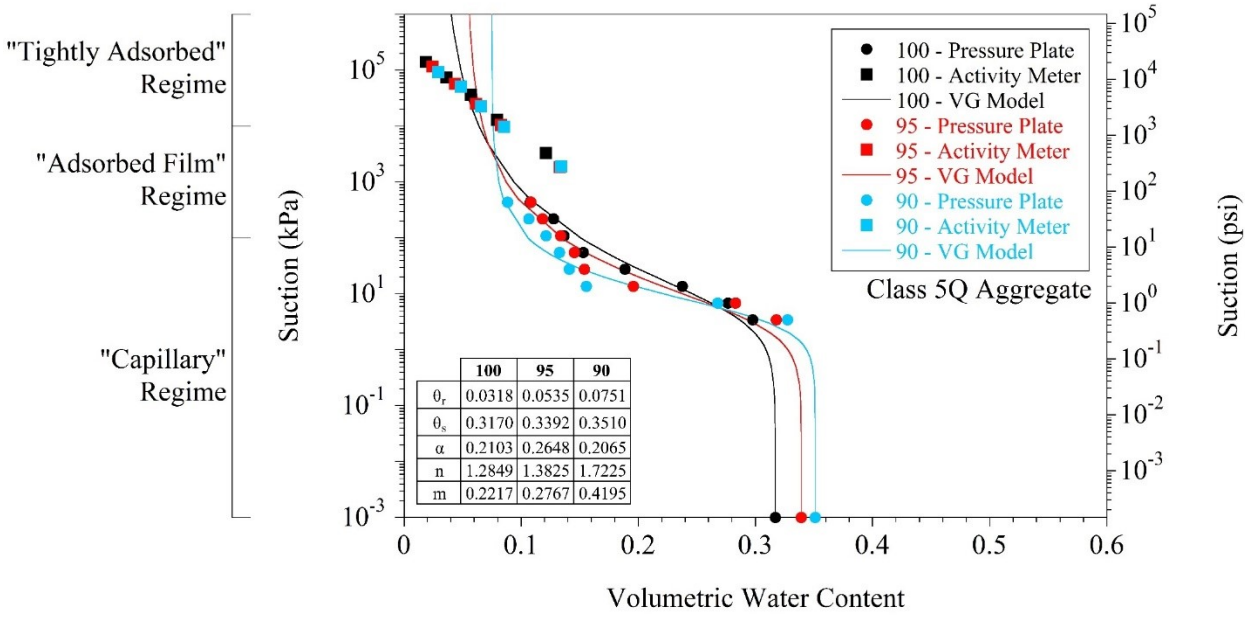

Figure 4.55. Effect of degree of compaction (DOC) on soil-water characteristic curve (SWCC) of Class 5Q Aggregate

Table 4.10. Volumetric water content (VWC) at fully saturated condition and air-entry pressure of each material at different degree of compaction (DOC)

Material	DOC (%)	Initial VWC	Air-Entry Pressure	
			(kPa)	(psi)
Sand Subgrade	100	0.1785	5	0.73
	95	0.2185	4.8	0.70
	90	0.2475	3.5	0.51
Clay Loam	100	0.3051	14.5	2.10
	95	0.3321	10	1.45
	90	0.3526	5	0.73
Coarse RCA	100	0.2765	3	0.44
	95	0.3096	10	1.45
	90	0.3420	9	1.31
Fine RCA	100	0.2812	10.5	1.52
	90	0.3614	2	0.29
	80	0.4334	5	0.73
Limestone	100	0.2134	2.5	0.36
	95	0.2388	1.5	0.22
	90	0.2521	1.25	0.18
RCA+RAP	100	0.2531	3.5	0.51
	95	0.2864	3	0.44
	90	0.3134	1.5	0.22
Class 6 Aggregate	100	0.2607	3	0.44
	95	0.2953	2.5	0.36
	90	0.3239	3	0.44
Class 5Q Aggregate	100	0.3170	1.75	0.25
	95	0.3392	1.25	0.18
	90	0.3510	1.75	0.25

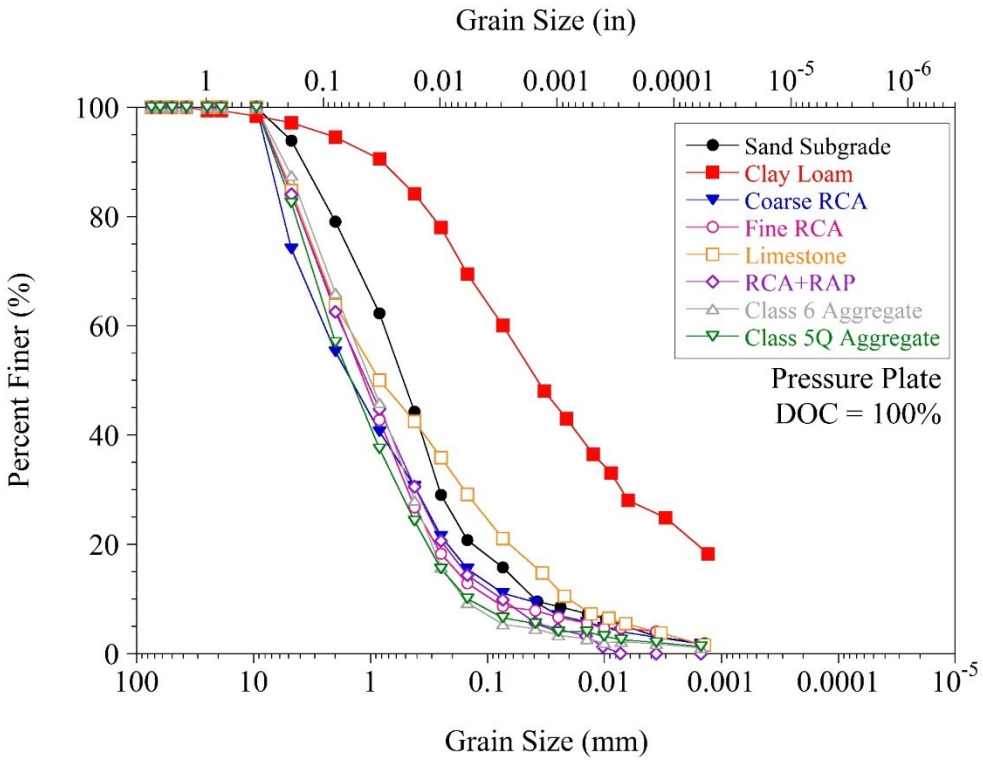

Figure 4.56. Particle size distribution of pressure plate test specimens

Table 4.11. Compositions of pressure plate test specimens

Material	Gravel (%)	Sand (%)	Fines (%)
Coarse RCA	25.9	63.0	11.1
Fine RCA	15.1	76.2	8.7
Limestone	15.2	63.7	21.1
RCA+RAP	15.9	74.2	9.9
Class 6 Aggregate	12.5	82.1	5.4
Class 5Q Aggregate	17.5	75.9	6.6
Sand Subgrade	6.1	78.1	15.8
Clay Loam	2.8	37.1	60.1

4.4 STEREOPHOTOGRAPHY

Particle size and shape characteristics of aggregates must be well known since the engineering properties of aggregates (shear strength, stiffness, permeability, etc.) are significantly affected by these parameters (Cosentino et al. 2003; Tan et al. 2014; Zheng and Hryciw 2014, 2017). The conventional method to determine the particle shape characteristics (elongation and flatness) of aggregates is to measure the length, width, and thickness of the particles by a caliper device (ASTM D4791). Since aggregate particles are evaluated individually by the conventional method, the process is slow (Zheng

and Hryciw 2017). In addition, due to the limitations of the size of the existing test equipment, sieve analysis may not be practical for testing of large stones. Several digital imaging techniques have been developed by researchers as an alternative to standard sieve and particle shape analyses (Fletcher et al. 2003; Kumara et al. 2012; Altuhafi et al. 2013; Ohm and Hryciw 2013; Kazmee et al. 2016). Overall, these techniques were successful. However, most of them contained imperfections such as neglecting or roughly predicting the thickness of aggregate particles, or they were impractical. The length and width of an aggregate particle can be determined from a 2-D model, which is simply a single image of the particle at a known scale (Ghalib and Hryciw 1999; Hryciw and Ohm 2012; Ohm and Hryciw 2013). However, the thickness of the aggregate particle cannot be measured by the 2-D model (Zheng and Hryciw 2014, 2017). Stereophotography is a promising technique to determine particle size and shape (sphericity and roundness) characteristics of aggregates. In stereophotography, the image analysis algorithm combines two images, which are captured from two different positions, and creates a 3-D half surface model to determine such characteristics of aggregates (Zheng and Hryciw 2014, 2017). The image analysis algorithm includes basic matching, dynamic programming, pyramidal matching, and sub-pixel estimation functions (Zheng and Hryciw 2014, 2017). These functions identify corresponding points between two images and back-calculate the physical distance between the points in the image and the camera. Detailed mathematical derivation of the process is provided by Zheng and Hryciw (2014, 2017).

4.4.1 Test Method

Stereophotography was performed on all the materials except Sand Subgrade, Clay Loam, and Select Granular Borrow. For Coarse RCA, Fine RCA, Limestone, RCA+RAP, Class 6 Aggregate, and Class 5Q Aggregate, sieve analyses were performed without any problem. However, for LSSB Material, sieve analysis was not practical because most of the large particles had to be sieved one by one. The 12-in diameter sieves, which were on hand, could not be stacked on top of each other since a great number of particles were larger than the stacked height (around 1.6 in) of the half-height sieves. In addition, since the sieves could not be stacked, a mechanical sieve shaker could not be used effectively to sieve LSSB Material.

The stereophotography system, which was developed for this study, is shown in Figure 4.57. The system was set up on an audio visual (AV) cart [Figure 4.57(a)]. A camera, a camera slider, and LED lighting were installed on the bottom face of the top shelf of the AV cart [Figure 4.57(a), Figure 4.57(b), and Figure 4.57(c)]. It is recommended by Zheng and Hryciw (2017) that two cameras at fixed locations could be placed. The system, developed for this study, had one camera. The camera was a 20.2-megapixel digital camera, which could capture images up to 5184 x 3888 pixels. The camera could be moved horizontally along the camera slider [Figure 4.57(b) and Figure 4.57(c)]. LED lighting provided uniform illumination and improved image sharpness [Figure 4.57(b) and Figure 4.57(c)]. A test surface was set up on the top surface of the bottom shelf of the AV cart [Figure 4.57(a), Figure 4.57(b), and Figure 4.57(d)]. Self-adhesive measuring tapes were placed on the test surface in two directions to specify the area that test material could be placed and to indicate the scales in both directions [Figure 4.57(d)]. A replaceable white ledger size paper (11 x 17 in) was placed on the area that was specified by the measuring tapes (the color of the paper could be different depending upon the color of the aggregate particles).

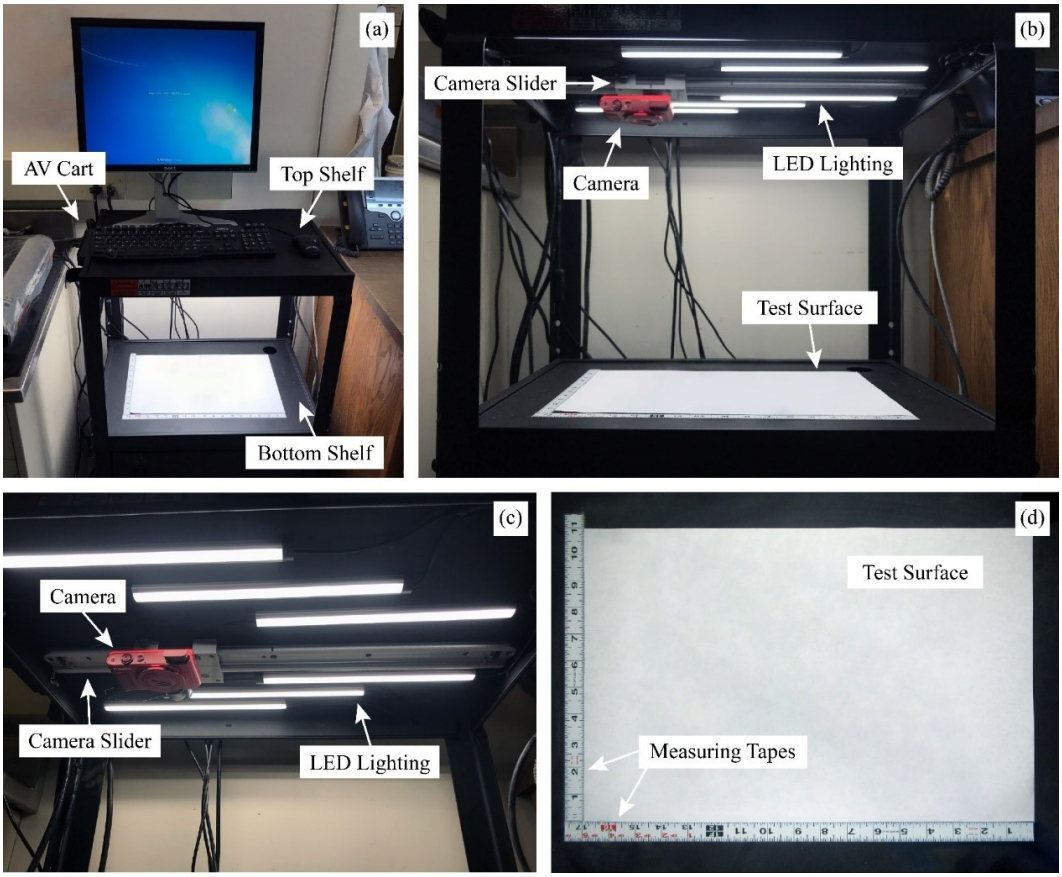

Figure 4.57. (a) Audio visual (AV) cart and top and bottom shelves, (b) main components of stereophotography system, (c) camera, camera slider, and LED lighting, and (d) test surface and self-adhesive measuring tapes

The key parameters for constructing the stereophotography system include the vertical distance between the camera center and the test surface (D_B), the camera separation distance (L), the focal length of the camera (*f*) (Figure 4.58). These parameters can be determined by a system calibration process (Zheng and Hryciw 2014, 2017).

Different D_B values were evaluated by adjusting the height of the top shelf of the AV cart [Figure 4.57(a)]. It was determined that a height of 15.4 in yielded a satisfactory field of view and depth of focus for the evaluation of the size and shape characteristics of aggregate particles. After fixing the D_B value, different L values were evaluated by sliding the camera to different locations. A large L value may cause a reduction in the number of aggregate particles that could be captured. On the other hand, a small L value may not be suitable to capture the two different sides of aggregate particles effectively. The most appropriate L value was found to be 4 in. After the determination of the D_B and L values, the *f* value was fixed to 1869 pixels. The detailed information about the system calibration is provided by Zheng and Hryciw (2017).

Particles were placed on the test surface in groups and not allowed to touch each other to eliminate the process of watershed analysis (Zheng and Hryciw 2016). For each group, two pictures [Figure 4.59(a) and Figure 4.59(b)] were taken by shifting the camera at the distance of L = 4 in (Figure 4.58). Then, the

image taken from the left position (the other image could also be used) was converted into a binary image (2-D) by a Photoshop program [Figure 4.59(c)] to determine the two dimensions of the particles in the group. As the final step, the two images [Figure 4.59(a) and Figure 4.59(b)] and the binary image [Figure 4.59(c)] were input into a computer code developed in MATLAB (Zheng and Hryciw 2017), which generated the 3-D half surface model of the particles in the group (Figure 4.60). In the 3-D half surface model, the X- and Y-axes show the 2-D dimensions of the particles (Figure 4.60). A color legend is also provided to show the variations of the 3rd dimension of the particles in the group (Z-axis) (Figure 4.60). The dark blue color represents the test surface at Z = 0 in (Figure 4.60) and the dark red color represents the highest surface points of the particles (from the test surface, Z = 0 in) (Figure 4.60). All the particles larger than No. 4 sieve (4.75 mm) were selected and analyzed by this method. In total, 4766 LSSB particles, 5160 Coarse RCA particles, 6671 Fine RCA particles, 5527 Limestone particles, 5893 RCA+RAP particles, 5507 Class 6 Aggregate particles, and 5762 Class 5Q Aggregate particles were analyzed.

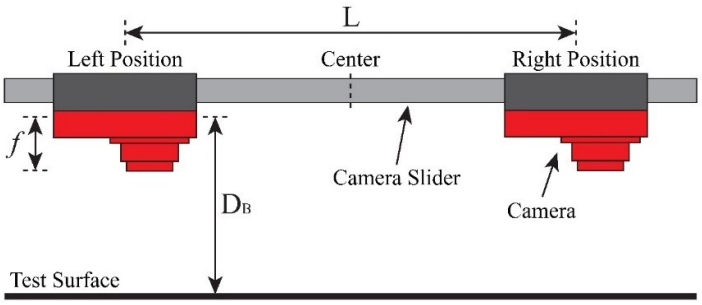

Figure 4.58. Vertical distance between camera center and test surface (D_B), camera separation distance (L), and focal length of camera (*f*) (not to scale)

Figure 4.59. (a) Image taken from left position, (b) image taken from right position, and (c) binary image for LSSB Material

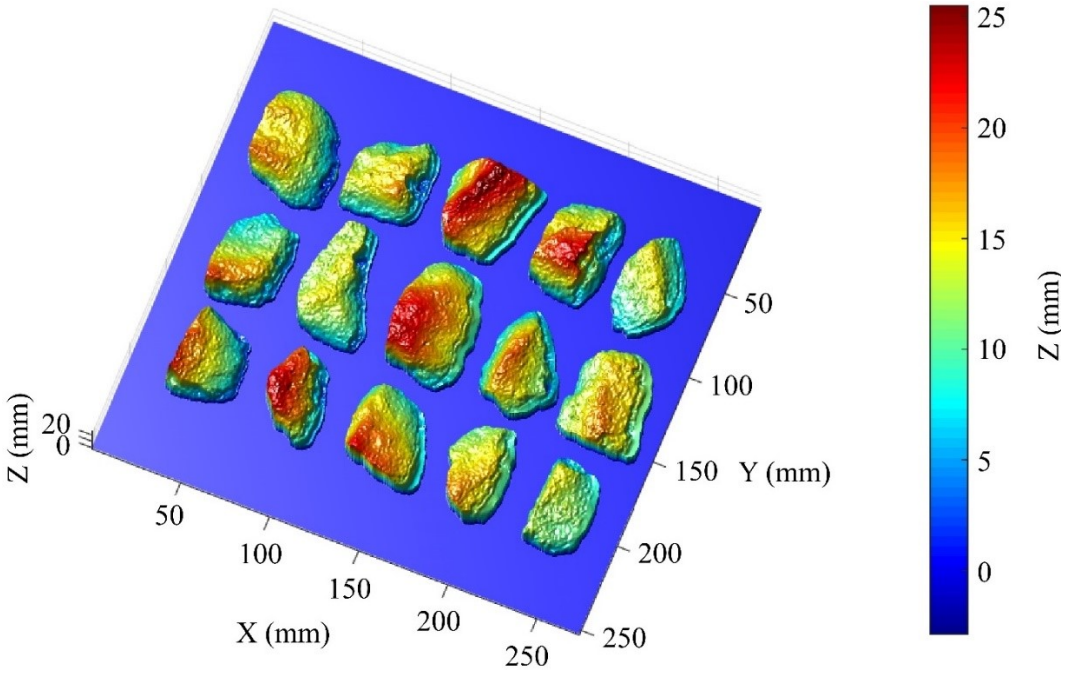

Figure 4.60. 3-D half surface model of group of particles for LSSB Material

4.4.2 Particle Size Analysis

The length (d_1), width (d_2), and thickness (d_3) of each aggregate particle were described as the largest, intermediate, and smallest dimensions, respectively (Zheng and Hryciw 2014, 2017). An ellipsoidal particle model [Figure 4.61(a)] was considered to determine the equivalent sieve opening size (d_e) of each aggregate particle [Figure 4.61(b)] (Zheng and Hryciw 2014, 2017). Equation (4.2) was used to determine the de values (Zheng and Hryciw 2014, 2017).

$$d_e = \sqrt{\frac{d_2^2 + d_3^2}{2}} \tag{4.2}$$

The volume (V) of each aggregate particle was calculated by Equation (4.3) (Zheng and Hryciw 2014, 2017). Then, the particle size distribution of the material (by volume) was determined.

$$V = d_1 \times d_2 \times d_3 \tag{4.3}$$

Stereophotography test results for LSSB Material, Coarse RCA, Fine RCA, Limestone, RCA+RAP, Class 6 Aggregate, and Class 5Q Aggregate are provided in Figure 4.62, Figure 4.63, Figure 4.64, Figure 4.65, Figure 4.66, Figure 4.67, and Figure 4.68, respectively. Gradations of the materials, provided in Figure 4.2, are also provided in the figures to compare the results of stereophotography and sieve analysis. Sand and fines contents of the materials could not be determined by stereophotography because only

the particles retained on No. 4 sieve (4.75 mm) were used as noted earlier. For LSSB Material, it was determined by sieve analysis that sand, silt, and clay particles were only 0.4% by dry weight (Figure 4.2 and Table 4.1). Therefore, even with eliminating the particles passing through No. 4 sieve (4.75 mm), stereophotography provided almost the entire gradation curve for LSSB Material. However, since Coarse RCA, Fine RCA, Limestone, RCA+RAP, Class 6 Aggregate, and Class 5Q Aggregate contained considerable amounts of particles finer than No. 4 sieve (4.75 mm) (Figure 4.2 and Table 4.1), significant portions of the gradation curves of these materials could not be determined by stereophotography. However, for all materials, the result of stereophotography remarkably matched with the result of sieve analysis for the particles larger than No. 4 sieve (4.75 mm).

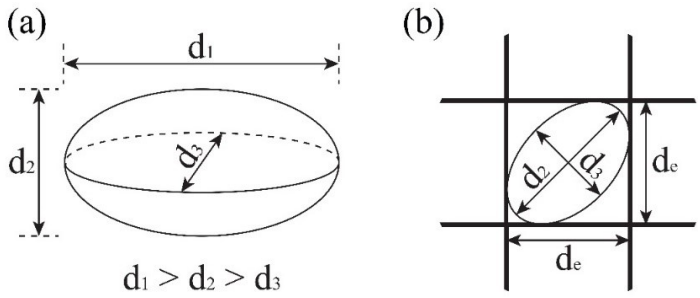

Figure 4.61. (a) Length (d_1), width (d_2), and thickness (d_3), and (b) equivalent sieve opening size (d_e) of particles (Zheng and Hryciw 2014, 2017)

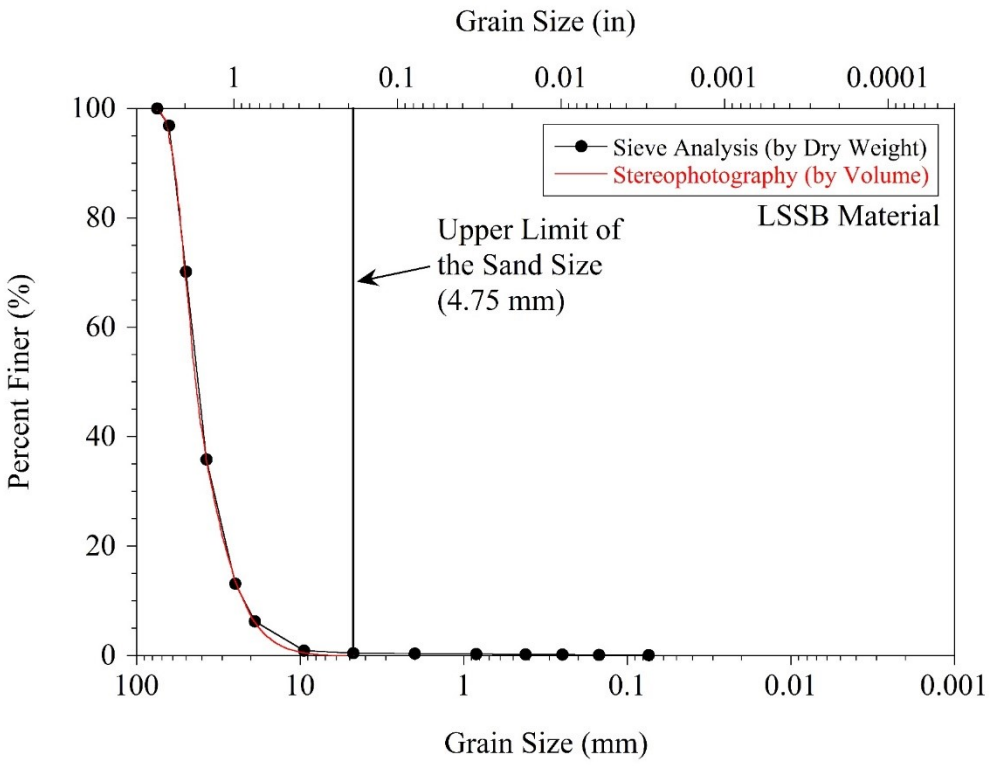

Figure 4.62. Gradations of LSSB Material determined by sieve analysis and stereophotography

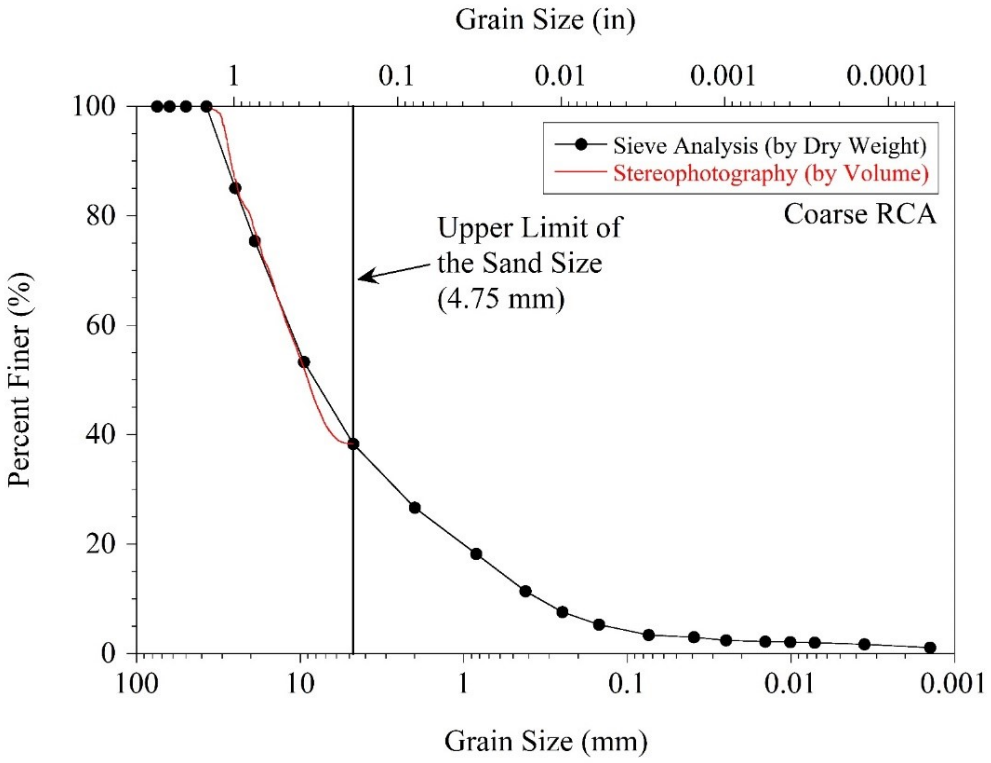

Figure 4.63. Gradations of Coarse RCA determined by sieve analysis and stereophotography

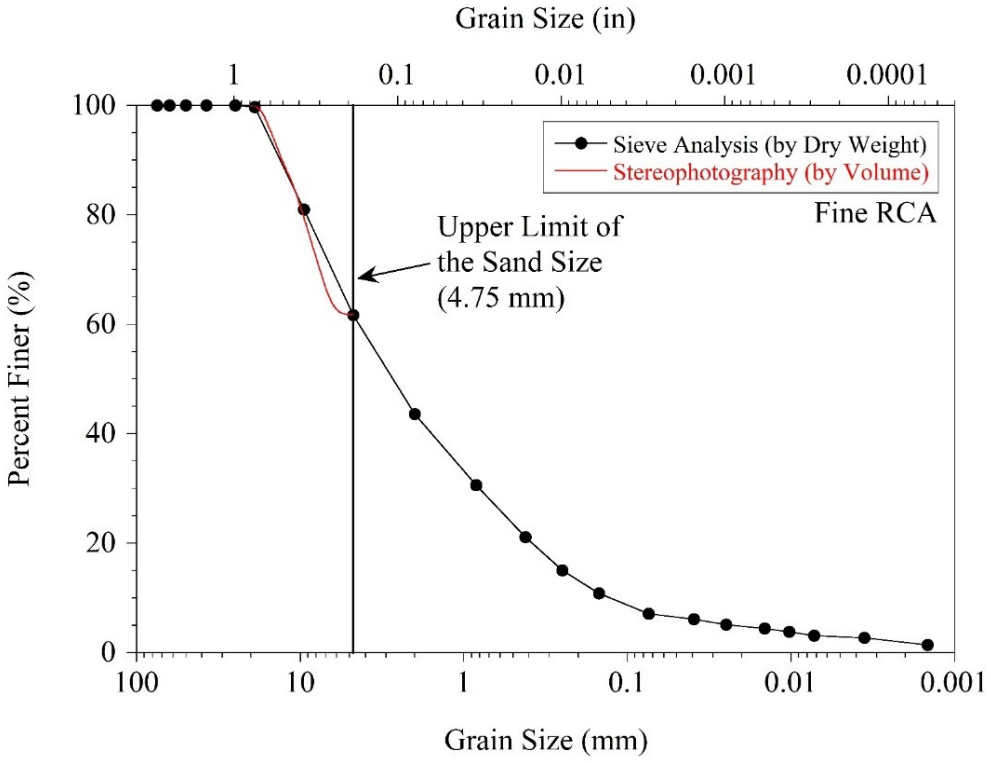

Figure 4.64. Gradations of Fine RCA determined by sieve analysis and stereophotography

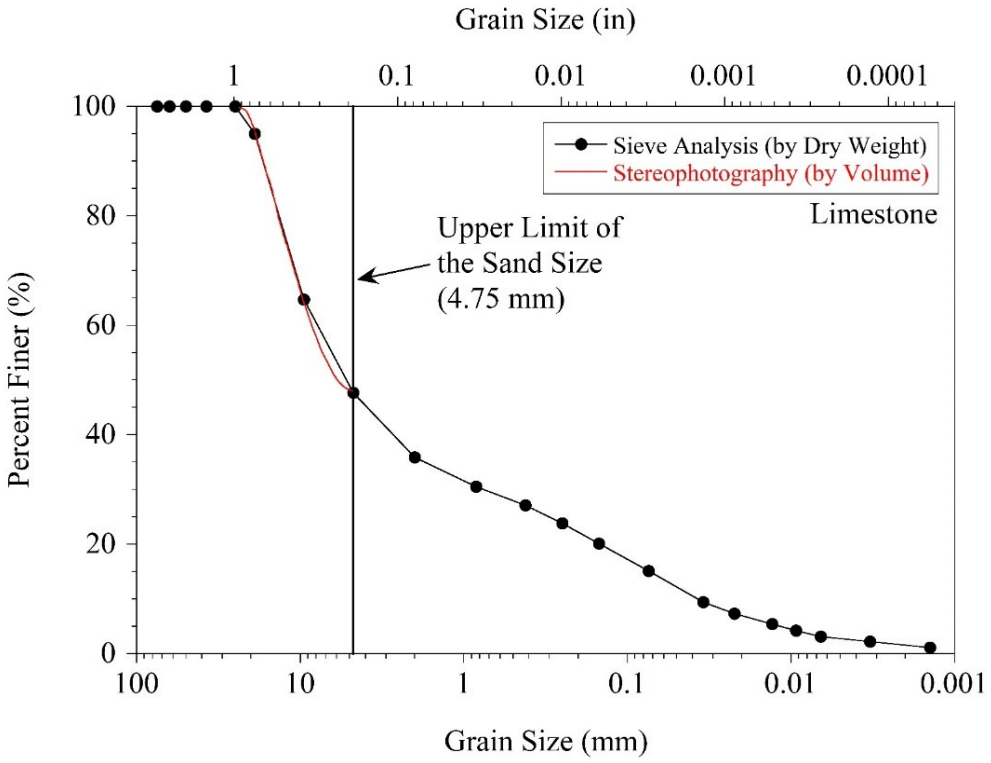

Figure 4.65. Gradations of Limestone determined by sieve analysis and stereophotography

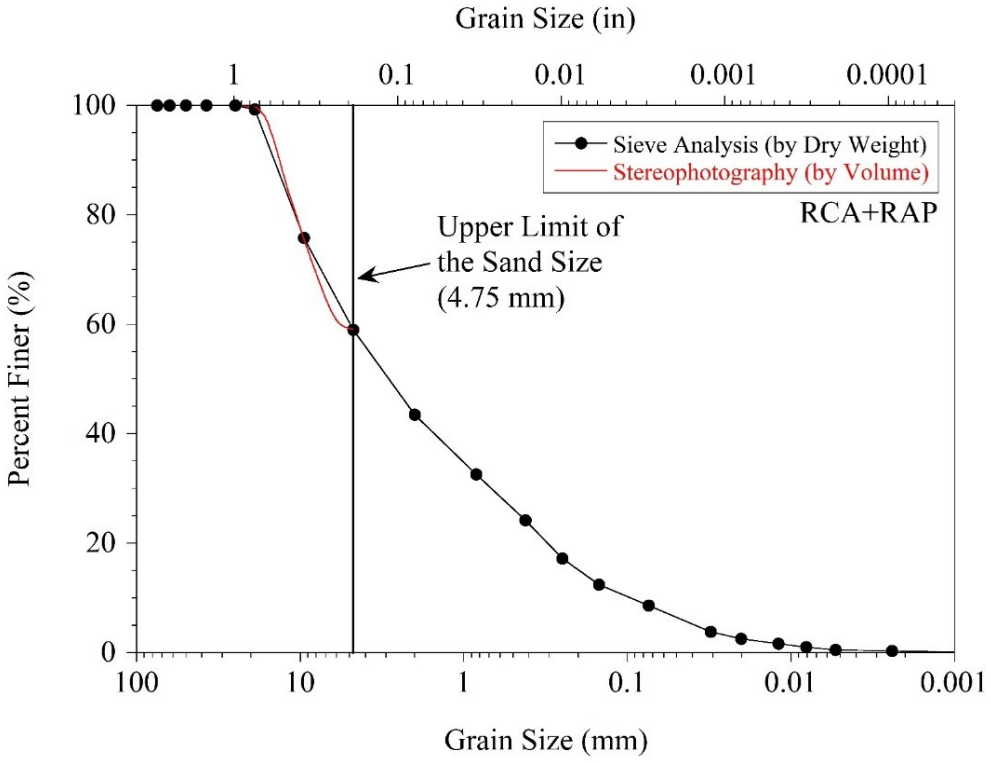

Figure 4.66. Gradations of RCA+RAP determined by sieve analysis and stereophotography

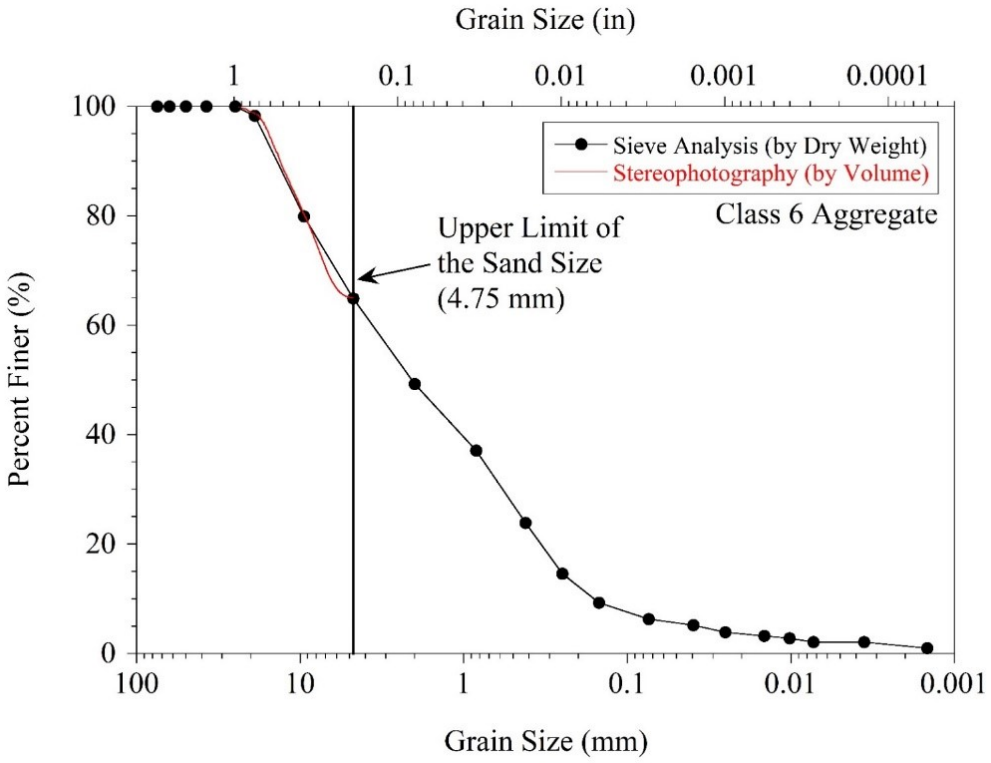

Figure 4.67. Gradations of Class 6 Aggregate determined by sieve analysis and stereophotography

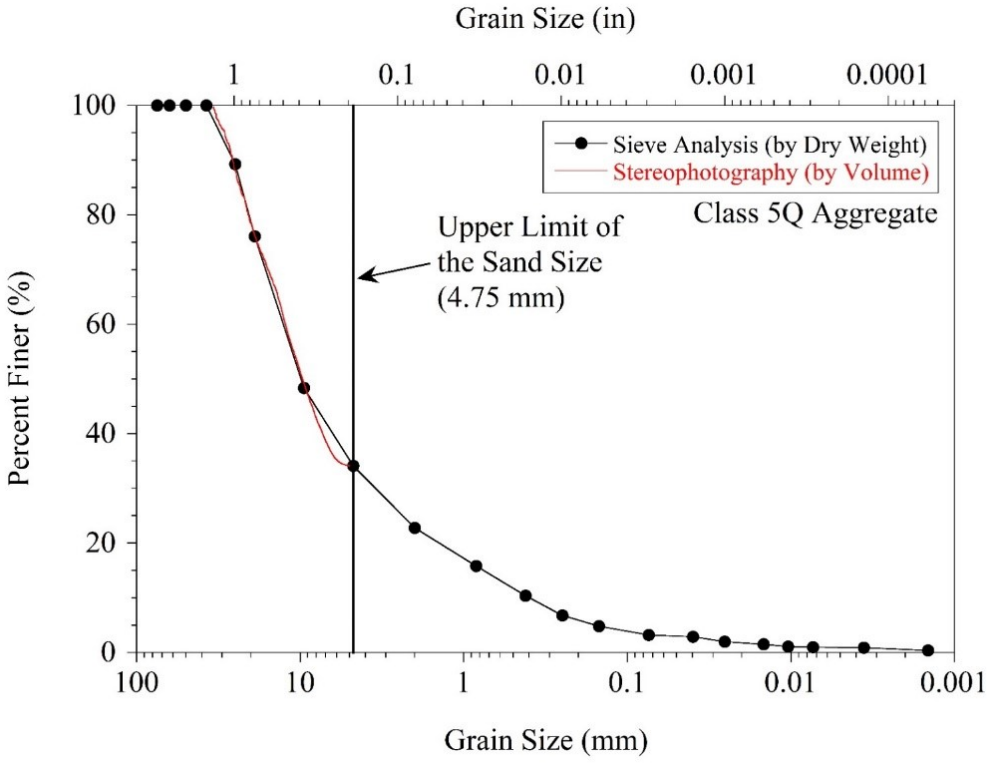

Figure 4.68. Gradations of Class 5Q Aggregate determined by sieve analysis and stereophotography

4.4.3 Particle Shape Analysis

Particle shape characteristics of the materials were also determined by stereophotography. The MATLAB code provided eight different parameters: area sphericity, diameter sphericity, circle ratio sphericity, perimeter sphericity, width-to-length ratio sphericity, circularity, convexity, and roundness. Each parameter is summarized in Table 4.12. Zheng and Hryciw (2015) stated that the width-to-length ratio sphericity (S_{WL}), defined by Krumbein and Sloss (1951) [Figure 4.69(a)], is the most useful approach to evaluate sphericity and yields the widest range of sphericity values (between 0 and 1). In addition, S_{WL} parameter does not depend on particle roundness, defined by Wadell (1932, 1933, 1935) [Figure 4.69(b)] (Zheng and Hryciw 2015; Hryciw et al. 2016). The Krumbein-Sloss chart (Figure 4.70) is a very well-known chart, which combines S_{WL} and roundness parameters (Zheng and Hryciw 2015; Kim et al. 2019). Therefore, in this study, S_{WL} and roundness (R) parameters were used to evaluate the particle shape characteristics.

Table 4.12. Particle shape parameters determined by stereophotography

Parameter	Formula	Description	Reference
Area Sphericity	$S_A = \frac{A}{A_{cir}}$	The ratio of the area of the particle (A) to the area of the smallest circumscribing circle (A_{cir}).	Riley (1941)
Diameter Sphericity	$S_D = \frac{D_e}{D_{cir}}$	The ratio of the diameter of a circle having the same area as the original particle (D_e) to the diameter of the minimum circumscribing circle (D_{cir}).	Wadell (1935)
Circle Ratio Sphericity	$S_C = \frac{D_{ins}}{D_{cir}}$	The ratio of the diameter of the largest inscribed circle of the particle (Dins) to the smallest circumscribing circle of the particle (D_{cir}).	Santamarina and Cho (2004)
Perimeter Sphericity	$S_P = \frac{P_e}{P}$	The ratio of the perimeter of the circle having the same area as the particle (P_e) to the real perimeter of the particle (P).	Kuo and Freeman (2000)
Width-to-Length Ratio Sphericity (Aspect Ratio, Elongation)	$S_{WL} = \frac{d_2}{d_1}$	The ratio of the width of the particle (d_2) to the length of the particle (d_1).	Krumbein and Sloss (1951)
Circularity	$C = \frac{4\pi A}{P^2}$	The ratio of the area of the particle (A) to the area of the circle having the same perimeter as the particle ($P^2/4\pi$).	ISO (2008)
Convexity (Solidity)	$C_x = \frac{A}{A_c}$	The ratio of the area of the particle (A) to the area of the minimum convex boundary circumscribing the particle (A_c).	Mora and Kwan (2000)
Roundness (Angularity)	$R = \frac{\sum_{i=1}^{N} r_i / N}{r_{ins}}$	The ratio of the average radius of corner circles of the particles (r_i is the radius of i^{th} corner and N is the number of corners) to the radius of the maximum inscribed circle (r_{ins}).	Wadell (1932, 1933, and 1935)

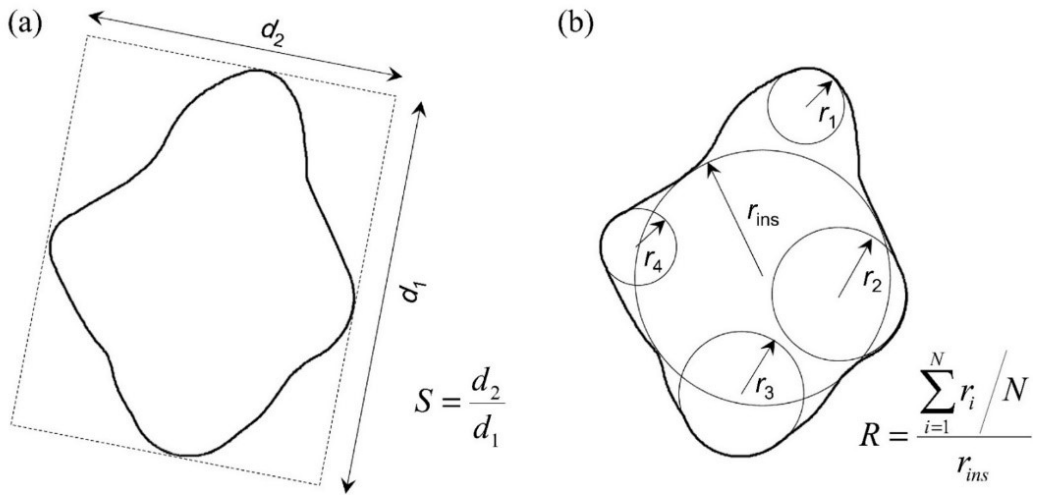

Figure 4.69. Definitions of (a) width-to-length ratio sphericity (Krumbein and Sloss 1951; Hryciw et al. 2016) and (b) roundness (Wadell 1932, 1933, and 1935)

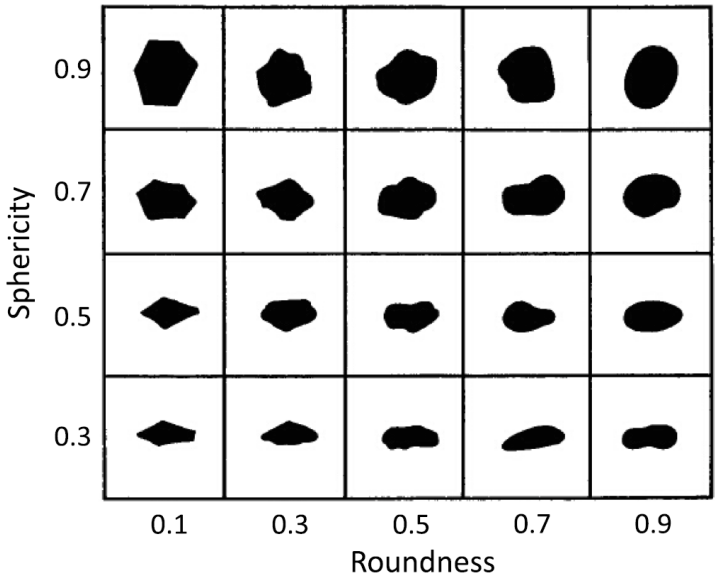

Figure 4.70. Krumbein-Sloss chart (Krumbein and Sloss 1951; Hryciw et al. 2016)

Particle distributions based on their width-to-length ratio sphericity and roundness values are provided in Figure 4.71 and Figure 4.72, respectively. Summaries of the width-to-length ratio sphericity and roundness distributions are provided in Table 4.13 and Table 4.14, respectively. For the distributions, the number of particles was considered instead of the volume of particles. If the volume of particles was considered, particle size would affect the particle shape distributions (Li et al. 2017). To avoid this, the number of particles was used in order to evaluate the distributions.

For all materials, there was no particle exhibiting an S_{WL} value smaller than 0.3 (Figure 4.71 and Table 4.13). Base layer aggregates exhibited similar S_{WL} distributions (Figure 4.71). However, LSSB particles were less spherical than base layer aggregates overall (Figure 4.71). In terms of roundness, none of the

particles exhibited roundness value at around 0.1 (Figure 4.72 and Table 4.14). While base layer aggregates yielded similar roundness distributions, the roundness distribution of LSSB particles was considerably different from those of base layer aggregates (Figure 4.72). LSSB particles were relatively less rounded (more angular) than base layer aggregates (Figure 4.72).

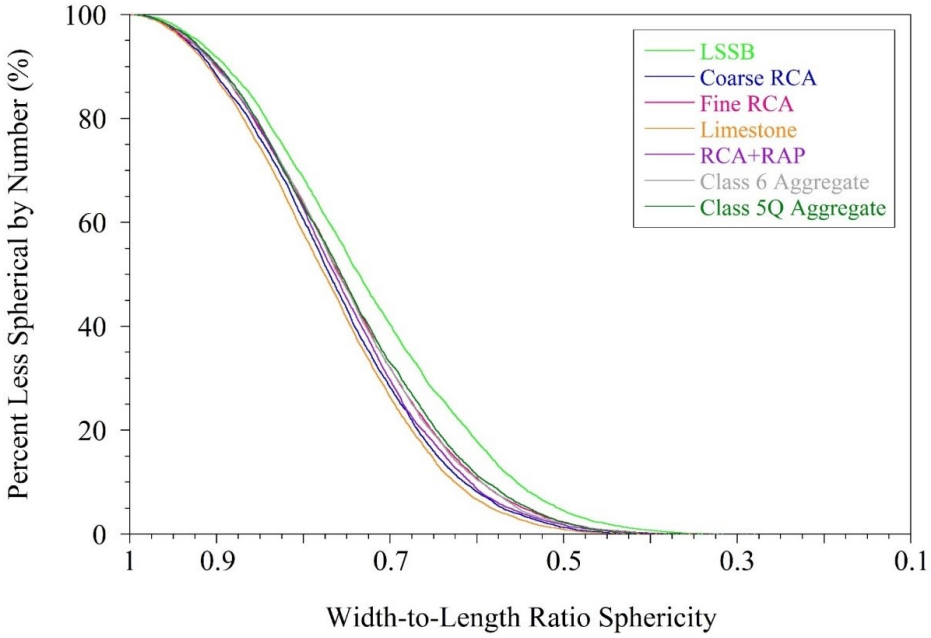

Figure 4.71. Width-to-length ratio sphericity distributions of materials determined by stereophotography

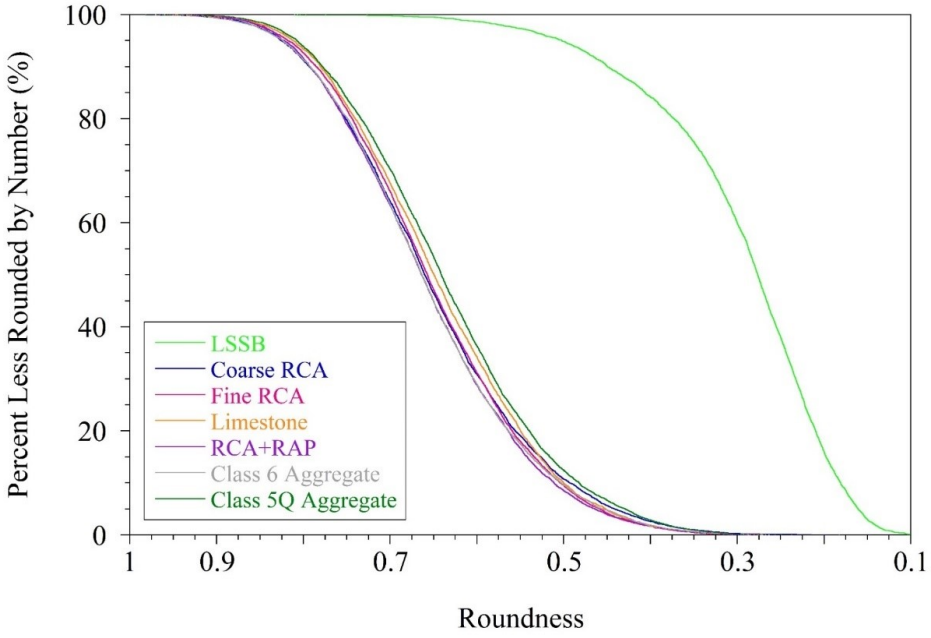

Figure 4.72. Roundness distributions of materials determined by stereophotography

Table 4.13. Summary of width-to-length ratio sphericity distributions

Material	Percent Less Spherical by Number (%)				
	0.9	0.7	0.5	0.3	0.1
LSSB	92	40	4.5	0	0
Coarse RCA	88	28	1	0	0
Fine RCA	90	32	2.5	0	0
Limestone	88	26	1	0	0
RCA+RAP	90.5	30	2	0	0
Class 6 Aggregate	90	32	2	0	0
Class 5Q Aggregate	90.5	33	2	0	0

Table 4.14. Summary of roundness distributions

Material	Percent Less Rounded by Number (%)				
	0.9	0.7	0.5	0.3	0.1
LSSB	100	100	95	60	0
Coarse RCA	99.5	64	11	0.5	0
Fine RCA	99.5	66	9.5	0	0
Limestone	99.5	67.5	10	0	0
RCA+RAP	100	63.5	8.5	0	0
Class 6 Aggregate	99	63.5	10	0	0
Class 5Q Aggregate	100	70	12.5	0	0

4.5 GYRATORY COMPACTION AND ABRASION

Degradation (or abrasion) of aggregates used in aggregate base layers can significantly affect the engineering properties of the pavement systems (Zeghal 2009). Due to degradation, aggregates become finer and reduction in aggregate sizes may decrease permeability and freeze-thaw (F-T) durability (Cho et al. 2006; Vallejo et al. 2006; White and Vennapusa 2014). Gradation, mineralogy, morphology, and loading conditions affect the degradation of aggregates (Li et al. 2017). Los Angeles (LA) abrasion (ASTM C131) and Micro-Deval tests (ASTM D6928) are the most commonly used tests to evaluate the degradation of aggregates. Specimens must be prepared at standard gradations to be tested by these two methods. However, each aggregate has a different gradation and the gradation affects the engineering properties of aggregates significantly (shear strength, stiffness, permeability, etc.) (Cosentino et al. 2003; Tan et al. 2014; Zheng and Hryciw 2014, 2017). Preparing aggregate specimens at standard (or predetermined) gradations cannot represent the actual behavior of aggregates in the field; therefore, aggregates should be tested at their original gradations determined by conventional particle size distribution analyses (Li et al. 2017). In addition, it is stated by Li et al. (2017) that the LA abrasion and Micro-Deval tests do not simulate the field loading conditions.

To overcome such problems, the Gyratory Abrasion and Image Analysis (GAIA) method was developed by Li et al. (2017). Gyratory compaction is generally used for testing asphalt materials (Harman et al.

2002). In addition, it is also used for soils and aggregates as an alternative to Proctor compaction (Kim et al. 2007; Li et al. 2015). Previously, the 2-D image analysis was used by Li et al. (2017). However, in this study, stereophotography, which is the previously described 3-D image processing technique, was performed. Changes in the particle size and shape characteristics of aggregates due to gyratory compaction effort were evaluated by the image analysis. In the GAIA method, aggregates were tested at their actual gradations.

4.5.1 Test Method

The GAIA method was performed on Coarse RCA, Fine RCA, Limestone, RCA+RAP, Class 6 Aggregate, and Class 5Q Aggregate. First, sieve analysis was performed on each material and the particles retained on the sieves (1 in, 3/4 in, 3/8 in, No. 4, No. 10, No. 20, No. 40, No. 60, No. 100, and No. 200 sieves) were separated, washed (particles passing No. 200 sieve were not washed), and dried in an oven at 110°C for 24 hours. The weight of each specimen was determined to be 4500 g and the required amount of each particle size (separated by the sieves) was calculated based on the original gradation of the material (Figure 4.2). Two particle fractions were kept in two different sealed bags: one for the particles larger than No. 4 sieve (4.75 mm) and another one for the particles finer than No. 4 sieve [Figure 4.73(a)]. Three specimens were prepared for each material (18 specimens in total from six different materials). Then, stereophotography, as described previously, was performed on the particles larger than No. 4 sieve (4.75 mm). After the completion of the image analysis, the two sealed bags were mixed in a pan prior to gyratory compaction Figure 4.73(b)].

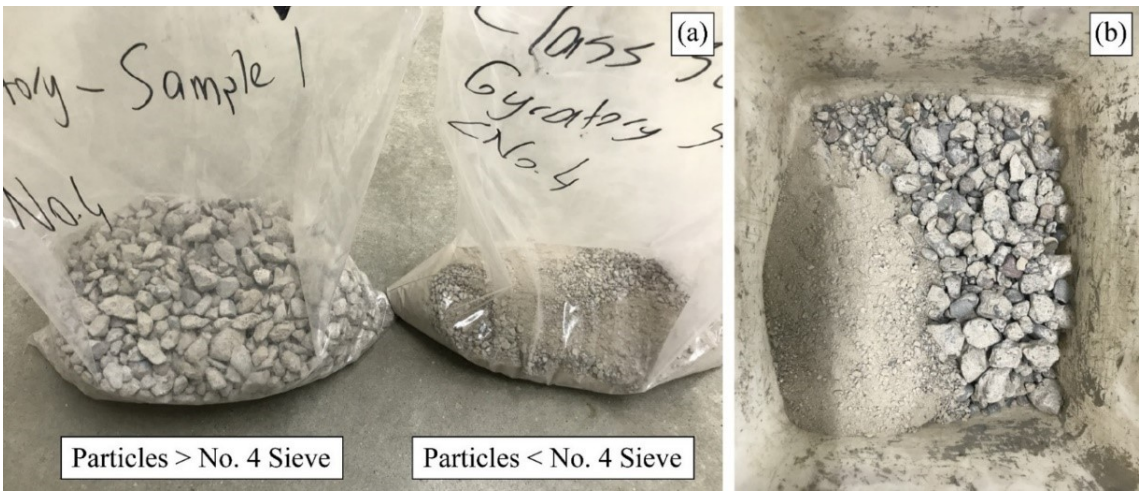

Figure 4.73. (a) Particle groups stored in different sealed bags and (b) mixing all particle groups prior to gyratory compaction

The gyratory compactor, used in this study, is shown in Figure 4.74. The information regarding the specimen sizes and the operation parameters is summarized in Table 4.15 (ASTM D6925). For three specimens from the same material, the first, the second, and the third specimen were subjected to 100, 300, and 500 gyrations, respectively. 100 and 300 gyrations were applied in a single test for the first and the second specimens. In fact, for the second specimen, 299 gyrations were applied since it was the maximum number of gyrations that could be applied in a single test. However, the number was rounded

to 300 for simplicity. To apply 500 gyrations for the third specimen, two consecutive 250-gyration tests were applied. Examples of the particles crushed due to the gyratory compaction effort are provided in Figure 4.75.

After compaction, similar sieving, separating, washing, and drying operations were performed on the compacted materials. Stereophotography, described previously, was performed on the particles retained on No. 4 sieve (4.75 mm). Then, the particle size and shape characteristics of the particles larger than No. 4 sieve before and after the gyratory compaction effort were compared.

Figure 4.74. Picture of gyratory compactor used in this study

Table 4.15. Specimen sizes and operation parameters of gyratory compactor

Parameter	Value
Compaction Mold Diameter [in (mm)]	6 (150)
Specimen Height [in (mm)]	6 - 7.25 (150 - 185)
Vertical Applied Pressure [psf (kPa)]	12,530 (600)
Number of Gyrations	100, 300[a], 500[b]
Angle of Gyration (°)	1.25 ± 0.02
Frequency of Gyration (gyrations/min)	30 ± 0.5
Number of Dwell Gyrations	2

[a]In fact, 299 gyrations (maximum number of gyrations that can be applied per test) were applied. However, the number is rounded to 300 for simplicity. [b]Applied in two consecutive tests with 250 gyrations each.

Figure 4.75. Examples of crushed particles after gyratory compaction

4.5.2 Compaction Analysis

Height changes of the specimens during the gyratory compaction were recorded at each gyration by the compactor's integral displacement transducer. From the recorded heights and known diameter of the compaction mold (6 in), volume changes of the specimens during the compaction were calculated. Then, based on the specimen weight and volume changes during the compaction, changes in the dry unit weight (γ_{dry}) of the specimens were calculated and shown in Figure 4.76.

As expected, the γ_{dry} of each specimen increased during gyratory compaction. Applying 100 and 300 gyrations yielded uninterrupted curves showing the increase in the dry unit weight of the specimens. On the other hand, applying 500 gyrations yielded interrupted curves. As stated previously, two sets of 250-gyration tests were performed to be able to apply 500 gyrations in total. At the end of the first set of the 250 gyrations, the test stopped automatically and was restarted manually. When the test stopped, the gyratory compactor released the vertical pressure (12,530 psf) and applied two dwell gyrations in order to zero the angle of gyration (1.25 ± 0.02°). This caused some disturbance of the data for 500 gyrations (Li et al. 2017). However, in Figure 4.76, the disturbance was eliminated, and dashed lines were added between the end of the first 250-gyration stage and the point, where the dry unit weight values went back to the actual trend.

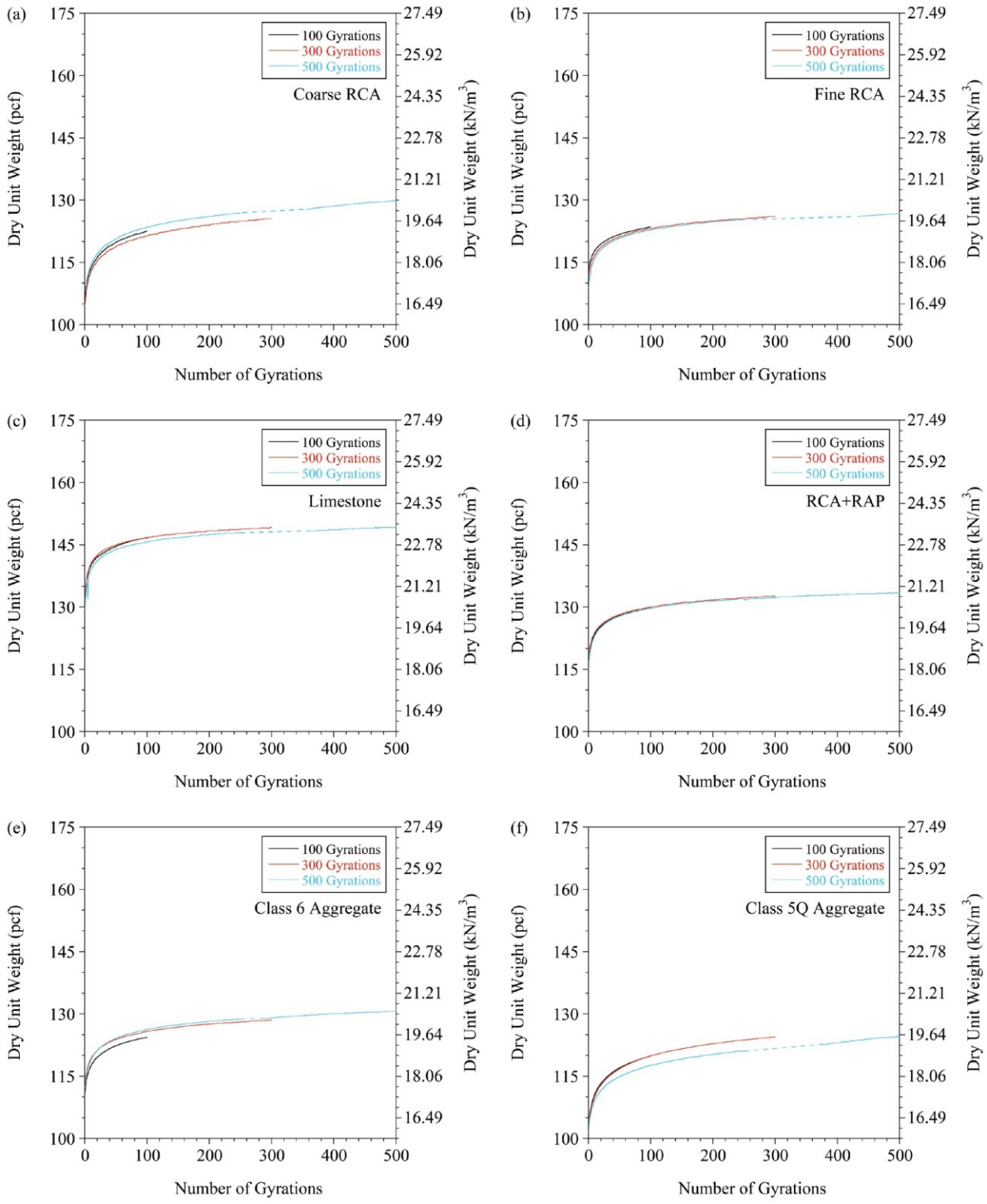

Figure 4.76. Changes of dry unit weight of specimens during gyratory compaction (a) Coarse RCA, (b) Fine RCA, (c) Limestone, (d) RCA+RAP, (e) Class 6 Aggregate, (f) Class 5Q Aggregate

4.5.3 Abrasion on Particle Size

The gradations of the materials before and after the gyratory compaction (after 100, 300, and 500 gyrations) are shown in Figure 4.77, Figure 4.78, Figure 4.79, Figure 4.80, Figure 4.81, and Figure 4.82 for Coarse RCA, Fine RCA, Limestone, RCA+RAP, Class 6 Aggregate, and Class 5Q Aggregate, respectively. To evaluate the degradation during compaction, breakage potential (B_p), total breakage (B_t), and relative breakage (B_r) parameters, described by Hardin (1985), were used. B_p is defined as the area between the initial gradation curve (before compaction) and the line, which defines the upper limit of the silt size (0.075 mm) (Hardin 1985) (Figure 4.83). B_t is defined as the area between the initial (before compaction) and the final (after compaction) gradation curves (Hardin 1985) (Figure 4.83). For B_p and B_t, the areas are the relative areas compared to the unit area, which is the area of one log cycle (Hardin 1985). B_r is the ratio between the B_t and B_p (Figure 4.83). B_p, B_t, and B_r of the materials are summarized in Figure 4.84, Figure 4.85, and Figure 4.86, respectively.

Coarse RCA and Class 5Q Aggregates exhibited higher B_p than the other materials (1.81 and 1.86, respectively) (Figure 4.84). In fact, the highest B_p was observed with Class 5Q Aggregate (1.86) (Figure 4.84). According to these results, Coarse RCA and Class 5Q Aggregate were expected to exhibit higher degradation compared to other materials. This behavior could be related to the coarser gradations of these two materials. Coarse RCA and Class 5Q Aggregate consisted of 96.6% (61.7% gravel and 34.9% sand) and 96.8% (65.9% gravel and 30.9% sand) gravel- and sand-size particles, respectively (Figure 4.2 and Table 4.1). These amounts were higher than other materials (Table 4.1). According to Hardin (1985), the larger the particle size the higher the B_p. This is because less stress is required to break up the larger particles compared to the finer particles (Hardin 1985). In descending order, B_p values of 1.47, 1.40, 1.40, and 1.35 were determined for Limestone, Fine RCA, RCA+RAP, and Class 6 Aggregate (Figure 4.84).

Coarse RCA and Class 5Q Aggregate showed larger B_t than the other materials (from 0.06 to 0.12 for Coarse RCA and from 0.09 to 0.15 for Class 5Q Aggregate) for each number of gyrations (Figure 4.85). Class 5Q Aggregate actually exhibited the highest B_t values (from 0.09 to 0.15) (Figure 4.85). This means that Class 5Q Aggregate experienced the highest degradation, which was followed by Coarse RCA, for each number of gyrations. This result was compatible with the B_p values, explained previously (Figure 4.84). Li et al. (2017) also observed that there was a linear relationship between the initial gravel content of the materials, used in that study, and B_t. While Fine RCA's B_p value (1.40) was lower than and equal to those of Limestone (1.47) and RCA+RAP (1.40) (Figure 4.84), respectively, it exhibited higher B_t (from 0.04 to 0.07) than Limestone (from 0.02 to 0.04) and RCA+RAP (from 0.03 to 0.04) for each number of gyrations (Figure 4.85). In the literature, it is stated that an increase in the residual mortar content can yield an increase in aggregate degradation because of the crushing and degradation of the porous mortar (de Juan and Gutiérrez 2009; Butler et al. 2011; Bhasya and Bharatkumar 2018). In addition, Coarse RCA and Class 5Q Aggregate exhibited higher degradation because of not only their coarser gradations but also their residual mortar content. Both Coarse RCA and Class 5Q Aggregates may have gravel size cemented aggregates, which could break down right away under pressure. Thus, higher B_t values could be observed for these two materials. B_r values of the materials (Figure 4.86) exhibited a similar trend as observed for the B_t values (Figure 4.85).

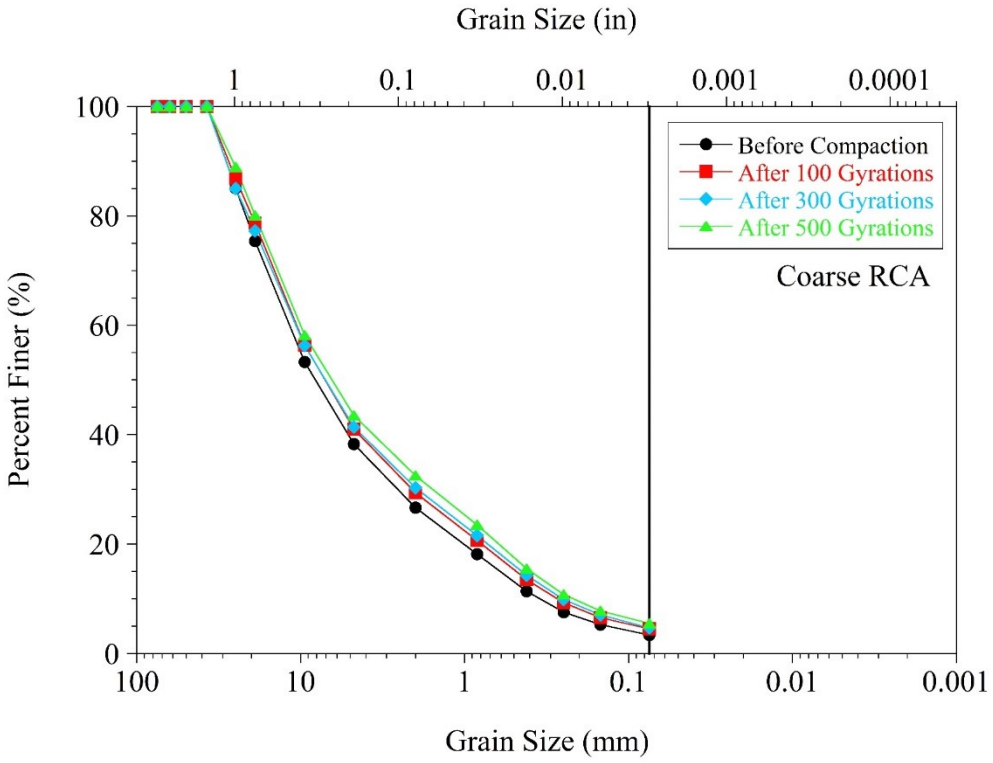

Figure 4.77. Gradations of Coarse RCA before and after gyratory compaction

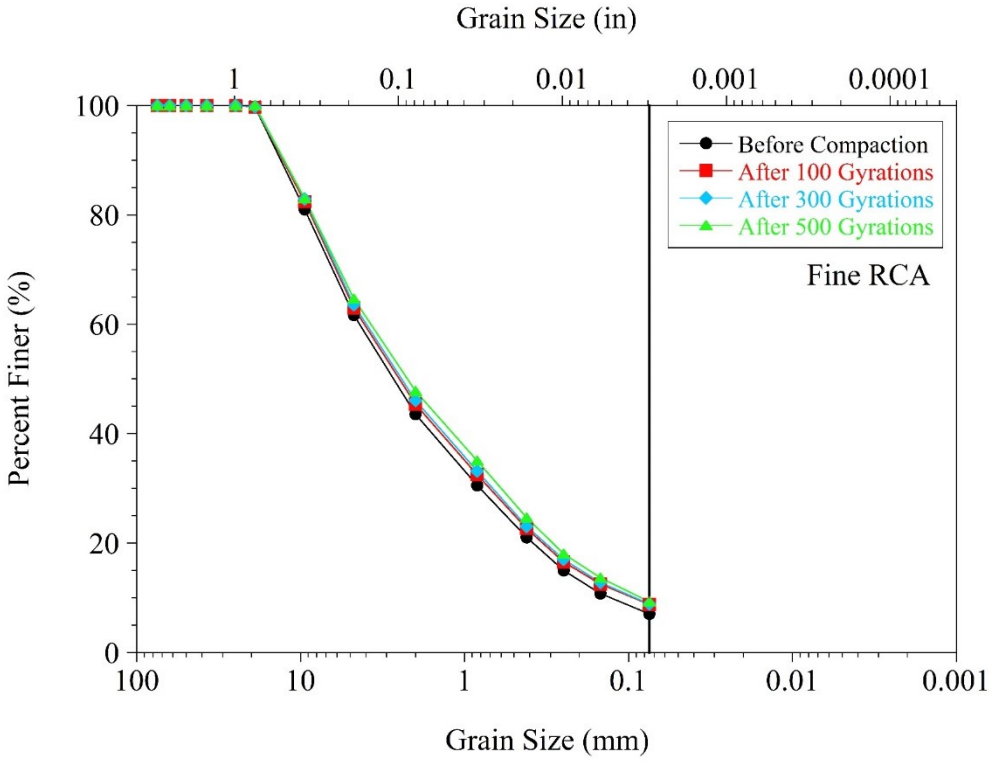

Figure 4.78. Gradations of Fine RCA before and after gyratory compaction

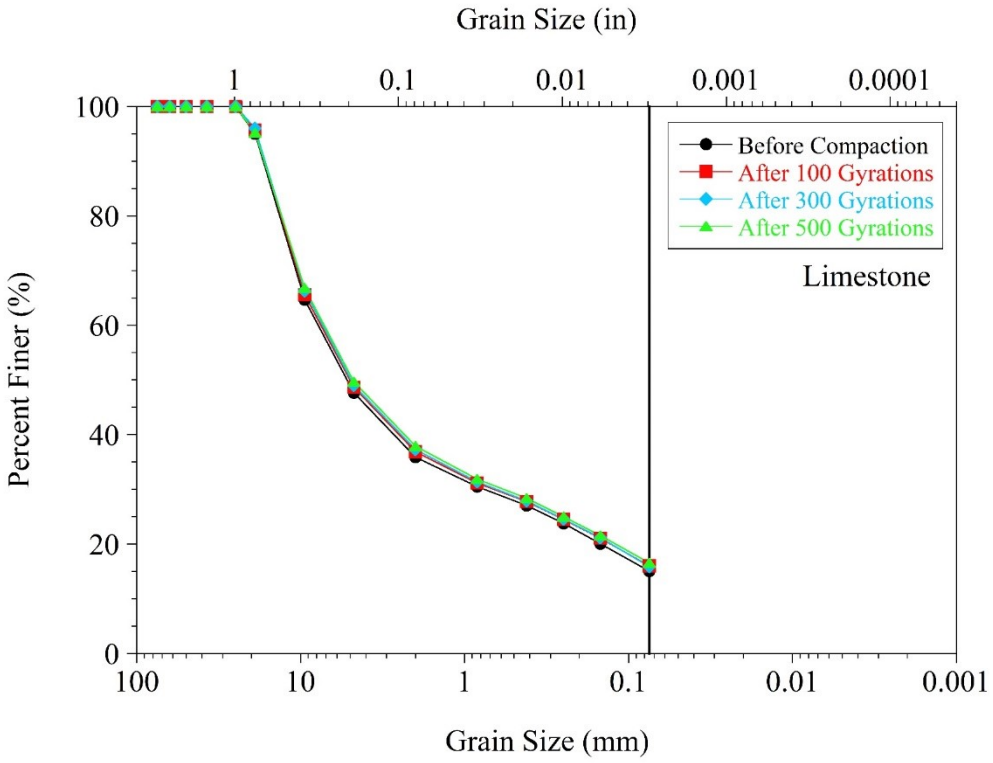

Figure 4.79. Gradations of Limestone before and after gyratory compaction

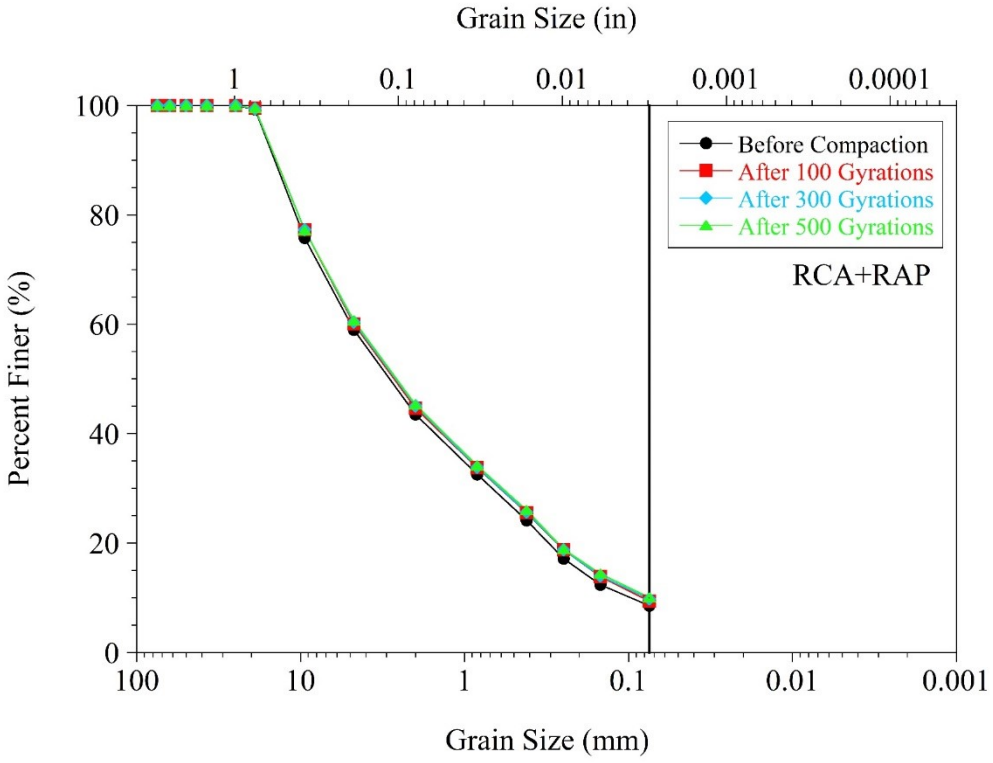

Figure 4.80. Gradations of RCA+RAP before and after gyratory compaction

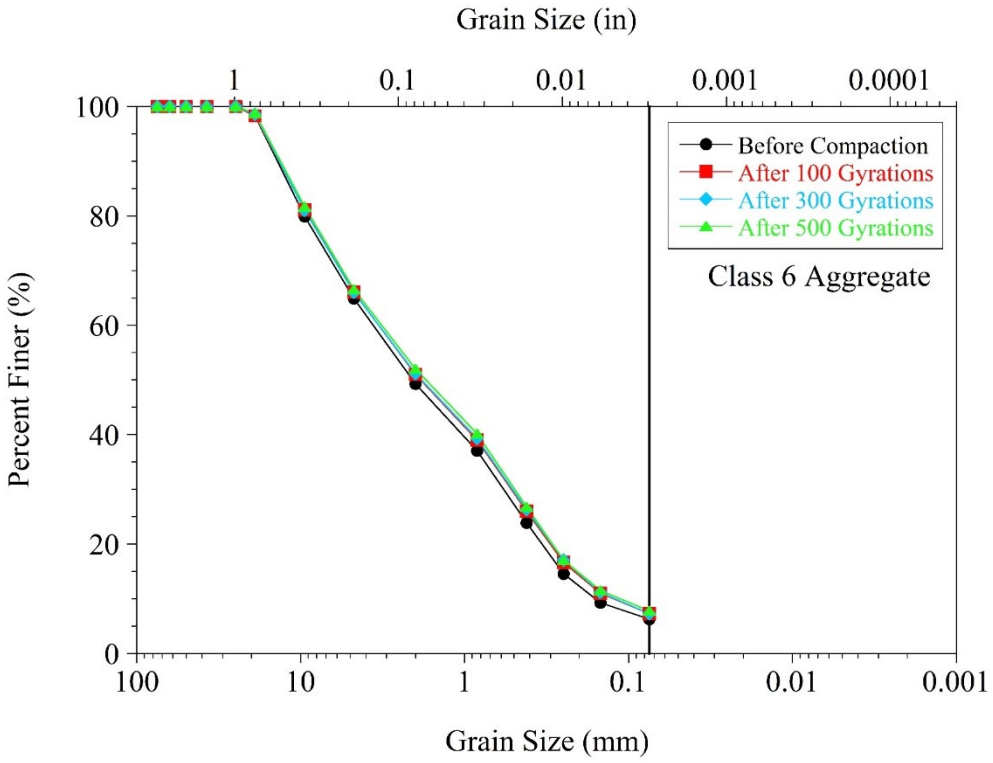

Figure 4.81. Gradations of Class 6 Aggregate before and after gyratory compaction

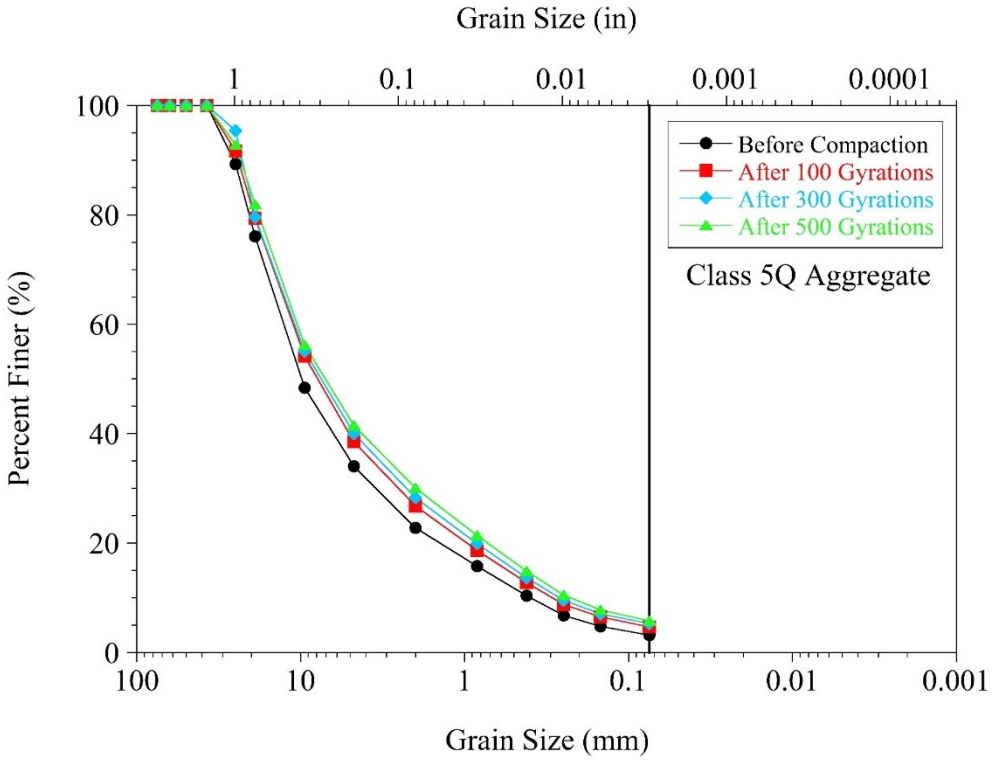

Figure 4.82. Gradations of Class 5Q Aggregate before and after gyratory compaction

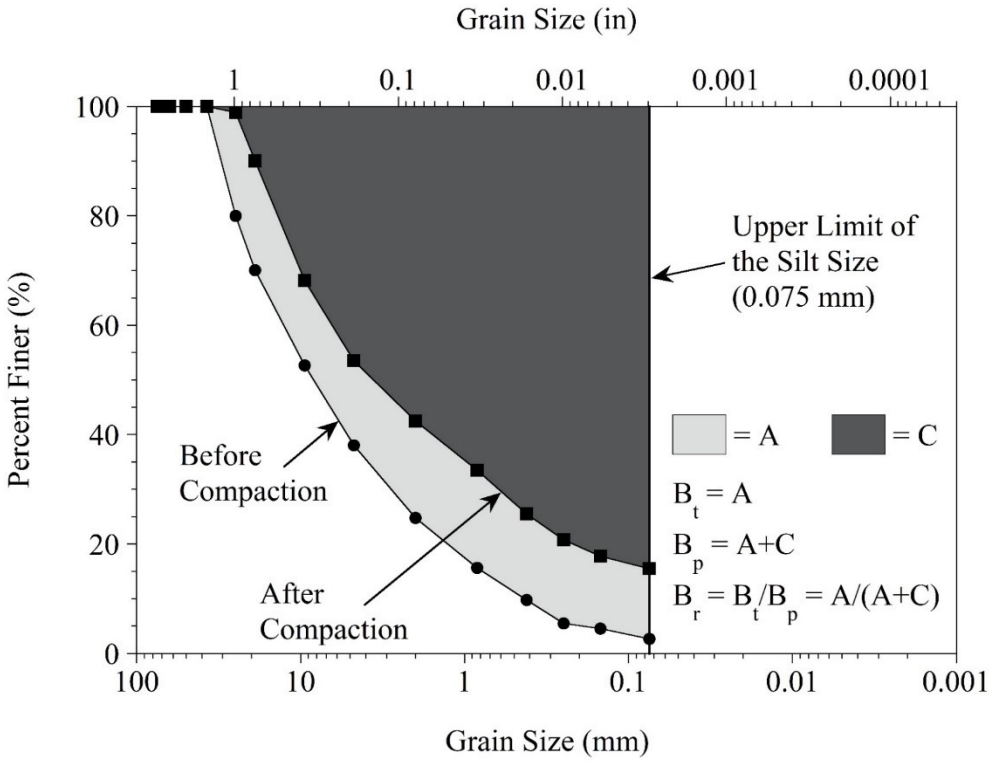

Figure 4.83. Hardin's concept to evaluate degradation of aggregates

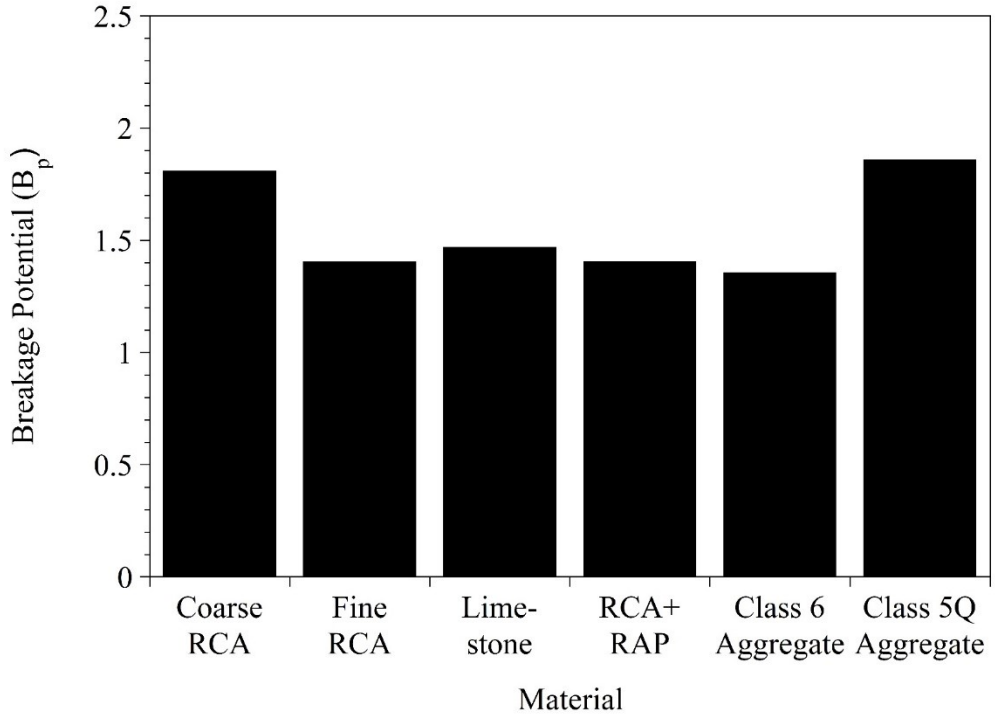

Figure 4.84. Breakage potential (B_p) of materials

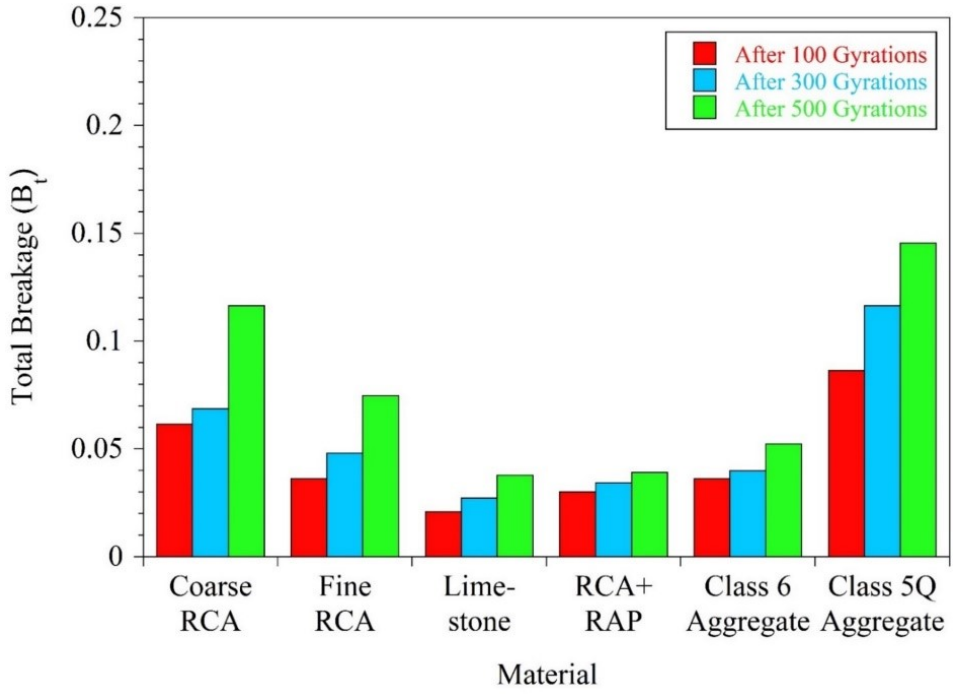

Figure 4.85. Total breakage (B_t) of materials

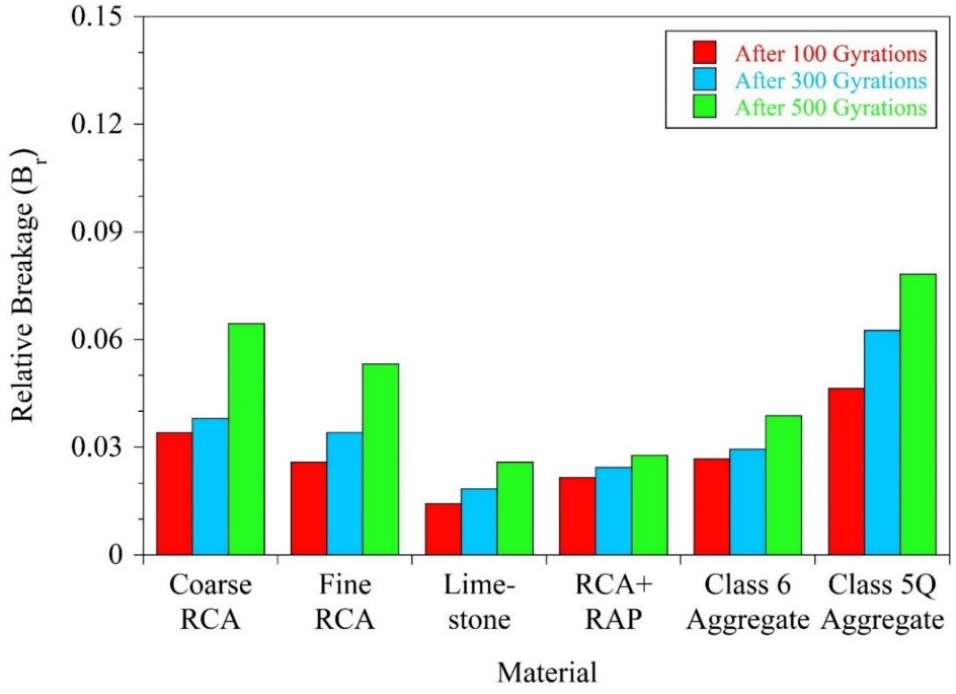

Figure 4.86. Relative breakage (B_r) of materials

4.5.4 Abrasion on Particle Shape

The width-to-length ratio sphericity and roundness of the materials (Table 4.12 and Figure 4.69) before and after compaction were evaluated. Figure 4.87 and Figure 4.88 provide examples of the changes in the width-to-length ratio sphericity and roundness of Coarse RCA due to gyratory compaction, respectively. Overall, it was concluded that an increase in the gyration number yielded higher changes in the particle shapes.

Summaries of the test results are provided in Figure 4.89, Figure 4.90, and Figure 4.91 for 100, 300, and 500 gyrations, respectively. Box plots were used for the evaluation of the abrasion on the particle shape. Similar to the results obtained by Li et al. (2017), the materials became slightly more spherical and rounded due to abrasion caused by gyratory compaction.

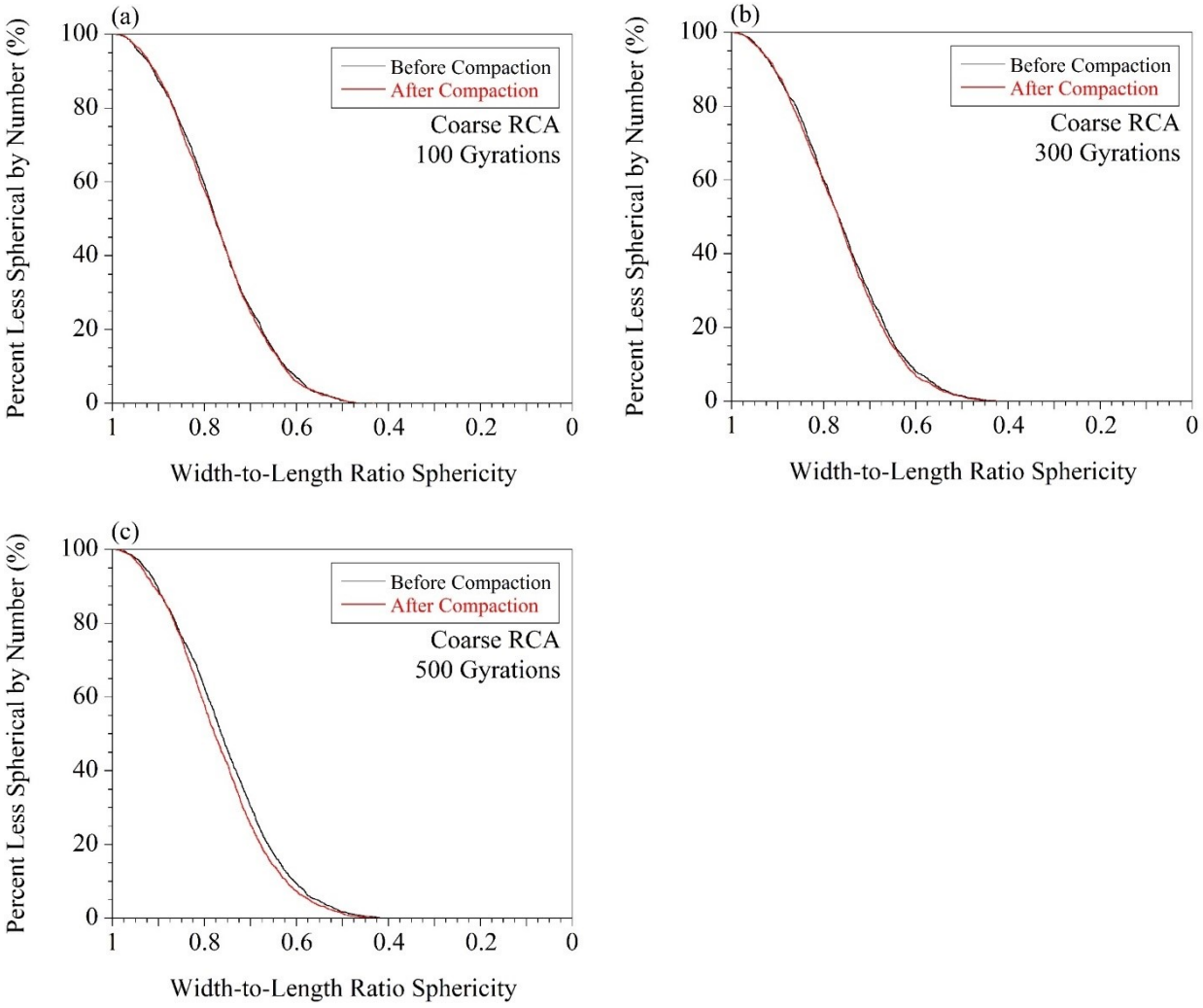

Figure 4.87. Abrasion on width-to-length ratio sphericity of Coarse RCA after (a) 100 gyrations, (b) 300 gyration, and (c) 500 gyrations

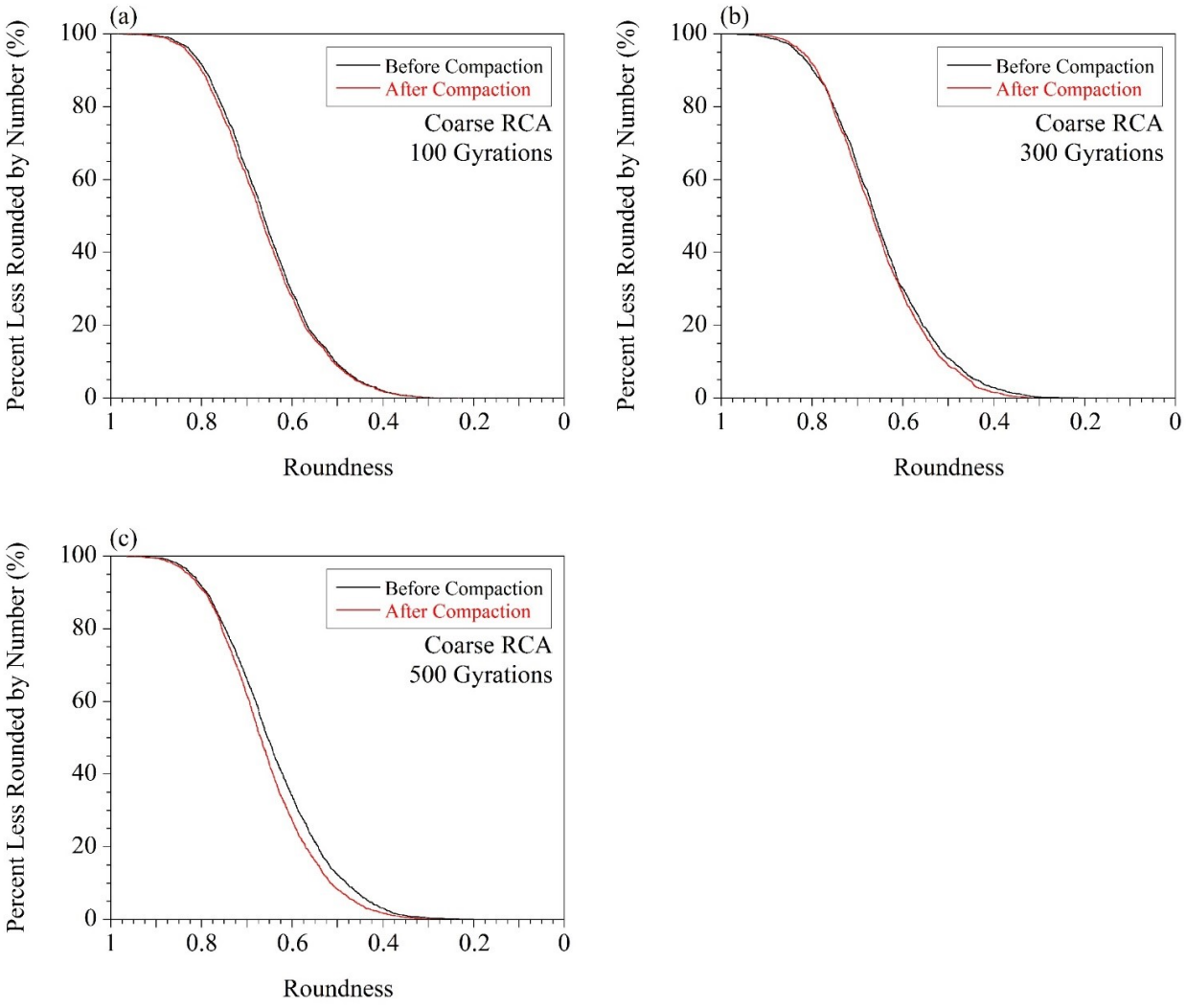

Figure 4.88. Abrasion on roundness of Coarse RCA after (a) 100 gyrations, (b) 300 gyration, and (c) 500 gyrations

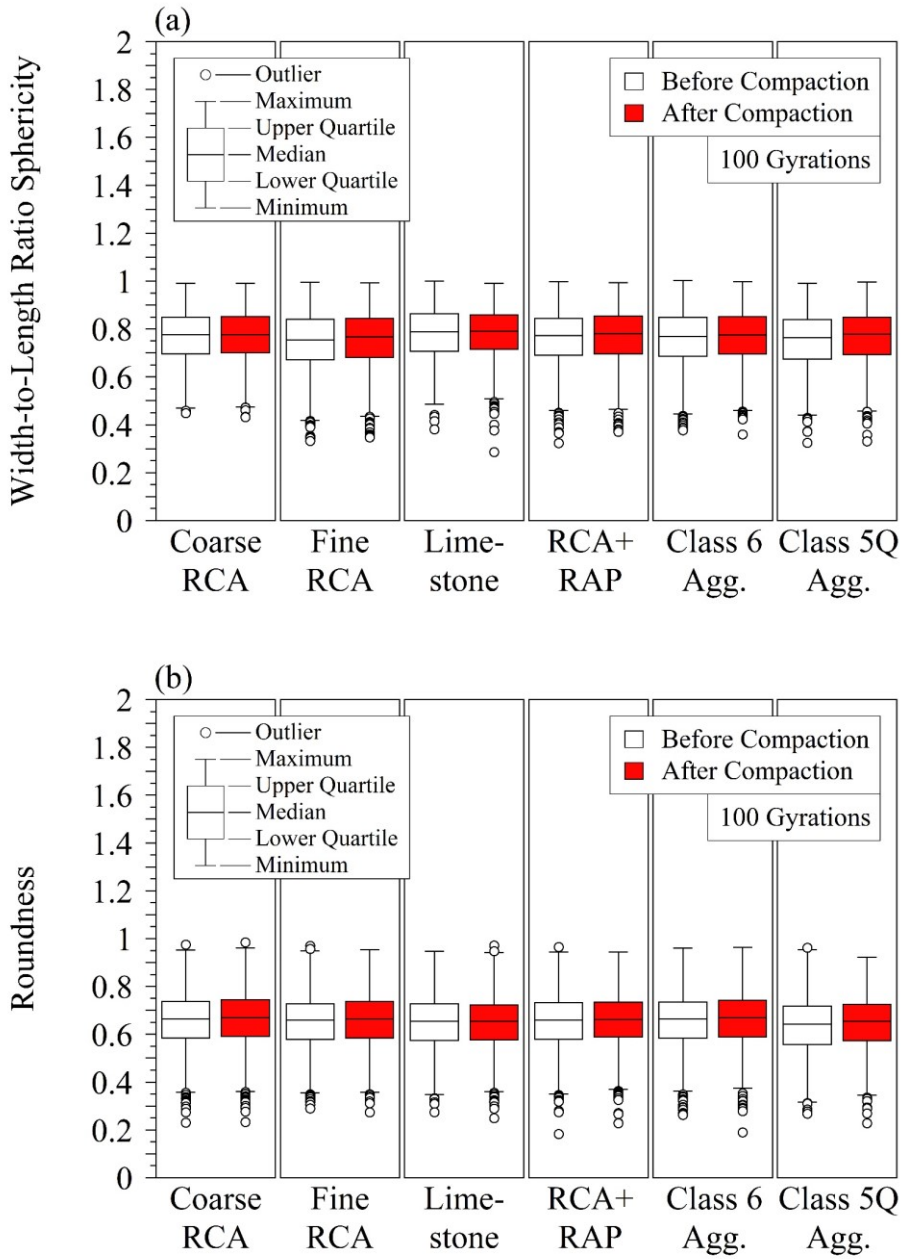

Figure 4.89. Abrasion on particle shape after 100 gyrations in terms of (a) width-to-length ratio sphericity and (b) roundness

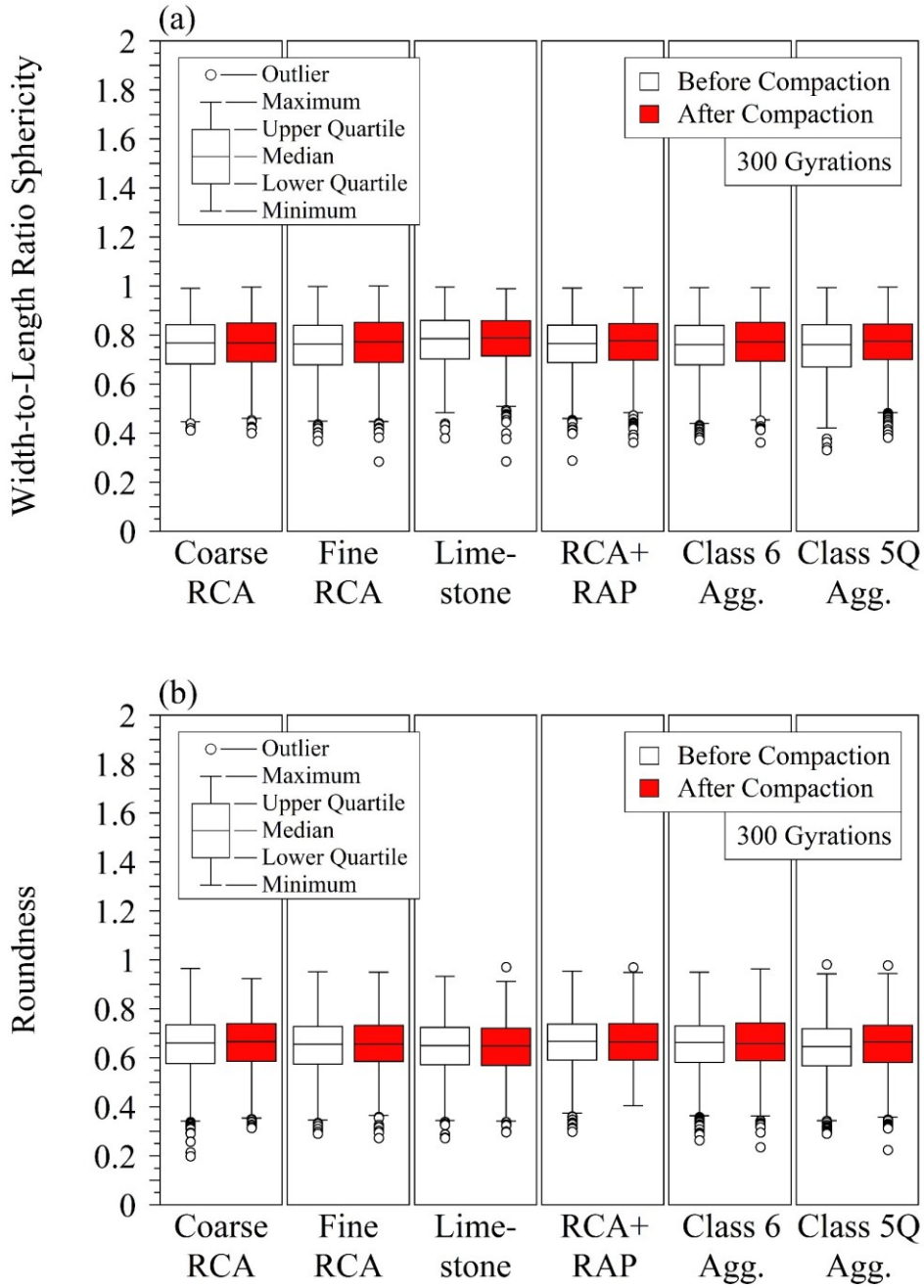

Figure 4.90. Abrasion on particle shape after 300 gyrations in terms of (a) width-to-length ratio sphericity and (b) roundness

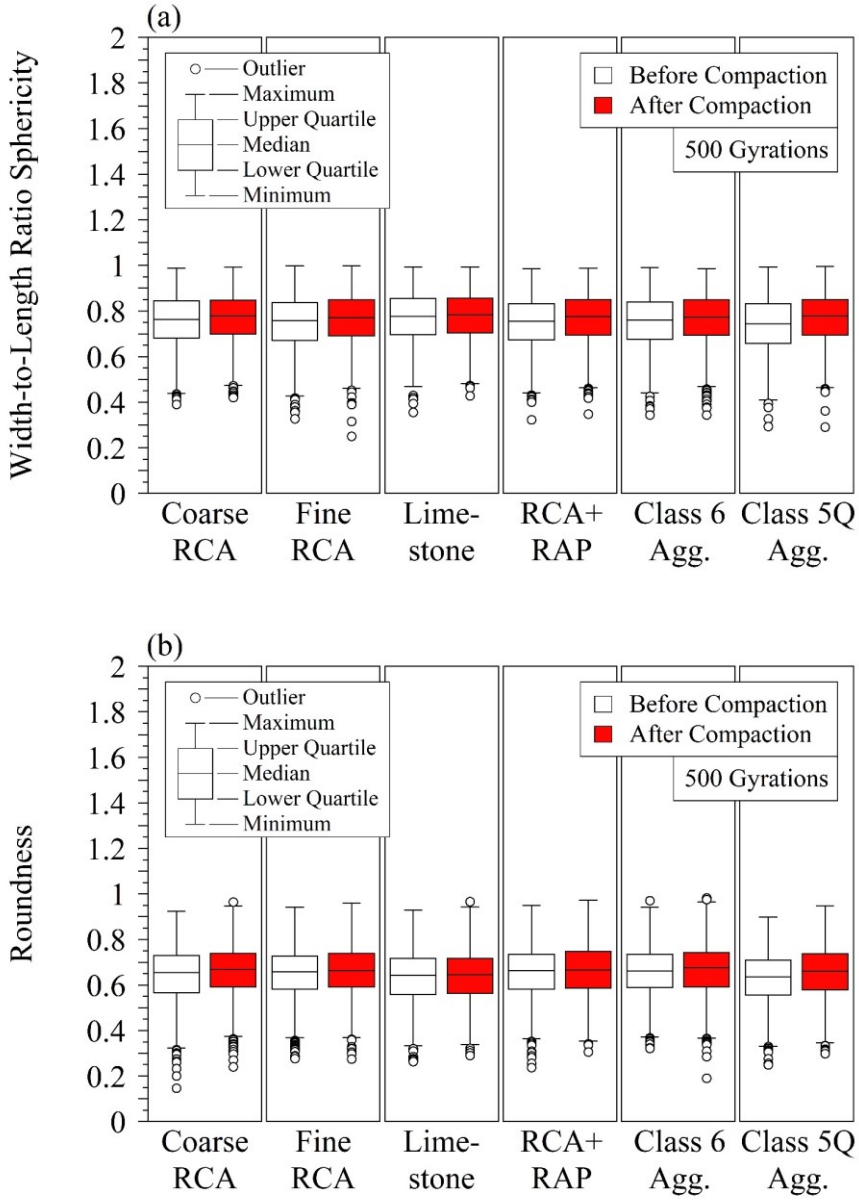

Figure 4.91. Abrasion on particle shape after 500 gyrations in terms of (a) width-to-length ratio sphericity and (b) roundness

4.6 CHAPTER CONCLUSIONS

In this chapter, detailed information about the laboratory characteristics of the materials used to construct the cells was provided. Index properties as well as saturated and unsaturated hydraulic properties of the materials were provided. In addition, the stereophotography system used to evaluate the particle size and shape characteristics of the materials and their abrasion characteristics were discussed. From the findings of this chapter, the following conclusions were drawn:

- Each material contained less than 0.1% (by dry weight) deleterious materials and met the quality requirements determined by the MnDOT. These deleterious materials included plant roots, leaves, wood chips, plastic, and fabric. No reinforcing steel was observed in the materials.

- Each material contained RAP particles to some extent. However, those RAP particles were considered to be part of the materials, and therefore, were not removed.

- Coarse RCA, Fine RCA, and RCA+RAP exhibited lower G_s than Limestone due to their residual mortar content and porous structure. Low-density asphalt binder and trapped air between the asphalt and aggregate particles were also the reason for the lower G_s of RCA+RAP. Fine RCA exhibited lower G_s than Coarse RCA. It was concluded that Class 6 Aggregate and Class 5Q Aggregate contained considerable amounts of recycled aggregates (RCA and RAP for Class 6 Aggregate and mainly RCA for Class 5Q Aggregate) because their G_s values were considerably lower than Limestone.

- Coarse RCA, Fine RCA, and RCA+RAP exhibited higher absorption than Limestone due to their residual mortar content and porous structure. Fine RCA exhibited higher absorption than Coarse RCA. RCA+RAP exhibited lower absorption than Coarse RCA and Fine RCA due to the presence of hydrophobic RAP material. Class 6 Aggregate and Class 5Q Aggregate also exhibited higher absorption than that of Limestone. These results were another sign of the presence of the recycled aggregates in Class 6 Aggregate and Class 5Q Aggregate.

- Coarse RCA, Fine RCA, and RCA+RAP exhibited lower MDU and higher OMC than Limestone because of the presence of residual mortar and cementation of unhydrated cement particles in the RCA matrix. Fine RCA exhibited lower MDU and higher OMC than those of Coarse RCA and RCA+RAP. Class 6 Aggregate and Class 5Q Aggregate exhibited lower MDU and higher OMC than Limestone due to the presence of the recycled aggregates in their matrices.

- The ignition method yielded higher asphalt binder contents compared to the quantitative extraction method and this was attributed to burned mineral fines and loss of fines in the ventilation system during ignition.

- For both the ignition and the quantitative extraction methods, the asphalt binder contents of RCA+RAP and Class 6 Aggregate were higher than those of other materials. Relatively lower asphalt binder contents were observed with Coarse RCA, Limestone, and Class 5Q Aggregate. According to the ignition method, asphalt binder content of Fine RCA was close to those of RCA+RAP and Class 6 Aggregate. However, according to the quantitative extraction method, Fine RCA contained considerably lower asphalt binder compared to RCA+RAP and Class 6 Aggregate. This result was attributed to the G_s of Fine RCA. It was concluded that the rate of loss of fines by the ventilation for Fine RCA was higher due to its relatively lower G_s.

- The freeze-thaw method developed by Abbas et al. (2007) to determine the residual mortar contents of the materials was successful. The residual mortar contents of Class 5Q Aggregate and Coarse RCA were higher than those of other materials. Fine RCA exhibited higher residual mortar content than Class 6 Aggregate and RCA+RAP. Limestone did not contain a considerable amount of residual mortar.

- Coarse RCA, Fine RCA, Limestone, and Class 5Q Aggregate exhibited 0° apparent contact angle and WDPT less than 5 seconds. Therefore, these materials were classified as wettable or hydrophilic. Apparent contact angles of RCA+RAP and Class 6 Aggregate were 83° and 86°, respectively. In addition, the water drops did not infiltrate through RCA+RAP and Class 6 Aggregate even after 3600 seconds from the placement of the water drops. As a result, these materials were classified as water repellent or hydrophobic.

- In the constant head permeability tests, the specimens could not be compacted sufficiently by the light hammering in the membrane because the degree of compaction (DOC) values were lower than 100%. Fine RCA yielded the highest permeability values with a narrower range. Sand Subgrade, Coarse RCA, and RCA+RAP exhibited relatively lower K_{sat} values with wider ranges. Class 6 Aggregate and Class 5Q Aggregate also exhibited similar K_{sat} values (Class 6 Aggregate exhibited a narrower range). Limestone exhibited similar K_{sat} values compared to Class 6 Aggregate and Class 5Q Aggregate; however, the minimum K_{sat} value of Limestone was much lower than those of Class 6 Aggregate and Class 5Q Aggregate.

- In the falling head permeability tests, the compaction process was more efficient by compacting the specimens in the rigid compaction mold. Overall, the K_{sat} values obtained by the falling head permeability were in narrower ranges compared to those obtained by the constant head permeability, in which the specimens were compacted by light hammering in the membrane. According to the falling head permeability tests, Clay Loam exhibited the lowest K_{sat} values as expected. Coarse RCA, Fine RCA, and RCA+RAP exhibited similar K_{sat} values (K_{sat} values of Fine RCA were in a narrower range) and they were higher than those of Limestone.

- Lowering the DOC yielded higher K_{sat} values for all materials. Less compaction, yielding lower DOC values, was obtained by applying lower compaction energies and these materials exhibited a more porous structure which allowed water to pass through faster.

- The hanging column tests for evaluating the soil-water characteristic curves (SWCCs) of materials were generally successful on Sand Subgrade and Class 6 Aggregate. However, results obtained for Class 5Q Aggregate and Fine RCA were not reliable. This result was attributed to the cementation of the unhydrated cement in the RCA matrix. Cementation occurred during the long testing period and it caused difficulty for the water outflow and created a risk regarding ceramic pore-clogging. Another reason could be related to the fines content of the Class 5Q and Fine RCA specimens. Hanging column test is more suitable for coarse materials.

- The pressure plate and activity meter tests were successful on Clay Loam, Coarse RCA, Fine RCA, Limestone, and RCA+RAP. In addition, the pressure plate and activity meter tests yielded narrower ranges for the specimens from the same materials compared to the hanging column tests. It was concluded that pressure plate and activity meter tests were more suitable for materials that contained RCA or that contained higher fines contents.

- It was observed that the higher the DOC of the specimens, the lower the initial volumetric water content (VWC) of the specimens at the fully saturated condition. This was due to the denser structure of the specimens. The denser structure of the specimens yielded lower void ratio values, which in turn lowered the initial VWC at fully saturated conditions.

- Sand and fines contents of the materials could not be determined by stereophotography because only the particles retained on No. 4 sieve (4.75 mm) could be used for this technique. For LSSB Material, the entire gradation curve could be obtained because a very small portion of the particles was finer than No. 4 sieve. However, for Coarse RCA, Fine RCA, Limestone, RCA+RAP, Class 6 Aggregate, and Class 5Q Aggregate, significant portions of the gradation curves of these materials could not be determined by stereophotography because those materials contained significant amounts of particles passing No. 4 sieve. Overall, for all materials, the result of stereophotography remarkably matched with the result of sieve analysis for the particles retained on No. 4 sieve.

- Base layer aggregates exhibited similar width-to-length ratio sphericity (S_{WL}) distributions. However, LSSB particles were less spherical than base layer aggregates overall. While base layer aggregates yielded similar roundness distributions, the roundness distribution of LSSB particles was considerably different from those of base layer aggregates. LSSB particles were relatively less rounded (more angular) than base layer aggregates.

- The dry unit weight of each specimen increased during the gyratory compaction. Applying 100 and 300 gyrations yielded uninterrupted curves showing the increase in the dry unit weight of the specimens. On the other hand, applying 500 gyrations yielded interrupted curves because the test stopped automatically and was restarted manually at the end of the first set of the 250 gyrations.

- The highest breakage potential (B_p) was observed with Class 5Q Aggregate followed by Coarse RCA because of their coarser gradations. The B_p values of Fine RCA, RCA+RAP, and Class 6 Aggregate were not very different from each other.

- The highest total breakage (B_t) was observed with Class 5Q Aggregate followed by Coarse RCA for each number of gyrations. This result was compatible with the B_p values of these two aggregates, which were higher than the other materials. While Fine RCA's B_p value was lower than and equal to those of Limestone and RCA+RAP, respectively, it exhibited higher B_t than those materials for each number of gyrations. This result was attributed to the higher residual mortar content of Fine RCA. B_r values of the materials exhibited a similar trend as observed for the B_t values.

- Overall, it was concluded that an increase in the gyration number yielded higher changes in the particle shapes. In addition, the materials became slightly more spherical and rounded due to abrasion caused by gyratory compaction.

4.7 DISCUSSIONS

- The use of Coarse RCA and Class 5Q Aggregate in aggregate base layers may cause several problems according to the laboratory test results. Results showed that Coarse RCA and Class 5Q Aggregate exhibited higher breakage potential (B_p) and higher total breakage (B_t). Higher breakage of particles may decrease the permeability of aggregate base layers which can then affect the long-term pavement performance negatively.

- Breakage of Coarse RCA and Class 5Q Aggregate may also cause a release of unhydrated cement content which is present in the RCA particle's matrix. This may increase the potential for tufa formation and ultimately reduce the permeability of the aggregate base layer.

- All the materials containing RCA (Coarse RCA, Fine RCA, RCA+RAP, Class 6 Aggregate, and Class 5Q Aggregate) may attract more water due to their higher absorption capacity and hydrophilicity [in fact, RCA+RAP and Class 6 Aggregate exhibit hydrophobic properties as described in Chapter 4. The hydrophobicity of these two materials mainly comes from the presence of RAP and its dust (i.e., finer RAP particles). RCA itself is prone to being hydrophilic while RCA particles covered with fine RAP particles (or RAP dust) tend to exhibit hydrophobic properties. An increase in RCA content in RCA+RAP may increase water absorption]. An increase in the water-holding capacity of aggregate base layers may cause a decrease in the freeze-thaw (F-T) resistance.

- The hanging column test method was not suitable to determine the SWCC characteristics of RCA materials due to the cementation of the unhydrated cement in the RCA matrix.

4.8 RECOMMENDATIONS

Based on laboratory test results, the following recommendations were made for practical applications:

- It can be concluded that any base layer aggregate with asphalt binder contents higher than 3% (per the ignition method) and 1.5% (per the extraction method) would exhibit hydrophobic properties. This would result in materials with higher freeze-thaw durability and better drainage properties.

- DOC of coarse-grained RCA materials should be between 90% and 95% due to their higher breakage potential and total breakage performances.

- Base layer aggregates should be treated as RCA materials if their absorption contents and mortar contents are equal to or higher than 6% and 25%, respectively.

- Gradation characteristics of RCA materials collected from sources should be determined after compactions tests to ensure that the gradation of the materials do not change significantly.

CHAPTER 5: LONG-TERM PERFORMANCE EVALUATION OF TEST CELLS

5.1 METEOROLOGICAL DATA

Meteorological data was collected by the external weather stations located at the MnROAD LVR test facility (MnDOT 2014a). Table 5.1 shows the list of equipment of which the weather stations contain. Air temperature and precipitation data (average of the two weather stations) during and after construction are provided in Figure 5.1 and Figure 5.2, respectively (detailed information about the construction dates is provided in Appendix D). Relative humidity and average wind speed data are also shown in Appendix N.

Between July 2017-April 2019, the minimum and maximum air temperatures were observed to be -29.6°F (-34.2°C) and 98°F (36.6°C), respectively (Figure 5.1). Air temperature data contained two freezing periods when the temperatures were mainly below 32°F (0°C). The first freezing period was between November 2017-April 2018, and the second freezing period was between October 2018-April 2019 (Figure 5.1).

The precipitation data contained two main rainy periods. The first and second rainy periods were between July 2017-November 2017 and May 2018- November 2018, respectively (Figure 5.2). The maximum precipitation was observed to be 0.675 in (17.1 mm) (Figure 5.2).

Table 5.1. MnROAD weather stations (NW = northwest and SE = southeast)

Equipment	NW/SE Weather Stations
Datalogger	Campbell Scientific CR1000s
Temperature/Relative Humidity Sensors	Vaisala probe Model HMP45AC/HMP45C
Wind Monitor Sensors	RM Young Model 05103
Ambient Pressure Sensor	Campbell Scientific CS106 (Vaisla PTB110)
Precipitation Sensor	Tipping bucket - Met One Instruments 380/385
Radiometer	Kipp & Zonen NR Lite 2

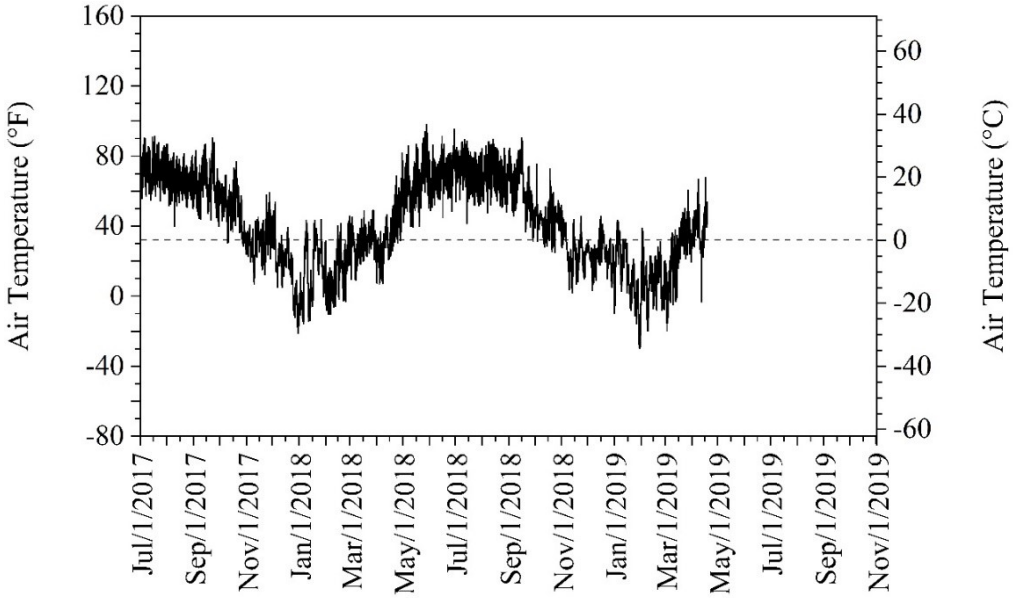

Figure 5.1. Air temperature data collected from weather stations

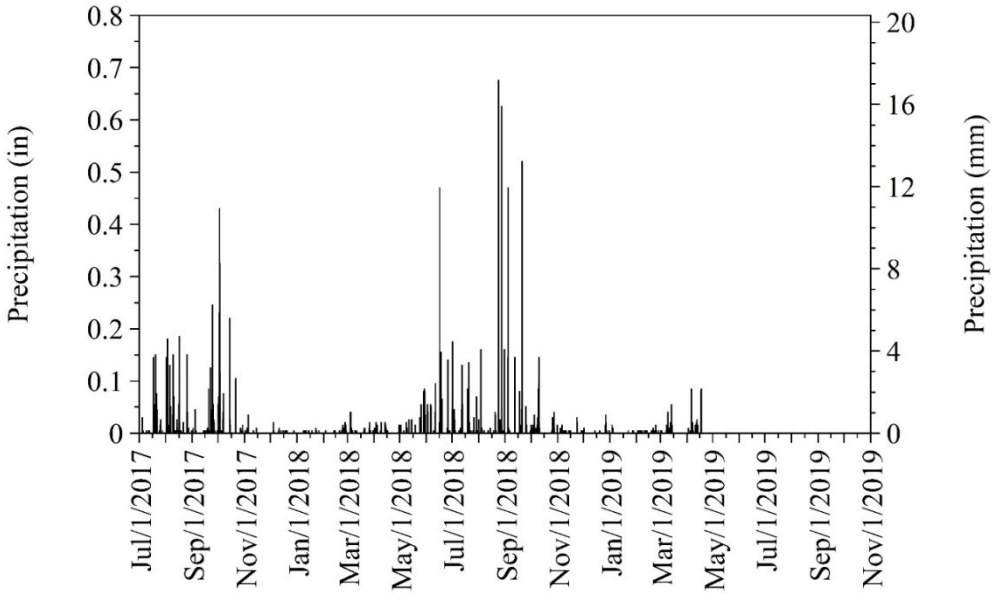

Figure 5.2. Precipitation data collected from weather stations

5.2 TEMPERATURE AND MOISTURE MONITORING

5.2.1 Monitoring Systems

Temperature and moisture measurements at various depths were taken every 15 minutes by thermocouples (TCs) (MnROAD 2014b) (Figure 5.3) and moisture probes (ECs) (Figure 5.4) (MnROAD 2014c), respectively. The sensors were installed only in Cells 185 (12-in Coarse RCA), 186 (12-in Fine RCA), 188 (12-in Limestone), 189 (12-in RCA+RAP), 127 (18-in LSSB), and 728 (9-in LSSB). The number of

sensors installed in those test cells is summarized in Table 5.2. Plan and profile views of the sensor locations are provided in Figure 5.5, Figure 5.6, Figure 5.7, Figure 5.8, Figure 5.9, and Figure 5.10 for Cells 185 (12-in Coarse RCA), 186 (12-in Fine RCA), 188 (12-in Limestone), 189 (12-in RCA+RAP), 127 (18-in LSSB), and 728 (9-in LSSB), respectively. Appendix O provides more information about the locations of the sensors.

Figure 5.3. Thermocouple array in PVC pipe (MnDOT 2014b)

Figure 5.4. Decagon 5TE moisture probe (MnDOT 2014c)

Table 5.2. Type and number of sensors installed (Van Deusen et al. 2018)

Cell Number	Cell Description	Number of Environmental Sensors	
		Thermocouple (TC)	Moisture Probe (EC)
185	12-in Coarse RCA	12	4
186	12-in Fine RCA	12	4
188	12-in Limestone	12	4
189	12-in RCA+RAP	12	4
127	18-in LSSB	12	3
728	9-in LSSB	16	4

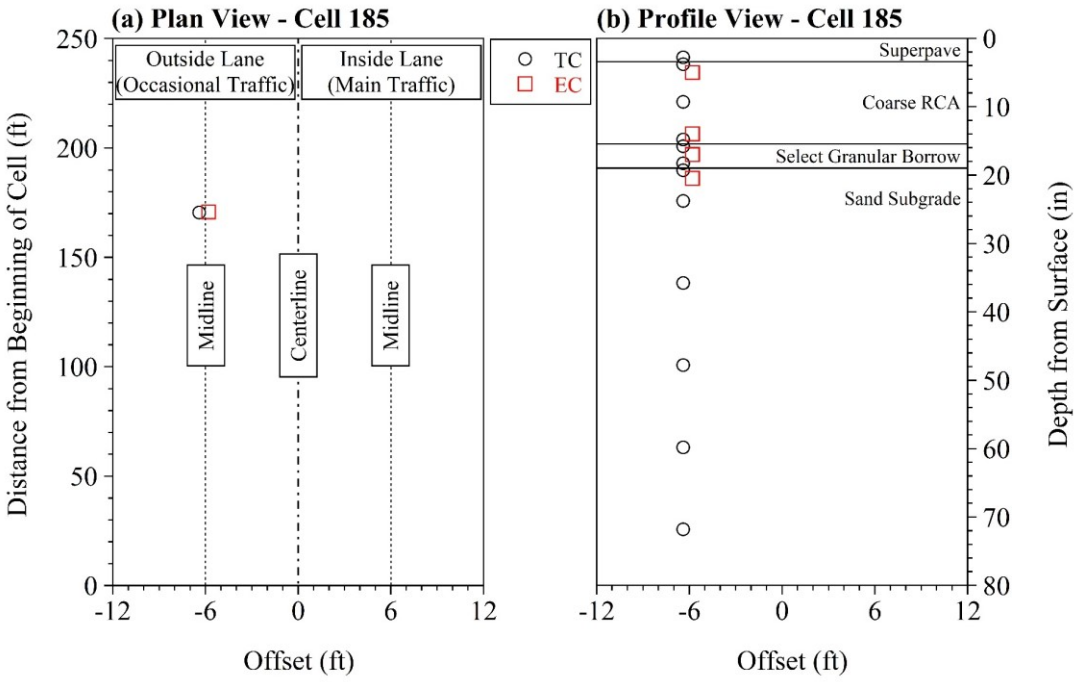

Figure 5.5. (a) Plan and (b) profile view of sensor locations in Cell 185 (12-in Coarse RCA) (TC = thermocouple, EC = moisture probe)

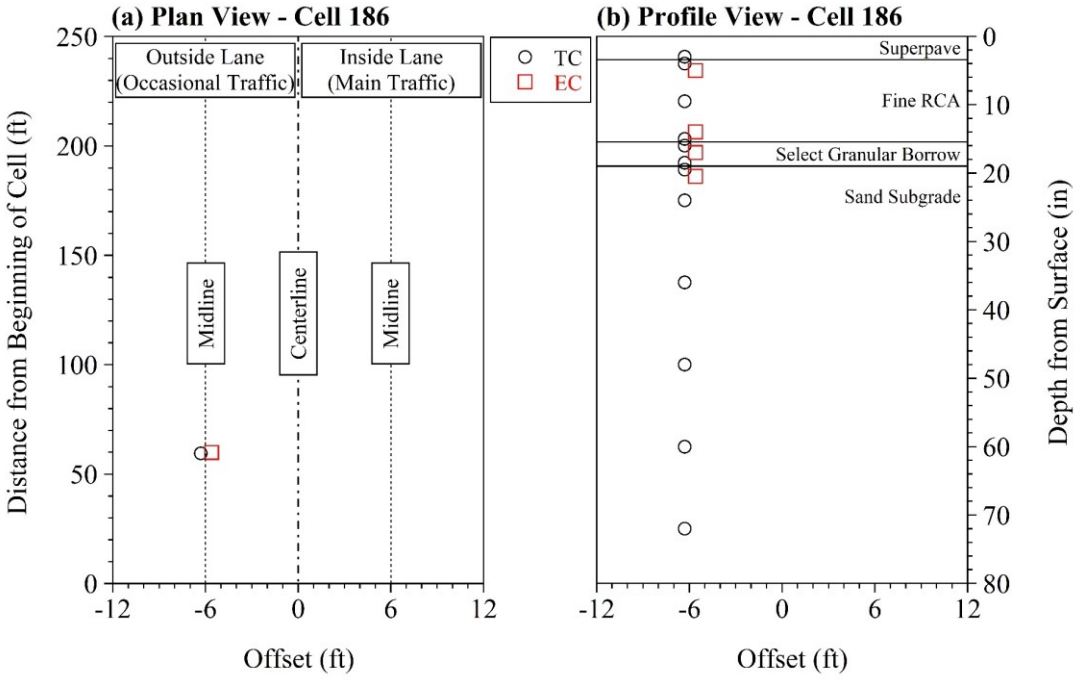

Figure 5.6. (a) Plan and (b) profile view of sensor locations in Cell 186 (12-in Fine RCA) (TC = thermocouple, EC = moisture probe)

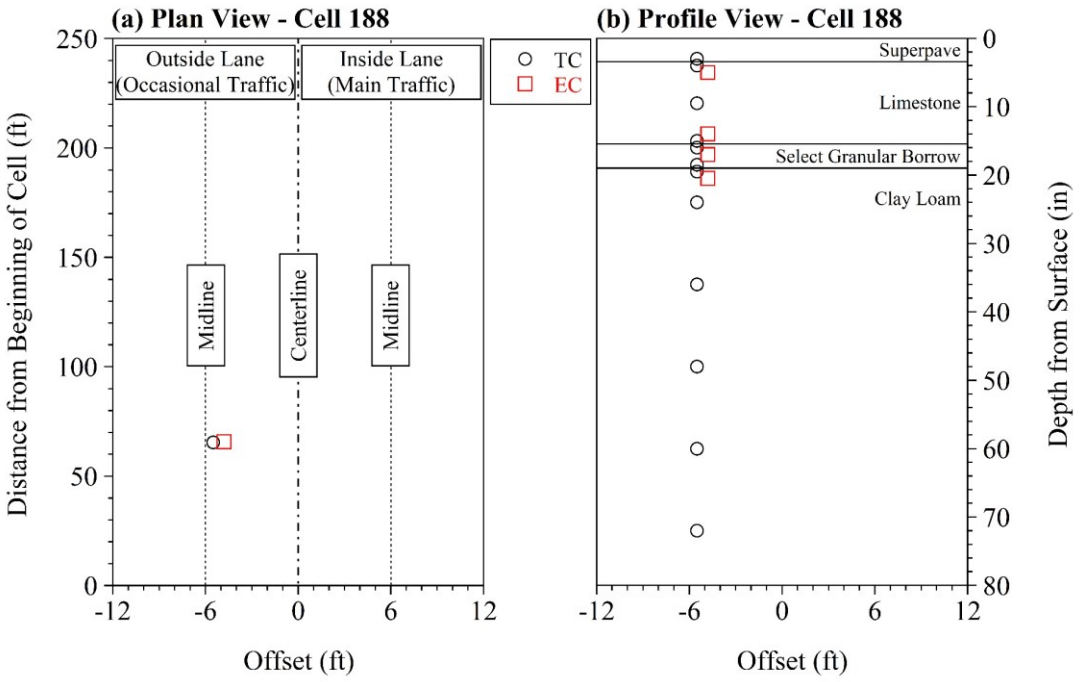

Figure 5.7. (a) Plan and (b) profile view of sensor locations in Cell 188 (12-in Limestone) (TC = thermocouple, EC = moisture probe)

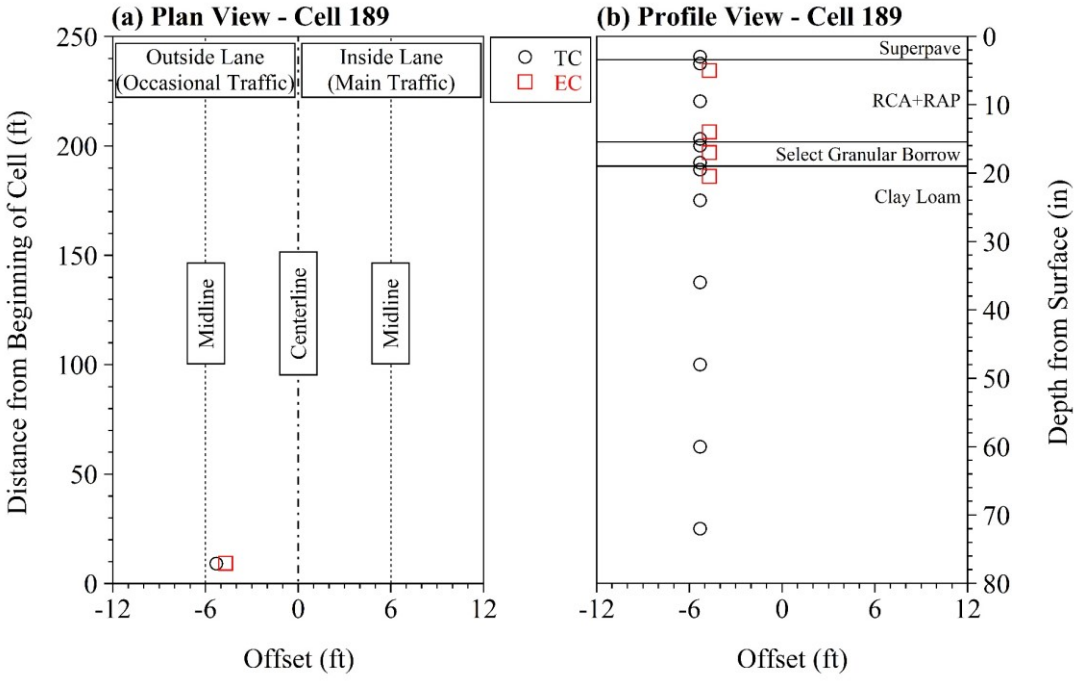

Figure 5.8. (a) Plan and (b) profile view of sensor locations in Cell 189 (12-in RCA+RAP) (TC = thermocouple, EC = moisture probe)

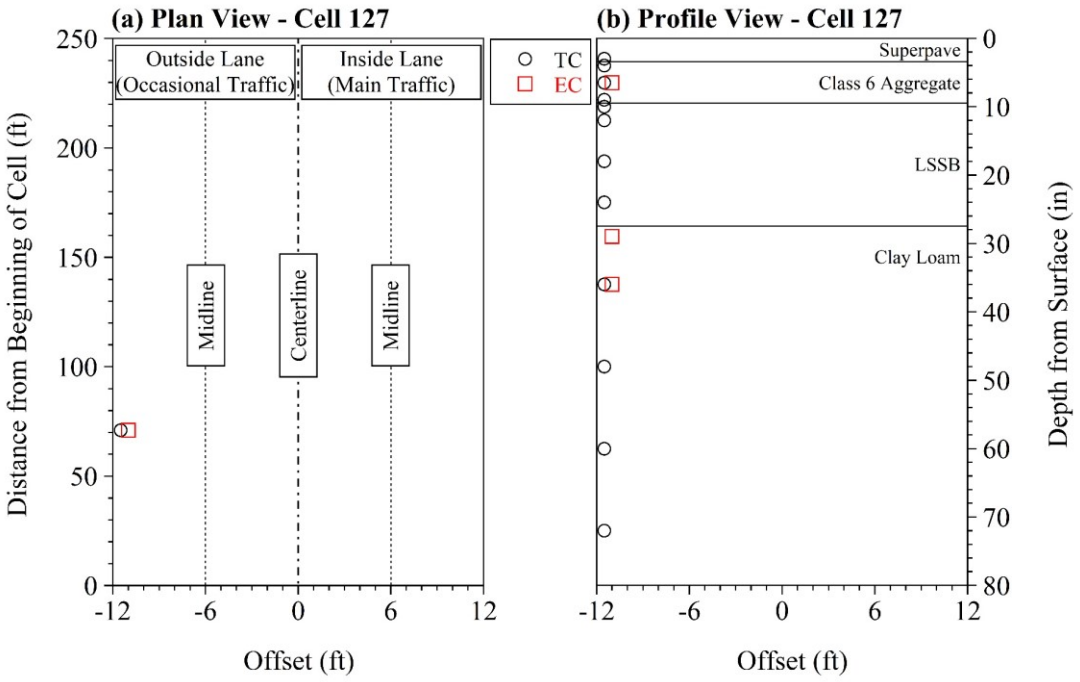

Figure 5.9. (a) Plan and (b) profile view of sensor locations in Cell 127 (18-in LSSB) (TC = thermocouple, EC = moisture probe)

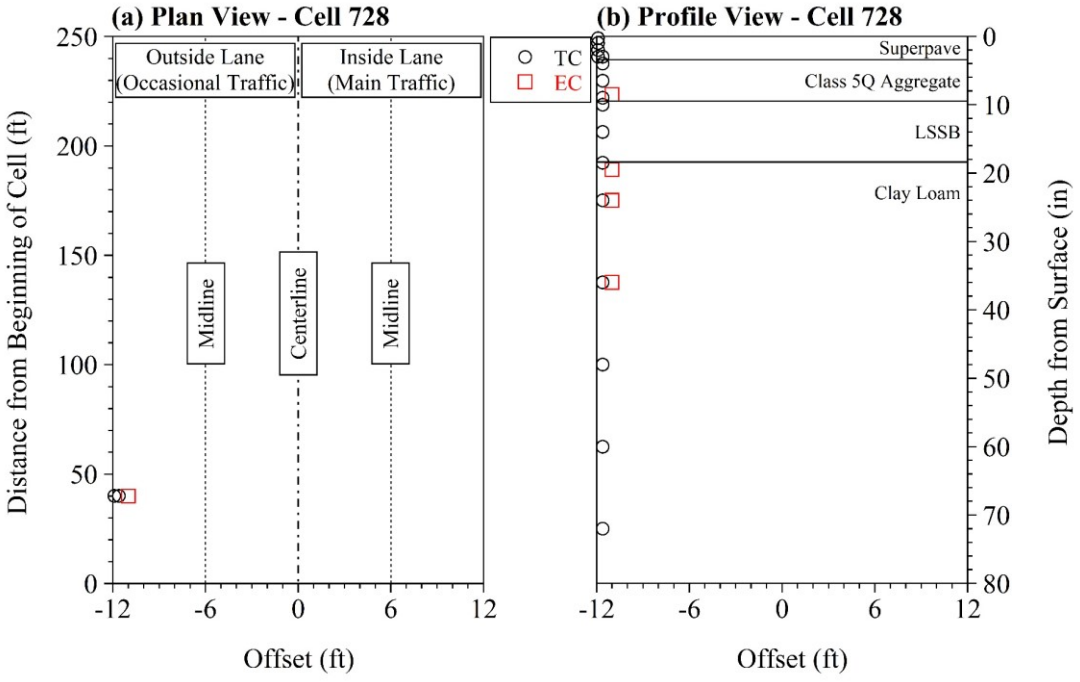

Figure 5.10. (a) Plan and (b) profile view of sensor locations in Cell 728 (9-in LSSB) (TC = thermocouple, EC = moisture probe)

5.2.2 Temperature Profiles of Select Test Cells

In general, the temperature of an asphalt pavement surface is prone to be different from air temperature. The difference is related to the composition, thermal properties, color, and texture of the asphalt material (Guan 2011). Light-colored materials have a higher albedo and can reflect more light than dark-colored materials. On the contrary, dark-colored materials tend to absorb heat and show lower albedo (Sailor 1995; Guan 2011). Since asphalt materials have a dark color (asphalt layer's color may fade depending on the age of the material), they are prone to absorb a high heat load and exhibit higher temperatures than air temperature (Guan 2011). Relatively rougher surfaces have more surface areas than smoother surfaces; therefore, materials having rougher surface properties can absorb more heat (Doulos et al. 2004). Briefly, asphalt surface layers are expected to be warmer than air under daylight. In addition, asphalt surface layers are expected to release the heat slowly over the night, which allows them to be warmer than air during night times (Buyantuyev and Wu 2010).

To compare the differences between air temperature and asphalt temperature at the test cells, the shallowest thermocouple [the one located at 0.3 in (7.6 mm) depth in the asphalt layer in Cell 728 (9-in LSSB)] was selected. As expected, relatively higher temperature values were observed in the asphalt layer compared to air temperature (Figure 5.11).

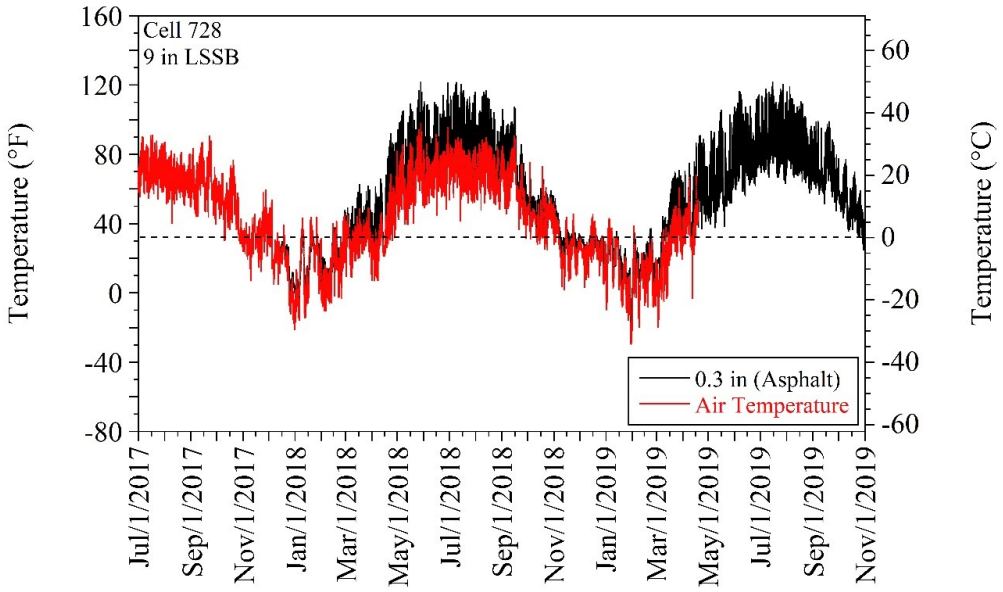

Figure 5.11. Differences between asphalt temperature and air temperature in Cell 728 (9-in LSSB)

In the one-dimensional conduction heat transfer theory, the analytical solution to determine the soil temperature at a specific depth (z) and time (t) is shown in Equation (5.1) (Horton et al. 1983). In the given theory, the amplitude (A) decreases as soil depth increases, and the sinusoidal-like temperature curve shifts to the right as soil depth increases due to the phase constant (C_4) (Figure 5.12) (Hanson et al. 2000). Time is required for heat transfer from higher elevations (closer to the surface) to lower elevations (deeper levels).

$$T(z,t) = \overline{T} + A_0 e^{-z\sqrt{\frac{\omega}{2\alpha}}} \sin\left(\omega t - z\sqrt{\frac{\omega}{2\alpha}} + C_4\right) \quad (5.1)$$

where $\overline{T}$ is the average temperature at the soil surface, A_0 is the amplitude at the soil surface, ω is the radial frequency $\left(\frac{2\pi}{p}\right)$, p is the period, α is the thermal diffusivity, and C_4 is the phase constant.

Temperature readings taken from Cells 185 (12-in Coarse RCA), 186 (12-in Fine RCA), 188 (12-in Limestone), 189 (12-in RCA+RAP), 127 (18-in LSSB), and 728 (9-in LSSB) are provided in Figure 5.13, Figure 5.14, Figure 5.15, Figure 5.16, Figure 5.17, and Figure 5.18, respectively. As the depth increased, the amplitude of the soil temperature curves decreased, and the curves shifted to the right. In addition, the temperature readings exhibited relatively higher fluctuations at the depths closer to the surface. On the other hand, the temperature readings became more stable and showed relatively lower fluctuations with depth over time. Thermocouple readings, taken from the asphalt layer in Cell 728 (9-in LSSB) (at between 0.3-3 in depth), are provided in Appendix P.

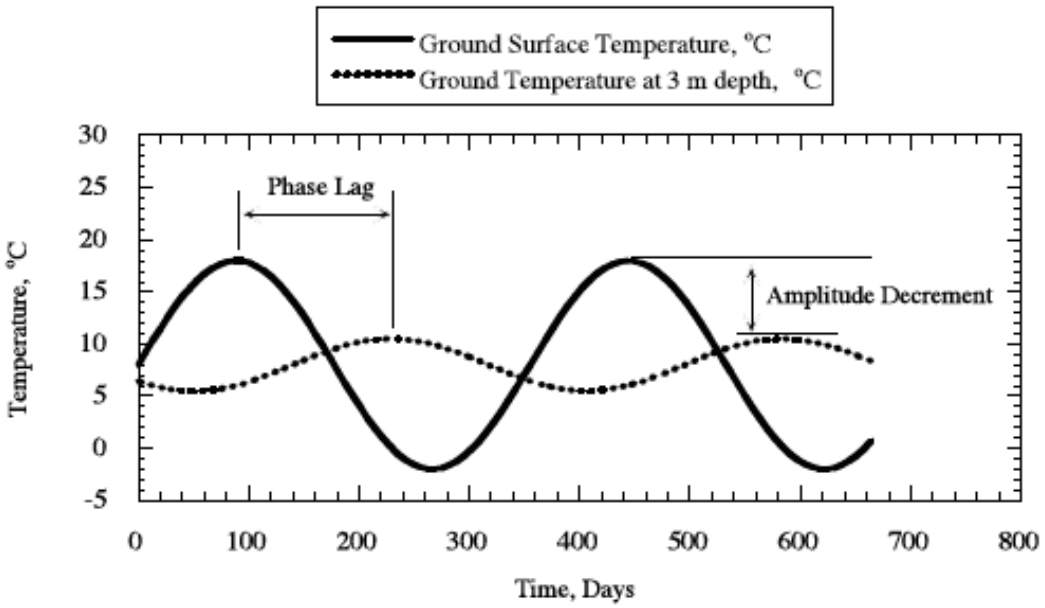

Figure 5.12. Effect of depth on soil temperature curves (Hanson et al. 2000)

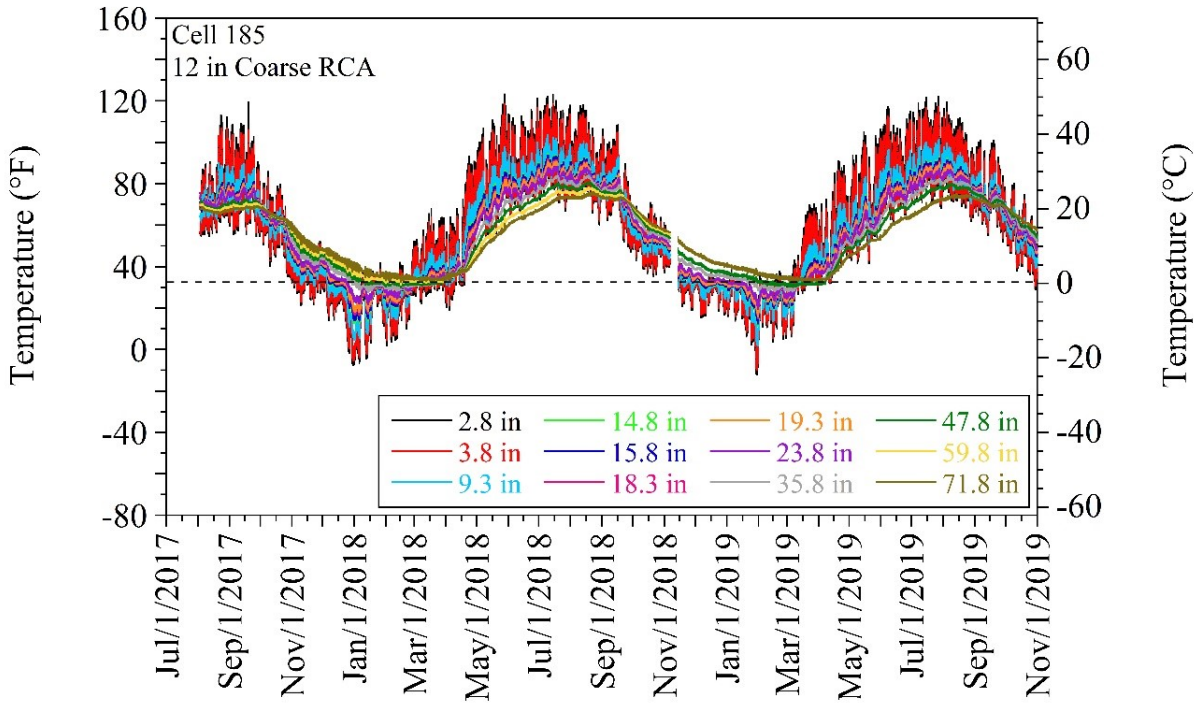

Figure 5.13. Temperature readings taken from Cell 185 (12-in Coarse RCA)

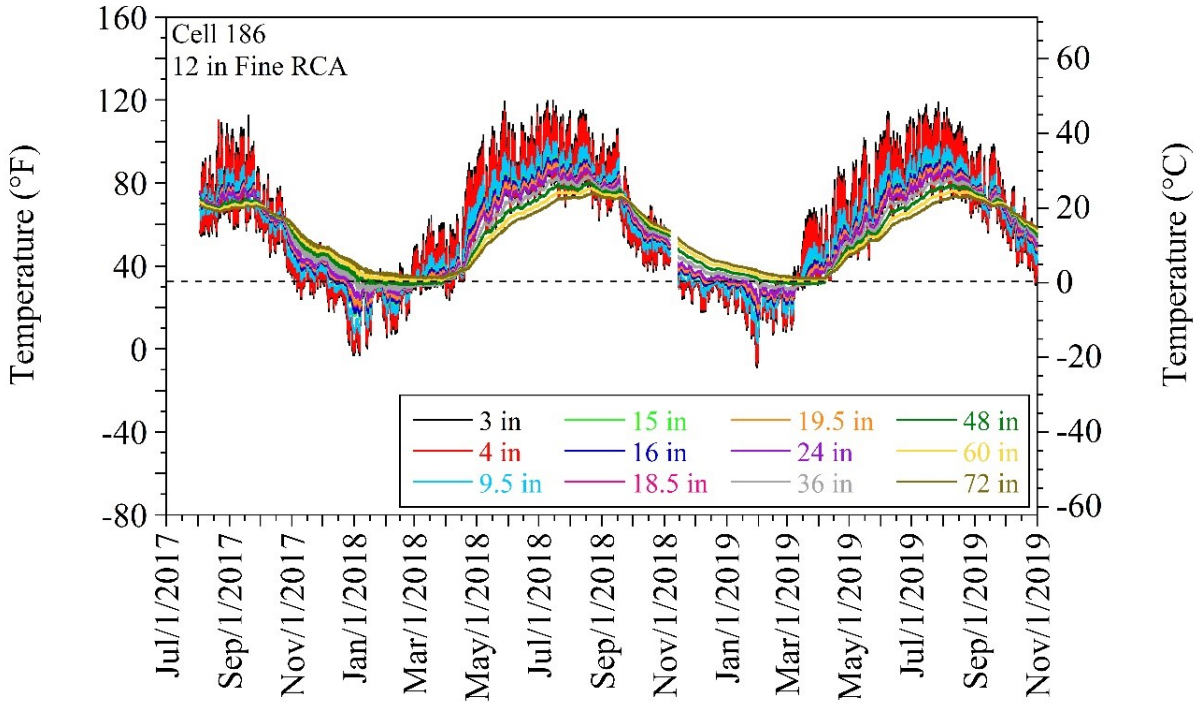

Figure 5.14. Temperature readings taken from Cell 186 (12-in Fine RCA)

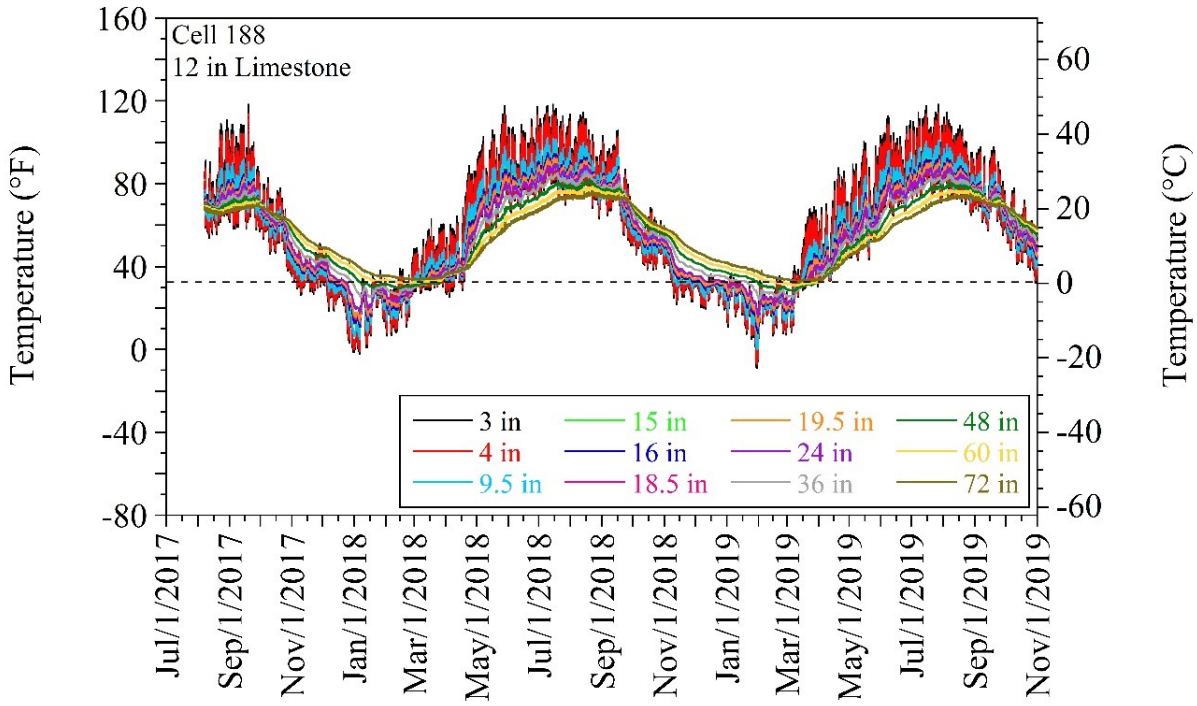

Figure 5.15. Temperature readings taken from Cell 188 (12-in Limestone)

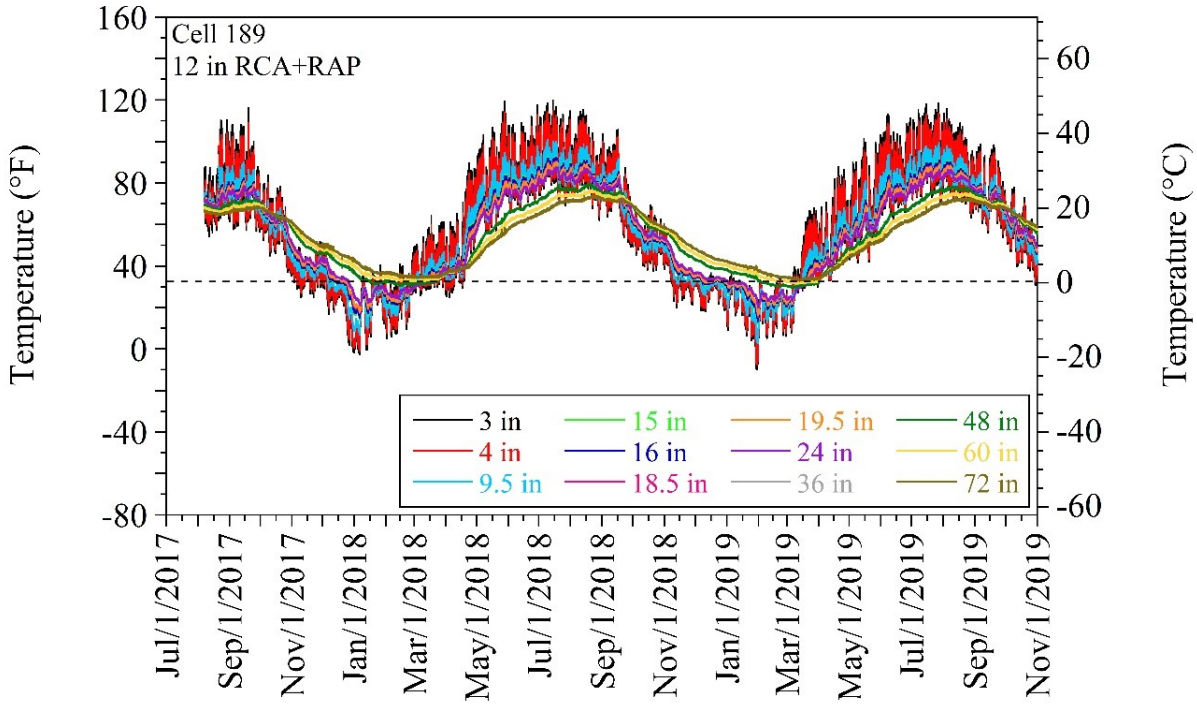

Figure 5.16. Temperature readings taken from Cell 189 (12-in RCA+RAP)

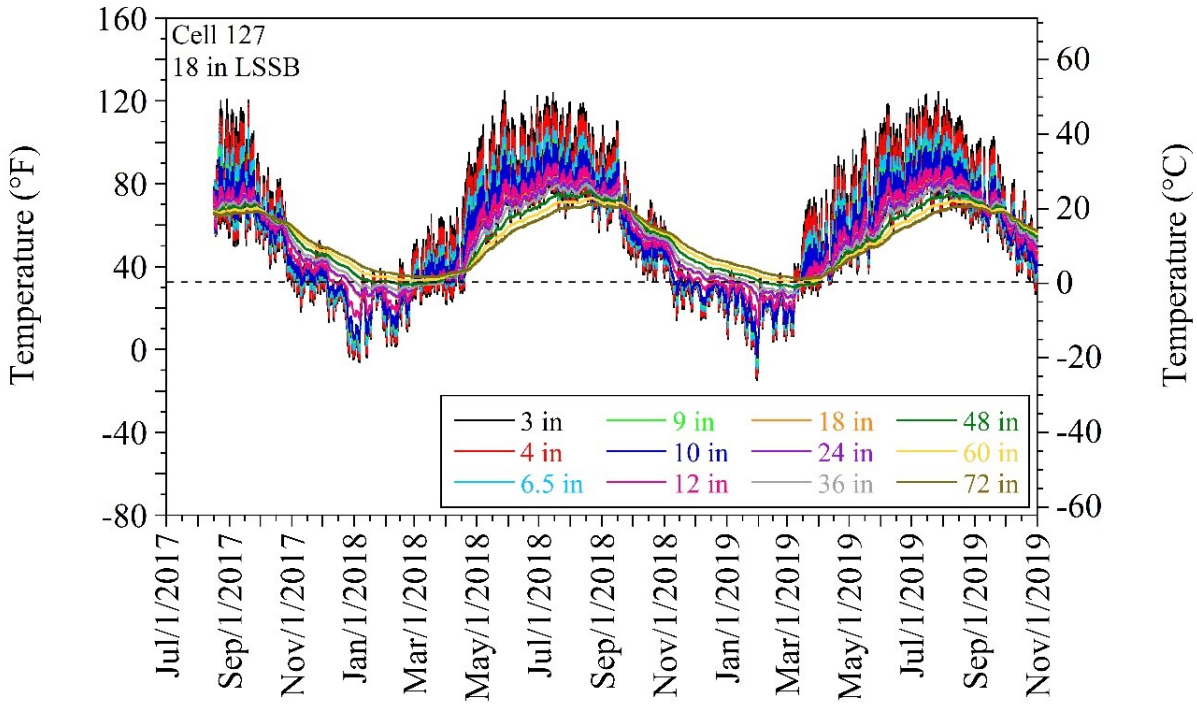

Figure 5.17. Temperature readings taken from Cell 127 (18-in LSSB)

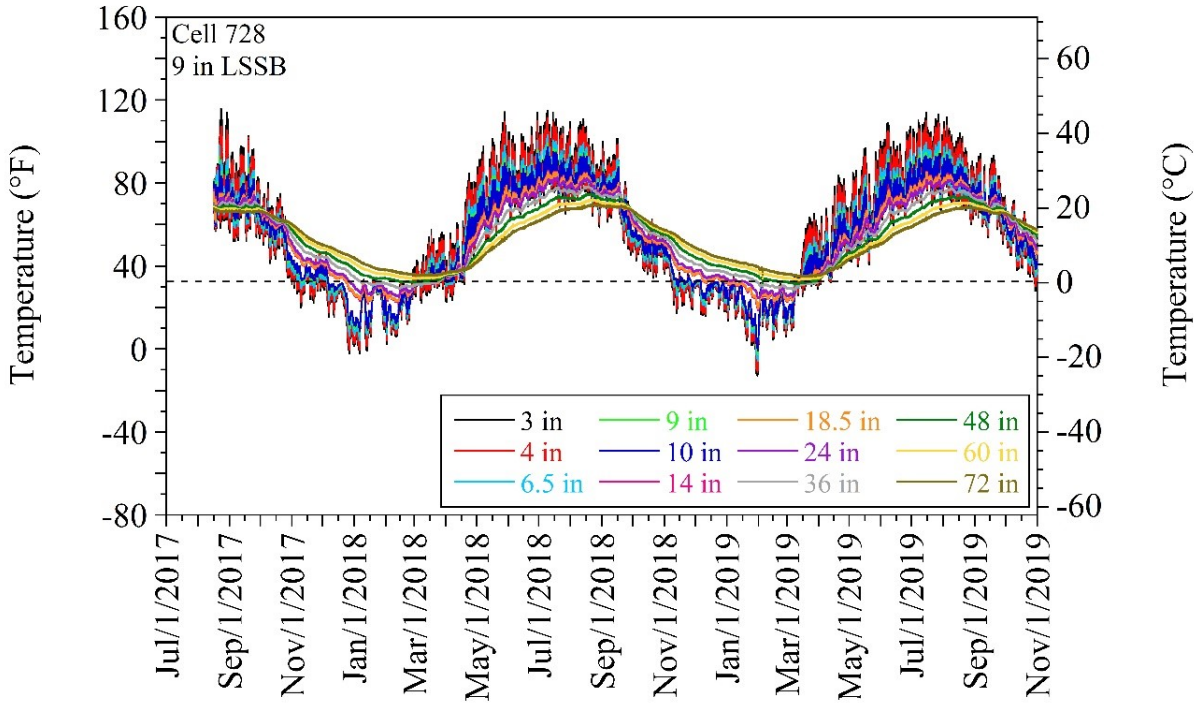

Figure 5.18. Temperature readings taken from Cell 728 (9-in LSSB)

5.2.3 Volumetric Water Content (VWC) Profiles of Select Test Cells

Moisture probes embedded in the test cells used the differences between dielectric constants of different soil phases to estimate VWC in the soil matrix. While air and dry soil have dielectric constants of about 1 and 4-16, respectively, the dielectric constant of liquid water is about 80 (Wraith and Or 1999; Bittelli 2011; Hallikainen et al. 1985). Therefore, soil medium with higher liquid water content has a higher dielectric constant.

When liquid water starts to freeze and transform to ice, its dielectric constant (about 80) begins to reduce, which also reduces the dielectric constant of the soil medium. Therefore, freezing events can be detected by observing sudden reductions in the VWC values over time. When the soil is fully frozen, its dielectric constant is expected to stay constant since there will be no change in the liquid water content under fully frozen conditions. Following the freezing and fully frozen conditions, thawing events can be determined from sudden increases in the VWC values over time. It is expected that the data obtained by the moisture probes to be compatible with the data collected by the thermocouples and demonstrate the freezing and thawing periods properly (Genc 2019).

Decagon's recommended calibration procedure was followed by the MnROAD staff to develop material-specific calibration equations for various aggregate base and subgrade materials to convert the collected raw data into VWC (MnDOT 2013b). The developed calibration equations are provided in Appendix Q.

Two-year VWC values for Cells 185 (12-in Coarse RCA), 186 (12-in Fine RCA), 188 (12-in Limestone), 189 (12-in RCA+RAP), 127 (18-in LSSB), and 728 (9-in LSSB) are provided in Figure 5.19, Figure 5.20, Figure 5.21, Figure 5.22, Figure 5.23, and Figure 5.24, respectively [degree of saturation (DOS) values are provided in Appendix Q]. The VWC values of the materials at the optimum moisture content (OMC) and maximum dry unit weight (MDU) (determined by modified Proctor testing) are summarized in Table 5.3. Nuclear density gauge (NDG) readings, taken from the outside lanes of the test cells during construction (detailed information on NDG is provided in Chapter 3), were converted to the VWC values, and the results are provided as box plots in Figure 5.25 and briefly summarized in Table 5.3. In addition, relative dry unit weight and moisture content values of the aggregate base and subgrade layers in the outside lanes of Cells 185 (12-in Coarse RCA), 186 (12-in Fine RCA), 188 (12-in Limestone), 189 (12-in RCA+RAP), 127 (18-in LSSB), and 728 (9-in LSSB) (calculated based on the NDG measurements and laboratory OMC and MDU of the materials) are summarized in Figure 5.26 and Figure 5.27, respectively. Overall, the results showed that the VWC values calculated from the NDG data collected from the outside lanes during construction were lower than the VWC values of the materials calculated based on laboratory compaction data at OMC and MDU (Table 5.3). In addition, it was observed that the aggregate base layers in the outside lanes of the test cells were compacted at the dry side of OMC (Figure 5.27). Therefore, the relative dry unit weight values of the aggregate base layers were lower than 100% (Figure 5.26).

For Cell 185 (12-in Coarse RCA), continuous readings could not be taken from any of the pavement layers due to the malfunctioning of the moisture probes embedded in the test cell (Figure 5.19). For the 12-in Coarse RCA base layer, the median VWC values recorded by the moisture probes on

August/3/2017 [0.09 and 0.05 for the sensors at 5 and 14 in depths, respectively (Figure 5.19)] were lower than the VWC value of Coarse RCA at OMC and MDU [0.20 (Table 5.3)] and the VWC values observed by NDG during construction on August/1/2017 [between 0.12 and 0.15 (Table 5.3)]. For the Select Granular Borrow subbase layer, the median VWC value recorded by the moisture probe on August/3/2017 [0.06 for the sensor at 17 in depth (Figure 5.19)] was lower than the VWC values of Select Granular Borrow at OMC and MDU [0.12 (Table 5.3)]. For the Sand Subgrade layer, the median VWC value recorded by the moisture probe on August/3/2017 [0.07 for the sensor at 20.5 in depth (Figure 5.19)] was lower than the VWC values of Sand Subgrade at OMC and MDU [0.12 (Table 5.3)] and comparable with the VWC values observed by NDG during construction on July/21/2017 [between 0.07 and 0.13 (Table 5.3)]. The data collected from Cell 185 (12-in Coarse RCA) between August 2017-October 2017 showed that the Coarse RCA base layer (sensors were at 5 and 14 in depths) contained relatively higher VWC than the Select Granular Borrow subbase (sensor was at 17 in depth) and Sand Subgrade layers (sensor was at 20.5 in depth) (Figure 5.19).

For Cell 186 (12-in Fine RCA), no continuous VWC readings were able to be taken from the Select Granular Borrow subbase (sensor was at 17 in depth) and the bottom of the Fine RCA base layer (sensor was at 14 in depth). Also, the sensor embedded at 20.5 in depth (in the Sand Subgrade layer) exhibited highly fluctuated data, which could be the indication of malfunctioning of that sensor. For the 12-in Fine RCA base layer, the median VWC values recorded by the moisture probes on August/3/2017 [0.11 for both of the sensors at 5 and 14 in depths (Figure 5.20)] were lower than the VWC values of Fine RCA at OMC and MDU [0.22 (Table 5.3)] and the VWC values observed by NDG during construction on August/1/2017 [between 0.13 and 0.17 (Table 5.3)]. For the Select Granular Borrow subbase layer, the median VWC value recorded by the moisture probe on August/3/2017 [0.05 for the sensor at 17 in depth (Figure 5.20)] was lower than the VWC value of Select Granular Borrow at OMC and MDU [0.12 (Table 5.3)]. For the Sand Subgrade layer, the median VWC value recorded by the moisture probe on August/3/2017 [0.06 for the sensor at 20.5 in depth (Figure 5.20)] was lower than the VWC value of Sand Subgrade at OMC and MDU [0.12 (Table 5.3)]. For the top of the Fine RCA base layer (sensor was at 5 in depth), the VWC values reacted to freezing (decrease in the values) and thawing (increase in the values) between November 2017-April 2018 and November 2018-April 2019. Other times when no freezing or thawing occurred, the VWC values reacted to precipitation (Figure 5.2). During precipitation (July 2017- November 2017 and May 2018- October 2019) (Figure 5.2), slight increases in the VWC values were observed.

For Cell 188 (12-in Limestone), continuous readings were taken from the pavement sublayers. For the 12-in Limestone base layer, the median VWC values recorded by the moisture probes on August/7/2017 [0.02 and 0.03 for the sensors at 5 and 14 in, respectively (Figure 5.21)] were lower than the VWC value of Limestone at OMC and MDU [0.14 (Table 5.3)] and the VWC values observed by NDG during construction on August/1/2017 [between 0.09 and 0.11 (Table 5.3)]. For the Select Granular Borrow subbase layer, the median VWC value recorded by the moisture probe on August/7/2017 [0.05 for the sensor at 17 in depth (Figure 5.21)] was lower than the VWC value of Select Granular Borrow at OMC and MDU [0.12 (Table 5.3)]. For the Clay Loam subgrade layer, the median VWC value recorded by the moisture probe on August/7/2017 [0.07 for the sensor at 20.5 in depth (Figure 5.21)] was lower than the

VWC value of Clay Loam at OMC and MDU [0.20 (Table 5.3)] and comparable with the VWC values observed by NDG during construction on July/25/2017 [between 0.04 and 0.15 (Table 5.3)]. For the top and bottom of the Limestone base layer (sensors were at 5 and 14 in depths, respectively), similar VWC values were observed, and these values were lower than those observed in the Select Granular Borrow subbase (sensor was at 17 in depth) and Clay Loam subgrade layers (sensor was at 20.5 in depth). The VWC values of the Select Granular Borrow subbase (sensor was at 17 in depth) were slightly lower than those of the Clay Loam subgrade (sensor was at 20.5 in depth) (the difference was more considerable between freezing and thawing events). The sensor data showed that the VWC values reacted to freezing and thawing between November 2017-April 2018 and November 2018-April 2019.

For Cell 189 (12-in RCA+RAP), continuous readings were taken from the pavement sublayers. For the 12-in RCA+RAP base layer, the median VWC values recorded by the moisture probes on August/7/2017 [0.07 and 0.04 for the sensors at 5 and 14 in, respectively (Figure 5.22)] were lower than the VWC value of RCA+RAP at OMC and MDU [0.20 (Table 5.3)] and the VWC values observed by NDG during construction on August/1/2017 [between 0.09 and 0.14 (Table 5.3)]. For the Select Granular Borrow subbase layer, the median VWC value recorded by the moisture probe on August/7/2017 [0.10 for the sensor at 17 in depth (Figure 5.22)] was lower than the VWC value of Select Granular Borrow at OMC and MDU [0.12 (Table 5.3)]. For the Clay Loam subgrade layer, the median VWC value recorded by the moisture probe on August/7/2017 [0.11 for the sensor at 20.5 in depth (Figure 5.22)] was lower than the VWC value of Clay Loam at OMC and MDU [0.20 (Table 5.3)] and comparable with the VWC values observed by NDG during construction on July/25/2017 [between 0.06 and 0.13 (Table 5.3)]. Unlike the trend observed in the Limestone base layer in Cell 188 (12-in Limestone), the bottom of the RCA+RAP base layer (sensor was at 14 in depth) exhibited lower VWC values than the top of the same layer (sensor was at 5 in depth). Overall, the VWC values of the RCA+RAP base layer (sensors were at 5 in and 14 in depths) were lower than those of the Select Granular Borrow subbase (sensor was at 17 in depth) and Clay Loam subgrade layers (sensor was at 20.5 in depth). The Select Granular Borrow subbase layer (sensor was at 17 in depth) exhibited lower VWC values than the Clay Loam subgrade layer (sensor was at 20.5 in depth). The sensor data showed that the VWC values reacted to freezing and thawing between November 2017-April 2018 and November 2018-April 2019. During late spring, summer, and fall seasons (July 2017- November 2017 and May 2018- October 2019), slight increases in the VWC values were observed due to precipitation (Figure 5.2).

For Cell 127 (18-in LSSB), continuous readings were taken from the pavement sublayers. For the 6 in Class 6 Aggregate base layer, the median VWC value recorded by the moisture probe on August/28/2017 [0.08 for the sensor at 6.5 in depth (Figure 5.23)] was lower than the VWC value of Class 6 Aggregate at OMC and MDU [0.17 (Table 5.3)] and the VWC values observed by NDG during construction on August/21/2017 [between 0.10 and 0.11 (Table 5.3)]. For the Clay Loam subgrade layer, the median VWC values recorded by the moisture probes on August/16/2017 [0.29 and 0.27 for the sensors at 29 and 36 in depths, respectively (Figure 5.23)] was higher than the VWC value of Clay Loam at OMC and MDU [0.20 (Table 5.3)]. The middle of the Class 6 Aggregate base layer (sensor was at 6.5 in depth) exhibited considerably lower VWC values than the Clay Loam subgrade layer (sensors were at 29 and 36 in depths). This could indicate that the drainage provided by the 18-in LSSB layer was efficient.

The sensor at a higher elevation (at 29 in depth) in the Clay Loam subgrade layer exhibited slightly higher VWC values than the sensor at a lower elevation (at 36 in depth) in the same layer. All of the sensor readings at this cell reacted to freezing and thawing between November 2017-April 2018 and November 2018-April 2019. In addition, rainy periods (July 2017- November 2017 and May 2018- October 2019) (Figure 5.2) caused slight increases in the VWC values of the Clay Loam subgrade (sensors were at 29 and 36 in depths). On the other hand, the middle of the Class 6 Aggregate base layer (sensor was at 6.5 in depth) did not exhibit such an increase due to precipitation. This could also indicate the presence of an effective drainage system due to the 18-in LSSB layer.

For Cell 728 (9-in LSSB), continuous readings were taken from the pavement sublayers. For the 6 in Class 5Q Aggregate base layer, the median VWC value recorded by the moisture probe on August/21/2017 [0.11 for the sensor at 8.5 in depth (Figure 5.24)] was lower than the VWC value of Class 5Q Aggregate at OMC and MDU [0.20 (Table 5.3)] and the VWC values observed by NDG during construction on August/21/2017 [between 0.15 and 0.16 (Table 5.3)]. For the Clay Loam subgrade layer, the median VWC values recorded by the moisture probes on August/16/2017 [0.20, 0.16, and 0.24 for the sensors at 19.5, 24, and 36 in depths, respectively (Figure 5.24)] were lower than, equal to, or higher than the VWC value of Clay Loam at OMC and MDU [0.20 (Table 5.3)]. The bottom of the Class 5Q Aggregate base layer (sensor was at 8.5 in depth) exhibited considerably lower VWC values than the Clay Loam subgrade layer (sensors were at 19.5, 24, and 36 in depths). Similar to Cell 127 (18-in LSSB), this result could indicate that effective drainage was provided by the 9-in LSSB layer in Cell 728. Different VWC values were observed at different elevations in the Clay Loam subgrade (sensors were at 19.5, 24, and 36 in depths). While the top of the Clay Loam subgrade (sensor was at 19.5 in depth) exhibited lower VWC values than the lower subgrade levels, the VWC values were higher at 24 in depth (from the surface) in the subgrade layer. Similar to the other cells, all of the sensor readings in Cell 728 (9-in LSSB) reacted to freezing and thawing between November 2017-April 2018 and November 2018-April 2019. In addition, precipitation events caused slight increases in the VWC values of the subgrade layer during the rainy periods [July 2017- November 2017 and May 2018- November 2018] (Figure 5.2). No considerable change in the VWC was observed in the bottom of the Class 5Q Aggregate base layer, possibly due to the good drainage properties of the 9-in LSSB layer.

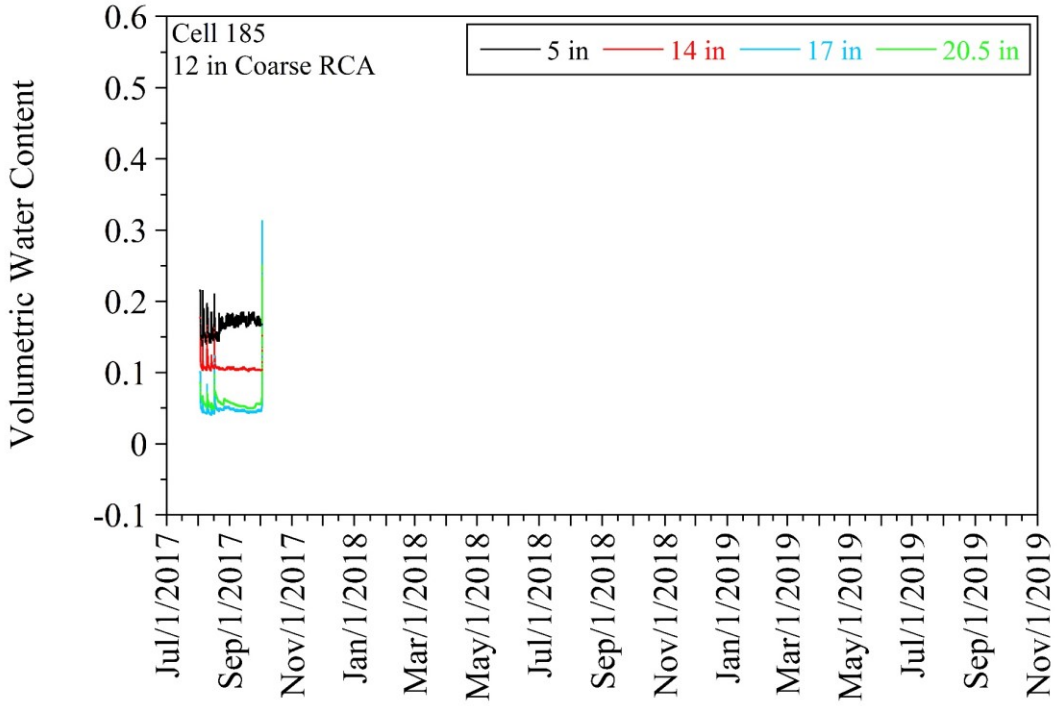

Figure 5.19. Volumetric water content (VWC) data taken from Cell 185 (12-in Coarse RCA)

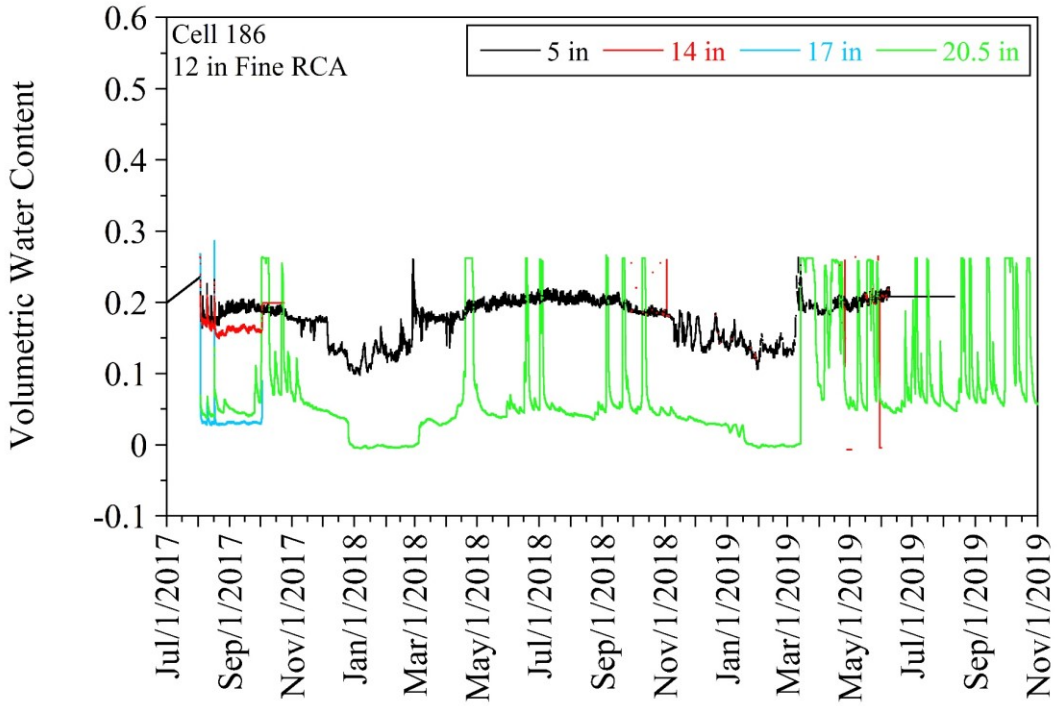

Figure 5.20. Volumetric water content (VWC) data taken from Cell 186 (12-in Fine RCA)

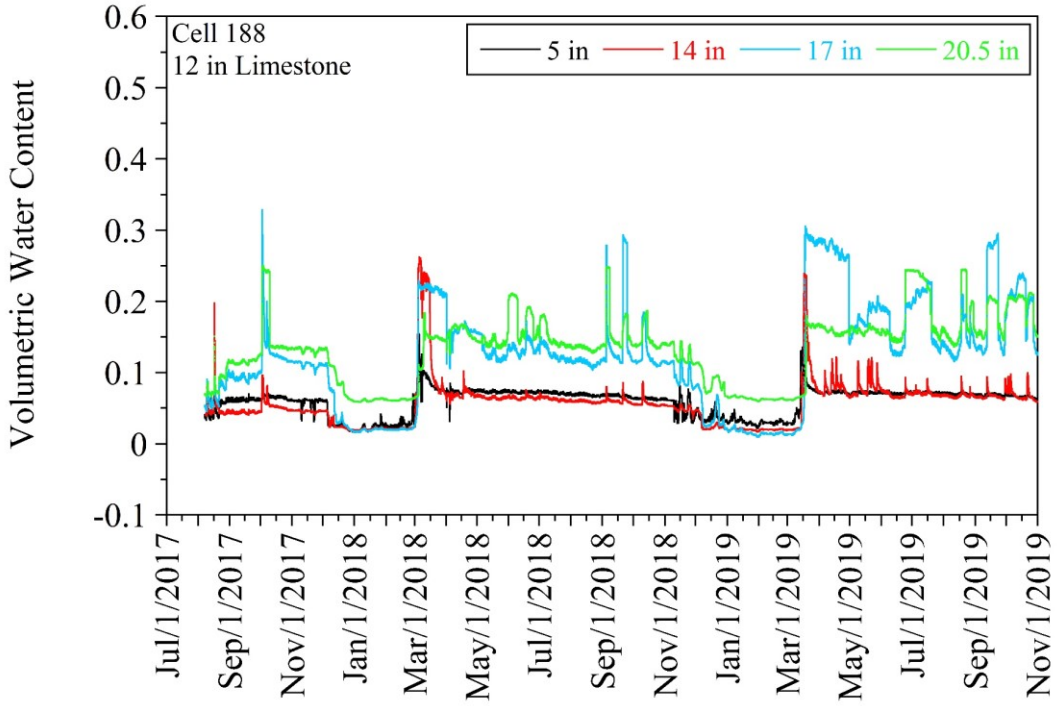

Figure 5.21. Volumetric water content (VWC) data taken from Cell 188 (12-in Limestone)

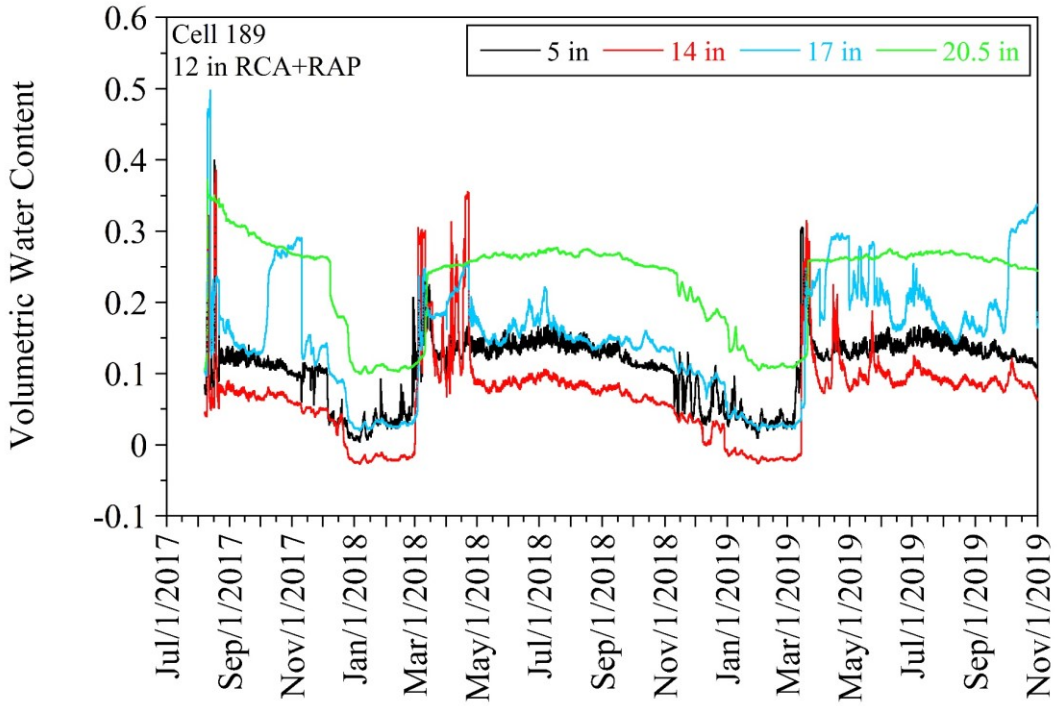

Figure 5.22. Volumetric water content (VWC) data taken from Cell 189 (12-in RCA+RAP)

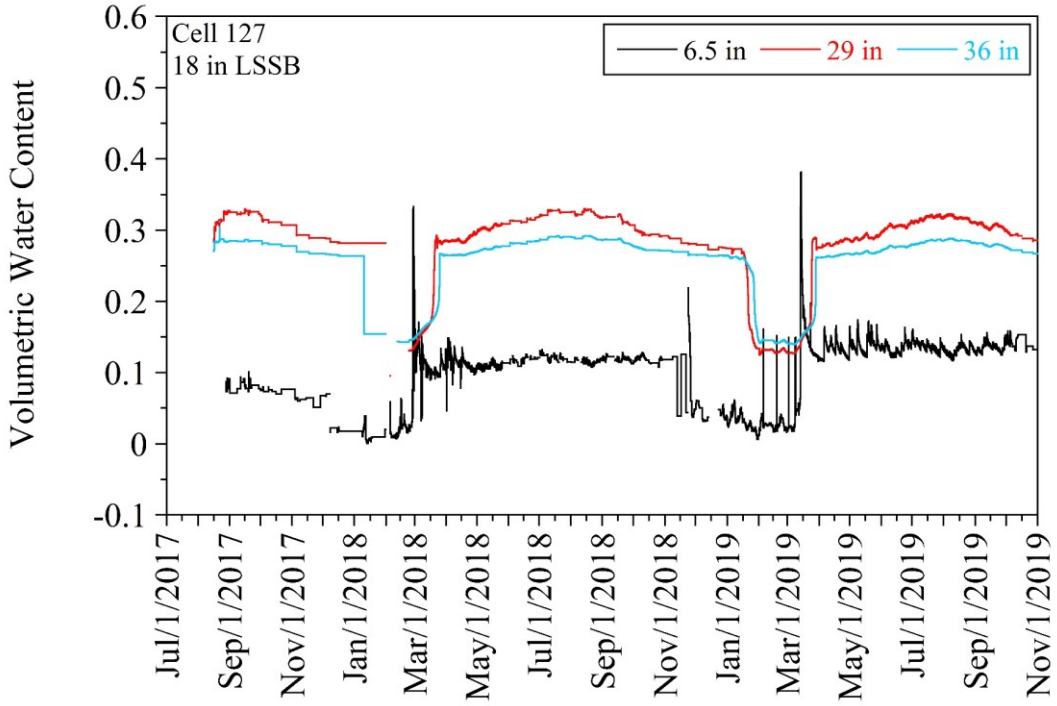

Figure 5.23. Volumetric water content (VWC) data taken from Cell 127 (18-in LSSB)

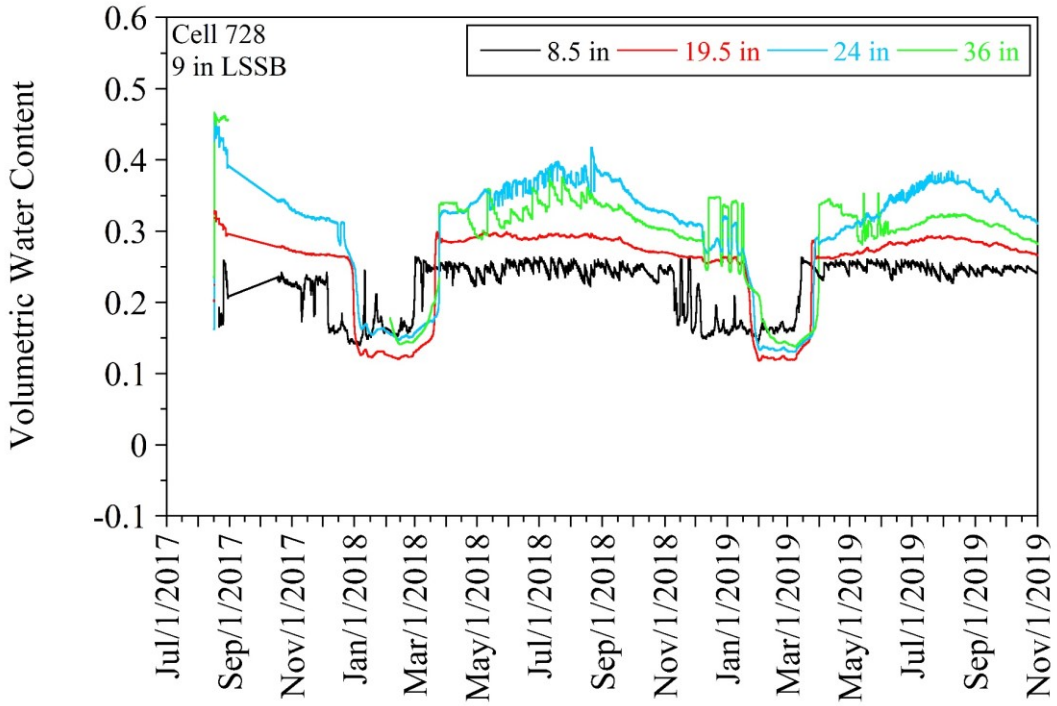

Figure 5.24. Volumetric water content (VWC) data taken from Cell 728 (9-in LSSB)

Table 5.3. Volumetric water content (VWC) values of materials calculated based on laboratory compaction data at optimum moisture content (OMC) and maximum dry unit weight (MDU) and VWC values calculated from nuclear density gauge (NDG) data taken from outside lanes of test cells during construction

Material	VWC at OMC and MDU	VWC Taken by NDG During Construction
Sand Subgrade	0.12	0.07 - 0.13 (Cell 185)
Clay Loam	0.20	0.04 - 0.15 (Cell 188) 0.06 - 0.13 (Cell 189)
Select Granular Borrow	0.12	NA
LSSB	NA	NA
Coarse RCA	0.20	0.12 - 0.15 (Cell 185)
Fine RCA	0.22	0.13 - 0.17 (Cell 186)
Limestone	0.14	0.09 - 0.11 (Cell 188)
RCA+RAP	0.20	0.09 - 0.14 (Cell 189)
Class 6 Aggregate	0.17	0.10 - 0.11 (Cell 127)
Class 5Q Aggregate	0.20	0.15 - 0.16 (Cell 728)

NA = not available.

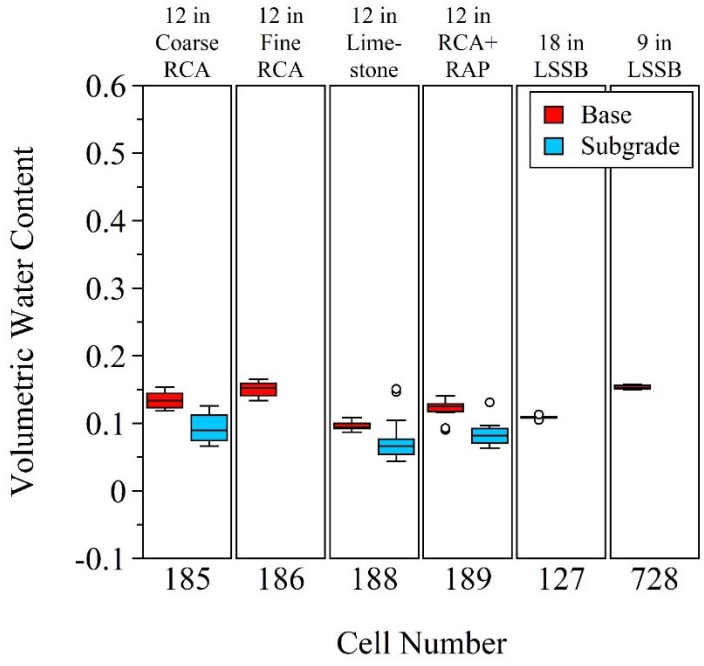

Figure 5.25. Volumetric water content (VWC) data calculated from nuclear density gauge (NDG) data taken from outside lanes of test cells during construction

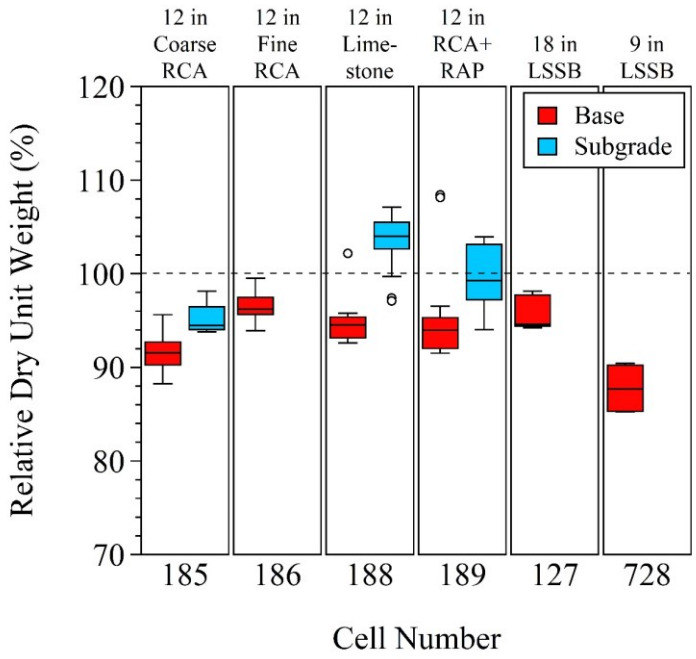

Figure 5.26. Relative dry unit weight of base and subgrade layers in outside lanes of Cells 185 (12-in Coarse RCA), 186 (12-in Fine RCA), 188 (12-in Limestone), 189 (12-in RCA+RAP), 127 (18-in LSSB), and 728 (9-in LSSB)

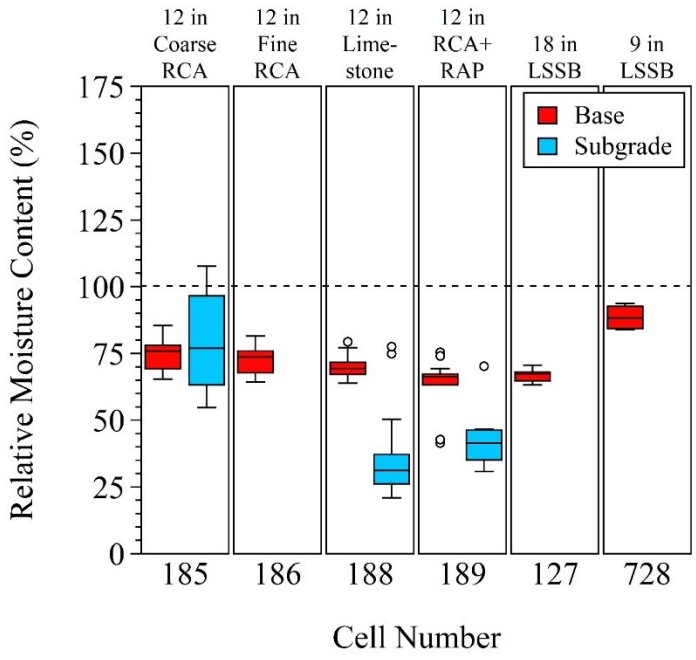

Figure 5.27. Relative moisture content of base and subgrade layers in outside lanes of Cells 185 (12-in Coarse RCA), 186 (12-in Fine RCA), 188 (12-in Limestone), 189 (12-in RCA+RAP), 127 (18-in LSSB), and 728 (9-in LSSB)

5.2.4 Annual Frost Penetration Depths

Water in soil/aggregate voids is expected to exhibit a freezing point that is lower than 32°F (0°C) (freezing-point depression) due to the presence of solutes (minerals, other chemicals, etc.). Rosa et al. (2016) and Edil et al. (2017) reported different freezing point temperatures for different soils and aggregates. According to Edil et al. (2017), while the freezing point of water in natural aggregate [Class 5 (MnDOT 2018)] was -5.2°C (22.6°F), it was -10°C (14°F) for RAP materials. However, many studies considered the freezing point of soil/aggregate water to be 0°C (Genc 2019). Since there was no sensor installed in the test cells that could determine the impurity of the soil/aggregate water, 0°C was selected to be the freezing point of water in this research.

0°C isotherm points were selected from the temperature profiles [Figure 5.13, Figure 5.14, Figure 5.15, Figure 5.16, Figure 5.17, and Figure 5.18 for Cells 185 (12-in Coarse RCA), 186 (12-in Fine RCA), 188 (12-in Limestone), 189 (12-in RCA+RAP), 127 (18-in LSSB), and 728 (9-in LSSB), respectively] (Andersland and Ladanyi 2004; Zhang 2016; Li 2017) to determine the frost penetration depth of each test cell over time. A group of 0°C isotherm points generated a 0°C isotherm region, and the inner area of such a region represented the frozen zones (Zhang 2016). The deepest 0°C isotherm points were used to determine the maximum frost penetration depth. An example of the determination of the maximum frost penetration depth and freezing and thawing periods is provided in Figure 5.28.

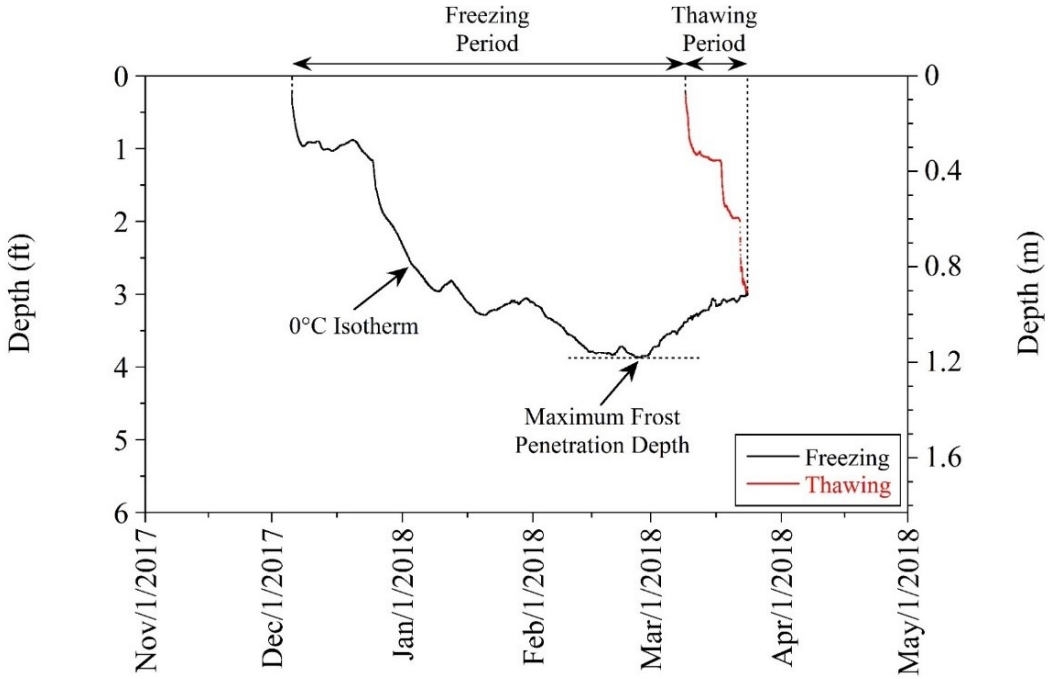

Figure 5.28. Maximum frost penetration depth and freezing and thawing periods

Two-year frost penetration depths determined for Cells 185 (12-in Coarse RCA), 186 (12-in Fine RCA), 188 (12-in Limestone), 189 (12-in RCA+RAP), 127 (18-in LSSB), and 728 (9-in LSSB) are provided in Figure 5.29, Figure 5.30, Figure 5.31, Figure 5.32, Figure 5.33, and Figure 5.34, respectively. Summaries of the maximum frost penetration depths and the freezing and thawing periods for the monitored test cells

[Cells 185 (12-in Coarse RCA), 186 (12-in Fine RCA), 188 (12-in Limestone), 189 (12-in RCA+RAP), 127 (18-in LSSB), and 728 (9-in LSSB)] are provided in Table 5.4 and Table 5.5, respectively.

In the 2017-2018 winter, the shallowest maximum frost penetration depth was 3.87 ft (1.18 m), and it was observed in Cell 728 (9-in LSSB). In the same winter, the deepest maximum penetration depth was 4.9 ft (1.49 m), and it was observed in Cell 188 (12-in Limestone). For Cells 185 (12-in Coarse RCA), 186 (12-in Fine RCA), 189 (12-in RCA+RAP), and 127 (18-in LSSB), the maximum frost penetration depths were 4.44 ft (1.35 m), 4.24 ft (1.29 m), 4.47 ft (1.36 m), and 4.29 ft (1.31 m), respectively, in the 2017-2018 winter. In the 2018-2019 winter, all of the observed frost penetration depths were deeper than those observed in the 2017-2018 winter [the difference between the maximum frost penetration depths in these winters were between 0.15-0.62 ft (0.05-0.19 m)]. In the 2018-2019 winter, the shallowest maximum frost penetration depth was 4.17 ft (1.27 m), and it was observed in Cell 728 (9-in LSSB). In the same winter, the deepest maximum frost penetration depth was 5.52 ft (1.68 m), and it was observed in Cell 188 (12-in Limestone). The maximum frost penetration depths of Cells 185 (12-in Coarse RCA), 186 (12-in Fine RCA), 189 (12-in RCA+RAP), and 127 (18-in LSSB) in the 2018-2019 winter were 4.75 ft (1.45m), 4.39 ft (1.34 m), 5.09 ft (1.55 m), and 4.81 ft (1.47 m), respectively.

In 2017-2018, the freezing periods were between 83 and 94 days. For Cells 185 (12-in Coarse RCA), 186 (12-in Fine RCA), 188 (12-in Limestone), 189 (12-in RCA+RAP), 127 (18-in LSSB), and 728 (9-in LSSB), the freezing periods were 83, 84, 84, 84, 84, and 94 days, respectively. In the same year, the thawing periods were much shorter than the freezing periods, and they were between 15 and 28 days. For Cells 185 (12-in Coarse RCA), 186 (12-in Fine RCA), 188 (12-in Limestone), 189 (12-in RCA+RAP), 127 (18-in LSSB), and 728 (9-in LSSB), the thawing periods were 25, 28, 18, 16, 28, and 15 days, respectively. In 2018-2019, the freezing period was determined to be 108 days for each cell, and the effect of the 2018-2019 winter was expected to be higher than the 2017-2018 winter. Similar to 2017-2018, the thawing periods (between 17 and 25 days) in 2018-2019 were much shorter than the freezing periods (108 days). While it was determined that the 2018-2019 winter was much longer than the 2017-2018 winter, no significant differences were observed between the two years in terms of the thawing periods. This indicates that the thawing periods of the aggregate base and subbase layers do not change significantly with a difference within different seasonal changes in the weather.

It was speculated that the difference in the maximum frost penetration depths and the freezing and thawing periods for different test cells can be related to the thermal properties (thermal conductivity, heat capacity, and thermal diffusivity) of each material used in the test cells. It is recommended as a future study to prove this theory. The thermal diffusivity of each material was calculated from the field observations [Figure 5.13, Figure 5.14, Figure 5.15, Figure 5.16, Figure 5.17, and Figure 5.18 for Cells 185 (12-in Coarse RCA), 186 (12-in Fine RCA), 188 (12-in Limestone), 189 (12-in RCA+RAP), 127 (18-in LSSB), and 728 (9-in LSSB), respectively].

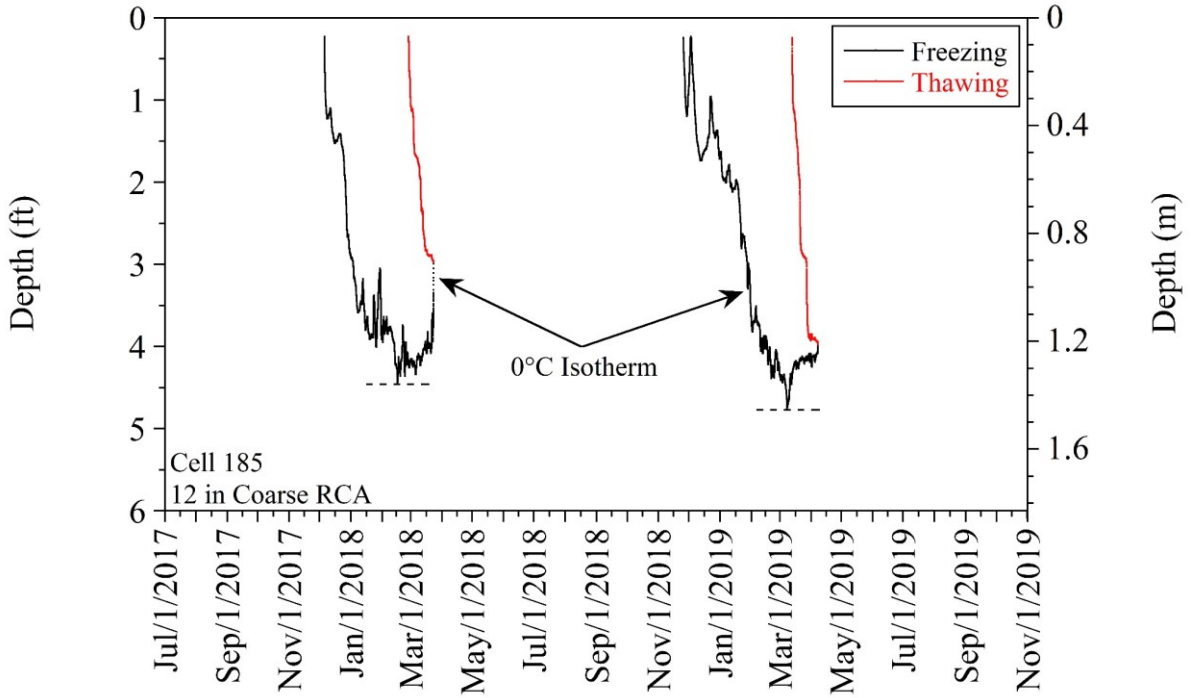

Figure 5.29. Two-year frost penetration depths in Cell 185 (12-in Coarse RCA)

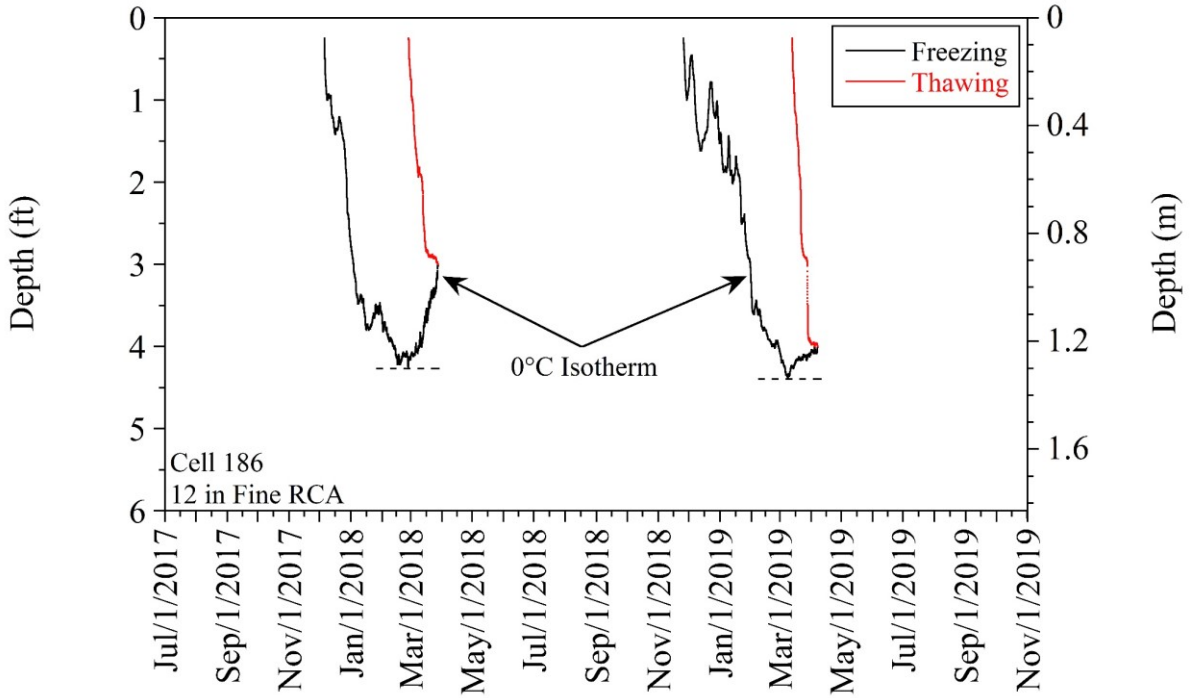

Figure 5.30. Two-year frost penetration depths in Cell 186 (12-in Fine RCA)

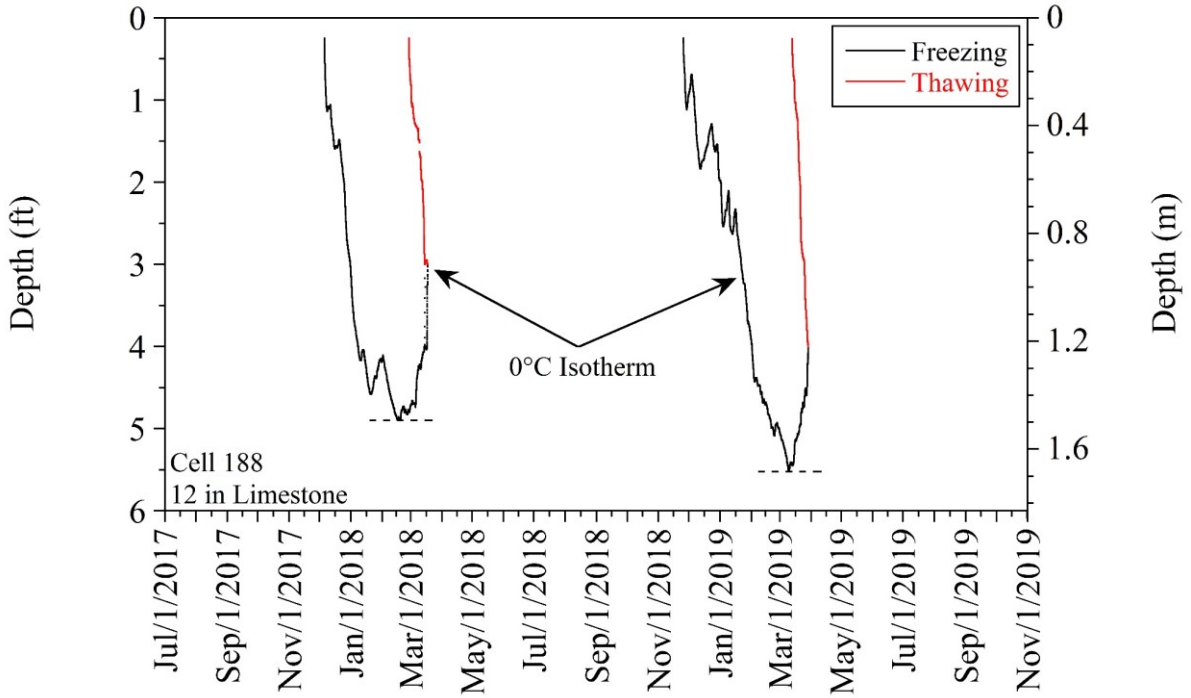

Figure 5.31. Two-year frost penetration depths in Cell 188 (12-in Limestone)

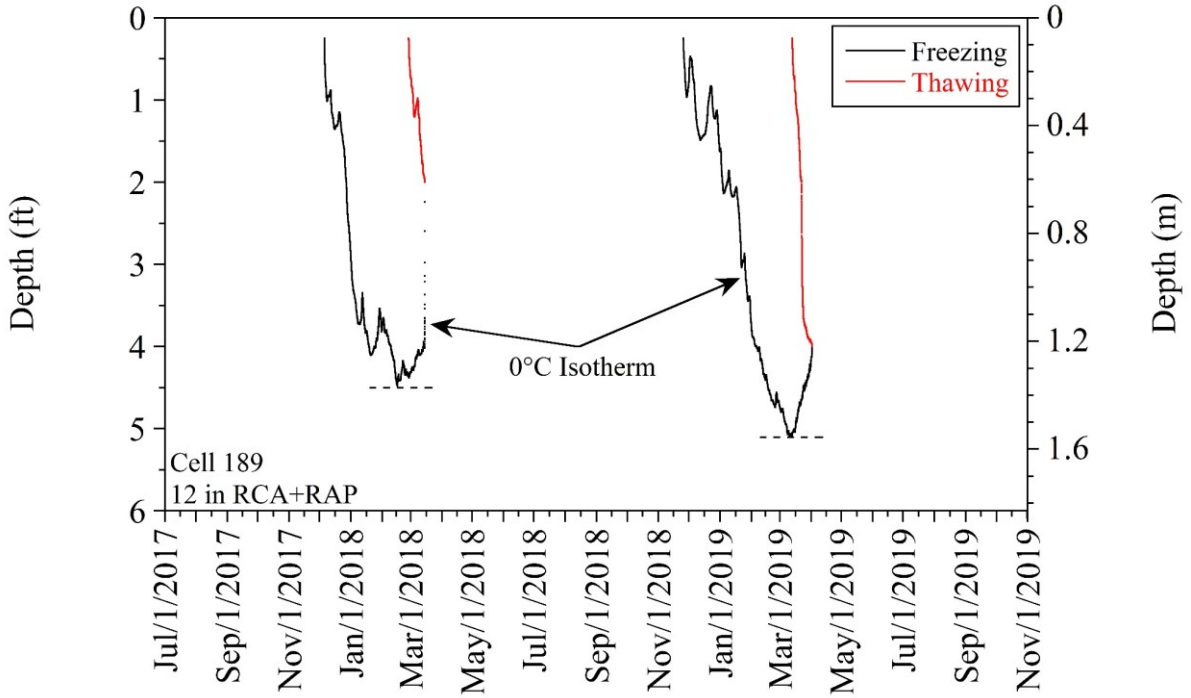

Figure 5.32. Two-year frost penetration depths in Cell 189 (12-in RCA+RAP)

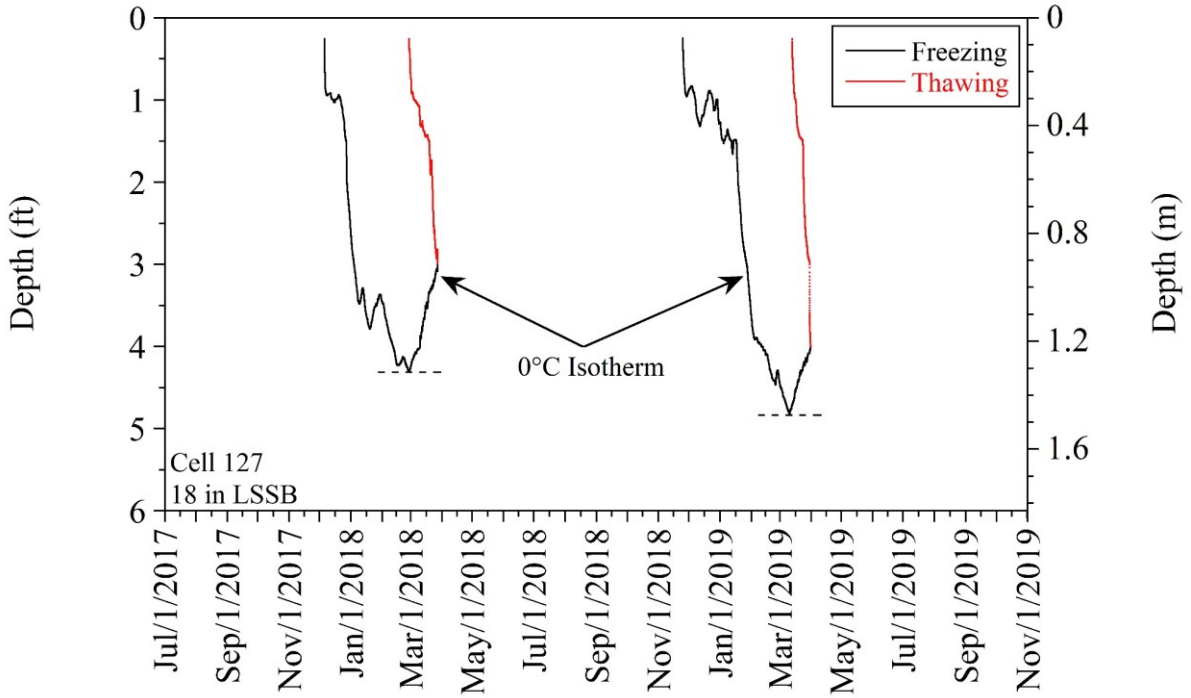

Figure 5.33. Two-year frost penetration depths in Cell 127 (18-in LSSB)

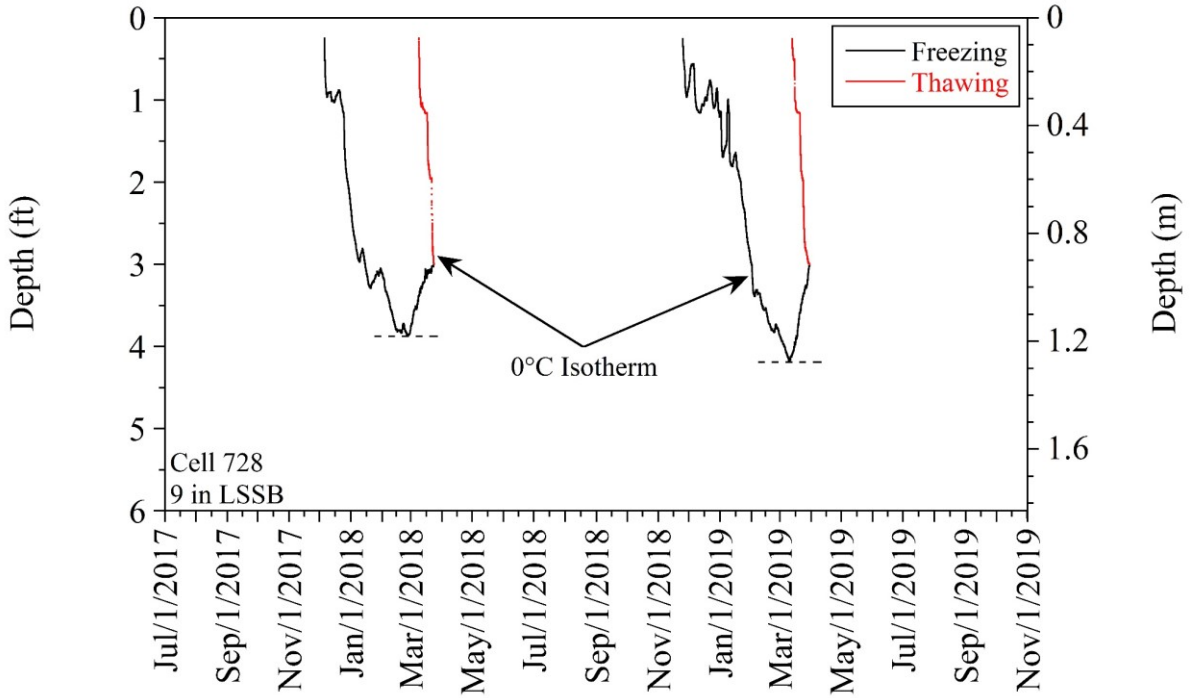

Figure 5.34. Two-year frost penetration depths in Cell 728 (9-in LSSB)

Table 5.4. Two-year maximum frost penetration depths

Cell Number	Cell Description	2017-2018 Maximum Frost Penetration Depth		2018-2019 Maximum Frost Penetration Depth	
		(ft)	(m)	(ft)	(m)
185	12-in Coarse RCA	4.44	1.35	4.75	1.45
186	12-in Fine RCA	4.24	1.29	4.39	1.34
188	12-in Limestone	4.9	1.49	5.52	1.68
189	12-in RCA+RAP	4.47	1.36	5.09	1.55
127	18-in LSSB	4.29	1.31	4.81	1.47
728	9-in LSSB	3.87	1.18	4.17	1.27

Table 5.5. Two-year freezing and thawing periods

Cell Number	Cell Description	2017-2018		2018-2019	
		Freezing Duration (days)	Thawing Duration (days)	Freezing Duration (days)	Thawing Duration (days)
185	12-in Coarse RCA	83	25	108	25
186	12-in Fine RCA	84	28	108	25
188	12-in Limestone	84	18	108	16
189	12-in RCA+RAP	84	16	108	19
127	18-in LSSB	84	28	108	18
728	9-in LSSB	94	15	108	17

5.2.5 Determination of Thermal Diffusivities

The theory described by Equation (5.1) has several assumptions that may affect the accuracy of the estimations made from field temperature profiles, including the following:

- Heat flow by conduction only,
- One-dimensional heat flow,
- The soil is homogeneous,
- The soil is semi-infinite in space,
- The soil surface temperature is a sinusoidal function of time (Figure 5.12 and Figure 5.35), and
- The sine wave is assumed to be repeating (Figure 5.12).

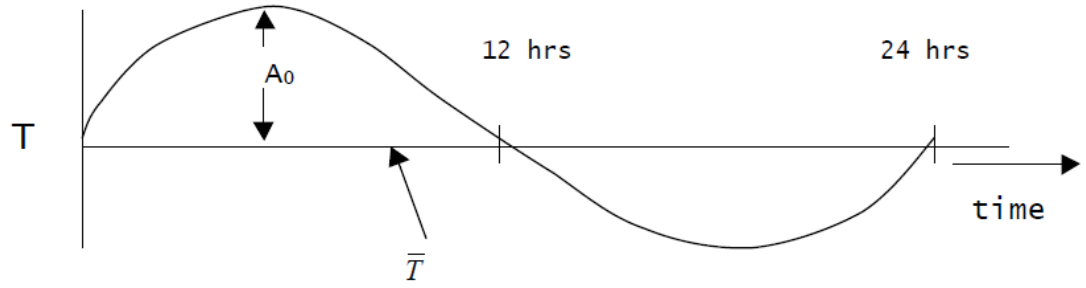

Figure 5.35. Daily soil surface temperature as sinusoidal function of time (T = temperature, A_0 = amplitude at soil surface, $\overline{T}$ = average temperature at soil surface)

Thermal conductivity (λ), volumetric heat capacity (C), and thermal diffusivity (α) are the three thermal properties of soils. λ is defined as a soils' ability to conduct heat, and C is defined as the amount of heat required to increase the temperature of a mass of soil by 1°C. α is defined as the ratio between λ and C, as shown in Equation (5.2). VWC of a soil affects its λ and C properties, as shown in Figure 5.36. Since both λ and C are affected by soil VWC, α is also affected by soil VWC (Figure 5.36). λ, C, and α of soils can be measured through laboratory testing by using a thermal properties analyzer such as a Decagon KD2 Pro. In addition to laboratory testing, α can also be determined from soil temperature profiles recorded in the field by temperature sensors (e.g., thermocouples used in this project). Amplitude and phase equations derived from Equation (5.1) and provided in Equations (5.3) and (5.4), respectively, can be used to determine soil α in the field.

$$\alpha = \frac{\lambda}{C} \tag{5.2}$$

where α is the thermal diffusivity, λ is the thermal conductivity, and C is the volumetric heat capacity.

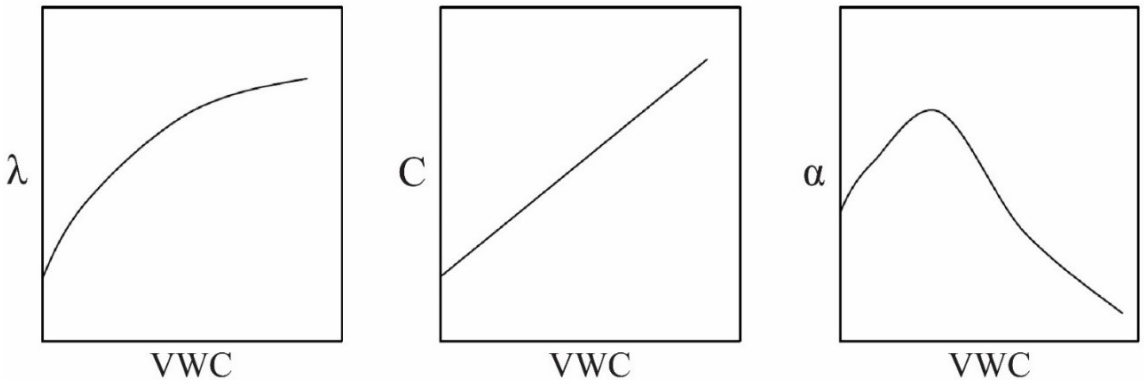

Figure 5.36. Thermal properties of soils (λ = thermal conductivity, C = heat capacity, and α = thermal diffusivity, VWC = volumetric water content) (Jury and Horton 2004)

$$\alpha = \left(\frac{\omega}{2}\right)\left[\frac{z_2 - z_1}{\ln\left(\frac{A_1}{A_2}\right)}\right]^2 \quad (5.3)$$

$$\alpha = \left(\frac{1}{2\omega}\right)\left[\frac{z_2 - z_1}{\Delta t_{max}}\right]^2 \quad (5.4)$$

where ω is the radial frequency $\left(\frac{2\pi}{p}\right)$, p is the period, z_1 and z_2 are the two elevations where the measurements are taken, A_1 and A_2 are the amplitudes measured at z_1 and z_2, and Δt_{max} is the time difference between maximum temperatures at z_1 and z_2.

Amplitude and phase equations, provided in Equations (5.3) and (5.4), respectively, were used to determine α values based on field temperature profiles throughout Coarse RCA base (Cell 185), Fine RCA base (Cell 186), Limestone base (Cell 188), RCA+RAP base (Cell 189), and LSSB layers (Cells 127 and 728). As shown in Figure 5.35, there should be 12 hours of daytime and 12 hours of nighttime to obtain more reliable results by using the one-dimensional conduction heat transfer theory. Since equinoxes, dates when day and night are of equal length (12 hours/each), occur in March (around March 21) and September (around September 23), α values of the selected pavement sublayers were determined only near those dates.

In 12-in Coarse RCA (Cell 185), Fine RCA (Cell 186), Limestone (Cell 188), and RCA+RAP (Cell 189) base layers, there were three thermocouples (TCs): (1) top TC, (2) middle TC, and (3) bottom TC. Figure 5.37 is an example that shows the locations of the TC sensors in 12-in Coarse RCA (Cell 185). Since the α values of soil are affected by the VWC of soils, evaluating the moisture probe readings, if taken close to the TC sensors, could also be beneficial in understanding the α values calculated by the amplitude equation [Equation (5.3)] and phase equation [Equation (5.4)]. In the same aggregate base layers, there were two moisture probes (ECs): (1) top EC and (2) bottom EC. Figure 5.37 is also an example that shows the locations of the EC sensors in 12-in Coarse RCA (Cell 185). The EC sensors were at the same locations in 12-in Fine RCA (Cell 186), Limestone (Cell 188), and RCA+RAP (Cell 189) base layers; therefore, their locations are not shown separately. The top EC and bottom EC sensors were close to the top TC and bottom TC sensors, respectively. In 18-in LSSB layer (Cell 127), there were four TC sensors: (1) top TC, (2) middle 1 TC, (3) middle 2 TC, and (4) bottom TC (Figure 5.38). In 9-in LSSB layer (Cell 728), there were three TC sensors: (1) top TC, (2) middle TC, and (3) bottom TC (Figure 5.39). There were no EC sensors in any of the LSSB layers [Figure 5.38 for 18-in LSSB layer (Cell 127) and Figure 5.39 for 9-in LSSB layer (Cell 728)].

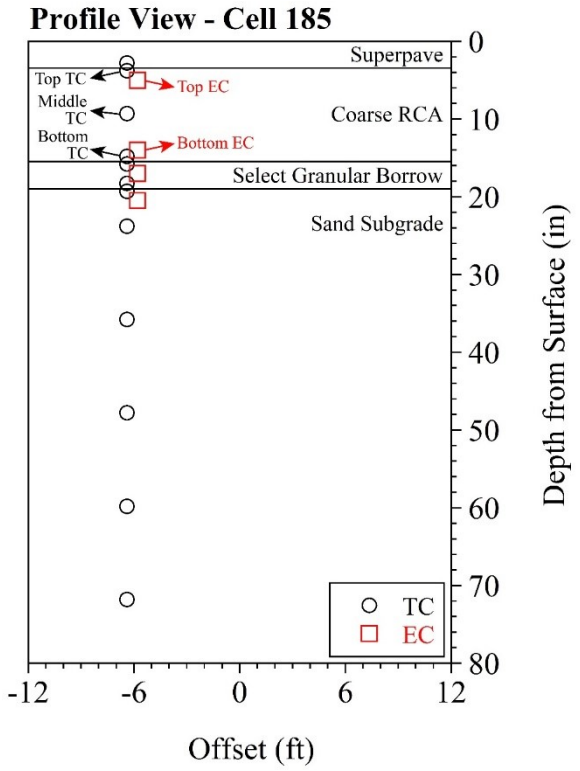

Figure 5.37. Locations of thermocouples (TC) and moisture probes (EC) in 12-in Coarse RCA (Cell 185)

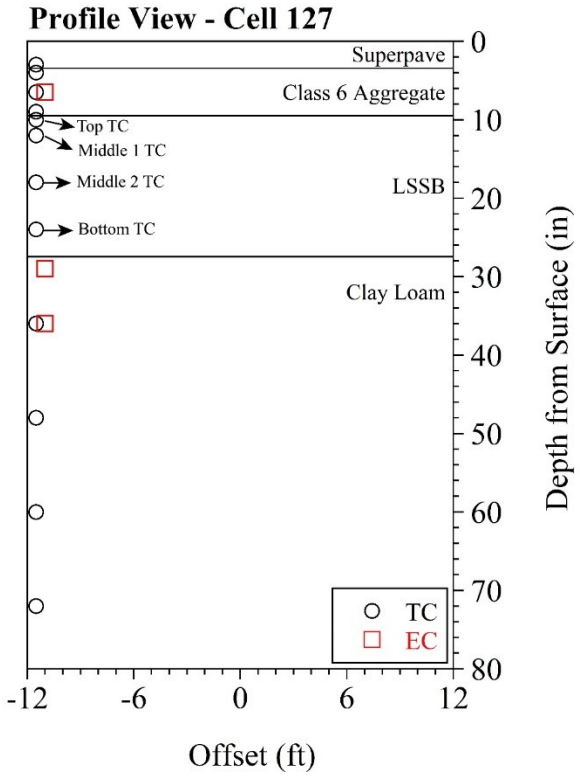

Figure 5.38. Locations of thermocouples (TC) and moisture probes (EC) in 18-in LSSB (Cell 127)

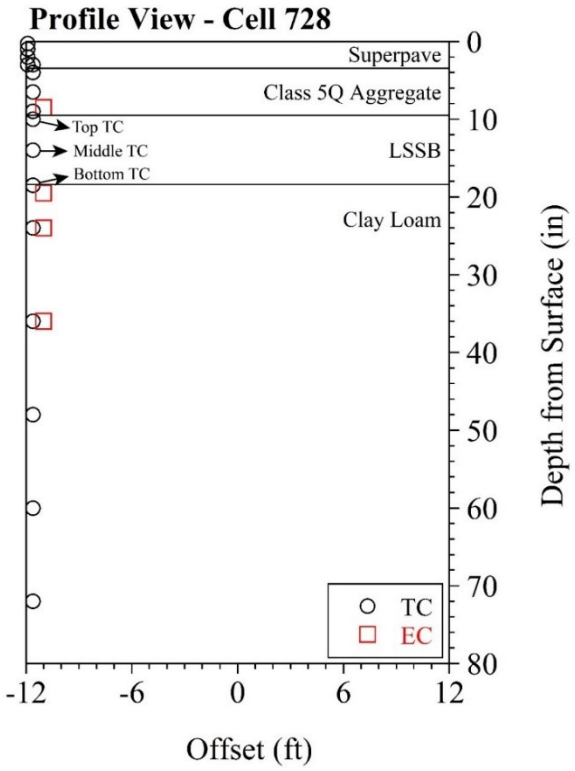

Figure 5.39. Locations of thermocouples (TC) and moisture probes (EC) in 9-in LSSB (Cell 728)

For 12-in Coarse RCA (Cell 185), Fine RCA (Cell 186), Limestone (Cell 188), and RCA+RAP (Cell 189) base layers, overall, the α values determined by the amplitude equation [Equation (5.3)] were located in a smaller range than those calculated by the phase equation [Equation (5.4)]. Figure 5.40 and Figure 5.41 are examples that show the α values determined by the amplitude and phase equations, respectively, for 12-in Coarse RCA base layer (Cell 185). The α values determined for 12-in Fine RCA (Cell 186), Limestone (Cell 188), and RCA+RAP (Cell 189) base layers are provided in Appendix R. The VWC values (median) around the equinox dates were also determined for 12-in aggregate base layers (Appendix R); however, no consistent trend was observed between the VWC values and the α values.

Overall, 12-in Limestone (Cell 188) base layer exhibited higher α values (between 40 and 53 cm^2/h) than the other 12-in aggregate base layers in Cell 185 (Coarse RCA) (between 26 and 31 cm^2/h), Cell 186 (Fine RCA) (between 24 and 31 cm^2/h), and Cell 189 (RCA+RAP) (between 28 and 35 cm^2/h). This could be due to two reasons: (1) different thermal properties of the materials and (2) different VWC values in the aggregate base layers (Figure 5.36). As stated previously, no consistent trend was observed between the VWC values and the α values, so it was speculated that 12-in Limestone (Cell 188) exhibited higher α values than other 12-in aggregate base layers because of Limestone's different thermal properties. Figure 5.42 is an example that shows the α values calculated from top-bottom TC sensors in 12-in aggregate base layers. Comparisons between top-middle and middle-bottom TC sensors in 12-in aggregate base layers are provided in Appendix S.

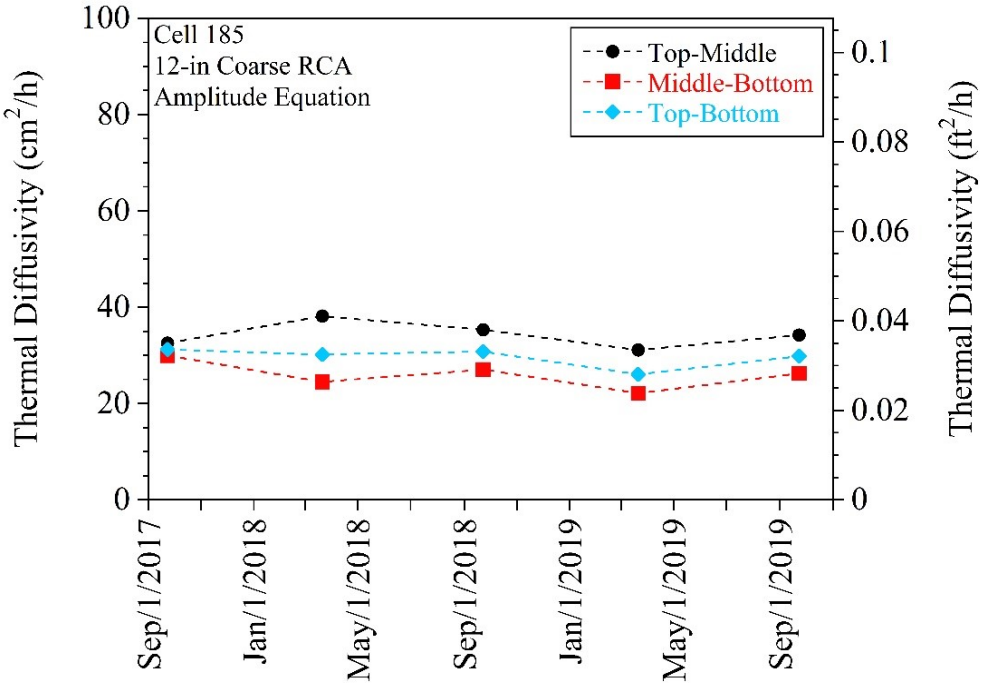

Figure 5.40. Thermal diffusivity (α) values determined by amplitude equation for 12-in Coarse RCA base (Cell 185)

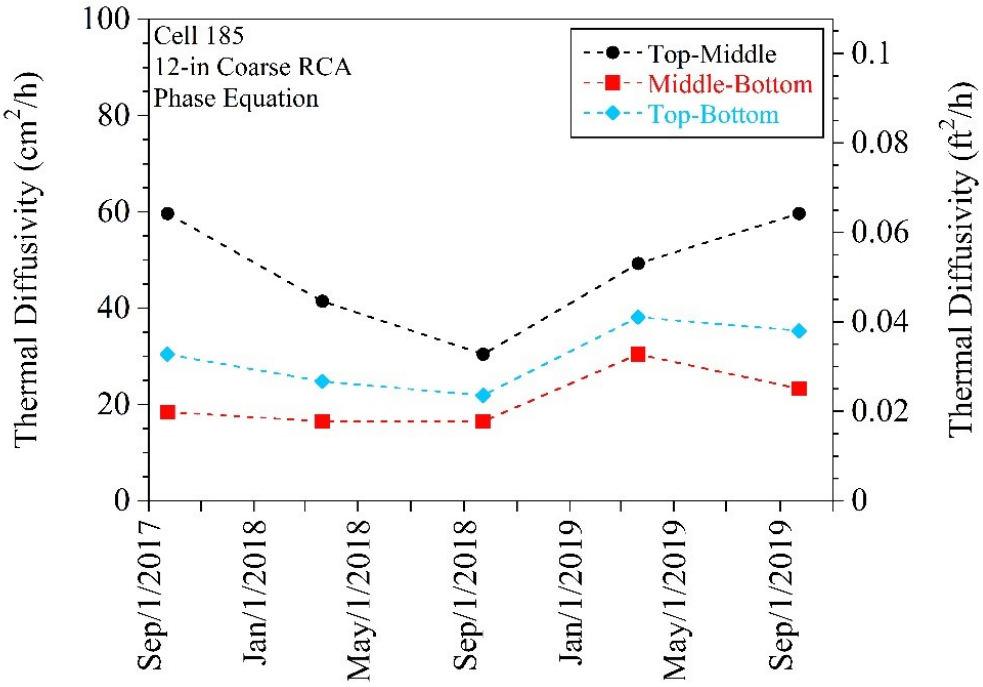

Figure 5.41. Thermal diffusivity (α) values determined by phase equation for 12-in Coarse RCA base (Cell 185)

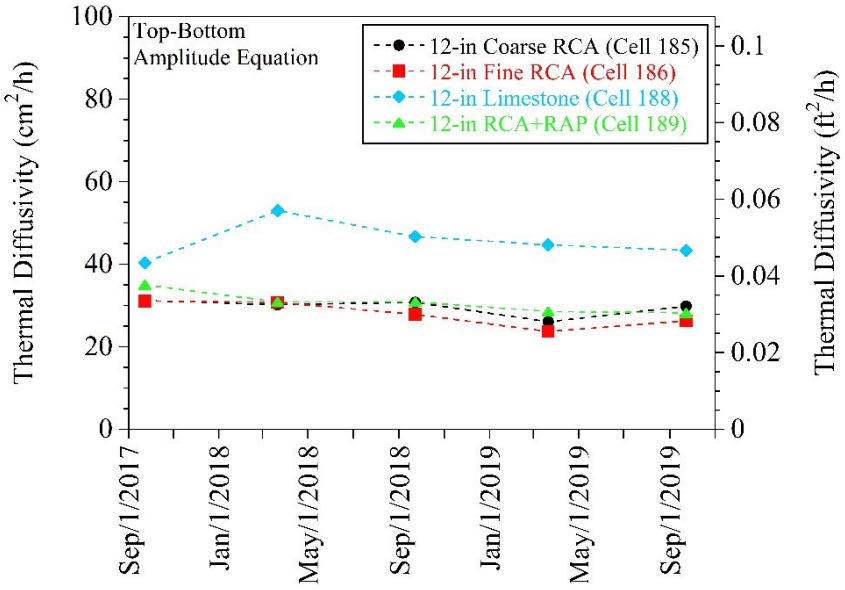

Figure 5.42. Thermal diffusivity (α) values determined from top-bottom thermocouples (TCs) by amplitude equation for 12-in aggregate base layers

The α values determined by the amplitude equation [Equation (5.3)] and phase equation [Equation (5.4)] for 18-in LSSB layer in Cell 127 are provided in Figure 5.43 and Figure 5.44, respectively. Only the top, middle 1, and middle 2 TC sensors were considered for the calculation since the bottom and middle 2 TC sensors exhibited similar temperature profiles. As explained previously, as soil depth increases, amplitude reduces (Figure 5.12), and soil temperatures at deeper elevations tend to be similar to one another. No comparison between the α values and VWC values could be made since 18-in LSSB layer in Cell 127 did not contain any EC sensors (Figure 5.38).

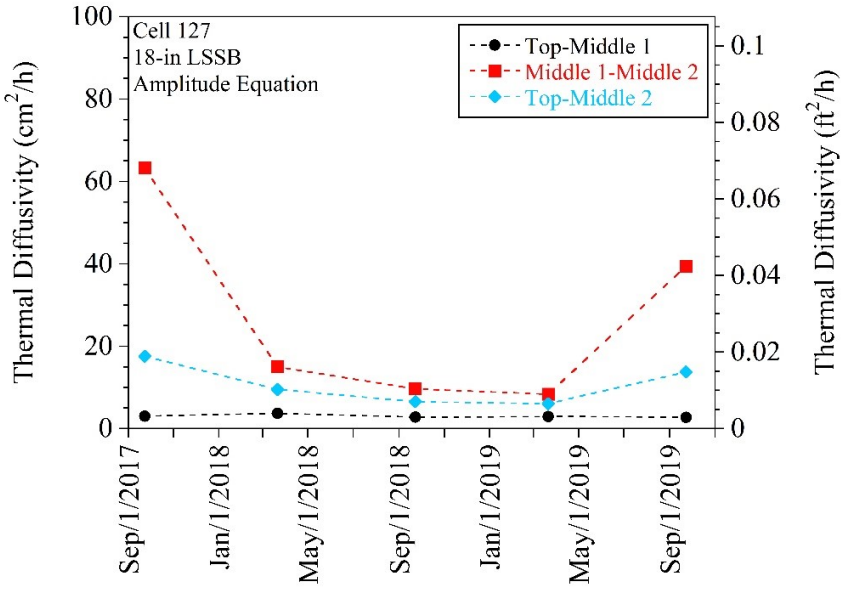

Figure 5.43. Thermal diffusivity (α) values determined by amplitude equation for 18-in LSSB (Cell 127)

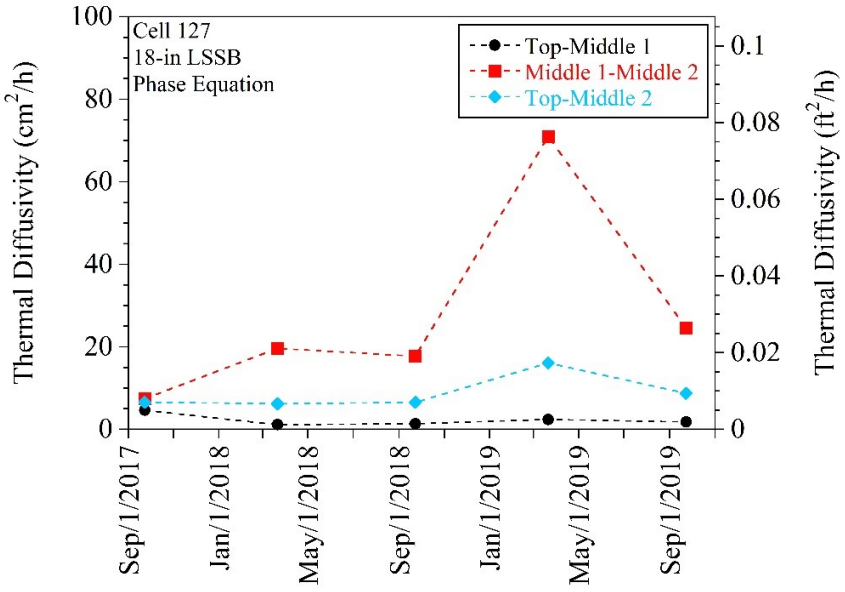

Figure 5.44. Thermal diffusivity (α) values determined by phase equation for 18-in LSSB (Cell 127)

The α values determined by the amplitude equation [Equation (5.3)] and phase equation [Equation (5.4)] for 9-in LSSB layer in Cell 728 are provided in Figure 5.45 and Figure 5.46, respectively. Only the top and middle TC sensors were considered because the bottom TC sensor and the middle TC sensor exhibited similar temperature profiles. As explained previously, as soil depth increases, amplitude diminishes, and soil temperature profiles become similar to one another (Figure 5.12). No comparison between the α values and VWC values could be made since 9-in LSSB layer in Cell 728 did not contain any EC sensors (Figure 5.39).

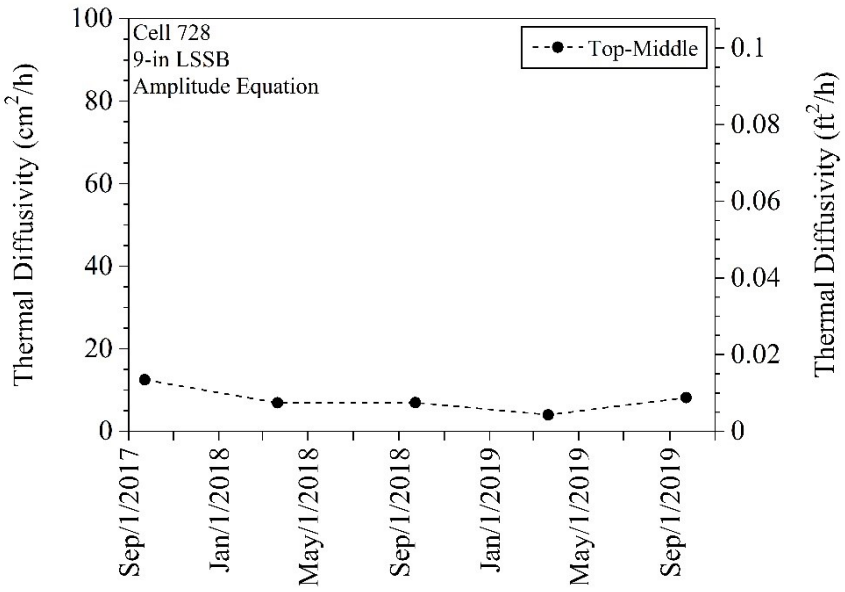

Figure 5.45. Thermal diffusivity (α) values determined by amplitude equation for 9-in LSSB (Cell 728)

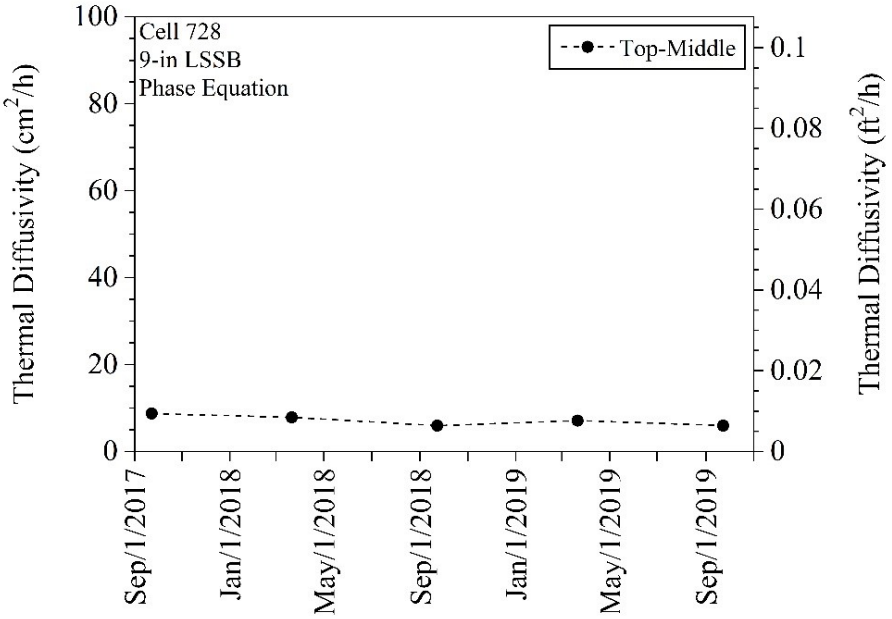

Figure 5.46. Thermal diffusivity (α) values determined by phase equation for 9-in LSSB (Cell 728)

Thermal properties of soils would affect the freeze-thaw (F-T) durability and frost penetration depth of pavement sublayers. For more reliable evaluation of the thermal properties of soils (λ, C, and α), laboratory testing rather than using the amplitude [Equation (5.3)] and phase equations [Equation (5.4)] is recommended. As described previously, the one-dimensional conduction heat transfer theory is based on several assumptions that would affect the reliability of such equations in determining soil α. However, determining the λ, C, and α properties of soils is beyond the scope of this project; therefore, it was not included in this study.

5.2.6 Comparisons between Volumetric Water Content (VWC) Values in First (2017-2018) and Second (2018-2019) Freezing and Thawing Periods

An effort was made to compare VWC values during the first (2017-2018) and second (2018-2019) freezing and thawing periods. Since the EC sensors were prone to stop working properly when the ground was frozen, no specific evaluation was made for such differences between VWC values recorded during the December-February periods.

When liquid water begins to freeze and transform into ice, its dielectric constant (about 80) begins to diminish, which also reduces the dielectric constant of the soil medium. Therefore, freezing events can be detected by noting sudden reductions in VWC values over time. When the soil has become fully frozen, its dielectric constant tends to stay constant because there will be no change in the liquid water content under such conditions. Following freezing and fully frozen conditions, thawing events can be determined by noting sudden increases in VWC values over time. It is expected that data obtained by the moisture probes would be compatible with data collected by the thermocouples and properly demonstrate the freezing and thawing periods (Genc 2019).

For Cell 185 (12-in Coarse RCA), VWC readings could not be taken from any of the pavement sublayers after October 2017 due to the malfunctioning of the moisture probes embedded in the test cell; therefore, no comparisons could be made between the VWC values during two freezing and thawing periods. For Cell 186 (12-in Fine RCA), the only consistent VWC readings could be taken from the top EC sensor in 12-in Fine RCA base layer. For Cell 186 (12-in Fine RCA), no continuous VWC readings could be taken from the Select Granular Borrow subbase (sensor was at 17-in depth) and the bottom of the Fine RCA base layer (sensor was at 14-in depth). Also, the EC sensor embedded in the Sand Subgrade layer (sensor was at 20.5-in depth) exhibited highly fluctuated data, possibly indicating malfunctioning of that sensor, too.

For 12-in Fine RCA (Cell 186), Limestone (Cell 188), and RCA+RAP (Cell 189) base layers, the VWC values before both freezing periods were similar to one another. The VWC values after both thawing periods were also similar. The only difference was that the thawing period in 2018-2019 started around 15 days later than that in 2017-2018 because the 2018-2019 winter was longer. Figure 5.47, Figure 5.48, and Figure 5.49 are examples showing the VWC values for the EC sensors at 5-in depths in 12-in Fine RCA (Cell 186), Limestone (Cell 188), and RCA+RAP (Cell 189) base layers, respectively. The comparisons for the other EC sensors are provided in Appendix T.

For Cells 127 (18-in LSSB) and 728 (9-in LSSB), since there were no EC sensors embedded in the LSSB layers, no comparison could be made for those layers. However, comparisons for 6-in Class 6 Aggregate base layer (Cell 127), Class 5Q Aggregate base layer (Cell 728), and Clay Loam subgrade layers (both Cells 127 and 728) were made and are provided in Appendix T.

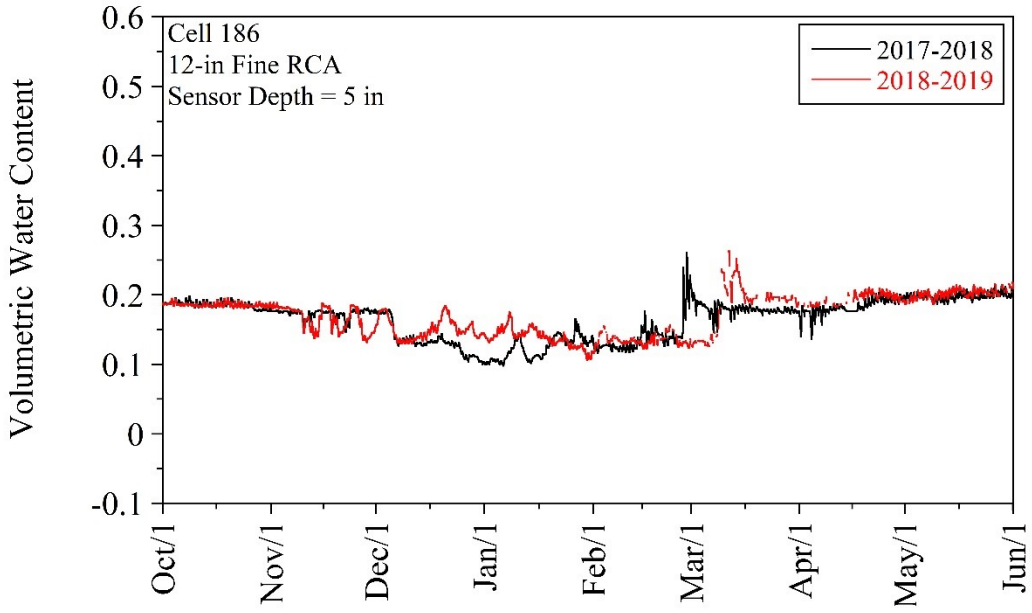

Figure 5.47. Volumetric water content (VWC) values for sensor at 5-in depth in 12-in Fine RCA base layer (Cell 186) during two freezing and thawing periods (dates on x-axis represent time periods for both 2017-2018 and 2018-2019 years)

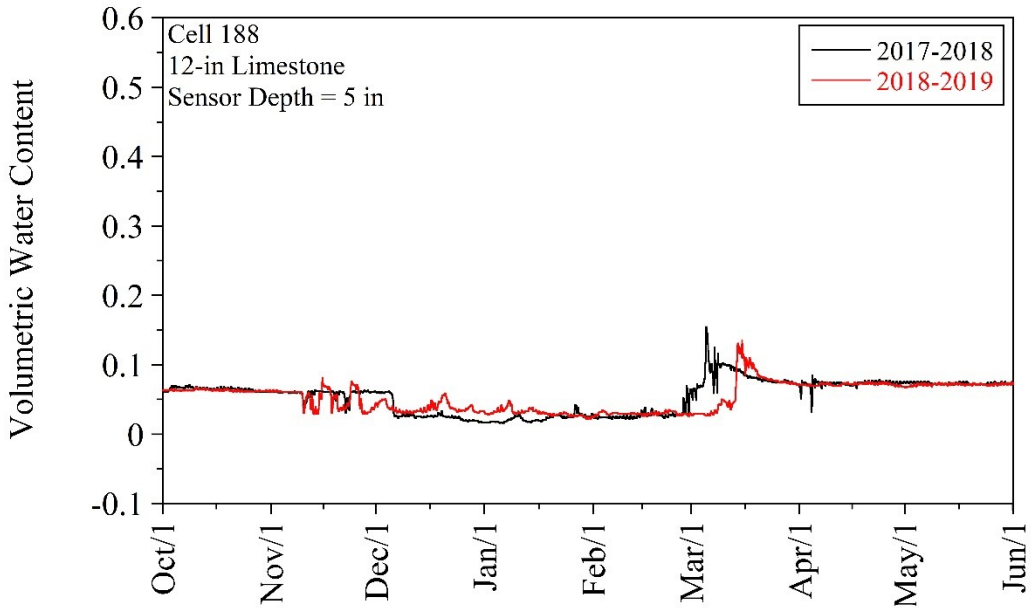

Figure 5.48. Volumetric water content (VWC) values for sensor at 5-in depth in 12-in Limestone base layer (Cell 188) during two freezing and thawing periods (dates on x-axis represent time periods for both 2017-2018 and 2018-2019 years)

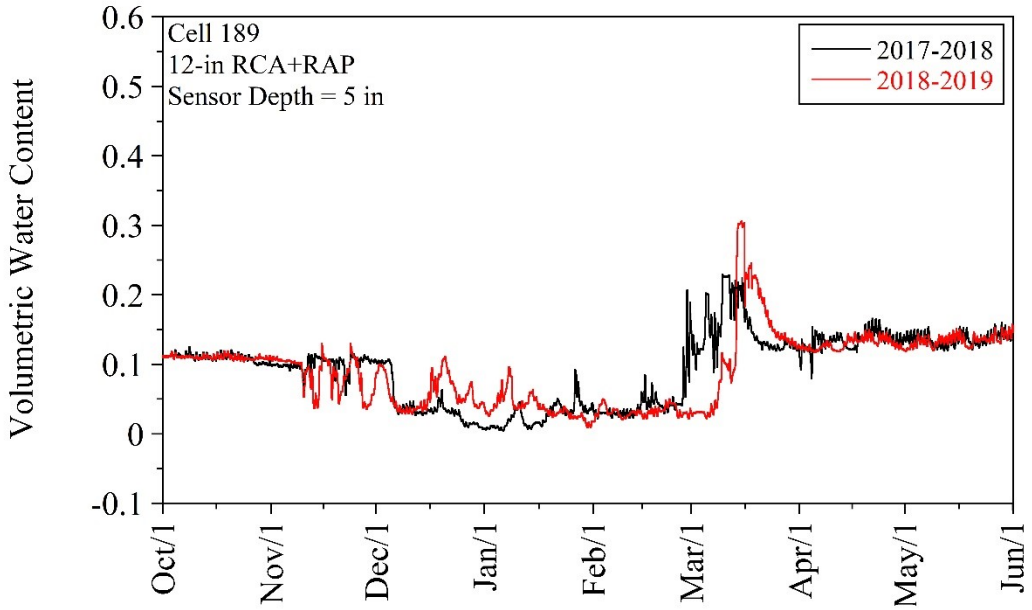

Figure 5.49. Volumetric water content (VWC) values for sensor at 5-in depth in 12-in RCA+RAP base layer (Cell 189) during two freezing and thawing periods (dates on x-axis represent time periods for both 2017-2018 and 2018-2019 years)

5.3 FALLING WEIGHT DEFLECTOMETER (FWD) TESTS

5.3.1 Test Method and Data Analysis

Falling weight deflectometer (FWD) tests were performed to measure maximum deflection and FWD elastic modulus (E_{FWD}) values throughout the test cells. A trailer-mounted FWD device with a plate (rigid) diameter of 11.8 in (300 mm) was used (Figure 5.50). Nine geophones were placed at the center of the loading plate and distances of 8 in (203 mm), 12 in (300 mm), 18 in (460 mm), 24 in (610 mm), 36 in (914 mm), 48 in (1219 mm), 60 in (1524 mm), and 72 in (1829 mm) from the center of the loading plate. Three different loads were applied [the first, second, and third loads were normalized to 6,000 lb (26.7 kN), 9,000 (40 kN), and 12,000 lb (53.4 kN), respectively]. The influence depth of each load ranged from 11.8 to 17.7 in (300 to 450 mm) (1 to 1.5 times the plate diameter) (Mooney et al. 2010; Vennapusa et al. 2012). Two analyses were performed for the determination of the E_{FWD} values: (1) composite analysis, and (2) layered analysis (Figure 5.51).

Figure 5.50. Trailer-mounted Dynatest Model 8002 falling weight deflectometer (FWD) device

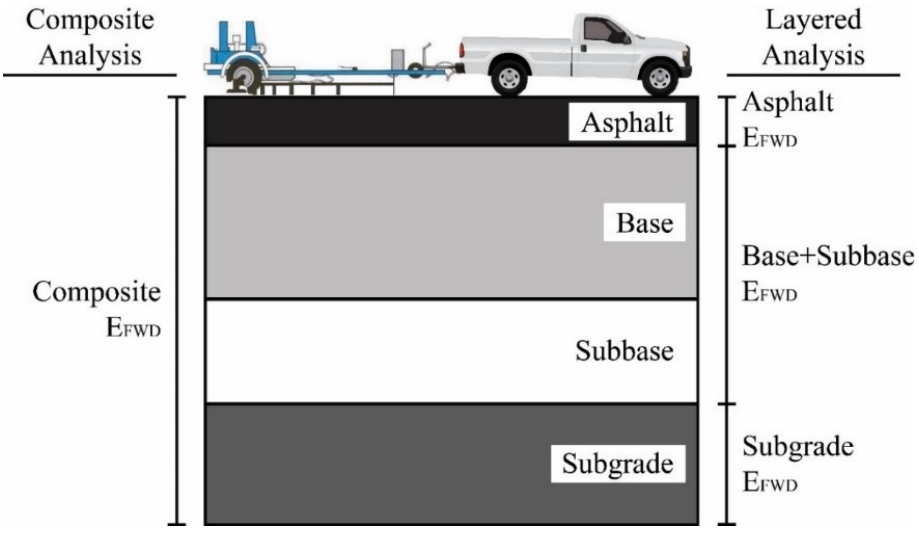

Figure 5.51. Composite and layered falling weight deflectometer (FWD) analysis

For the composite analysis (Figure 5.51), only the deflections under the loading plate (maximum deflections) were considered. Boussinesq elastic half-space equation, shown in Equation (5.5), was used to determine the composite E_{FWD} values for the entire pavement structure (Figure 5.51) (Vennapusa and White 2009; Li et al. 2019).

$$\text{Composite } E_{FWD} = \frac{(1 - \nu^2)\sigma_0 r}{d_0} f \tag{5.5}$$

where composite E_{FWD} is the composite FWD elastic modulus (MPa), v is the Poisson's ratio (assumed to be 0.35), σ_0 is the applied stress (MPa), r is the radius of the loading plate (mm), d0 is the average deflection (mm), and f is the shape factor [assumed to be 8/3 (a rigid plate on a granular material) (Vennapusa and White 2009)].

For the layered analysis (Figure 5.51), deflection basins (recorded by the geophones) were considered. The MODULUS 7.0 program, which was developed at the Texas A&M Transportation Institute (TTI) based on linear-elastic theory, was used for back-calculation (Edil et al. 2012). This program is mainly for flexible pavements and uses the database method to determine the layered E_{FWD} values (William 1999; Baladi et al. 2011).

Per Newcomb et al. (1995), the water table at the MnROAD test facility is relatively shallow and must be considered for back-calculation. Under dynamic loads, such as those applied during FWD testing, there is no time for pore water pressure to dissipate. Therefore, the pore water pressure increases suddenly under dynamic loads and withstands the loads. As a result, saturated soils tend to exhibit higher stiffness under dynamic loads. To be able to consider a shallow water table for back-calculation, the thickness of the unsaturated zone (between the subgrade layer surface and water table) must be determined. To do so, the depth-to-bedrock analysis must be performed (Rohde et al. 1992). By using the depth-to-bedrock analysis, not only the presence of bedrock but also the depth of the water table can be estimated (Liu and Scullion 2001; Chatti et al. 2017). If the subgrade layer is assumed as semi-infinite and the location of the water table is ignored, higher-than-actual subgrade layer stiffness can be observed. In addition, incorrect back-calculation for the upper layers (asphalt, aggregate base, and subbase layers) can be made by selecting a semi-infinite subgrade layer in case the water table is shallow (Newcomb et al. 1995). In addition, the subgrade/bedrock modular ratio of 100 is recommended for the depth-to-bedrock analysis. However, since the case in this study was the presence of a shallow water table rather than bedrock, a ratio of 5 was used for back-calculation as recommended by Liu and Scullion (2001). For the subgrade layers, Poisson's ratio (υ) was considered to be 0.40. The aggregate base and subbase layers were combined and considered as a single layer (base+subbase layer). The total design thickness of the base+subbase layer (aggregate base layer thickness + subbase layer thickness) was entered manually (υ was considered to be 0.35). For the asphalt layers, the design thickness [3.5 in (90 mm)] was entered manually into the program (υ was considered to be 0.30).

5.3.2 Falling Weight Deflectometer (FWD) Test Results Under Different Loads

5.3.2.1 Maximum Deflection

Regardless of the test location and date (detailed information about the effects of the test location and the date on the FWD test results are provided in Sections 5.3.3 and 5.3.4, respectively), higher maximum deflections were observed under higher loads for each test cell as expected. Figure 5.52 is an example that shows the two-year maximum deflection data for the inside lane (main traffic) - OWP of Cell 188 (12-in Limestone) under each load. All of the maximum deflection graphs for each test cell and test location are provided in Appendix U.

5.3.2.2 Composite E_{FWD}

Regardless of the test location and date, the composite E_{FWD} values calculated for 6,000 lb (26.7 kN) load were slightly lower than or similar to those calculated for 9,000 lb (40 kN) and 12,000 lb (53.4 kN) loads. The composite E_{FWD} values calculated for 9,000 lb (40 kN) and 12,000 lb (53.4 kN) loads were similar. Figure 5.53 is an example that shows the two-year composite E_{FWD} data for the inside lane (main traffic) - OWP of Cell 188 (12-in Limestone) under each load. All other graphs for the composite E_{FWD} of each test cell and test location are provided in Appendix V.

5.3.2.3 Asphalt and Base+Subbase E_{FWD}

Regardless of the test location and date, the asphalt and base+subbase E_{FWD} values determined for 6,000 lb (26.7 kN) load were slightly lower than or similar to those determined for 9,000 lb (40 kN) and 12,000 lb (53.4 kN) loads (similar to the trend observed for the composite E_{FWD}). Again, similar to the composite E_{FWD} values, the asphalt and base+subbase E_{FWD} values determined for 9,000 lb (40 kN) and 12,000 lb (53.4 kN) loads were similar to each other overall. Figure 5.54 is an example that shows the two-year asphalt E_{FWD} data for the inside lane (main traffic) - OWP of Cell 188 (12-in Limestone) under each load. Figure 5.55 is an example that shows the two-year base+subbase E_{FWD} data for the same location of the same test cell under each load. All of the asphalt and base+subbase E_{FWD} graphs for each test cell and test location are provided in Appendix W and Appendix X, respectively.

5.3.2.4 Subgrade E_{FWD}

Regardless of the test location and date, all of the loads yielded similar subgrade E_{FWD} values. Figure 5.56 is an example that shows the two-year subgrade E_{FWD} data for the inside lane (main traffic) - OWP of Cell 188 (12-in Limestone) under each load. All of the subgrade E_{FWD} graphs for each test cell and test location are provided in Appendix Y.

By considering the effects of different loads on the FWD test results and several other studies (Baladi et al. 2011; Edil et al. 2012; Bilodeau et al. 2014; Becker 2016; Zhang 2016), only the FWD test results under 9,000 lb (40 kN) [one-half equivalent single axle load (ESAL)] are discussed in the following sections.

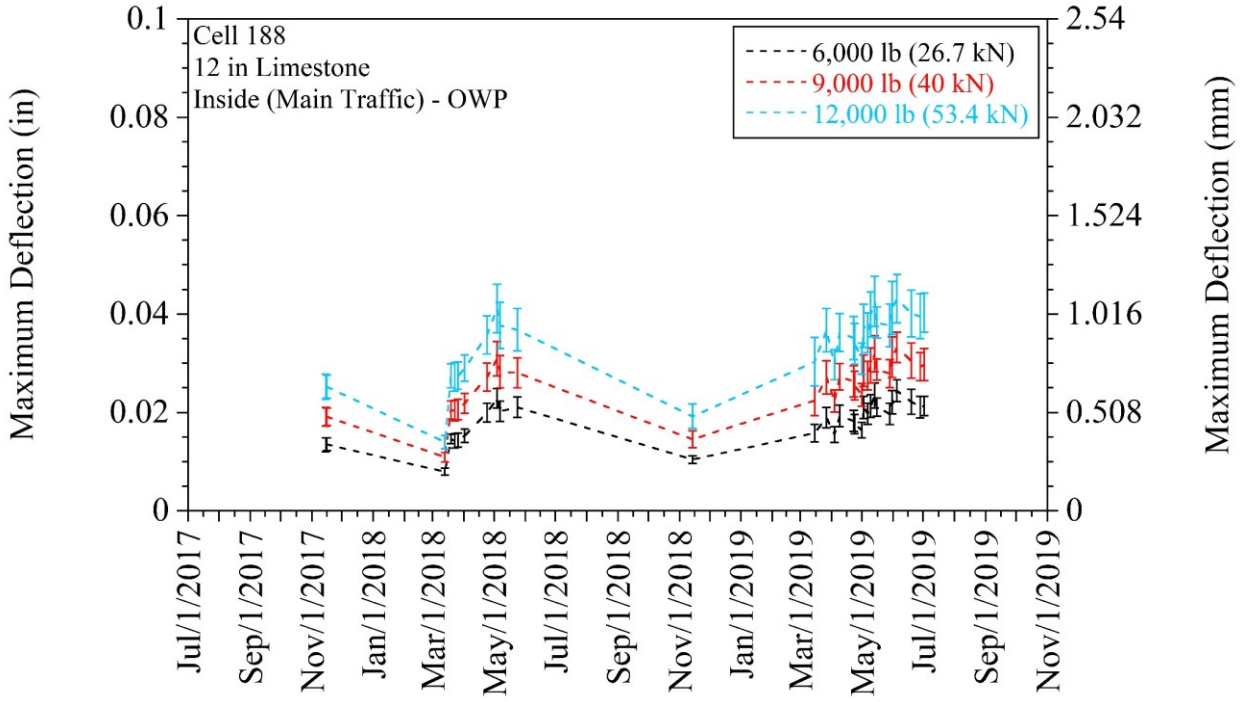

Figure 5.52. Maximum deflections for inside lane (main traffic) - outer wheel path (OWP) of Cell 188 (12-in Limestone) under different loads (error bars represent one standard deviation of data)

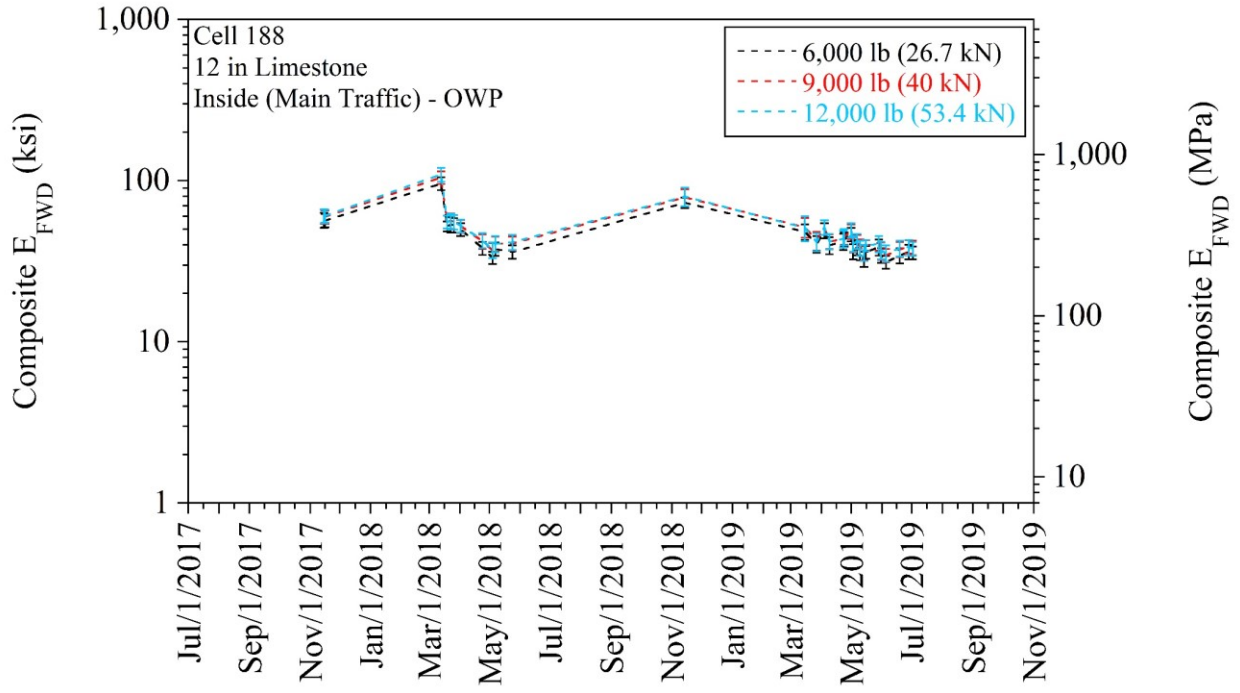

Figure 5.53. Composite falling weight deflectometer (FWD) elastic modulus (E_{FWD}) for inside lane (main traffic) - outer wheel path (OWP) of Cell 188 (12-in Limestone) under different loads (error bars represent one standard deviation of data)

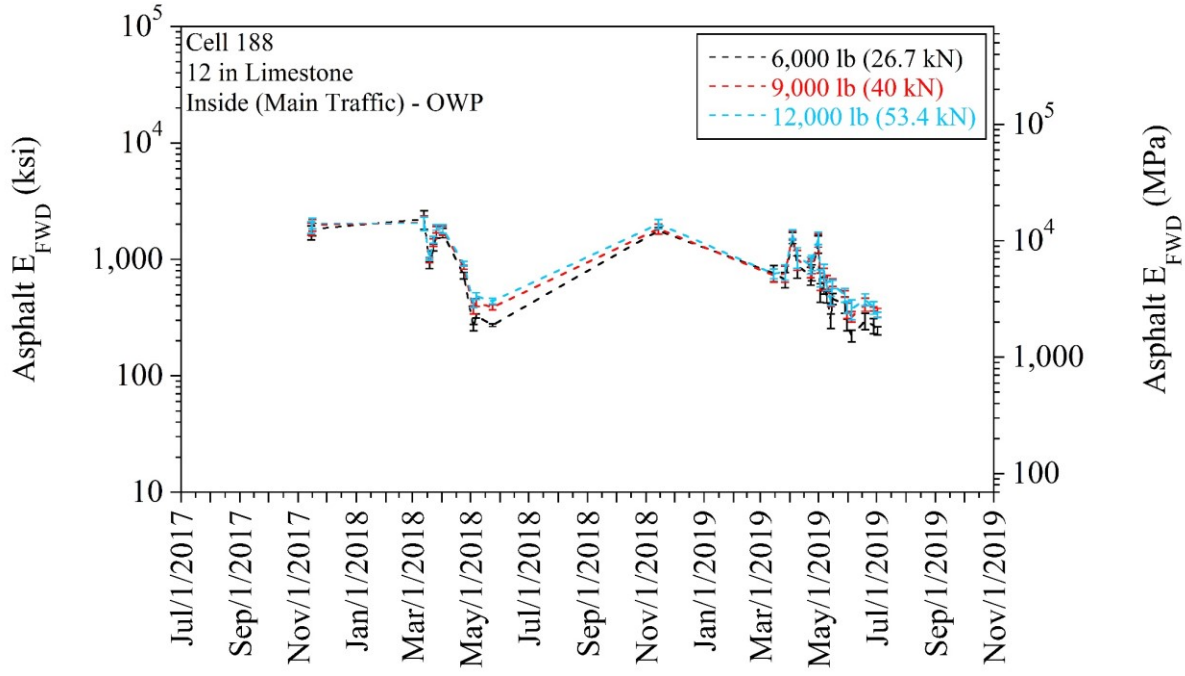

Figure 5.54. Asphalt falling weight deflectometer (FWD) elastic modulus (E_{FWD}) for inside lane (main traffic) - outer wheel path (OWP) of Cell 188 (12-in Limestone) under different loads (error bars represent one standard deviation of data)

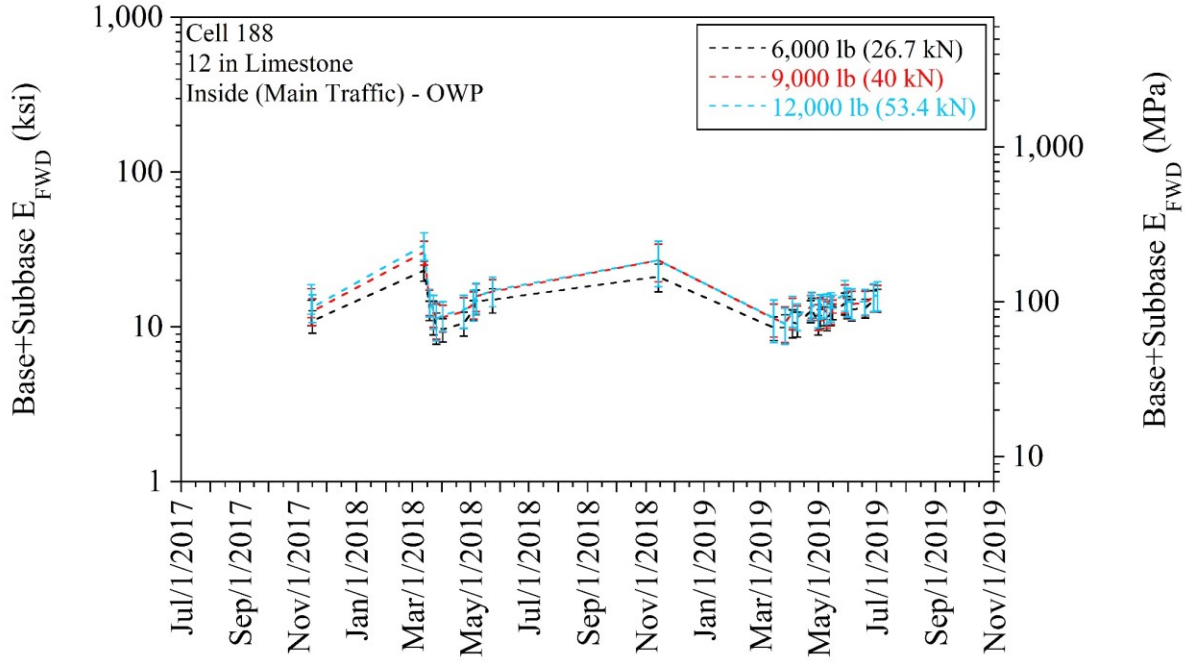

Figure 5.55. Base+subbase falling weight deflectometer (FWD) elastic modulus (E_{FWD}) for inside lane (main traffic) - outer wheel path (OWP) of Cell 188 (12-in Limestone) under different loads (error bars represent one standard deviation of data)

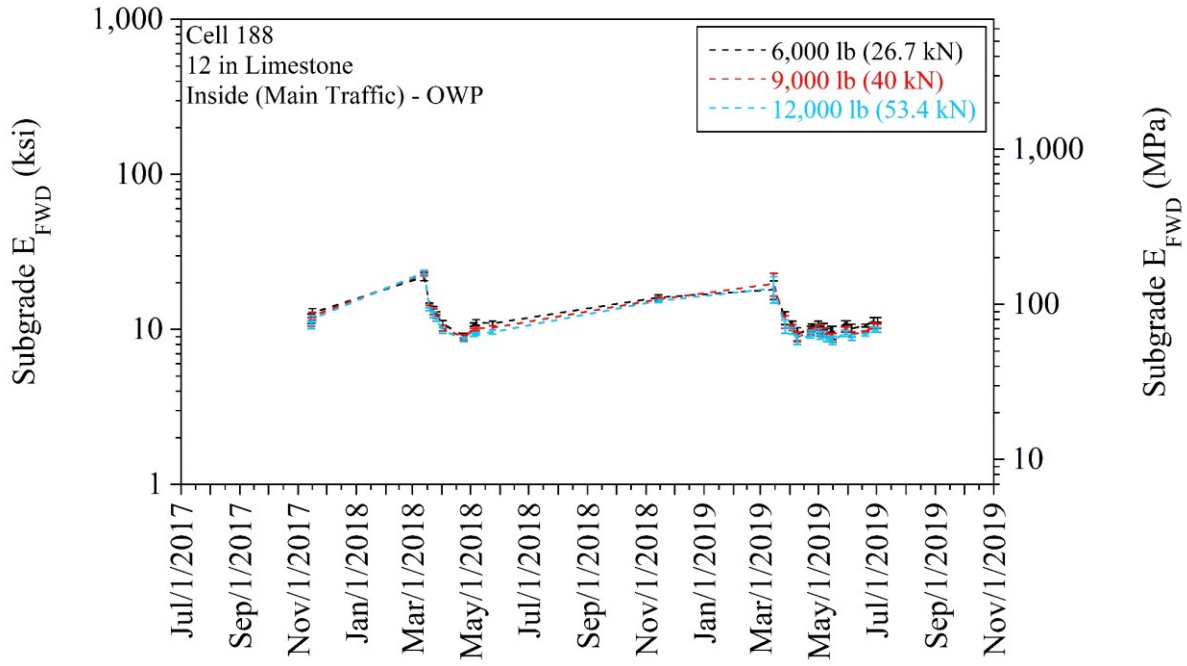

Figure 5.56. Subgrade falling weight deflectometer (FWD) elastic modulus (E_{FWD}) for inside lane (main traffic) - outer wheel path (OWP) of Cell 188 (12-in Limestone) under different loads (error bars represent one standard deviation of data)

5.3.3 Falling Weight Deflectometer (FWD) Test Results at Different Test Locations

5.3.3.1 Maximum Deflection

Regardless of the date (detailed information about the effects of the date on the FWD test results will be provided in Section 5.3.4), the outside lane (occasional traffic) - OWP yielded relatively higher maximum deflections than the other locations [outside lane (occasional traffic) - MID, inside lane (main traffic) - OWP, and inside lane (main traffic) - MID] under 9,000 lb (40 kN) load. The maximum deflections observed in the outside lane (occasional traffic) - MID were higher than or similar to those observed in the inside lane (main traffic). Overall, it was concluded that the maximum deflections observed in the inside lane (main traffic) were lower than those observed in the outside lane (occasional traffic). Furthermore, since the inside lane (main traffic) was subjected to more traffic [provided by the MnROAD truck weighing 80 kip (36.3 Mg)] than the outside lane (occasional traffic), the inside lane (main traffic) experienced a greater degree of compaction (DOC) over time. Thus, the further compaction of the pavement sublayers for the inside lane (main traffic) yielded denser material matrices, which improved the overall stiffness of the materials (Edil et al. 2012). In particular, the inside lane (main traffic) - OWP was expected to exhibit lower maximum deflections than the inside lane (main traffic) - MID since the weight of the MnROAD truck [80 kip (36.3 Mg)] directly impacted the inside lane (main traffic) - OWP. However, in this study, this trend could not be observed clearly. Figure 5.57 is an example that shows the two-year maximum deflection data for each test location of Cell 227 (18-in LSSB). All of the maximum deflection graphs for each test cell are provided in Appendix Z.

5.3.3.2 Composite E_{FWD}

Regardless of the date, the trends observed in the composite E_{FWD} values were exactly compatible with those observed in the maximum deflections under 9,000 lb (40 kN) load. Higher maximum deflections yielded lower composite E_{FWD} values, and lower maximum deflections yielded higher composite E_{FWD} values consistently. This was because the composite E_{FWD} values were inversely proportional to the maximum deflections under the same load [9,000 lb (40 kN)] based on Equation (5.5). Overall, the outside lane (occasional traffic) - OWP exhibited relatively lower composite E_{FWD} values than those measured at other locations. The composite E_{FWD} values calculated for the outside lane (occasional traffic) - MID were lower than or similar to those calculated for the inside lane (main traffic). In general, the inside lane (main traffic) yielded higher composite E_{FWD} values than the outside lane (occasional traffic) due to the aforementioned further compaction. Just like the observations made for the maximum deflections, no clear trend was observed between the inside lane (main traffic) - OWP and the inside lane - MID. Figure 5.58 is an example that shows the two-year composite E_{FWD} data for each test location of Cell 227 (18-in LSSB). All of the composite E_{FWD} graphs for each test cell are provided in Appendix AA.

5.3.3.3 Asphalt and Base+Subbase E_{FWD}

Regardless of the date, the trends observed in the asphalt and base+subbase E_{FWD} values were similar to those observed in the composite E_{FWD} values under 9,000 lb (40 kN) load. Figure 5.59 is an example that shows the two-year asphalt E_{FWD} data for each test location of Cell 227 (18-in LSSB). Figure 5.60 is an example that shows the two-year base+subbase E_{FWD} data for each test location of the same test cell. All of the asphalt E_{FWD} and base+subbase E_{FWD} graphs for each test cell are provided in Appendix AB and Appendix AC, respectively.

5.3.3.4 Subgrade E_{FWD}

Regardless of the date, no significant differences were observed in the subgrade E_{FWD} values for different test locations of each test cell under 9,000 lb (40 kN) load. Figure 5.61 is an example that shows the two-year subgrade E_{FWD} data for each test location of Cell 227 (18-in LSSB). All of the subgrade E_{FWD} graphs for each test cell are provided in Appendix AD.

Since the traffic load provided by the MnROAD truck [80 kip (36.3 Mg)] directly applied to the inside lane (main traffic) - OWP of each test cell, the FWD test results in the long-term are discussed only for that specific test location [under 9,000 lb (40 kN) load (the reason for the selection of that load was explained previously)] in the following sections.

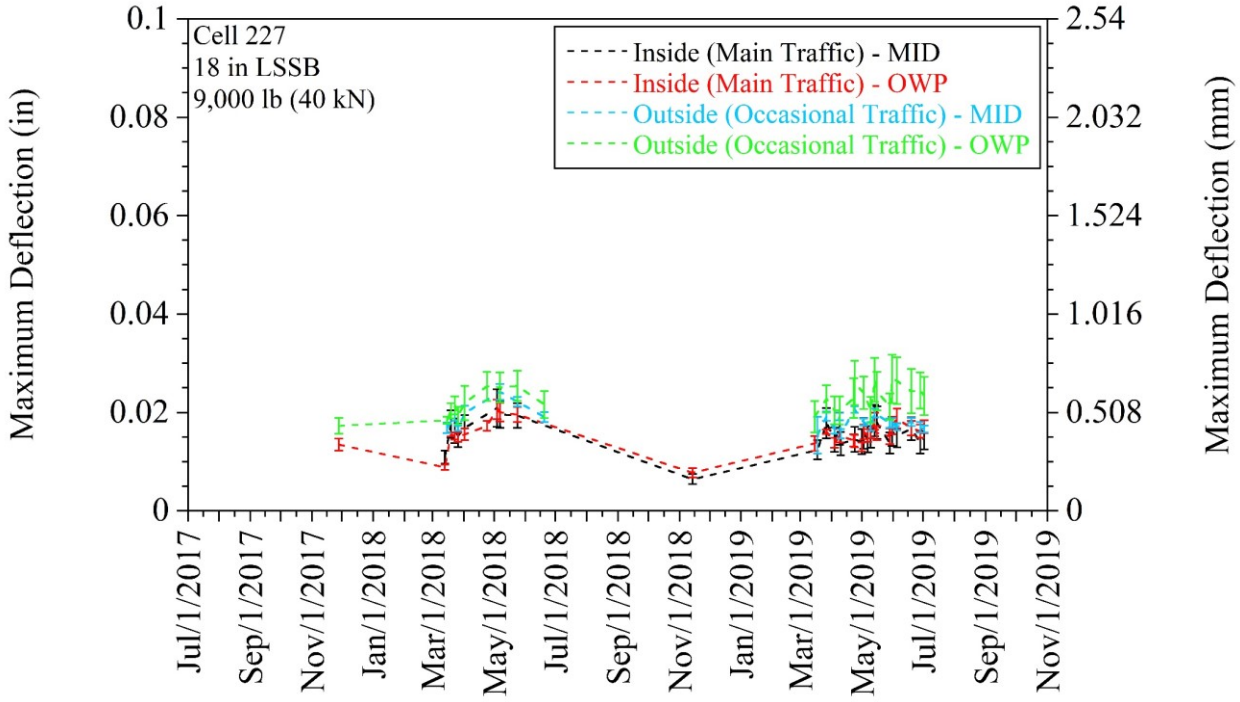

Figure 5.57. Maximum deflections for Cell 227 (18-in LSSB) under 9,000 lb (40 kN) load (error bars represent one standard deviation of data)

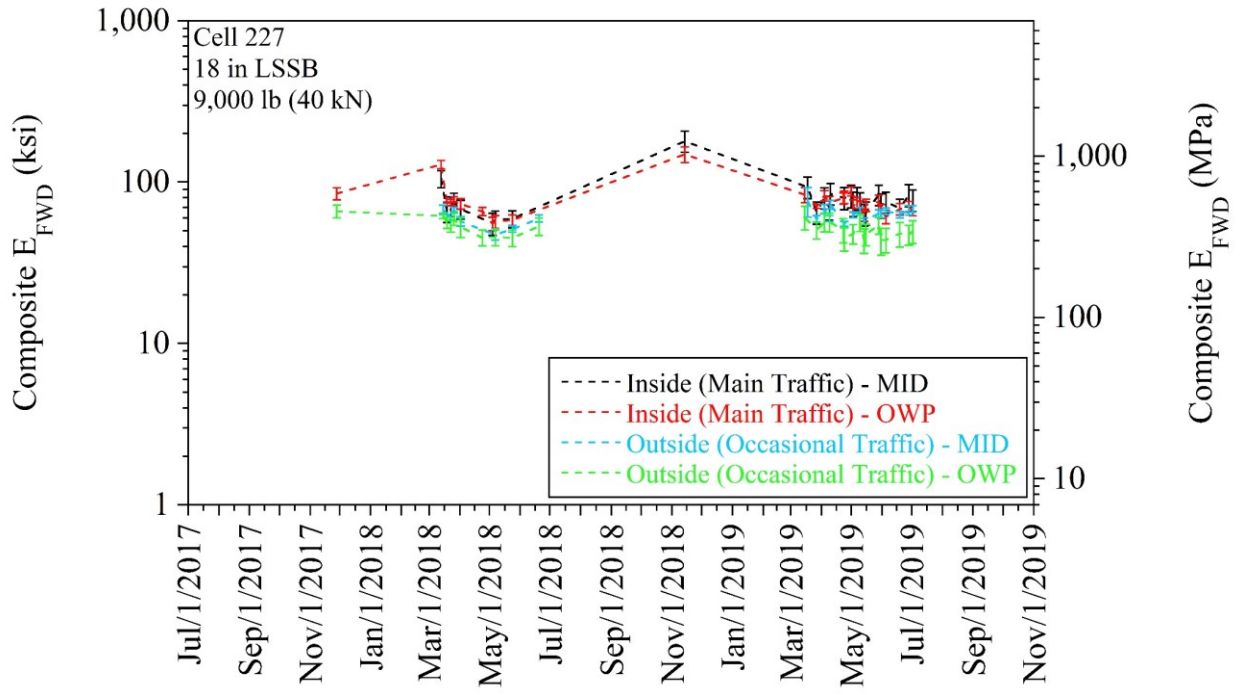

Figure 5.58. Composite falling weight deflectometer (FWD) elastic modulus (E_{FWD}) for Cell 227 (18-in LSSB) under 9,000 lb (40 kN) load (error bars represent one standard deviation of data)

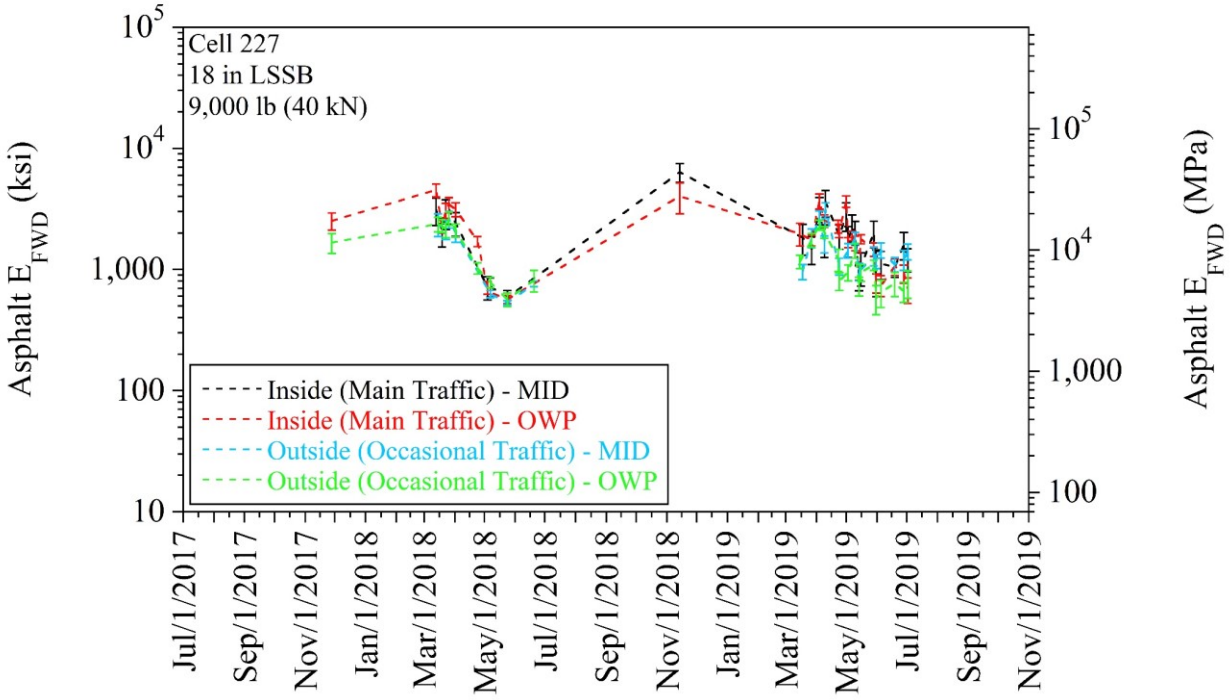

Figure 5.59. Asphalt falling weight deflectometer (FWD) elastic modulus (E_{FWD}) for Cell 227 (18-in LSSB) under 9,000 lb (40 kN) load (error bars represent one standard deviation of data)

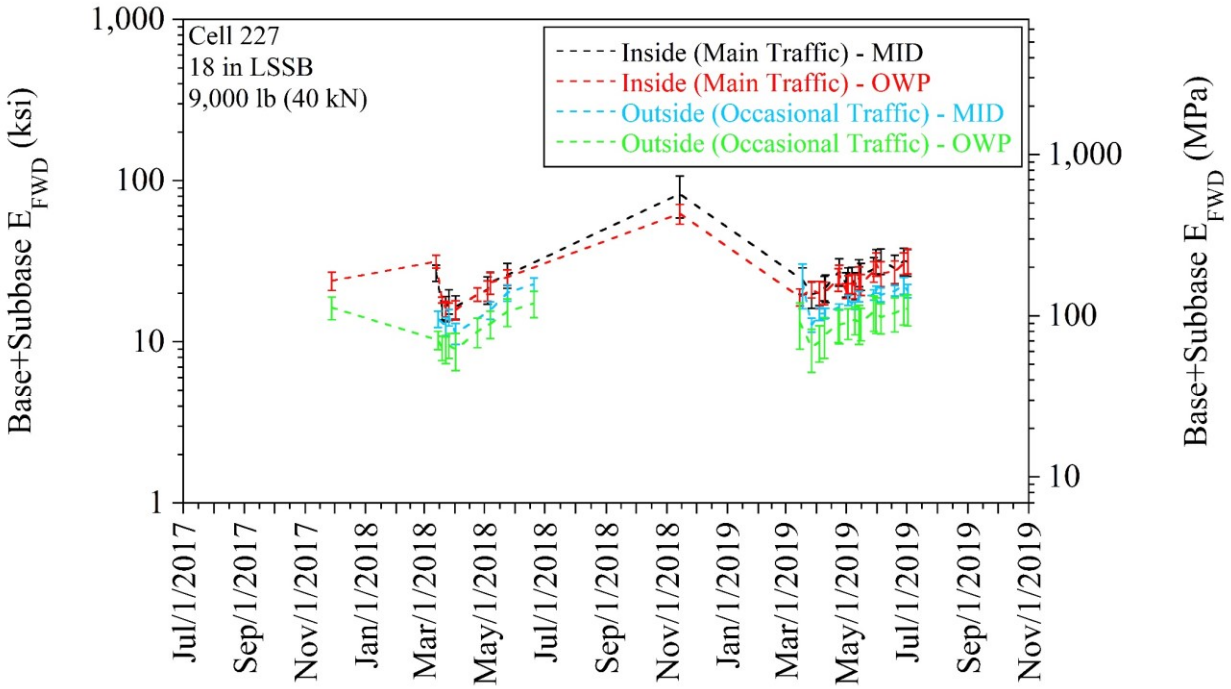

Figure 5.60. Base+subbase falling weight deflectometer (FWD) elastic modulus (E_{FWD}) for Cell 227 (18-in LSSB) under 9,000 lb (40 kN) load (error bars represent one standard deviation of data)

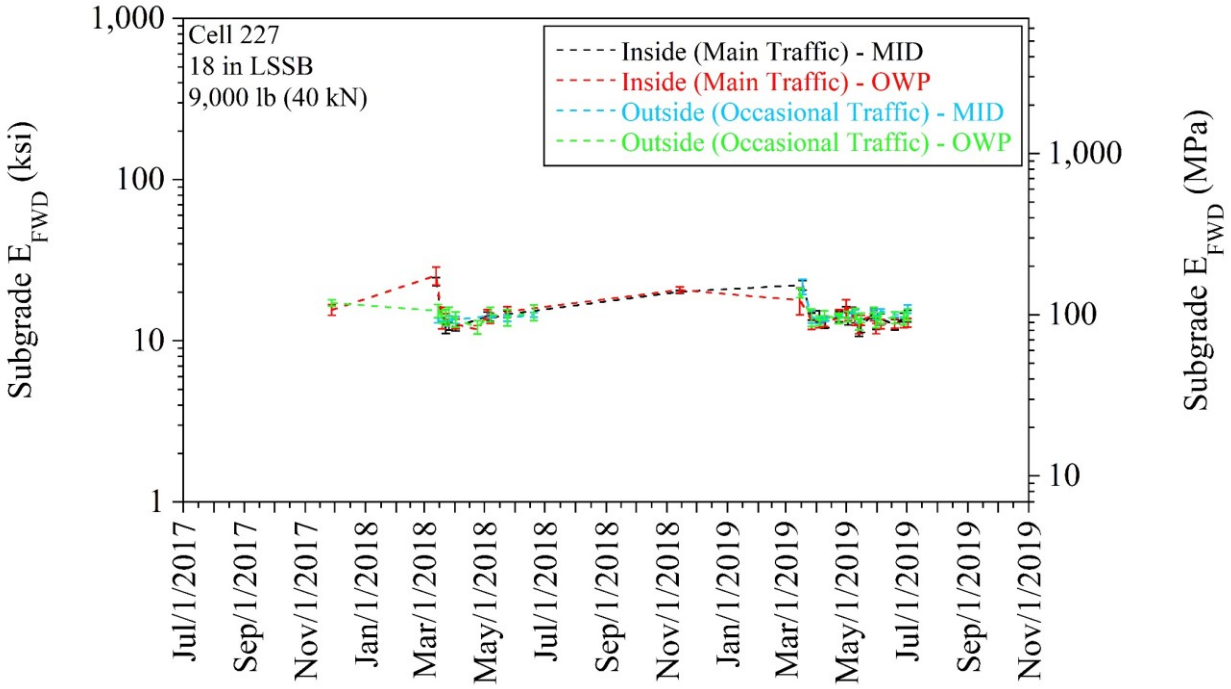

Figure 5.61. Subgrade falling weight deflectometer (FWD) elastic modulus (E_{FWD}) for Cell 227 (18-in LSSB) under 9,000 lb (40 kN) load (error bars represent one standard deviation of data)

5.3.4 Effects of Freeze-Thaw (F-T) Cycles and Temperature Changes on Falling Weight Deflectometer (FWD) Test Results

The engineering properties of pavement foundation systems can change considerably in the long term due to seasonal variations in weather conditions (Rosa et al. 2016). In cold regions, pavement structures experience several freeze-thaw (F-T) cycles. During the freezing period, water freezes and turns into ice with an increase (around 10%) in its volume. Frozen soils or aggregates are expected to exhibit higher stiffness than unfrozen soils; therefore, the stiffness of pavement systems increases during the freezing period. During the thawing period, ice melts with a reduction in its volume and it leaves a relatively more porous structure in the soil or aggregate matrix. In addition, expansion of the water molecules during freezing generates internal pressures in the soil or aggregate matrix. Thus, it may deteriorate soil or aggregate particles. During the thawing period, the fines content of the soils or aggregates may increase due to the deterioration of coarser particles. Such an increase in the fines content may yield an increase in the water absorption capacity of the soils or aggregates due to an increase in the specific surface area of the soil or aggregate (Edil et al. 2012; Rosa et al. 2017). Higher fines content and water absorption capacity may cause further detrimental effects during another freezing period as more water may turn into ice.

The long-term performances of the test cells are summarized in Figure 5.62, Figure 5.63, Figure 5.64, Figure 5.65, and Figure 5.66 for the maximum deflection, composite E_{FWD}, asphalt E_{FWD}, base+subbase E_{FWD}, and subgrade E_{FWD}, respectively [the results shown are only for the inside lane (main traffic) - OWP of each test cell under 9,000 lb (40 kN) load]. For the comparisons, the FWD test results obtained in

November 2017 (before the first freezing period), March 2018 (in the first thawing period), March 2019 (in the second thawing period), and July 2019 (the latest test date) were selected.

5.3.4.1 Falling Weight Deflectometer (FWD) Test Results Before the First Freezing Period

MAXIMUM DEFLECTION

In November 2017 (before the first freezing period) (Figure 5.62), Cells 186 (12-in Fine RCA), 127 (18-in LSSB), and 227 (18-in LSSB) yielded lower maximum deflections than the other cells. Cell 185 (12-in Coarse RCA) exhibited higher maximum deflections than Cells 186 (12-in Fine RCA), 127 (18-in LSSB), and 227 (18-in LSSB) and lower maximum deflections than Cell 189 (12-in RCA+RAP). Cells 188 (12-in Limestone), 328 (9-in LSSB - TX), and 728 (9-in LSSB) exhibited higher deflections than Cell 189 (12-in RCA+RAP). Cells 428 (9-in LSSB - TX+GT), 528 (9-in LSSB - BX+GT), and 628 (9-in LSSB - BX) yielded higher deflections than the other test cells.

COMPOSITE E_{FWD}

In November 2017 (before the first freezing period) (Figure 5.63), the trends observed in the composite E_{FWD} values were exactly compatible with those observed in the maximum deflections. Higher maximum deflections yielded lower composite E_{FWD} values. On the contrary, lower maximum deflections yielded higher composite E_{FWD} values. This was due to the inversely proportional relationship of composite E_{FWD} with the maximum deflections under the same load [9,000 lb (40 kN)] based on Equation (5.5).

ASPHALT E_{FWD}

In November 2017 (before the first freezing period) (Figure 5.64), Cells 188 (12-in Limestone), 189 (12-in RCA+RAP), 328 (9-in LSSB - TX), 428 (9-in LSSB - TX+GT), 528 (9-in LSSB - BX+GT), and 628 (9-in LSSB - BX) yielded similar asphalt E_{FWD} values which were lower than those of the other cells. Cells 185 (12-in Coarse RCA) and 728 (9-in LSSB) exhibited intermediate asphalt E_{FWD} values. Cells 186 (12-in Fine RCA), 127 (18-in LSSB), and 227 (18-in LSSB) provided higher asphalt E_{FWD} values than the other cells [Cell 127 (18-in LSSB) yielded the highest asphalt E_{FWD} values]. Asphalt E_{FWD} values exhibited relatively higher standard deviations, possibly due to the temperature-dependency of the asphalt material. The stiffness of asphalt material is inversely proportional to the air temperature due to viscosity (Edil et al. 2012). At higher temperatures, the viscosity of the asphalt material decreases, and this reduces the asphalt stiffness (Edil et al. 2012). On the other hand, the viscosity of the asphalt material increases at lower temperatures which increases the asphalt stiffness (Edil et al. 2012). It is very well known that even the test time on the same day (early in the morning, in the afternoon, etc.) can affect the asphalt stiffness significantly.

BASE+SUBBASE E_{FWD}

In November 2017 (before the first freezing period) (Figure 5.65), the Coarse RCA and Fine RCA base+subbase layers [placed over Select Granular Borrow and Sand Subgrade layers in Cells 185 (12-in Coarse RCA) and 186 (12-in Fine RCA), respectively] exhibited higher E_{FWD} values than the Limestone and

RCA+RAP base+subbase layers [placed over Select Granular Borrow and Clay Loam subgrade layers in Cells 188 (12-in Limestone) and 189 (12-in RCA+RAP), respectively]. This was attributed to the cementation of unhydrated cement of the Coarse RCA and Fine RCA materials. In addition, higher E_{FWD} values were also attributed to rougher surfaces of the Coarse RCA and Fine RCA materials due to cement mortar (Kuo et al. 2002; Edil et al. 2012). In fact, the Fine RCA base+subbase layer [Cell 186 (12-in Fine RCA)] yielded higher E_{FWD} values than the Coarse RCA base+subbase layer [Cells 185 (12-in Coarse RCA)]. It was speculated that the unhydrated cement content of the Fine RCA material was higher than that of the Coarse RCA material due to its higher fines content (ACPA 2009). The RCA+RAP base+subbase layer [Cell 189 (12-in RCA+RAP)] showed lower E_{FWD} values than the Coarse RCA and Fine RCA base+subbase layers [Cells 185 (12-in Coarse RCA) and 186 (12-in Fine RCA), respectively]. Because of the hydrophobicity of RAP, lower absorption would be expected for the RCA+RAP material compared to the RCA materials (Edil et al. 2012; Rahardjo et al. 2010). Therefore, it was speculated that the RAP particles in the RCA+RAP material reduced the amount of water that could be in contact with the RCA particles for cementation. In the literature, RCA and RAP materials tend to exhibit higher stiffness than virgin aggregates (VAs) (Edil et al. 2012; Stolle et al. 2014; Rosa et al. 2017). Since the Limestone material was a VA, the Limestone base+subbase layer exhibited lower E_{FWD} values than the Coarse RCA, Fine RCA, and RCA+RAP base+subbase layers [Cells 185 (12-in Coarse RCA), 186 (12-in Fine RCA), and 189 (12-in RCA+RAP), respectively]. It was determined from laboratory testing that the Class 5Q Aggregate was similar to the Coarse RCA material and the Class 6 Aggregate was similar to the RCA+RAP material. Therefore, the aggregate base layers constructed with the Class 5Q Aggregate [Cells 328 (9-in LSSB - TX), 428 (9-in LSSB - TX+GT), 528 (9-in LSSB - BX+GT), 628 (9-in LSSB - BX), and 728 (9-in LSSB)] were expected to show greater stiffness than those constructed with the Class 6 Aggregate [Cells 127 (18-in LSSB) and 227 (18-in LSSB)] due to cementation and rougher surface. However, in this study, the Class 6 Aggregate base+subbase layers [Cells 127 (18-in LSSB) and 227 (18-in LSSB)] exhibited higher E_{FWD} values than the Class 5Q Aggregate base+subbase layers [Cells 328 (9-in LSSB - TX), 428 (9-in LSSB - TX+GT), 528 (9-in LSSB - BX+GT), 628 (9-in LSSB - BX), and 728 (9-in LSSB)]. For flexible pavements, higher stiffness is expected for thicker layers as a result of an improvement in the load distribution with an increase in the layer thickness (Tanyu et al. 2003). Therefore, it was concluded that 18-in LSSB layers [Cells 127 (18-in LSSB) and 227 (18-in LSSB)] performed considerably better than 9-in LSSB layers [Cells 328 (9-in LSSB - TX), 428 (9-in LSSB - TX+GT), 528 (9-in LSSB - BX+GT), 628 (9-in LSSB - BX), and 728 (9-in LSSB)] due to their higher thickness.

SUBGRADE E_{FWD}

In November 2017 (before the first freezing period) (Figure 5.66), the Sand Subgrade layers in Cells 185 (12-in Coarse RCA) and 186 (12-in Fine RCA) provided higher E_{FWD} values than the Clay Loam subgrade layers in Cells 188 (12-in Limestone) and 189 (12-in RCA+RAP). The coarser materials were prone to exhibit higher E_{FWD} values than the finer materials because of the interlocking between coarser particles (Lekarp et al. 200; Cunningham et al. 2013). The Clay Loam subgrade layers in Cells 127 (18-in LSSB) and 227 (18-in LSSB) exhibited higher E_{FWD} values than the Clay Loam subgrade layers in Cells 328 (9-in LSSB - TX), 428 (9-in LSSB - TX+GT), 528 (9-in LSSB - BX+GT), 628 (9-in LSSB - BX), and 728 (9-in LSSB). Pavement foundation layers cannot be evaluated independently since the stress distribution throughout the

pavement system significantly affects the performance of each foundation layer. Since the thickness of the 18-in LSSB layers was higher than the thickness of the 9-in LSSB layers, the stress distribution was more effective throughout the 18-in LSSB layers. Improved stress distribution in 18-in LSSB layers caused a reduction in the stresses that could reach to the Clay Loam subgrade layers underlying 18-in LSSB layers. Since fine-grained soils are prone to exhibiting stress-softening behavior, the Clay Loam subgrade layers underlying thicker LSSB layers potentially exhibited higher stiffness under FWD loading.

5.3.4.2 Falling Weight Deflectometer (FWD) Test Results in the First Thawing Period

MAXIMUM DEFLECTION

In March 2018 (in the first thawing period) (Figure 5.62), Cells 186 (12-in Fine RCA), 328 (9-in LSSB - TX), 428 (9-in LSSB - TX+GT), 528 (9-in LSSB - BX+GT), and 628 (9-in LSSB - BX) yielded slightly lower maximum deflections compared to those observed in November 2017 (before the first freezing period). Cells 185 (12-in Coarse RCA) and 728 (9-in LSSB) exhibited slightly higher maximum deflections in March 2018 (in the first thawing period) compared to those observed in November 2017 (before the first freezing period), possibly indicating that those cells were not as durable as Cells 186 (12-in Fine RCA), 328 (9-in LSSB - TX), 428 (9-in LSSB - TX+GT), 528 (9-in LSSB - BX+GT), and 628 (9-in LSSB - BX) against the first F-T period. For Cells 188 (12-in Limestone), 189 (12-in RCA+RAP), 127 (18-in LSSB), and 227 (18-in LSSB), higher maximum deflections were observed in March 2018 (in the first thawing period) compared to those observed in November 2017 (before the freezing period of 2017-2018), indicating that these cells were not as durable as the other test cells against the first F-T period.

COMPOSITE E_{FWD}

In March 2018 (in the first thawing period) (Figure 5.63), the trends observed in the composite E_{FWD} values [relative to those observed in November 2017 (before the first freezing period)] were exactly compatible with those observed in the maximum deflections [relative to those observed in November 2017 (before the first freezing period)]. Higher maximum deflections yielded lower composite E_{FWD} values. On the contrary, lower maximum deflections yielded higher composite E_{FWD} values. This was due to the inversely proportional relationship of composite E_{FWD} with the maximum deflections under the same load [9,000 lb (40 kN)] based on Equation (5.5).

ASPHALT E_{FWD}

In March 2018 (in the first thawing period) (Figure 5.64), lower asphalt E_{FWD} values were observed in all the test cells (except Cell 728) compared to those observed in November 2017 (before the first freezing period). This was possibly due to the softening of the asphalt layers at relatively higher temperatures in March 2018 (in the first thawing period) compared to those in November 2017 (before the first freezing period).

BASE+SUBBASE E_{FWD}

In March 2018 (in the first thawing period) (Figure 5.65), considerably higher E_{FWD} values were observed in the Coarse RCA and Fine RCA base+subbase layers [Cells 185 (12-in Coarse RCA) and 186 (12-in Fine RCA), respectively] compared to those observed in November 2017 (before the first freezing period). For those cells, it was speculated that the cementation of Coarse RCA and Fine RCA materials overcame the negative effects of the first F-T period. More traffic loads were transferred to the Coarse RCA and Fine RCA base+subbase layers [Cells 185 (12-in Coarse RCA) and 186 (12-in Fine RCA), respectively] due to the softening of the asphalt layers. Aggregates generally show a stress-hardening behavior due to the reorientation of the particles into a denser state under higher loads (Ceylan et al. 2009; White et al. 2018). However, aggregates can exhibit decreasing stiffness values after reaching the breakpoint stress due to the presence of underlying softer or wetter subgrade conditions (White et al. 2018). Therefore, it was also speculated that the Coarse RCA and Fine RCA base+subbase layers [Cells 185 (12-in Coarse RCA) and 186 (12-in Fine RCA), respectively] exhibited stress-hardening behavior since they were on the Sand Subgrade layers (Ceylan et al. 2009; White et al. 2018). On the contrary, the Limestone and RCA+RAP base+subbase layers [Cells 188 (12-in Limestone) and 189 (12-in RCA+RAP), respectively] did not show higher E_{FWD} values in March 2018 (in the first thawing period) compared to those observed in November 2017 (before the first freezing period). Limestone in the aggregate base layer of Cell 188 (12-in Limestone) was a virgin aggregate and did not contain any RCA and no cementation occurred. For the RCA+RAP material in the aggregate base layer of Cell 189 (12-in RCA+RAP), the activity of the cementation of RCA was possibly low due to the presence of hydrophobic RAP material. For Cells 127 (18-in LSSB) and 227 (18-in LSSB), the Class 6 Aggregate base+subbase layers exhibited lower E_{FWD} values in March 2018 (in the first thawing period) compared to those observed in November 2017 (before the first freezing period). As mentioned previously, the Class 6 Aggregate was similar to the RCA+RAP material. Therefore, it was speculated that the RCA material in the Class 6 Aggregate matrix exhibited a lower rate of cementation compared to the Coarse RCA and Fine RCA materials. In addition, the Class 6 Aggregate base+subbase layers [Cells 127 (18-in LSSB) and 227 (18-in LSSB)] may have shown stress-softening behavior after the breakpoint stress under the relatively softer asphalt layers. The Class 5Q Aggregate base+subbase layers in Cells 328 (9-in LSSB - TX), 428 (9-in LSSB - TX+GT), 528 (9-in LSSB - BX+GT), and 628 (9-in LSSB - BX) did not exhibit considerable changes in March 2018 (in the first thawing period) compared to those observed in November 2017 (before the first freezing period). However, for the Class 5Q Aggregate base+subbase layer in Cell 728 (9-in LSSB), slightly lower E_{FWD} values were observed in March 2018 (in the first thawing) compared to those observed in November 2017 (before the first freezing period). Overall, it was speculated that the cementation of the Class 5Q Aggregate (as mentioned previously, the Class 5Q Aggregate was similar to the Coarse RCA material) and effective drainage provided by 9-in LSSB layer neutralized the negative effects of the first F-T period. In addition, it was observed that the use of geosynthetics in Cells 328 (9-in LSSB - TX), 428 (9-in LSSB - TX+GT), 528 (9-in LSSB - BX+GT), and 628 (9-in LSSB - BX) contributed to the durability of the test cells against freezing and thawing. It was speculated that the use of geosynthetics reduced the stresses acting on the Clay Loam subgrade layers by improving the distribution of the loads coming from the Class 5Q Aggregate base+subbase layers and this improved the stiffness (fine-grained materials are expected to show stress-softening behavior; therefore, a decrease in the stress applied to fine-grained subgrade

layers tends to cause an improvement in the stiffness of such subgrade layers) and durability of the Clay Loam subgrade layers. Improved stiffness and durability of the Clay Loam subgrade layers are expected to improve the durability of the pavement sublayers overlying the subgrade layers.

SUBGRADE E_{FWD}

In March 2018 (in the first thawing period) (Figure 5.66), the Sand Subgrade layers in Cells 185 (12-in Coarse RCA) and 186 (12-in Fine RCA) and the Clay Loam layers in Cells 188 (12-in Limestone) and 189 (12-in RCA+RAP) yielded higher E_{FWD} values compared to those observed in November 2017 (before the first freezing period). The Clay Loam subgrade layers in Cells 127 (18-in LSSB) and 227 (18-in LSSB) exhibited lower E_{FWD} values than those observed in November 2017 (before the first freezing period). The Clay Loam subgrade layers of Cells 328 (9-in LSSB - TX), 428 (9-in LSSB - TX+GT), and 728 (9-in LSSB) did not exhibit significant differences in the E_{FWD} values in March 2018 (in the first thawing period) compared to those observed in November 2017 (before the first freezing period). On the other hand, the Clay Loam subgrade layers of Cells 528 (9-in LSSB - BX+GT) and 628 (9-in LSSB - BX) yielded higher E_{FWD} values in March 2018 (in the first thawing period) compared to those observed in November 2017 (before the first freezing period). Explaining the behaviors of subgrade layers is considerably complex because none of the pavement layers could be considered by itself with the tests conducted in this study. Observing lower or higher subgrade stiffness due to freezing and thawing could be due to several factors. One of these reasons could be the actual softening or hardening of the subgrade layer under loading conditions. The other reason could be the softening or hardening of base+subbase layer. When a base+subbase layer softens, the stress distribution throughout the layer is prone to worsen. Fine-grained soils tend to exhibit stress-softening behavior under insufficient stress distribution associated with the soft upper layer(s). When a fine-grained subgrade layer receives higher stresses from the base+subbase layer, the subgrade layer tends to exhibit lower stiffness. On the other hand, when the fine-grained subgrade layer receives fewer stresses from the base+subbase layer due to the stiffening of the base+subbase layer, the subgrade layer is prone to exhibit higher stiffness.

5.3.4.3 Falling Weight Deflectometer (FWD) Test Results in the Second Thawing Period

MAXIMUM DEFLECTION

In March 2019 (in the second thawing period) (Figure 5.62) (the VWC values determined for the second thawing period are summarized in Appendix AE), overall, all of the test cells [except Cell 127 (18-in LSSB)] exhibited higher maximum deflections than those observed in March 2018 (in the first thawing period). The increases in the maximum deflections from March 2018 (in the first thawing period) to March 2019 (in the second thawing period) were higher for Cells 185 (12-in Coarse RCA), 186 (12-in Fine RCA), 188 (12-in Limestone), and 189 (12-in RCA+RAP), possibly indicating that those test cells were not as durable as the other test cells against the second F-T period. For Cell 227 (18-in LSSB), the maximum deflections observed in March 2019 (in the second thawing period) were only slightly higher (almost equal) than those observed in March 2018 (in the first thawing period). Therefore, it was concluded that Cells 127 (18-in LSSB) and 227 (18-in LSSB) were more durable than the other cells against the second F-T period. It was speculated that the main contributors to the observed performance of Cells 127 (18-in

LSSB) and 227 (18-in LSSB) were effective drainage and relatively higher thickness of the 18-in LSSB layers (compared to other subbase layers). Higher stiffness is expected for thicker layers as a result of an improvement in the load distribution with an increase in the layer thickness due to the strain effect (Tanyu et al. 2003).

COMPOSITE E_{FWD}

In March 2019 (in the second thawing period) (Figure 5.63), the trends observed in the composite E_{FWD} values [relative to those observed in March 2018 (in the first thawing period)] were exactly compatible with those observed in the maximum deflections [relative to those observed in March 2018 (in the first thawing period)]. Higher maximum deflections yielded lower composite E_{FWD} values. On the contrary, lower maximum deflections yielded higher composite E_{FWD} values. This was due to the inversely proportional relationship of composite E_{FWD} with the maximum deflections under the same load [9,000 lb (40 kN)] based on Equation (5.5).

ASPHALT E_{FWD}

In March 2019 (in the second thawing period) (Figure 5.64), lower asphalt E_{FWD} values were observed in all the test cells compared to those observed in March 2018 (in the first thawing period). This result was possibly due to the softening of the asphalt layers at relatively higher temperatures in March 2019 (in the second thawing period) compared to March 2018 (in the first thawing).

BASE+SUBBASE E_{FWD}

In March 2019 (in the second thawing period) (Figure 5.65), the Coarse RCA, Fine RCA, Limestone, and RCA+RAP base+subbase layers in Cells 185 (12-in Coarse RCA), 186 (12-in Fine RCA), 188 (12-in Limestone), and 189 (12-in RCA+RAP), respectively, yielded lower E_{FWD} values than those observed in March 2018 (in the first thawing period). It was speculated that no more cementation of the Coarse RCA and Fine RCA materials continued in the second thawing period. Therefore, the Coarse RCA and Fine RCA base+subbase layers [Cells 185 (12-in Coarse RCA) and 186 (12-in Fine RCA), respectively] experienced a reduction in stiffness during the second F-T period. However, the E_{FWD} values of the Coarse RCA and Fine RCA base+subbase layers [Cells 185 (12-in Coarse RCA) and 186 (12-in Fine RCA), respectively] were still higher than those observed for the Limestone and RCA+RAP base+subbase layers [Cells 188 (12-in Limestone) and 189 (12-in RCA+RAP), respectively] in March 2019 (in the second thawing period). In March 2019 (in the second thawing period), the E_{FWD} values of the Class 6 Aggregate base+subbase layers [Cells 127 (18-in LSSB) and 227 (18-in LSSB)] and the Class 5Q Aggregate base+subbase layers [Cells 328 (9-in LSSB - TX), 428 (9-in LSSB - TX+GT), 528 (9-in LSSB - BX+GT), 628 (9-in LSSB - BX), and 728 (9-in LSSB)] were higher than or similar to those observed in March 2018 (in the first thawing period). While the Class 6 Aggregate base+subbase layers [Cells 127 (18-in LSSB) and 227 (18-in LSSB)] were not durable against the first F-T period, they were more durable against the second F-T period compare to the first F-T period. In general, the most drastic decreases in the stiffness of soils/aggregates are observed after the first F-T cycle, and the soils/aggregates become more stable as F-T cycles continue over time (Coban 2017). It was speculated that such a mechanism was observed in

the Class 6 Aggregate base+subbase layers [Cells 127 (18-in LSSB) and 227 (18-in LSSB)]. In addition, it was speculated that 18-in LSSB layers in Cells 127 (18-in LSSB) and 227 (18-in LSSB) provided durability against F-T cycles in the long-term due to effective drainage and better load distribution due to relatively higher thickness of the 18-in LSSB layers (compared to other subbase layers) (Tanyu et al. 2003). The Class 5Q Aggregate base+subbase layers in Cells 328 (9-in LSSB - TX), 428 (9-in LSSB - TX+GT), 528 (9-in LSSB - BX+GT), 628 (9-in LSSB - BX), and 728 (9-in LSSB) were also durable against the second F-T period (those layers were also durable against the first F-T period).

SUBGRADE E_{FWD}

In March 2019 (in the second thawing period) (Figure 5.66), no consistent trends in the E_{FWD} values were observed. While the Sand Subgrade layer in Cell 185 (12-in Coarse RCA) exhibited similar E_{FWD} values in March 2019 (in the second thawing period) compared to those observed in March 2018 (in the first thawing period), the Sand Subgrade layer in Cell 186 (12-in Fine RCA) yielded higher E_{FWD} values in March 2019 (in the second thawing period) compared to those observed in March 2018 (in the first thawing period). While the Clay Loam subgrade layer in Cell 188 (12-in Limestone) exhibited lower E_{FWD} values in March 2019 (in the second thawing period) compared to those observed in March 2018 (in the first thawing period), the Clay Loam subgrade layer in Cell 189 (12-in RCA+RAP) yielded higher E_{FWD} values in March 2019 (in the second thawing period) compared to those observed in March 2018 (in the first thawing period). The Clay Loam subgrade layers in Cells 328 (9-in LSSB - TX), 428 (9-in LSSB - TX+GT), 528 (9-in LSSB - BX+GT), 628 (9-in LSSB - BX), and 728 (9-in LSSB) exhibited relatively similar results in March 2019 (in the second thawing period) compared to those observed in March 2018 (in the first thawing period).

5.3.4.4 Falling Weight Deflectometer (FWD) Test Results After the Second Thawing Period

MAXIMUM DEFLECTION

In July 2019 (after the second thawing period) (Figure 5.62), Cells 185 (12-in Coarse RCA), 186 (12-in Fine RCA), and 189 (12-in RCA+RAP) exhibited lower maximum deflections than those observed in March 2019 (in the second thawing period). On the other hand, Cells 188 (12-in Limestone), 127 (18-in LSSB), 227 (18-in LSSB), 328 (9-in LSSB - TX), 428 (9-in LSSB - TX+GT), 528 (9-in LSSB - BX+GT), 628 (9-in LSSB - BX), and 728 (9-in LSSB) exhibited higher maximum deflections in July 2019 (after the second thawing) than those observed in March 2019 (in the second thawing period). The increases in the maximum deflections from March 2019 (in the second thawing period) to July 2019 (after the second thawing period) were higher for Cells 328 (9-in LSSB - TX), 428 (9-in LSSB - TX+GT), 528 (9-in LSSB - BX+GT), 628 (9-in LSSB - BX), and 728 (9-in LSSB).

COMPOSITE E_{FWD}

In July 2019 (after the second thawing period) (Figure 5.63), the trends observed in the composite E_{FWD} values [relative to those observed in March 2019 (in the second thawing period)] were exactly compatible with those observed in the maximum deflections [relative to those observed in March 2019 (in the second thawing period)]. Higher maximum deflections yielded lower composite E_{FWD} values. On

the contrary, lower maximum deflections yielded higher composite E_{FWD} values. This was due to the inversely proportional relationship of composite E_{FWD} with the maximum deflections under the same load [9,000 lb (40 kN)] based on Equation (5.5).

ASPHALT E_{FWD}

In July 2019 (after the second thawing period) (Figure 5.64), considerably lower asphalt E_{FWD} values were observed in all of the test cells compared to those observed in March 2019 (in the second thawing period). This was possibly due to the softening of the asphalt layers at relatively higher temperatures in July 2019 (after the second thawing period) compared to those observed in March 2019 (in the second thawing period).

BASE+SUBBASE E_{FWD}

In July 2019 (after the second thawing period) (Figure 5.65), all of the base+subbase layers exhibited higher E_{FWD} values than those observed in March 2019 (in the second thawing period). The increases in the E_{FWD} values were considerably higher for the Coarse RCA and Fine RCA base+subbase layers [Cells 185 (12-in Coarse RCA) and 186 (12-in Fine RCA), respectively)]. As the asphalt layers became softer at higher temperatures, more traffic loads were transferred to the Coarse RCA and Fine RCA base+subbase layers [Cells 185 (12-in Coarse RCA) and 186 (12-in Fine RCA), respectively)], and higher E_{FWD} values were observed in both base+subbase layers due to their stress-hardening behavior. The Fine RCA base+subbase layer [Cell 186 (12-in Fine RCA)] exhibited higher E_{FWD} values than the Coarse RCA base+subbase layer [Cell 185 (12-in Coarse RCA)]. As seen in Figure 5.64, the asphalt E_{FWD} values of Cell 186 (12-in Fine RCA) were lower than those of Cell 185 (12-in Coarse RCA). The Fine RCA base+subbase layer [Cell 186 (12-in Fine RCA)] experienced greater traffic loads than the Coarse RCA base+subbase layer [Cell 185 (12-in Coarse RCA)]. The Fine RCA base+subbase layer [Cell 186 (12-in Fine RCA) exhibited higher E_{FWD} values than the Coarse RCA base+subbase layer [Cell 185 (Coarse RCA)] due to the stress-hardening behavior. For the other base+subbase layers, it was speculated that the base+subbase layers densified and became stiffer over time under the traffic provided by the MnROAD truck [80 kip (36.3 Mg)].

SUBGRADE E_{FWD}

In July 2019 (after the second thawing period) (Figure 5.66), overall, the E_{FWD} values of the subgrade layers were lower than or similar to those observed in March 2019 (in the second thawing period). The most considerable difference was observed in the Sand Subgrade layer in Cell 186 (12-in Fine RCA). The Sand Subgrade layer in Cell 186 (12-in Fine RCA) exhibited considerably lower E_{FWD} in July 2019 (after the second thawing period) than those observed in March 2019 (in the second thawing period).

In conclusion, according to the results observed from November 2017 (before the first freezing period) to July 2019 (after the second thawing period), Cells 185 (12-in Coarse RCA) and 186 (12-in Fine RCA), constructed over Sand Subgrade layers, performed considerably better than the other cells. After approximately two years, Cells 185 (12-in Coarse RCA) and 186 (12-in Fine RCA) exhibited lower maximum deflections and higher composite E_{FWD} values. In fact, Cell 186 (12-in Fine RCA) performed

better than Cell 185 (12-in Coarse RCA) as it exhibited relatively lower maximum deflections and higher composite E_{FWD} values compared to Cell 185 (12-in Coarse RCA). This could indicate that the Fine RCA material would be a better option to construct aggregate base layers than the Coarse RCA material. After approximately two years, Cell 189 (12-in RCA+RAP) exhibited lower maximum deflections and higher composite E_{FWD} values than Cell 188 (12-in Limestone) (both test cells were constructed over Clay Loam subgrade layers). Overall, these results indicate that the Sand Subgrade layers in Cells 185 (12-in Coarse RCA) and 186 (12-in Fine RCA) performed better than the Clay Loam subgrade layers in Cells 188 (12-in Limestone) and 189 (12-in RCA+RAP). Although there were two different subgrade layers [Sand Subgrade layers in Cells 185 (12-in Coarse RCA) and 186 (12-in Fine RCA) and Clay Loam subgrade layers in Cells 188 (12-in Limestone) and 189 (12-in RCA+RAP)], the following material selection can be recommended for building aggregate base layers from the most preferred to least preferred, based on the FWD test results: (1) Fine RCA, (2) Coarse RCA, (3) RCA+RAP, and (4) Limestone. However, further investigation may be needed to verify this recommendation. While this recommendation about the material selection was made based on the first two-year performance of the built cells, it could be said that the two-year performance of the built cells would reflect the potential performance trends of the cells in the following years based on a study performed by Titi et al. (2019). Lastly, Cells 127 (18-in LSSB) and 227 (18-in LSSB) exhibited lower deflections and higher composite E_{FWD} values than Cells 328 (9-in LSSB - TX), 428 (9-in LSSB - TX+GT), 528 (9-in LSSB - BX+GT), 628 (9-in LSSB - BX), and 728 (9-in LSSB) and it could be indicated that thicker LSSB layers should be built in pavement foundation systems. This conclusion is compatible with the recommendations provided by IDOT (IDOT 2015) and WisDOT (WisDOT 2019) regarding the design thickness of the layers overlying subgrade layers. In brief, having strong and well-performing aggregate base, subbase, and subgrade layers is essential for overall pavement performance. From the results obtained from this field study, it can be concluded that constructing Fine RCA base and sufficiently thick LSSB layers together would maximize the overall pavement performance.

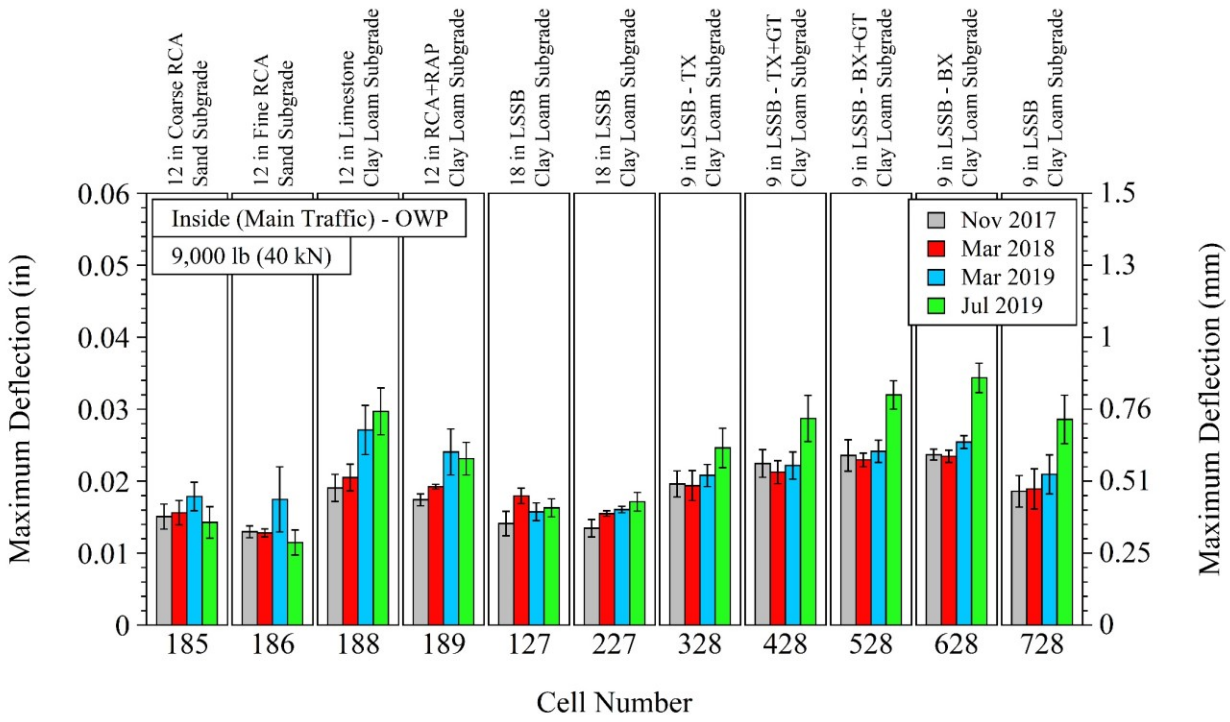

Figure 5.62. Summary of maximum deflections of test cells under 9,000 lb (40 kN) load (error bars represent one standard deviation of data)

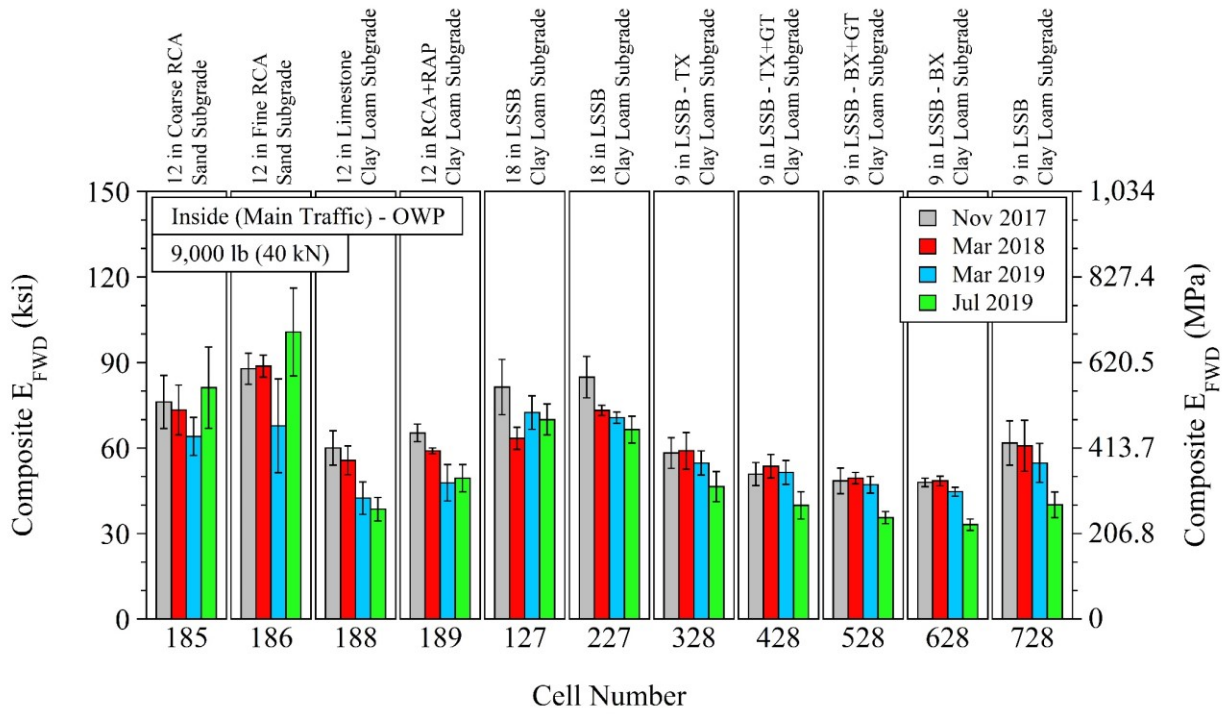

Figure 5.63. Summary of composite falling weight deflectometer (FWD) elastic modulus (E_{FWD}) of test cells under 9,000 lb (40 kN) load (error bars represent one standard deviation of data)

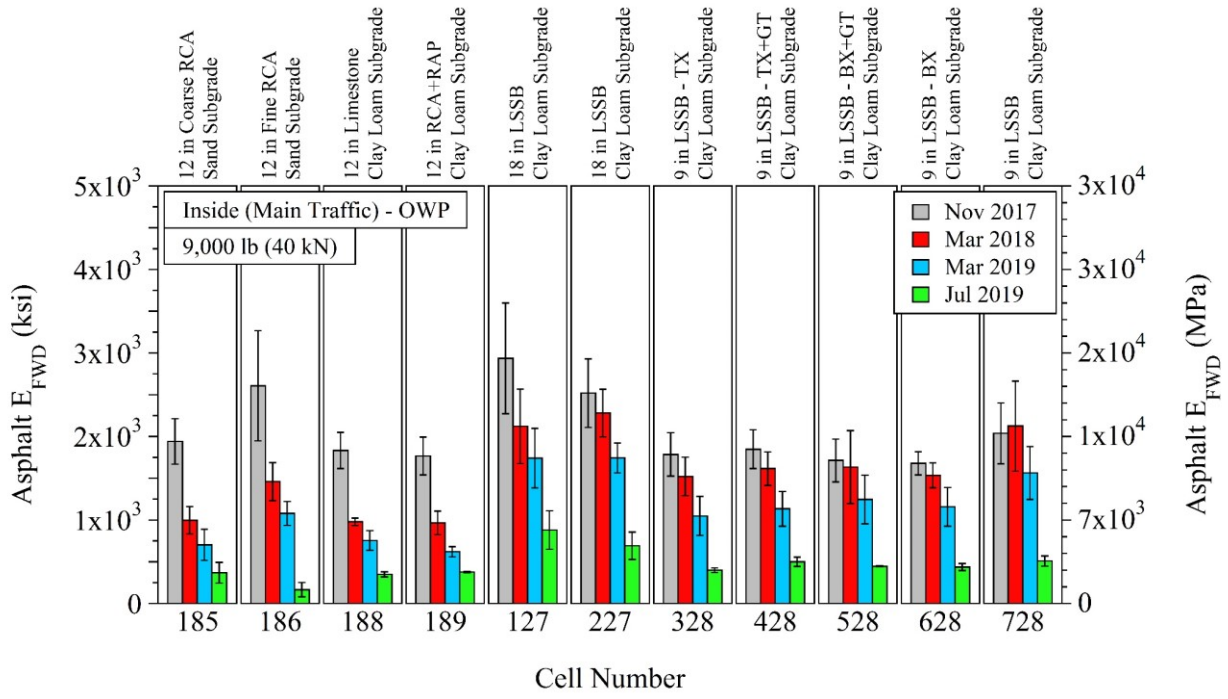

Figure 5.64. Summary of asphalt falling weight deflectometer (FWD) elastic modulus (E_{FWD}) of test cells under 9,000 lb (40 kN) load (error bars represent one standard deviation of data)

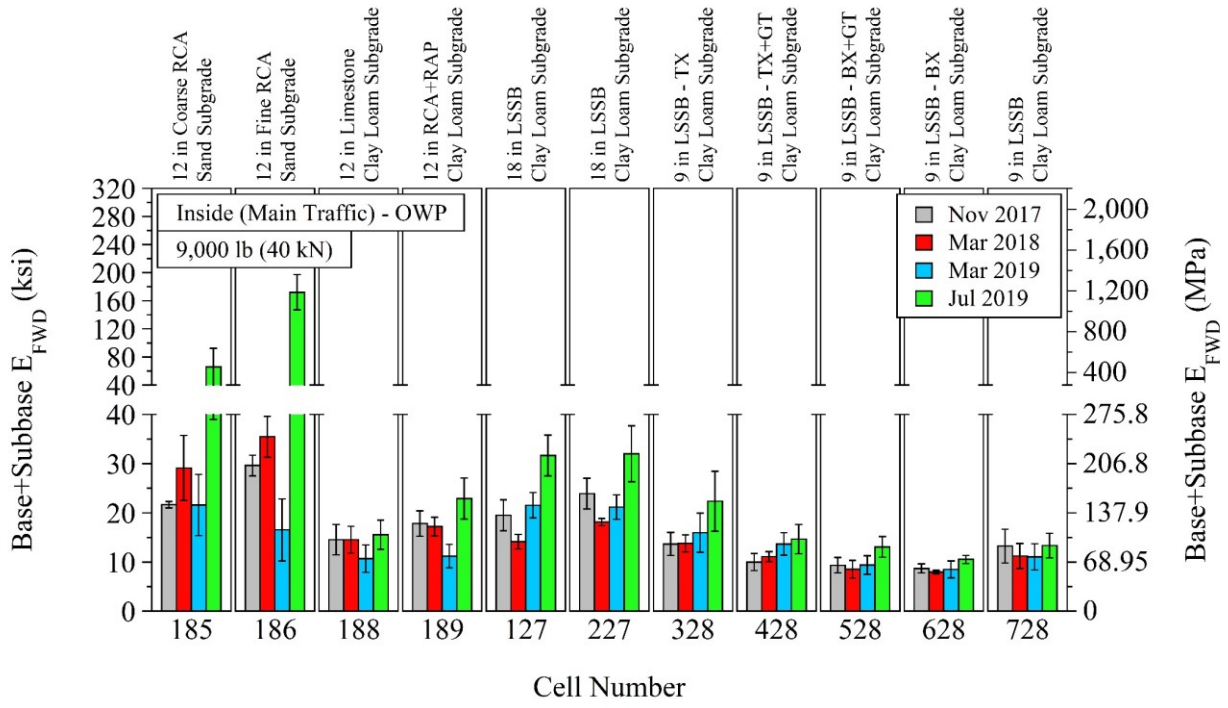

Figure 5.65. Summary of base+subbase falling weight deflectometer (FWD) elastic modulus (E_{FWD}) of test cells under 9,000 lb (40 kN) load (error bars represent one standard deviation of data)

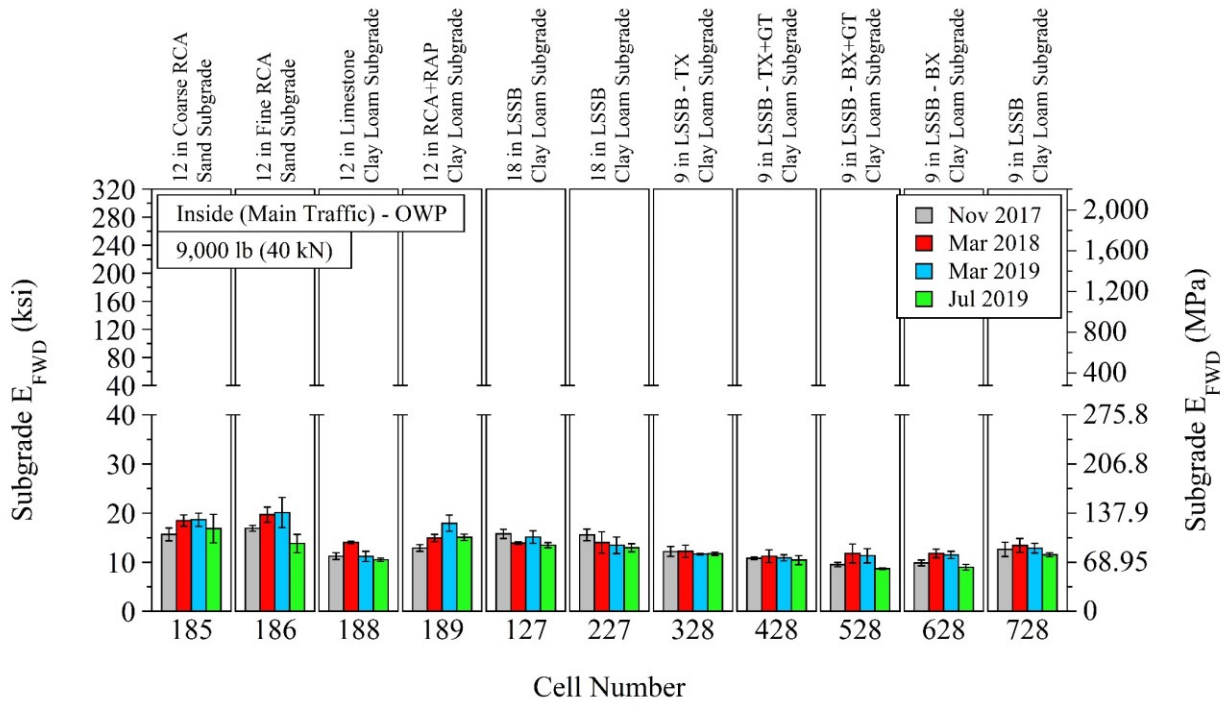

Figure 5.66. Summary of subgrade falling weight deflectometer (FWD) elastic modulus (E_{FWD}) of test cells under 9,000 lb (40 kN) load (error bars represent one standard deviation of data)

5.4 FROST HEAVE AND THAW SETTLEMENT MEASUREMENTS

During the freezing period, water freezes and turns into ice with an increase (around 10%) in its volume, and this event causes frost heave in the pavement structure. On the contrary, during the thawing period, ice melts with a reduction in its volume and this event causes thaw settlement in the pavement structure. Seasonal frost heave and thaw settlement can cause pavement distresses that decrease the long-term performance and the service life of pavements.

Several stations were selected for each test cell and five test points were marked on each station before taking elevation measurements. The same points were tested at different dates. Figure 5.67 is an example that shows the locations of the test points for two stations in Cell 185 (12-in Coarse RCA). Leveling readings were taken from the five test points on each station and elevation profiles were plotted. Figure 5.68 is an example that shows the elevation profiles of one station in Cell 185 (12-in Coarse RCA) at different dates. Elevation profiles for all of the test cells are provided in Appendix AF. The elevation changes due to frost heave and thaw settlement were evaluated from the elevation profiles (no statistical analysis was performed in this report). In Figure 5.69, the elevation measurements taken on December/4/2017 (the early stage of the first freezing period) were considered as zero (reference elevation), and the relative elevation measurements taken on December/18/2017 (the later stage of the first freezing period compared to the date of December/4/2017) and March/21/2018 (the final stage of the first thawing period or after fully thawing) are summarized and evaluated visually.

On December/18/2017 (the later stage of the first freezing period compared to the date of December/4/2017), no considerable frost heave was observed in Cells 185 (12-in Coarse RCA), 189 (12-in RCA+RAP), 127 (18-in LSSB), 227 (18-in LSSB), 428 (9-in LSSB - TX+GT), 528 (9-in LSSB - BX+GT), 628 (9-in LSSB - BX), and 728 (9-in LSSB) (Figure 5.69). On the other hand, Cells 186 (12-in Fine RCA), 188 (12-in Limestone), and 328 (9-in LSSB - TX) exhibited relatively more considerable frost heave (Figure 5.69). These differences could be related to the amount of water available for freezing. The freezing of a higher amount of water can cause greater frost heave than the freezing of a less amount of water. In addition, due to different thermal properties of the aggregate base, subbase, and subgrade materials, the materials in the test cells could have different freezing levels.

On March/21/2018 (the final stage of the first thawing period or after thawing), the greatest thaw settlements were observed in Cells 185 (12-in Coarse RCA) and 186 (12-in Fine RCA) (Figure 5.69), and this could be related to the water absorption capacities of Coarse RCA and Fine RCA materials. It was determined from laboratory testing that the water absorptions of Coarse RCA and Fine RCA materials were higher than those of the other materials. For Cells 185 (12-in Coarse RCA) and 186 (12-in Fine RCA), it was speculated that the thawing of higher amounts of water in the Coarse RCA and Fine RCA base layers yielded greater thaw settlements. Cell 188 (12-in Limestone) yielded less thaw settlement than Cell 189 (12-in RCA+RAP) (Figure 5.69). From laboratory testing, it was determined that water absorption of Limestone was lower than that of RCA+RAP material. Therefore, it was speculated that the Limestone base layer [Cell 188 (12-in Limestone)] yielded less thaw settlement than the RCA+RAP base layer [Cell 189 (RCA+RAP)] due to the thawing of fewer amounts of water. Although the thaw settlements of Cells 127 (18-in LSSB) and 227 (18-in LSSB) were expected to be lower due to good drainage properties of 18-in LSSB layers, considerable thaw settlements were observed in those test cells (Figure 5.69). The lowest thaw settlements were observed in Cells 428 (9-in LSSB - TX+GT), 528 (9-in LSSB - BX+GT), 628 (9-in LSSB - BX), and 728 (9-in LSSB) (Figure 5.69). For Cell 328 (9-in LSSB - TX), the elevations recorded on March/21/2018 (the final stage of the first thawing period or after fully thawing) were higher than those recorded on December/18/2017 (the later stage of the first freezing period compared to the date of December/4/2017) (Figure 5.69). This result was attributed to an experimental error. Overall, it was speculated that the effective drainage provided by 9-in LSSB layers decreased frost heave and thaw settlement.

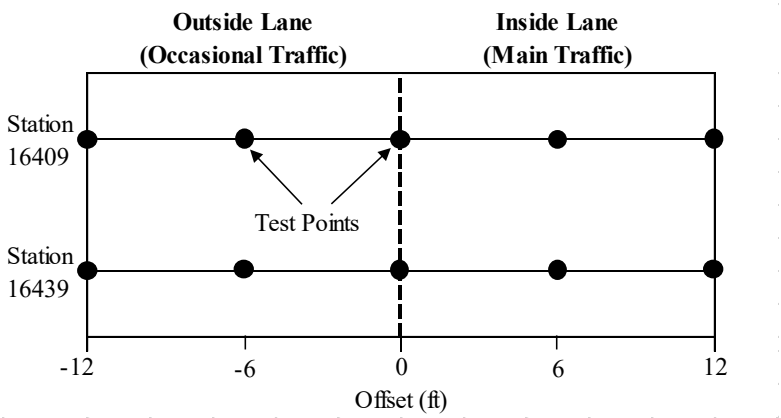

Figure 5.67. Locations of test points for two stations in Cell 185 (12-in Coarse RCA)

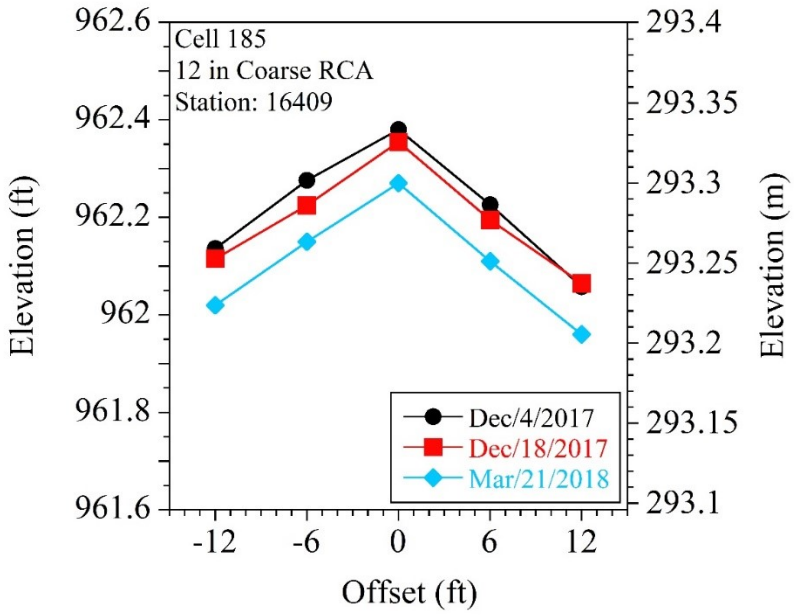

Figure 5.68. Elevation profiles of one station in Cell 185 (12-in Coarse RCA) at different dates

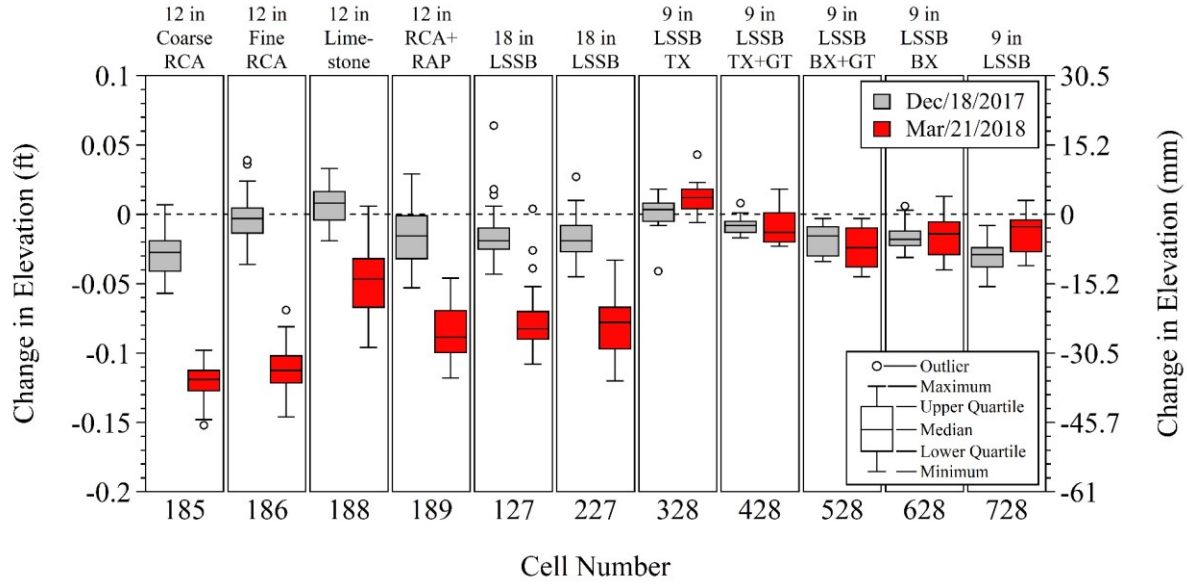

Figure 5.69. Summary of changes in elevations of test cells

5.5 RUTTING MEASUREMENTS

Rutting measurements were taken by using an automated laser profile system (ALPS) (MnDOT 2003; MnDOT 2009b) for each lane at 50 ft intervals (Figure 5.70). For the ALPS measurements, the ALPS beam [the length of the beam was 12 ft 10 in (3.9 m)] was centered on the lane by locating it between two previously marked paint marks. The beam was stationary while testing was conducted, and 616 data points were collected for each test. Since the width of each lane was 12 ft (3.7 m), which was 10 in (25.4

cm) shorter than the beam length [12 ft 10 in (3.9 m)], 5 in (12.7 cm) from the other lane and 5 in (12.7 cm) from the shoulder were also captured during testing. The ALPS data was then analyzed by using a macro in Excel that generated a digital pavement lane profile for each test and smoothed the data by using a 16-point moving average. The readings were adjusted to eliminate extreme outlying data points by the macro, and straight edges were simulated for the inside wheel path (IWP) and OWP of the generated pavement profile (Figure 5.71). Then, the maximum rut depths were determined by taking the differences between the simulated straight edges and the smoothed digital pavement profiles.

Figure 5.70. Automated laser profile system (ALPS) (MnDOT 2003)

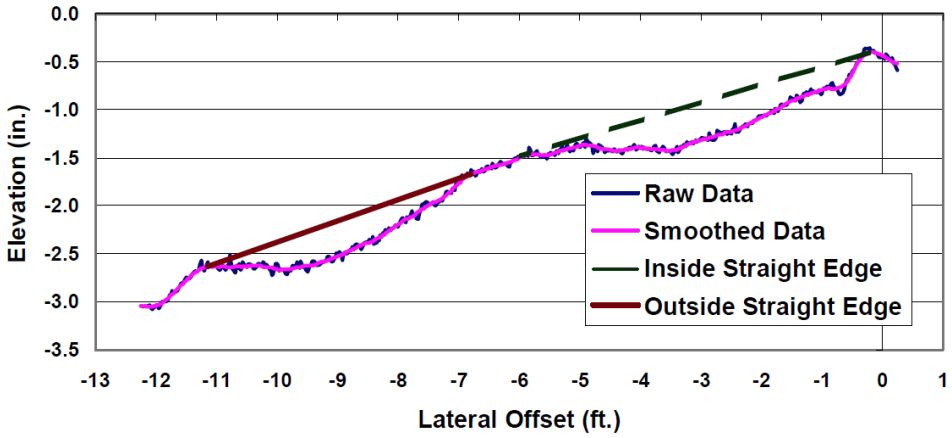

Figure 5.71. Automated laser profile system (ALPS) rutting data (MnDOT 2003)

It was observed in several test results that the macro was not able to simulate straight edges on the IWP or OWP. In addition, the digital separation of the IWP and OWP could not be made for several test cells due to relatively higher rut depths throughout the lane. Therefore, the rut depths are not summarized separately for the IWP and OWP of one lane hereinafter to overcome such problems. The rut depths are summarized simply for the inside lane (main traffic) and outside lane (occasional traffic).

For each test cell, the rut depths observed in the inside lane (main traffic) were higher than those observed in the outside lane (occasional traffic). Since the inside lane (main traffic) was subjected to more traffic [provided by the MnROAD truck weighing 80 kip (36.3 Mg)] than the outside lane

(occasional traffic), it was expected to observe higher rutting in the inside lane (main traffic). It was also concluded that the rut depths became more stable as time progressed. Figure 5.72 is an example that shows the rut depth measurements for Cell 428 (9-in LSSB - TX+GT). All of the rut depth measurements for the test cells are provided in Appendix AG.

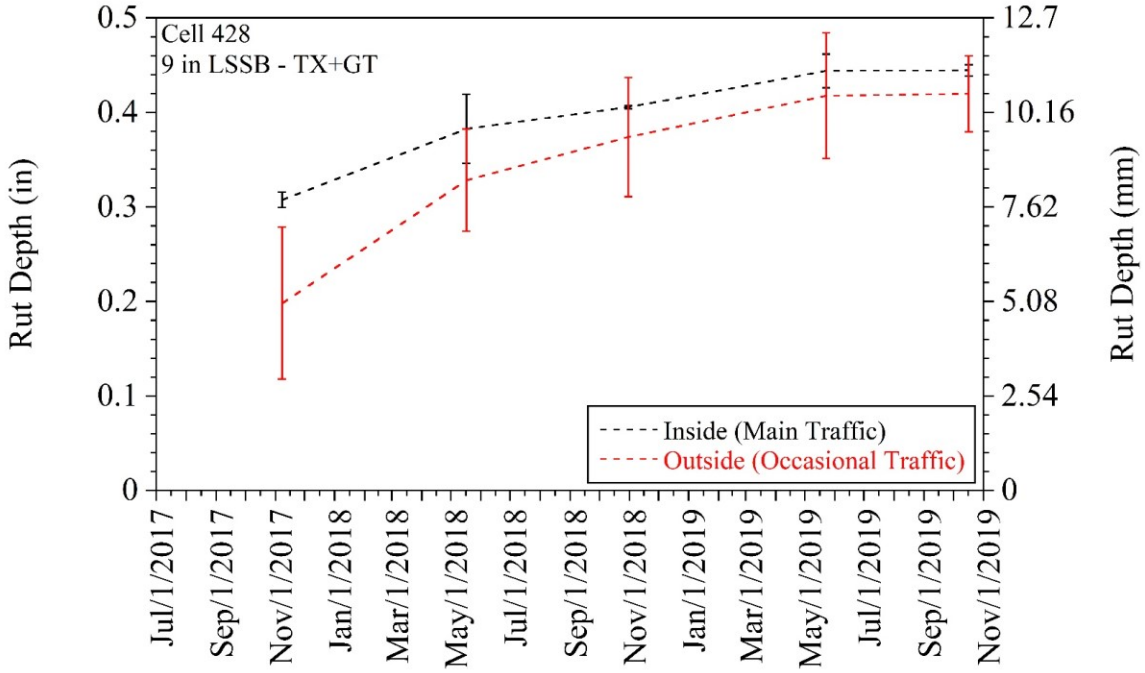

Figure 5.72. Rut depth measurements for Cell 428 (9-in LSSB - TX+GT) (error bars represent one standard deviation of data)

A summary of the rut depths observed in the inside lane (main traffic) of the test cells is provided in Figure 5.73. Overall, Cells 328 (9-in LSSB - TX), 428 (9-in LSSB - TX+GT), 528 (9-in LSSB - BX+GT), and 628 (9-in LSSB - BX) exhibited higher rut depths than the other cells. It was speculated that 9-in LSSB layers could not be compacted properly due to the nature of the large stones and relatively lower thickness of 9-in LSSB layers compared to 18-in LSSB layers in Cells 127 (18-in LSSB) and 227 (18-in LSSB). In addition, the Class 5Q Aggregate base layers in Cells 328 (9-in LSSB - TX), 428 (9-in LSSB - TX+GT), 528 (9-in LSSB - BX+GT), and 628 (9-in LSSB - BX) was not compacted adequately. In fact, Cells 328 (9-in LSSB - TX) and 628 (9-in LSSB BX) exhibited lower rut depths than Cells 428 (9-in LSSB - TX+GT) and 528 (9-in LSSB - BX+GT). As determined in Chapter 3, lower in-situ dry unit weight values were observed for the Class 5Q Aggregate base layers in Cells 428 (9-in LSSB - TX+GT) and 528 (9-in LSSB - BX+GT) compared to those observed in Cells 328 (9-in LSSB - TX) and 628 (9-in LSSB - BX). Thus, it resulted in higher rutting values for Cells 428 (9-in LSSB - TX+GT) and 528 (9-in LSSB - BX+GT) [compared to Cells 328 (9-in LSSB - TX) and 628 (9-in LSSB - BX)]. The lowest rut depths were observed in Cell 728 (9-in LSSB). Cells 185 (12-in Coarse RCA), 186 (12-in Fine RCA), 127 (18-in LSSB), and 227 (18-in LSSB) exhibited similar rut depths which were lower than those observed in Cells 188 (12-in Limestone) and 189 (12-in RCA+RAP). Cell 188 (12-in Limestone) exhibited higher rut depths than Cell 189 (12-in RCA+RAP).

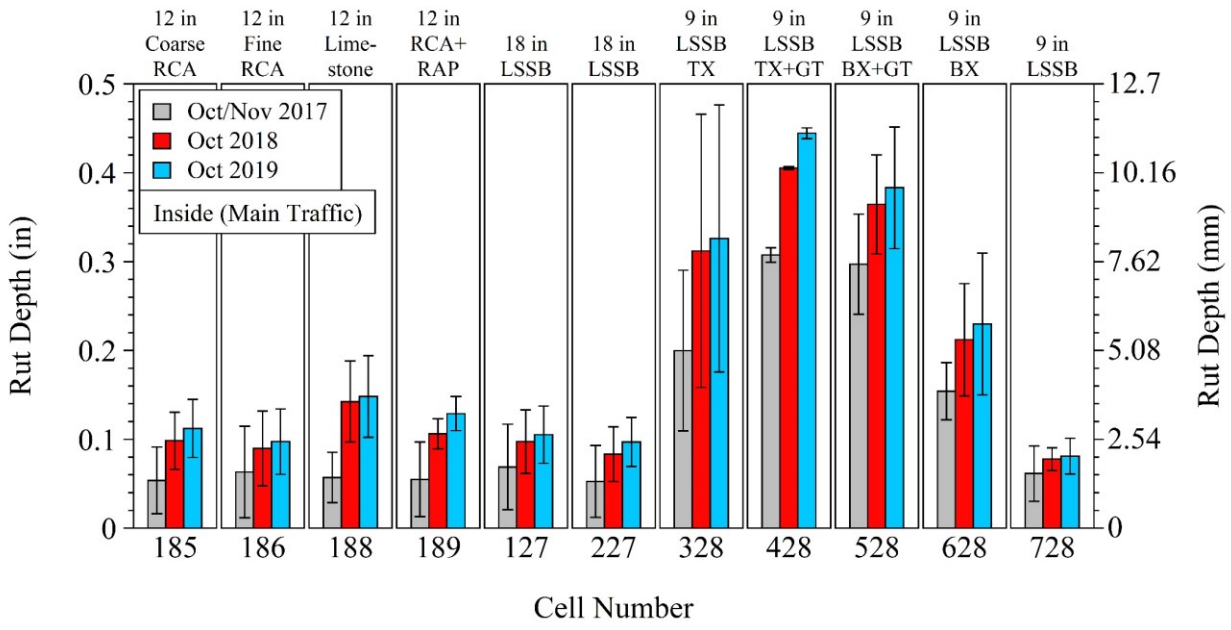

Figure 5.73. Summary of rut depth measurements for test cells (error bars represent one standard deviation of data)

5.6 INTERNATIONAL ROUGHNESS INDEX (IRI) MEASUREMENTS

The international roughness index (IRI) is a standard measure of pavement smoothness and ride quality (Akkari and Izevbekhai 2012). The IRI measurements were taken by a lightweight internal surface analyzer (LISA) profiler mounted on a utility vehicle (Figure 5.74) (MnDOT 2009c). The LISA profiler measured the amount of vertical rise over a horizontal distance [tire pressure = 10 psi (69 kPa)] [vehicle speed = 10-12 mph (16-19 kph)] (MnDOT 2009c). The profiler contained two laser sources on the two sides of the vehicle. One of the lasers took continuous profile measurements over a 4 in path. The second laser measured three discrete profiles across the 4 in path. The IRI was calculated from the data obtained by the lasers (Akkari and Izevbekhai 2012).

The FHWA describes condition criteria for different IRI values (Table 5.6). While the IRI values lower than 2.68 m/km (169.8 in/mile) are acceptable for the ride quality, the values greater than 2.68 m/km (169.8 in/mile) are considered unacceptable. Overall, by considering all of the test cells, no consistent trends were observed between different test locations [inside (main traffic) - IWP, inside (main traffic) - OWP, outside (occasional traffic) - IWP, and outside (occasional traffic (OWP)]. Although some fluctuations were observed over time, the general trend was that the IRI values increased over time. Figure 5.75 is an example that shows the IRI measurements for Cell 227 (18-in LSSB). All of the IRI measurements for each test cell are provided in Appendix AH.

Figure 5.74. Lightweight inertial surface analyzer (LISA) profiler (MnDOT 2009c)

Table 5.6. FHWA international roughness index (IRI) condition criteria (Elbheiry et al. 2011)

Condition Term	IRI	Ride Quality
Very Good	< 0.95 m/km	Acceptable 0 – 2.68 m/km
Good	0.95 – 1.49 m/km	
Fair	1.50 – 1.88 m/km	
Poor	1.89 – 2.68 m/km	
Very Poor	> 2.68 m/km	Unacceptable

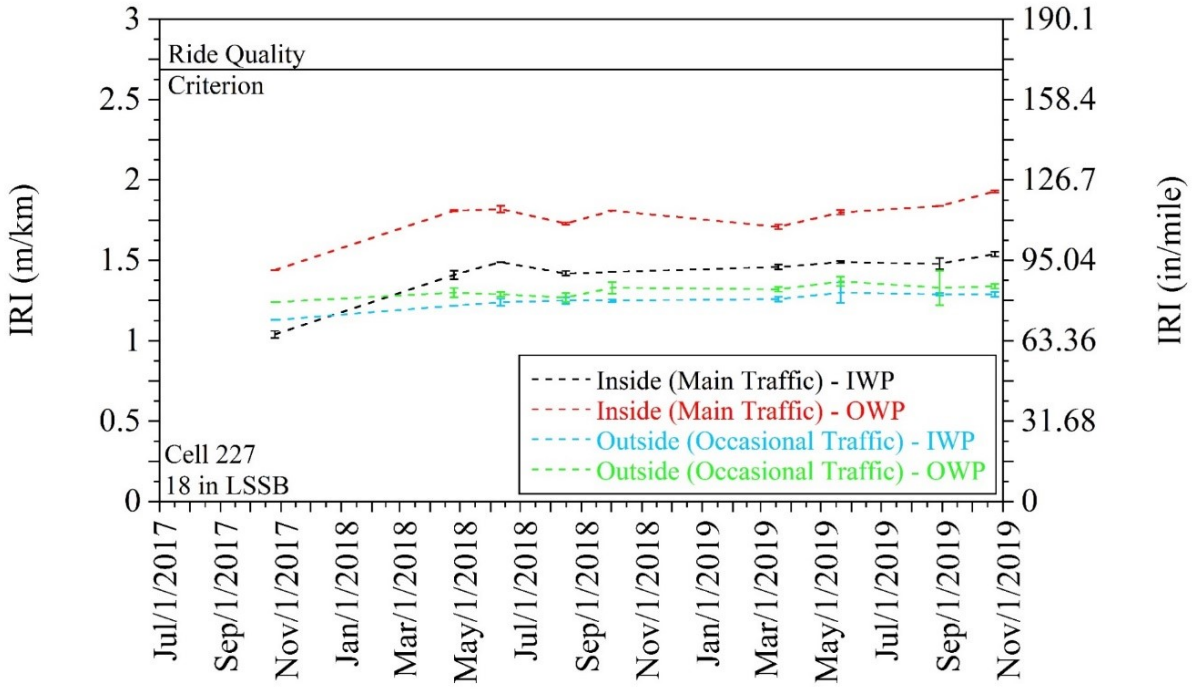

Figure 5.75. International roughness index (IRI) measurements for Cell 227 (18-in LSSB) (error bars represent one standard deviation of data) (IWP = inner wheel path, OWP = outer wheel path)

A summary of the IRI measurements for the inside lane (main traffic) - OWP of the test cells is provided in Figure 5.76. Appendix AI shows the IRI measurements for the inside lane (main traffic) - OWP of the test cells. Cells 628 (9-in LSSB - BX) and 728 (9-in LSSB) exhibited higher IRI values than the other cells. Cells 127 (18-in LSSB), 227 (18-in LSSB), 328 (9-in LSSB - TX), and 428 (9-in LSSB - TX+GT) yielded higher IRI values than Cells 185 (12-in Coarse RCA), 186 (12-in Fine RCA), 188 (12-in Limestone), 189 (12-in RCA+RAP), and 528 (9-in LSSB - BX+GT). The lower IRI values were observed in Cells 186 (12-in Fine RCA) and 189 (12-in RCA+RAP).

Overall, except Cell 728 (9-in LSSB), all other IRI values were lower than 2.68 m/km (169.8 in/mile) (Figure 5.76), which indicated that the ride quality was acceptable throughout all the test cells except Cell 728 (9-in LSSB) according to the FHWA (Table 5.6). For Cell 728 (9-in LSSB), while the initial IRI values were lower than 2.68 m/km (169.8 in/mile) in October 2017, the values slightly exceeded that criterion over time, which indicated that the ride quality was unacceptable.

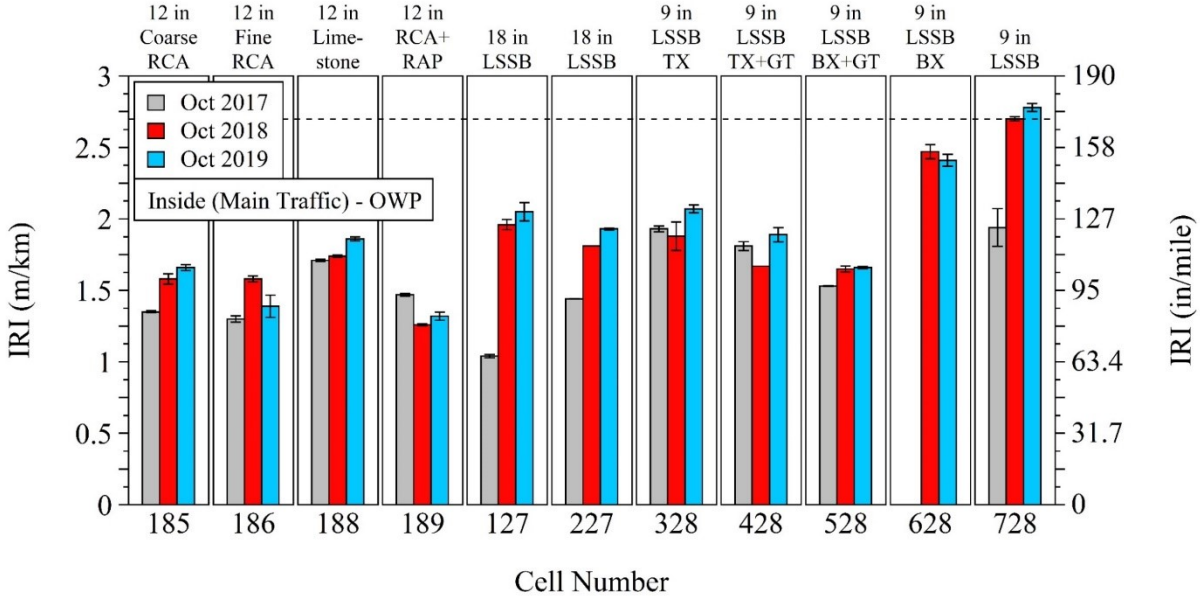

Figure 5.76. Summary of international roughness index (IRI) measurements for inside lane (main traffic) - outer wheel path (OWP)

5.7 PAVEMENT DISTRESSES

Pavement distress surveys were performed by the MnROAD Operations staff to monitor the field performance of the test cells. The data collected included the distress type, extent or amount of distress, and the severity of the distress. For the evaluation, a modified distress identification manual for the long-term pavement performance program (LTTP) was used (Miller and Bellinger 2014). The visible failure mechanisms were marked on the maps (Figure 5.77) and then entered into an Excel spreadsheet.

Table 5.7 summarizes the pavement distress types for flexible pavements as described in the distress identification manual for the LTTP (Miller and Bellinger 2014). Among all the distress types, only transverse cracking (cracks that are predominantly perpendicular to the pavement centerline),

longitudinal cracking (cracks predominantly parallel to pavement centerline), and raveling (wearing away of the pavement surface caused by the dislodging of aggregate particles and loss of asphalt binder) were observed in the test cells (Table 5.7). The severity levels for transverse cracking and longitudinal cracking were determined to be low (a crack with a mean width $\leq$ 6 mm). In addition, the severity level for raveling was determined as low to medium.

Figure 5.78 and Figure 5.79 summarize the transverse cracking on the inside lane (main traffic) and outside lane (occasional traffic) of the test cells, respectively. The lengths were reported as the number of the unit squares shown in Figure 5.77. For both lanes, transverse cracking was only observed in Cells 189 (12-in RCA+RAP), 227 (18-in LSSB), 328 (9-in LSSB - TX), 528 (9-in LSSB - BX+GT), and 728 (9-in LSSB).

Figure 5.80 summarizes the longitudinal cracking on the inside lane (main traffic) of the test cells. All the cracks were observed on the inside lane (main traffic) only, and the locations of the cracks were right by the centerline (non-wheel path). Longitudinal cracking was only observed on the inside lane (main traffic) of Cells 328 (9-in LSSB - TX), 528 (9-in LSSB - BX+GT), 728 (9-in LSSB). While the shortest longitudinal cracking (total length) was observed in Cells 328 (9-in LSSB - TX), the longest cracking (total length) was observed in Cell 528 (9-in LSSB - BX+GT).

Since raveling is related to the quality and the long-term performance of the asphalt material only, no discussion was included in the context of the report. However, survey results for raveling can be seen in Appendix AJ.

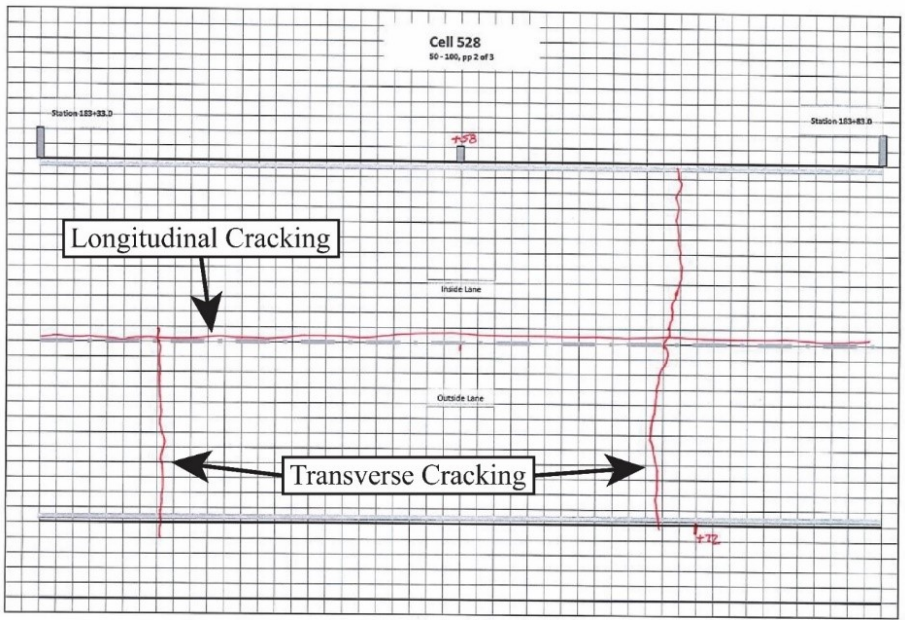

Figure 5.77. Pavement distress map for Cell 528 (9-in LSSB - BX+GT)

Table 5.7. List of flexible pavement distresses (NA = not available)

Distress Category	Distress Type	Observed	Severity
Cracking	Fatigue Cracking	No	NA
	Block Cracking	No	NA
	Edge Cracking	No	NA
	Longitudinal Cracking	Yes	Low
	Reflection Cracking at Joints	No	NA
	Transverse Cracking	Yes	Low
Patching and Potholes	Patch/Patch Deterioration	No	NA
	Potholes	No	NA
Surface Deformation	Rutting	See Section 5.5	NA
	Shoving	No	NA
Surface Defects	Bleeding	No	NA
	Polished Aggregate	No	NA
	Raveling	Yes	Low/Moderate
Miscellaneous Distresses	Lane-to-Shoulder Dropoff	No	NA
	Water Bleeding and Pumping	No	NA

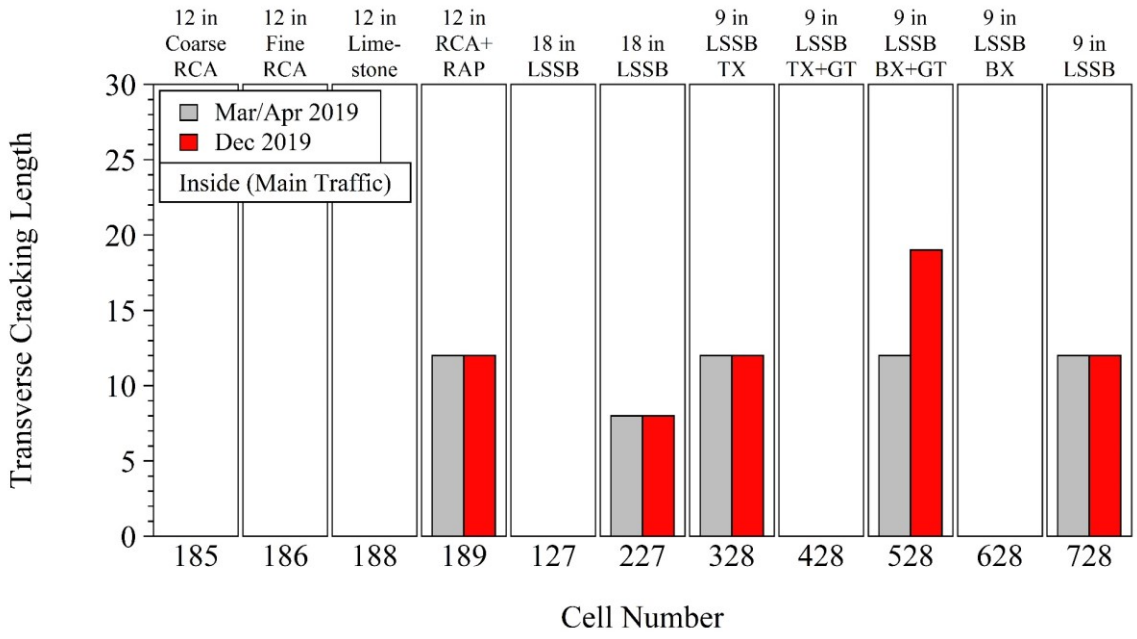

Figure 5.78. Summary of transverse cracking lengths on inside lane (main traffic) of test cells (lengths are number of unit squares shown in distress maps)

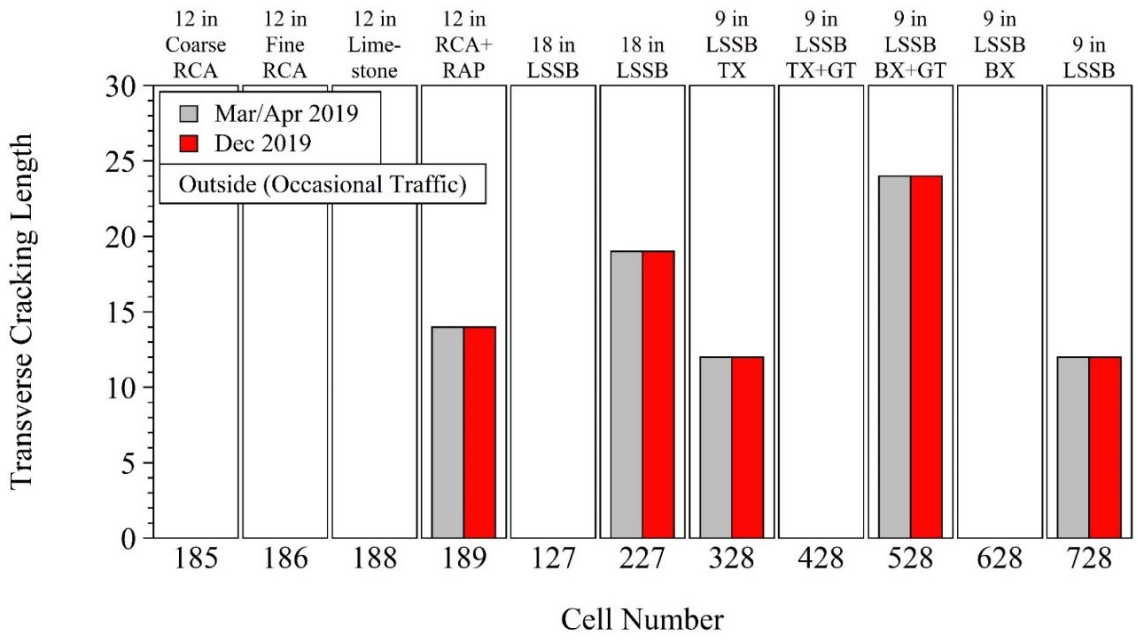

Figure 5.79. Summary of transverse cracking lengths on outside lane (occasional traffic) of test cells (lengths are number of unit squares shown in distress maps)

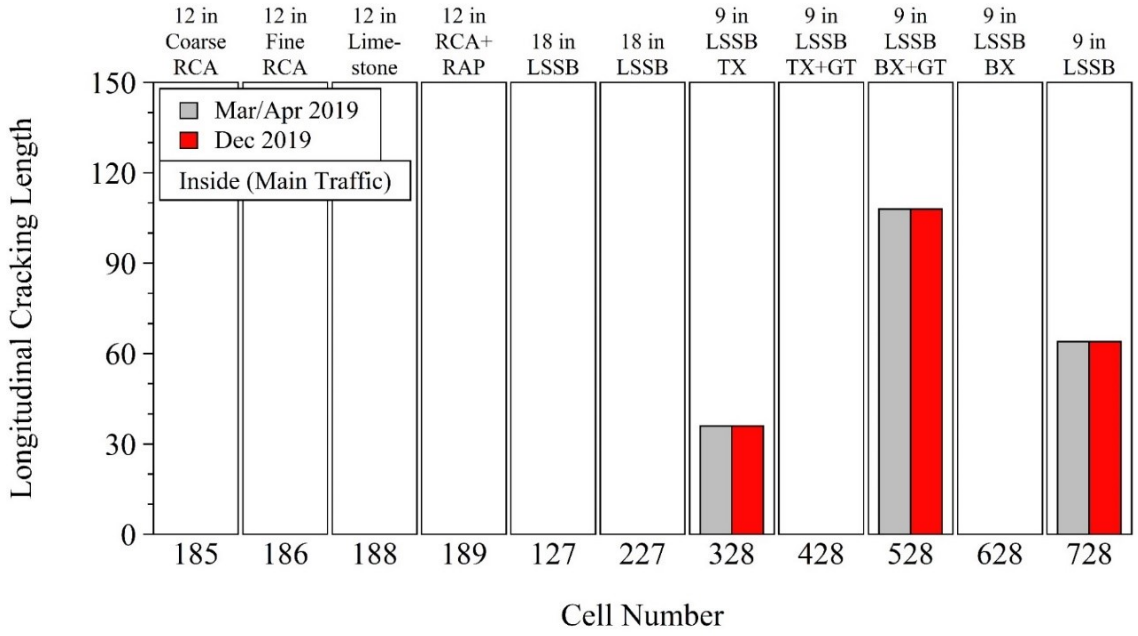

Figure 5.80. Summary of longitudinal cracking lengths of test cells (lengths are number of unit squares shown in distress maps)

5.8 EFFECT OF FIELD DEGREE OF COMPACTION (DOC) ON PERFORMANCE OF TEST CELLS

5.8.1 Nuclear Density Gauge (NDG) Measurements for Base and Subgrade Layers of Test Cells

Modified Proctor compaction test results [maximum dry unit weight (MDU) and optimum moisture content (OMC)] and in-situ nuclear density gauge (NDG) measurements were compared for subgrade and aggregate base layers to determine the relative dry unit weight (i.e., field DOC) and relative moisture content values. NDG tests could not be performed for the subgrade layers in Cells 127 (18-in LSSB), 227 (18-in LSSB), 328 (9-in LSSB + TX), 428 (9-in LSSB + TX+GT), 528 (9-in LSSB + BX+GT), 628 (9-in LSSB + BX), and 728 (9-in LSSB) since a very non-traditional subgrade preparation procedure was followed during the construction of these cells to create a weak subgrade with a dynamic cone penetration (DCP) index (DCPI) value between 2.5 and 3.5 in/blow (65 and 90 mm/blow) (ASTM D6951) for the upper 1 ft (0.3 m) of the Clay Loam subgrade soil [in fact, no field testing (except DCP) was performed on the prepared subgrade layers not to disturb these layers]. For NDG measurements to be valid, particles bigger than 38 mm (1½ in) should not be more than 40% of test material by weight (Roads and Maritime Services 2015). Since 64% of the particles in the LSSB material was larger than 38 mm (1½ in), NDG measurements were not taken for LSSB cells (Cells 127 to 728). For all the subbase layers, a quality compaction method, in which the compacted layer was visually observed for consolidation, pumping, and lateral movement, was used (MnDOT 2018). Detailed information regarding the NDG measurements is provided in Chapter 3. Figure 5.81 and Figure 5.82 summarize the relative dry unit weight and relative moisture content values for the aggregate base and subgrade layers, respectively.

The Sand Subgrade layer in Cell 185 (12-in Coarse RCA) exhibited lower relative dry unit weight values (between 89 and 99%) than the Clay Loam subgrade layers in Cells 188 (12-in Limestone) and 189 (12-in RCA+RAP) (between 94 and 112%) (Figure 5.81). In general, the relative moisture content values of these subgrade layers were lower than 100%. (Figure 5.82). All three subgrade layers exhibited similar calibrated in-place moisture content values (between 1.6 and 5.3%). However, since the OMC of the Sand Subgrade (5.6%) was lower than that of Clay Loam (10%) (Table 4.3), the Sand Subgrade layer in Cell 185 (12-in Coarse RCA) exhibited higher relative moisture content values (median value of 85%) than the Clay Loam subgrade layers in Cells 188 (12-in Limestone) and 189 (12-in RCA+RAP) (median values of 26 and 39%, respectively) (Figure 5.82).

The relative dry unit weight values of 12-in Coarse RCA (Cell 185), Fine RCA (Cell 186), Limestone (Cell 188), and RCA+RAP (Cell 189) base layers were between 88% and 100% (Figure 5.81). The relative moisture content values of these aggregate base layers were lower than 100%, indicating that each aggregate base layer was compacted at the dry side of the OMC of the corresponding material (Figure 5.82), so MDU values could not be obtained and lower relative dry unit weight values were observed (Kazmee and Tutumluer 2015). Overall, the relative dry unit weight values of 12-in Coarse RCA base layer (Cell 185) were lower than those of 12-in Fine RCA (Cell 186), Limestone (Cell 188), and RCA+RAP (Cell 189) base layers. However, since different materials were used in 12-in aggregate base layers, no specific comparison was made between the NDG measurements and the performance of these layers.

The relative dry unit weight values of the Class 6 Aggregate base layers (Cells 127 and 227) (between 91 and 95%) were higher than those of the Class 5Q Aggregate base layers (Cells 328, 428, 528, 628, and 728) (between 78 and 92%) (Figure 5.81). Similar to the 12-in aggregate base layers, each 6-in aggregate base layer [Class 6 Aggregate (Cells 127-227) and Class 5Q Aggregate (Cells 328-728) base layers] was compacted at the dry side of the OMC of the corresponding material [the relative moisture content values of the Class 6 Aggregate (Cells 127-227) and Class 5Q Aggregate (Cells 328-728) base layers were lower than 100%)] (Figure 5.82).

During compaction, lower relative dry unit weight values were expected to be observed for materials containing large voids associated with large particles due to particle reorientation (Kazmee and Tutumluer 2015). It was concluded that 9-in LSSB layers could not provide a stable foundation for the Class 5Q Aggregate base layers, and therefore, reduced the effectiveness of compaction for the Class 5Q Aggregate base layers due to the reorientation of large particles during compaction. By considering that the main contribution of the geosynthetics placed beneath 9-in LSSB layers would be to the subgrade layers, placing geosynthetics on top of 9-in LSSB layers would improve the stability of 9-in LSSB layers during compaction of the Class 5Q Aggregate base layers due to improved load distribution. A similar result was not observed with 18-in LSSB layers, possibly indicating that 18-in LSSB layers were more suitable for pavement construction than 9-in LSSB layers. Higher layer stiffness would be expected for thicker layers because of improvement in load distribution with an increase in the layer thickness (Tanyu et al. 2003).

Specifically, the 6-in Class 5Q Aggregate base layer in Cell 528 (overlying 9-in LSSB layer) exhibited lower relative dry unit weight values compared to the other 6-in Class 5Q Aggregate base layers (overlying 9-in LSSB layers) in Cells 328, 428, 628, and 728. In addition, the relative moisture content values of 6-in Class 5Q Aggregate base layer (overlying 9-in LSSB layer) in Cell 528 were lower than those of the other Class 5Q Aggregate base layers (overlying 9-in LSSB layers) in Cells 328, 428, 682, and 728. Compacting drier soil at the same compaction energy is expected to result in lower compacted dry unit weight due to the lack of lubricant effect provided by the water. Therefore, lower relative dry unit weight values observed in the Class 5Q Aggregate base layer (overlying 9-in LSSB layer) in Cell 528 were possibly due to the lack of sufficient water in the aggregate matrix.

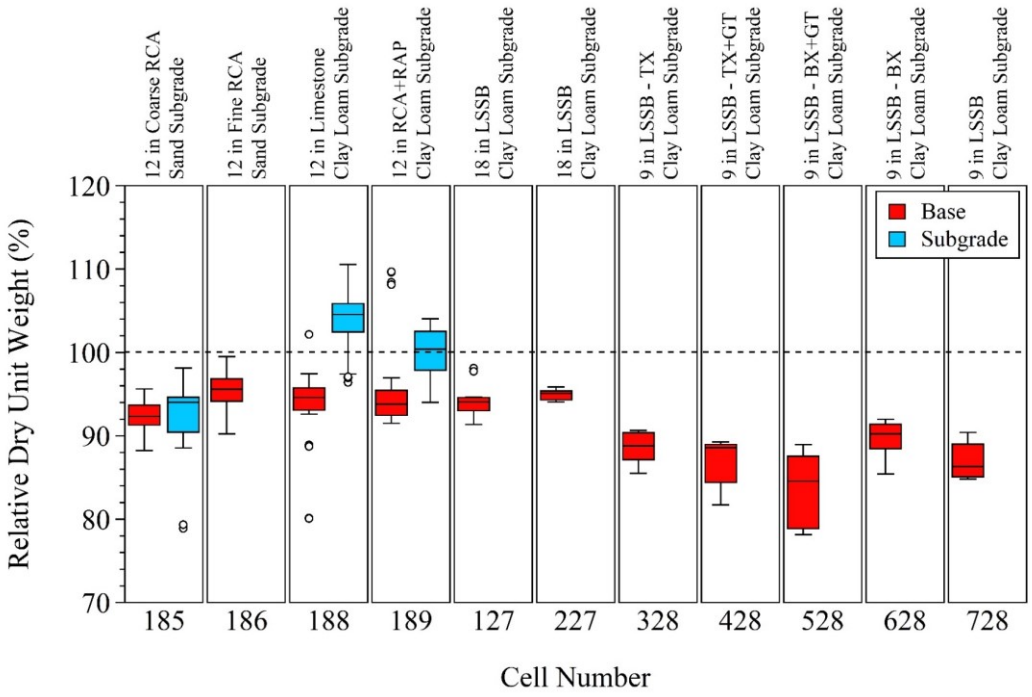

Figure 5.81. Relative dry unit weight values for aggregate base and subgrade layers (red boxes shown for Cells 127 and 227 are for Class 6 Aggregate base layers and those shown for Cells 328-728 are for Class 5Q Aggregate base layers)

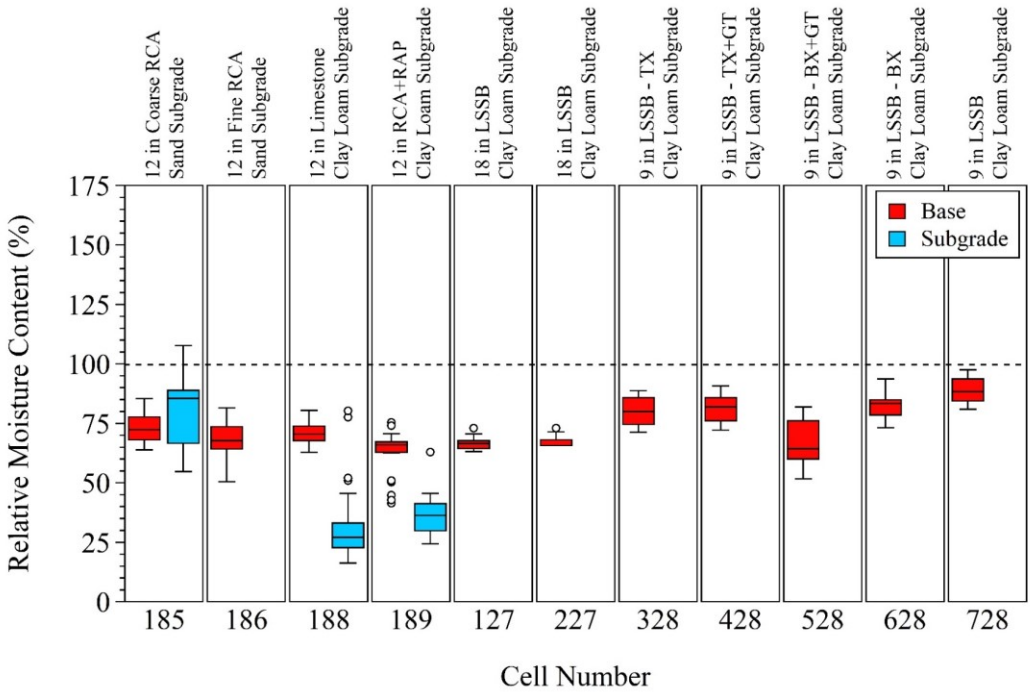

Figure 5.82. Relative moisture content values for aggregate base and subgrade layers (red boxes shown for Cells 127 and 227 are for Class 6 Aggregate base layers and those shown for Cells 328-728 are for Class 5Q Aggregate base layers)

5.8.2 Effect of Inadequate Compaction of Class 5Q Aggregate Base Layers Overlying 9-in Large Stone Subbase (LSSB) Layers

As previously shown in Figure 5.81, the relative dry unit weight values of all of the aggregate base layers were lower than 95%-100%. Specifically, the relative dry unit weight values of 6-in Class 5Q Aggregate base layers overlying 9-in LSSB layers were lower than other aggregate base layers due to the instability of 9-in LSSB layers under compaction. To focus on the effect of the instability of 9-in LSSB layers under compaction on the performance of the test cells, Figure 5.81 and Figure 5.82 were revised into Figure 5.83 and Figure 5.84, respectively.

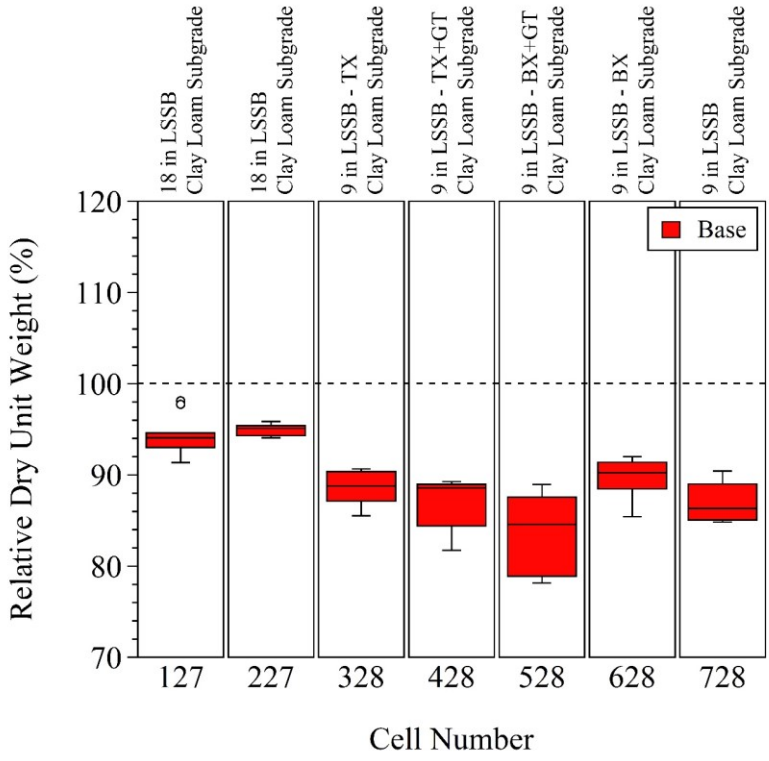

Figure 5.83. Relative dry unit weight values for aggregate base layers overlying LSSB layers

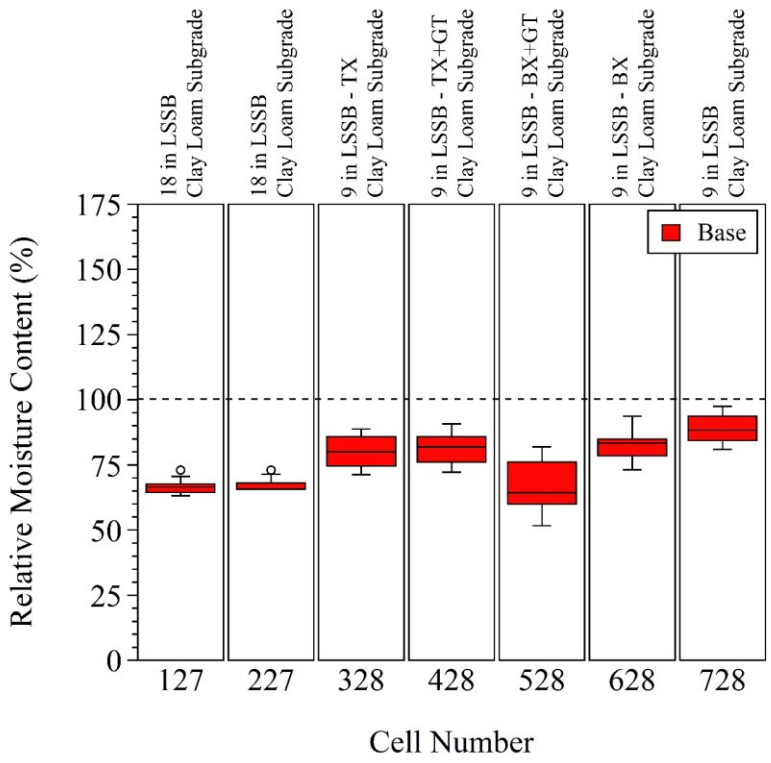

Figure 5.84. Relative moisture content values for aggregate base layers overlying LSSB layers

Figure 5.85, Figure 5.86, and Figure 5.87 show light weight deflectometer (LWD) elastic modulus (E_{LWD}), falling weight deflectometer (FWD) elastic modulus (E_{FWD}), and intelligent compaction (IC) M_R values, respectively, for the base+subase layers through Cells 127-728 (these results were taken from Chapter 3). As can be seen in these figures, the base+subbase layers in Cells 127 and 227 (6-in Class 6 Aggregate base + 18-in LSSB layers) generally provided greater stiffness than the base+subbase layers of Cells 328-728 (6-in Class 5Q Aggregate base + 9-in LSSB layers). There were two principal reasons for this: (1) 18-in LSSB provided better structural support than 9-in LSSB due to higher thickness (Tanyu et al. 2003) and (2) Class 6 Aggregate base layers overlying 18-in LSSB layers were better compacted than Class 5Q Aggregate base layers overlying 9-in LSSB layers. LWD, FWD, and IC test results (Figure 5.85, Figure 5.86, and Figure 5.87, respectively) exhibited that stiffness trends were similar to the trends observed in relative dry unit weight values (Figure 5.83). Specifically, the base+subbase layer in Cell 528 (Class 5Q Aggregate base + 9-in LSSB layers) exhibited the lowest base+subbase stiffness compared to the similar base+subbase layers in Cells 328, 428, 628, and 728. This occurred because the Class 5Q Aggregate base layer in Cell 528 exhibited the lowest relative dry unit weight compared to the other Class 5Q Aggregate base layers in Cells 328, 428, 628, and 728 (Figure 5.83). Therefore, it was concluded that the structural benefits of the geosynthetics could not be clearly observed by LWD, FWD, and IC testing due to the overall instability of 9-in LSSB layers and lower relative dry unit weight of 6-in Class 5Q Aggregate base layers. In addition, it was also speculated that the loads applied by LWD, FWD, or IC testing were insufficient to permit observation of the structural benefits of geosynthetics. A heavy weight deflectometer (HWD), a type of FWD equipment applying higher loads, could be used for this purpose.

As discussed in Chapter 3, after the placement of 9-in LSSB layers over Clay Loam subgrade layers, subgrade soil pumping into 9-in LSSB layers was observed in the originally constructed test cells (Cells 128 and 228) under construction traffic. In addition, as the construction of those originally constructed test cells (Cells 128 and 228) continued, rutting was observed in the aggregate base and asphalt layers when subjected to construction traffic. To overcome these subgrade soil pumping and rutting issues, the originally constructed test cells (Cells 128 and 228) were excavated to their subgrade layers for reconstruction. Cell 228 could not be fully removed because of the presence of near-surface utilities in an area to the east, so around 130 ft (39.6 m) of that cell was kept in place and renumbered as Cell 728. The newly designed test cells were named as Cells 328, 428, 528, and 628. During reconstruction, geosynthetics were placed on top of the Clay Loam subgrade layers in Cells 328, 428, 528, and 628 to improve load distribution and separate the Clay Loam subgrade and the LSSB layers. The placement of the geosynthetics provided important benefits such as improving workability and the rest of the construction was completed without any further problem related to subgrade soil pumping and rutting. As stated previously, the area where Cell 728 was located could not be reconstructed due to near-surface utilities, so no geosynthetics were placed there. However, even without placement of any geosynthetics, no observable issue was encountered in Cell 728. While no field data was available to make a scientific evaluation of this behavior, it was speculated that the top 1 ft (0.3 m) of the Clay Loam subgrade layer in Cell 728 was not as loose as that of other Clay Loam subgrade layers underlying 9-in LSSB layers. Therefore, for Cell 728, upward movement of the Clay Loam subgrade soil and downward movement of the LSSB particles were expected to be limited. While another factor could be the effect of the existing underground utilities on the pavement responses with respect to loading, no specific investigation was performed on this matter. Forensic analysis is recommended to better understand the behavior of the 9-in LSSB layers including Cell 728.

In fact, it would be highly possible that if no loosening had been applied to the top 1 ft (0.3 m) of the Clay Loam subgrade layer in the originally constructed test cells (Cells 128 and 228), no severe subgrade soil pumping or aggregate base/asphalt rutting would have been observed. Since the loosened Clay Loam subgrade thickness [1 ft (0.3 m)] was thicker than the 9-in LSSB layers, the Clay Loam subgrade soil could reach up to the top of the 9-in LSSB layers in the originally constructed test cells (Cells 128 and 228). However, since the 18-in LSSB layers were thicker than the loosened Clay Loam subgrade thickness [1 ft (0.3 m)], no subgrade soil pumping was observed on the surface of the 18-in LSSB layers during construction. On the other hand, it seemed quite possible that the loosened Clay Loam subgrade soil mixed with the large stones at some degree in 18-in LSSB. The reason why rutting was not observed during construction in the test cells constructed with 18-in LSSB layers (Cells 127 and 228) could be the greater structural support provided by 18-in LSSB compared to 9-in LSSB (Tanyu et al. 2003).

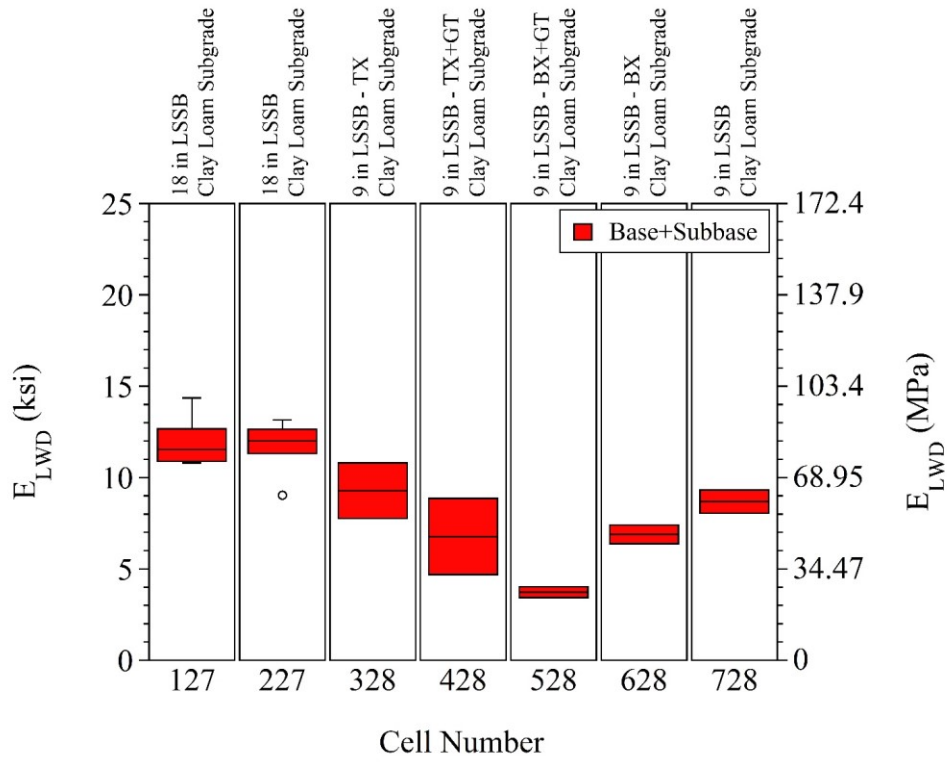

Figure 5.85. Light weight deflectometer (LWD) elastic modulus (E_{LWD}) of base+subbase layers in Cells 127-728

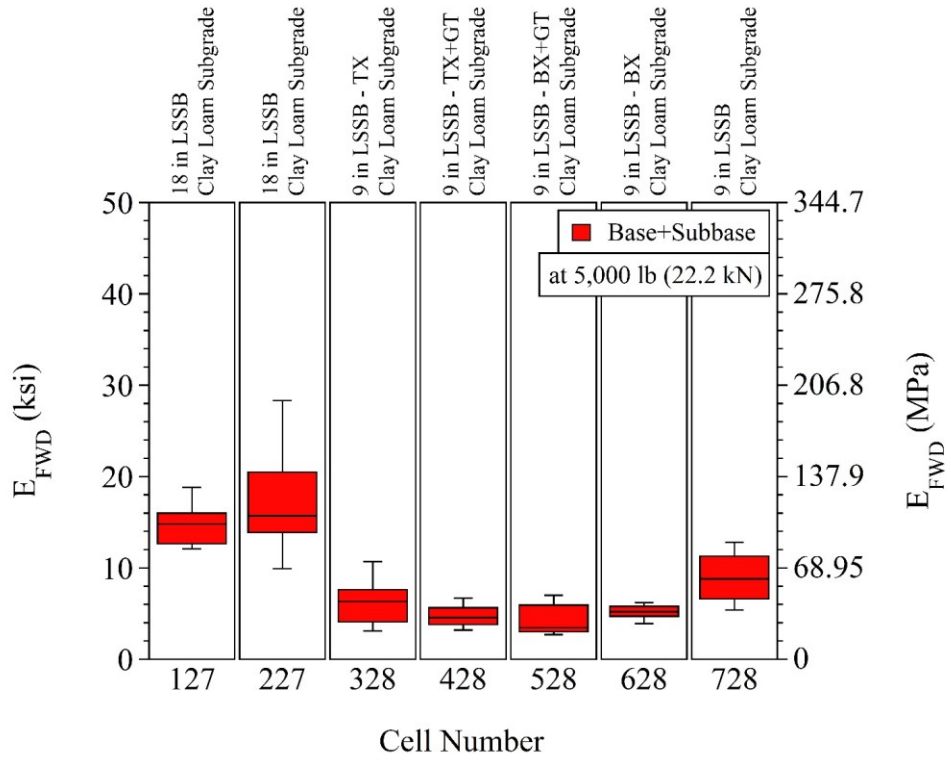

Figure 5.86. Falling weight deflectometer (FWD) elastic modulus (E_{FWD}) of base+subbase layers in Cells 127-728

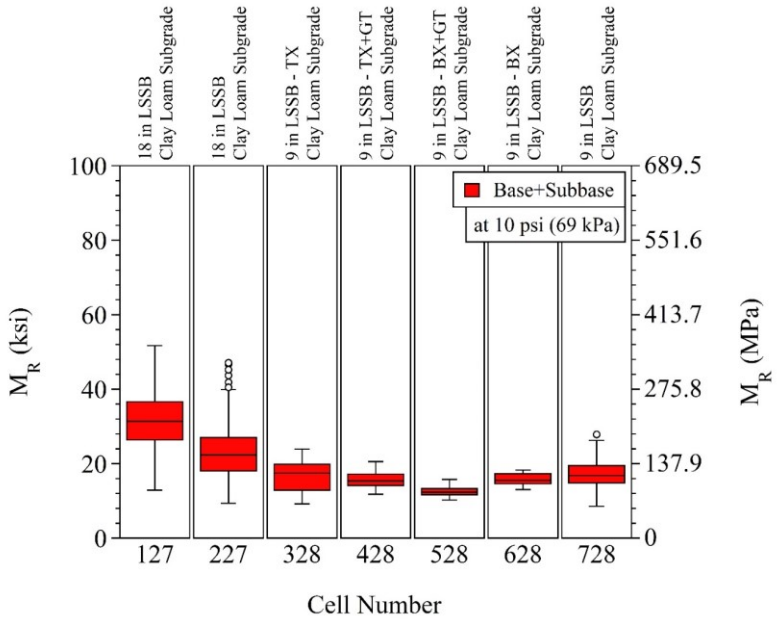

Figure 5.87. Intelligent compaction (IC) resilient modulus (M_R) of base+subbase layers in Cells 127-728

In terms of the long-term base+subbase E_{FWD} values in the inside lanes (main traffic) of the cells (Figure 5.88), the base+subbase layers in Cells 127 and 227 (6-in Class 6 Aggregate base + 18-in LSSB layers) exhibited higher stiffness than those in Cells 328, 428, 528, 628, and 728 (6-in Class 5Q Aggregate base + 9-in LSSB layers). This indicated that 18-in LSSB layers should be more preferable than 9-in LSSB layers in pavement foundations systems. Overall, no consistent trend was observed between the relative dry unit weight values of the test cells (Figure 5.83) and their base+subbase E_{FWD} values (Figure 5.88).

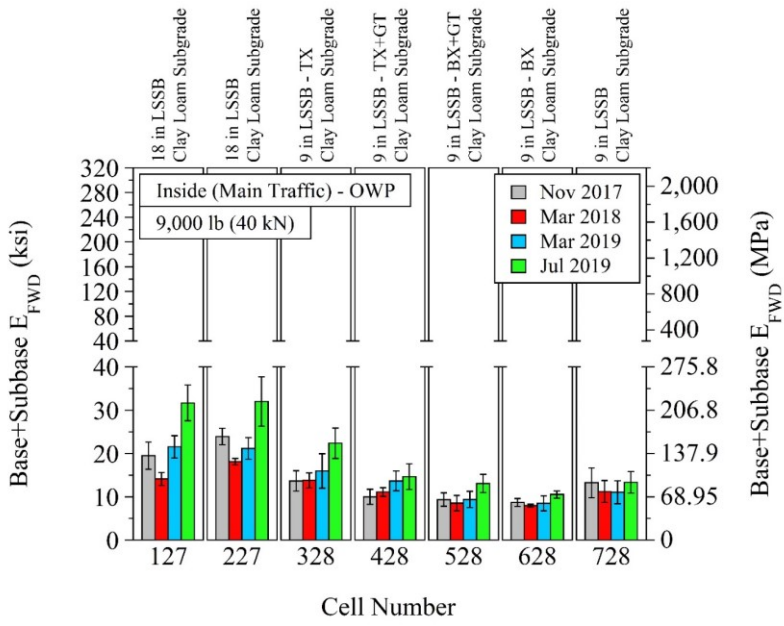

Figure 5.88. Base+subbase E_{FWD} of Cells 127-728 under 9,000 lb (40 kN) load (error bars represent one standard deviation of data)

In terms of the long-term rutting observed in the inside lanes (main traffic) of the test cells (Figure 5.89), Cells 328 (9-in LSSB - TX), 428 (9-in LSSB - TX+GT), 528 (9-in LSSB - BX+GT), and 628 (9-in LSSB - BX) exhibited greater rutting than the other cells. This was because the 9-in LSSB layers and Class 5Q Aggregate base layers could not be compacted properly during construction due to the nature of the large stones and lack of structural support provided by 9-in LSSB layers (as a result of inadequate layer thickness). In fact, Cells 328 (9-in LSSB - TX) and 628 (9-in LSSB BX) exhibited shallower rut depths than Cells 428 (9-in LSSB - TX+GT) and 528 (9-in LSSB - BX+GT). As shown in Figure 5.83, lower in-situ dry unit weight values were observed for the Class 5Q Aggregate base layers in Cells 428 (9-in LSSB - TX+GT) and 528 (9-in LSSB - BX+GT) compared to those observed in Cells 328 (9-in LSSB - TX) and 628 (9-in LSSB - BX). Thus, it resulted in higher rutting values for Cells 428 (9-in LSSB - TX+GT) and 528 (9-in LSSB - BX+GT) compared to Cells 328 (9-in LSSB - TX) and 628 (9-in LSSB - BX). The least rutting was observed in Cell 728 (9-in LSSB). It was previously speculated that the top 1 ft (0.3 m) of the Clay Loam subgrade layer in Cell 728 was not as loose as other Clay Loam subgrade layers underlying 9-in LSSB layers and this could possibly be the reason why the least rutting was observed in Cell 728 (9-in LSSB).

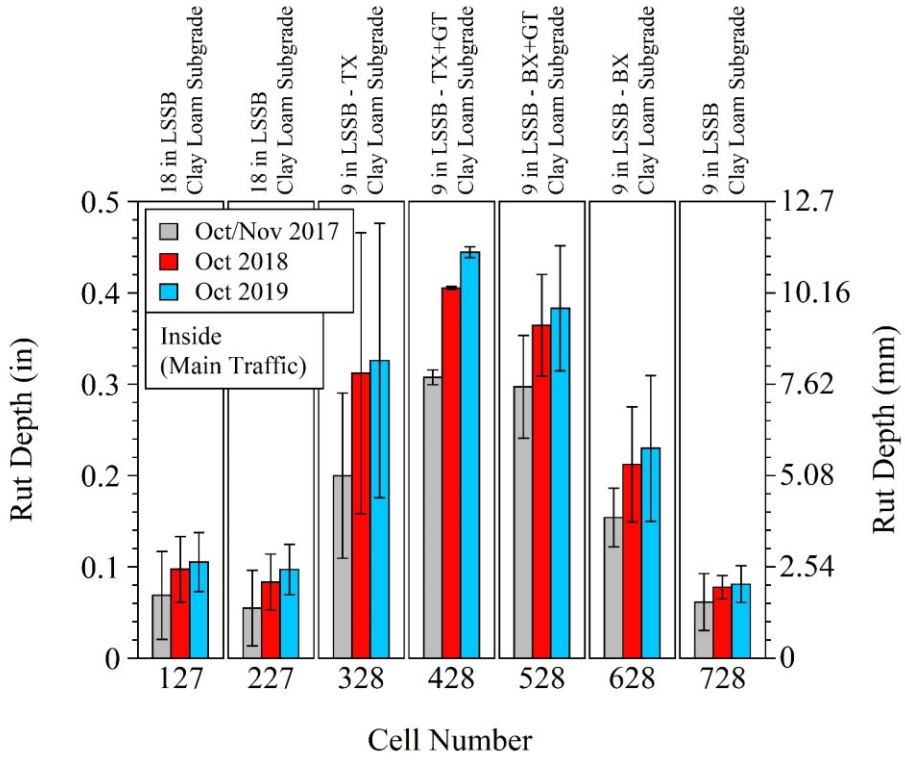

Figure 5.89. Rut depth measurements for Cells 127-728 (error bars represent one standard deviation of data)

International roughness index (IRI) measurements for the inside lane (main traffic) - OWP of the test cells are provided in Figure 5.90. Cells 628 (9-in LSSB - BX) and 728 (9-in LSSB) exhibited higher IRI values than the other cells. Overall, except for Cell 728 (9-in LSSB), all other IRI values were lower than 2.68 m/km (170 in/mile), which indicated that the ride quality was acceptable throughout all the test cells except Cell 728 (9-in LSSB) according to the FHWA. For Cell 728 (9-in LSSB), while the initial IRI values were lower than 2.68 m/km (170 in/mile) in October 2017, the values slightly exceeded that criterion

over time, which indicated that the ride quality was unacceptable. No consistent trend was observed between the relative dry unit weight values of the test cells (Figure 5.83) and their long-term IRI values (Figure 5.90).

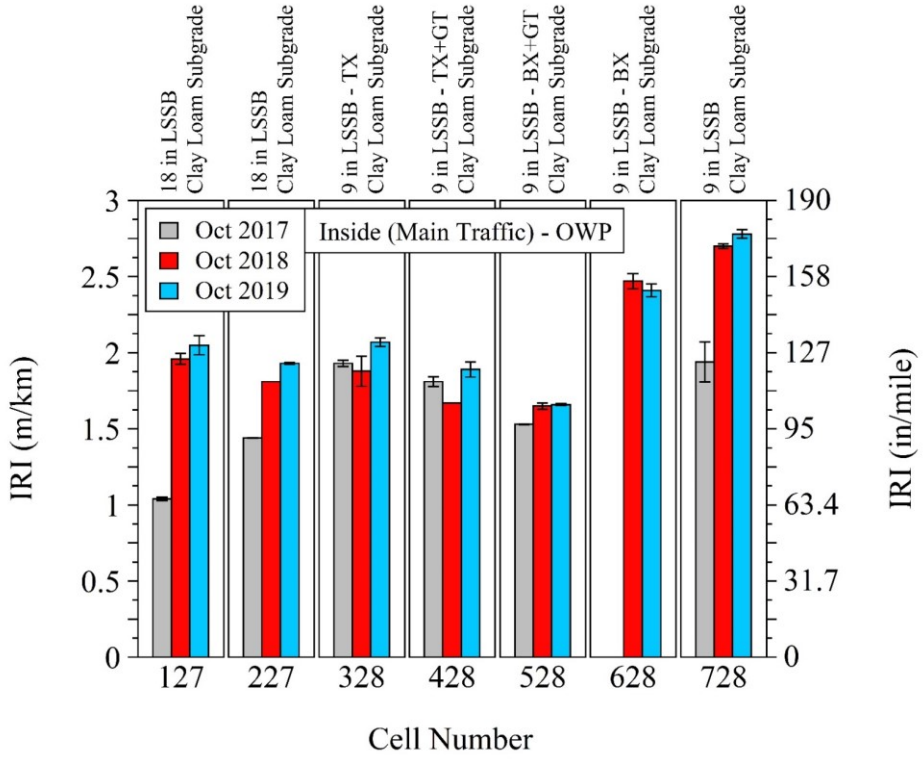

Figure 5.90. International roughness index (IRI) measurements for inside lane (main traffic) - outer wheel path (OWP)

Figure 5.91 summarizes transverse cracking behavior in the inside lane (main traffic) of the test cells. Transverse cracking was observed only in Cells 227 (18-in LSSB), 328 (9-in LSSB - TX), 528 (9-in LSSB - BX+GT), and 728 (9-in LSSB). While no change was observed in the transverse cracking length in Cells 227 (18-in LSSB), 328 (9-in LSSB - TX), and 728 (9-in LSSB) after March/April 2019, the crack length increased in Cell 528 (9-in LSSB - BX+GT) after that testing period. While this increasing transverse cracking length in Cell 528 (9-in LSSB + BX+GT) could be due to the lower relative dry unit weight values of the cell (Figure 5.83), no consistent trend was observed between these two parameters.

Figure 5.92 summarizes longitudinal cracking behavior in the inside lane (main traffic) of the test cells. Crack locations were just to the right of the centerline (non-wheel path). Longitudinal cracking was observed only in the inside lane (main traffic) of Cells 328 (9-in LSSB - TX), 528 (9-in LSSB - BX+GT), and 728 (9-in LSSB). While the shortest longitudinal cracking (total length) was observed in Cells 328 (9-in LSSB - TX), the longest cracking (total length) was observed in Cell 528 (9-in LSSB - BX+GT). Although the higher longitudinal cracking length in Cell 528 (9-in LSSB - BX+GT) could possibly be due to the lower relative dry unit weight values of the cell (Figure 5.83), no consistent trend was observed between these two parameters.

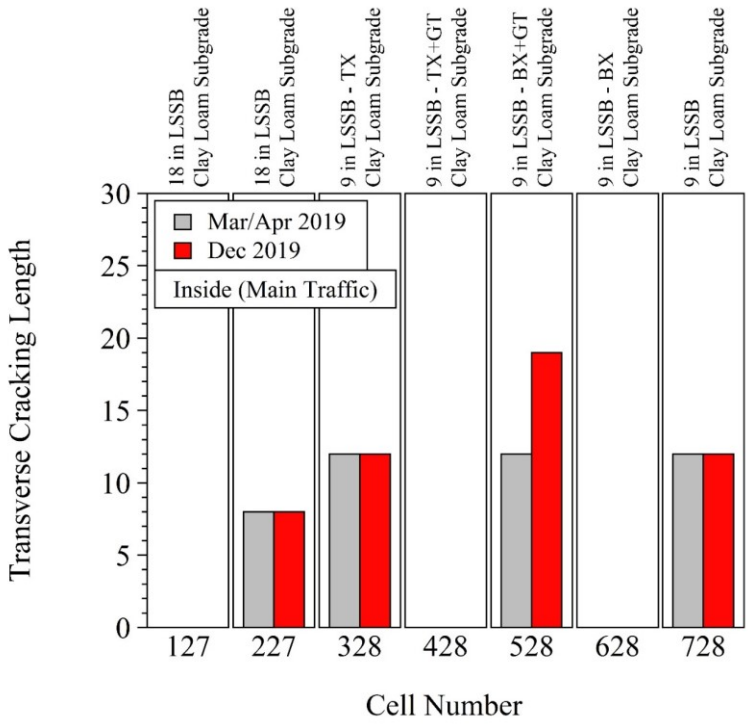

Figure 5.91. Transverse cracking lengths in inside lane (main traffic) of test cells (lengths are number of unit squares shown in distress maps)

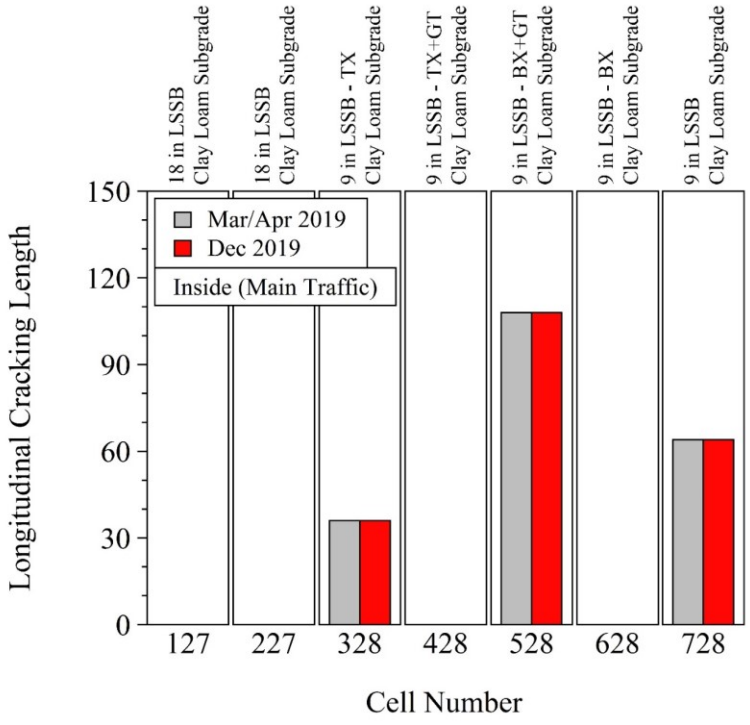

Figure 5.92. Longitudinal cracking lengths in inside lane (main traffic) of test cells (lengths are number of unit squares shown in distress maps)

5.9 CHAPTER CONCLUSIONS

In this chapter, the long-term performance of the built test cells was discussed. Meteorological data and data collected by soil temperature and moisture monitoring were provided. In addition, data collected by falling weight deflectometer (FWD) tests, frost heave and thaw settlement measurements, rutting measurements, international roughness index (IRI) measurements, and pavement distress evaluations was provided. From the findings of this chapter, the following conclusions were drawn:

- Moisture probe readings were compatible with thermocouple readings and both sensors' readings demonstrated the freezing and thawing periods properly. The Class 6 Aggregate [Cell 127 (18-in LSSB)] and the Class 5Q Aggregate [Cell 728 (9-in LSSB)] base layers did not exhibit an increase in the VWC values in the rainy periods. This indicates that a good drainage system is provided by the LSSB layers in Cell 127 (18-in LSSB) and Cell 728 (9-in LSSB).

- Different maximum frost penetration depths and freezing and thawing periods were observed for each test cell. It was speculated that such parameters were affected by the thermal properties of each material used in the test cells. Therefore, the thermal properties of the materials (heat capacity, thermal conductivity, and thermal diffusivity) should be evaluated to better understand the freezing and thawing characteristics of the materials.

- For the FWD tests, according to the two-year test results, Cells 185 (12-in Coarse RCA) and 186 (12-in Fine RCA), constructed over Sand Subgrade layers, performed considerably better (lower maximum deflections and higher composite E_{FWD} values) than the other cells. In fact, Cell 186 (12-in Fine RCA) performed better than Cell 185 (12-in Coarse RCA). This could indicate that the Fine RCA material would be a better option to construct aggregate base layers than the Coarse RCA material.

- After approximately two years, Cell 189 (12-in RCA+RAP) performed better than Cell 188 (12-in Limestone) (both test cells were constructed over Clay Loam subgrade layers). This could indicate that the RCA+RAP material would be a better option to construct aggregate base layers than the Limestone material.

- After approximately two years, Cells 127 (18-in LSSB) and 227 (18-in LSSB) performed better than Cells 328 (9-in LSSB - TX), 428 (9-in LSSB - TX+GT), 528 (9-in LSSB - BX+GT), 628 (9-in LSSB - BX), and 728 (9-in LSSB). This could indicate that constructing 18-in LSSB layers would be a better option than constructing 9-in LSSB layers.

- Cells 185 (12-in Coarse RCA), 186 (12-in Fine RCA), 127 (18-in LSSB), and 227 (18-in LSSB) exhibited less rutting than Cells 188 (12-in Limestone) and 189 (12-in RCA+RAP). Cell 188 (12-in Limestone) exhibited more rutting than Cell 189 (12-in RCA+RAP). Cells 328 (9-in LSSB - TX), 428 (9-in LSSB - TX+GT), 528 (9-in LSSB BX+GT), and 628 (9-in LSSB - BX) yielded more rutting than the other cells.

- It was speculated that 9-in LSSB layers could not be compacted properly due to the nature of the large stones, the relatively lower thickness of 9-in LSSB layers compared to 18-in LSSB layers in Cells 127 (18-in LSSB) and 227 (18-in LSSB), and purposely weakened Clay Loam subgrade layer. In

addition, the Class 5Q Aggregate base layers in Cells 328 (9-in LSSB - TX), 428 (9-in LSSB - TX+GT), 528 (9-in LSSB - BX+GT), and 628 (9-in LSSB - BX) could not be compacted adequately. In fact, Cells 328 (9-in LSSB - TX) and 628 (9-in LSSB BX) exhibited less rut depths than Cells 428 (9-in LSSB - TX+GT) and 528 (9-in LSSB - BX+GT). As determined in Chapter 3, lower in-situ dry unit weight values were observed for the Class 5Q Aggregate base layers in Cells 428 (9-in LSSB - TX+GT) and 528 (9-in LSSB - BX+GT) compared to those observed in Cells 328 (9-in LSSB - TX) and 628 (9-in LSSB - BX). Thus, it resulted in higher rutting values for Cells 428 (9-in LSSB - TX+GT) and 528 (9-in LSSB - BX+GT) [compared to Cells 328 (9-in LSSB - TX) and 628 (9-in LSSB - BX)]. The lowest rut depths were observed in Cell 728 (9-in LSSB).

- Except for Cell 728 (9-in LSSB), all other test cells exhibited IRI values lower than 2.68 m/km (169.8 in/mile), indicating that the ride quality was acceptable throughout all the test cells except Cell 728 (9-in LSSB). For Cell 728 (9-in LSSB), while the initial IRI values were lower than 2.68 m/km (169.8 in/mile), the values slightly exceeded that criterion over time, which indicated that the ride quality was unacceptable. Cells 628 (9-in LSSB - BX) and 728 (9-in LSSB) exhibited higher IRI values than the other cells. On the other hand, Cells 127 (18-in LSSB), 227 (18-in LSSB), 328 (9-in LSSB - TX), and 428 (9-in LSSB - TX+GT) yielded higher IRI values than Cells 185 (12-in Coarse RCA), 186 (12-in Fine RCA), 188 (12-in Limestone), 189 (12-in RCA+RAP), and 528 (9-in LSSB - BX+GT). The lowest IRI values were observed in Cells 186 (12-in Fine RCA) and 189 (12-in RCA+RAP).

- For both the inside lane (main traffic) and outside lane (occasional traffic), transverse cracking was only observed in Cells 189 (12-in RCA+RAP), 227 (18-in LSSB), 328 (9-in LSSB - TX), 528 (9-in LSSB - BX+GT), and 728 (9-in LSSB). Longitudinal cracking was observed on the inside lane (main traffic) only, and the locations of the cracks were right by the centerline (non-wheel path). Longitudinal cracking was only observed on the inside lane (main traffic) of Cells 328 (9-in LSSB - TX), 528 (9-in LSSB - BX+GT), 728 (9-in LSSB). While the shortest longitudinal cracking (total length) was observed in Cells 328 (9-in LSSB - TX), the longest cracking (total length) was observed in Cell 528 (9-in LSSB - BX+GT).

5.10 DISCUSSION & RECOMMENDATION

- Aggregates generally show a stress-hardening behavior due to the reorientation of the particles into a denser state under higher loads. However, aggregates can exhibit decreasing stiffness values after reaching the breakpoint stress due to the presence of underlying softer or wetter subgrade conditions. Stress-hardening and stress-softening behavior of each road material, as well as stresses at layer interfaces (asphalt/base and base+subbase/subgrade), should be investigated to better understand the performances of the pavement layers and the interactions between the pavement layers in the long-term.

- For the RAB group, the FWD results showed that RCA-included base layers performed superior to those built with Limestone. Results showed that Fine RCA performed the best followed by the Coarse RCA and RCA+RAP while Limestone performed the lowest within the test cells that were not built with LSSB. Based on the FWD test results, the following material selection can be

recommended for building aggregate base layers with recycled aggregate materials from the most preferred to least preferred: (1) Fine RCA, (2) Coarse RCA, (3) RCA+RAP, and (4) Limestone. However, since there were two different subgrade layers [Sand Subgrade layers in Cells 185 (12-in Coarse RCA) and 186 (12-in Fine RCA) and Clay Loam subgrade layers in Cells 188 (12-in Limestone) and 189 (12-in RCA+RAP)], further investigation may be needed to verify this recommendation.

- The thickness of the LSSB layers should be sufficient enough to provide good drainage and structural support and the results of this study showed that 18-in LSSB layers performed better than 9-in LSSB layers. It should also be noted that the FWD test may not be appropriate to evaluate the impact of geosynthetics in the LSSB system and heavy weight deflectometer (HWD) tests should be conducted in the future studies on the LSSB sections.

- LSSB Material used in this study (a crushed granite stone) was poorly graded. Poorly graded large stones contain large voids that weak subgrade soil can move into. Large voids can also cause excessive particle reorientation during compaction and cause a less stable foundation for the construction of the upper layers. By using well-graded large stones having fewer voids, such problems could be reduced.

- While LSSB layers are expected to show good drainage properties, conditions that could lower the permeability of the LSSB layers (e.g., contamination by the subgrade soil) should be investigated. The placement of geocomposite layers in the LSSB layers (preferably in the middle of the layers) should be investigated to improve the lateral drainage.

- The thermal properties of each road material should be investigated to understand the different maximum frost penetration depths and freezing and thawing periods observed for each test cell.

CHAPTER 6: ESTIMATION OF LABORATORY AND FIELD TEST RESULTS

6.1 ESTIMATION OF LABORATORY TEST RESULTS

For the estimation of laboratory test results, a forward stepwise regression technique, which is one of the two stepwise regression methods (the other method is known as backward stepwise regression) was used to obtain simple and easily interpretable models (Edil et al. 2012; Bareither et al. 2008). Initially, a significance level of 0.05 [alpha (α) = 0.05 (95% confidence)], was used to determine whether the model was statistically significant. The p-value of each parameter in the model and the significance F value of the whole model must be smaller than 0.05 for statistical significance. However, when no statistically significant model could be determined at α = 0.05, the confidence level was reduced to 90% (α = 0.1). The statistical significance of the intercept, which was the constant value in the model, was ignored. In addition, all of the statistically significant models were checked for physical significance. The sample size for all of the regression analyses shown in this section was six (each base layer aggregate was one sample) except the analyses performed to estimate M_R of the base layer aggregates. For the estimation of the M_R of the base layer aggregates, the sample size was only four since the M_R tests were performed only on Coarse RCA, Fine RCA, Limestone, and RCA+RAP materials.

Forward stepwise regression analyses were performed only for the base layer aggregates in all the test cells (Figure 3.2). These base layer aggregates were Coarse RCA, Fine RCA, Limestone, RCA+RAP, Class 6 Aggregate, and Class 5Q Aggregate (Figure 4.1). Detailed information regarding laboratory test results of these aggregates is provided in Chapter 4. In addition, summaries of the laboratory test results of the base layer aggregates that were used in the forward stepwise regression analyses are provided in Appendix AK.

6.1.1 Proctor Compaction Characteristics

For aggregates, determining Proctor compaction characteristics consisted of two stages: (1) conventional Proctor testing [modified Proctor compaction testing was used in this project (ASTM D1557)] and (2) correction of unit weight and water content for soils containing oversize particles (ASTM D4718). The optimum moisture content (OMC) and maximum dry unit weight (MDU) parameters determined only through conventional modified Proctor compaction testing (ASTM D1557) are referred to as “uncorrected OMC” and “uncorrected MDU”, respectively, hereinafter. On the other hand, the OMC and MDU parameters determined after applying the correction for oversize particles (ASTM D4718) are referred to as “corrected OMC” and “corrected MDU”, respectively, hereinafter.

6.1.1.1 Uncorrected Optimum Moisture Content (OMC) and Maximum Dry Unit Weight (MDU)

Table 6.1 and Table 6.2 summarize the regression equations that can be used to estimate uncorrected optimum moisture content (OMC) and maximum dry unit weight (MDU) values of the base layer aggregates, respectively. All of the equations listed in Table 6.1 and Table 6.2 are statistically significant at α = 0.05. Additional equations are provided in Appendix AL.

Table 6.1. Equations to estimate uncorrected optimum moisture content (OMC) (%)

Equation	R^2	Adj. R^2	Std. Error
0.3740*Fine Absorption (%) - 7.4767*Fine Apparent G_s + 0.4845*C_c + 25.5829	1	1	0.12
-10.1413*Fine SSD G_s - 0.8009*Asphalt Binder Content by Extraction (%) + 34.1067	1	0.99	0.15
-7.8353*Fine OD G_s - 0.0271*Sand (%) + 28.0680	1	0.99	0.17
0.4022*Fine Absorption (%) - 5.8618*Fine Apparent G_s + 21.9079	0.98	0.96	0.38
-7.5866*Fine OD G_s + 26.3385	0.97	0.96	0.39
-10.0533*Fine SSD G_s + 33.3040	0.91	0.89	0.67
0.4404*Fine Absorption (%) + 6.4150	0.86	0.83	0.84
1.9516*Coarse Absorption (%) + 3.0264	0.83	0.79	0.93
0.1411*Residual Mortar Content (%) + 6.1902	0.8	0.75	1.01
-19.1560*Coarse OD G_s + 56.8998	0.78	0.73	1.06
-22.9161*Coarse SSD G_s + 68.0771	0.72	0.65	1.2

G_s = specific gravity; C_c = coefficient of curvature; SSD = saturated-surface-dry; OD = oven-dry

Table 6.2. Equations to estimate uncorrected maximum dry unit weight (MDU) (kN/m^3)

Equation	R^2	Adj. R^2	Std. Error
6.2770*Combined OD G_s - 1.5330*D_{10} (mm) + 5.6493	1	0.99	0.1
-0.3473*Uncorrected OMC (%) + 0.0079*C_u + 22.8208	1	0.99	0.11
8.4437*Combined SSD G_s - 0.2150*D_{30} (mm) - 0.3574	0.99	0.98	0.15
9.5728*Combined SSD G_s - 0.4428*Gravel-to-Sand Ratio - 2.8983	0.99	0.98	0.18
4.5679*Fine OD G_s + 9.9306	0.98	0.97	0.21
-0.2100*Fine Absorption (%) + 5.1046*Fine Apparent G_s + 8.2741	0.98	0.96	0.25
-1.8681*Coarse Absorption (%) + 0.6488*D_{30} (mm) + 25.2969	0.97	0.96	0.25
-0.3256*Fine Absorption (%) - 0.9333*Asphalt Binder Content by Extraction (%) + 23.0652	0.96	0.94	0.31
-0.5755*Uncorrected OMC (%) + 25.5324	0.92	0.90	0.39
12.2566*Coarse OD G_s - 10.2530	0.89	0.86	0.46
-0.0887*Residual Mortar Content (%) + 22.1542	0.88	0.85	0.48
15.0737*Coarse SSD G_s - 18.4532	0.86	0.83	0.51
-1.1371*Coarse Absorption (%) + 23.8381	0.78	0.73	0.64
-0.2432*Fine Absorption (%) + 21.7656	0.73	0.66	0.71

OD = oven-dry; SSD = saturated-surface-dry; G_s = specific gravity; C_u = coefficient of uniformity; OMC = optimum moisture content. To determine the combined G_s values, the weighted average of the G_s values of the coarse [> No. 4 sieve (4.75 mm)] and fine (< No. 4) fractions of the materials were used.

6.1.1.2 Corrected Optimum Moisture Content (OMC) and Maximum Dry Unit Weight (MDU)

Table 6.3 and Table 6.4 summarize the regression equations that can be used to estimate corrected optimum moisture content (OMC) and maximum dry unit weight (MDU) values of the base layer aggregates, respectively. All of the equations listed in Table 6.3 and Table 6.4 are statistically significant at $\alpha = 0.05$. Additional equations are provided in Appendix AM.

Table 6.3. Equations to estimate corrected optimum moisture content (OMC) (%)

Equation	R^2	Adj. R^2	Std. Error
0.5026*Combined Absorption (%) - 6.0058*Fine Apparent G_s + 22.0333	0.96	0.94	0.41
-9.1895*Combined OD G_s + 30.5418	0.92	0.91	0.51
-8.1230*Fine SSD G_s + 28.2286	0.89	0.86	0.61
-5.9208*Fine OD G_s + 22.1405	0.88	0.85	0.64
0.5912*Combined Absorption (%) + 5.9768	0.79	0.73	0.85

G_s = specific gravity; OD = oven-dry; SSD = saturated-surface-dry. To determine the combined G_s or absorption values, the weighted average of the G_s or absorption values of the coarse [> No. 4 sieve (4.75 mm)] and fine (< No. 4) fractions of the materials were used.

Table 6.4. Equations to estimate corrected maximum dry unit weight (MDU) (kN/m^3)

Equation	R^2	Adj. R^2	Std. Error
5.4563*Combined OD G_s - 0.4420*Asphalt Binder Content by Ignition (%) + 8.7018	0.99	0.99	0.12
6.4234*Combined OD G_s + 0.0551*D_{60} (mm) + 4.8986	0.99	0.98	0.16
3.2017*Fine OD G_s - 0.7433*Asphalt Binder Content by Ignition (%) + 15.1387	0.99	0.98	0.16
5.6348*Fine SSD G_s + 0.0264*Gravel (%) + 5.7557	0.98	0.96	0.23
4.1482*Fine OD G_s + 0.0345*Gravel (%) + 9.4952	0.98	0.96	0.22
8.5169*Combined SSD G_s - 0.5435	0.96	0.95	0.24
6.4424*Combined OD G_s + 5.2901	0.95	0.94	0.29
-0.6590*Corrected OMC (%) + 26.3182	0.91	0.88	0.39
5.6169*Fine SSD G_s + 7.0948	0.89	0.86	0.43
3.9711*Fine OD G_s + 11.5752	0.83	0.79	0.53
12.4780*Coarse SSD G_s - 11.5034	0.66	0.58	0.74

OD = oven-dry; G_s = specific gravity; SSD = saturated-surface-dry; OMC = optimum moisture content. To determine the combined G_s values, the weighted average of the G_s values of the coarse [> No. 4 sieve (4.75 mm)] and fine (< No. 4) fractions of the materials were used.

6.1.2 Saturated Hydraulic Conductivity (K_{sat})

Forward stepwise regression analyses were performed only to correlate saturated hydraulic conductivity (K_{sat}) values of the base layer aggregates determined by falling head permeability testing at 100% DOC. Table 6.5 summarizes the regression equations that can be used to estimate K_{sat} values of the base layer aggregates. All of the equations listed in Table 6.5 are statistically significant at $\alpha = 0.05$. Additional equations are provided in Appendix AN.

Table 6.5. Equations to estimate saturated hydraulic conductivity (K_{sat}) (cm/sec)

Equation	R^2	Adj. R^2	Std. Error
0.002992*e - 0.000136*Fine Apparent G_s - 0.000222	1	1	7.16E-06
0.002635*e - 2.26E-05*Corrected MDU (kN/m^3) - 1.89E-05	1	1	7.7E-06
0.002534*e + 1.78E-05*Corrected OMC (%) - 0.000611	1	1	8.98E-06
-0.000190*Corrected MDU (kN/m^3) + 0.001358*Combined Apparent G_s + 0.000523	1	0.99	1.25E-05
0.005083*n - 0.000844	0.99	0.99	1.75E-05
0.003073*e - 0.000598	0.99	0.98	1.9E-05
-0.000183*Corrected MDU (kN/m^3) + 0.000933*Fine Apparent G_s + 0.001539	0.98	0.96	2.95E-05
0.016696*e^3/(1+e) - 4.05*E-05	0.96	0.95	3.36E-05
5.52E-05*Combined Absorption (%) - 4.50E-05	0.91	0.89	4.71E-05
7.80E-05*Corrected OMC (%) - 0.000464	0.81	0.76	6.99E-05
-0.000716*Combined OD G_s + 0.001917	0.75	0.68	8.07E-05
2.90E-05*Fine Absorption (%) + 3.46E-05	0.75	0.68	8.1E-05
-0.000106*Corrected MDU (kN/m^3) + 0.002409	0.72	0.65	8.46E-05
-0.0004586*Fine OD G_s + 0.001257	0.71	0.63	8.72E-05
-9.74E-05*Uncorrected MDU (kN/m^3) + 0.002195	0.68	0.6	9.06E-05
5.77E-05*Uncorrected OMC (%) - 0.000309	0.66	0.58	9.33E-05

e = void ratio [based on corrected MDU and apparent specific gravity (G_s)]; n = porosity [n = e/(1+e)]; G_s = specific gravity; MDU = maximum dry unit weight; OMC = optimum moisture content; OD = oven-dry. To determine the combined G_s or absorption values, the weighted average of the G_s or absorption values of the coarse [> No. 4 sieve (4.75 mm)] and fine (< No. 4) fractions of the materials were used.

6.1.3 Soil-Water Characteristic Curve (SWCC) Parameters

Forward stepwise regression analyses were performed only to correlate SWCC parameters of the base layer aggregates determined by pressure plate and activity meter tests at 100% DOC. As stated in Chapter 4, the van Genuchten model (van Genuchten 1980) [Equation (4.1)] was used to plot SWCC curves of the base layer aggregates. Among the parameters shown in Equation (4.1), forward stepwise regression analyses were performed only to estimate the residual VWC (θ_r) and the saturated VWC (θ_s). Forward stepwise regression analyses were also run to estimate air-entry pressure (or bubbling pressure) values required to initiate desaturation of the largest pores in the soils/aggregates (Fredlund and Rahardjo 1993).

6.1.3.1 Residual Volumetric Water Content (VWC) (θ_r)

Table 6.6 shows the only equation that can be used to estimate the θ_r values of the base layer aggregates, and it is statistically significant at $\alpha = 0.1$.

Table 6.6. Equation to estimate residual volumetric water content (VWC) (θ_r)

Equation	R^2	Adj. R^2	Std. Error
#-0.0100*Corrected OMC (%) + 0.1127	0.55	0.44	0.02

OMC = optimum moisture content; #statistically significant at alpha = 0.1

6.1.3.2 Saturated Volumetric Water Content (VWC) (θ_s)

Table 6.7 shows the equations that can be used to estimate the θ_s values of the base layer aggregates. The equations listed in Table 6.7 are statistically significant at $\alpha = 0.05$.

Table 6.7. Equations to estimate saturated volumetric water content (VWC) (θ_s)

Equation	R^2	Adj. R^2	Std. Error
-0.1382*Combined OD G_s + 0.0213*C_c + 0.5672	0.91	0.85	0.01
0.0271*Coarse Absorption (%) + 0.1845	0.9	0.88	0.01
0.0018*Residual Mortar Content (%) + 0.2315	0.77	0.71	0.01
0.0116*Uncorrected OMC (%) + 0.1647	0.76	0.7	0.01
-0.0188*Uncorrected MDU (kN/m^3) + 0.6526	0.72	0.65	0.02
-0.2413*Coarse OD G_s + 0.8718	0.7	0.62	0.02
-0.0848*Fine OD G_s + 0.4632	0.68	0.6	0.02

OD = oven-dry; G_s = specific gravity; C_c = coefficient of curvature; OMC = optimum moisture content; MDU = maximum dry unit weight. To determine the combined G_s values, the weighted average of the G_s values of the coarse [> No. 4 sieve (4.75 mm)] and fine (< No. 4) fractions of the materials were used.

6.1.3.3 Air-Entry Pressure

Table 6.8 shows the equations that can be used to estimate the air-entry pressure values of the base layer aggregates. The equations listed in Table 6.8 are statistically significant at $\alpha = 0.05$. However, further evaluation would be required to check the physical significance of these equations.

Table 6.8. Equations to estimate air-entry pressure (kPa)

Equation	R^2	Adj. R^2	Std. Error
48.5469*e - 2.2888*Coarse Absorption (%) - 0.1958*Fines (%) - 1.2909	1	0.99	0.15
78.8067*n - 1.4732*Coarse Absorption (%) - 9.0649	0.97	0.94	0.38
46.0499*e - 1.3624*Coarse Absorption (%) - 5.1737	0.96	0.93	0.41
31.5864*e - 0.6861*D_{30} (mm) - 4.7364	0.93	0.89	0.53
52.2180*n - 0.7107*D_{30} (mm) - 7.2297	0.93	0.88	0.56

e = void ratio [based on corrected MDU and apparent specific gravity (G_s)]; n = porosity [n = e/(1+e)]

6.1.4 Resilient Modulus (M_R) Characteristics

Laboratory M_R tests were performed on Coarse RCA, Fine RCA, Limestone, RCA+RAP, Sand Subgrade, and Clay Loam subgrade materials per AASHTO T 307 by the University of Texas at El Paso (UTEP). Since no information regarding M_R testing for the base layer aggregates was given in Chapter 4, the test methodology used for the base layer aggregates is explained in the following. Nazarian et al. (2020) provides more information regarding M_R testing for Sand Subgrade and Clay Loam subgrade.

The base layer aggregates were air-dried, and aggregations were broken up rigorously to preserve the natural size of the aggregate particles. Since the aggregates were classified as Type I (AASHTO T 307), 152 mm by 305 mm cylindrical specimens were prepared. Variation in compaction moisture content affects the degree of saturation (DOS) of aggregates and changes pore water pressure or matric suction in the aggregates (Dawson et al. 2000). Such changes in aggregates affect their M_R significantly (Edil et al. 2012). To determine the relationship between the moisture content (or matric suction) and M_R values, the aggregates were compacted with modified Proctor effort at different moisture contents (dry side of OMC, OMC, and wet side of OMC) in six lifts of equal mass with a 4.5-kg impact hammer. Duplicate specimens were prepared for each compaction moisture content and mellowed for 24 hours prior to testing. Elastic deformations, recorded during the last five cycles of each loading sequence, were considered and the model introduced by Ooi et al. (2004) was used to determine the M_R. The model introduced by Ooi et al. (2004) is known as the modified MEPDG model [Equation (6.1)]. Most of the highway agencies use the conventional MEPDG model [Equation (6.2)]. To convert the modified MEPDG model [Equation (6.1)] into the conventional MEPDG model [Equation (6.2)], the modified fitting parameters (k_1', k_2', and k_3') [Equation (6.1)] were converted into the conventional fitting parameters (k_1, k_2, and k_3) [Equation (6.2)] (Nazarian et al. 2014). Conversions of the fitting parameters are shown in Equations (6.3), (6.4), and (6.5) for $k_1' \rightarrow k_1$, $k_2' \rightarrow k_2$, and $k_3' \rightarrow k_3$, respectively.

$$M_R' = k_1' P_a \left(\frac{\theta}{P_a} + 1\right)^{k_2'} \left(\frac{\tau_{oct}}{P_a} + 1\right)^{k_3'} \tag{6.1}$$

$$M_R = k_1 P_a \left(\frac{\theta}{P_a}\right)^{k_2} \left(\frac{\tau_{oct}}{P_a} + 1\right)^{k_3} \tag{6.2}$$

where P_a is the atmospheric pressure, θ is the bulk stress ($\theta = \sigma_1 + \sigma_2 + \sigma_3 = \sigma_1 + 2\sigma_3 = \sigma_d + 3\sigma_3$), σ_1, σ_2, and σ_3 are the principal stresses, σ_d is the deviator stress ($\sigma_d = \sigma_1 - \sigma_3$), τ_{oct} is the octahedral shear stress [$\tau_{oct} = 1/3\sqrt{(\sigma_1 - \sigma_2)^2 + (\sigma_1 - \sigma_3)^2 + (\sigma_2 - \sigma_3)^2} = (\sqrt{2}/3)\sigma_d$], and k_1', k_2', k_3' are modified fitting parameters, and k_1, k_2, and k_3 are the conventional fitting parameters.

$$k_1' = k_1 e^{-1.32k_2} \quad (6.3)$$

$$k_2' = 1.88k_2 \quad (6.4)$$

$$k_3' = k_3 \quad (6.5)$$

where k_1', k_2', k_3' are modified fitting parameters, and k_1, k_2, k_3 are the conventional fitting parameters.

NCHRP 1-28A suggests that an M_R at θ = 214 kPa (31 psi) and τ_{oct} = 52 kPa (7.5 psi) can be considered to be a summary M_R (SM_R) for base layer aggregates (Mazari et al. 2014; Nazarian et al. 2014). Figure 6.1, Figure 6.2, Figure 6.3, and Figure 6.4 summarize the SM_R values at various moisture content values for Coarse RCA, Fine RCA, Limestone, and RCA+RAP, respectively. In these figures, linear trendlines were added to show SM_R as a function of moisture content. More figures showing exponential, logarithmic, and power relationships between SM_R and moisture content are provided in Appendix AO. Appendix AP and Appendix AQ contain more figures showing SM_R vs. degree of saturation (DOS) and SM_R vs. VWC, respectively. Overall, it was concluded that increasing the moisture content, DOS, or VWC yielded lower M_R values. It was also concluded that this result agreed with findings in the literature.

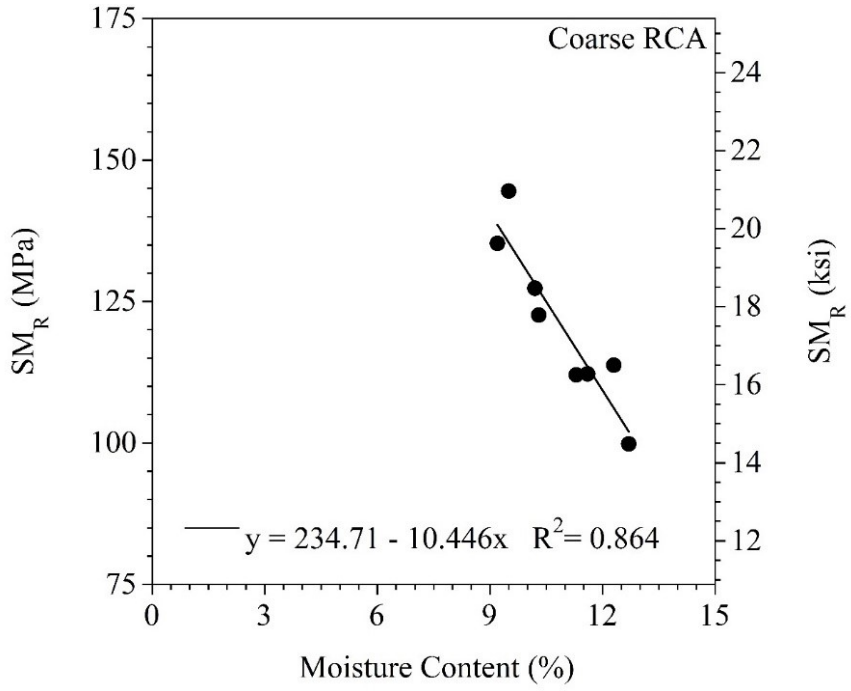

Figure 6.1. Summary resilient modulus (SM_R) values at different moisture contents for Coarse RCA

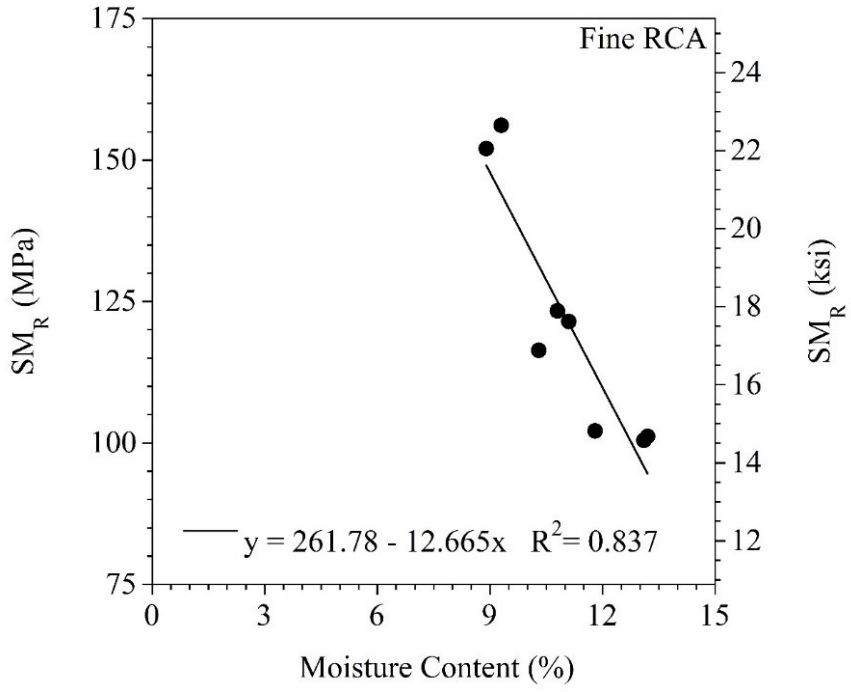

Figure 6.2. Summary resilient modulus (SM_R) values at different moisture contents for Fine RCA

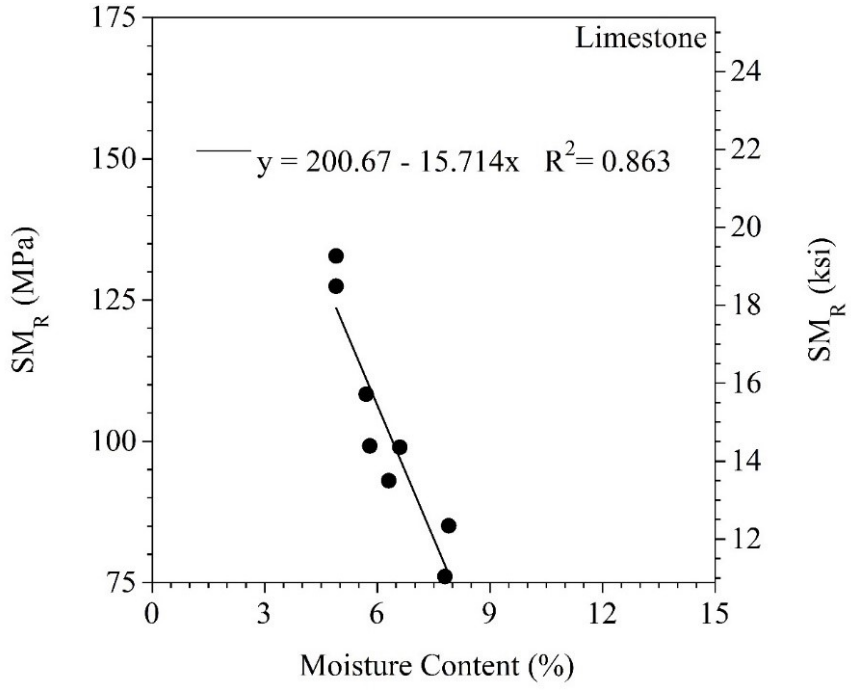

Figure 6.3. Summary resilient modulus (SM_R) values at different moisture contents for Limestone

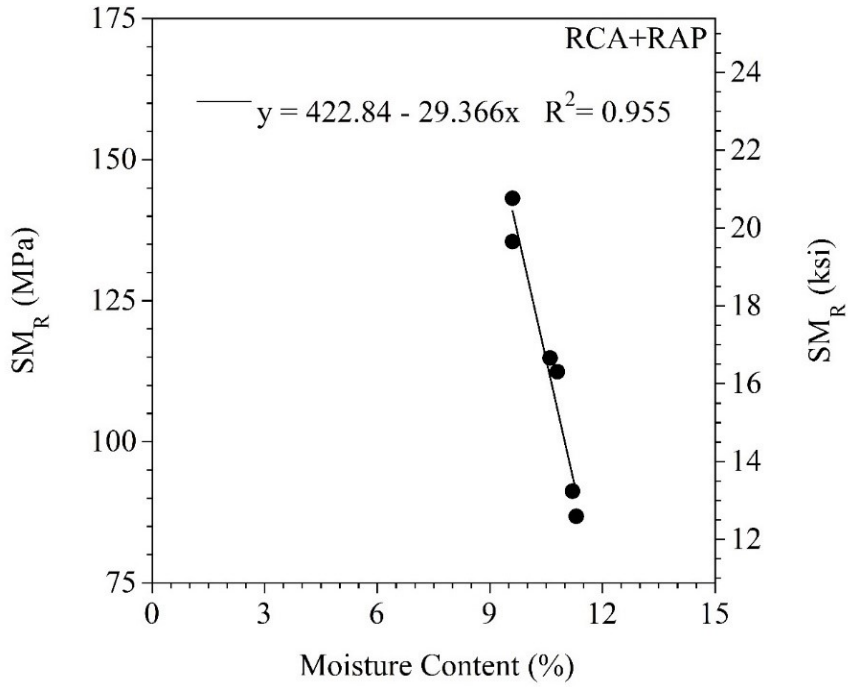

Figure 6.4. Summary resilient modulus (SM_R) values at different moisture contents for RCA+RAP

Soil suction is composed of osmotic suction and matric suction (Mehrotra 2014). Khoury et al. (2004) stated that changes in M_R of unsaturated soils/aggregates were mostly affected by changes in matric suction. Previous studies have indicated that M_R was better correlated to matric suction than to moisture content (Edil et al. 2012; Ba et al. 2013; Nokkaew 2014; Mehrotra 2014; Nazarian et al. 2014; Banerjee et al. 2020; Chu 2020). In a soil/aggregate matrix, matric suction affects the stress existing in the soil/aggregate particle with pore water pressure (Ba et al. 2013; Nokkaew 2014; Chu 2020). In addition, a force that reinforces the particle bonding is generated by matric suction (Chu 2020). Overall, soil/aggregate M_R is expected to increase when the matric suction in soil/aggregate matrix increases (Edil et al. 2012; Mehrotra 2014).

The effect of matric suction on M_R of unsaturated soils/aggregates depends on the air-entry pressure. In a study performed by Banerjee et al. (2020), for ML and CH soils (ASTM D2487), while considerable increases in the M_R values were observed at matric suctions higher than air-entry pressures of the soils, no significant changes in the M_R values were observed at matric suctions lower than the air-entry pressures of the soils.

In this study, an effort was made to compare the SM_R values determined for Coarse RCA, Fine RCA, Limestone, and RCA+RAP with the matric suction values, determined from the SWCC properties of these materials (first, VWC values of the M_R test specimens were calculated using the gravimetric water content and dry density of the specimens. Then, using the SWCC test results and van Genuchten model parameters determined for each test material, the suction values were determined for a range of moisture contents for a given material) [detailed information regarding the SWCC of these aggregates is provided in Chapter 4]. Figure 6.5, Figure 6.6, Figure 6.7, and Figure 6.8 show the relationships between

the SM_R and matric suction for Coarse RCA, Fine RCA, Limestone, and RCA+RAP, respectively. In these figures, logarithmic trendlines were added to show SM_R as a function of matric suction. In addition, air-entry pressure values, determined from the SWCC properties of the aggregates, were also added to these figures. More figures showing linear, exponential, and power relationships between SM_R and matric suction are provided in Appendix AR. Unlike in the study performed by Banerjee et al. (2020), all the matric suction values were higher than the air-entry pressures of the base layer aggregates, i.e., no M_R data presented at matric suctions lower than the air-entry pressures of the base layer aggregates. Since all the matric suction values were higher than the air-entry pressures of the base layer aggregates, higher SM_R values were observed at higher matric suctions (Banerjee et al. 2020).

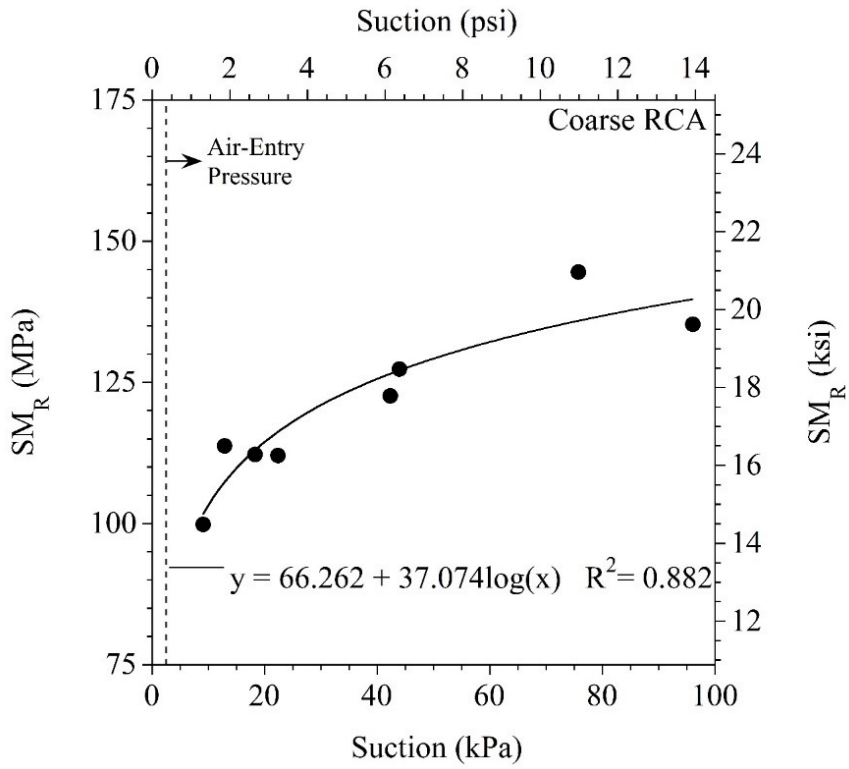

Figure 6.5. Summary resilient modulus (SM_R) at different matric suctions for Coarse RCA

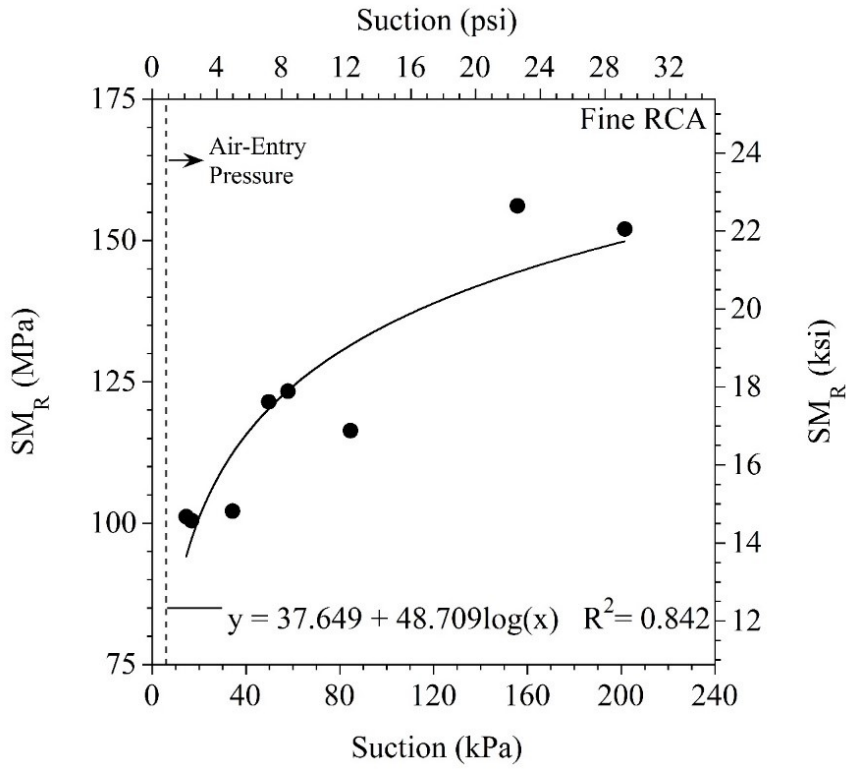

Figure 6.6. Summary resilient modulus (SM_R) at different matric suctions for Fine RCA

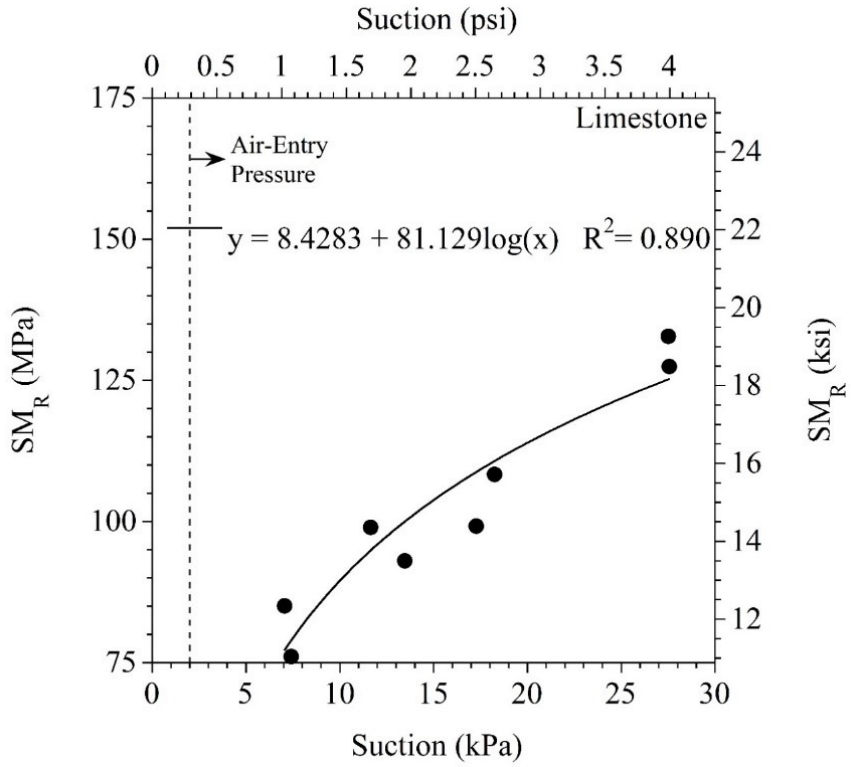

Figure 6.7. Summary resilient modulus (SM_R) at different matric suctions for Limestone

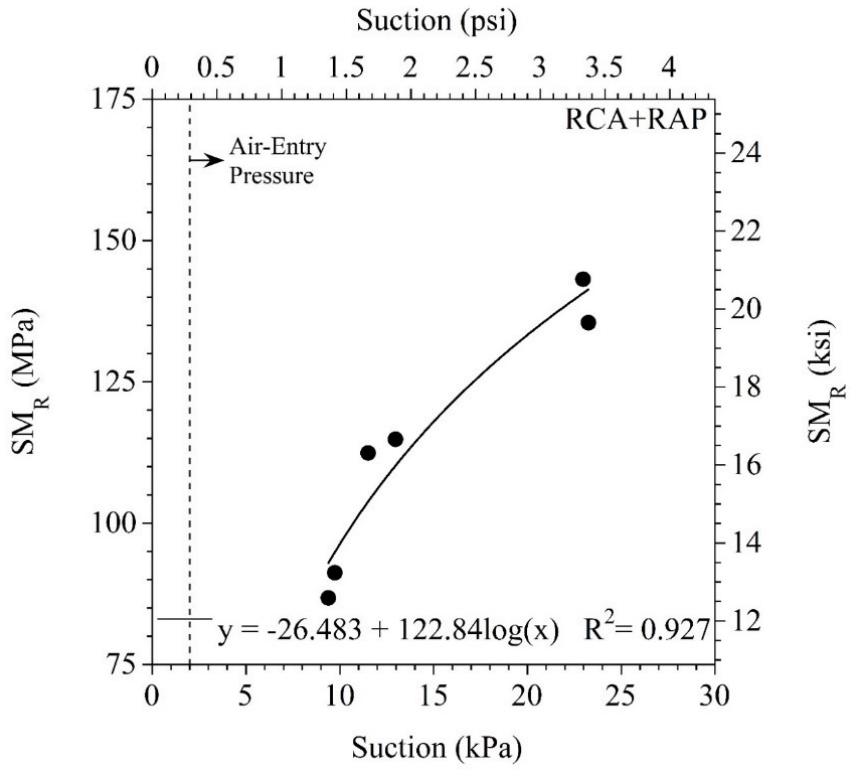

Figure 6.8. Summary resilient modulus (SM_R) at different matric suctions for RCA+RAP

6.1.4.1 Summary Resilient Modulus (SM_R)

Table 6.9 summarizes the regression equations that can be used to estimate SM_R at optimum moisture content (OMC). All of the equations listed in Table 6.9 are statistically significant at $\alpha = 0.05$. More equations are provided in Appendix AS.

Table 6.9. Equations to estimate summary resilient modulus (SM_R) (MPa) at optimum moisture content (OMC)

Equation	R^2	Adj. R^2	Std. Error
0.9121*Residual Mortar Content (%) + 95.0309	1	1	0.51
13.9035*Coarse Absorption (%) + 69.9919	0.99	0.99	1.32
5.4794*Uncorrected OMC (%) + 61.4114	0.98	0.97	2.19
-39.5364*Fine OD G_s + 201.5303	0.97	0.95	2.8
-118.4860*Coarse OD G_s + 409.3854	0.95	0.92	3.73
-8.4659*Uncorrected MDU (kN/m^3) + 284.6113	0.94	0.91	3.89
-143.1262*Coarse SSD G_s + 482.0049	0.92	0.88	4.61
2.4855*Fine Absorption (%) + 95.5617	0.92	0.88	4.62

OMC = optimum moisture content; OD = oven-dry; SSD = saturated-surface-dry; G_s = specific gravity; MDU = maximum dry unit weight

6.1.4.2 MEPDG Constitutive Model Coefficients (k_1, k_2, and k_3)

Table 6.10, Table 6.11, and Table 6.12 summarize the equations that can be used to estimate k_1, k_2, and k_3 conventional fitting parameters [Equation (6.2)]. All of the equations listed in Table 6.10, Table 6.11, and Table 6.12 are statistically significant at $\alpha = 0.05$.

Table 6.10. Equations to estimate k_1 conventional fitting parameter

Equation	R^2	Adj. R^2	Std. Error
11.6644*Fine Absorption (%) + 16.1631*D_{30} (mm) + 731.5558	1	1	0.73
83.7374*Coarse Absorption (%) + 153.4469*Fine Apparent G_s + 173.1523	1	1	0.26
13.4873*Fine Absorption (%) + 738.4029	0.96	0.94	16.51
70.6962*Coarse Absorption (%) + 614.7812	0.92	0.87	24.80

G_s = specific gravity

Table 6.11. Equations to estimate k_2 conventional fitting parameter

Equation	R^2	Adj. R^2	Std. Error
-0.5822*Combined Apparent G_s - 0.0136*Corrected MDU (kN/m^3) + 2.250	1	1	0
-0.5946*Combined Apparent G_s + 0.0092*Corrected OMC (%) + 1.9211	1	1	0
-0.4716*Fine Apparent G_s + 0.0061*Combined Absorption (%) + 1.6280	1	1	0
-0.7294*Combined Apparent G_s + 2.3626	0.98	0.97	0.01
-0.5161*Fine Apparent G_s + 1.7773	0.96	0.93	0.02

G_s = specific gravity; MDU = maximum dry unit weight; OMC = optimum moisture content. To determine the combined G_s or absorption values, the weighted average of the G_s or absorption values of the coarse [> No. 4 sieve (4.75 mm)] and fine (< No. 4) fractions of the materials were used.

Table 6.12. Equations to estimate k_3 conventional fitting parameter

Equation	R^2	Adj. R^2	Std. Error
0.2190*Fine Apparent G_s + 0.0048*Combined Absorption (%) - 0.6708	1	1	0
0.5910*Fine Apparent G_s + 0.7889*k_2 - 1.9552	1	1	0

G_s = specific gravity; k_2 = conventional fitting parameter. To determine the combined absorption values, the weighted average of the absorption values of the coarse [> No. 4 sieve (4.75 mm)] and fine (< No. 4) fractions of the materials were used.

6.1.5 Aggregate Abrasion Characteristics

To evaluate degradation during compaction, breakage potential (B_p), total breakage (B_t), and relative breakage (B_r) parameters, as described by Hardin (1985), were used in Chapter 4. B_p is defined as the area between the initial gradation curve (before compaction) and the line defining the upper limit of silt size (0.075 mm) (Hardin 1985). B_t is defined as the area between initial (before compaction) and final (after compaction) gradation curves (Hardin 1985). B_p and B_t are relative areas compared to the unit area, which is the area of one log cycle (Hardin 1985). B_r is the ratio between the B_t and B_p.

According to Hardin (1985), the larger the particle size, the higher the B_p value. Based on the test results provided in Chapter 4, Coarse RCA and Class 5Q Aggregate exhibited higher B_p than other materials due to their gradation characteristics. In fact, the highest B_p was observed with Class 5Q Aggregate, which was the coarsest aggregate. According to these results, Coarse RCA and Class 5Q Aggregate would be expected to exhibit higher B_t than other materials because less stress is required to break up larger particles compared to finer particles (Hardin 1985).

In the literature, it is stated that an increase in the residual mortar content can yield an increase in aggregate degradation through crushing and degradation of porous mortar (de Juan and Gutiérrez 2009; Butler et al. 2011; Bhasya and Bharatkumar 2018). Therefore, Coarse RCA and Class 5Q Aggregate exhibited higher B_t because of not only their coarser gradations but also their high residual mortar content. Since both Coarse RCA and Class 5Q Aggregate may have gravel size cemented aggregates that could instantly break down under compaction pressure, these two aggregates exhibited higher B_t values. These two aggregates also exhibited higher B_r values than other aggregates.

In this study, an effort was made to model abrasion characteristics of the base layer aggregates. To do so, B_r values of the base layer aggregates were considered. Table 6.13, Table 6.14, and Table 6.15 summarize the equations that can be used to estimate B_r after 100, 300, and 500 gyrations. All of the equations listed in Table 6.13, Table 6.14, and Table 6.15 are statistically significant at $\alpha = 0.1$.

Table 6.13. Equations to estimate relative breakage (B_r) after 100 gyrations

Equation	R^2	Adj. R^2	Std. Error
-0.0702*Coarse OD G_s + 0.0048*$PLR_{0.5}$ (%) + 0.1524	0.98	0.96	0
-0.1056*Coarse OD G_s - 0.6655*Median Roundness + 0.7250	0.97	0.96	0
0.0005*Residual Mortar Content (%) + 0.0042*$PLR_{0.5}$ (%) - 0.0281	0.96	0.94	0
-0.1052*Coarse OD G_s + 0.0022*$PLR_{0.7}$ (%) + 0.1451	0.95	0.91	0
#0.0007*Residual Mortar Content (%) - 0.5216*Median Roundness + 0.3519	0.94	0.9	0
0.0008*Residual Mortar Content (%) + 0.0096	0.76	0.7	0.01
-0.0986*Coarse OD G_s + 0.2713	0.69	0.61	0.01
0.0067*$PLR_{0.5}$ (%) - 0.0407	0.69	0.61	0.01

OD = oven-dry; G_s = specific gravity; $PLR_{0.5}$ = percent less rounded than 0.5; $PLR_{0.7}$ = percent less rounded than 0.7 (the definitions of $PLR_{0.5}$, $PLR_{0.7}$, and median roundness are provided in Figure 6.9). For the distribution shown in Figure 6.9, the number of particles was considered instead of the volume of particles. If the volume of particles was considered, particle size would affect the particle shape distributions. To avoid this, the number of particles was used in order to evaluate the distributions. More detailed information can be found in Chapter 4.
#statistically significant at alpha = 0.1

Table 6.14. Equations to estimate relative breakage (B_r) after 300 gyrations

Equation	R^2	Adj. R^2	Std. Error
-0.1327*Coarse OD G_s - 1.1803*Median Roundness + 1.1357	1	0.99	0
-0.1324*Coarse OD G_s + 0.0040*$PLR_{0.7}$ (%) + 0.0992	0.99	0.98	0
0.0009*Residual Mortar Content (%) - 0.9992*Median Roundness + 0.6665	0.98	0.97	0
0.0009*Residual Mortar Content (%) + 0.0033*$PLR_{0.7}$ (%) - 0.2066	0.96	0.94	0
#0.0006*Residual Mortar Content (%) + 0.0066*$PLR_{0.5}$ (%) - 0.0485	0.9	0.84	0.01
0.0095*$PLR_{0.5}$ (%) - 0.0630	0.71	0.64	0.01
#0.0010*Residual Mortar Content (%) + 0.0109	0.64	0.55	0.01
#-0.1203*Coarse OD G_s + 0.3312	0.53	0.42	0.01

OD = oven-dry; G_s = specific gravity; $PLR_{0.5}$ = percent less rounded than 0.5; $PLR_{0.7}$ = percent less rounded than 0.7 (the definitions of $PLR_{0.5}$, $PLR_{0.7}$, and median roundness are provided in Figure 6.9). For the distribution shown in Figure 6.9, the number of particles was considered instead of the volume of particles. If the volume of particles was considered, particle size would affect the particle shape distributions. To avoid this, the number of particles was used in order to evaluate the distributions. More detailed information can be found in Chapter 4.

#statistically significant at alpha = 0.1

Table 6.15. Equations to estimate relative breakage (B_r) after 500 gyrations

Equation	R^2	Adj. R^2	Std. Error
0.0009*Residual Mortar Content (%) + 0.0083*$PLR_{0.5}$ (%) - 0.0601	0.94	0.91	0.01
0.0014*Residual Mortar Content (%) - 1.0793*Median Roundness + 0.7221	0.94	0.9	0.01
#0.0014*Residual Mortar Content (%) + 0.0035*$PLR_{0.7}$ (%) - 0.2165	0.92	0.86	0.01
#-0.1121*Coarse OD G_s + 0.0096*$PLR_{0.5}$ (%) + 0.2258	0.9	0.84	0.01
#-0.1836*Coarse OD G_s - 1.3319*Median Roundness + 1.3744	0.89	0.82	0.01
#-0.1832*Coarse OD G_s + 0.0044*$PLR_{0.7}$ (%) + 0.2075	0.88	0.8	0.01
0.0014*Residual Mortar Content (%) + 0.0139	0.73	0.66	0.01
0.0128*$PLR_{0.5}$ (%) - 0.0827	0.69	0.62	0.01
#-0.1697*Coarse OD G_s + 0.4665	0.57	0.47	0.02

OD = oven-dry; G_s = specific gravity; $PLR_{0.5}$ = percent less rounded than 0.5; $PLR_{0.7}$ = percent less rounded than 0.7 (the definitions of $PLR_{0.5}$, $PLR_{0.7}$, and median roundness are provided in Figure 6.9). For the distribution shown in Figure 6.9, the number of particles was considered instead of the volume of particles. If the volume of particles was considered, particle size would affect the particle shape distributions. To avoid this, the number of particles was used in order to evaluate the distributions. More detailed information can be found in Chapter 4.

#statistically significant at alpha = 0.1

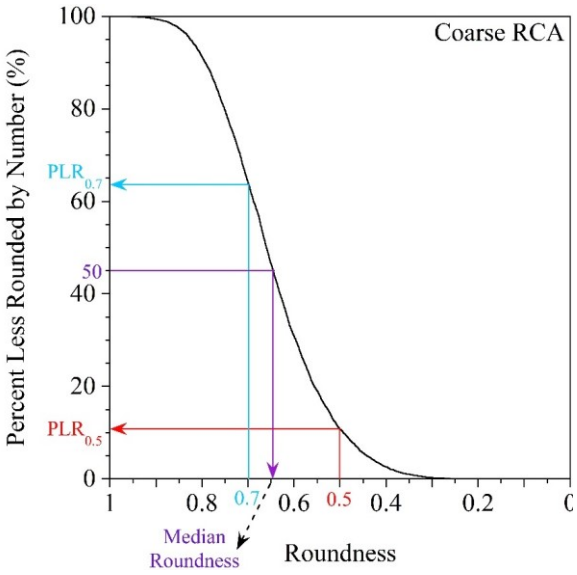

Figure 6.9. Definitions of $PLR_{0.5}$, $PLR_{0.7}$, and median roundness parameters

6.1.6 Reassessment of Models Provided in Edil et al. (2012) for More General Equations

Edil et al. (2012) conducted a study on recycled aggregates that were collected from different sources throughout the US. Thus, it was considered that it would be useful to retrieve the data and analysis results provided in Edil et al. (2012) and evaluate whether they can be combined together to expand the database for recycled aggregate materials. The laboratory test results that are summarized in Appendix AK (also reported in Chapter 4) and the laboratory test results from Edil et al. (2012) in Appendix AT were combined to obtain more general equations to predict engineering properties of these materials by considering simple index properties. The test methods were first compared to see whether they were similar, and after the comparisons forward stepwise regression analyses were run to obtain more general equations to estimate the uncorrected OMC and MDU values of the materials. However, no satisfactory equations were determined because some of the laboratory data [coarse & fine OD G_s, coarse & fine SSD G_s, coarse apparent G_s, fine absorption, and combined absorption values of the aggregates] were not available in Edil et al. (2012). In Edil et al. (2012), the G_s of aggregates were determined by ASTM D854, which can only give fine apparent G_s. However, in this study, ASTM C127 and C128 were followed to obtain OD, SSD, apparent, and combined G_s values for both coarse and fine fractions of the aggregates. In addition, in this study, coarse, fine, and combined absorption values of the aggregates were reported (ASTM C127 and C128) while only the coarse absorption (ASTM C127) was reported in Edil et al. (2012). Lastly, in this study, a method developed by Abbas et al. (2007) was used to determine the residual mortar content of the aggregates (the method is defined as the combination of freeze-thaw testing and aggregate soundness testing by using a saturated sodium sulfate solution). In Abbas et al. (2007), for each aggregate, 2000 g of the particles retained on a 1-in sieve (if any), 2000 g of the particles retained on a 3/4-in sieve (if any), 1000 g of the particles retained on a 3/8-in sieve, and 1000 g of the particles retained on a No. 4 sieve were collected. This method gave the opportunity to consider a wide range of gravel fractions to determine residual mortar content. However, in Edil et al. (2012), a method described in Nokkaew (2014) was used to determine mortar contents of RCA materials

by immersing 500 g of specimen in a 10% HCl solution for 24 h. The specimens were then sieved through a 5-mm sieve and aggregate weight loss was calculated (Gokce 2001; Nokkaew 2014). Due to the smaller specimen size in the method described in Nokkaew (2014), the mortar content values reported in Edil et al. (2012) may not be as representative as the residual mortar content values reported in this study. However, since no direct comparisons between the two test methods to determine the residual mortar content of RCA materials was made in this study, the previous statement was left as speculation.

The M_R test results reported in this study and in Edil et al. (2012) could not be combined for further analysis. While NCHRP 1-28A was followed for the specimens compacted at 95% MDU in Edil et al. (2012), AASHTO T 307 was used for the specimens compacted at 100% MDU in this study. In addition, while the NCHRP model (NCHRP 2004b) was used in Edil et al. (2012), the MEPDG method [Equation (6.2)] was used in this study to analyze the test data. As stated by Mazari et al. (2014) and Nazarian et al. (2014), since these test methods differed in loading time, stress sequence, and type and location of the linear variable displacement transducers (LVDT), different M_R values were obtained by these two test methods (Mazari et al. 2014), and therefore, their results could not be combined.

In addition to the equations provided in this section, uncorrected OMC, uncorrected MDU, and SM_R [expressed as SRM in Edil et al. (2012)] models provided in Edil et al. (2012) were reassessed. Those assessments are provided in Appendix AT. Additionally, the revised correlations generated using the data provided by Edil et al. (2012) are also provided in Appendix AT.

6.2 ESTIMATION OF FIELD TEST RESULTS DURING CONSTRUCTION

Forward stepwise regression technique was also used to obtain simple and easily interpretable models for the estimation of field test results collected during construction (Bareither et al. 2008; Edil et al. 2012). The median values [the middle value in a sorted (ascending or descending) list of values] of the test results (obtained from NDG, DCP, LWD, FWD, and IC testing) provided in Chapter 3 were used in the regression analyses. The sample size for all of the regression analyses shown in this section was eleven (there were eleven test cells). Initially, a significance level of 0.05 [alpha (α) = 0.05 (95% confidence)], was used to determine whether the model was statistically significant. The p-value of each parameter in the model and the significance F value of the whole model must be smaller than 0.05 for statistical significance. However, when no statistically significant model could be determined at $\alpha = 0.05$, the confidence level was reduced to 90% ($\alpha = 0.1$). The statistical significance of the intercept, which was the constant value in the model, was ignored. In addition, all of the statistically significant models were checked for physical significance.

Forward stepwise regression analyses were only performed for the aggregate base or base+subbase layers in all the test cells (Figure 3.2). Detailed information regarding the laboratory test results of all the research materials (Figure 4.1) is provided in Chapter 4 (Appendix AK also contains information about the summaries of the laboratory test results for the base layer aggregates). Summaries of the field test results that were used in the forward stepwise regression analyses are provided in Appendix AU. Detailed information regarding the field tests performed during construction and their results is provided in Chapter 3.

6.2.1 Dynamic Cone Penetration (DCP) Parameters

6.2.1.1 Dynamic Cone Penetration (DCP) Index (DCPI)

Table 6.16 summarizes the equations that can be used to estimate the dynamic cone penetration (DCP) index (DCPI) values of the constructed test cells. All of the equations listed in Table 6.16 are statistically significant at $\alpha = 0.05$.

Table 6.16. Equations to estimate dynamic cone penetration (DCP) index (DCPI) (mm/blow)

Equation	R^2	Adj. R^2	Std. Error
-1.6462*Median NDG Dry Unit Weight (kN/m^3) + 11.3118*Combined OD G_s + 13.2990	0.63	0.54	0.91
-0.2650*Median Relative MDU (%) + 33.2674	0.56	0.51	0.94

NDG = nuclear density gauge; OD = oven-dry; G_s = specific gravity; MDU = maximum dry unit weight. To determine the combined G_s values, the weighted average of the G_s values of the coarse [> No. 4 sieve (4.75 mm)] and fine (< No. 4) fractions of the materials were used.

6.2.1.2 Field California Bearing Ratio (CBR)

Table 6.17 provides the equation that can be used to estimate field California bearing ratio (CBR) based on the DCPI values collected by dynamic cone penetrometer (DCP) [Equation (6.6) (ASTM D6951)]. The equation shown in Table 6.17 is statistically significant at $\alpha = 0.05$.

Table 6.17. Equations to estimate field California bearing ratio (CBR) (%)

Equation	R^2	Adj. R^2	Std. Error
0.8407*Median Relative MDU (%) - 51.3895	0.53	0.48	3.17

MDU = maximum dry unit weight

$$\text{CBR}\ (\%) = \frac{292}{\text{DCPI}^{1.12}} \tag{6.6}$$

where CBR is the California bearing ratio (%), and DCPI is the dynamic cone penetration (DCP) index (mm/blow).

6.2.2 Light Weight Deflectometer (LWD) Elastic Modulus (E_{LWD})

Table 6.18 summarizes the equations that can be used to estimate E_{LWD} values based on laboratory and field testing. The equations listed in Table 6.18 are statistically significant at $\alpha = 0.05$. The equations that show E_{LWD} as a linear function of DCPI or CBR in Table 6.18 are also graphically illustrated in Figure 6.10.

Table 6.18. Equations to estimate light weight deflectometer (LWD) elastic modulus (E_{LWD}) (MPa)

Equation	R^2	Adj. R^2	Std. Error
31.7980*Median NDG Dry Unit Weight (kN/m^3) - 217.5777*Combined OD G_s - 14.4437	0.81	0.76	11.25
27.6348*Median NDG Dry Unit Weight (kN/m^3) - 240.6255*Combined SDD G_s + 145.4250	0.73	0.67	13.26
34.2796*Median NDG Dry Unit Weight (kN/m^3) - 144.5733*Fine OD G_s - 251.1844	0.73	0.66	13.33
33.7399*Median NDG Dry Unit Weight (kN/m^3) - 198.3377*Fine SSD G_s - 92.1880	0.72	0.65	13.51
5.1192*Median Relative MDU (%) - 398.1386	0.71	0.68	13.01
24.4016*Median NDG Dry Unit Weight (kN/m^3) - 9.7645*Combined Absorption (%) - 435.6365	0.64	0.55	15.44
-13.2604*Median DCPI (mm/blow) + 189.5575	0.6	0.56	15.31
4.0215*Median CBR (%) - 32.8065	0.59	0.54	15.56

NDG = nuclear density gauge; OD = oven-dry; G_s = specific gravity; SSD = saturated-surface-dry; MDU = maximum dry unit weight; DCPI = dynamic cone penetration (DCP) index; CBR = field California bearing ratio. To determine the combined G_s or absorption values, the weighted average of the G_s or absorption values of the coarse [> No. 4 sieve (4.75 mm)] and fine (< No. 4) fractions of the materials were used.

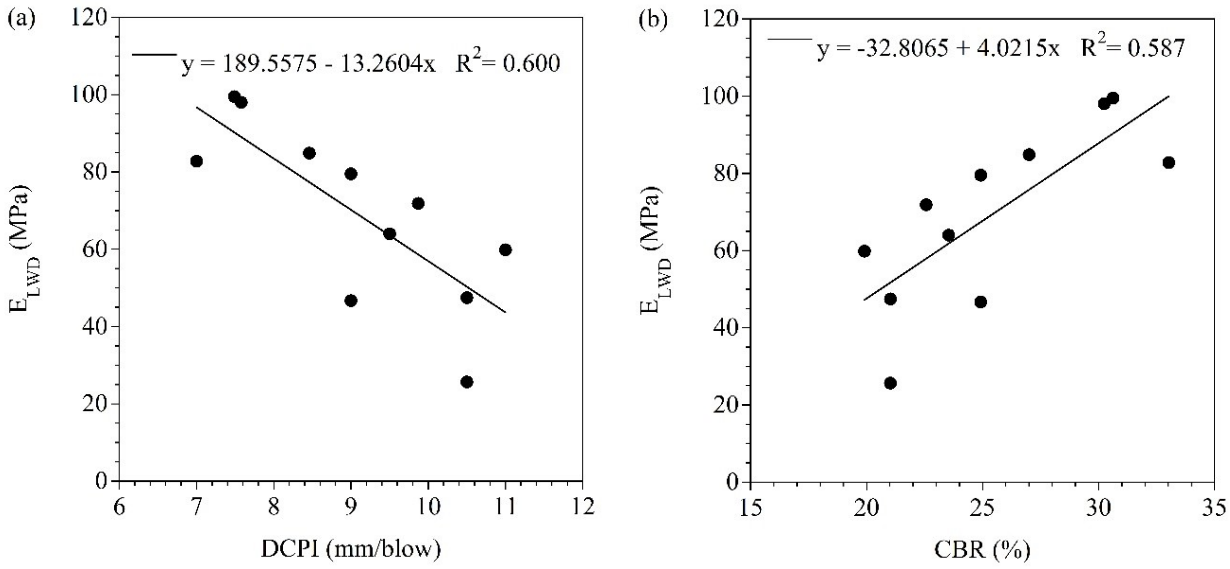

Figure 6.10. (a) Light weight deflectometer (LWD) elastic modulus (E_{LWD}) vs. dynamic cone penetration (DCP) index (DCPI) and (b) E_{LWD} vs. field California bearing ratio (CBR)

6.2.3 Falling Weight Deflectometer (FWD) Elastic Modulus (E_{FWD})

Table 6.19 summarizes the equations that can be used to estimate E_{FWD} values based on laboratory and field testing. The equations listed in Table 6.19 are statistically significant at $\alpha = 0.05$. The equations that show E_{FWD} as a linear function of DCPI, CBR, or E_{LWD} in Table 6.19 are also graphically illustrated in Figure

6.11 (for E_{FWD} vs. DCPI or CBR) and Figure 6.12 (for E_{FWD} vs. E_{LWD}). In addition to the linear relationship between E_{FWD} and E_{LWD} (Table 6.19), Figure 6.12 also shows E_{FWD} as exponential and power functions of E_{LWD}.

Table 6.19. Equations to estimate falling weight deflectometer (FWD) elastic modulus (E_{FWD}) (MPa)

Equation	R^2	Adj. R^2	Std. Error
2.2010*Median E_{LWD} (MPa) + 20.8064*Combined Absorption (%) - 21.8024*Median NDG Moisture Content (%) - 30.8626	0.95	0.93	15.7
-40.4818*D_{30} (mm) + 21.5511*Fine Absorption (%) + 31.0942*Median NDG Dry Unit Weight (kN/m^3) - 563.7491	0.95	0.92	17.07
2.2769*Median E_{LWD} (MPa) + 11.8182*Combined Absorption (%) - 1.8902*Median Relative OMC (%) + 4.5147	0.94	0.92	17.37
1.8589*Median E_{LWD} (MPa) + 16.4004*Combined Absorption (%) - 165.2143*D_{10} (mm) - 86.5880	0.94	0.91	18.11
2.4732*Median E_{LWD} (MPa) + 9.7178*Combined Absorption (%) - 136.4322	0.89	0.86	22.87
2.3858*Median E_{LWD} (MPa) - 76.4845	0.8	0.78	29.04
16.1040*Median Relative MDU (%) + 10.1868*Fine Absorption (%) - 1461.9277	0.77	0.72	32.71
10.6542*Median CBR (%) - 181.6171	0.58	0.53	42.02
-34.4403*Median DCPI (mm/blow) + 401.2251	0.57	0.52	42.51
11.7122*Median Relative MDU (%) - 980.6099	0.52	0.47	44.69

E_{LWD} = light weight deflectometer (LWD) elastic modulus; NDG = nuclear density gauge; OMC = optimum moisture content; MDU = maximum dry unit weight; CBR = field California bearing ratio; DCPI = dynamic cone penetration (DCP) index. To determine the combined absorption values, the weighted average of the absorption values of the coarse [> No. 4 sieve (4.75 mm)] and fine (< No. 4) fractions of the materials were used.

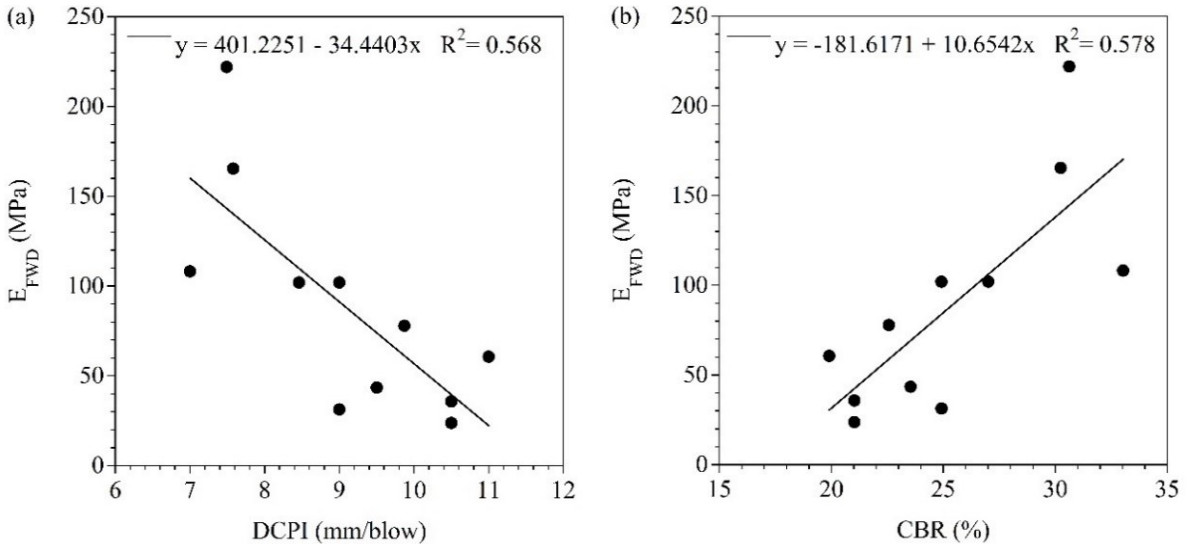

Figure 6.11. (a) Falling weight deflectometer (FWD) elastic modulus (E_{FWD}) vs. dynamic cone penetration (DCP) index (DCPI) and (b) E_{FWD} vs. field California bearing ratio (CBR)

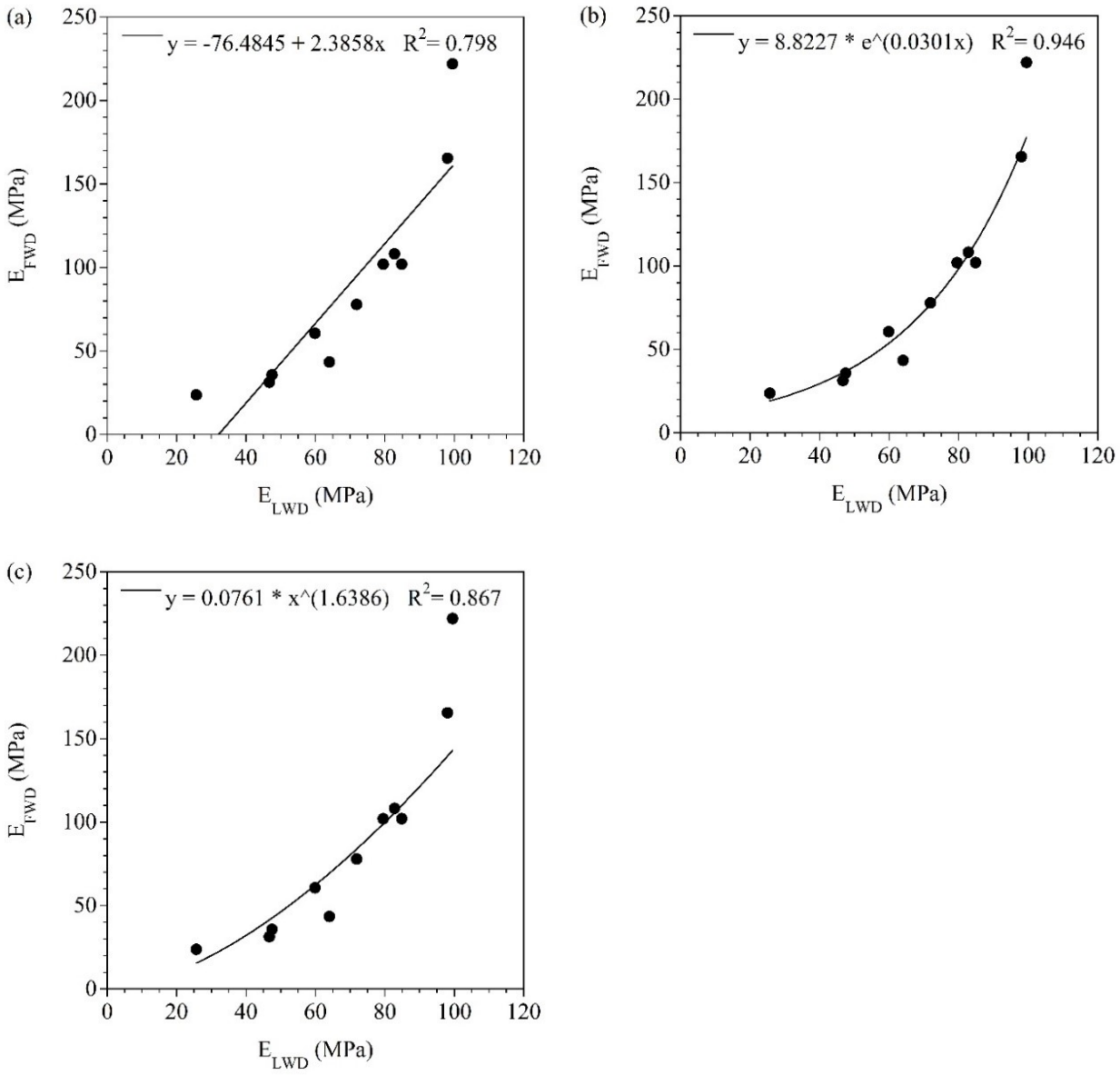

Figure 6.12. Falling weight deflectometer (FWD) elastic modulus (E_{FWD}) vs. light weight deflectometer (LWD) elastic modulus (E_{LWD}): (a) linear, (b) exponential, and (c) power trendline

6.2.4 Intelligent Compaction (IC) Resilient Modulus (M_R) at 10 psi (69 kPa)

Table 6.20 summarizes the equations that can be used to estimate intelligent compaction (IC) M_R at 10 psi (69 kPa) based on laboratory and field testing. The equations listed in Table 6.20 are statistically significant at $\alpha = 0.05$. The equations that show IC M_R [at 10 psi (69 kPa)] as a linear function of DCPI, CBR, E_{LWD}, or E_{FWD} in Table 6.20 are also graphically illustrated in Figure 6.13 (for IC M_R vs. DCPI), Figure 6.14 (for IC M_R vs. CBR), Figure 6.15 (for IC M_R vs. E_{LWD}), and Figure 6.16 (for IC M_R vs. E_{FWD}). In addition to the linear relationship between the parameters, Figure 6.13, Figure 6.14, Figure 6.15, and Figure 6.16 also show nonlinear relationships between the parameters.

Table 6.20. Equations to estimate intelligent compaction (IC) resilient modulus (M_R) (MPa) at 10 psi (69 kPa)

Equation	R^2	Adj. R^2	Std. Error
1.0258*Median E_{FWD} (MPa) + 69.5686	0.91	0.9	20.93
2.5583*Median E_{LWD} (MPa) - 16.5596	0.79	0.77	31.62
16.8683*Median Relative MDU (%) + 10.4512*Fine Absorption (%) - 1461.9308	0.73	0.66	38.29
-35.2625*Median DCPI (mm/blow) + 480.5413	0.52	0.46	48.46
12.3625*Median Relative MDU (%) - 968.1201	0.5	0.45	49.04
10.5220*Median CBR (%) - 106.4179	0.49	0.43	49.81

E_{FWD} = falling weight deflectometer (FWD) elastic modulus; E_{LWD} = light weight deflectometer (LWD) elastic modulus; MDU = maximum dry unit weight; DCPI = dynamic cone penetration (DCP) index; CBR = field California bearing ratio

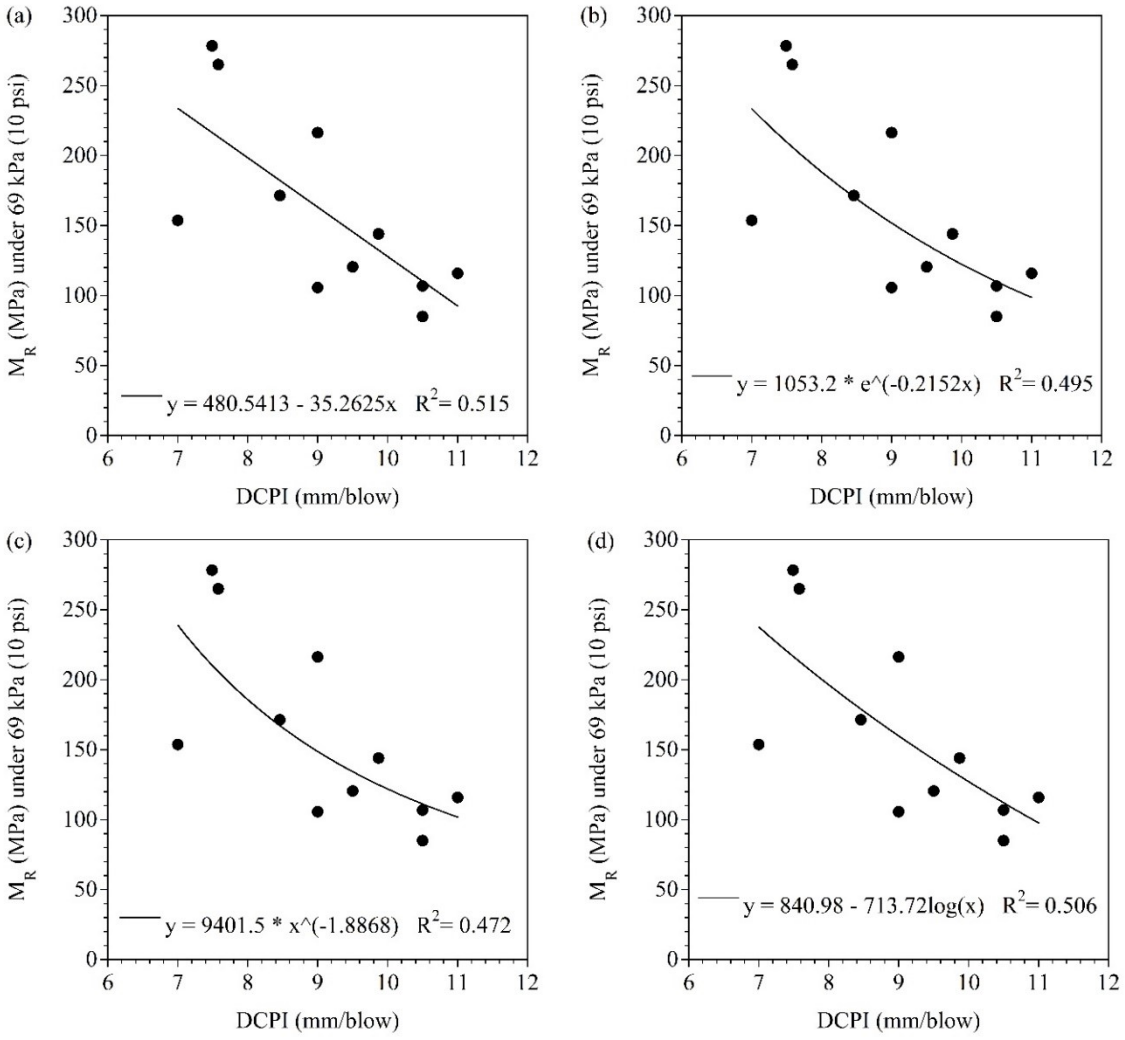

Figure 6.13. Intelligent compaction (IC) resilient modulus (M_R) [at 10 psi (69 kPa)] vs. dynamic cone penetration (DCP) index (DCPI): (a) linear, (b) exponential, (c) power, and (d) logarithmic relationships

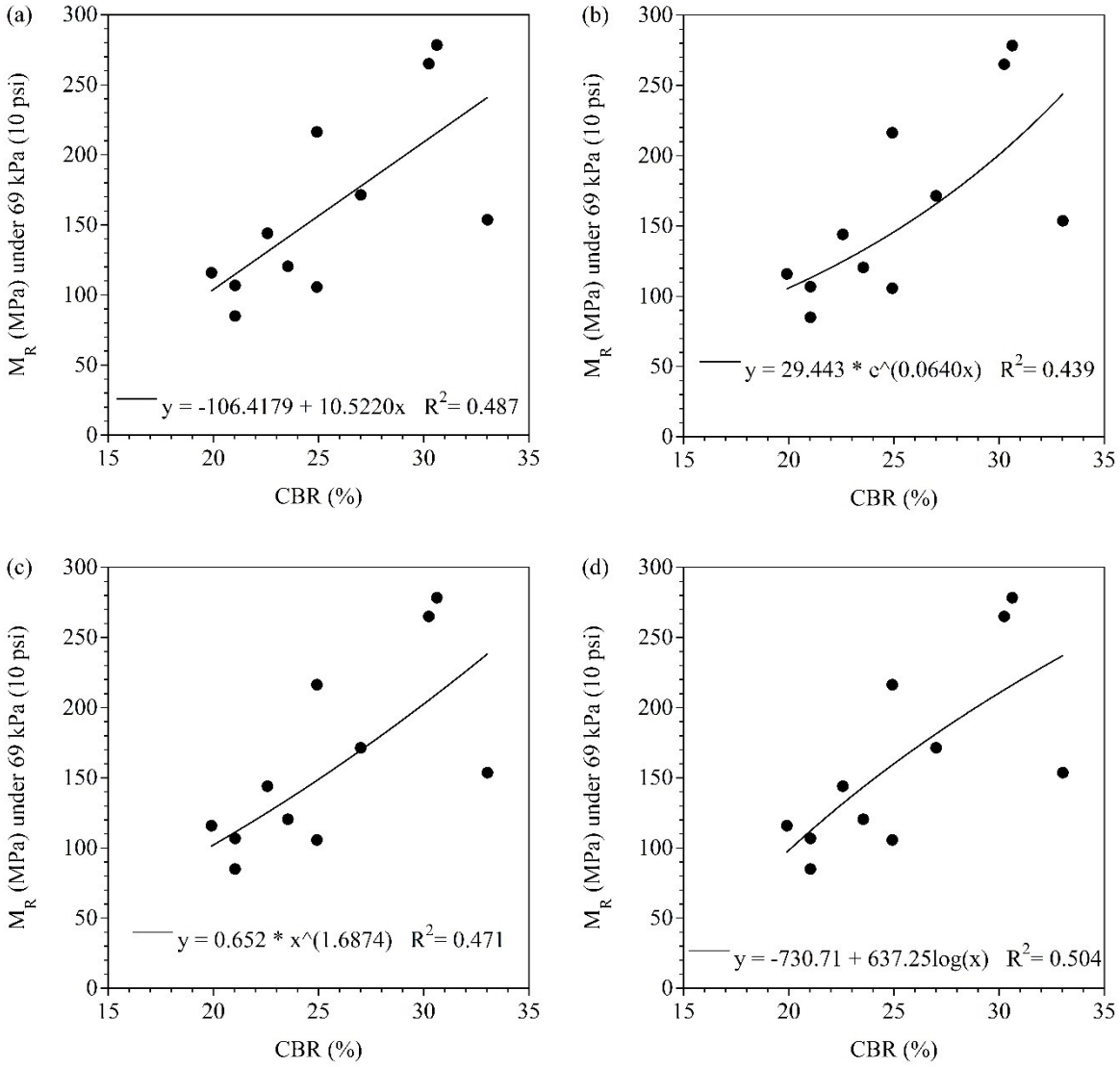

Figure 6.14. Intelligent compaction (IC) resilient modulus (M_R) [at 10 psi (69 kPa)] vs. field California Bearing Ratio (CBR): (a) linear, (b) exponential, (c) power, and (d) logarithmic relationships

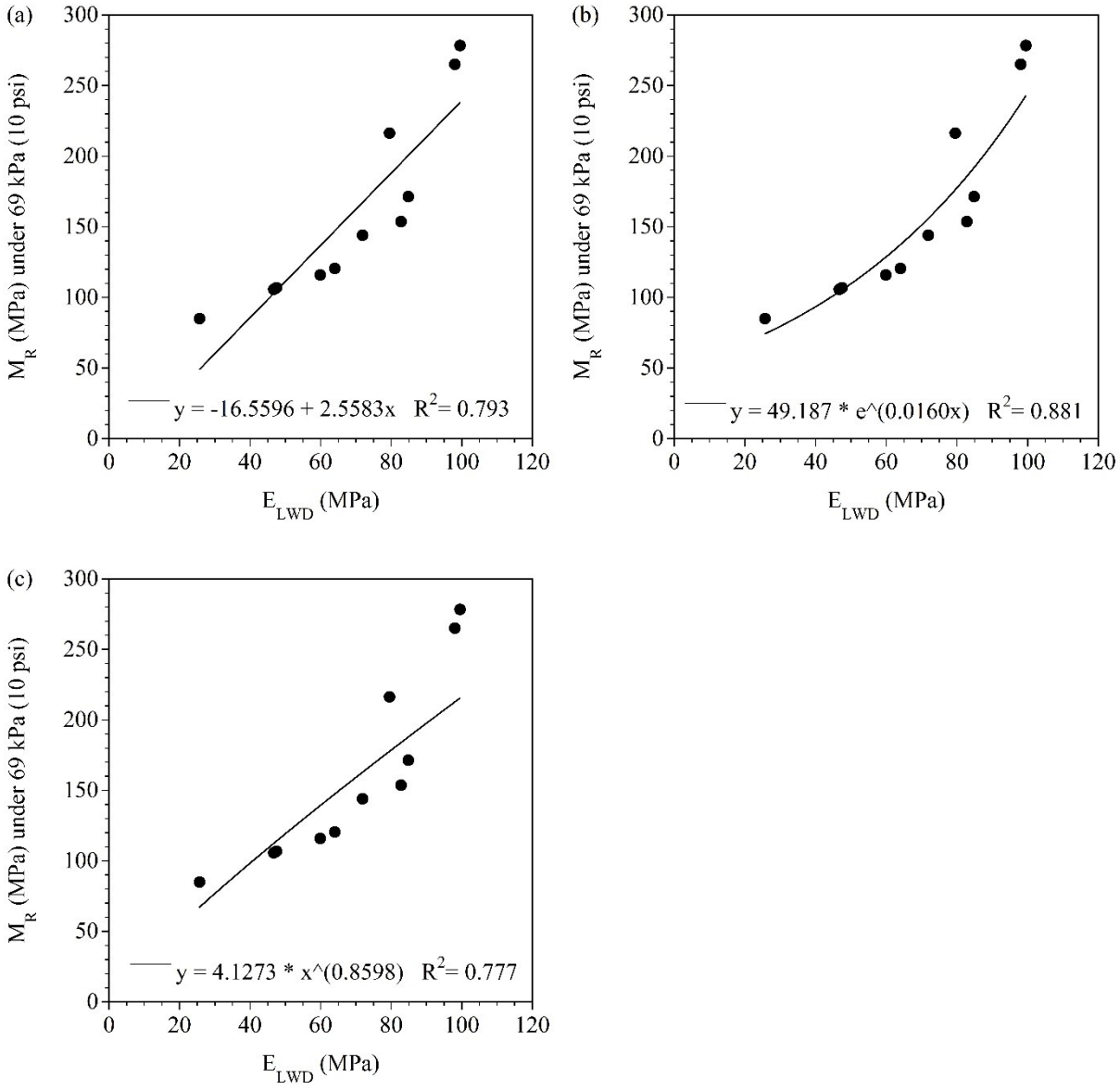

Figure 6.15. Intelligent compaction (IC) resilient modulus (M_R) [at 10 psi (69 kPa)] vs. light weight deflectometer (LWD) elastic modulus (E_{LWD}): (a) linear, (b) exponential, (c) power trendline

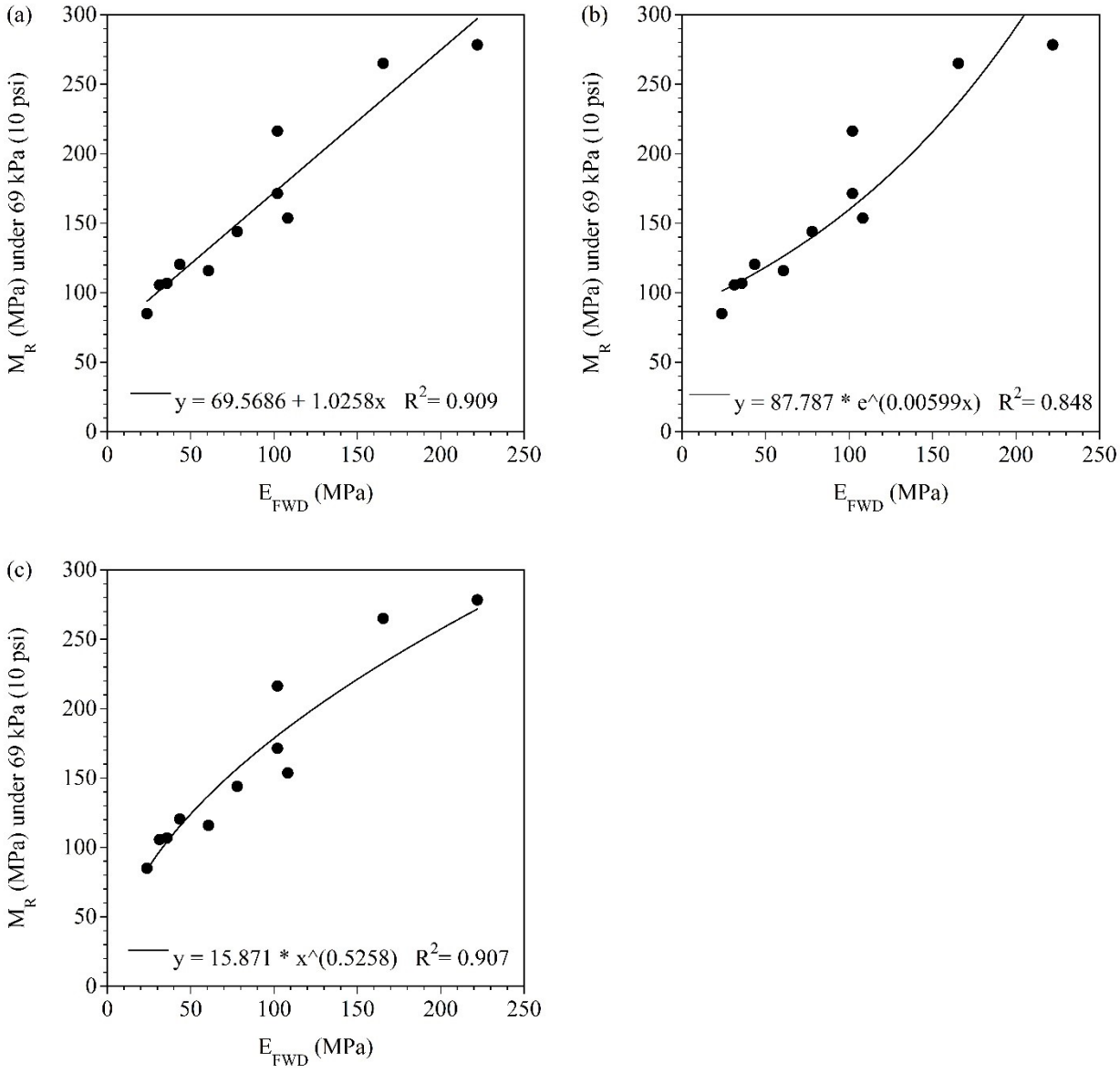

Figure 6.16. Intelligent compaction (IC) resilient modulus (M_R) [at 10 psi (69 kPa)] vs. falling weight deflectometer (FWD) elastic modulus (E_{FWD}): (a) linear, (b) exponential, and (c) power trendline

6.2.5 Intelligent Compaction (IC) Resilient Modulus (M_R) at 30 psi (207 kPa)

Table 6.21 summarizes the regression equations that can be used to estimate intelligent compaction (IC) M_R at 30 psi (207 kPa) based on laboratory and field testing. Additional equations are provided in Appendix AV. The equations listed in Table 6.21 are statistically significant at $\alpha = 0.05$. The equations that show IC M_R [at 30 psi (207 kPa)] as a linear function of DCPI, CBR, E_{LWD}, or E_{FWD} in Table 6.21 are also graphically illustrated in Figure 6.17 (for IC M_R vs. DCPI or CBR), Figure 6.18 (for IC M_R vs. E_{LWD}), and Figure 6.19 (for IC M_R vs. E_{FWD}). In addition to the linear relationship between IC M_R [at 30 psi (207 kPa)] and E_{LWD} or E_{FWD} (Table 6.21), Figure 6.18 and Figure 6.19 also show IC M_R [at 30 psi (207 kPa)] as exponential and power functions of E_{LWD} and E_{FWD}, respectively.

Table 6.21. Equations to estimate intelligent compaction (IC) resilient modulus (M_R) (MPa) at 30 psi (207 kPa)

Equation	R^2	Adj. R^2	Std. Error
1.2907*Median M_R at 69 kPa (MPa) - 50.5300	0.99	0.99	9.97
1.3445*Median E_{FWD} (MPa) + 37.4498	0.93	0.92	24.5
3.2745*Median E_{LWD} (MPa) - 70.0008	0.77	0.75	43.25
21.5095*Median Relative MDU (%) + 14.9378*Fine Absorption (%) - 1924.9268	0.72	0.65	50.79
-44.8505*Median DCPI (mm/blow) + 563.6878	0.49	0.44	64.28
13.5485*Median CBR (%) - 187.0635	0.48	0.42	65.21
15.0695*Median Relative MDU (%) - 1219.1306	0.44	0.38	67.41

M_R = resilient modulus; E_{FWD} = falling weight deflectometer (FWD) elastic modulus; E_{LWD} = light weight deflectometer (LWD) elastic modulus; MDU = maximum dry unit weight; DCPI = dynamic cone penetration (DCP) index; CBR = field California bearing ratio

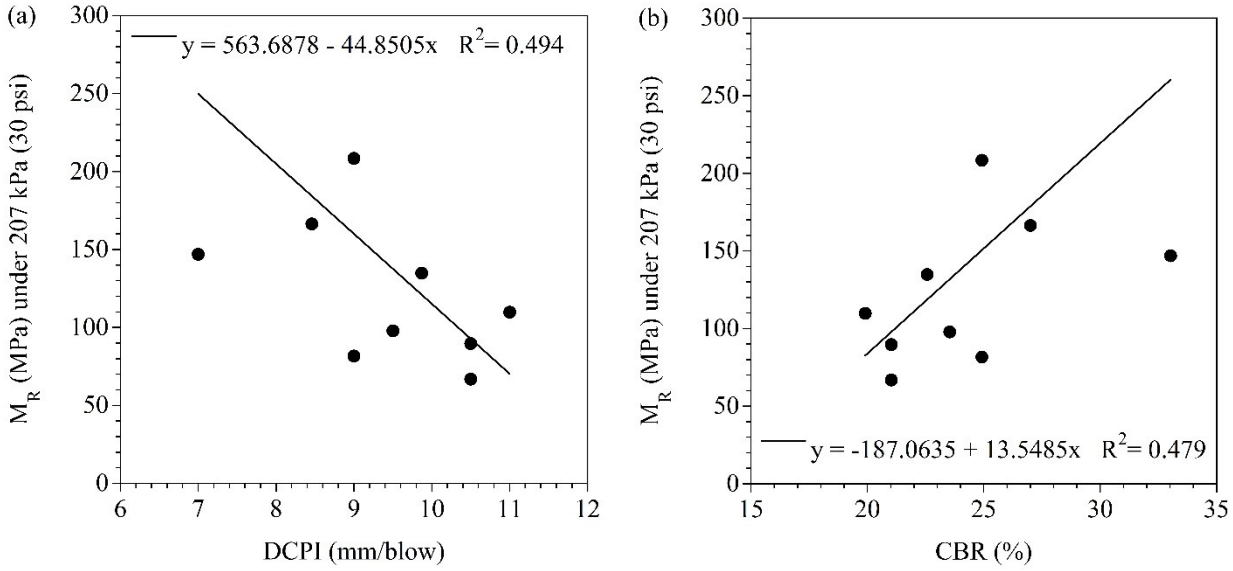

Figure 6.17. (a) Intelligent compaction (IC) resilient modulus (M_R) [at 30 psi (207 kPa)] vs. dynamic cone penetration (DCP) index (DCPI) and (b) IC M_R [at 30 psi (207 kPa)] vs. field California bearing ratio (CBR)

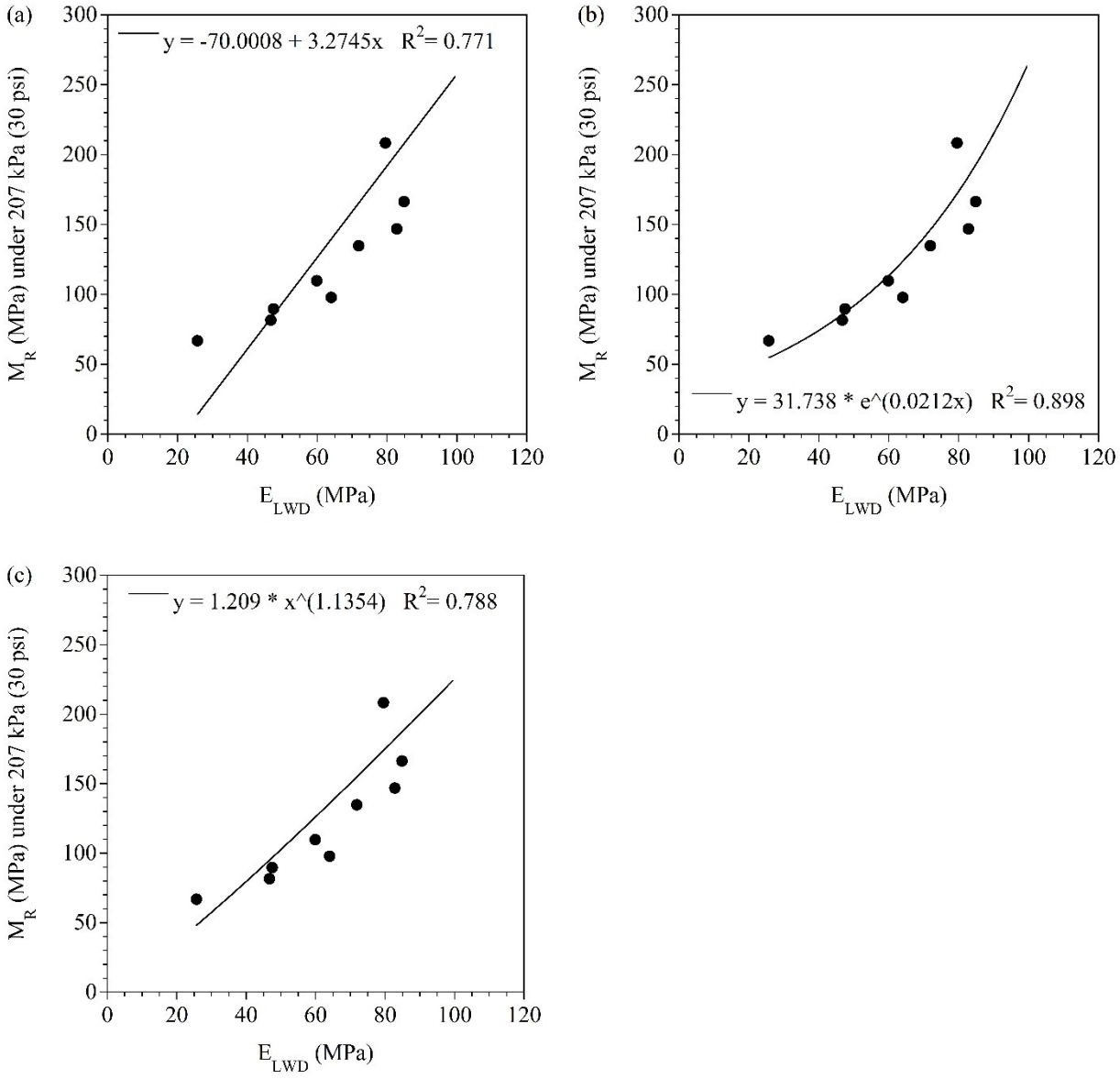

Figure 6.18. Intelligent compaction (IC) resilient modulus (M_R) [at 30 psi (207 kPa)] vs. light weight deflectometer (LWD) elastic modulus (E_{LWD}): (a) linear, (b) exponential, and (c) power trendline

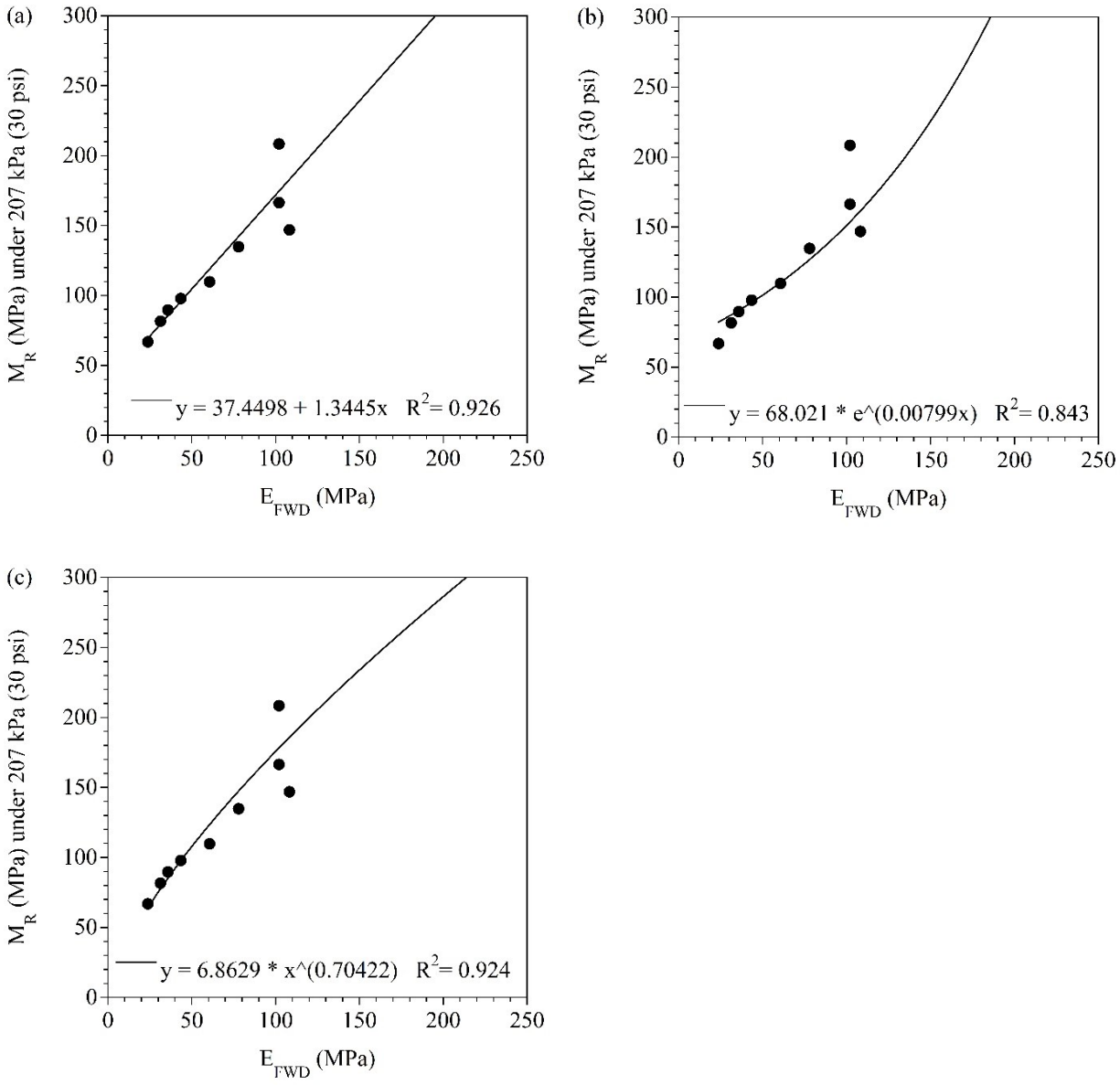

Figure 6.19. Intelligent compaction (IC) resilient modulus (M_R) [at 30 psi (207 kPa)] vs. falling weight deflectometer (FWD) elastic modulus (E_{FWD}): (a) linear, (b) exponential, and (c) power trendline

6.3 CHAPTER CONCLUSIONS

In this chapter, regression models were developed using the forward stepwise regression technique to obtain simple and easily interpretable models for the estimation of laboratory and field test (collected during construction) results. From the findings of this chapter, the following conclusions were drawn:

- Stepwise regression analysis results revealed that the common parameters that could be used to estimate the uncorrected and corrected optimum moisture content (OMC) and maximum dry unit weight (MDU) values of base layer aggregates used in this study (Coarse RCA, Fine RCA, Limestone, RCA+RAP, Class 5Q Aggregate, and Class 6 Aggregate) are specific gravity (G_s), absorption, and

gradation characteristics. Residual mortar content could also be used to estimate uncorrected OMC and MDU values of base layer aggregates containing RCA.

- For estimation of saturated hydraulic conductivity (K_{sat}), stepwise regression analysis results showed that G_s, absorption, OMC and MDU (both uncorrected and corrected), and void ratio/porosity parameters could be used. To calculate the void ratio or porosity, G_s and MDU of the aggregate must be known [$e = (G_s\gamma_w/\gamma_d) - 1$ and $n = e/(1 + e)$]. However, it should be kept in mind that since aggregate base layers were compacted at lower dry densities than MDU in the field, the models may not be representative for field conditions.

- Residual volumetric water content (VWC) (θ_r), saturated VWC (θ_s), and air-entry pressure parameters, which are soil-water characteristic curve (SWCC) parameters, could also be estimated by using the index properties of the base layer aggregates. It was also determined that corrected OMC could be used to estimate θ_r. G_s, absorption, residual mortar content, and uncorrected OMC and MDU could be used to predict θ_s. To estimate air-entry pressures, void ratio/porosity, absorption, and gradation could be used.

- As expected, the M_R values of the base layer aggregates were inversely related to the moisture contents of the materials. A direct relationship was presented between the M_R values of the base layer aggregates and the matric suctions of the aggregate materials (matric suctions were higher than the air-entry pressures).

- It was determined that G_s, absorption, uncorrected OMC and MDU, and residual mortar content could be used to estimate the summary resilient modulus (SM_R) values of the base layer aggregates. In addition, G_s and absorption could commonly be used for the estimation of k_1, k_2, and k_3 (conventional Pavement ME fitting parameters).

- It was determined that the breakage characteristics of the base layer aggregates were affected by not only their gradations, but also their coarse oven-dry (OD) G_s, residual mortar content, and roundness characteristics. The stepwise regression analyses revealed that the relative breakage (B_r) of the base layer aggregates increased with their residual mortar content. In addition, it was determined that the B_r and coarse OD G_s or roundness of the base layer aggregates were inversely related.

- Overall, it was concluded that the aggregate base dynamic cone penetration (DCP) index (DCPI), the aggregate base field California bearing ratio (CBR), the base+subbase light weight deflectometer (LWD) elastic modulus (E_{LWD}), the base+subbase falling weight deflectometer (FWD) elastic modulus (E_{FWD}), and the base+subbase intelligent compaction (IC) M_R values were all related to one another. While base+subbase E_{LWD}, E_{FWD}, and IC M_R values were inversely related to the aggregate base DCPI values, they were directly related to the aggregate base field CBR values. In addition, the base+subbase E_{LWD}, E_{FWD}, and IC M_R values were directly related to each other. Therefore, it was concluded that the results obtained from relatively simpler field tests (e.g., DCP and/or LWD tests) could be used to estimate the results of relatively more advanced field tests (e.g., FWD and IC tests).

CHAPTER 7: MECHANISTIC-EMPIRICAL (ME) PAVEMENT PERFORMANCE MODELS

The AASHTOWare Pavement ME Design program (version 2.5.5) was used to provide recommendations on aggregate base and subbase layer thicknesses. The following sections give detailed information about general model inputs, material inputs, and evaluation of the performance prediction models. Since the use of local calibration is not within the scope of this study, global (default) calibration was used in the analyses.

7.1.1 General Model Inputs

General design inputs are summarized in Table 7.1. The design life of flexible pavement models was determined to be 20 years (Velasquez et al. 2009; Ceylan et al. 2015b). For the aggregate base and pavement construction dates, actual construction dates of the test cells (Figure 3.2) were used (Appendix D). The initial international roughness index (IRI) value was determined to be 63 in/mile (Izevbekhai and Akkari 2011; Ceylan et al. 2015b).

Table 7.1. General design inputs for Pavement ME

Parameter	Input/Value
Design Life (years)	20
Design Type	Flexible
Base Construction	August 2017
Pavement Construction	September 2017
Traffic Opening	September 2017
Initial IRI (in/mile)	63

IRI = international roughness index

Target values and reliability levels for different pavement distresses are summarized in Table 7.2. For all distresses, a reliability level of 90% was used. According to the FHWA, while IRI values lower than 2.68 m/km (170 in/mile) might be acceptable in terms of ride quality, values greater than 2.68 m/km (170 in/mile) are considered unacceptable (Elbheiry et al. 2011). Therefore, the terminal IRI value was determined to be 170 in/mile (Elbheiry et al. 2011). Other pavement distress target values were selected based on Ceylan et al. (2015b).

Table 7.2. Pavement distress types, target values, and reliability levels

Parameter	Target Value	Reliability (%)
Terminal IRI (in/mile)	170	90
AC Bottom-Up Fatigue Cracking (% lane area)	25	90
AC Thermal Cracking (ft/mile)	1,000	90
AC Top-Down Fatigue Cracking (ft/mile)	2,000	90
Permanent Deformation - AC Only (in)	0.25	90
Permanent Deformation - Total Pavement (in)	0.75	90

IRI = international roughness index; AC = asphalt concrete

Climatic parameters and regional information are summarized in Table 7.3. The MnROAD LVR test facility (Figure 3.1), where the test cells were located, was selected, and to enable specific selection of the MnROAD LVR test facility, a virtual weather station was created by selecting six neighboring weather stations. The coordinates and the locations of the neighboring weather stations are shown in Table 7.3 and Figure 7.1, respectively. Water table depth was selected to be 10 ft based on Schwartz et al. (2011). Monthly rainfall statistics, monthly climate summary, and hourly air temperature distribution by month for the MnROAD LVR test facility location are provided in Appendix AW.

Table 7.3. Climatic parameters and regional information

Parameter	Input/Value	Coordinates
Climate Location	MnROAD LVR	45.5016205, -93.7609675
		45.001088, -93.7521709
		45.5003105, -93.1249918
		45.0003614, -93.1247624
		45.4994913, -94.3722707
		45.0000331, -94.368383
Mean Annual Air Temperature (°F)	43.8	
Mean Annual Precipitation (in)	39	
Freezing Index (°F - days)	1894	
Average Annual Number of Freeze/Thaw Cycles	80	
Water Table Depth (ft)	10	

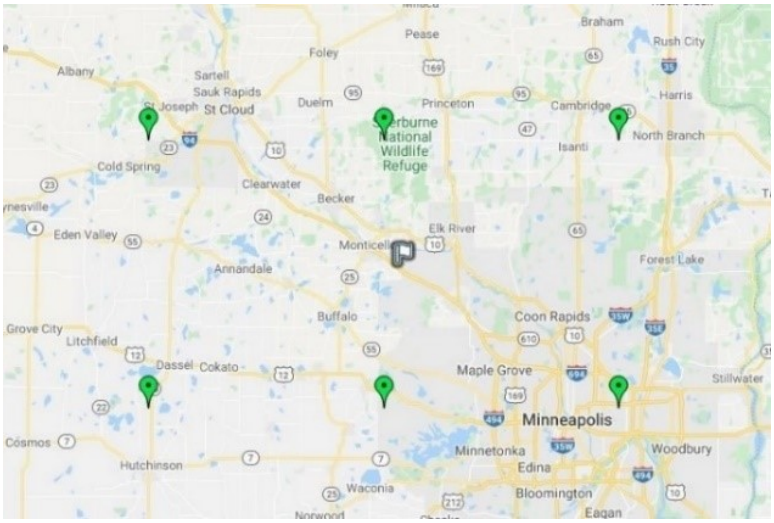

Figure 7.1. Locations of six neighboring weather stations and MnROAD LVR test facility (green pins represent neighboring weather stations and white flag represents location of MnROAD LVR)

Traffic information is provided in two parts in Table 7.4 (part 1) and Table 7.5 (part 2). Operational speed was determined to be 50 mph (Izevbekhai and Akkari 2011; Schwartz et al. 2011) (Table 7.4). Truck traffic category (TTC) was selected to be 4 (level 3 default vehicle distribution) (Schwartz et al. (2011) with a default growth factor of 3% (linear) (Table 7.4). Five different traffic levels were used (Table 7.5)

(Schwartz et al. 2011). Average annual daily truck traffic (AADTT) values of 100, 500, and 1,000 represented low traffic levels (Table 7.5) (Schwartz et al. 2011). In addition, AADTT values of 7,500 and 25,000 represented medium and high traffic levels, respectively (Table 7.5) (Schwartz et al. 2011). Graphical and tabular representations of the traffic inputs are provided in Appendix AX.

Table 7.4. Traffic information - part 1

Parameter	Input/Value
Operational Speed (mph)	50
Truck Traffic Category (TTC)	4 (Level 3)
Growth Factor (%)	3 (Linear)

Table 7.5. Traffic information - part 2

Parameter	Low Traffic			Medium Traffic	High Traffic
	100 AADTT	500 AADTT	1,000 AADTT	7,500 AADTT	25,000 AADTT
Number of Lanes in Design Direction	1	2	2	3	3
Percent of Trucks in Design Direction (%)	50	50	50	50	50
Percent of Trucks in Design Lane (%)	100	75	75	55	50

AADTT = average annual daily truck traffic

7.1.2 Recycled Aggregate Base (RAB) Group

7.1.2.1 Aggregate Base Layer Design

In the MnROAD LVR test facility, the recycled aggregate base (RAB) group contained the test cells built with 12-in Coarse RCA (Cell 185), Fine RCA (Cell 186), Limestone (Cell 188), and RCA+RAP (Cell 189) base layers. To evaluate the effect of aggregate base layer thickness on pavement performance using Pavement ME, thinner aggregate base layers (10 in, 8 in, 6 in, and 4 in) were modeled in addition to the original aggregate base layer thickness of 12 in. In addition, as can be seen in Figure 3.2 for the RAB group, while two of the test cells contained Sand Subgrade layers (Cells 185 and 186), the other two test cells contained Clay Loam subgrade layers (Cells 188 and 189). In Pavement ME, first, Coarse RCA, Fine RCA, Limestone, and RCA+RAP base layers were placed on Sand Subgrade layers. Then, the same aggregate base layers were placed on Clay Loam subgrade layers. Asphalt and subbase layer thicknesses were kept the same as the original (3.5 in/each). Figure 7.2 is an example that shows different Coarse RCA base layer thicknesses that were modeled with Pavement ME.

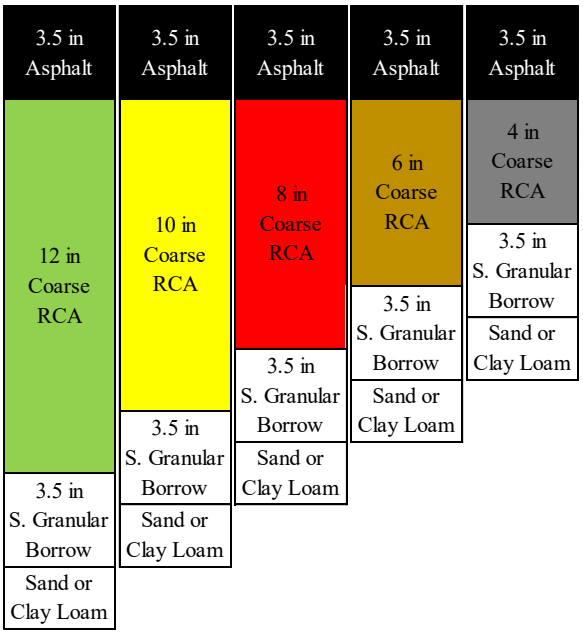

Figure 7.2. Pavement ME models for Coarse RCA base layer at different layer thicknesses

7.1.2.2 Material Inputs

Van Deusen et al. (2018) reported that the asphalt mixture type used in the construction of the test cells (Figure 3.2) was 12.5 mm nominal maximum aggregate size (NMAS) Superpave performance grade (PG) 58S-34 [58 = maximum pavement design temperature (°C), S = standard traffic level, -34 = minimum pavement design temperature (°C)]. Therefore, for modeling the asphalt layers, Superpave PG 58-34 was selected (level 3). Appendix AY provides detailed information about the level 3 parameters for the modeled asphalt layer.

Table 7.6 summarizes the input parameters for aggregate base, subbase, and subgrade layers that were used in the models. For each pavement sublayer, the coefficient of lateral earth pressure (K0) was kept at the default (0.5). For M_R inputs of the aggregate base and subgrade layers, the previously explained actual SM_R values were used (level 2). For Select Granular Borrow subbase layers, no laboratory M_R testing was performed, so the equations that were found to estimate the SM_R values for Coarse RCA, Fine RCA, Limestone, and RCA+RAP (Table 6.9 and Appendix AS) were used to estimate Select Granular Borrow's SM_R (Appendix AZ). After using the suitable equations to estimate the SM_R values of Select Granular Borrow, the median SM_R value (12,888.8 psi) was determined and compared with the SM_R values of other materials. After comparison, the estimated SM_R value of Select Granular Borrow (12,888.8 psi) was determined to be in an acceptable range, and therefore, it was used in the models (Table 7.6). In addition, no K_{sat} testing was performed for Select Granular Borrow. Unlike the procedure followed to estimate the SM_R of Select Granular Borrow [as stated previously, the correlations shown in Table 6.9 and Appendix AS were used to estimate the SM_R of Select Granular Borrow], the K_{sat} (2.71E-03 ft/hr) value for Select Granular Borrow material was predicted by the Pavement ME program in level 2 analysis (Table 7.6). Lastly, as described previously, the SWCC characteristics of the materials were determined using the van Genuchten model (van Genuchten 1980) [Equation (4.1)] in this study. Since

the Pavement ME program uses the Fredlund and Xing (1994) SWCC model, the SWCC inputs [af, bf, cf, hr fitting parameters (Fredlund and Xing 1994)] were not user-defined for any of the materials listed in Table 7.6.

Table 7.6. Material inputs used for pavement sublayers in Pavement ME models

Parameter		Coarse RCA Base	Fine RCA Base	Lime-stone Base	RCA+ RAP Base	Select Granular Borrow Subbase	Sand Subgrade	Clay Loam Subgrade
AASHTO Classification		A-1-a	A-1-a	A-1-b	A-1-a	A-1-b	A-1-b	A-6
Poisson's Ratio		0.35	0.35	0.35	0.35	0.35	0.4	0.4
M_R (psi)		18,129	17,760.9	13,926.3	16,487.7	12,888.8[#]	11,336.1	8,630.9
LL		0	32.7	17.9	27.4	18.9	19.9	36.3
PI		0	0	0	0	0	0	12.4
Corrected MDU (pcf)		128.6	121.7	143.2	125.8	140.3	137.7	124.9
K_{sat} (ft/hr)		3.15E-02	5.73E-02	5.74E-03	2.44E-02	2.71E-03*	3.24E-02	1.62E-05
Combined OD G_s		2.25	2.17	2.66	2.28	2.62	2.6	2.68
Corrected OMC (%)		9.5	11.1	6.3	10	5.3	5.6	10
Percent Passing (%)	No. 200	3.4	7.1	15.1	8.6	12.4	12.6	59.7
	No. 100	5.3	10.8	20.1	12.4	14.4	16.9	68.9
	No. 60	7.6	15	23.8	17.2	20.1	24.4	77.6
	No. 40	11.4	21.1	27.1	24.2	32.6	38.2	84.6
	No. 20	18.2	30.6	30.5	32.6	48	53.6	90.1
	No. 10	26.7	43.6	35.9	43.5	59.9	62.8	94
	No. 4	38.3	61.7	47.7	59	68.9	72.4	96.9
	3/8 in	53.3	81	64.7	75.8	77.4	81.5	98.4
	3/4 in	75.4	99.7	95	99.3	93.3	95.8	99.4
	1 in	85.1	100	100	100	100	99.9	99.5
	1 1/2 in	100	100	100	100	100	100	100
	2 in	100	100	100	100	100	100	100
	2.5 in	100	100	100	100	100	100	100
	3 in	100	100	100	100	100	100	100

M_R = resilient modulus; LL = liquid limit; PI = plasticity index; MDU = maximum dry unit weight; K_{sat} = saturated hydraulic conductivity; OD = oven-dry; G_s = specific gravity; OMC = optimum moisture content. To determine the combined G_s values, the weighted average of the G_s values of the coarse [> No. 4 sieve (4.75 mm)] and fine (< No. 4) fractions of the materials were used.

[#]Determined based on the M_R models developed in this study (Table 6.9 and Appendix AS)

*Not user-defined

7.1.2.3 Effect of Aggregate Base Layer Thickness on Pavement Performance Prediction Models

As stated previously, aggregate base layer thicknesses ranging between 4 in and 12 in were used in the models (Figure 7.2) to evaluate the effect of the aggregate base layer thickness on long-term pavement performance prediction models. Overall, for all types of base layer aggregates, increasing the aggregate base layer thickness decreased pavement distresses at the end of typical flexible pavement design life (20 years) and increased the service life of pavements (service life is defined as the pavement age at failure). Figure 7.3, Figure 7.4, Figure 7.5, and Figure 7.6 are examples that show the effect of the aggregate base layer thickness on IRI, rutting, alligator cracking, and longitudinal cracking, respectively, for the pavement models that contained Sand Subgrade layers and were subjected to 1,000 AADTT. More results for other pavement models are provided in Appendix BA.

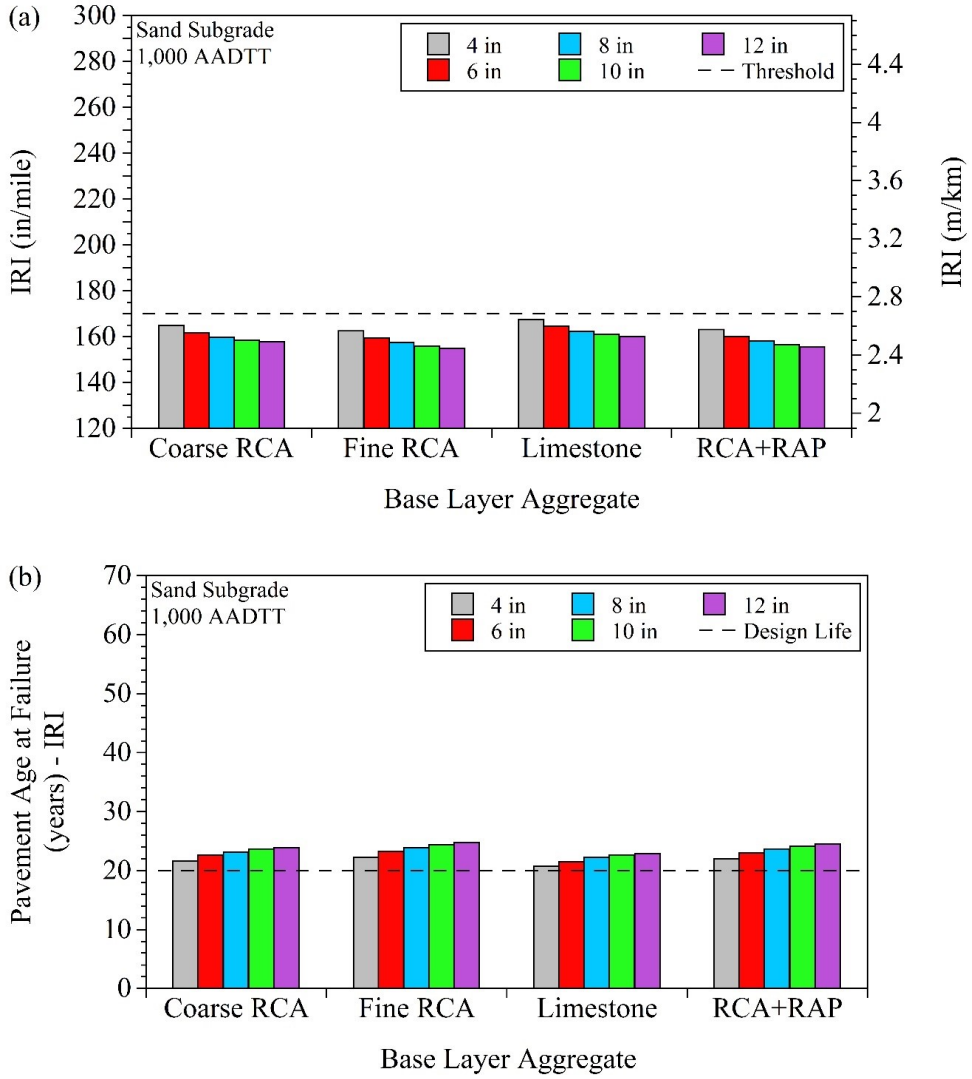

Figure 7.3. Effect of aggregate base layer thickness on (a) international roughness index (IRI) at the end of design life (20 years) and (b) pavement age at IRI failure

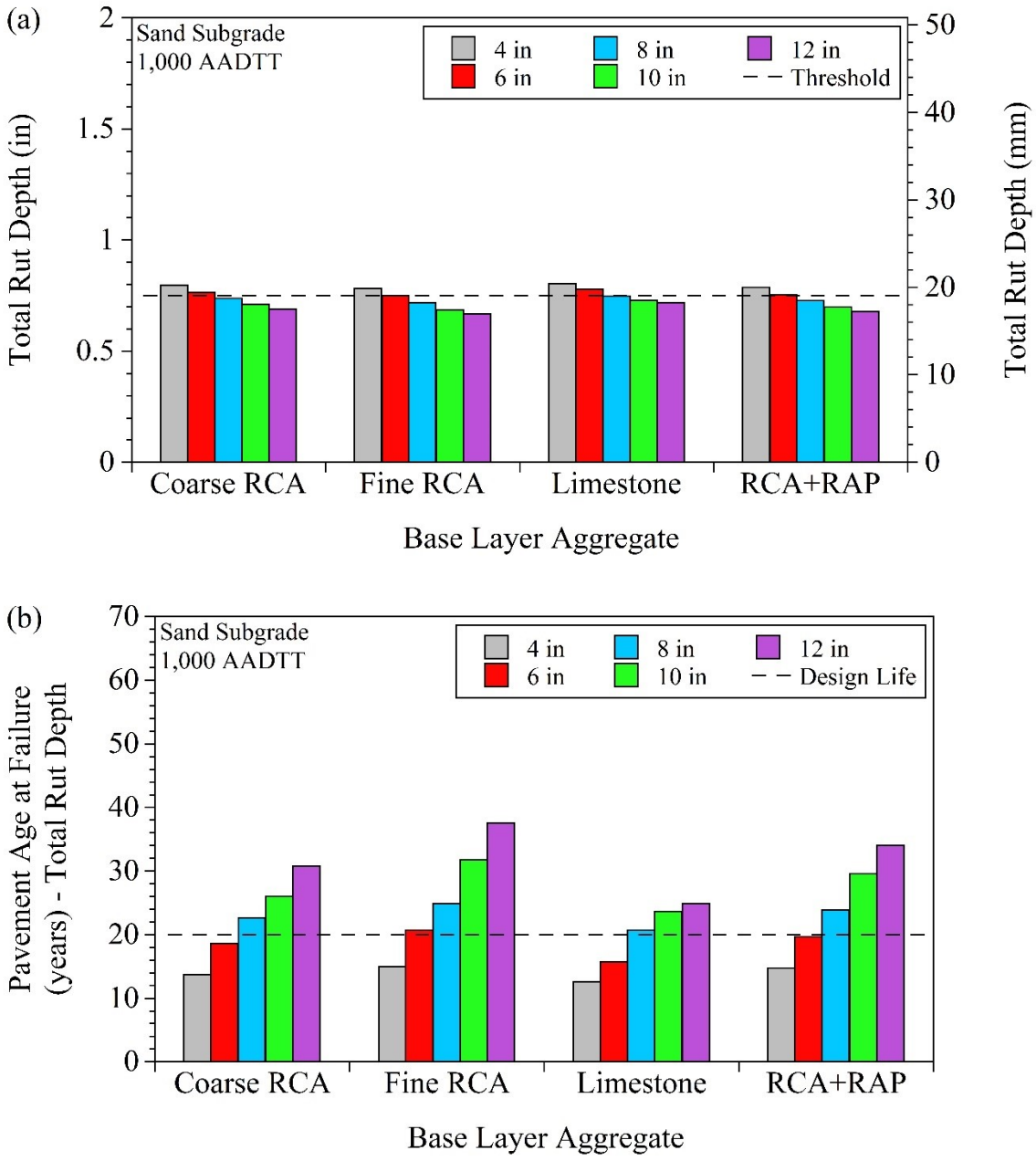

Figure 7.4. Effect of aggregate base layer thickness on (a) total rut depth at the end of design life (20 years) and (b) pavement age at total rut depth failure

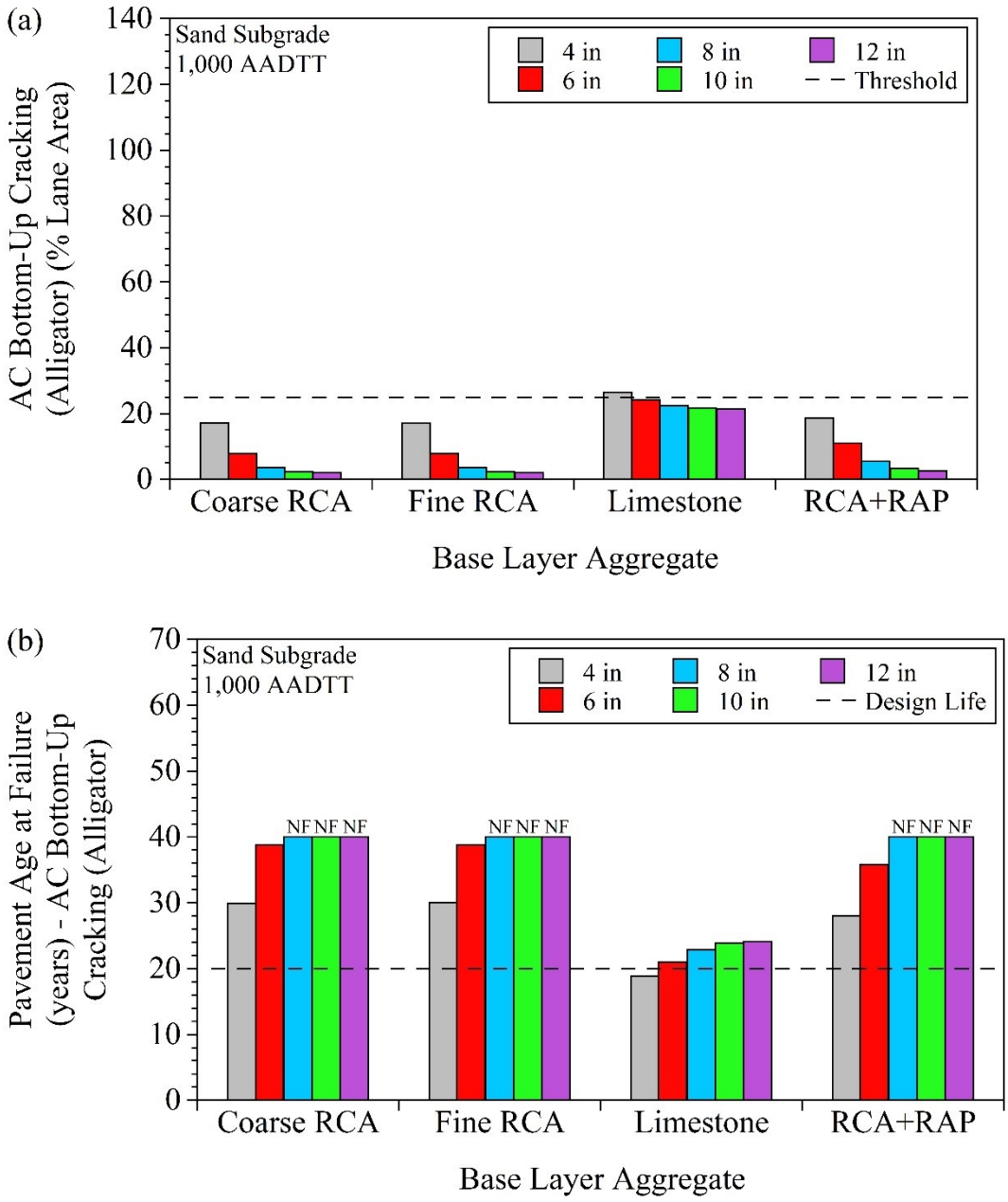

Figure 7.5. Effect of aggregate base layer thickness on (a) alligator cracking at the end of design life (20 years) and (b) pavement age at alligator cracking failure (NF = no failure)

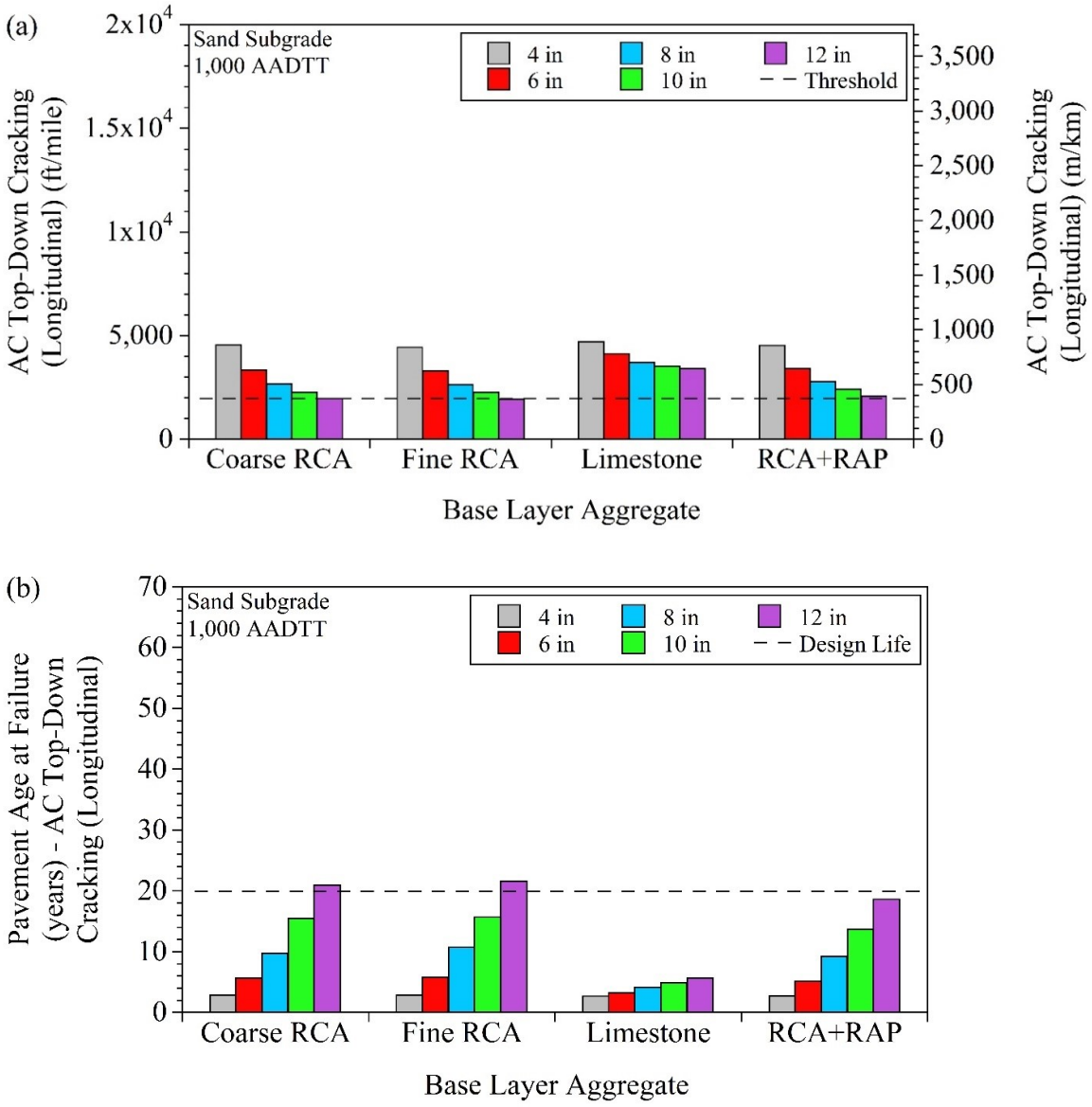

Figure 7.6. Effect of aggregate base layer thickness on (a) longitudinal cracking at the end of design life (20 years) and (b) pavement age at longitudinal cracking failure

7.1.2.4 Effect of Base Layer Aggregate Type on Pavement Performance Prediction Models

As stated previously, Coarse RCA, Fine RCA, Limestone, and RCA+RAP were used to model the aggregate base layers at each different layer thickness (12, 10, 8, 6, and 4 in) (Figure 7.2). Overall, for all aggregate base layer thicknesses, it was observed that using Limestone resulted in higher pavement distresses at the end of the pavement design period (20 years) and lower pavement service life. Figure 7.7, Figure 7.8, Figure 7.9, and Figure 7.10 are examples that show the effect of the base layer aggregate type on IRI, rutting, alligator cracking, and longitudinal cracking, respectively, for pavement models that contained Sand Subgrade layers and were subjected to 1,000 AADTT. More results for other pavement models can be found in Appendix BB.

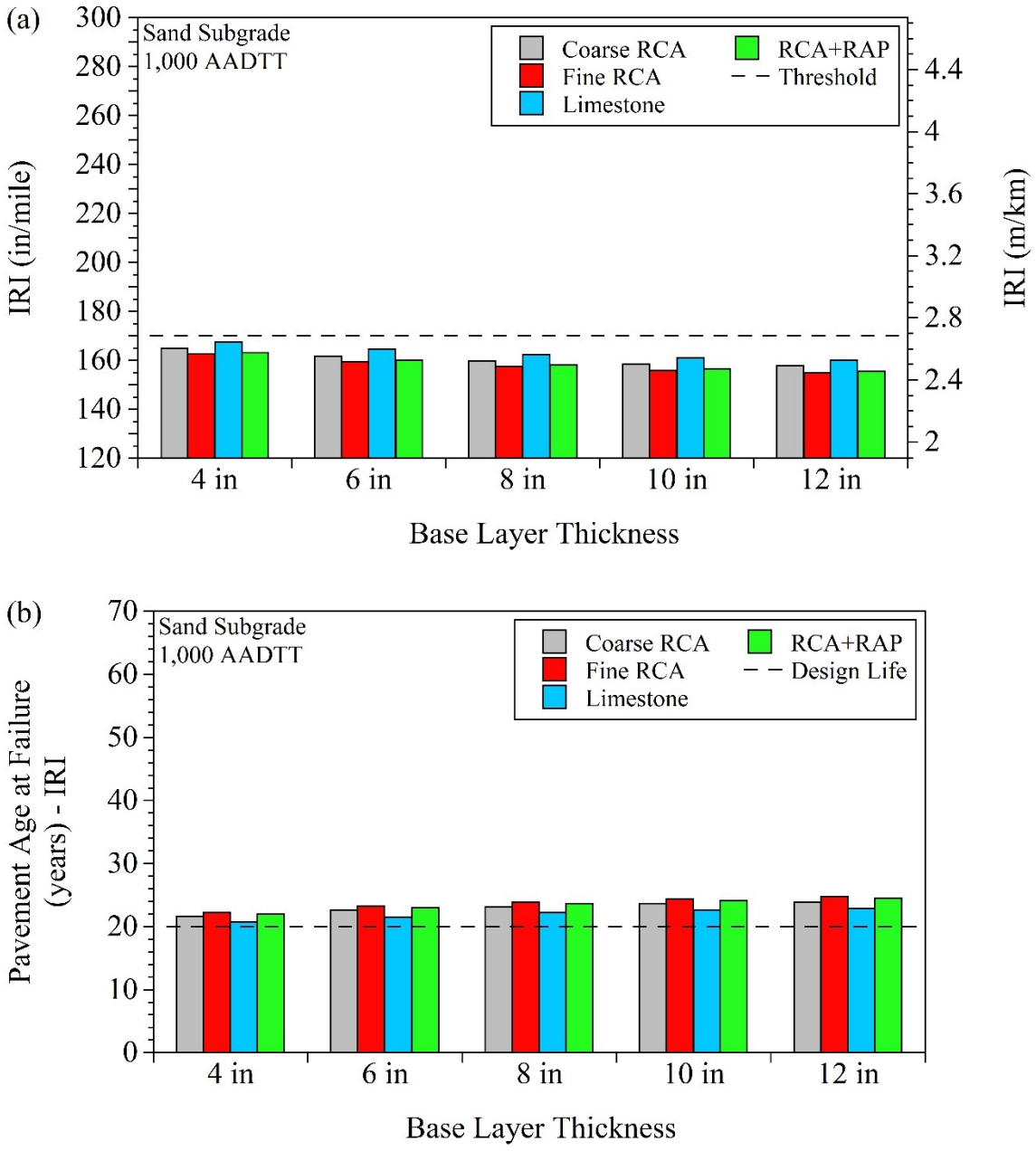

Figure 7.7. Effect of base layer aggregate type on (a) international roughness index (IRI) at the end of design life (20 years) and (b) pavement age at IRI failure

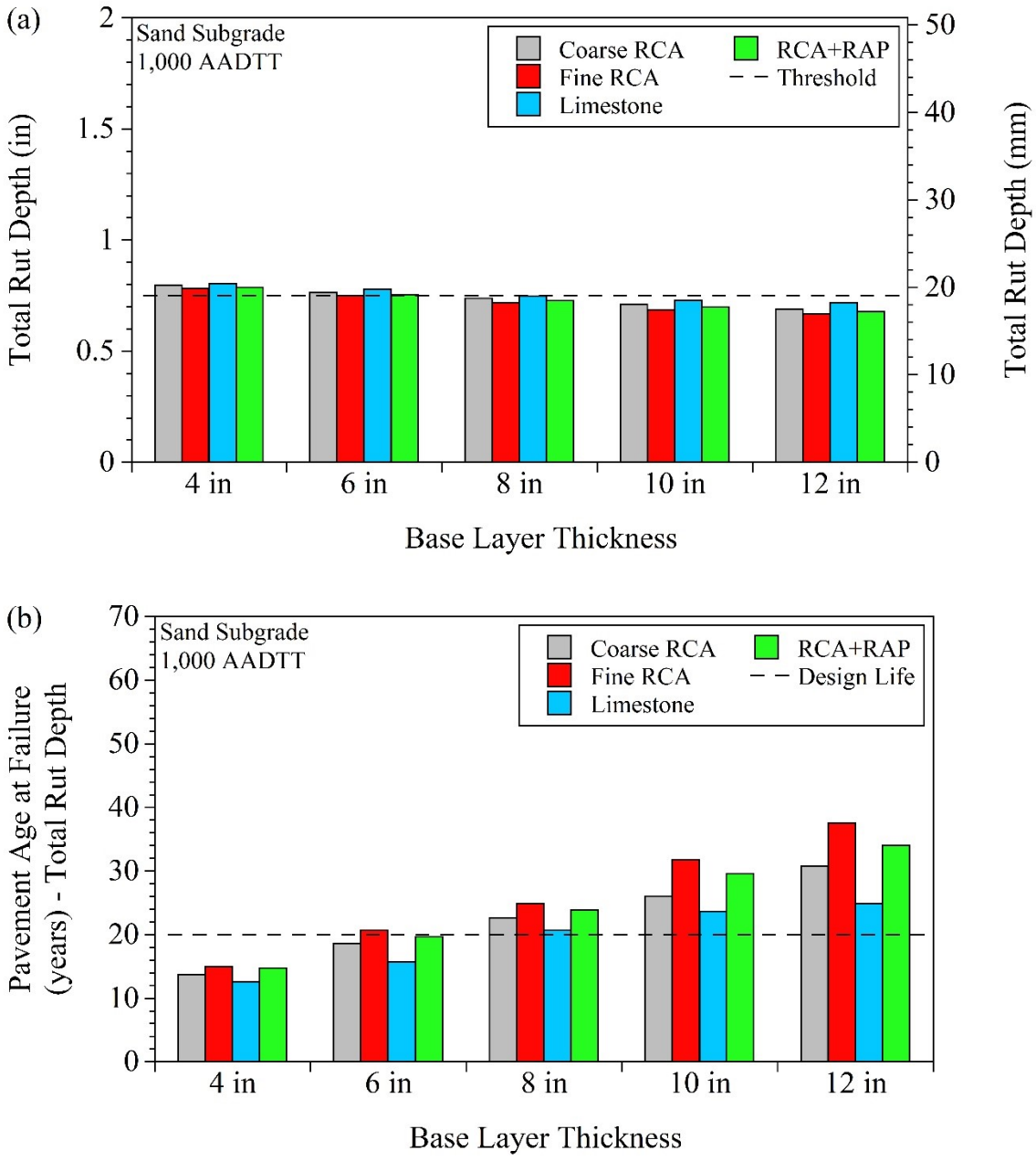

Figure 7.8. Effect of base layer aggregate type on (a) total rut depth at the end of design life (20 years) and (b) pavement age at total rut depth failure

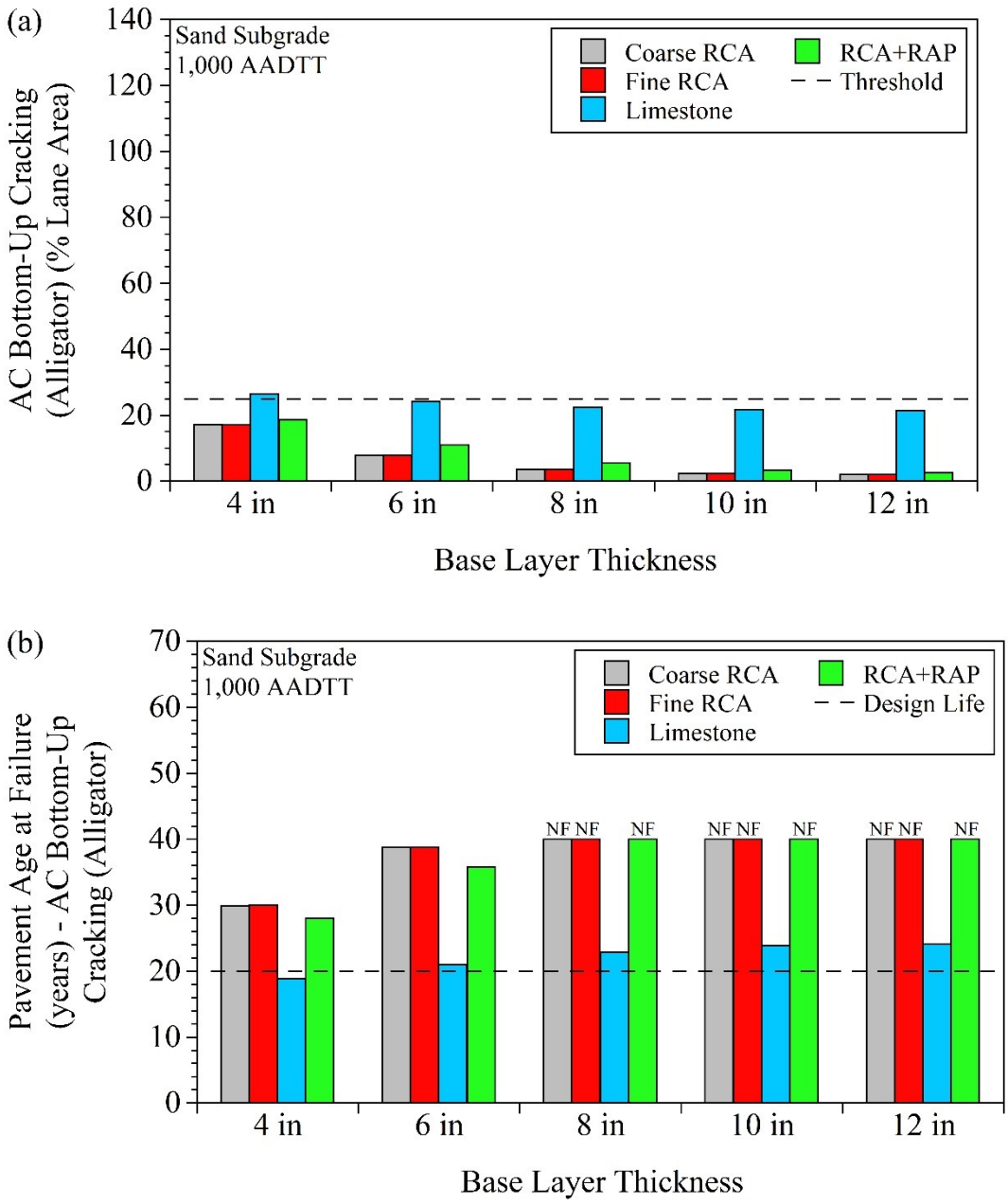

Figure 7.9. Effect of base layer aggregate type on (a) alligator cracking at the end of design life (20 years) and (b) pavement age at alligator cracking failure (NF = no failure)

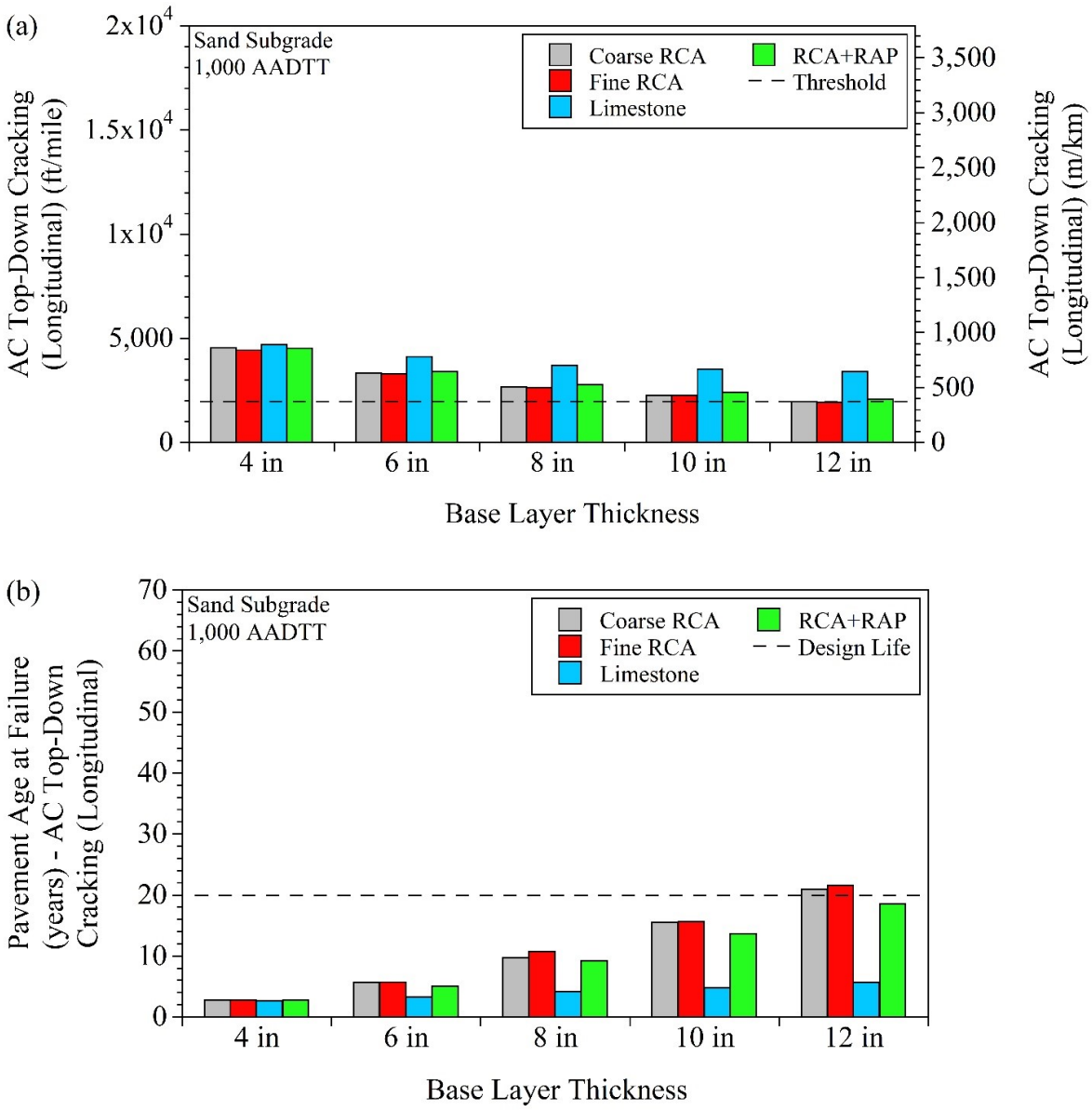

Figure 7.10. Effect of base layer aggregate type on (a) longitudinal cracking at the end of design life (20 years) and (b) pavement age at longitudinal cracking failure

7.1.2.5 Layer Rutting at 50% Reliability

Layer rutting for asphalt, base+subbase, and subgrade layers was also evaluated at 50% reliability (Pavement ME can only give 50% reliability for layer rutting). For asphalt layer rutting, the asphalt layers overlying Limestone base layers (at different thicknesses) provided slightly higher asphalt rutting. However, overall, it could be said that no significant difference was observed among the asphalt layers placed on Coarse RCA, Fine RCA, Limestone, and RCA+RAP base layers (at different thicknesses) in the modeling results.

For base+subbase layer rutting, overall, Limestone base+Select Granular Borrow subbase layers yielded higher rutting than the other base+subbase layers (for each aggregate base layer thickness). For subgrade layer rutting, the Sand Subgrade layers underlying Limestone base+Select Granular Borrow subbase layers yielded slightly lower rutting. Figure 7.11, Figure 7.12, and Figure 7.13 are examples that show the asphalt, base+subbase, and subgrade rutting for the pavement models that contained Sand Subgrade layers and were subjected to 1,000 AADTT. More results for other pavement modeling results are provided in Appendix BC.

As expected, it was observed from the model results that the highest amount of layer rutting was observed in subgrade layers. In addition, increasing the aggregate base layer thickness increased the base+subbase rutting overall. However, it should be kept in mind that the higher rutting in thicker layers does not mean that the thicker layer's performance is lower than the thinner layer's performance. Figure 7.14 is an example that shows total, asphalt, base+subbase, and subgrade rutting for the pavement models that contained Sand Subgrade and Coarse RCA base layers and were subjected to 1,000 AADTT (more results for other pavement models are provided in Appendix BD). As can be seen in Figure 7.14, although there was a slight increase in base+subbase layer rutting with an increase in the aggregate base layer thickness, the subgrade layer rutting reduced significantly. However, in real life, a similar result would be observed because increased aggregate base layer thickness tends to improve the load distribution mechanism and reduce the stresses applied to the subgrade layers. Reduced loading on subgrade layers yields lower subgrade rutting. Since subgrade layer rutting is the major contributor to the total pavement rutting, reduced subgrade layer rutting reduces total rutting.

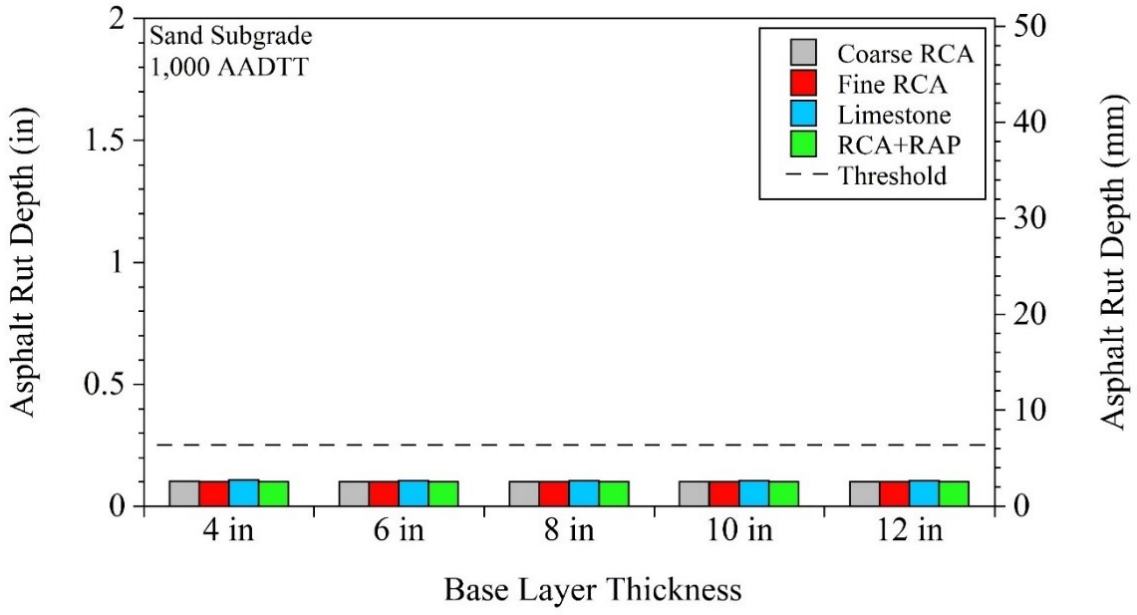

Figure 7.11. Asphalt rut depths (at 50% reliability) for pavement models that contained Sand Subgrade and were subjected to 1,000 AADTT

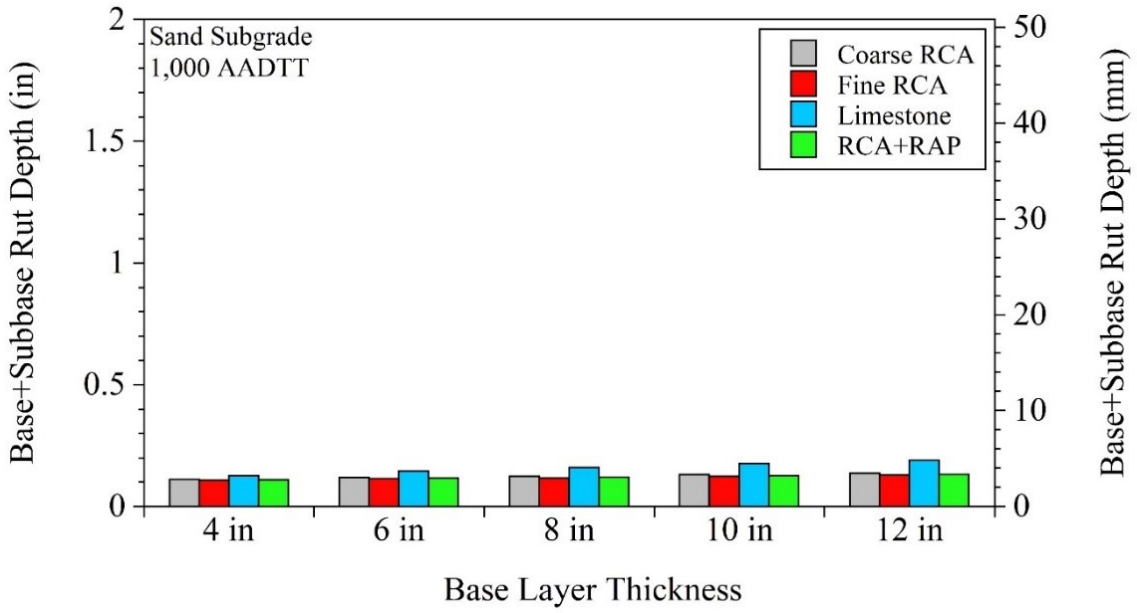

Figure 7.12. Base+subbase rut depths (at 50% reliability) for pavement models that contained Sand Subgrade and were subjected to 1,000 AADTT

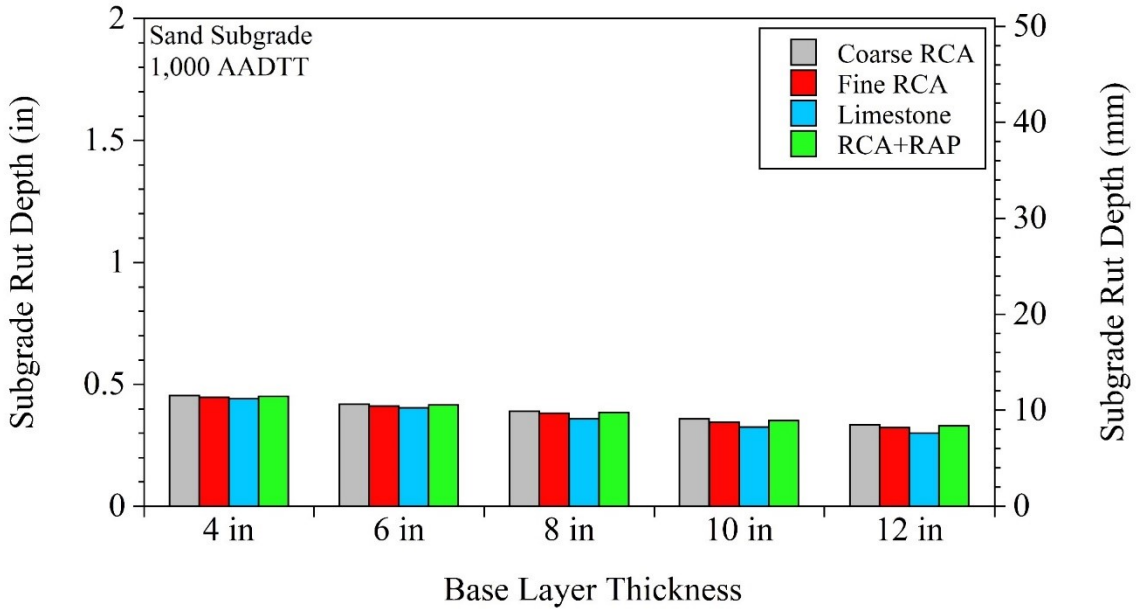

Figure 7.13. Subgrade rut depths (at 50% reliability) for pavement models that contained Sand Subgrade and were subjected to 1,000 AADTT

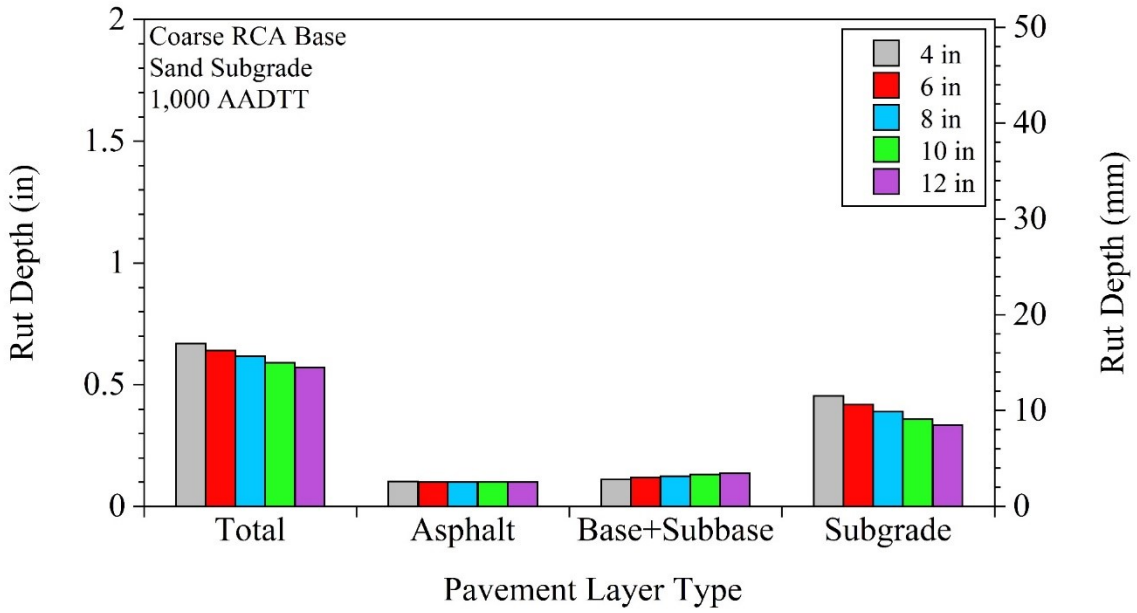

Figure 7.14. Total and layer rut depths (at 50% reliability) for pavement models that contained Sand Subgrade and Coarse RCA base layers and were subjected to 1,000 AADTT

7.1.2.6 Effect of Traffic Levels on Pavement Performance Prediction Models

As stated previously, five different traffic levels were applied to the models (Table 7.5). Overall, as expected, increasing the AADTT level yielded greater pavement distresses and shorter pavement service life. Performance prediction models exhibited that while acceptable pavement distresses and service lives were obtained at 100, 500, and 1,000 AADTT levels (low traffic), excessive failures occurred at 7,500 (medium traffic) and 25,000 (high traffic) AADTT levels (Table 7.5). Since the test cells were located in the MnROAD LVR and were designed as low volume road sections, it could be concluded that the model results complied with the actual case. Figure 7.15, Figure 7.16, Figure 7.17, and Figure 7.18 are examples that show the effect of traffic levels on IRI, rutting, alligator cracking, and longitudinal cracking, respectively, for pavement models that contained Sand Subgrade layers and 12-in aggregate base layers. More results for other pavement models are provided in Appendix BE.

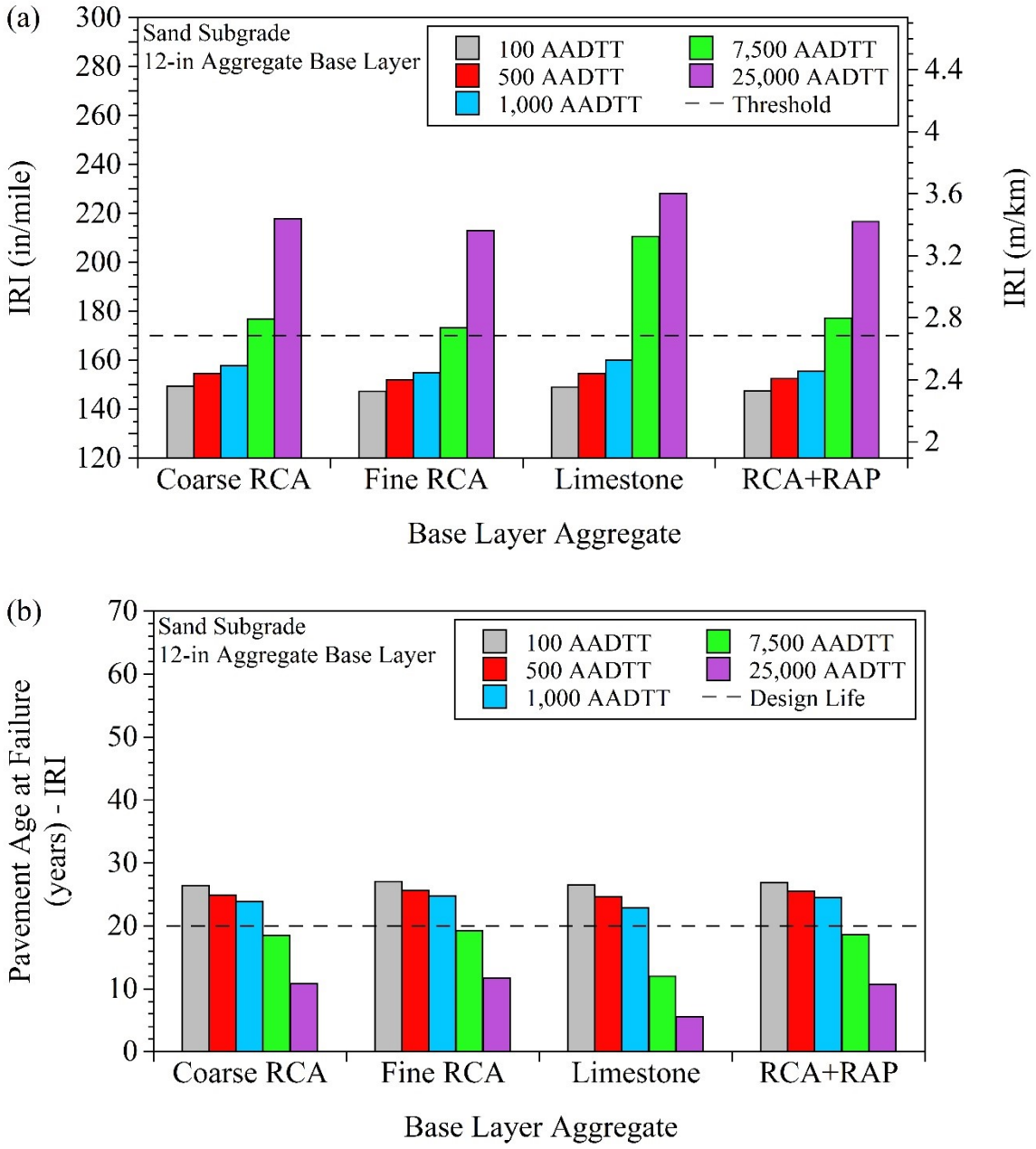

Figure 7.15. Effect of traffic level on (a) international roughness index (IRI) at the end of design life (20 years) and (b) pavement age at IRI failure

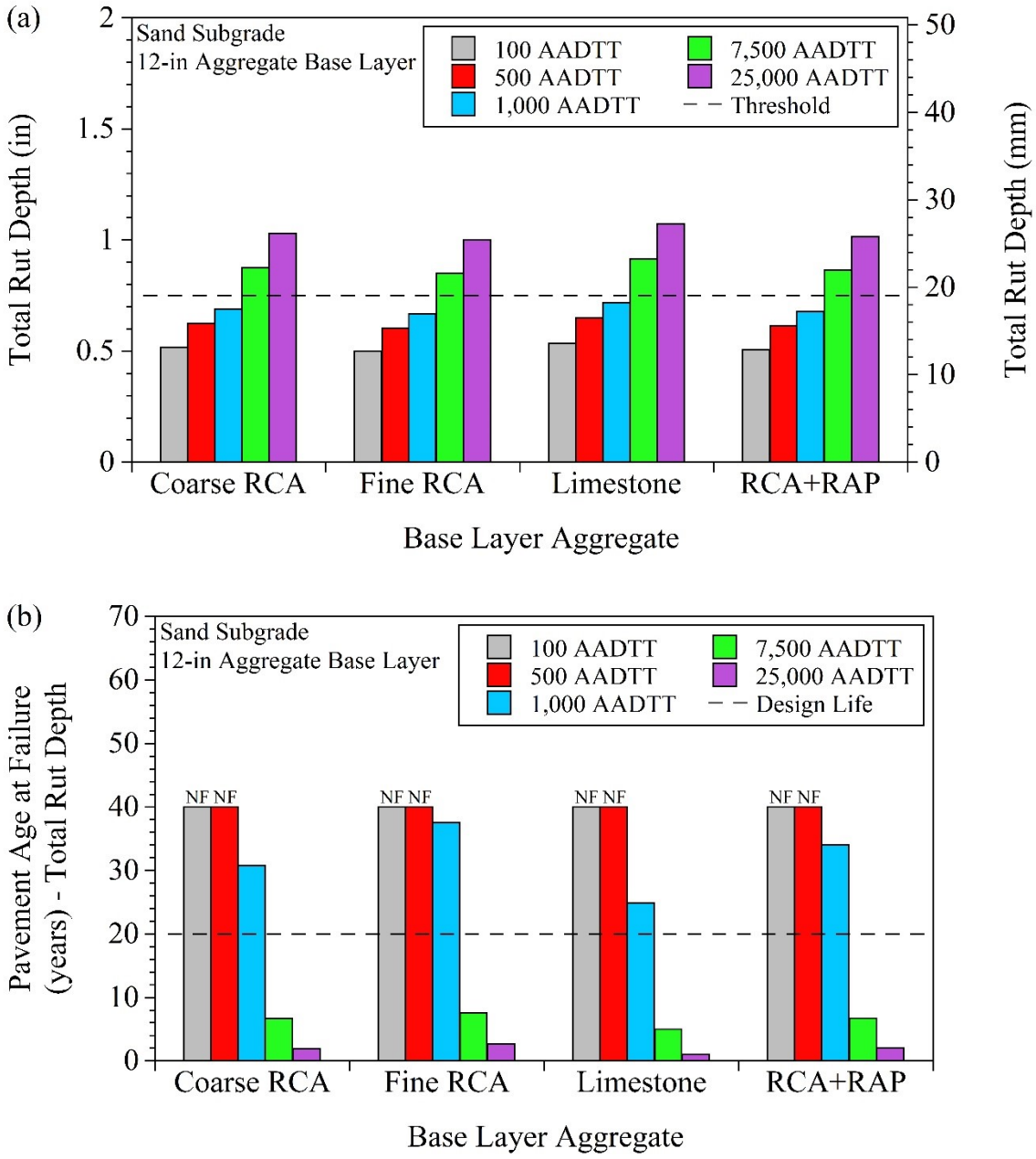

Figure 7.16. Effect of traffic level on (a) rutting at the end of design life (20 years) and (b) pavement age at rutting failure (NF = no failure)

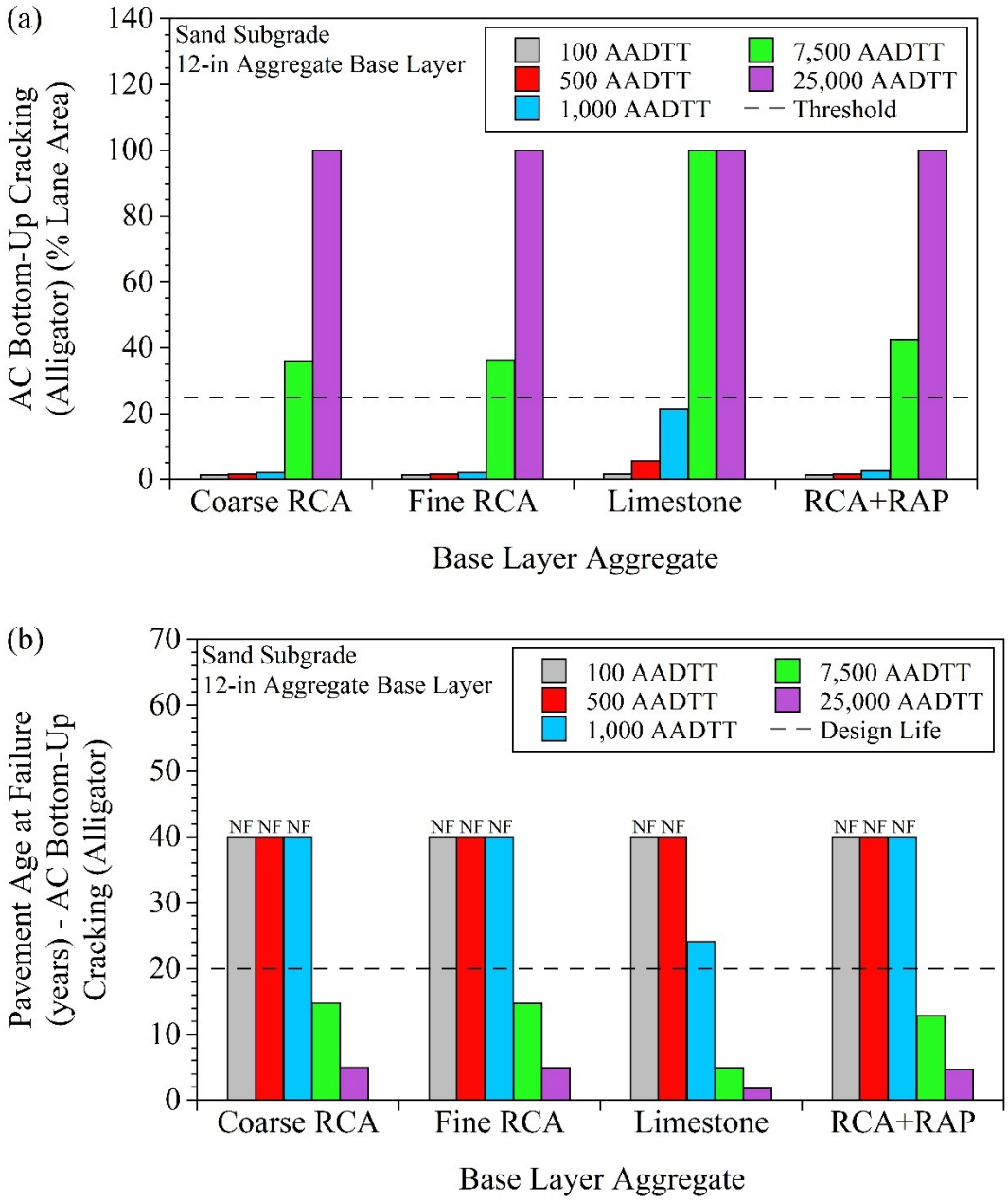

Figure 7.17. Effect of traffic level on (a) alligator cracking at the end of design life (20 years) and (b) pavement age at alligator cracking failure (NF = no failure)

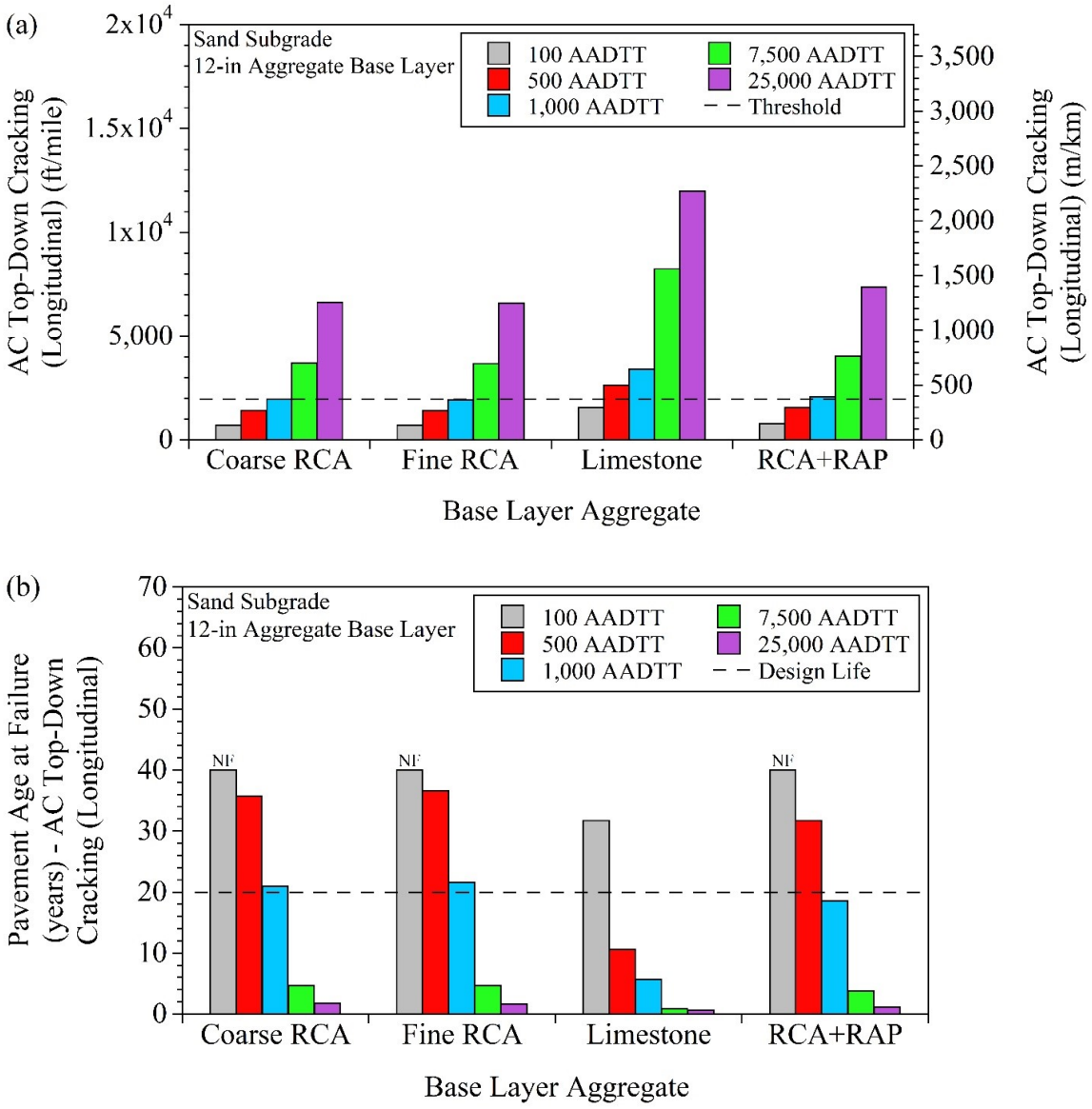

Figure 7.18. Effect of traffic level on (a) longitudinal cracking at the end of design life (20 years) and (b) pavement age at longitudinal cracking failure (NF = no failure)

7.1.2.7 Recycled Aggregate Base (RAB) Layer Thicknesses Alternative to 12-in Limestone Base Layer

To make thickness recommendations for RAB layers constructed with Coarse RCA, Fine RCA, and RCA+RAP, the pavement performance prediction models for the pavements that contained 12-in Limestone base layer were compared to those for the pavements that contained RAB layers at different thicknesses (ranging from 4 in to 12 in). Since it was previously discussed that AADTT levels of 7,500 and 25,000 yielded excessive pavement distresses and the overall designs of the pavement models were more suitable for lower traffic levels, comparisons were made only for the pavement models that were subjected to low traffic levels [100, 500, and 1,000 AADTT (Table 7.5)].

Overall, based on the models, it was concluded that thinner RAB layers (4, 6, 8, or 10 in) could be constructed with Coarse RCA, Fine RCA, or RCA+RAP materials instead of constructing a 12-in Limestone base layer. This was mainly due to the input SM_R values used for Coarse RCA (18,129 psi), Fine RCA (17,760.9 psi), and RCA+RAP (16,487.7 psi) base layers all of which were higher than those used for Limestone base layers (13,926.3 psi). Figure 7.19, Figure 7.20, Figure 7.21, and Figure 7.22 are examples that show relative recycled aggregate base (RAB) layer thicknesses as alternatives to 12-in Limestone base layers in terms of IRI, rutting, alligator cracking, and longitudinal cracking, respectively [for pavement models that contained Sand Subgrade layers and were subjected to 1,000 AADTT]. More results for other pavement models are provided in Appendix BF. A summary of all RAB layer thicknesses alternative to 12-in Limestone base layer based on different pavement distresses is provided in Table 7.7.

Based on the IRI predictions, while the input SM_R value used for Coarse RCA (18,129 psi) was higher than those used for Fine RCA (17,760.9 psi) and RCA+RAP (16,487.7 psi), the model results showed that the Fine RCA and RCA+RAP base layers could be even thinner than Coarse RCA base layers (Table 7.7). This demonstrated that not only the input SM_R value, but also other input parameters (e.g., K_{sat} and gradation) could be important for the determination of the aggregate base layer design thickness. Based on rutting predictions, similar alternative RAB thicknesses (10 in) were determined for the sections built with RAB layers on Sand Subgrade layers. However, for the RAB layers overlying Clay Loam subgrade layers, rutting predictions showed that Fine RCA and RCA+RAP base layers could be 4-in thick and Coarse RCA base layer could be 6-in thick. Based on alligator cracking predictions, the alternative RAB layer thicknesses were 4 in. Lastly, based on longitudinal cracking predictions, while 6 in was the alternative layer thickness for Coarse RCA and Fine RCA base layers, it was 8 in for RCA+RAP base layers.

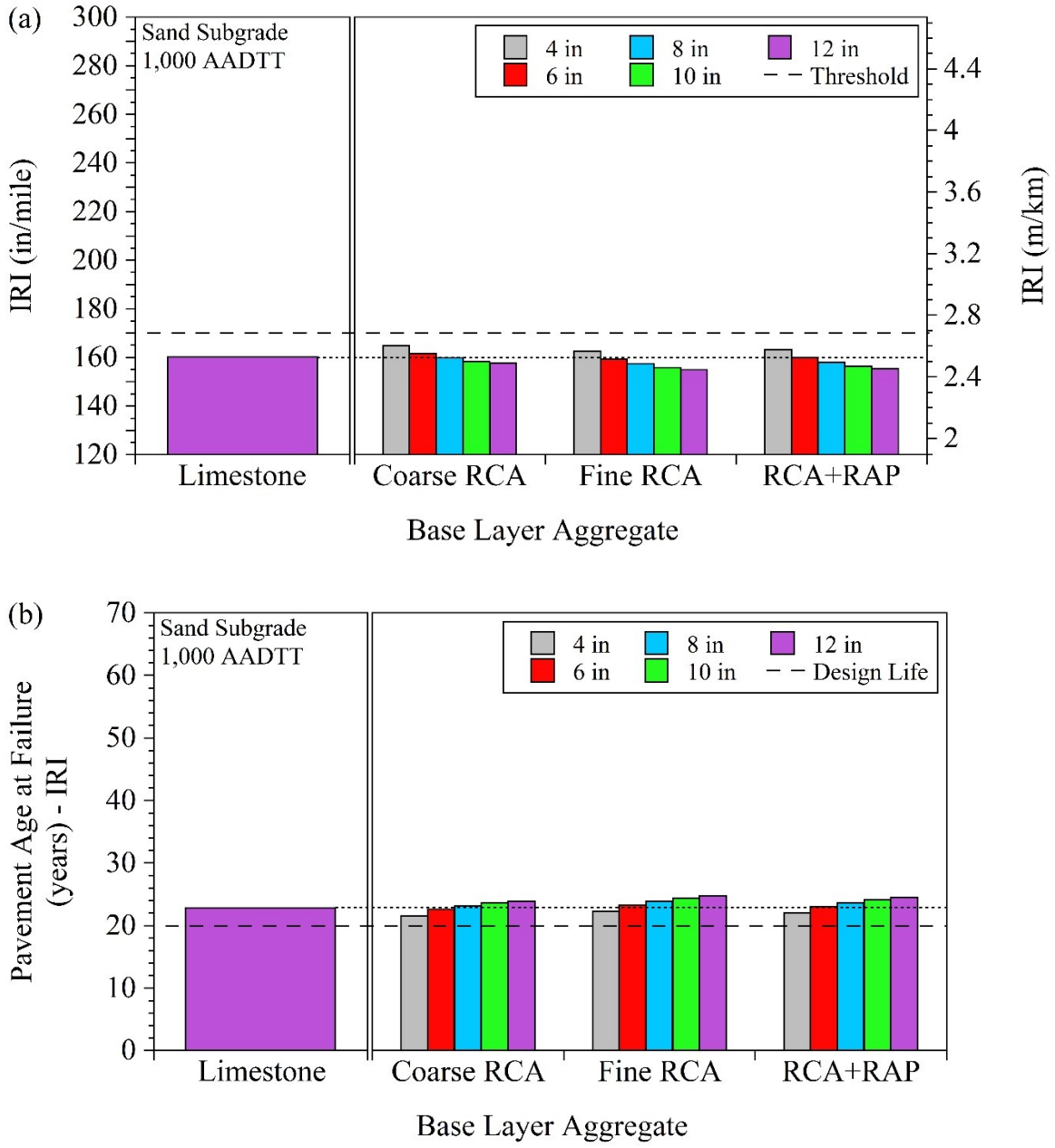

Figure 7.19. Relative recycled aggregate base (RAB) layer thicknesses alternative to 12-in Limestone base layer in terms of (a) international roughness index (IRI) at the end of design life (20 years) and (b) pavement age at IRI failure

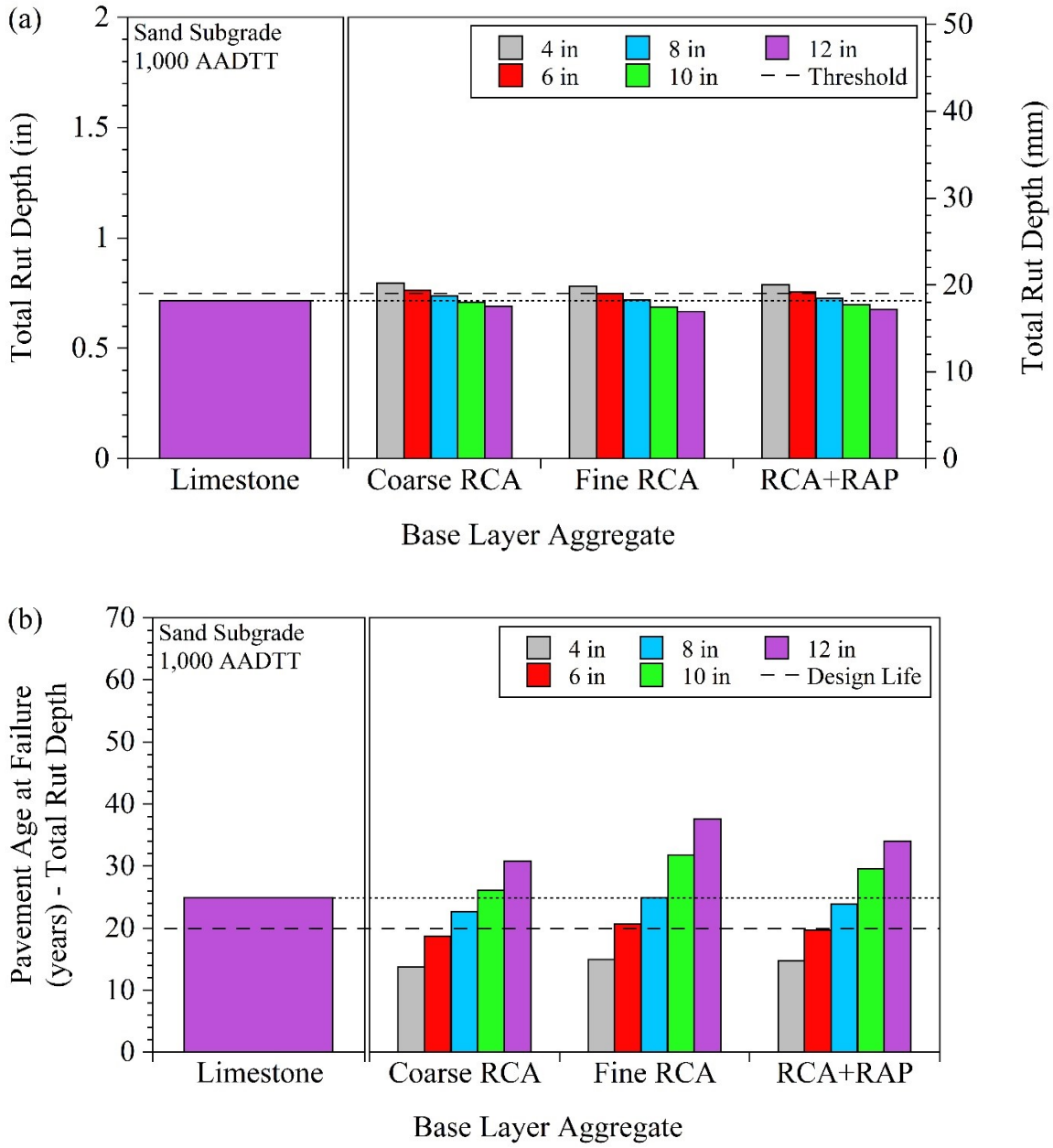

Figure 7.20. Relative recycled aggregate base (RAB) layer thicknesses alternative to 12-in Limestone base layer in terms of (a) rutting at the end of design life (20 years) and (b) pavement age at rutting failure

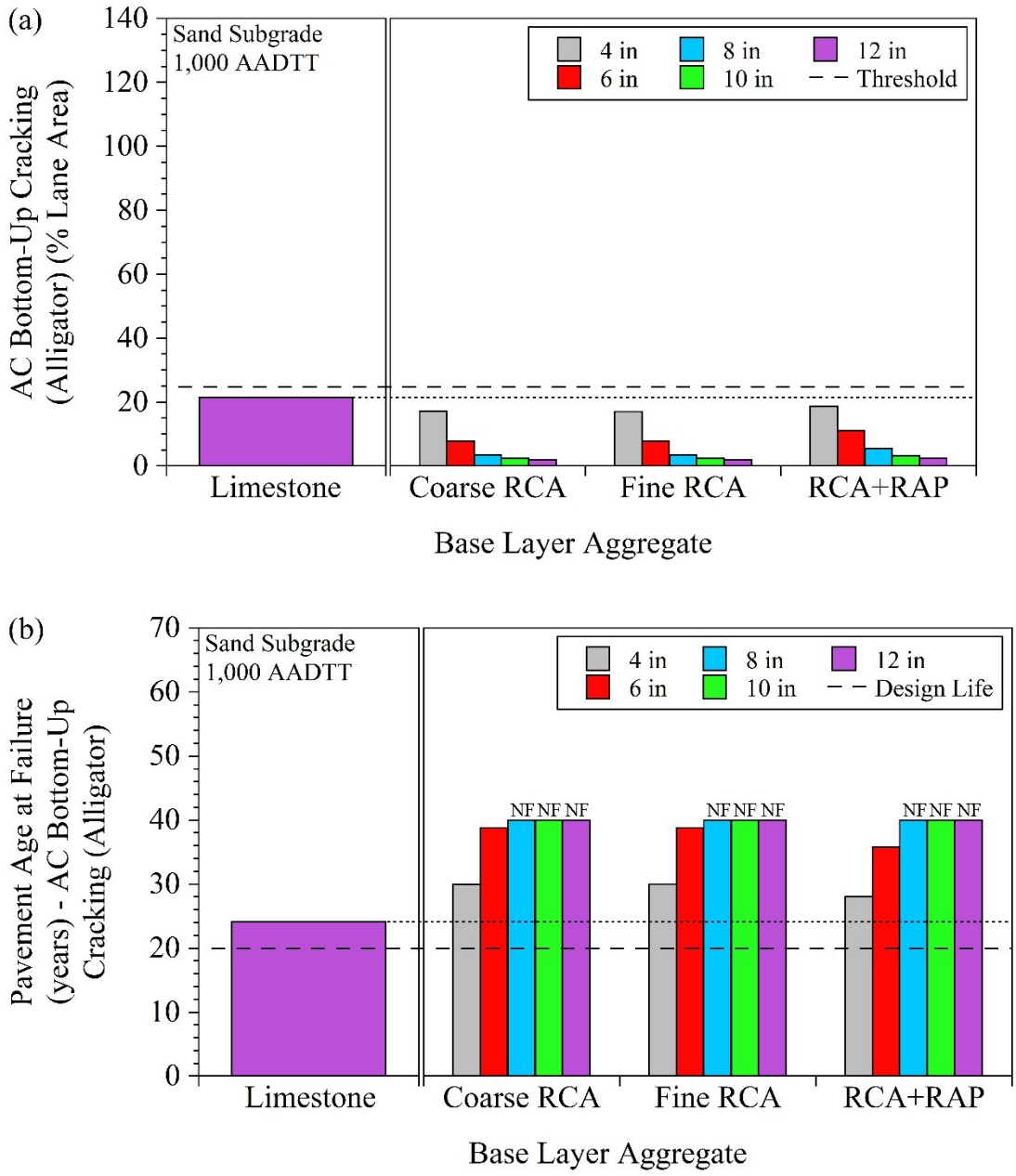

Figure 7.21. Relative recycled aggregate base (RAB) layer thicknesses alternative to 12-in Limestone base layer in terms of (a) alligator cracking at the end of design life (20 years) and (b) pavement age at alligator cracking failure (NF = no failure)

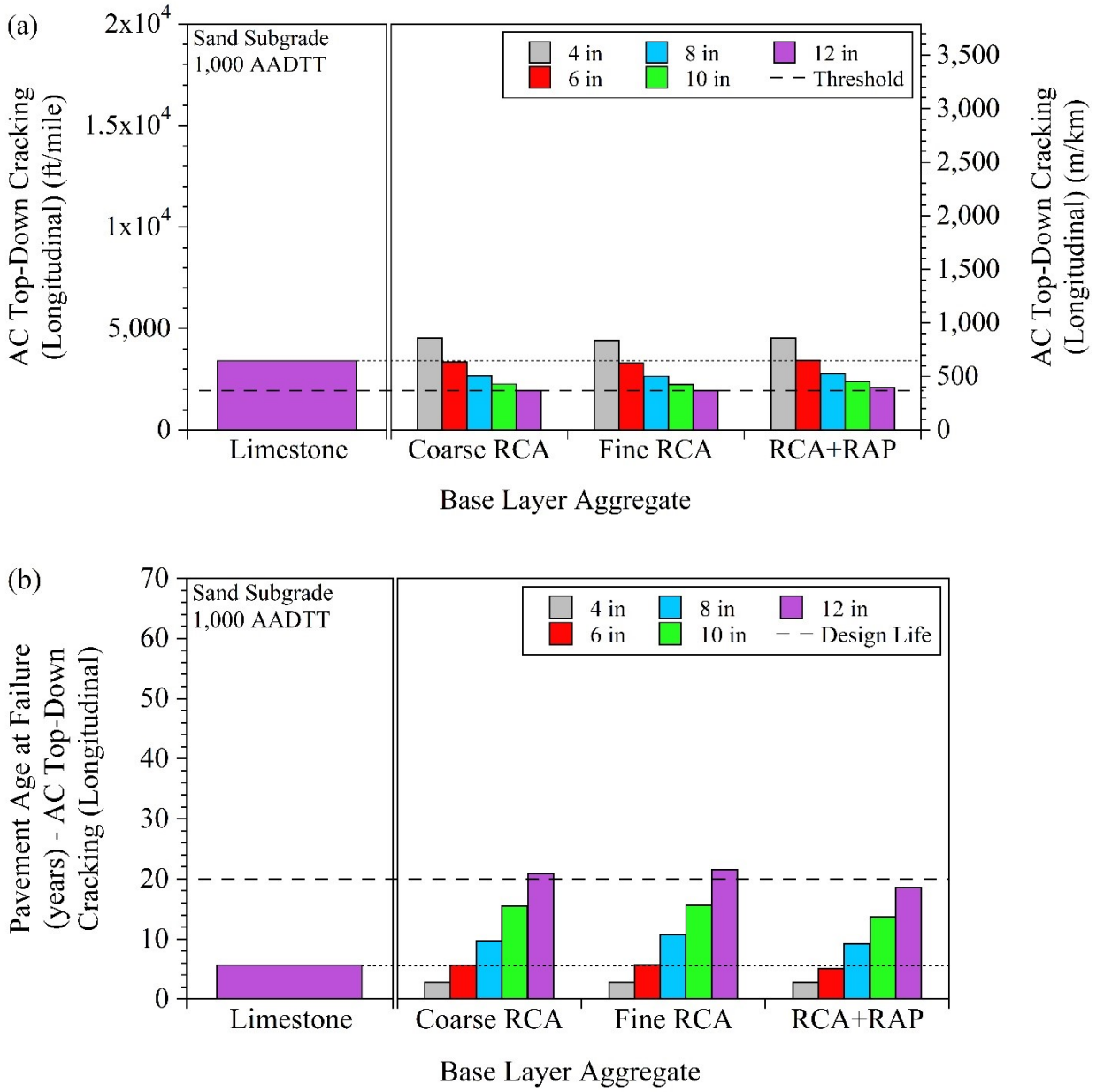

Figure 7.22. Relative recycled aggregate base (RAB) layer thicknesses alternative to 12-in Limestone base layer in terms of (a) longitudinal cracking at the end of design life (20 years) and (b) pavement age at longitudinal cracking failure

Table 7.7. Summary of RAB layer thicknesses alternative to 12-in Limestone base layer

AADTT Level	Recycled Aggregate Base (RAB) Layer Thickness Alternative to 12-in Limestone (in)							
	Alter-native Material	Based on IRI		Based on Rutting		Based on Alligator Cracking		Based on Longitudinal Cracking
		Sand Subgrade	Clay Loam Subgrade	Sand Subgrade	Clay Loam Subgrade	Sand Subgrade	Clay Loam Subgrade	Sand Subgrade
100	Coarse RCA	12	10	10	6	4	4	6
	Fine RCA	10	6	10	4	4	4	6
	RCA+ RAP	10	4	10	4	4	4	8
500	Coarse RCA	12	8	10	6	4	4	6
	Fine RCA	8	6	10	4	4	4	6
	RCA+ RAP	8	6	10	4	4	4	8
1,000	Coarse RCA	8	6	10	6	4	4	6
	Fine RCA	6	6	10	4	4	4	6
	RCA+ RAP	6	4	10	4	4	4	8

AADTT = average annual daily truck traffic; IRI = international roughness index

7.1.3 Large Stone Subbase (LSSB) Groups

7.1.3.1 Large Stone Subbase (LSSB) Layer Design

In the MnROAD LVR test facility, LSSB layers were constructed at two different thicknesses: (1) 18-in LSSB layers (Cells 127 and 227) and (2) 9-in LSSB layers (Cells 328-728). To evaluate the effect of the LSSB layer thickness on pavement performance prediction models in Pavement ME, 12-in LSSB and 15-in LSSB layers were also modeled in addition to the original LSSB layer thicknesses (18 in and 9 in). In addition, as can be seen in Figure 3.2 for the LSSB groups, while Cells 127 and 227 (18-in LSSB) contained Class 6 Aggregate base layers, Cells 328-728 (9-in LSSB) contained Class 5Q Aggregate base layers. In Pavement ME, first, 6-in Class 6 Aggregate base layers were placed on top of the LSSB layers [asphalt layer thicknesses were kept as original (3.5 in), and similar Clay Loam subgrade layers were used]. Then, 6-in Class 5Q Aggregate base layers were placed on top of the LSSB layers. Figure 7.23 is an example that shows different LSSB layer thicknesses that were modeled on top of the Clay Loam subgrade layers.

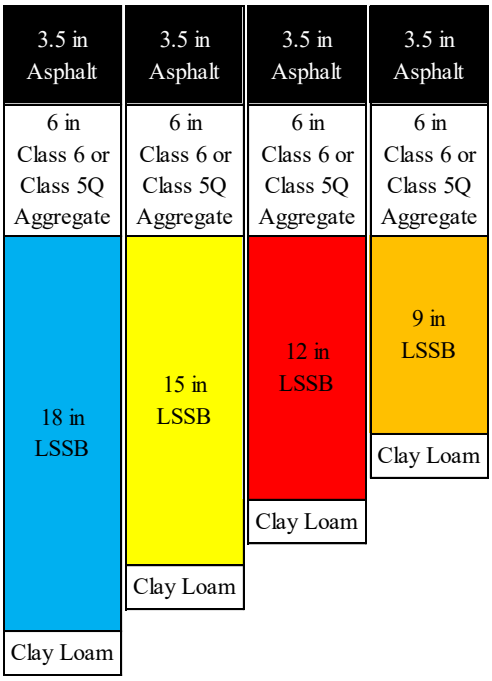

Figure 7.23. Pavement ME models for large stone subbase (LSSB) layers at different layer thicknesses

7.1.3.2 Material Inputs

Similar to the RAB group, Superpave PG 58-34 was selected (level 3) to model the 3.5-in asphalt layers. Appendix AY provides detailed information about level 3 parameters for the modeled asphalt layer. Table 7.8 summarizes the input parameters (level 2) for aggregate base, LSSB, and Clay Loam subgrade layers that were used in the models.

For each pavement sublayer, the coefficient of lateral earth pressure (K0) was kept at its default value (0.5). Since no laboratory M_R tests were performed for Class 6 Aggregate and Class 5Q Aggregate, the equations were found to estimate the SM_R for Coarse RCA, Fine RCA, Limestone, and RCA+RAP (Table 6.9 and Appendix AS) were used for Class 6 Aggregate and Class 5Q Aggregate to estimate their SM_R values (Appendix AZ). After using the equations suitable to estimate the SM_R values of Class 6 Aggregate and Class 5Q Aggregate, the median SM_R values (16,478.9 psi and 18,651.1 psi for Class 6 Aggregate and Class 5Q Aggregate, respectively) were determined and compared with the SM_R values of Coarse RCA (18,129 psi), Fine RCA (17,760.9 psi), Limestone (13,926.3 psi), and RCA+RAP (16,487.7 psi). Since the comparison showed that the estimated SM_R values of Class 6 Aggregate (16,478.9 psi) and Class 5Q Aggregate (18,651.1 psi) were in an acceptable range, they were used in the modeling analyses (Table 7.8).

For the SM_R of LSSB layers, based on the literature, three SM_R levels were used in the modeling analyses: (1) 10,000 psi, (2) 30,000 psi, and (3) 50,000 psi. MDU, K_{sat}, and OMC values for the LSSB layers were not user-defined, and their values, provided by the Pavement ME program during level 2 analysis, were used for LSSB (80 pcf for MDU, 1.18E+03 ft/hr for K_{sat}, and 0% for OMC). The input parameters for Clay Loam subgrade layers were identical to those used in the models created for the RAB group. Lastly, as

described previously, the SWCC characteristics of the materials were determined by the van Genuchten model (van Genuchten 1980) [Equation (4.1)] in this study. Since the Pavement ME program uses the Fredlund and Xing (1994) SWCC model, the SWCC inputs [af, bf, cf, hr fitting parameters (Fredlund and Xing 1994)] were not user-defined for Class 6 Aggregate, Class 5Q Aggregate, and Clay Loam subgrade (no matric suction would be expected for LSSB due to the presence of large stones).

Table 7.8. Material inputs used for pavement sublayers in Pavement ME models

Parameter		Class 6 Aggregate Base	Class 5Q Aggregate Base	LSSB	Clay Loam Subgrade
AASHTO Classification		A-1-a	A-1-a	A-1-a	A-6
Poisson's Ratio		0.35	0.35	0.35	0.4
M_R (psi)		16,478.9[#]	18,651.1[#]	10,000 psi[+] 30,000 psi[+] 50,000 psi[+]	8,630.9
LL		27.4	0	0	36.3
PI		0	0	0	12.4
Corrected MDU (pcf)		128.5	128	80*	124.9
K_{sat} (ft/hr)		2.26E-02	3.44E-02	1.18E+03*	1.62E-05
Combined OD G_s		2.35	2.28	2.60	2.68
Corrected OMC (%)		8.3	9.6	0*	10
Percent Passing (%)	No. 200	6.3	3.2	0.1	59.7
	No. 100	9.3	4.8	0.1	68.9
	No. 60	14.6	6.8	0.2	77.6
	No. 40	23.9	10.4	0.2	84.6
	No. 20	37.1	15.8	0.3	90.1
	No. 10	49.3	22.8	0.4	94
	No. 4	64.9	34.1	0.4	96.9
	3/8 in	79.9	48.4	0.9	98.4
	3/4 in	98.3	76.1	6.3	99.4
	1 in	100	89.3	13.1	99.5
	1 1/2 in	100	100	35.8	100
	2 in	100	100	70.2	100
	2.5 in	100	100	96.9	100
	3 in	100	100	100	100

M_R = resilient modulus; LL = liquid limit; PI = plasticity index; MDU = maximum dry unit weight; K_{sat} = saturated hydraulic conductivity; OD = oven-dry; G_s = specific gravity; OMC = optimum moisture content. To determine the combined G_s values, the weighted average of the G_s values of the coarse [> No. 4 sieve (4.75 mm)] and fine (< No. 4) fractions of the materials were used.

[#]Determined based on the M_R models developed in this study (Table 6.9, Appendix AS, and Appendix AZ)

*Not user-defined (level 2)

[+]Estimated based on the literature to provide a wide range of M_R values

7.1.3.3 Effect of Large Stone Subbase (LSSB) Thickness on Pavement Performance Prediction Models

As stated previously, LSSB layer thicknesses ranging between 9 in and 18 in were used in the modeling analyses (Figure 7.23) to evaluate the effect of the LSSB layer thickness on long-term pavement performance predictions. For IRI, no consistent trend was observed between the IRI predictions and LSSB layer thickness. On the other hand, increasing the LSSB layer thickness generally decreased rutting and alligator cracking at the end of the pavement design life (20 years). Figure 7.24, Figure 7.25, and Figure 7.26 are examples that show the effect of the LSSB thickness on IRI, rutting, and alligator cracking, respectively, for the pavement models that contained Class 6 Aggregate base layers and were subjected to 1,000 AADTT. More results for other pavement modeling analyses are provided in Appendix BG.

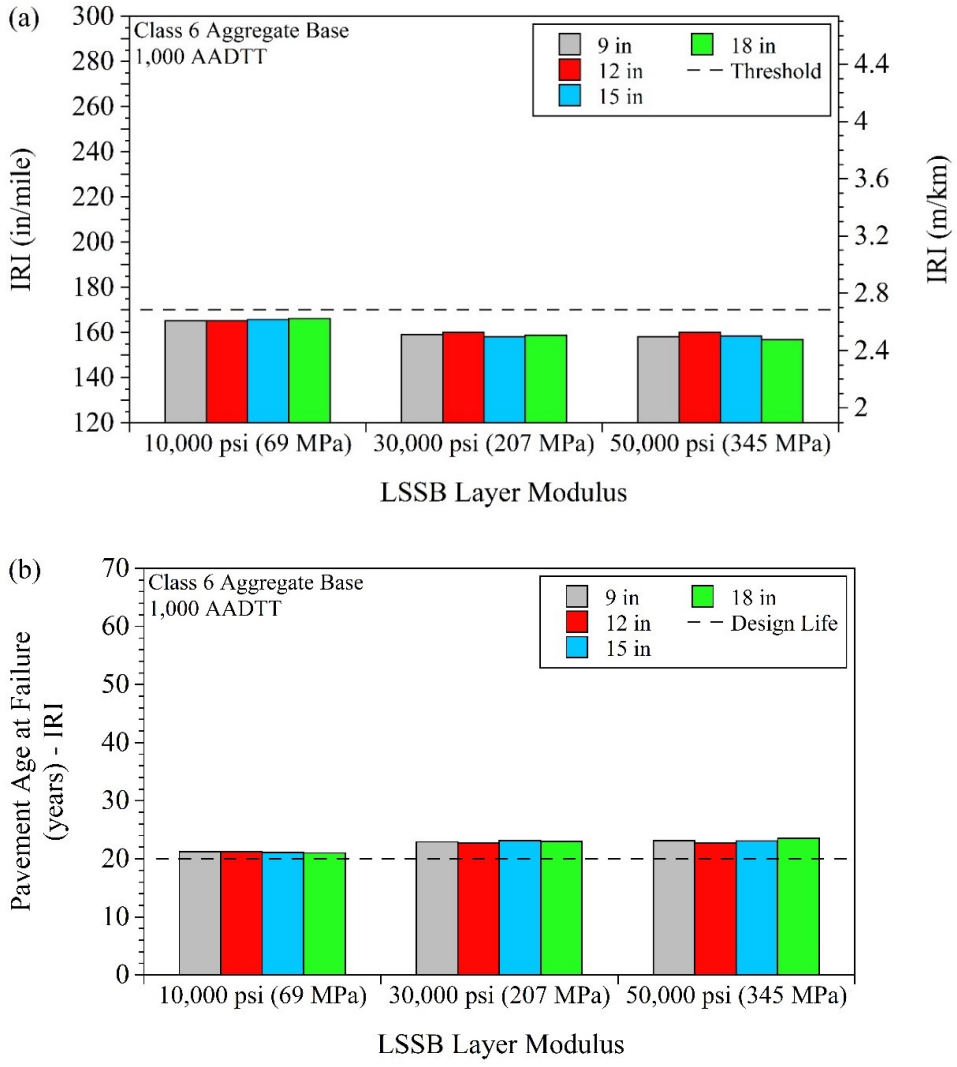

Figure 7.24. Effect of large stone subbase (LSSB) layer thickness on (a) international roughness index (IRI) at the end of design life (20 years) and (b) pavement age at IRI failure

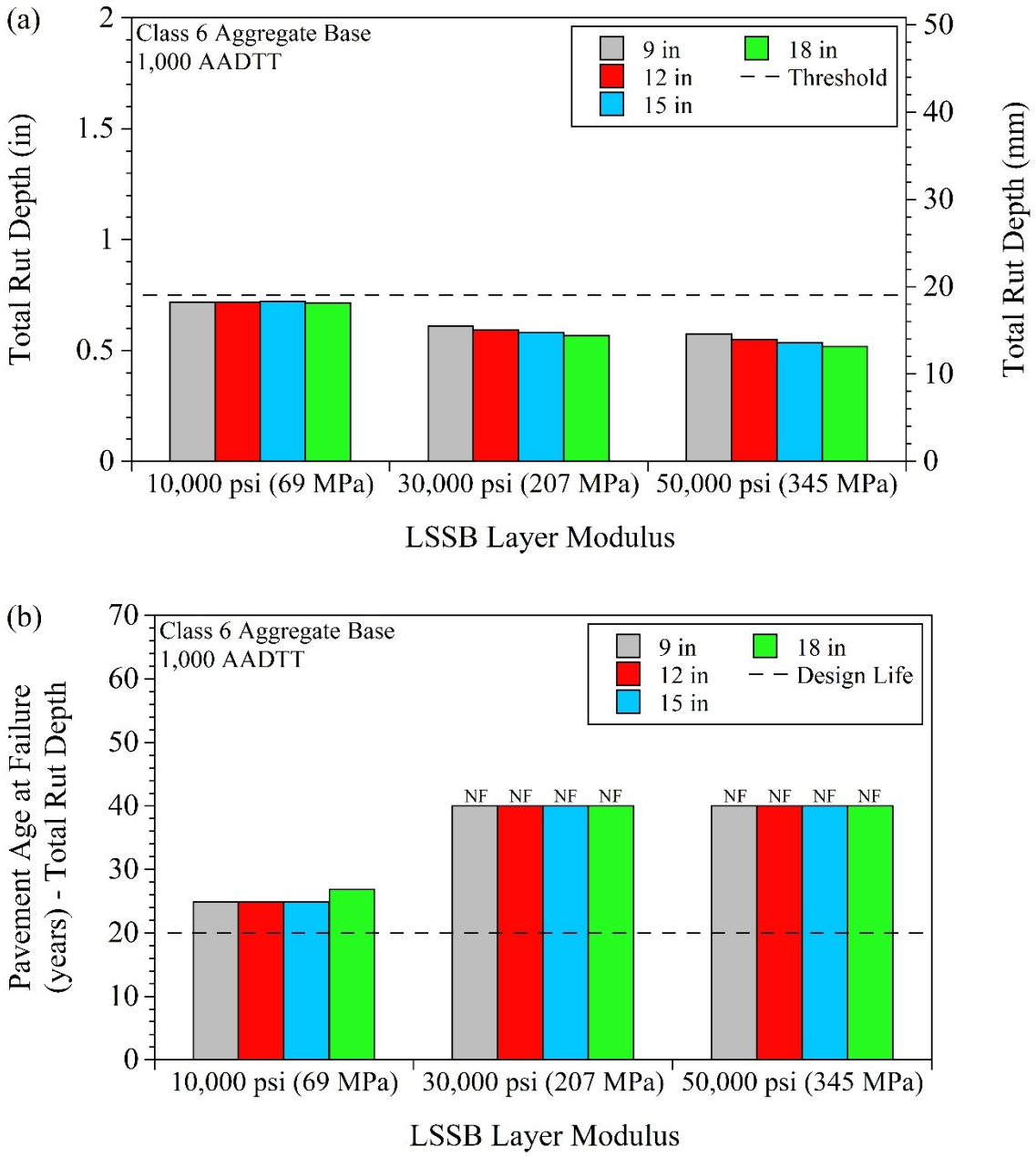

Figure 7.25. Effect of large stone subbase (LSSB) layer thickness on (a) rutting at the end of design life (20 years) and (b) pavement age at rutting failure (NF = no failure)

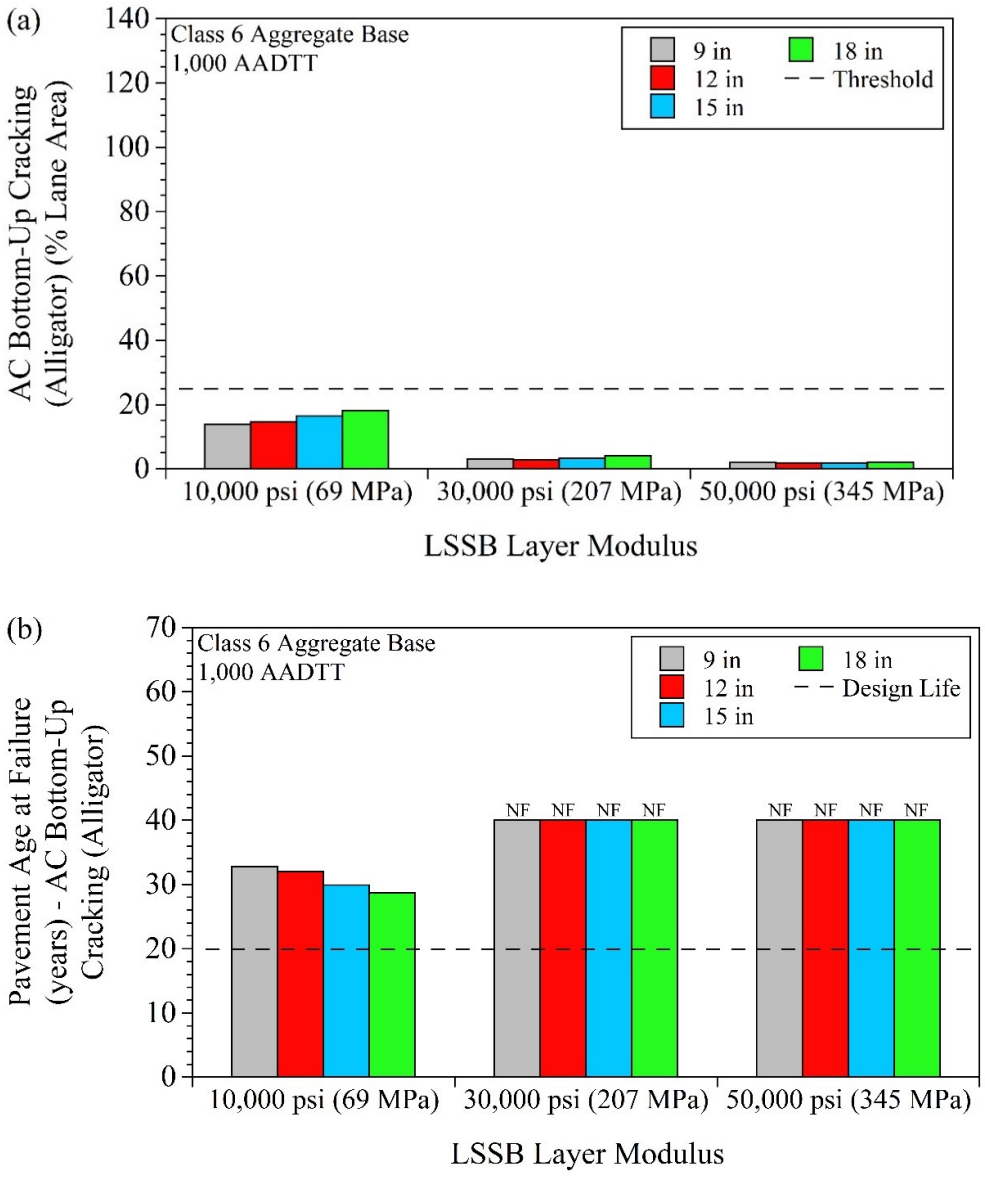

Figure 7.26. Effect of large stone subbase (LSSB) layer thickness on (a) alligator cracking at the end of design life (20 years) and (b) pavement age at alligator cracking failure (NF = no failure)

7.1.3.4 Effect of Large Stone Subbase (LSSB) Stiffness on Pavement Performance Prediction Models

As stated previously, three different SM_R values were used in the models for LSSB: (1) 10,000 psi, (2) 30,000 psi, and (3) 50,000 psi. Overall, it was concluded that increasing the LSSB SM_R value resulted in lower pavement distress at the end of the pavement design life (20 years) and an increase in pavement service life. Figure 7.27, Figure 7.28, and Figure 7.29 are examples that show the effect of LSSB M_R on IRI, rutting, and alligator cracking, respectively, for the pavement models that contained Class 6 Aggregate base layers and were subjected to 1,000 AADTT. More results for other pavement modeling analyses are provided in Appendix BH.

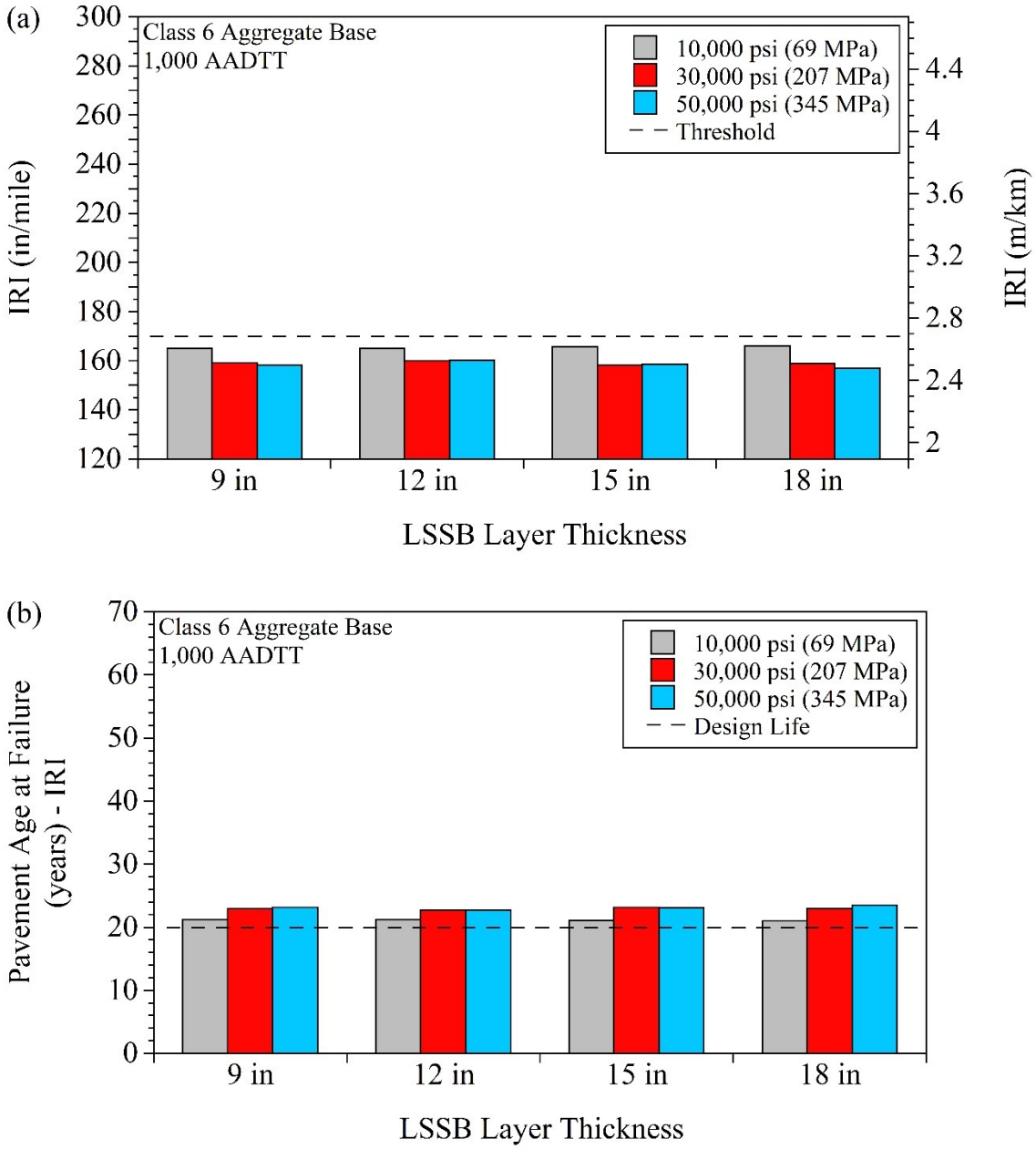

Figure 7.27. Effect of large stone subbase (LSSB) layer modulus on (a) international roughness index (IRI) at the end of design life (20 years) and (b) pavement age at IRI failure

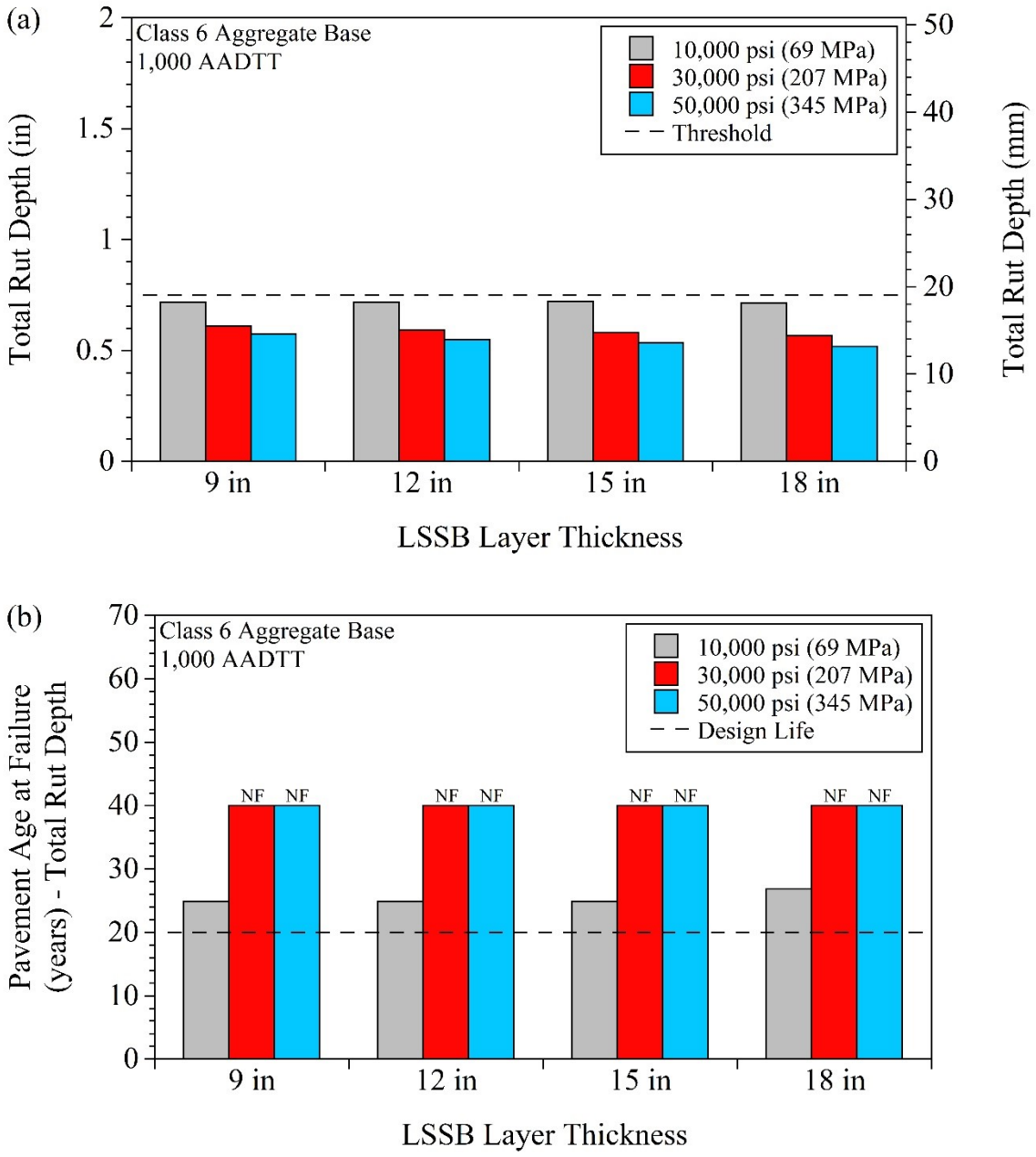

Figure 7.28. Effect of large stone subbase (LSSB) layer modulus on (a) rutting at the end of design life (20 years) and (b) pavement age at rutting failure (NF = no failure)

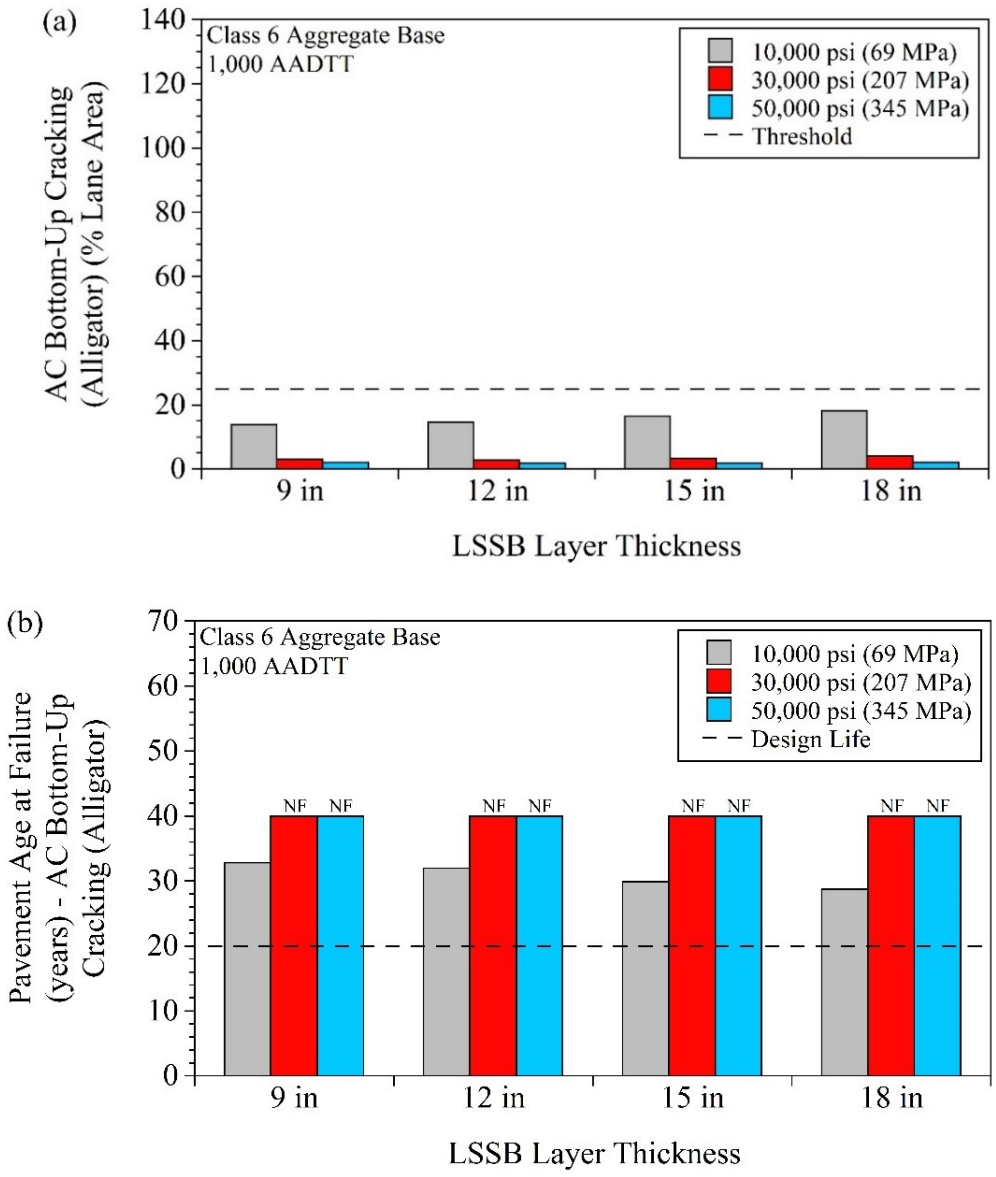

Figure 7.29. Effect of large stone subbase (LSSB) layer modulus on (a) alligator cracking at the end of design life (20 years) and (b) pavement age at alligator cracking failure (NF = no failure)

7.1.3.5 Layer Rutting at 50% Reliability

Layer rutting for asphalt, base+subbase, and subgrade was also evaluated at 50% reliability (Pavement ME can only give 50% reliability for layer rutting) based on the outputs obtained from Pavement ME. For asphalt layer rutting, there was generally no significant difference between the asphalt layers placed on LSSB layers at different thicknesses and with different M_R values in the modeling analyses.

For base+subbase layer rutting, increasing the LSSB thickness generally yielded higher LSSB layer rutting. For subgrade layer rutting, the subgrade layers underlying thinner LSSB layers exhibited higher rutting. Figure 7.30, Figure 7.31, and Figure 7.32 are examples that show the asphalt, base+subbase, and

subgrade rut depths for the pavement models that contained Class 6 Aggregate base layers and were subjected to 1,000 AADTT. More results for other pavement modeling analyses are provided in Appendix BI.

As expected, the modeling analyses showed that the highest layer rutting was observed in the subgrade layers. In addition, increasing the LSSB M_R value decreased both base+subbase and subgrade layer rutting. It was concluded that the model results complied with general expectations. Figure 7.33 is an example that shows the total, asphalt, base+subbase, and subgrade rutting for the pavement models that contained Class 6 Aggregate base layers and were subjected to 1,000 AADTT. More results for other pavement modeling analyses are provided in Appendix BJ.

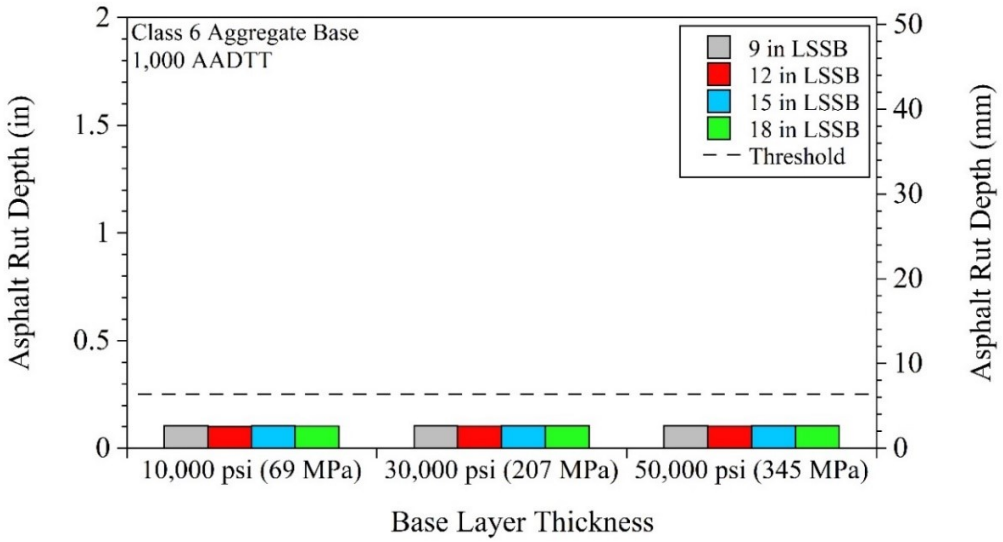

Figure 7.30. Asphalt rut depths (at 50% reliability) for pavement models that were subjected to 1,000 AADTT

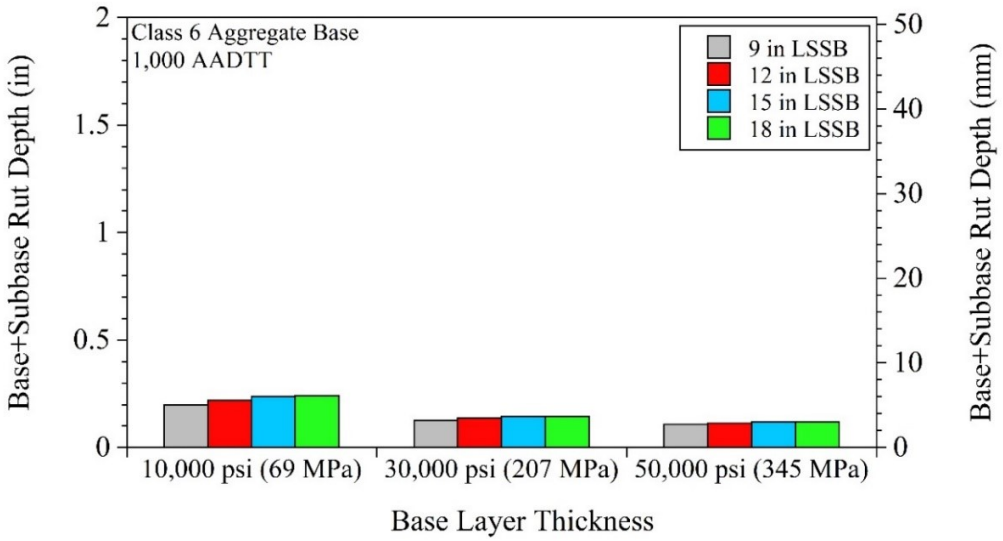

Figure 7.31. Base+subbase rut depths (at 50% reliability) for pavement models that were subjected to 1,000 AADTT

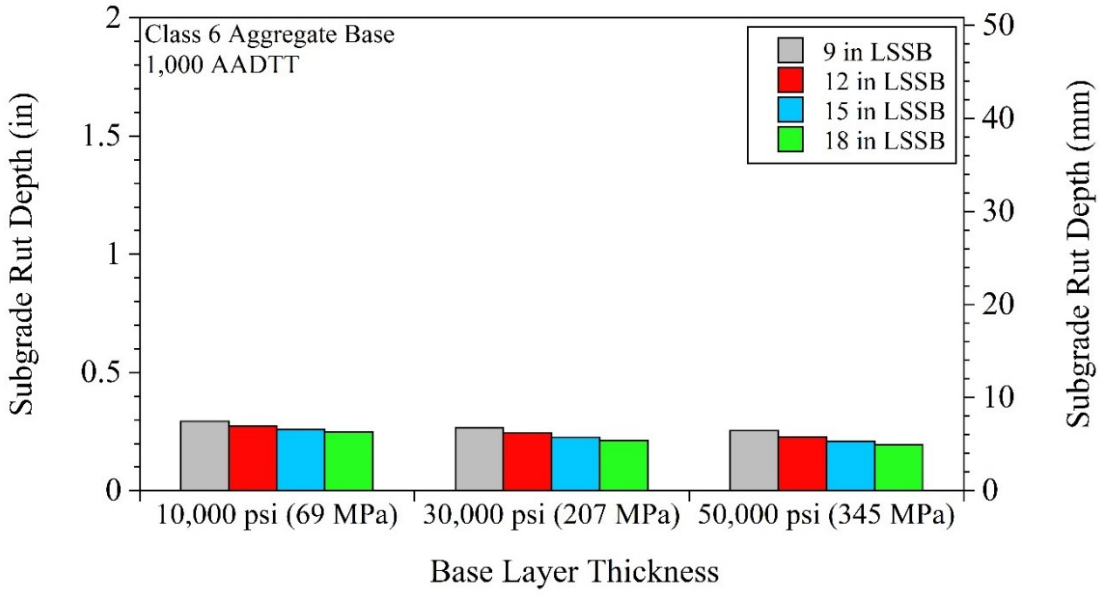

Figure 7.32. Subgrade rut depths (at 50% reliability) for pavement models that were subjected to 1,000 AADTT

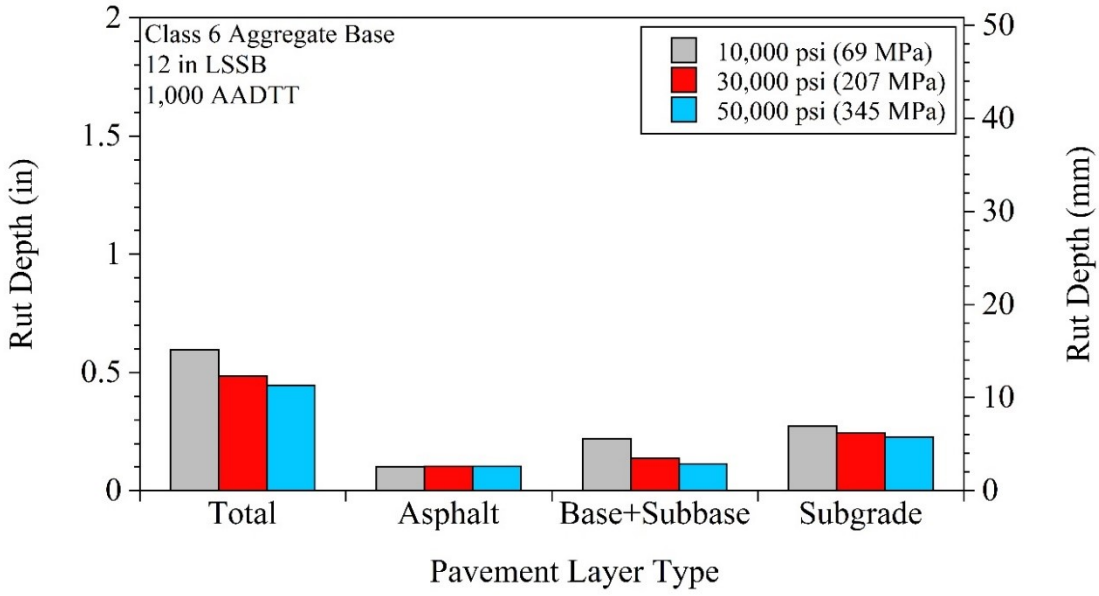

Figure 7.33. Total and layer rut depths (at 50% reliability) for pavement models that contained 12-in large stone subbase (LSSB) layers and were subjected to 1,000 AADTT

7.1.3.6 Effect of Traffic Level on Pavement Performance Prediction Models

Similar to the observations made for the RAB group, increasing the AADTT level yielded greater pavement distresses and shorter pavement service life. Figure 7.34, Figure 7.35, and Figure 7.36 are examples that show the effect of traffic levels on IRI, rutting, and alligator cracking, respectively, for pavement modeling analyses that contained Class 6 Aggregate base layers and LSSB layers having an SM_R of 10,000 psi. More results for other pavement modeling analyses are provided in Appendix BK.

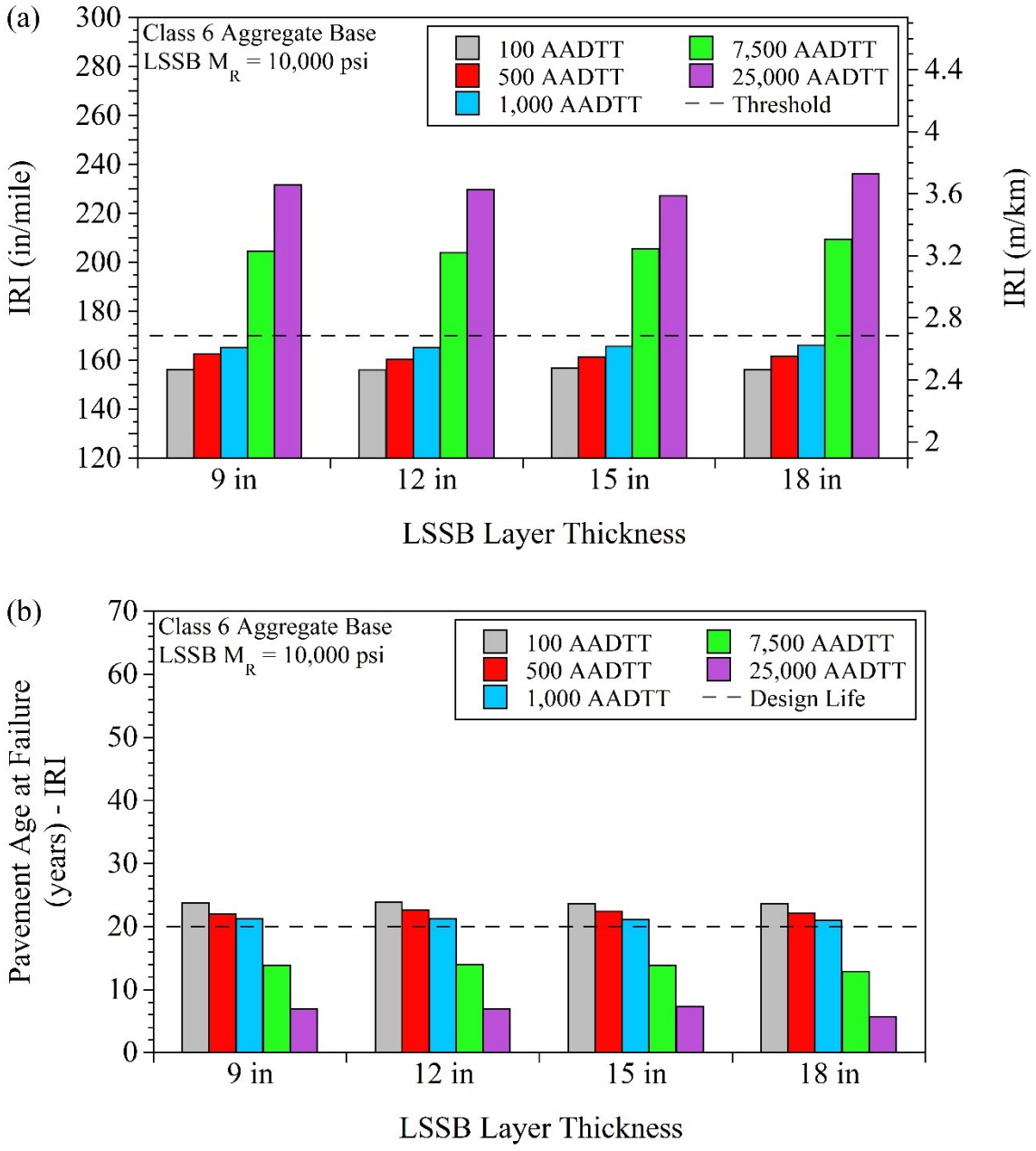

Figure 7.34. Effect of traffic level on (a) international roughness index (IRI) at the end of design life (20 years) and (b) pavement age at IRI failure

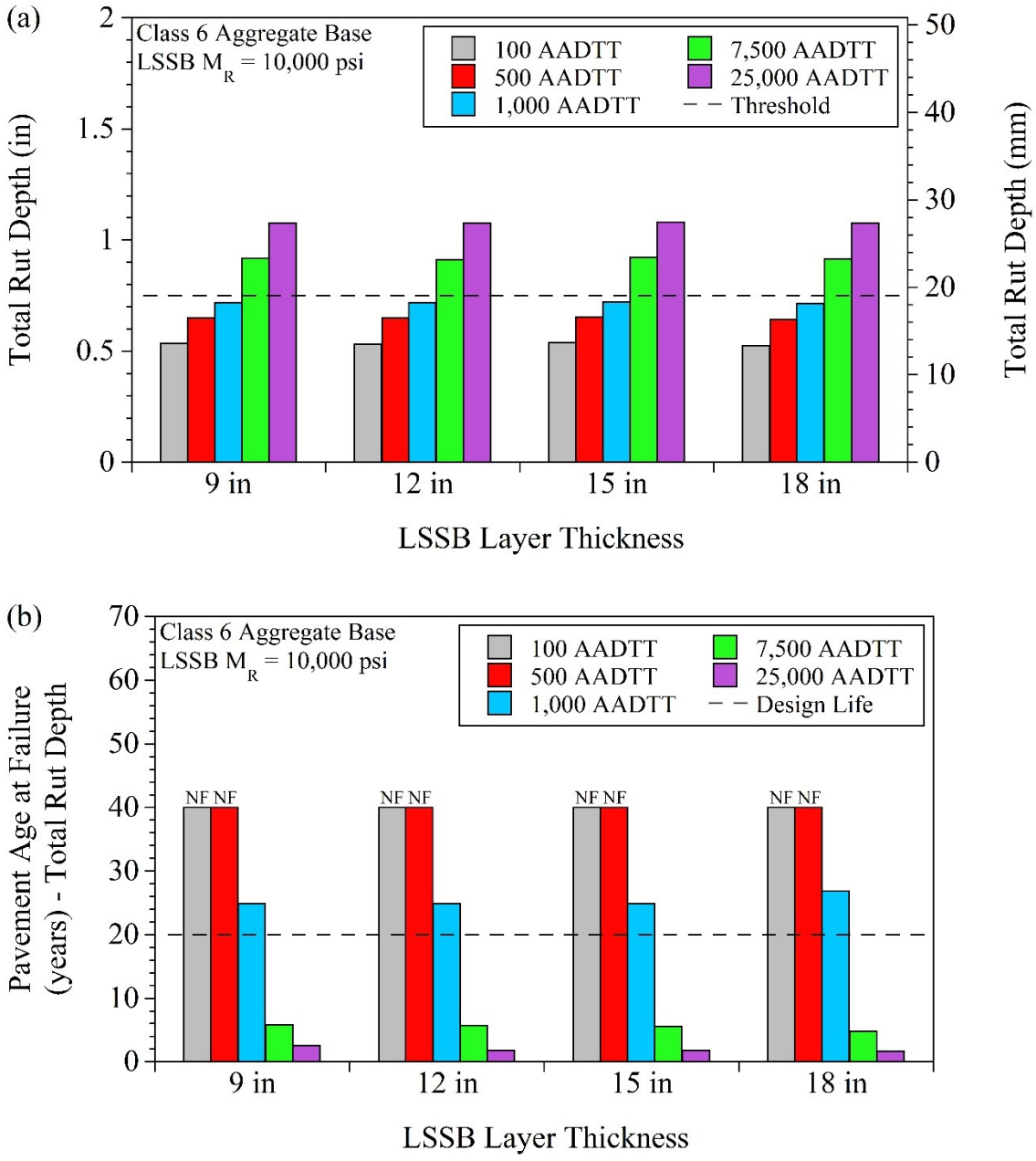

Figure 7.35. Effect of traffic level on (a) rutting at the end of design life (20 years) and (b) pavement age at rutting failure (NF = no failure)

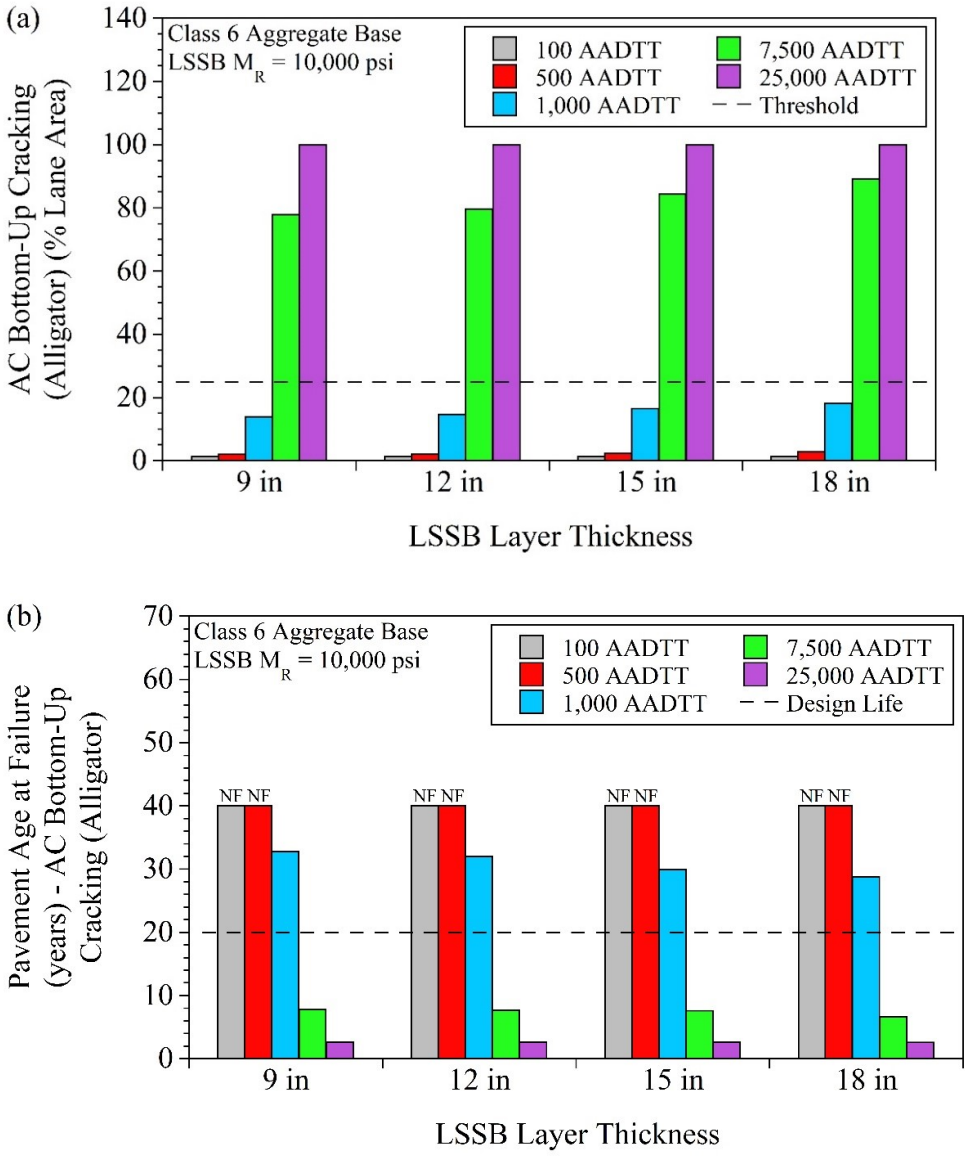

Figure 7.36. Effect of traffic level on (a) alligator cracking at the end of design life (20 years) and (b) pavement age at alligator cracking failure (NF = no failure)

In addition to all the Pavement ME analyses shown above, an effort was made to compare the actual field data obtained from the MnROAD test facility with that of the Pavement ME models. The Pavement ME models were not calibrated with the local calibrations since that is outside the scope of this study. Therefore, a relatively poor fitting would be expected between the field data and the models. These comparisons were not included in the main context of this study. Appendix BL contains information about comparison between field data and model data.

An effort was also made to analyze pavement overlays [asphalt concrete (AC) over AC] for the originally constructed test cells (Figure 3.2). However, the results of those analyses were not included in the main context of this study and are provided in Appendix BM.

7.2 CHAPTER CONCLUSIONS

The following conclusions were made based on the Pavement ME analyses performed for the recycled aggregate base (RAB) group:

- Increasing the aggregate base layer (Coarse RCA, Fine RCA, Limestone, RCA+RAP) thicknesses decreased the predicted pavement distress values at the end of the flexible pavement design life (20 years) and increased pavement service life.
- Using Limestone in the aggregate base layer models (at different thicknesses) resulted in greater pavement distresses at the end of the pavement design period (20 years) and lower pavement service life in the Pavement ME models than the recycled aggregates (for each aggregate base layer thickness).
- For base+subbase layer rutting, overall, Limestone base+Select Granular Borrow subbase layers yielded higher rutting than the other base+subbase layers (for each aggregate base layer thickness).
- As expected, increasing the AADTT level yielded greater pavement distresses and shorter pavement service life. While performance prediction models showed that acceptable pavement distresses and service lives were obtained at 100, 500, and 1,000 AADTT levels (low traffic), excessive failures occurred at 7,500 (medium traffic) and 25,000 (high traffic) AADTT levels.
- It was concluded that thinner RAB layers (4, 6, 8, or 10 in) could be constructed with Coarse RCA, Fine RCA, or RCA+RAP materials rather than constructing a 12-in Limestone base layer depending on the distress values that are of interest to an agency.

The following conclusions were made based on the Pavement ME analyses performed for the large stone subbase (LSSB) groups:

- No consistent trend was observed between IRI predictions and LSSB layer thickness. On the other hand, increasing the LSSB layer thickness generally decreased rutting and alligator cracking at the end of the pavement design life (20 years).
- It was concluded that increasing the LSSB SM_R value resulted in lower pavement distresses at the end of the pavement design life (20 years) and increased pavement service life.
- There was no significant difference between the rutting of the asphalt layers placed on LSSB layers at different thicknesses and having different M_R values in the models. For base+subbase layer rutting, increasing the LSSB thickness resulted in greater LSSB layer rutting. The subgrade layers underlying thinner LSSB layers exhibited higher rutting. As expected, the greatest amount of layer rutting was observed in subgrade layers. In addition, increasing the LSSB M_R value decreased both base+subbase and subgrade layer rutting.
- Similar to the observations made for the RAB group, increasing the AADTT level yielded greater pavement distresses and shorter pavement service life.

CHAPTER 8: GENERAL CONCLUSIONS AND RECOMMENDATIONS

This chapter provides general conclusions drawn from this project and recommendations for future research and practice. The conclusions are presented in four sections related to the topics of this research. Specific conclusions and key findings of each topic are provided in the previous chapters.

8.1 MATERIAL SELECTION FOR RECYCLED AGGREGATE BASE (RAB) LAYERS

- In this study, for the materials containing RCA (all the base layer aggregates except Limestone), the oven-dry specific gravity (OD G_s) values were ranging between 2.17 and 2.35 (OD G_s of Limestone was 2.66). The water absorption was ranging between 3.86% and 8.65% for the materials containing RCA (water absorption of Limestone was 1.72%). In addition, the residual mortar contents of those materials were ranging between 20.1% and 37.1% (residual mortar content of Limestone was 1.3%). As can be seen from these results, the aggregates used in this study could be separated by assessing their OD G_s, absorption, and residual mortar content values. RCA materials tend to exhibit lower G_s (due to their porous structure) and higher absorption (due to their porous structure, hydrophilicity, and unhydrated cement content).

- The following relationship was observed between the water absorptions of the base layer aggregates used in this study: Fine RCA > Coarse RCA > Class 5Q Aggregate > RCA+RAP > Class 6 Aggregate > Limestone. The materials containing RCA may attract more water due to their higher absorption capacity. An increase in the water-holding capacity of aggregate base layers constructed with RCA materials may increase the amount of water available to freeze throughout the layer. Such an increase in water content can increase frost heaving and thaw settlement, and thereby, reduce the overall freeze-thaw (F-T) durability.

- In this study, since RCA+RAP and Class 6 Aggregate exhibited lower absorption than Fine RCA, Coarse RCA, and Class 5Q Aggregate, it can be affirmed that RCA can be mixed with RAP to reduce the absorption. In this study, the absorption values of Limestone, RCA+RAP, and Class 6 Aggregate were 1.7%, 4.3%, and 3.9%, respectively. Therefore, it can be recommended to mix RCA with RAP. In addition, coarser RCA materials (Coarse RCA and Class 5Q Aggregate) would be more preferable than Fine RCA because their absorption values (7% and 6.3% for Coarse RCA and Class 5Q Aggregate, respectively) were relatively lower than that of Fine RCA (8.65%). It is expected that material with a higher absorption value is prone to exhibiting lower F-T durability in the long term. Therefore, it can be recommended that an RCA material with a relatively lower absorption value may be preferable.

- It can be concluded that any base layer aggregate with asphalt binder contents higher than 3% (per the ignition method) and 1.5% (per the quantitative extraction method) would exhibit hydrophobic properties, resulting in materials with higher freeze-thaw durability and better drainage properties.

- The following relationship was observed with respect to breakage (due to compaction) of the base layer aggregates used in this study: Class 5Q Aggregate > Coarse RCA > Fine RCA > Class 6 Aggregate > RCA+RAP > Limestone. It was concluded that not only gradation but also the residual mortar content and roundness of aggregate particles affected the breakage characteristics of the base layer aggregates.

- It was concluded that breakage increases as the roundness of the particles decreases (angularity increases). Higher breakage of particles may decrease the permeability of aggregate base layers, possibly negatively affecting long-term pavement performance. Breakage of RCA materials may also cause a release of unhydrated cement content that is present in the RCA particle's matrix. While this may further improve the stiffness of RCA later, it may also increase the potential for tufa formation, and drainage properties of aggregate base layers constructed with RCA can be reduced as a result of the tufa formation. Due to the high breakage of Coarse RCA and Class 5Q Aggregate, the field degree of compaction (DOC) of coarse-grained RCA materials can be lowered (e.g., between 90% and 95%). For coarse-grained RCA materials, the gradation after compaction is recommended to be used to consider breakage.

- The following relationship was observed between the saturated hydraulic conductivity (K_{sat}) of the base layer aggregates used in this study: Fine RCA > Class 5Q Aggregate > Coarse RCA > RCA+RAP > Class 6 Aggregate > Limestone. It was concluded that there was a direct relationship between the aggregate's void ratio/porosity and K_{sat}. It was concluded that Fine RCA yielded the highest void ratio/porosity and can be used if greater K_{sat} is preferred in the pavement structure.

- Both preliminary and long-term performance evaluation of the test cells showed that the cells built with the Coarse RCA and Fine RCA base layers, built over Select Granular Borrow and Sand Subgrade layers (Cells 185 and 186, respectively), performed better (e.g., higher modulus, lower rutting) than the other cells overall (Cells 188 and 189 were built on Select Granular Borrow and Clay Loam subgrade layers). In fact, the cell built with the Fine RCA base layer (Cell 186) performed better than that built with the Coarse RCA base layer (Cell 185). This could indicate that Fine RCA could be a better option than Coarse RCA to construct aggregate base layers.

- The cell built with the RCA+RAP base layer (Cell 189) performed better (higher modulus, lower rutting, etc.) than the cell built with the Limestone base layer (Cell 188). Therefore, it could be concluded that RCA+RAP would be a better option to construct aggregate base layers than Limestone. Overall, it could be concluded from the test results that the cells constructed with Coarse RCA and Fine RCA base layers (Cells 185 and 186, respectively) performed better (higher modulus, lower rutting, etc.) than that constructed with the RCA+RAP base layer (Cell 189). This could indicate that RCA+RAP could be less preferable to Coarse RCA and Fine RCA to construct aggregate base layers. However, since there were two different subgrade layers [Sand Subgrade layers in Cells 185 (12-in Coarse RCA) and 186 (12-in Fine RCA) and Clay Loam subgrade layers in Cells 188 (12-in Limestone)], further investigation may be needed to verify this recommendation.

In summary, the following material selection can be recommended to build RAB layers from the most preferred to least preferred based on laboratory and field test results obtained in this study: (1) finer RCA material (named Fine RCA in this study and contained 38.3% gravel, 54.6% sand, and 7.1% fines), (2) coarser RCA material (named Coarse RCA in this study and contained 61.7% gravel, 34.9% sand, and 3.4% fines), (3) blend of RCA and RAP materials (named RCA+RAP in this study), and (4) crushed limestone aggregate (named Limestone in this study).

8.2 MATERIAL SELECTION FOR LARGE STONE SUBBASE (LSSB) LAYERS

- LSSB Material used in this study (a crushed granite stone) to construct LSSB layers was poorly graded. During the construction of the pavement test cells containing LSSB layers, subgrade soil pumping and aggregate base/asphalt rutting were observed. Poorly graded large stones contain large voids that weak subgrade soil can move into. Large voids can also cause excessive particle reorientation during compaction and cause a less stable foundation for the construction of the upper layers. By using well-graded large stones, such problems could be reduced. A well-graded structure can provide a packed structure with fewer voids so that weak subgrade soils cannot easily move into the voids. In addition, such a packed LSSB structure can provide a more stable foundation for construction and compaction of aggregate base layers placed on top of the LSSB layers.

8.3 RECYCLED AGGREGATE BASE (RAB) LAYER DESIGN

- Different agencies may assign different priorities to pavement distresses (IRI, rutting, alligator cracking, or longitudinal cracking or a combination of several distresses) in optimizing their pavement design. Therefore, in this study, RAB thicknesses, possibly considered as an alternative to 12-in Limestone, were evaluated with respect to different pavement distress mechanisms, and the results were summarized to provide guidance to the agencies. Based on the pavement ME models that were created in this study, instead of 12-in Limestone base layers, RAB layers as thin as 4 in could be satisfactorily constructed.

- RCA materials may attract more water due to their higher absorption capacity and hydrophilicity. In addition, tufa formation may occur in an RCA matrix as a result of carbonation, and this may reduce the permeability of RCA materials. To minimize water-related issues associated with RCA materials, highly permeable subbase layers can be placed beneath the RCA base layers. In addition, suitable geosynthetic(s) (e.g., geocomposites with appropriate properties) can be placed between aggregate base and subbase layers or in the middle of RCA base layers to improve drainage.

- Due to the relatively higher breakage of RCA materials compared to virgin aggregates, gradation after compaction is recommended to be used to consider breakage, particularly for coarse-grained RCA materials.

- In Pavement ME, the fundamental materials inputs for base layer aggregates are resilient modulus (M_R), maximum dry unit weight (MDU) (corrected MDU is preferred), optimum moisture content (OMC) (corrected OMC is preferred), saturated hydraulic conductivity (K_{sat}), specific gravity (G_s) [oven-dry (OD) G_s is preferred], and gradation. In this study, several equations with both statistical and physical significance were provided for the estimation of summary M_R (SM_R), corrected OMC and MDU, and K_{sat}. Among those equations, the common parameters were determined to be G_s and absorption. This study showed that the G_s and absorption parameters, determined by ASTM C127 and C128, can be used to estimate the other material inputs required for pavement design.

8.4 LARGE STONE SUBBASE (LSSB) LAYER DESIGN

- As stated previously, geosynthetics had to be placed in the field to minimize subgrade soil pumping and aggregate base/asphalt rutting in the test cells containing 9-in LSSB layers. However, no significant problem was observed in constructing 18-in LSSB layers. In addition, while LSSB layers would be expected to show good drainage properties, conditions that can lower their permeability (e.g., contamination by subgrade soil pumping) should be considered. Special care must be taken during construction of thinner LSSB layers, and placement of geosynthetic(s) between the thinner LSSB layers and weak subgrade layers should be considered.

- In this study, placement of the geosynthetics between 9-in LSSB layers and Clay Loam subgrade layers were indeed found to provide important benefits such as workability improvement because the rest of the construction was completed without a problem regarding subgrade soil pumping and rutting. However, structural benefits of the geosynthetics could not be observed clearly using light weight deflectometer (LWD), falling weight deflectometer (FWD), or intelligent compaction (IC) testing due to the lower relative dry unit weight of the Class 5Q Aggregate base layers. In addition, the loads applied by LWD, FWD, or IC testing were not sufficient to allow observation of the structural benefits of the geosynthetics. Therefore, no specific recommendation could be made for the selection of the most suitable geosynthetics. A heavy weight deflectometer (HWD), which is a type of FWD equipment providing higher loads, could be used for this purpose.

- Coarse-grained aggregates can interlock between grid openings of geogrids and the interlocking mechanism increases the integrity and stiffness of pavement layers. If placement of geogrids between an LSSB layer and a Clay Loam subgrade layer is intended, special attention must be given to the geogrid aperture size. There are only a few geogrids with grid apertures suitable for use with large stones to provide adequate interlocking. In this study, Tensar TriAx TX190L (triaxial geogrid) and Tensar BX1300 (biaxial geogrid) were used. Tensar TriAx TX190L had a rib pitch of 60 mm (2.4 in). Aperture dimensions of Tensar BX1300 were 46 mm (1.8 in) in machine direction (MD) and 64 mm (2.5 in) in cross-machine direction (XMD).

- LSSB materials and subgrade soils can mix in case there is no separation/reinforcement between these materials using geosynthetics. The intermingling of subgrade soils and LSSB materials may reduce the permeability and drainage capabilities of LSSB layers. While agencies or engineers may consider placing geocomposite layers in the middle of LSSB layers to improve lateral drainage in case

there is an intermingling of subgrade soils and LSSB materials, field monitoring during construction revealed that two-lift construction was not practical for LSSB layers [the reason is that subgrade soil pumping and rutting were encountered during the construction of the 9-in (230-mm) LSSB layers without geosynthetics], so placing a geocomposite between two LSSB lifts would not be practical and should be avoided.

- As stated previously, Class 5Q Aggregate base layers overlying 9-in LSSB layers could not be compacted effectively due to the instability of 9-in LSSB layers under loading. Such a problem was not observed in Class 6 Aggregate base layers overlying 18-in LSSB layers. Therefore, the LSSB layer thickness must be sufficient to provide sufficient structural support. If not, geosynthetic(s) can be placed on top of the LSSB layers to provide reinforcement before the placement of the aggregate base layers. Using geosynthetic(s) on top of LSSB layers can help to distribute load more effectively and increase the stability of LSSB layers under loading. Another option would be to consider SM_R values at a lower DOC (as low as 80%) for the aggregate base layers overlying 9-in LSSB layers during the design process, optimizing the thickness of the aggregate base layer overlying the 9-in LSSB layer.

REFERENCES

AASHTO (1993). *AASHTO Guide for Design of Pavement Structures*. American Association of State Highway and Transportation Officials, Washington, DC.

AASHTO (2002). *Standard Specifications for Highway Bridges*. American Association of State Highway and Transportation Officials, Washington, DC.

Abbas, A., Fathifazl, G., Isgor, O. B., Razaqpur, A. G., Fournier, B., & Foo, S. (2007). Proposed method for determining the residual mortar content of recycled concrete aggregates. *Journal of ASTM International*, *5*(1), 1-12.

Abbaspour, A., Tanyu, B. F., & Cetin, B. (2016). Impact of aging on leaching characteristics of recycled concrete aggregate. *Environmental Science and Pollution Research*, *23*(20), 20835-20852.

Abdelrahman, M., Alam, T., & Zollars, J. (2010). Performance of high recycled asphalt pavement (RAP) content as base layer in flexible pavement. *The Journal of Solid Waste Technology and Management*, *36*(3), 131-142.

Abu-Farsakh, M., Hanandeh, S., Mohammad, L., & Chen, Q. (2016). Performance of geosynthetic reinforced/stabilized paved roads built over soft soil under cyclic plate loads. *Geotextiles and Geomembranes*, *44*(6), 845-853.

ACPA (2009). Recycling concrete pavements (Engineering Bulletin 043P). American Concrete Paving Association, Skokie, IL.

Akkari, A., & Izevbekhai, B. (2012). *Composite Pavements and Exposed Aggregate Texturing at MnROAD: Cells 70, 71, and 72, Construction Report and Early Performance Evaluation* (No. MN/RC 2012-29). Minnesota Department of Transportation, Research Services Section, St. Paul, MN.

Altuhafi, F., O'sullivan, C., & Cavarretta, I. (2013). Analysis of an image-based method to quantify the size and shape of sand particles. *Journal of Geotechnical and Geoenvironmental Engineering*, *139*(8), 1290-1307.

Andersland, O. B., & Ladanyi, B. (2004). *Frozen Ground Engineering*. John Wiley & Sons, Hoboken, NJ.

ARTF (2018). *Aggregate Resources Task Force*. Final Report to the Minnesota Legislature, St. Paul, MN. Retrieved from https://www.lcc.leg.mn/artf/meetings/2017%20ARTF%20Final%20Report.pdf

Attia, M. I. E. S. (2010). Characterization of the structural behavior of reclaimed asphalt pavement as pavement base layer (Doctoral dissertation). North Dakota State University, Fargo, ND.

Attia, M., & Abdelrahman, M. (2010). Modeling the effect of moisture on resilient modulus of untreated reclaimed asphalt pavement. *Transportation Research Record*, *2167*(1), 30-40.

Ba, M., Nokkaew, K., Fall, M., & Tinjum, J. M. (2013). Effect of matric suction on resilient modulus of compacted aggregate base courses. *Geotechnical and Geological Engineering*, *31*(5), 1497-1510.

Baek, S. O., Field, R. A., Goldstone, M. E., Kirk, P. W., Lester, J. N., & Perry, R. (1991). A review of atmospheric polycyclic aromatic hydrocarbons: Sources, fate and behavior. *Water, Air, and Soil Pollution*, *60*(3-4), 279-300.

Baladi, G. Y., Thottempudi, A., & Dawson, T. (2011). *Backcalculation of Unbound Granular Layer Moduli* (No. RC-1548). Michigan Department of Transportation Construction & Technology Division, Lansing, MI.

Banerjee, A., Puppala, A. J., Congress, S. S., Chakraborty, S., Likos, W. J., & Hoyos, L. R. (2020). Variation of resilient modulus of subgrade soils over a wide range of suction states. *Journal of Geotechnical and Geoenvironmental Engineering*, *146*(9), 04020096.

Bareither, C. A., Edil, T. B., Benson, C. H., & Mickelson, D. M. (2008). Geological and physical factors affecting the friction angle of compacted sands. *Journal of Geotechnical and Geoenvironmental Engineering*, *134*(10), 1476-1489.

Becker, P. J. (2016). The Central Iowa Expo site pavement foundation stabilization and paving project: An investigation into the influence of pavement foundation stiffness on pavement design, construction, and performance (Doctoral dissertation). Iowa State University, Ames, IA.

Bennert, T., & Maher, A. (2005). *The Development of a Performance Specification for Granular Base and Subbase Material* (No. FHWA-NJ-2005-003). New Jersey Department of Transportation, Trenton, NJ.

Bennert, T., Papp Jr, W. J., Maher, A., & Gucunski, N. (2000). Utilization of construction and demolition debris under traffic-type loading in base and subbase applications. *Transportation Research Record*, *1714*(1), 33-39.

Bestgen, J. O., Hatipoglu, M., Cetin, B., & Aydilek, A. H. (2016a). Mechanical and environmental suitability of recycled concrete aggregate as a highway base material. *Journal of Materials in Civil Engineering*, *28*(9), 04016067.

Bestgen, J. O., Cetin, B., & Tanyu, B. F. (2016b). Effects of extraction methods and factors on leaching of metals from recycled concrete aggregates. *Environmental Science and Pollution Research*, *23*(13), 12983-13002.

Bhasya, V., & Bharatkumar, B. H. (2018). Mechanical and durability properties of concrete produced with treated recycled concrete aggregate. *ACI Materials Journal*, *115*(2), 209-217.

Bilodeau, J. P., Doré, G., & Perier, L. (2014). Falling weight deflectometer analysis of flexible pavement structure built with geotextile drainage layers. *Canadian Journal of Civil Engineering*, *41*(6), 540-549.

Bittelli, M. (2011). Measuring soil water content: A review. *HortTechnology*, *21*(3), 293-300.

Blankenagel, B. J., & Guthrie, W. S. (2006). Laboratory characterization of recycled concrete for use as pavement base material. *Transportation Research Record*, *1952*(1), 21-27.

Bleakley, A. M., Cosentino, P. J., Kalajian, E. H., & Patel, M. J. (2014). Strength and creep characteristics of reclaimed asphalt pavement-sand blend backfill in mechanically stabilized earth walls. *Transportation Research Record*, *2462*(1), 18-27.

Bozyurt, O., Keene, A., Tinjum, J., Edil, T., & Fratta, D. (2013). Freeze-thaw effects on stiffness of unbound recycled road base. In *Mechanical Properties of Frozen Soil*. ASTM International, West Conshohocken, PA.

Bozyurt, O., Tinjum, J. M., Son, Y. H., Edil, T. B., & Benson, C. H. (2012). Resilient modulus of recycled asphalt pavement and recycled concrete aggregate. In *GeoCongress 2012: State of the Art and Practice in Geotechnical Engineering* (pp. 3901-3910).

Brandt, H. C. A., & De Groot, P. C. (2001). Aqueous leaching of polycyclic aromatic hydrocarbons from bitumen and asphalt. *Water Research*, *35*(17), 4200-4207.

BTS (2017). *Bureau of Transportation Statistics*. United States Department of Transportation, Washington, DC.

Bush, A. L., & Thompson, M. R. (1990). Predicting capacities of low volume airfield pavements. In *Proc.*, *the 3rd Int. Conf. on Bearing Capacity of Roads and Airfields*, Trondheim, Norway.

Butler, L., West, J. S., & Tighe, S. L. (2011). Quantification of recycled concrete aggregate (RCA) properties for usage in bridges and pavements: An Ontario case study. In *the Innovative Developments in Sustainable Pavements Session of the 2011 Annual Conf. of the Transport, Assoc. of Canada,* Edmonton, Alberta.

Buyantuyev, A., & Wu, J. (2010). Urban heat islands and landscape heterogeneity: Linking spatiotemporal variations in surface temperatures to land-cover and socioeconomic patterns. *Landscape Ecology*, *25*(1), 17-33.

CalRecycle (2014). *Construction and Demolition Debris Recycling, Caltrans Specifications for Aggregate Base and Subbase*. California Department of Resources Recycling and Recovery. Retrieved from http://www.calrecycle.ca.gov/Condemo/Specs/CaltransAgg.htm

Caltrans (2015). *Standard Specifications*. California Department of Transportation, Sacramento, CA.

Cedergren, H. R. (1988). Why all important pavements should be well drained. *Transportation Research Record*, *1188*, 56-62.

Cetin, A., Kaya, Z., Cetin, B., & Aydilek, A. H. (2014). Influence of laboratory compaction method on mechanical and hydraulic characteristics of unbound granular base materials. *Road Materials and Pavement Design*, *15*(1), 220-235.

Cetin, B., Aydilek, A. H., & Guney, Y. (2010). Stabilization of recycled base materials with high carbon fly ash. *Resources, Conservation and Recycling*, *54*(11), 878-892.

Cetin, B., Aydilek, A. H., & Li, L. (2012). Experimental and numerical analysis of metal leaching from fly ash-amended highway bases. *Waste Management*, *32*(5), 965-978.

Cetin, B., Aydilek, A. H., & Li, L. (2013). Trace metal leaching from embankment soils amended with high-carbon fly ash. *Journal of Geotechnical and Geoenvironmental Engineering*, *140*(1), 1-13.

Ceylan, H., Gopalakrishnan, K., & Kim, S. (2009). *MEPDG Work Plan Task No. 5: Characterization of Unbound Materials (Soils/Aggregates) for Mechanistic-Empirical Pavement Design Guide* (CTRE Project 06–271). Iowa Department of Transportation, Ames, IA.

Ceylan, H., Gopalakrishnan, K., Kim, S., & Steffes, R. F. (2013). *Evaluating Roadway Subsurface Drainage Practices* (No. IHRB Project TR-643). Institute for Transportation, Iowa State University, Ames, IA.

Ceylan, H., Kim, S., Gopalakrishnan, K., Steffes, R. F., & Yang B. (2015a). *Evaluating Roadway Subsurface Drainage Practices – Phase II* (No. IHRB Project TR-662). Institute for Transportation, Iowa State University, Ames, IA.

Ceylan, H., Gopalakrishnan, K., & Kim, S. (2015b). *Investigation of AASHTOWare Pavement ME Design/DARWin-ME Performance Prediction Models for Iowa Pavement Analysis and Design* (No. InTrans Project 14-496). Iowa Department of Transportation, Ames, IA.

Chatti, K., Kutay, M. E., Lajnef, N., Zaabar, I., Varma, S., & Lee, H. S. (2017). *Enhanced Analysis of Falling Weight Deflectometer Data for Use with Mechanistic-Empirical Flexible Pavement Design and Analysis and Recommendations for Improvements to Falling Weight Deflectometers* (No. FHWA-HRT-15-063). Turner-Fairbank Highway Research Center, McLean, VA.

Chen, J., & Brown, B. (2012). Leaching characteristics of recycled aggregate used as road base. *University of Wisconsin System Solid Waste Research Program Student Project Report*, Madison, WI.

Chen, J., Tinjum, J. M., & Edil, T. B. (2013). Leaching of alkaline substances and heavy metals from recycled concrete aggregate used as unbound base course. *Transportation Research Record*, *2349*(1), 81-90.

Chesner, W. H., Collins, R .J., & MacKay, M. H. (1998). *User Guidelines for Waste and Byproduct Materials in Pavement Construction* (No. FHWA-RD-97-148). Federal Highway Administration (FHWA), US Department of Transportation, Washington, DC.

Cho, G. C., Dodds, J., & Santamarina, J. C. (2006). Particle shape effects on packing density, stiffness, and strength: Natural and crushed sands. *Journal of Geotechnical and Geoenvironmental Engineering*, *132*(5), 591-602.

Chu, X. (2020). A review on the resilient response of unsaturated subgrade soils. *Advances in Civil Engineering*, Volume *2020,* 7367484.

Clyne, T. R. (2011). *Monitoring Geosynthetics in Local Roadways (LRRB 768) 10-Year Performance Summary* (Report No. MN/RC 2011-20). Minnesota Department of Transportation, St. Paul, MN.

Cooley, L. A., & Hornsby, H. (2012). *Evaluation of Crushed Concrete Base Strength* (No. FHWA/MS-DOT-RD-12-238). Mississippi. Department of Transportation, Jackson, MS.

Copeland, A. (2011). *Reclaimed Asphalt Pavement in Asphalt Mixtures: State of the Practice* (No. FHWA-HRT-11-021). Turner-Fairbank Highway Research Center, Federal Highway Administration (FHWA), McLean, VA.

Cosentino, P. J., & Kalajian, E. H. (2001). *Developing Specifications for Using Recycled Asphalt Pavement as Base, Subbase, or General Fill Materials: Final Report*. State Materials Office, Florida Department of Transportation, Gainesville, FL.

Cosentino, P. J., Kalajian, E. H., Bleakley, A. M., Diouf, B. S., Misilo, T. J., Petersen, A. J., Krajcik, R. E., & Sajjadi, A. M. (2012). *Improving the Properties of Reclaimed Asphalt Pavement for Roadway Base Applications* (No. FL/DOT/BDK81 97702). Florida Department of Transportation, Tallahassee, FL.

Cosentino, P. J., Kalajian, E. H., Shieh, C. S., Mathurin, W. J. K., Gomez, F. A., Cleary, E. D., & Treeratrakoon, A. (2003). *Developing Specifications for Using Recycled Asphalt Pavement as Base, Subbase or General Fill Materials, Phase II* (No. FL/DOT/RMC/06650-7754). Florida Department of Transportation, Tallahassee, FL.

Cunningham, C. N., Evans, T. M., & Tayebali, A. A. (2013). Gradation effects on the mechanical response of crushed stone aggregate. *International Journal of Pavement Engineering*, *14*(3), 231-241.

Dawson, A. R., Mundy, M. J., & Huhtala, M. (2000). European research into granular material for pavement bases and subbases. *Transportation Research Record*, *1721*(1), 91-99.

Dawson, A., & Kolisoja, P. (2006). *Managing Rutting in Low Volume Roads: Executive Summary*. ROADEX III Project, the Swedish Road Administration, Northern Region, Luleå, Sweden.

de Juan, M. S., & Gutiérrez, P. A. (2009). Study on the influence of attached mortar content on the properties of recycled concrete aggregate. *Construction and Building Materials*, *23*(2), 872-877.

Dikova, D. (2006). Creep behavior of RAP-soil mixtures in earthwork applications (M.S. thesis). Florida Institute of Technology, Melbourne, FL.

Doulos, L., Santamouris, M., & Livada, I. (2004). Passive cooling of outdoor urban spaces. The role of materials. *Solar Energy*, *77*(2), 231-249.

Ebrahimi-Birang, N., Fredlund, D. G., & Samarasekera, L. (2007). Hysteresis of the soil-water characteristic curve in the high suction range. In *Proc. OttawaGeo Conf* (pp. 1061-1068).

Edil, T. (2011). *Specifications and Recommendations for Recycled Materials Used as Unbound Base Course*. Recycled Materials Resource Center, University of Wisconsin-Madison, Madison, WI.

Edil, T. B., & Cetin, B. (2015). Freeze-thaw performance of chemically stabilized natural and recycled highway materials. *Sciences in Cold and Arid Regions*, *7*(5), 482-491.

Edil, T. B., Cetin, B., & Soleimanbeigi, A. (2017). Laboratory and field performance of recycled aggregate base in a seasonally cold region. *Sciences in Cold and Arid Regions*, *9*(3), 183-191.

Edil, T. B., Tinjum, J. M., & Benson, C. H. (2012). *Recycled Unbound Materials* (No. 2012-35). Minnesota Department of Transportation. St. Paul, MN.

Elbheiry, M. R., Kandil, K. A., & Kotb, A. S. (2011). Investigation of factors affecting pavement roughness (M.S. thesis). Arab Academy for Science and Technology and Maritime Transport, Abou Kir, Alexandria - Egypt.

Engelsen, C. J., van der Sloot, H. A., & Petkovic, G. (2017). Long-term leaching from recycled concrete aggregates applied as sub-base material in road construction. *Science of the Total Environment*, *587*, 94-101.

Engelsen, C. J., Van der Sloot, H. A., Wibetoe, G., Justnes, H., Lund, W., & Stoltenberg-Hansson, E. (2010). Leaching characterisation and geochemical modelling of minor and trace elements released from recycled concrete aggregates. *Cement and Concrete Research*, *40*(12), 1639-1649.

Engelsen, C. J., van der Sloot, H. A., Wibetoe, G., Petkovic, G., Stoltenberg-Hansson, E., & Lund, W. (2009). Release of major elements from recycled concrete aggregates and geochemical modelling. *Cement and Concrete Research*, *39*(5), 446-459.

Engelsen, C. J., Wibetoe, G., van der Sloot, H. A., Lund, W., & Petkovic, G. (2012). Field site leaching from recycled concrete aggregates applied as sub-base material in road construction. *Science of the Total Environment*, *427*, 86-97.

Erickson, H., & Drescher, A. (2001). *The Use of Geosynthetics to Reinforce Low Volume Roads* (No. MN/RC-2001-15). Minnesota Department of Transportation, St. Paul, MN.

Esfahani, M. A., & Goli, A. (2018). Effects of aggregate gradation on resilient modulus and CBR in unbound granular materials. *International Journal of Transportation Engineering*, *5*(4), 367-381.

FDOT (2018). *Standard Specifications for Road and Bridge Construction*. Florida Department of Transportation, Tallahassee, FL.

Feldmann, R. M., Biros, D. J., & Middleton, D. L. (1982). Tufa precipitation and its effect on drainage of interstate highways in northeastern Ohio. *Bulletin of the Association of Engineering Geologists*, *19*(4), 347-370.

FHWA (2016). *Highway Statistics 2016.* Office of Highway Policy Information, Federal Highway Administration, Washington, DC.

Fletcher, T., Chandan, C., Masad, E., & Sivakumar, K. (2003). Aggregate imaging system for characterizing the shape of fine and coarse aggregates. *Transportation Research Record*, *1832*(1), 67-77.

Fredlund, D. G., & Rahardjo, H. (1993). *Soil Mechanics for Unsaturated Soils*. John Wiley & Sons, Inc., New York.

Fredlund, D. G., & Xing, A. (1994). Equations for the soil-water characteristic curve. *Canadian Geotechnical Journal*, *31*(4), 521-532.

Garach, L., López, M., Agrela, F., Ordóñez, J., Alegre, J., & Moya, J. A. (2015). Improvement of bearing capacity in recycled aggregates suitable for use as unbound road sub-base. *Materials*, *8*(12), 8804-8816.

Garg, N., & Thompson, M. R. (1996). Lincoln Avenue reclaimed asphalt pavement base project. *Transportation Research Record*, *1547*(1), 89-95.

Garrabrants, A. C., Sanchez, F., & Kosson, D. S. (2004). Changes in constituent equilibrium leaching and pore water characteristics of a Portland cement mortar as a result of carbonation. *Waste Management*, *24*(1), 19-36.

Genc, D. (2019). Development, installation and preliminary data collection of an environmental sensor system for freeze–thaw monitoring under granular-surfaced roadways (M.S. thesis). Iowa State University, Ames, IA.

Gervais, C., Garrabrants, A. C., Sanchez, F., Barna, R., Moszkowicz, P., & Kosson, D. S. (2004). The effects of carbonation and drying during intermittent leaching on the release of inorganic constituents from a cement-based matrix. *Cement and Concrete Research*, *34*(1), 119-131.

Ghalib, A. M., & Hryciw, R. D. (1999). Soil particle size distribution by mosaic imaging and watershed analysis. *Journal of Computing in Civil Engineering*, *13*(2), 80-87.

Gokce, A. (2001). Investigation of the parameters controlling frost resistance of recycled aggregate concrete (Doctoral thesis). Niigata University, Niigata, Japan.

Gonzalez, G. P., & Moo-Young, H. K. (2004). *Transportation Applications of Recycled Concrete Aggregate.* FHWA State of the Practice National Review, U.S. Department of Transportation, FHWA, Washington, DC.

Gray, J. E. (1962). Characteristics of graded base course aggregates determined by triaxial tests (Engineering Bulletin No. 12). National Crushed Stone Association.

Greenbook (2009). *Construction Materials, Section 200-Rock Materials*. In Greenbook Standard Specifications for Public Works Construction. Retrieved from http://www.greenbookspecs.org/documents/change/change218ns.pdf

Grosenheider, K., Bloom, P., Halbach, T., & Simcik, M. (2006). *Chemical Inventory and Database Development for Recycled Material Substitutes* (No. MN/RC-2006-28). Minnesota Department of Transportation, St. Paul, MN.

Guan, K. K. (2011). Surface and ambient air temperatures associated with different ground material: A case study at the University of California, Berkeley. *Environmental Science*, *196*, 1-14.

Gupta, J. D., & Dollimore D. (2002). *Magnitude Assessment of Free Lime and Hydrated Limes Present in RPCC Aggregates*. (No. FHWA/OH-2002/014). Ohio Department of Transportation, Toledo, OH.

Gupta, N., Kluge, M., Chadik, P. A., & Townsend, T. G. (2018). Recycled concrete aggregate as road base: Leaching constituents and neutralization by soil interactions and dilution. *Waste Management*, *72*, 354-361.

Gupta, S., Kang, D. H., & Ranaivoson, A. (2009). *Hydraulic and Mechanical Properties of Recycled Materials* (No. 2009-32). Minnesota Department of Transportation, St. Paul, MN.

Gupta, S., Singh, A., & Ranaivoson, A. (2004). *Moisture Retention Characteristics of Base and Sub-base Materials* (No. MN/RC-2005-06). Minnesota Department of Transportation, St. Paul, MN.

Guthrie, W. S., Cooley, D., & Eggett, D. L. (2007). Effects of reclaimed asphalt pavement on mechanical properties of base materials. *Transportation Research Record*, *2005*(1), 44-52.

Haider, I., Kaya, Z., Cetin, A., Hatipoglu, M., Cetin, B., & Aydilek, A. H. (2014). Drainage and mechanical behavior of highway base materials. *Journal of Irrigation and Drainage Engineering*, *140*(6), 04014012.

Hallikainen, M. T., Ulaby, F. T., Dobson, M. C., El-Rayes, M. A., & Wu, L. K. (1985). Microwave dielectric behavior of wet soil-part 1: Empirical models and experimental observations. *IEEE Transactions on Geoscience and Remote Sensing*, (1), 25-34.

Hanson, J. L., Edil, T. B., & Yesiller, N. (2000). Thermal properties of high water content materials. In *Geotechnics of High Water Content Materials*. ASTM International, West Conshohocken, PA.

Hardin, B. O. (1985). Crushing of soil particles. *Journal of Geotechnical Engineering*, *111*(10), 1177-1192.

Harman, T., Bukowski, J. R., Moutier, F., Huber, G., & McGennis, R. (2002). History and future challenges of gyratory compaction: 1939 to 2001. *Transportation Research Record*, *1789*(1), 200-207.

Hatipoglu, M., Cetin, B., & Aydilek, A. H. (2020). Effects of fines content on hydraulic and mechanical performance of unbound granular base aggregates. *Journal of Transportation Engineering, Part B: Pavements*, *146*(1), 04019036.

Hewitt, C. N., & Rashed, M. B. (1990). An integrated budget for selected pollutants for a major rural highway. *Science of the Total Environment*, *93*, 375-384.

Hillel, D. (1980). *Fundamental of Soil Physics*. Academic Press, Inc., San Diego, CA.

Hiller, J. E., Deshpande, Y. S., Qin, Y., Shorkey, C. J., & Peterson, K. (2011). *Efficient Use of Recycled Concrete in Transportation Infrastructure* (No. RC-1544). Michigan Department of Transportation, Lansing, MI.

Holtz, R. D., Christopher, B. R., & Berg, R. R. (1998). *Geosynthetic Design and Construction Guidelines* (No. FHWA HI-95-038). National Highway Institute, Federal Highway Administration (FHWA), US Department of Transportation, Washington, DC.

Hoppe, E. J., Lane, D. S., Fitch, G. M., & Shetty, S. (2015). *Feasibility of Reclaimed Asphalt Pavement (RAP) Use as Road Base and Subbase Material* (No. VCTIR 15-R6). Virginia Department of Transportation, Richmond, VA.

Horton, R., Wierenga, P. J., & Nielsen, D. R. (1983). Evaluation of methods for determining the apparent thermal diffusivity of soil near the surface. *Soil Science Society of America Journal*, *47*(1), 25-32.

Hryciw, R. D., & Ohm, H.-S. (2012). *Feasibility of Digital Imaging to Characterize Earth Materials* (No. RC1557). Michigan Department of Transportation, Lansing, MI.

Hryciw, R. D., Zheng, J., & Shetler, K. (2016). Particle roundness and sphericity from images of assemblies by chart estimates and computer methods. *Journal of Geotechnical and Geoenvironmental Engineering*, *142*(9), 04016038.

Hussain, M., & Dash, S. K. (2010). Influence of lime on plasticity behaviour of soils. In *Proc. Indian Geotechnical Conference* (pp. 537-540).

IDOT (2005). *Subgrade Stability Manual.* Illinois Department of Transportation, Bureau of Bridges and Structures, Springfield, IL.

IDOT (2016). *Standard Specifications for Road and Bridge Construction*. Illinois Department of Transportation, Springfield, IL.

ISO (2008). *Representation of results of particle size analysis—part 6: Descriptive and quantitative representation of particle shape and morphology* (Protocol ISO 9276–6). International Organization for Standardization, Geneva, Switzerland.

Izevbekhai, B. I., & Akkari, A. (2011). *Pervious Concrete Test Cells on MnROAD Low-Volume Road* (No. MN/RC 2011-23). Minnesota Department of Transportation, Research Services Section, St. Paul, MN.

Jayakody, S., Gallage, C., & Kumar, A. (2012). Assessment of recycled concrete aggregate for road base and sub-base. In *Proceedings of the Second International Conference on Geotechnique, Construction Materials and Environment* (pp. 575-579).

Jury, W.A. & Horton R. (2004). *Soil Physics*. John Wiley & Sons. Hoboken, NJ.

Kang, D. H., Gupta, S. C., Bloom, P. R., Ranaivoson, A. Z., Roberson, R., & Siekmeier, J. (2011). Recycled materials as substitutes for virgin aggregates in road construction: II. Inorganic contaminant leaching. *Soil Science Society of America Journal*, *75*(4), 1276-1284.

Kazmee, H., & Tutumluer, E. (2015). *Evaluation of Aggregate Subgrade Materials Used as Pavement Subgrade/Granular Subbase* (No. FHWA-ICT-15-013). Illinois Department of Transportation, Springfield, IL.

Kazmee, H., Mishra, D., & Tutumluer, E. (2015). Sustainable alternatives in low volume road base course applications evaluated through accelerated pavement testing. In *IFCEE 2015*, 409-418, ASCE, San Antonio, TX.

Kazmee, H., Tutumluer, E., & Beshears, S. (2016). Pavement working platforms constructed with large-size unconventional aggregates. *Transportation Research Record*, *2578*(1), 1-11.

Khoury, N. N., & Zaman, M. M. (2004). Correlation between resilient modulus, moisture variation, and soil suction for subgrade soils. *Transportation Research Record*, *1874*(1), 99-107.

Kim, W. H., Edil, T. B., Benson, C. H., & Tanyu, B. F. (2005). Structural contribution of geosynthetic-reinforced working platforms in flexible pavement. *Transportation Research Record*, *1936*(1), 43-50.

Kim, W., & Labuz, J. F. (2007). *Resilient Modulus and Strength of Base Course with Recycled Bituminous Material* (No. MN/RC-2007-05). Minnesota Department of Transportation, St. Paul, MN.

Kim, W., Labuz, J. F., & Dai, S. (2007). Resilient modulus of base course containing recycled asphalt pavement. *Transportation Research Record*, *2005*(1), 27-35.

Kim, Y., Suh, H. S., & Yun, T. S. (2019). Reliability and applicability of the Krumbein-Sloss chart for estimating geomechanical properties in sands. *Engineering Geology*, *248*, 117-123.

Konrad, J. M., & Lemieux, N. (2005). Influence of fines on frost heave characteristics of a well-graded base-course material. *Canadian Geotechnical Journal*, *42*(2), 515-527.

Kootstra, B. R., Ebrahimi, A., Edil, T. B., & Benson, C. H. (2010). Plastic deformation of recycled base materials. In *GeoFlorida 2010: Advances in Analysis, Modeling & Design* (pp. 2682-2691). ASCE, Orlando, FL.

Kriech, A. J., Kurek, J. T., Osborn, L. V., Wissel, H. L., & Sweeney, B. J. (2002). Determination of polycyclic aromatic compounds in asphalt and in corresponding leachate water. *Polycyclic Aromatic Compounds*, *22*(3-4), 517-535.

Krumbein, W. C., & Sloss, L. L. (1951). *Stratigraphy and Sedimentation*. W. H. Freeman and Company, San Francisco, CA.

Kumara, G. H. A., Hayano, K., & Ogiwara, K. (2012). Image analysis techniques on evaluation of particle size distribution of gravel. *Int. J. Geomate*, *3*(1), 290-297.

Kuo, C. Y., & Freeman, R. B. (2000). Imaging indices for quantification of shape, angularity, and surface texture of aggregates. *Transportation Research Record*, *1721*(1), 57-65.

Kuo, S. S., Mahgoub, H. S., & Nazef, A. (2002). Investigation of recycled concrete made with limestone aggregate for a base course in flexible pavement. *Transportation Research Record*, *1787*(1), 99-108.

Kwon, J., & Tutumluer, E. (2003). *Use of Geosynthetics in Working Platform and Pavement Construction.* (Unpublished White Paper, Project IHR-30). Department of Civil & Environment Engineering, UIUC, Urbana, IL.

Lee, J. C., Edil, T. B., Tinjum, J. M., & Benson, C. H. (2010). Quantitative assessment of environmental and economic benefits of recycled materials in highway construction. *Transportation Research Record*, *2158*(1), 138-142.

Lekarp, F., Isacsson, U., & Dawson, A. (2000). State of the art. II: Permanent strain response of unbound aggregates. *Journal of Transportation Engineering*, *126*(1), 76-83.

Letey, J., Carrillo, M. L. K., & Pang, X. P. (2000). Approaches to characterize the degree of water repellency. *Journal of Hydrology*, *231*, 61-65.

Li, C., Ashlock, J. C., White, D. J., & Vennapusa, P. K. (2019). Mechanistic-based comparisons of stabilised base and granular surface layers of low-volume roads. *International Journal of Pavement Engineering*, *20*(1), 112-124.

Li, C., Ashlock, J. C., White, D. J., Jahren, C. T., & Cetin, B. (2017). Gyratory abrasion with 2D image analysis test method for evaluation of mechanical degradation and changes in morphology and shear strength of compacted granular materials. *Construction and Building Materials*, *152*, 547-557.

Li, C., White, D. J., & Vennapusa, P. (2015). Moisture-density-strength-energy relationships for gyratory compacted geomaterials. *Geotechnical Testing Journal*, *38*(4), 461-473.

Likos, W. J., & Lu, N. (2003). Automated humidity system for measuring total suction characteristics of clay. *Geotechnical Testing Journal*, *26*(2), 179-190.

Likos, W. J., Lu, N., & Godt, J. W. (2013). Hysteresis and uncertainty in soil water-retention curve parameters. *Journal of Geotechnical and Geoenvironmental Engineering*, *140*(4), 04013050.

Little, D. N., & Nair, S. (2009). *Recommended Practice for Stabilization of Subgrade Soils and Base Materials.* National Cooperative Highway Research Program, Transportation Research Board of the National Academies, Washington, DC.

Liu, W., & Scullion, T. (2001). *MODULUS 6.0 for Windows: User's Manual* (No. FHWA/TX-05/0-1869-3). Texas Department of Transportation, Research and Technology Implementation Office, Austin, TX.

Locander, R. (2009). *Analysis of Using Reclaimed Asphalt Pavement (RAP) as a Base Course Material* (No. CDOT-2009-5). Colorado Department of Transportation, Materials/Geotechnical Branch, Denver, CO.

LRRB (2016). *Recycled Materials in Unbound Aggregate Base Layers in Minnesota. Transportation Research Synthesis* (TRS 1604). Local Road Research Board, Minnesota Department of Transportation, St. Paul, MN.

MacGregor, J. A., Highter, W. H., & DeGroot, D. J. (1999). Structural numbers for reclaimed asphalt pavement base and subbase course mixes. *Transportation Research Record*, *1687*(1), 22-28.

Mazari, M., Navarro, E., Abdallah, I., & Nazarian, S. (2014). Comparison of numerical and experimental responses of pavement systems using various resilient modulus models. *Soils and Foundations*, *54*(1), 36-44.

McGarrah, E. J. (2007). *Evaluation of Current Practices of Reclaimed Asphalt Pavement/Virgin Aggregate as Base Course Material* (No. WA-RD 713.1). Washington State Department of Transportation, Olympia, WA.

Mehrotra, A. (2014). Evaluating the influence of moisture variation on resilient modulus for unsaturated pavement subgrades (M.S. thesis). Louisiana State University, Baton Rouge, LA.

Miller, J. S., & Bellinger, W. Y. (2014). *Distress Identification Manual for the Long-Term Pavement Performance Program (Fifth Revised Edition)* (No. FHWA-HRT-13-092). Federal Highway Administration, Office of Infrastructure Research and Development, Washington, DC.

Mishra, D., & Tutumluer, E. (2012). Aggregate physical properties affecting modulus and deformation characteristics of unsurfaced pavements. *Journal of Materials in Civil Engineering*, *24*(9), 1144-1152.

Mishra, D., Tutumluer, E., & Butt, A. A. (2010). Quantifying effects of particle shape and type and amount of fines on unbound aggregate performance through controlled gradation. *Transportation Research Record*, *2167*(1), 61-71.

MnDOT (2003). *MnROAD Automated Laser Profile System "ALPS".* Minnesota Department of Transportation, Office of Materials and Road Research, St. Paul, MN.

MnDOT (2005). *Standard Specifications for Construction (2005 Edition)*. Minnesota Department of Transportation, St. Paul, MN.

MnDOT (2009a). *Density – Nuclear Density Gauge*. Retrieved from https://www.dot.state.mn.us/mnroad/instrumentation/pdfs/nucleardensity.pdf

MnDOT (2009b). *Rutting – ALPS.* Retrieved from http://www.dot.state.mn.us/mnroad/data/pdfs/alps.pdf

MnDOT (2009c). *Lightweight Internal Surface Analyzer – MnROAD Ride Measurement.* Retrieved from http://www.dot.state.mn.us/mnroad/data/pdfs/lisa.pdf

MnDOT (2013a). *MnROAD Semi Tractor Trailer*. Retrieved from https://www.dot.state.mn.us/mnroad/data/pdfs/MnROADSemiDescriptions(March%202013).pdf

MnDOT (2013b). *Moisture Sensing Documentation*. Retrieved from http://www.dot.mn.gov/mnroad/pdfs/Moisture%20Sensing%20at%20MnROAD(working%20document).pdf

MnDOT (2014a). *MnROAD Weather Stations*. Retrieved from https://www.dot.state.mn.us/mnroad/pdfs/MnROADWeather2014.pdf

MnDOT (2014b). *Building Temperature Sensing Arrays (Thermocouple Trees).* Retrieved from http://mndot.org/mnroad/data/pdfs/envsense/BuildingTemperatureSensors.pdf

MnDOT (2014c). *Moisture Content – EW (EC, ET)*. Retrieved from https://www.dot.state.mn.us/mnroad/data/pdfs/envsense/Base_Moisture_EC.pdf

MnDOT (2017). *MnROAD Safer, Smarter, Sustainable Pavements Through Innovative Research*. Minnesota Department of Transportation, St. Paul, MN. Retrieved from http://www.dot.state.mn.us/mnroad/pdfs/MnROAD%20Brochure%20(Jan%202011).pdf

MnDOT (2018). *Standard Specifications for Construction (2018 Edition)*. Minnesota Department of Transportation, St. Paul, MN.

MoDOT (2018). *Missouri Standard Specifications for Highway Construction*. Missouri Highways and Transportations Comission, Jefferson City, MO.

Mohod, M. V., & Kadam, K. N. (2016). A comparative study on rigid and flexible pavement: A review. *IOSR Journal of Mechanical and Civil Engineering (IOSR-JMCE)*, *13*(3), 84-88.

Molenaar, A. A., & van Niekerk, A. A. (2002). Effects of gradation, composition, and degree of compaction on the mechanical characteristics of recycled unbound materials. *Transportation Research Record*, *1787*(1), 73-82.

Montemayor, T. A. (1998). Compaction and strength-deformation characteristics of reclaimed asphalt pavement (M.S. thesis). Florida Institute of Technology, Melbourne, FL.

Mooney, M., Rinehart, R., White, D., Vennapusa, P., Facas, N., & Musimbi, O. (2010). *Intelligent Soil Compaction Systems* (No. NCHRP Report 676). Transportation Research Board, Washington, DC.

Moossazadeh, J., & Witczak, M. W. (1981). Prediction of subgrade moduli for soil that exhibits nonlinear behavior. *Transportation Research Record*, *810*, 10-17.

Mora, C. F., & Kwan, A. K. H. (2000). Sphericity, shape factor, and convexity measurement of coarse aggregate for concrete using digital image processing. *Cement and Concrete Research*, *30*(3), 351-358.

Muschack, W. (1990). Pollution of street run-off by traffic and local conditions. *The Science of the Total Environment*, *93*(3), 419-431.

Nataatmadja, A., & Tan, Y. L. (2001). Resilient response of recycled concrete road aggregates. *Journal of Transportation Engineering*, *127*(5), 450-453.

Nazarian, S., Fathi, A., Tirado, C., Kreinovich, V., Rocha, S., & Mazari, M. (2020). *Evaluating Mechanical Properties of Earth Material During Intelligent Compaction.* Pre-publication draft of NCHRP Research Report 933. Transportation Research Board, Washington, DC.

Nazarian, S., Mazari, M., Abdallah, I. N., Puppala, A. J., Mohammad, L. N., & Abu-Farsakh, M. Y. (2014). *Modulus-Based Construction Specification for Compaction of Earthwork and Unbound Aggregate* (No. NCHRP Project 10-84). Transportation Research Board of the National Academics, Washington, DC.

NCHRP (2004a). *Guide for Mechanistic-Empirical Design of Pavement Structures: Part 2 – Design Inputs*. ARA, Inc., ERES Consultants Division, Champaign, IL.

NCHRP (2004b). *Laboratory Determination of Resilient Modulus for Flexible Pavement Design*. NCHRP Research Results Digest, National Academies of Sciences, Engineering, and Medicine, Washington, DC. Retrieved from https://www.nap.edu/catalog/21960/laboratory-determination-of-resilient-modulus-for-flexible-pavement-design

NCHRP (2017a). *Measuring Modulus for Better-Performing Pavements* (No. NCHRP Project 10-84). National Cooperative Highway Research Program. Retrieved from http://www.trb.org/Main/Blurbs/176225.aspx

NCHRP (2017b). *Optimizing Materials QA to Improve Construction, Save Costs* (No. NCHRP Research Report 838). National Cooperative Highway Research Program. Retrieved from http://onlinepubs.trb.org/onlinepubs/nchrp/nchrp_readyresult_06.pdf

Newcomb, D. E., Van Deusen, D. A., Jiang, Y., & Mahoney, J. P. (1995). Considerations of saturated soil conditions in backcalculation of pavement layer moduli. *Transportation Research Record*, *1473*, 63-71.

Nokkaew, K. (2014). Hydraulic properties of recycled pavement aggregates and effect of soil suction on resilient modulus for pavement design (Doctoral dissertation). University of Wisconsin, Madison, WI.

Nokkaew, K., Tinjum, J. M., & Benson, C. H. (2012). Hydraulic properties of recycled asphalt pavement and recycled concrete aggregate. In *GeoCongress 2012: State of the Art and Practice in Geotechnical Engineering* (pp. 1476-1485), ASCE, Oakland, CA.

Ohm, H. S., & Hryciw, R. D. (2013). Translucent segregation table test for sand and gravel particle size distribution. *Geotechnical Testing Journal*, *36*(4), 592-605.

Okafor, F. O. (2010). Performance of recycled asphalt pavement as coarse aggregate in concrete. *Leonardo Electronic Journal of Practices and Technologies*, *17*(9), 47-58.

Ooi, P. S., Archilla, A. R., & Sandefur, K. G. (2004). Resilient modulus models for compacted cohesive soils. *Transportation Research Record*, *1874*(1), 115-124.

Ooi, P. S., Archilla, A. R., Song, Y., & Sagario, M. L. Q. (2010). *Application of Recycled Materials in Highway Projects* (No. HWY-L-2005-04). Hawaii Department of Transportation, Highway Division, Honolulu, HI.

Perkins, S. W., Bowders, J. J., Christopher, B. R., & Berg, R. R. (2005). Geosynthetic reinforcement for pavement systems: US perspectives. In *International Perspectives on Soil Reinforcement Applications* (pp. 1-13). ASCE, Austin, TX.

Poon, C. S., Qiao, X. C., & Chan, D. (2006). The cause and influence of self-cementing properties of fine recycled concrete aggregates on the properties of unbound sub-base. *Waste Management*, *26*(10), 1166-1172.

Rada, G., & Witczak, M. W. (1982). Material layer coefficients of unbound granular materials from resilient modulus. *Transportation Research Record*, *852*, 15-21.

Rahardjo, H., Vilayvong, K., & Leong, E. C. (2010). Water characteristic curves of recycled materials. *Geotechnical Testing Journal*, *34*(1), 89-96.

Read, J. & Whiteoak, D. (2003). *The Shell Bitumen Handbook* (Fifth Edition). Thomas Telford Publishing, London, UK.

Riley, N. A. (1941). Projection sphericity. *Journal of Sedimentary Research*, *11*(2), 94-95.

Roberts, F. L., Kandhal, P. S., Brown, E. R., Lee, D. Y., & Kennedy, T. W. (1996). *Hot Mix Asphalt Materials, Mixture Design, and Construction* (pp. 102-114). NAPA Education Foundation, Lanham, MD.

Rohde, G. T., Smith, R. E., & Scullion, T. (1992). Pavement deflection analysis on sections where the subgrade vary in stiffness with depth. In *7th International Conference on Asphalt Pavements,* Nottingham, UK.

Rosa, M. G., Cetin, B., Edil, T. B., & Benson, C. H. (2016). Development of a test procedure for freeze-thaw durability of geomaterials stabilized with fly ash. *Geotechnical Testing Journal*, *39*(6), 938-953.

Rosa, M. G., Cetin, B., Edil, T. B., & Benson, C. H. (2017). Freeze–thaw performance of fly ash–stabilized materials and recycled pavement materials. *Journal of Materials in Civil Engineering*, *29*(6), 04017015.

Roy, D. M. (1986). Mechanisms of cement paste degradation due to chemical and physical factor. *8th Int. Cong. on the Chemistry of Cement*, *1*, 362-380.

Sadler, R., Delamont, C., White, P., & Connell, D. (1999). Contaminants in soil as a result of leaching from asphalt. *Toxicological & Environmental Chemistry*, *68*(1-2), 71-81.

Saeed, A. (2008). *Performance-Related Tests of Recycled Aggregates for Use in Unbound Pavement Layers* (No. NCHRP Report 598). Transportation Research Board of the National Academies, Washington, DC.

Saeed, A., Hall Jr, J. W., & Barker, W. (2001). *Performance-Related Tests of Aggregates for Use in Unbound Pavement Layers* (No. NCHRP Report 453). Transportation Research Board, National Research Council, Washington, DC.

Sailor, D. J. (1995). Simulated urban climate response to modifications in surface albedo and vegetative cover. *Journal of Applied Meteorology*, *34*(7), 1694-1704.

Santamarina, J. C. & Cho, G. C. (2004). Soil behaviour: The role of particle shape. In *Advances in Geotechnical Engineering: The Skempton Conference* (pp. 604–617). London, UK.

Sayed, S. M., Pulsifer, J. M., & Schmitt, R. C. (1993). Construction and performance of shoulders using UNRAP base. *Journal of Materials in Civil Engineering*, *5*(3), 321-338.

Schaertl, G. J. (2010). Scaling and equivalency of bench-scale tests to field scale conditions (M.S. thesis). University of Wisconsin, Madison, WI.

Schuettpelz, C. C., Fratta, D., & Edil, T. B. (2010). Mechanistic corrections for determining the resilient modulus of base course materials based on elastic wave measurements. *Journal of Geotechnical and Geoenvironmental Engineering*, *136*(8), 1086-1094.

Schwartz, C. W., Li, R., Kim, S., Ceylan, H., & Gopalakrishnan, K. (2011). *Sensitivity Evaluation of MEPDG Performance Prediction* (No. Project 1-47). Transportation Research Board of the National Academies, Washington, DC.

Selvi, P. (2015). Fatigue and rutting strain analysis on lime stabilized subgrades to develop a pavement design chart. *Transportation Geotechnics*, *2*, 86-98.

Shedivy, R. F., Meier, A., Edil, T. B., Tinjum, J. M., & Benson, C. H. (2012). *Leaching Characteristics of Recycled Asphalt Pavement Used as Unbound Road Base* (University of Wisconsin System Solid Waste Research Program-Student Project Report). Madison, WI.

Siekmeier, J., & Casanova, J. (2016). *Geogrid Reinforced Aggregate Base Stiffness for Mechanistic Pavement Design* (No. MN/RC 2016-24). Minnesota Department of Transportation, St. Paul, MN.

Siekmeier, J., Pinta C., Merth S., Jensen J., Davich P., Camargo F., & Beyer M. (2009). *Using the Dynamic Cone Penetrometer and the Lightweight Deflectometer for Construction Quality Assurance* (No. MN/RC 2009-12). Minnesota Department of Transportation, St. Paul, MN.

Skok, E. L., Johnson, E. N., & Brown, M. (2003a). *Special Practices for Design and Construction of Subgrades in Poor, Wet and/or Saturated Soil Conditions* (No. MN/RC-2003-36). Minnesota Department of Transportation, St. Paul, MN.

Skok, E. L., Timm, D. H., Brown, M. L., Clyne, T. R., & Johnson, E. (2003b). *Best Practices for the Design and Construction of Low Volume Roads* (No. MN/RC-2002-17REV). Minnesota Department of Transportation, St. Paul, MN.

Snyder, M. (1995). *Use of Crushed Concrete Products in Minnesota Pavement Foundations* (No. MN/RC-96/12). Minnesota Department of Transportation, St. Paul, MN.

Snyder, M. B., & Bruinsma, J. E. (1996). Review of studies concerning effects of unbound crushed concrete bases on PCC pavement drainage. *Transportation Research Record*, *1519*(1), 51-58.

Snyder, M., Smith, K. D., Vandenbossche, J. M., & Wade, M. J. (1994). *Physical and Mechanical Properties of Recycled PCC Aggregate Concrete* (Interim Report–Task A, DTFH61-93C-00133). US Department of Transportation, Federal Highway Administration, Washington, DC.

Soleimanbeigi, A., & Edil, T. B. (2015). Compressibility of recycled materials for use as highway embankment fill. *Journal of Geotechnical and Geoenvironmental Engineering*, *141*(5), 04015011.

Soleimanbeigi, A., Shedivy, R. F., Tinjum, J. M., & Edil, T. B. (2015). Climatic effect on resilient modulus of recycled unbound aggregates. *Road Materials and Pavement Design*, *16*(4), 836-853.

Sposito, G. (1981). *The Thermodynamics of Soil Solutions*. Oxford University Press, Oxford, UK.

Steffes, R. (1999). *Laboratory Study of the Leachate from Crushed Portland Cement Concrete Base Material* (No. MLR-96-4). Iowa Department of Transportation, Ames, IA.

Stolle, D. F., Guo, P., & Emery, J. J. (2014). Mechanical properties of reclaimed asphalt pavement—natural aggregate blends for granular base. *Canadian Journal of Civil Engineering*, *41*(6), 493-499.

Taha, R., Ali, G., Basma, A., & Al-Turk, O. (1999). Evaluation of reclaimed asphalt pavement aggregate in road bases and subbases. *Transportation Research Record*, *1652*(1), 264-269.

Takada, H., Onda, T., & Ogura, N. (1990). Determination of polycyclic aromatic hydrocarbons in urban street dusts and their source materials by capillary gas chromatography. *Environmental Science & Technology*, *24*(8), 1179-1186.

Tamrakar, P., & Nazarian, S. (2016). *Impact of Gradation and Moisture Content on Stiffness Parameters of Base Materials* (No. CAIT-UTC-054). Center for Advanced Infrastructure and Transportation, Rutgers, The State University of New Jersey, Piscataway, NJ.

Tan, D., Hill, K., & Khazanovich L. (2014). *Quantifying Moisture Effects in DCP and LWD Tests Using Unsaturated Mechanics* (No. MN/RC 2014-13). Minnesota Department of Transportation, St. Paul, MN.

Tanyu, B. F., Benson, C. H., Edil, T. B., & Kim, W. H. (2004). Equivalency of crushed rock and three industrial by-products used for working platforms during pavement construction. *Transportation Research Record*, *1874*(1), 59-69.

Tanyu, B. F., Kim, W. H., Edil, T. B., & Benson, C. H. (2003). Comparison of laboratory resilient modulus with back-calculated elastic moduli from large-scale model experiments and FWD tests on granular materials. In *Resilient Modulus Testing for Pavement Components*. ASTM International, West Conshohocken, PA.

Taylor, H. F. (1997). *Cement Chemistry*. Thomas Telford Publishing, Thomas Telford Services Ltd, Heron Quays, London, UK.

Thakur, J. K., & Han, J. (2015). Recent development of recycled asphalt pavement (RAP) bases treated for roadway applications. *Transportation Infrastructure Geotechnology*, *2*(2), 68-86.

Thompson, M. R., & Smith, K. L. (1990). Repeated triaxial characterization of granular bases. *Transportation Research Record*, *1278*, 7-17.

Titi, H. H., Tabatabai, H., Ramirez, J., & Sooman, M. (2019). *Evaluation of Recycled Base Aggregates* (No. WHRP 0092-17-01). University of Wisconsin-Milwaukee, Milwaukee, WI.

Townsend, T. G., & Brantley, A. (1998). *Leaching Characteristics of Asphalt Road Waste* (No. #98-2). Florida Center for Solid and Hazardous Waste Management, Gainesville, FL.

Tutumluer, E. (2013). *Practices for Unbound Aggregate Pavement Layers: A Synthesis of Highway Practice* (No. NCHRP Synthesis 445). Transportation Research Board of the National Academies, Washington, DC.

Tutumluer, E., Huang, H., & Bian, X. (2012). Geogrid-aggregate interlock mechanism investigated through aggregate imaging-based discrete element modeling approach. *International Journal of Geomechanics*, *12*(4), 391-398.

Uhlmeyer, J. S., Pierce, L. M., Lovejoy, J. S., Gribner, M. R., Mahoney, J. P., & Olson, G. D. (2003). Design and construction of rock cap roadways: Case study in northeast Washington state. *Transportation Research Record*, *1821*(1), 39-46.

USGS (2018). *Mineral Commodity Summaries 2018*. U.S. Department of the Interior, U.S. Geological Survey, Reston, VA.

Vallejo, L. E., Lobo-Guerrero, S., & Hammer, K. (2006). Degradation of a granular base under a flexible pavement: DEM simulation. *International Journal of Geomechanics*, *6*(6), 435-439.

Van Dam, T., Smith, K., Truschke, C., & Vitton, S. (2011). *Using Recycled Concrete in MDOT's Transportation Infrastructure - Manual of Practice* (No. RC-1544). Michigan Department of Transportation, Lansing, MI.

Van Deusen, D., Burnham, T., Dai, S., Geib, J., Hanson, C., Izevbekhai, B., Johnson, E., Palek, L., Siekmeier, J., Vrtis, M., & Worel, B. (2018). *Report on 2017 MnROAD Construction Activities* (No. MN/RC 2018-16). Minnesota Department of Transportation, St. Paul, MN.

van Genuchten, M. T. (1980). A closed-form equation for predicting the hydraulic conductivity of unsaturated soils. *Soil Science Society of America Journal*, *44*(5), 892-898.

Velasquez, R., Hoegh, K., Yut, I., Funk, N., Cochran, G., Marasteanu, M., & Khazanovich, L. (2009). *Implementation of the MEPDG for New and Rehabilitated Pavement Structures for Design of Concrete and Asphalt Pavements in Minnesota* (No. MN/RC 2009-06). Minnesota Department of Transportation, St. Paul, MN.

Vennapusa, P. K. R., White, D. J., Siekmeier, J., & Embacher, R. A. (2012). In situ mechanistic characterisations of granular pavement foundation layers. *International Journal of Pavement Engineering*, *13*(1), 52-67.

Vennapusa, P. K., & White, D. J. (2009). Comparison of light weight deflectometer measurements for pavement foundation materials. *Geotechnical Testing Journal*, *32*(3), 1-13.

Wadell, H. (1932). Volume, shape, and roundness of rock particles. *The Journal of Geology*, *40*(5), 443-451.

Wadell, H. (1933). Sphericity and roundness of rock particles. *The Journal of Geology*, *41*(3), 310-331.

Wadell, H. (1935). Volume, shape, and roundness of quartz particles. *The Journal of Geology*, *43*(3), 250-280.

Wen, H., & Wu, M. (2011). *Evaluation of High Percentage Recycled Asphalt Pavement as Base Materials* (No. TNW2011-15). U.S. Department of Transportation, Northwest Regional Center, Seattle, WA.

Wen, H., Wu, M., & Uhlmeyer, J. (2011). Evaluation of the effects of climatic conditions on modulus of base materials with recycled asphalt pavement. *Journal of ASTM International*, *8*(10), 1-13.

West, R. (2010). *Reclaimed Asphalt Pavement Management: Best Practices*. National Center for Asphalt Technology, Auburn University, Auburn, AL.

Westover, T. M., Labuz, J. F., & Guzina, B. B. (2007). *Resilient Modulus Development of Aggregate Base and Subbase Containing Recycled Bituminous and Concrete for 2002 Design Guide and Mn/Pave Pavement Design* (No. MN/RC-2007-25). Minnesota Department of Transportation, St. Paul, MN.

White, D. J., & Vennapusa, P. (2014). Rapid in situ measurement of hydraulic conductivity for granular pavement foundations. In *Geo-Congress 2014: Geo-characterization and Modeling for Sustainability* (pp. 3005-3014). ASCE, Atlanta, GA.

White, D. J., & Vennapusa, P. (2017). *2017 MnROAD Unbound Layer Evaluation Using Intelligent Compaction: Ingios Validated Intelligent Compaction (VIC) Results* (No. 2017-043). Ingios Geotechnics, Northfield, MN.

White, D. J., Vennapusa, P. K., Becker, P., Rodriguez, J., Zhang, Y., & White, C. (2018). *Central Iowa Expo Pavement Test Sections: Pavement and Foundation Construction Testing and Performance Monitoring* (No. IHRB Project TR-671). Iowa Highway Research Board, Iowa Department of Transportation, Ames, IA, and Federal Highway Administration, U.S. Department of Transportation, Washington, DC.

White, D. J., Vennapusa, P. K., Eichner, D., Gieselman, H., Zhao, L., & Jahren, C. (2010). *Rapid, Self-Contained In-Situ Permeameter for Field QA/QC of Pavement Base/Subbase Materials* (No. NCHRP-130). IDEA Program, Transportation Research Board of the National Academies, Washington, DC.

White, D. J., Vennapusa, P. K., Suleiman, M. T., & Jahren, C. T. (2007). An In-situ Device for Rapid Determination of Permeability for Granular Bases. *Geotechnical Testing Journal*, *30*(4), 282-291.

William, G. W. (1999). Backcalculation of pavement layers moduli using 3D nonlinear explicit finite element analysis (M.S. thesis). West Virginia University Libraries, Morgantown, WV.

WisDOT (2018). *Standard Specifications*. Wisconsin Department of Transportation, Madison, WI.

WisDOT (2019). *Facilities Development Manual (FDM)*. Wisconsin Department of Transportation, Madison, WI.

Wraith, J. M., & Or, D. (1999). Temperature effects on soil bulk dielectric permittivity measured by time domain reflectometry: Experimental evidence and hypothesis development. *Water Resources Research*, *35*(2), 361-369.

Wu, Y., Parker, F., & Kandhal, P. S. (1998). Aggregate toughness/abrasion resistance and durability/soundness tests related to asphalt concrete performance in pavements. *Transportation Research Record*, *1638*(1), 85-93.

Yin, J., Soleimanbeigi, A., Likos, W. J., & Edil, T. B. (2016). Effects of temperature on creep behavior of compacted recycled asphalt pavement. *Journal of Geotechnical and Geoenvironmental Engineering*, *143*(4), 06016028.

Yohannes, B., Hill, K., & Khazanovich, L. (2009). *Mechanistic Modeling of Unbound Granular Materials* (No. MN/RC 2009-21). Minnesota Department of Transportation, St. Paul, MN.

Zeghal, M. (2009). The impact of grain crushing on road performance. *Geotechnical and Geological Engineering*, *27*(4), 549.

Zhang, Y. (2016). Assessing seasonal performance, stiffness, and support conditions of pavement foundations (Doctoral dissertation). Iowa State University, Ames, IA.

Zhao, L. (2011). In situ assessment of support and drainage for PCC subbase (M.S. thesis). Iowa State University, Ames, IA.

Zheng, J., & Hryciw, R. D. (2014). Soil particle size characterization by stereophotography. In *Geo-Congress 2014: Geo-characterization and Modeling for Sustainability* (pp. 64-73).

Zheng, J., & Hryciw, R. D. (2015). Traditional soil particle sphericity, roundness and surface roughness by computational geometry. *Géotechnique*, *65*(6), 494-506.

Zheng, J., & Hryciw, R. D. (2016). Segmentation of contacting soil particles in images by modified watershed analysis. *Computers and Geotechnics*, *73*, 142-152.

Zheng, J., & Hryciw, R. D. (2017). Soil particle size and shape distributions by stereophotography and image analysis. *Geotechnical Testing Journal*, *40*(2), 317-328.

Zornberg, J. G. (2012). Geosynthetic-reinforced pavement systems. In *5th European Geosynthetics Congress*, Valencia, Spain.

Zornberg, J. G. (2017). Functions and applications of geosynthetics in roadways. *Procedia Engineering*, *189*, 298-306.